General Disclaimer

One or more of the Following Statements may affect this Document

- This document has been reproduced from the best copy furnished by the organizational source. It is being released in the interest of making available as much information as possible.

- This document may contain data, which exceeds the sheet parameters. It was furnished in this condition by the organizational source and is the best copy available.

- This document may contain tone-on-tone or color graphs, charts and/or pictures, which have been reproduced in black and white.

- This document is paginated as submitted by the original source.

- Portions of this document are not fully legible due to the historical nature of some of the material. However, it is the best reproduction available from the original submission.

Produced by the NASA Center for Aerospace Information (CASI)

NATIONAL AERONAUTICS AND SPACE ADMINISTRATION

1129

EARTH RESOURCES AIRCRAFT PROGRAM

STATUS REVIEW

VOLUME I

GEOLOGY, GEOGRAPHY, AND SENSOR STUDIES

Presented at the

NASA Manned Spacecraft Center
Houston, Texas

September 16 to 18, 1968

N71-16126
(ACCESSION NUMBER)
571
(PAGES)
TMX62564
(NASA CR OR TMX OR AD NUMBER)
FACILITY FORM 602
N71-16146
(CODE)
13
(CATEGORY)
JAN 1970
RECEIVED

MANNED SPACECRAFT CENTER
HOUSTON, TEXAS

VOLUME I

GEOGRAPHY AND GEOLOGY

SECTION I

INTRODUCTION

On September 16, 17, and 18, a review of various aspects of the Earth Resources Program was held at the Manned Spacecraft Center, Houston, Texas. Particular emphasis was placed on the results of analysis of data obtained with the Manned Spacecraft Center and other aircraft which have contributed data to the program.

The review was arranged in conjunction with the Department of Interior, Department of Agriculture and the Department of the Navy. Attendees and participants at the meeting included program investigators, their immediate associates, and program representatives from the above named agencies and ESSA and NASA.

The review was divided into the disciplinary areas of Geology, Geography, Hydrology, Agriculture and Forestry, and Oceanography. An additional session was held on instrumentation. Program investigators presented the results of their work in each of these areas. The material presented is being published in three volumes:

Vol I — GEOLOGY, GEOGRAPHY, AND SENSOR STUDIES

Vol II — AGRICULTURE, FORESTRY, AND SENSOR STUDIES

Vol III — HYDROLOGY, OCEANOGRAPHY, AND SENSOR STUDIES

It should be noted that the instrumentation section is repeated in all three volumes as much of this material is of interest to more than one discipline.

The review provided a current assessment of the program for both management and technical personnel. It is important to note that the material presented represented the current status on ongoing programs and consequently complete technical analyses will be available at a later date.

PRECEDING PAGE BLANK NOT FILMED.

CONTENTS

Section		Page
1	INTRODUCTION	1-1
2	SUMMARY OF AIRCRAFT MISSIONS	2-1
3	MISSION 73 AND ASSOCIATED TESTS . . . . . By Robert H. Alexander	3-1
4	SOUTHERN CALIFORNIA REGIONAL RESOURCES STUDIES . . . . . By Leonard W. Bowden	4-1
5	LAND USE AND REGIONAL ANALYSIS . . . . . By Robert W. Peplies	5-1
6	REMOTE SENSING OF FIRE PHENOMENA IN TROPICAL GRASSLANDS: THE FLORIDA TEST SITES, 1967-68 . . . . . By Merle C. Prunty	6-1
7	REMOTE SENSING AND THE STUDY AND PLANNING OF URBAN AREAS . . . . . By Duane F. Marble and Frank E. Norton	7-1
8	THEMATIC LAND-USE MAPPING WITH SPACECRAFT PHOTOGRAPHY AND RADAR . . . . . By David S. Simonett	8-1
9	INSTRUMENTATION OF IMAGE ANALYSIS AND TELEVISION SIMULATION TECHNIQUES . . . . . By James P. Latham	9-1
10	INFRARED SURVEY OF THE PISGAH CRATER AREA, SAN BERNARDINO COUNTY, CALIFORNIA: A GEOLOGIC INTERPRETATION . . . . By Stephen J. Gawarecki	10-1

Section		Page
11	THERMAL ANOMALIES AND GEOLOGIC FEATURES OF THE MONO LAKE AREA, CALIFORNIA, AS REVEALED BY INFRARED IMAGERY	11-1
	By Jules D. Friedman	
12	GEOLOGIC EVALUATION OF THERMAL INFRARED IMAGERY, CALIENTE AND TEMBLOR RANGES, SOUTHERN CALIFORNIA	12-1
	By Edward W. Wolfe	
13	RADAR AND INFRARED IN GEOLOGICAL STUDIES OF NORTHERN ARIZONA	13-1
	By Gerald G. Schaber	
14	PLUSES AND MINUSES OF RADAR IN GEOLOGICAL EXPLORATION	14-1
	By L. F. Dellwig	
15	PROGRAM STATEMENT FOR REGIONAL GEOLOGIC STUDIES IN REMOTE SENSING, YELLOWSTONE NATIONAL PARK	15-1
	By Harry W. Smedes	
16	GEOTHERMAL INFRARED ANOMALIES OF LOW INTENSITY, YELLOWSTONE NATIONAL PARK	16-1
	By Donald E. White and Lee D. Miller	
17A	RADAR AND INFRARED IMAGERY, OREGON AND WASHINGTON COASTS	17A-1
	By Norman S. MacLeod and Parke D. Snavely, Jr.	
17B	PROGRESS IN APPLICATION OF REMOTE-SENSING TECHNIQUES TO MARINE GEOLOGY AND HYDROLOGY	17B-1
	By Ernest H. Lathram	
18	AIRBORNE MULTIFREQUENCY MICROWAVE RADIOMETRIC SENSING OF AN EXPOSED VOLCANIC PROVINCE	18-1
	By John C. Blinn III, Peter Chapman, and Jack Quade	

Section		Page
19	APPLICATION OF ULTRAVIOLET REFLECTANCE AND STIMULATED LUMINESCENCE TO THE REMOTE DETECTION OF NATURAL MATERIALS	19-1
	By William R. Hemphill	
50	RADAR PROGRESS IN THE NASA EARTH RESOURCES AIRCRAFT PROGRAM	50-1
	By R. K. Moore	
51	INFRARED STUDIES	51-1
	By D. S. Lowe	

TABLES

Table		Page
4-I	DATA RECEIVED FROM EARTH RESOURCES AIRCRAFT PROGRAM AT TEST SITE 130	4-2
5A-I	USE OF REMOTE-SENSING DATA	5A-3
5B-I	ASHEVILLE BASIN GROUND-TRUTH DATA COLLECTED DURING OVERFLIGHT	5B-1
8-I	SUMMARY OF DATA COLLECTED AND OF WORK AT LAWRENCE, KANSAS, TEST SITE 85	8-13
8-II	SUMMARY OF DATA OBTAINED AND USED FROM MSC MISSIONS ALONG THE OREGON COAST (TEST SITE 7)	8-14
10-I	MODAL ANALYSIS OF SUNSHINE AND PISGAH BASALTS	10-27
11-I	TIME RATE OF CHANGE OF IMAGE TONAL DENSITY DURING DIURNAL CYCLE, MONO CRATERS AREA, JULY 27 AND 28, 1966	11-23
11-II	INFRARED FLIGHT LOG DATA, MONO CRATERS AREA, JULY 27 AND 28, 1966	11-24
11-III	INTEGRATED 8μ TO 14μ EMISSIVITIES OF ROCKS FROM MONO CRATERS AREA	11-26
11-IV	RELATIONSHIP BETWEEN AMPLITUDE OF DIURNAL SURFACE-TEMPERATURE-CURVES AND THERMAL PARAMETERS FOR SELECTED LITHOLOGIES OF THE MONO LAKE AREA, JULY 27 AND 28, 1966	11-31
12-I	AIR AND GROUND TEMPERATURES MEASURED ALONG SAN ANDREAS FAULT EAST OF SODA LAKE, 4:30 a.m. OCTOBER 25, 1967	12-13
15-I	SUMMARY OF MISSIONS AND SENSORS	15-4
18-I	SUMMARY OF CHEMICAL ANALYSES IN PERCENTAGE	18-17
18-II	NEUTRON GAMMA-GAMMA PROBE DATA FROM ALTERED CINDER	18-18

Table		Page
18-III	AVERAGE TEMPERATURE MEASUREMENTS FOR DAY AND NIGHT FLIGHTS	18-19
18-IV	BEAM POSITION OFFSETS CAUSED BY DRIFT, FLIGHT 5	18-19
18-V	MAGNITUDE AND PEAK DEVIATIONS OF AIRCRAFT ROLL, PITCH, AND YAW RATES AND ALTITUDE	18-20
18-VI	RADIOMETER CALIBRATIONS	18-21
18-VII	ANTENNA TEMPERATURES OF SELECTED POINTS IN DEGREES KELVIN	18-22
18A-I	RADIOMETER RESOLUTION ELEMENTS FOR MISSION 55	18A-7
18A-II	THE ΔT's FOR MR-62 AND MR-64 RADIOMETERS	18A-7
18B-I	RADIOMETER POLARIZATIONS CORRESPONDING TO E- AND H-PLANES	18B-3
51-I	SCANNER-SPECTROGRAPH SPECIFICATIONS	51-4

FIGURES

Figure		Page
3-1	Location of mission 73 geographic experiments	3-10
3-2	Sensors and applications in mission 73	3-11
3-3	Agricultural land use, Imperial Valley	3-12
3-4	Ground photograph of month-old cotton, taken in Imperial Valley	3-13
3-5	Ground photograph of mature alfalfa, showing 100-percent ground cover	3-14
3-6	Agricultural land use in the Imperial Valley. Black and white print of color infrared photograph taken from 20 000 ft, 12-in. camera	3-15
3-7	Sugar beet harvesting operation, Imperial Valley . . .	3-16
3-8	Comparison of ultraviolet imagery from the AAS-5 scanner with thermal infrared imagery from the Reconofax IV scanner	
	a. Ultraviolet, AN/AAS-5 sensor, flown May 21, 1968	3-17
	b. Thermal IR, Reconofax IV sensor, flown May 21, 1968	3-17
3-9	Passive microwave imagery of Mexican-American border area, Imperial Valley	3-18
3-10	Portion of the Willowbrook district of Los Angeles, illustrating improving residential environmental conditions with increasing distance from railroad and junkyard	3-19
3-11	Obtaining ground truth for urban housing quality and environmental health studies	3-20
3-12	Urban field team obtaining ground-truth observations for Los Angeles area flight line in Santa Monica	3-21
3-13	Aerial view of smog over Los Angeles	3-22

Figure		Page
3-14	Plots of sulfur dioxide (concentration times path length) measurements obtained with Barringer absorption spectroscope	3-23
3-15	Multispectral photographs of calibrated color panels	
	a. Y-2 filter, f/8 at 1/250 (Plus X-1120)	3-24
	b. 25A filter, f/4 at 1/250 (Plus X-1125)	3-24
	c. 47 filter, f/5 at 1/250 (Plus X-1125)	3-25
	d. 58 filter, f/4 at 1/250 (Plus X-1127)	3-25
3-16	Passive microwave image of Salton Sea	
	a. Smooth sea	3-26
	b. Rough sea	3-26
3-17	Three playbacks of same passive microwave image of Salton Sea	3-27
3-18	Ground measurements of passive microwave temperature versus viewing angle, Coachella Valley	3-28
3-19	Cotton being irrigated, Imperial Valley	3-29
3-20	Fields under irrigation, showing advantage of thermal infrared image over panchromatic photograph for identification of moist area	
	a. Reconofax IV sensor, 8μ to 14μ	3-30
	b. RC-8 camera sensor, panchromatic film	3-31
3-21	Results of use in mission 73 (preliminary)	3-32
3-22	Recommendations for future research (mission 73 sensors)	3-33
4-1	Indio Area, Coachella Valley; Aero Ektachrome IR 8443 obtained on mission 42, NASA aircraft 927, March 1968; scale 1:78 000	4-14
4-2	Land-use map of Indio area	4-15

Figure		Page
4-3	A reduced image of west Los Angeles acquired on mission 42. The two maps were constructed entirely from the imagery	
	a. IR Imagery of west Los Angeles	4-16
	b. Maps constructed from IR imagery	4-17
4-4	Views of Century City Plaza	
	a. A black and white print made from the same transparencies roll as the copy in figure 4-3. The arrow points to the Century City Plaza photograph. The original roll is scale 1:60 000, imaged from 30 000 feet	4-18
	b. Century City Plaza as imaged by the automatic lock-on tracking system from 40 000 feet; scale 1:1500	4-19
4-5	Imagery from mission 22, test site 27	
	a. Black and white print of Alamo River Delta area taken on mission 22 (test site 27), scale 1:20 000 on original; outlines are index frames of images taken by the automatic lock-on tracking system	4-20
	b. Automatic lock-on tracking system 70-millimeter frame of the area shown in the upper outline in figure 4-5a. This print is a copy made from the original Anscochrome transparency	4-21
4-6	Salton Sea area	
	a. Photographed from Gemini V. Note the road, railroad, and vegetation pattern on the east (far) shore at the base of the Chocolate Mountains	4-22
	b. Aero Ektachrome IR 8443 taken on 35-mm film with 15 plus 80B filter during mission 73	4-23
4-7	Imagery from missions 73 and 102	
	a. Renconofax IV 8μ to 14μ image of the same area as shown in figures 4-6b and 4-7b taken at 23:00 hours on mission 73	4-24
	b. AN/APQ-97 side-looking radar of the east shore of the Salton Sea (Westinghouse mission 102) . . .	4-25

Figure		Page
4-8	The effects of various additive enhancement filters on type 8443 film, the results of a filter experiment conducted at the test site	
	a. A normal color view across the eastern end of the Los Angeles Basin on a moderately clear day	4-26
	b. The effect when only minus-blue (Wratten 15) filtration is used	4-26
	c. The effect when a CC30B additive enhancing filter is used. Mild IR reflection shows on the distant mountains	4-27
	d. The effect when an 80B is used as the additive filter. The conifer forests on the distant mountains are now yielding a strong IR record . . .	4-27
4-9	Color IR imagery of Canadian River of Oklahoma and Pomona-Claremont area of Southern California	
	a. In this view of the Canadian River of Oklahoma, taken with color IR film from an altitude of 40 000 feet, the false color blushes of newly sprouted winter wheat give a strong IR record . . .	4-28
	b. Pomona-Claremont area of Southern California taken on 35-mm color IR film at 17 000 feet with additive 80B filter through airliner window in late December	4-29
5-1	Flight line across the general "grain" of different geographical features which are typical of the Southern Appalachians	5-12
5-2	Radar imagery of a number of relatively distinct regions in the Asheville Basin, western North Carolina	5-13
5-3	Stereogram of linear features in the Asheville Basin	5-14
5-4	Black and white photograph of color infrared photograph showing road markings at road intersections	5-15
5-5	Traffic flow directions plotted on standard series topographic map, 1:29 280	5-16

Figure		Page
6-1	Location of test sites	6-10
6-2	Distribution of vegetation types, Pipeline Road	6-11
6-3	Distribution and age of burns, Pipeline Road	6-12
7-1	A framework for the collection and processing of urban data using remote sensor imagery	7-8
7-2	The planning process	7-9
8-1	Multiple-polarization identification of farm buildings on radar images	8-15
8-2	K-band radar image and transportation network of Lawrence, Kansas, in September 1965	8-16
8-3	Land-use map of Lawrence, Kansas	
	a. Urban land use as determined from the radar image	8-17
	b. These six land-use regions had been improperly interpreted from radar	8-17
8-4	K-band radar image of a portion of Woods County, Oklahoma	8-18
8-5	Soil associations normally distinguishable on K-band imagery, Woods County, Oklahoma	8-19
8-6	Soil associations which cannot be separated on K-band imagery, Woods County, Oklahoma	8-20
9-1	Test site 164 located at Boca Raton to Belle Glade is in central area of this image taken by Gemini mission	9-8
9-2	Coastal flight path from northern Boca Raton to Palm Beach, Florida, as printed from color IR transparency	9-9
9-3	Hillsboro canal and flood control dam along flight path over underdeveloped terrain between Boca Raton and Belle Glade, Florida	9-10

Figure		Page
9-4	Test site 164 located on West Palm Beach map sheet, with interior Belle Glade and coastal Boca Raton indicated	9-11
9-5	Sugar cane, cattle grazing, and settlement patterns recorded originally by color IR in Belle Glade Field Survey Site of test site 164	9-12
9-6	Belle Glade Field Survey Site with some field annotations indicated	9-13
9-7	Monitor and waveform analyzer equipment utilized for image control and for sampling image density or gray-tone percentage values used in land-use categorization	9-14
9-8	Selected land-use categories as cataloged for computer identification experiment	9-15
9-9	Sampled percentage values in matrix form for computer processing and values calculated for identification of each category	9-16
9-10	Land-use types selected as "unknowns" for computer identification and schematic illustrations of relation to terrain features and matrix matching process	9-17
9-11	Flow chart for computer processing to identify unknowns	9-18
9-12	Equipment system for simulating a television observation from space altitudes	9-19
9-13	Monitors and waveform analyzers used to control and display image	9-20
9-14	East-central Florida transportation patterns, reference scale of 1:1 000 000	9-21
9-15	East-central Florida transportation patterns, reference scale of 1:500 000	9-22
9-16	East-central Florida transportation patterns, reference scale of 1:250 000	9-23

Figure		Page
9-17	East-central Florida transportation patterns, reference scale of 1:131 250	9-24
9-18	East-central Florida transportation patterns, reference scale of 1:131 250	9-25
9-19	East-central Florida land-use patterns, reference scale of 1:1 000 000	9-26
9-20	East-central Florida land-use patterns, reference scale of 1:500 000	9-27
9-21	East-central Florida land-use patterns, reference scale of 1:250 000	9-28
9-22	East-central Florida land-use patterns, reference scale of 1:141 250	9-29
10-1	Index map showing location of Pisgah Crater area	10-28
10-2	Index Map of Pisgah Crater area, San Bernardino County, California	10-29
10-3	Geologic Map of Pisgah Crater area, San Bernardino County, California	10-30
10-4	Sunshine lava field viewed from Lavic Dry Lake . . .	10-31
10-5	Pisgah fault scarp with tumulus development	10-31
10-6	Typical pahoehoe surface of first Pisgah basalt flow (Qb_1) at station 66-2 near Lavic Dry Lake Lake	10-32
10-7	Fissured aa dome in first Pisgah flow (Qb_1)	10-32
10-8	Typical aa surface of second Pisgah basalt flow (Qb_2) at station 66-3 near Lavic Dry Lake	10-33
10-9	View of collapsed lava tubes in pahoehoe basalt of third Pisgah flow (Qb_3)	10-33
10-10	Interior view of Pisgah Cone	10-34
10-11	Road cut in slope of Pisgah Cone showing surface and buried silty horizons	10-34

Figures		Page
10-12	Typical moisture stripe boundary of giant desiccation polygon in Lavic Lake near center, section 27 . . .	10-35
10-13	Desiccation cracks in Lavic playa next to Pisgah flow at station 66-2	10-35
10-14	Infrared images along flight line 1, showing changes in thermal response of rock materials throughout a diurnal cycle	10-36
10-15	Infrared images along flight line 2, showing changes in thermal response of rock materials throughout a diurnal cycle	10-37
10-16	Infrared images along flight line 3, showing changes in thermal response of rock materials throughout a diurnal cycle	10-38
11-1	Flight lines, IR imagery surveys, July 27 and 28, 1966, Mono Craters area, California	11-33
11-2	Incident radiant solar flux and surface temperature, Mono Instrument Stations, Mono Lake area, July 27 and 28, 1966	
	a. Incident radiant solar flux	11-34
	b. Surface temperature	11-35
11-3	Surface radiant temperatures, Aeolian Buttes, Mono Lake area, July 27 and 28, 1966	11-36
11-4	Surface and near-surface temperatures determined by thermistor probe, Mono South Beach station, July 27 and 28, 1966	11-37
11-5	Change in temperature with depth, east pumice sand flat, Mono Lake area, July 27 and 28, 1966. (Instrument station 3, variable sequencer G258931.)	11-38
11-6	Surface temperature of Mono Lake, South Beach area, 120 feet out in 3-foot depth at 6 inches below surface (tempscribe), July 27 and 28, 1966	11-39

Figure — Page

11-7 Infrared imagery within the 8μ- to 14μ-wavelength region, July 27 and 28, 1966, Black Point, California

a. 07:25 hours 11-40
b. 11:57 hours 11-40
c. 16:31 hours 11-41
d. 20:29 hours 11-41
e. 23:59 hours 11-42
f. 04:00 hours 11-42

11-8 Infrared imagery within the 8μ- to 14μ-wavelength region, Paoha Island, Mono Lake, California, July 27 and 28, 1966

a. 08:11 hours 11-43
b. 12:07 hours 11-43
c. 16:12 hours 11-44
d. 20:10 hours 11-44
e. 00:07 hours 11-45
f. 04:07 hours 11-45

11-9 Infrared imagery of Aeolian Buttes, 3 miles west of Mono Craters complex, California, 8μ- to 14μ-wavelength region, July 27 and 28, 1966

a. 07:58 hours 11-46
b. 12:04 hours 11-46
c. 16:03 hours 11-47
d. 20:29 hours 11-47
e. 23:59 hours 11-48
f. 04:00 hours 11-48

11-10 Infrared imagery within the 8μ- to 14μ-wavelength region, July 27 and 28, 1966, North Coulee, Mono Craters rhyolite-obsidian complex

a. 08:11 hours 11-49
b. 12:07 hours 11-49
c. 16:41 hours 11-50
d. 20:38 hours 11-50
e. 00:33 hours 11-51
f. 04:07 hours 11-51

Figure		Page
11-11	Infrared imagery of the main rhyolite-obsidian complex at Mono Craters within the 8μ- to 14μ-wavelength region, 08:00 hours, June 4, 1965	11-52
11-12	Isodensity scan used in correlating surface temperatures with the image emulsion density scale (figs. 11-24 and 11-25). IR imagery, Wilson Creek delta, Black Point, Mono Lake, 07:50 hours, July 27, 1966	11-53
11-13	Isodensity scan used in correlating surface temperatures with image emulsion density scale (figs. 11-24 and 11-25). IR imagery, Wilson Creek, Black Point, Mono Lake, 12:33 hours, July 27, 1966	11-54
11-14	Isodensity scan used in correlating surface temperatures with image emulsion density scale (figs. 11-24 and 11-25). IR imagery, Wilson Creek, Black Point, Mono Lake, 16:31 hours, July 27, 1966	11-55
11-15	Isodensity scan used in correlation of surface temperatures with image emulsion density (figs. 11-24 and 11-25). IR imagery, Wilson Creek delta, Black Point, Mono Lake, 20:00 hours, July 27, 1966	11-56
11-16	Isodensity scan used in correlation of surface temperatures with the image emulsion density (figs. 11-24 and 11-25). IR imagery, Wilson Creek delta, Black Point, Mono Lake, 04:04 hours, July 28, 1966	11-57
11-17	Isodensity scan used in correlating surface temperatures and the image emulsion density scale (figs. 11-24 and 11-25). IR imagery of Wilson Creek delta, Black Point, Mono Lake, 04:00 hours, July 28, 1966	11-58
11-18	Isodensity scan of IR imagery, 23:59 hours, July 27, 1966, effluent from a hot spring near Deschambeau Ranch, Black Point, California	11-59

Figure		Page
11-19	Isodensity scan of IR imagery, northeastern Paoha Island, Mono Lake, 20:10, July 27, 1966	11-60
11-20	Isodensity scan of post-sunset IR imagery, northeastern Paoha Island, Mono Lake, 20:38, July 27, 1966	11-61
11-21	Isodensity scan, northeastern Paoha Island, Mono Lake, showing virtual disappearance of radiant-temperature distinctions between most lithologic units, July 28, 1966	11-62
11-22	Isodensity scan of IR imagery showing area of thermal anomalies, eastern Paoha Island, Mono Lake, 20:10, July 27, 1966	11-63
11-23	Isodensity scan of IR imagery showing area of thermal anomalies in detail, eastern Paoha Island, Mono Lake, 20:38, July 27, 1966	11-64
11-24	Infrared image density in relation to surface temperature, Black Point, Mono Lake, California, July 27 and 28, 1966	11-65
11-25	Change in relative film density with time during a diurnal cycle for three lithologies and water	11-66
11-26	Change in apparent emissivity ε_c as a function of cavity shape and integrated emissivity $\varepsilon_{\lambda,8\mu-14\mu}$ of cavity wall (ref. 11-6)	11-67
11-27	Graph of $f(\lambda,\delta,\omega,\tau)$ for a diurnal cycle at the summer solstice, autumnal equinox, and July 27 and 28, 1966, for latitude 38° N	11-68
11-28	Theoretical diurnal surface temperature variations for lacustrine carbonate deposits (QM) of Black Point and for olivine basalt lapilli-ash (Qvb) of Black Point, July 27 and 28, 1966	11-69
11-29	Theoretical variation in surface temperatures of upper unit of Bishop tuff (Qbt) and quartz monzonite (Ka) of Aeolian Buttes, July 27 and 28, 1966	11-70

Figure		Page
11-30	Recorded variations in apparent surface temperature with time during a period of IR survey, Black Point, California, for two lithologies, July 27 and 28, 1966	11-71
11-31	Recorded variations in blackbody-equivalent surface temperature with time during period of IR survey, Aeolian Buttes, California, July 27 and 28, 1966	11-72
11-32	Aerial photograph of Paoha Island showing areas scanned by isodensitracer technique. Arrows on east side indicate points of thermal emission	11-73
11-33	Photographs of thermal-spring deposits, recent andesite basalt volcanics, structural deformation of wavecut bench, and the water morphology of Paoha and Negit Islands	
	a. Thermal spring and fumarolic deposits forming a southward-jutting peninsula along the probable extension of a fracture zone, eastern Paoha Island	11-74
	b. Recent andesite-basalt volcanics (QpvA) cut by fracture zones containing epithermal or thermal-spring deposits. Hot springs are concentrated along the lakeward extension of fracture zones	11-74
	c. Structural deformation of lacustrine deposits (Qm) of wavecut bench, western Paoha Island	11-75
	d. Northern Paoha and Negit Islands (view west) . . .	11-75
11-34	Subsided Santorin (Thíra) caldera in the Cyclades archipelago, Aegean Sea	11-76
12-1	Index map showing major physiographic features and approximate locations of areas described and illustrated in this report	12-16
12-2	Generalized geologic map of study area	12-17

Figure		Page
12-3	Predawn IR image	
	a. Caliente Range and Carrizo Plain	12-18
	b. Carrizo Plain, Elkhorn Plain, and Temblor Range	12-19
	c. Temblor Range	12-20
12-4	Postsunrise IR image	
	a. Caliente Range and Carrizo Plain	12-21
	b. Carrizo Plain, Elkhorn Plain, and Temblor Range	12-22
	c. Temblor Range	12-23
12-5	Small-scale aerial photograph of Temblor Range southwest of Fellows	12-24
12-6	Radiation temperatures measured by Barnes IT-3 radiometer at locality 13, Temblor Range, May 22 to 24, 1967	12-25
12-7	Predawn IR image of part of Carrizo Plain east of Soda Lake	12-26
12-8	Predawn IR image near the southeast end of Carrizo Plain	12-27
13-1	Location map showing geologic test sites 101, 28, 71, and Grand Canyon, Arizona	13-13
13-2	Location map of San Francisco Volcanic Field showing radar and IR scanner coverage	13-14
13-3	Flight 103 run 16; north-northeast from the San Francisco Peaks	
	a. Plane polarized (HH) image	13-15
	b. Depolarized (HV) image	13-15
13-4	Flight 103 run 15; east-west flight over Flagstaff, Arizona	
	a. Plane-polarized (HH) image	13-16
	b. Depolarized (HV) image	13-16

Figure		Page
13-5	Flight 103 run 7; east-west flight north of the San Francisco Peaks	
	a. Plane-polarized (HH) image	13-17
	b. Depolarized (HV) image	13-17
13-6	Enlargement of figure 13-5	
	a. Enlarged portion of figure 13-5a showing Kana-a basalt flow emanating from Sunset Crater. Plane-polarized (HH) image	13-18
	b. Enlarged portion of figure 13-5b showing Kana-a basalt flow emanating from Sunset Crater. Depolarized (HV) image	13-19
13-7	Enlargement of figure 13-2	
	a. Enlarged portion of low-altitude Reconofax IV run over an area of the San Francisco Volcanic Field northeast of Flagstaff, Arizona	13-20
	b. Enlarged portion of low-altitude Reconofax IV run covering the same general region shown in figure 13-7a	13-21
13-8	Aerial photograph taken simultaneously with IR scan image shown in figure 13-7	
	a. Area A indicates the presence of the prehistoric Indian agricultural plots	13-22
	b. Area A indicates the presence of prehistoric Indian agricultural plots; area B indicates the site of Indian ruins	13-23
13-9	Radar image run 8	
	a. Plane-polarized (HH) image of Meteor Crater and vicinity, Arizona	13-24
	b. Cross-polarized (HV) image of Meteor Crater and vicinity, Arizona	13-24
13-10	Radar image enlargement from flight 103 run 14	13-25
13-11	Geologic map showing correlation between geology and radar image	13-26

Figure		Page
13-12	Side-looking radar image of Grand Canyon, Arizona . . .	13-27
13-13	Radar image of the Grand Canyon	
	a. Comparison of mapped, inferred lineaments with actual plotted faults	13-28
	b. Comparison of mapped, inferred lineaments as transferred from ref. 13-11	13-28
13-14	Radar image of Hopi Buttes, Arizona; flight 103 run 12	13-29
14-1	Darien Province, Republic of Panama, and Northwest Colombia	14-8
14-2	Radar imagery (AN/APQ-69) in the vicinity of Ozark, Arkansas	14-9
14-3	Boston Mountains-Arkansas River Valley, Franklin and Johnson Counties, Arkansas	14-10
14-4	Radar lineament zone on south flank of Ozark Dome, Arkansas	14-11
14-5	Wasatch Range	14-12
14-6	Postulated ancestral drainage and present drainage, Wasatch Range	14-13
14-7	Comparison of radar imagery and aerial photography, Cane Springs Area, Arizona	14-14
14-8	South Fork Cottonwood River, Plymouth to Matfield Green, Chase County, Kansas	14-15
14-9	Pisgah Crater, California	14-16
14-10	Major drainage pattern in a portion of the test site	14-17
17A-1	Comparison between photographically enlarged radar imagery (above) and conventional photography (below) in the Tenmile Creek area of coastal Oregon	17A-5

Figure		Page
17A-2	Radar image of area near Lincoln City, Oregon. Northeast trend of lineation is caused by large fault	17A-6
17A-3	Radar image of area near Seaside, Oregon, showing arcuate feature (arrows in center of image). Miocene gabbroic intrusive underlies curved ridge on northern part of arc; physiographic expression in southern part of arc is a manifestation of a fault	17A-7
17A-4	Infrared image of the Taholah, Washington, area showing thermal plume developed off the mouth of the Quinault River	17A-8
18-1	Index map of Mount Lassen Test Site	18-23
18-2	Aerial view of test site area	18-23
18-3	Geologic map of test site area	18-24
18-4	Sample location map showing sampling points for preflight studies	18-25
18-5	Major chemical variations along flight line 2	18-26
18-6	Particle-size variations along flight line 2	18-27
18-7	Cinder grain-size distribution and comparisons with radiometer wavelengths	18-28
18-8	Locations of overflight stations	18-29
18-9	Diurnal heating-cooling curves for basalt cinder	18-30
18-10	Aircraft flight path and radiometer response over cinder cone, flight 5	18-30
18-11	Aircraft flight path, day flight	18-31
18-12	Recorder deviation from linearity, 9.3-gigahertz channel	18-32
18-13	Recorder calibrations, mission 55, flight 5, 9.3 gigahertz channel	18-33

Figure		Page
18-14	Recorder calibrations, mission 55, flight 6, 9.3-gigahertz channel	18-34
18-15	Response of 34.0-gigahertz channel over flight line 1	18-35
18-16	Thermal IR imagery (8μ to 14μ)	18-36
18-17	Radiometer responses over water, lava, and cinder, flight 6, diagrammatic representation	18-37
18-18	Radiometer responses over water, lava, and cinder, flight 5, diagrammatic representation	18-37
18-19	Radiometer responses, cinder over lava, flight 6 at night (base line on 9.3 gigahertz adjusted by +90° K)	18-38
18-20	Radiometer responses over cinder cone, base lines adjusted	18-38
18-21	Temperature differences between vertically and horizontally polarized data	18-39
18A-1	Radiometric temperature of sea water (ref. 18-2)	18A-8
18A-2	Radiometric temperatures of limestone and sand (ref. 18-2)	18A-8
18B-1	System diagram of the Convair 240A aircraft microwave radiometer	18B-4
18B-2	Aircraft strip-chart recording	18B-5
18B-3	Steps in conversion of raw flight data to calibrated data	18B-6
18B-4	Computer plot of radiometer data	18B-7
18B-5	Computer print-out of radiometer data	18B-8
19-1	Curves showing ultraviolet and visible spectral reflectance of some common rocks	19-14
19-2	Curves showing transmission of specific ultraviolet and visible filters and the quantum efficiency of the S-13 photocathode	19-14

Figure		Page
19-3	Multiband imagery acquired with the University of Michigan's 18-channel scanner over Paoha Island, Mono Lake, California	19-15
19-4	Computer print-out of part of Paoha Island, Mono Lake, California, showing bedrock and surficial materials symbolized by letter. (Prepared in cooperation with the Department of Agriculture and Purdue University.)	19-16
19-5	Diagram showing operational components of an active ultraviolet imaging system	19-17
19-6	Photograph showing ultraviolet imaging system set up in laboratory. Transmitter, A; receiver, B; oscilloscope, C; and video monitor, D	19-17
19-7	Video monitor image indicating luminescence of dewey-lite in a quarry near Baltimore. Distance from the transmitter to the quarry face is 64 feet	19-18
19-8	Conventional photograph of same area shown in figure 19-7	19-18
19-9	Ultraviolet laser. (Courtesy of the Avco-Everett Research Laboratory.)	19-19
19-10	Diagram showing position of laser, sample, and photomultiplier detector for measurement of luminescent decay time	19-19
19-11	Oscilloscope traces for a suite of five feldspars . . .	19-20
19-12	Diagrams illustrating the Fraunhofer line-depth method	19-20
19-13	Schematic showing design of the optical unit of the line-discriminator prototype. (Courtesy of the Perkin-Elmer Corp.)	19-21
19-14	Prototype line discriminator showing the optical unit and the control console. (Courtesy of the Perkin-Elmer Corp.)	
	a. Optical unit	19-21
	b. Control console	19-22

Figure		Page
19-15	Excitation and emission spectra of Rhodamine dye. (After spectrofluorometric analyses furnished by G. K. Turner Associates, Palo Alto, California.)	19-22
50-1	Curves of radar differential scattering coefficient versus angle of incidence compared with photograph showing regions from which the data were obtained using the 13.3-gigahertz scatterometer	50-24
50-2	Curves of difference between radar differential scattering coefficient and values for a mean curve compared with photograph of Pisgah Crater area from which the data were obtained by the 13.3-gigahertz scatterometer	50-25
50-3	Color codes for the information obtained by scatterometer from the Pisgah Crater area, compared with a photograph of the area	50-26
50-4	Curves of radar differential scattering coefficient versus angle of incidence compared with a line map of the Garden City Test Site area from which the data were obtained with the 13.3-gigahertz scatterometer	50-27
50-5	Curves of difference between radar differential scattering coefficient and values for a mean curve compared with a line map of the Garden City Test Site area from which the data were obtained with the 13.3-gigahertz scatterometer	50-28
50-6	Variation of radar differential scattering cross section with frequency as reported by Daley of NRL (horizontal polarization). The parametric angle is the elevation angle, the complement of the angle of incidence	50-29
50-7	Variation of radar differential scattering cross section with frequency as reported by Daley of NRL (vertical polarization). The parametric angle is the elevation angle, the complement of the angle of incidence	50-30

Figure		Page
50-8	Frequency dependence of scattering coefficient obtained by ultrasonic simulation (undulating surface)	50-31
50-9	Frequency dependence of scattering coefficient obtained by ultrasonic simulation (undulating surface roughened with sand particles)	50-32
50-10	Effect of frequency average on image of sphere targets	
	a. Monochromatic image of two spheres (f = 1.5 MHz)	50-33
	b. Swept frequency image of two spheres (f = 1.5 MHz ± 10%)	50-33
50-11	Monochromatic images of the same target made at nearby frequencies compared with panchromatic images with ±3-percent and ±6-percent frequency variation. These images were produced in the ultrasonic simulator	50-34
50-12	Example of possible spectral-response-separated trichromatic radar	50-35
50-13	Block diagram of the IDECS and associated equipment	50-36
50-14	False color IDECS-enhanced image of Bucks Lake Test Site. Original data multispectral photographs from NASA aircraft 926 overflight	50-37
50-15	False-color IDECS-enhanced image of Bucks Lake Test Site. Original data multispectral photographs from NASA aircraft 926 overflight	50-38
50-16	False-color IDECS-enhanced image of Bucks Lake Test Site. Original data multispectral photographs from NASA aircraft 926 overflight	50-39
50-17	False-color IDECS-enhanced image of Bucks Lake Test Site. Original data multispectral photographs from NASA aircraft 926 overflight	50-40
50-18	False-color IDECS-enhanced image of Bucks Lake Test Site. Original data multispectral photographs from NASA aircraft 926 overflight	50-41

Figure		Page
50-19	Identification accuracy for August-September 1965 radar imagery	50-42
50-20	Identification accuracy for July 1966 radar imagery	50-43
50-21	Identification accuracy for Pisgah Crater scatterometer data	50-44
50-22	Scattergram of July 1966 Garden City radar image data projected on its first two principal axes	50-45
50-23	Scattergram of August 1965 to September 1965 Garden City radar image data projected on its first two principal axes	50-46
50-24	Image 1 of made-up data	50-47
50-25	Image 2 of made-up data	50-48
50-26	Image 3 of made-up data	50-49
50-27	Classified image of made-up data using spatial clustering	50-50
50-28	Classified image of made-up data using measurement space clustering	50-51
51-1	Schematic of multispectral scanner and data processor	51-7
51-2	Typical spectrometer video data	51-8
51-3	Typical x-y scope pictures	51-9
51-4	Raw spectrum of green paint	51-10
51-5	Light-green standard reflectance panel	51-11
51-6	Illustrative plots of relative signal versus scan angle for wheat field	51-12
51-7	Signal variation as a function of scan angle and direction	51-13

Figure		Page
51-8	Distribution of wheat-field signals data	51-14
51-9	Typical signal relationships of dwell time on land to water changes	51-15
51-10	Tonal variations arising from ac coupling	51-16
51-11	Thermal stripmap with gain set to observe thermal patterns in water	51-17

2. SUMMARY OF AIRCRAFT MISSIONS

Earth Resources Group
NASA Manned Spacecraft Center

The following table presents information on the missions which have been flown over each of the Earth Resources Aircraft Program test sites.

Site	Mission	Site	Mission
1	Not overflown	44	9, 52, 54, 72, 74, 77
2	2, 5, 7, 21, 44	45	Not overflown
3	2, 8, 13, 21, 30, 56, 78	46	14, 23, 34, 53, 65
4	10	47	Not overflown
5	5	48	8, 13, 55, 73
6	5	49	8, 13
7	13, 42, 55	50	13
8	13	51	13, 18, 44, 59
9	Not overflown	52	30, 44
10	Not overflown	53	Not overflown
11	32	54	Not overflown
12	21	55	Not overflown
13	Not overflown	56	55, 76, 78
14	12, 43	57	Not overflown
15	18	58	Not overflown
16	3	59	Not overflown
17	Not overflown	60	Not overflown
18	Not overflown	61	Not overflown
19	13, 30, 56, 78	62	Not overflown
20	8, 13, 30, 59, 73	63	Not overflown
21	18	64	Not overflown
22	5, 76	65	Not overflown
23	Not overflown	66	Not overflown
24	8, 28	67	Not overflown
25	Not overflown	68	Not overflown
26	2, 7	69	Not overflown
27	18, 73	70	Not overflown
28	18	71	Not overflown
29	4, 10, 12, 19, 43	72	73
30	Not overflown	73	Not overflown
31	12, 15, 18	74	Not overflown
32	11, 12, 16, 17, 24, 27, 35, 51, 951, 62, 64, 75	75	5, 76
33	Not overflown	76	32, 54, 61, 74, 77
34	Not overflown	77	Not overflown
35	Not overflown	78	Not overflown
36	Not overflown	79	61
37	Not overflown	80	Not overflown
38	Not overflown	81	Not overflown
39	Not overflown	82	Not overflown
40	13, 21, 29, 42, 78	83	Not overflown
41	72	84	Not overflown
42	Not overflown	85	54, 61, 74
43	14, 25, 31	86	20, 38

Site	Mission	Site	Mission
87	22	138	34
88	25	139	Not overflown
89	Not overflown	140	Not overflown
90	Not overflown	141	61
91	Not overflown	142	53, 65
92	Not overflown	143	47
93	47	144	54
94	Not overflown	145	67
95	23, 36, 50	146	57, 67
96	Not overflown	147	67
97	9	148	53, 77
98	23, 36	149	Not overflown
99	23, 34, 40, 49, 50	150	53, 65
100	Not overflown	151	53, 65
101	21, 43	152	53, 65
102	36, 40	153	53
103	36, 40	154	44
104	36, 40	155	49, 66, 79
105	23	156	55, 59, 78
106	23	157	56, 73
107	23	158	57
108	23, 50	159	59
109	Not overflown	160	60
110	Not overflown	161	65
111	Not overflown	162	66, 75
112	Not overflown	163	66
113	Not overflown	164	66, 79
114	28, 33, 39, 43	165	964, 67
115	Not overflown	166	70
116	Not overflown	167	72
117	Not overflown	168	74, 79
118	54	169	Not overflown
119	Not overflown	170	Not overflown
120	Not overflown	171	Not overflown
121	Not overflown	172	79
122	Not overflown	173	79
123	Not overflown	174	79
124	53, 65	175	3
125	Not overflown	Cape Kennedy, Florida	58
126	72		
127	Not overflown	Evansville, Indiana	3
128	26, 34, 37, 41, 50, 58, 66	Galveston Beach, Texas	6
129	61		
130	28, 29, 42, 56, 73	Junction City, Texas	64
131	Not overflown		
132	40, 62, 66	Mt. Diablo, California	7
133	40, 62		
134	40, 62	Titusville, Florida	58
135	30, 59		
136	Not overflown	Zuni Salt Lake, New Mexico	21
137	40, 62		

The following table presents information on the test sites overflown during each mission of the Earth Resources Aircraft Program.

Mission	Date	Site
1	June 30, 1964	Functional check flight
2	Nov. 30, 1964	2, 3, 26
3	Dec. 21, 1964	16, 175; Evansville, Indiana
4	Jan. 17, 1965	29
5	Feb. 11, 1965	2, 5, 6, 22, 75
6	Feb. 26, 1965	Galveston Beach, Texas
7	Apr. 20, 1965	2, 26; Mt. Diablo, California
8	June 2, 1965	3, 20, 24, 48, 49
9	June 9, 1965	44, 97
10	June 17, 1965	4, 29
11	June 21, 1965	32
12	July 2, 1965	14, 29, 31, 32
13	Sept. 22, 1965	3, 7, 8, 19, 20, 40, 48, 49, 50, 51
14	Nov. 15, 1965	43, 46
15	Dec. 17, 1965	31
16	Dec. 22, 1965	32
17	Jan. 5, 1966	32
18	Jan. 7, 1966	15, 21, 27, 28, 31, 51
19	Feb. 15, 1966	29
20	Mar. 6, 1966	86
21	Apr. 2, 1966	2, 3, 12, 40, 101; Zuni Salt Lake, New Mexico
22	Apr. 16, 1966	87
23	May 7, 1966	46, 95, 98, 99, 105, 106, 107, 108
24	May 14, 1966	32
25	June 30, 1966	43, 88
26	July 6, 1966	128
27	July 8, 1966	32
28	July 25, 1966	24, 114, 130
29	Aug. 8, 1966	40, 130
30	Aug. 30, 1966	3, 19, 20, 52, 135
31	Sept. 15, 1966	43
32	Sept. 19, 1966	11, 76
33	Oct. 3, 1966	114
34	Oct. 11, 1966	46, 99, 128, 138
35	Dec. 5, 1966	32
36	Dec. 6, 1966	95, 98, 102, 103, 104
37	Dec. 14, 1966	128
38	Jan. 22, 1967	86
39	Feb. 4, 1967	114
40	Feb. 21, 1967	99, 102, 103, 104, 132, 133, 134, 137
41	Feb. 24, 1967	128
42	Mar. 6, 1967	7, 40, 130
43	Mar. 14, 1967	14, 29, 101, 114
44	Mar. 21, 1967	2, 51, 52, 154
45	Canceled	
46	Canceled	
47	May 11, 1967	93, 143
48	Canceled	

Mission	Date	Site
49	June 8, 1967	99, 155
50	June 12, 1967	95, 99, 108, 128
51	June 23, 1967	32
951	July 6, 1967	32
52	June 27, 1967	44
53	July 10, 1967	46, 124, 142, 148, 150, 151, 152, 153
54	July 31, 1967	44, 76, 85, 118, 144
55	Aug. 14, 1967	7, 48, 56, 156
56	Sept. 5, 1967	3, 19, 130, 157
57	Sept. 18, 1967	146, 158
58	Aug. 30, 1967	128, Cape Kennedy, Florida, Titusville, Florida
59	Oct. 16, 1967	20, 51, 135, 156, 159
60	Oct. 30, 1967	160
61	Nov. 13, 1967	76, 79, 85, 129, 141
62	Dec. 4, 1967	32, 132, 133, 134, 137
63	Canceled	
964	Jan. 5, 1968	165
64	Jan. 9, 1968	32; Junction City, Texas
65	Jan. 16, 1968	46, 124, 142, 150, 151, 152, 161
66	Feb. 5, 1968	128, 132, 155, 162, 163, 164
67	Feb. 26, 1968	145, 146, 147, 165
68	Canceled	
69	Canceled	
70	Apr. 3, 1968	166
71	Canceled	
72	May 6, 1968	41, 44, 126, 167
73	May 21, 1968	20, 27, 48, 72, 130, 157
74	June 14, 1968	44, 76, 85, 168
75	July 1, 1968	32, 162
76	July 15, 1968	22, 56, 75
77	July 29, 1968	44, 76, 148
78	Aug. 26, 1968	3, 19, 40, 56, 156
79	Sept. 9, 1968	155, 164, 168, 172, 173, 174

N71-16127

MISSION 73 AND ASSOCIATED TESTS

By Robert H. Alexander
Geographic Applications Program
U.S. Geological Survey

INTRODUCTION

The Geographic Applications Program of the U.S. Geological Survey conducted a complex series of remote-sensing experiments in southern California this spring. Primary support of the experiments was provided by the NASA MSC Convair 240A, mission 73, Southern California Test Site for Geography, No. 130, May 21-24, 1968. We refer here to the whole series of aircraft flights and field data-gathering activities, extending from mid-April to mid-June, as mission 73, even though this is a somewhat broader meaning than that used in the Manned Spacecraft Center Aircraft Program.

The idea of a combined research effort by a number of investigators took shape in the fall of 1967 during the program review in the Washington Office of the Geographic Applications Program. Until that time, test site missions in the geography program were carried out on an individual basis, that is, with one investigator making all the arrangements for ground measurements, flight line planning, liaison with the Manned Spacecraft Center operational personnel, and, after the conclusion of the mission, data analysis, and interpretation. Under that procedure, a great deal was learned but none of the investigators had been able to conduct a truly multisensor mission, one in which photographic, thermal infrared, passive microwave, and radar sensors operated over a single site at a single time in the presence of appropriate ground-truth measurements.

After the geography investigators endorsed the idea of conducting a joint multisensor research mission at a single test site, it became possible to combine that research mission with the field demonstration of an aircraft and ground data-gathering mission for visiting Mexican and Brazilian scientists.

Detailed planning for what was to become mission 73 began immediately and extended over the next several months. The successful conclusion of the data-gathering phase of the effort (the coordinated air

and ground measurements program) was made possible by the cooperation of a large number of individuals and organizations, including university investigators, representatives of the U.S. Geological Survey and NASA, many local, state, and federal governmental organizations, and representatives of private industry.

The series of experiments was designed to advance the research objectives of the Geographic Applications Program which are, briefly stated, to apply the technology of remote sensing from aircraft and spacecraft to the science of geography and to practical applications of geography in earth resources studies and thereby to improve the habitability of this planet by monitoring surface environmental conditions and changes. Implied in these objectives are programs for channelling resulting environmental information to those who are in a position to shape resource management decisions. Therefore, these experiments focus on the spatial extent and regional scope of environmental problems. Public and private organizations which have regional environmental responsibilities and which would be among the consumers of remote-sensing data which may be ultimately obtained from earth-orbiting satellite systems were involved in the program.

Figure 3-1 illustrates the principal areas where the remote-sensing tests were carried out, specifically, Los Angeles and vicinity, the Coachella Valley, the Salton Sea, and the Imperial Valley in southern California. The specific objectives of mission 73 tests were to correlate multisensor and ground-truth observations and to evaluate the feasibility of sensors and sensor combinations as data-gathering components in aircraft and, eventually, spacecraft, in four areas of emphasis as illustrated in figure 3-2: first, land use; second, urban problems; third, surface energy balance; and fourth, soil moisture. The sensors employed in the test are listed across the top of the diagram, roughly in order of increasing wavelength. The basic aircraft was the NASA Convair 240 which carried the AAS-5 ultraviolet scanner, two RC-8 mapping cameras using black and white and color infrared film, four Hasselblad cameras with synchronized shutters using color infrared film, a Reconofax IV thermal infrared scanner operating in the 8 to 14 micron band, the radar scatterometer, and four passive microwave radiometers. The scanning microwave radiometer, producing images in the 19.35-GHz band, was carried by the NASA Convair 990 aircraft under the auspices of the Goddard Space Flight Center. The ultraviolet absorption spectroscope developed by Barringer Research, Limited, was carried aboard their own plane. A 12-inch mapping camera, another bank of Hasselblads furnished by the University of Tennessee, and a TV camera were carried aboard other aircraft. It should be clearly understood, however, that even though these latter aircraft were not NASA aircraft, they were incorporated into mission 73 as integral parts of the overall series of experiments with full knowledge, cooperation, and support of NASA officials.

This presentation must necessarily be only a summary description of what happened and a sampling of the preliminary results and conclusions. A preliminary report is already available,[1] and detailed reporting on the data analysis will take place at several centers over the next few months. Because of the diversity of the studies and the rather wide interest already generated, a 1-day general briefing on the results of mission 73 is under consideration.

LAND USE

For the land-use determinations, the basic sensor system employed was the camera with color infrared film. Special filter combinations were tested for their ability to make color infrared more effective for land-use discrimination through a column of atmosphere. The other sensors available were also tested for their ability to discriminate among different types of land use. Aerial photography taken just prior to the flights of the NASA aircraft proved to be of great value in speeding up the collection of basic land-use data. For example, the aerial extent of the type of land use revealed by the ground observation could be quickly determined by reference to the preflight photography. In addition, complete photographic coverage (with color infrared film) of the Imperial and Coachella Valleys was obtained 3 weeks after the Convair 240 flights in May to verify land use over the larger area imaged by the scanning microwave radiometer flown by the NASA Convair 990. An example of determination of land use with this photography is shown in figure 3-3, with simultaneous ground-truth photographs documenting month-old cotton and mature alfalfa shown in figures 3-4 and 3-5, respectively. The ground photographs were carefully indexed to be correlated later with the aerial photography and other sensor data. A similar land-use example is shown in figure 3-6, where the sharp tonal difference in the field is shown by ground observation (fig. 3-7) to be the dividing line between harvested and unharvested sugar beets. The harvesting machine is shown in figure 3-7 and can also be seen on the original color infrared photograph from which figure 3-6 was made. Data from the ground and aerial photographs are combined to be used later in correlating land use and percent of crop cover with radiometric temperatures obtained from the passive microwave imager.

---

[1] "Mission Summary and Data Catalog," USGS/NASA Southern California Remote-Sensing Test Program, by Richard F. Pascucci and Gary W. North, August 1968.

As a result of the experiments which culminated with mission 73, we have determined that color infrared film (Ektachrome Aero infrared type 8443), when used with 15 + 80B or 15 + 82B filters and properly exposed and processed, is the single most effective sensor for land-use determinations through considerable atmospheric distances. This film and filter combination is now ready to be tested in space.

Color infrared film, when specially filtered, can be processed to a negative. There are several advantages to this. First, black and white prints can be available within hours after the pictures are taken. This was accomplished for the first time in mission 73 with the result that land-use field mapping was considerably more efficient, and location in the field was greatly facilitated with fresh aerial photography. Second, many options are still available in the processing of the positive color infrared print. When the film is processed to a positive transparency, the original processing determines and limits the information content of the film for land-use mapping, and errors in exposure or processing are irretrievable.

We also learned that the scatterometer has definite potential for land-use discrimination. Mission 73 is the first test of the scatterometer for land-use determination. It is probable that signatures could be worked out for many types of land use. However, correlative photography is essential for realining the signal from the different angles so that the signatures can be correlated with the ground trace of the flight path rather than with the time the scattered return signal is received.

The thermal infrared scanner can be used for gross land-use determination (fig. 3-8) but is not as accurate for land use as photography. It is, however, effective at night and through smog. The AAS-5 ultraviolet scanner (fig. 3-8) reveals gross land-use features only if they are already known. Nothing appears to be added that is not available on the other sensors. Ground resolution is poor. The NASA/Goddard scanning microwave radiometer imagery shows gross correlation with land use. For example, the U.S.-Mexican border is clearly distinguishable in the imagery because of the sharp differences in land-use practices on each side, even though ground resolution is poor (fig. 3-9).

URBAN PROBLEMS

In the studies of urban problems, most effort was concentrated on two projects, both in the Los Angeles area: the determination of housing quality and residential neighborhood environmental health conditions primarily with data collected by cameras and color infrared film; and the remote measurement of the atmospheric pollutants, nitrogen dioxide and sulfur dioxide, by an absorption spectroscopy technique, correlated

with ground measurements of the same pollutants made by the air pollution control districts.

Several criteria for determining housing quality can be observed in black and white photography and even more on color infrared photography. An example is shown in figure 3-10, which is a block in the Willowbrook district of Los Angeles. Housing quality and neighborhood environmental conditions improve with increasing distance from a junkyard and railroad. Figures 3-11 and 3-12 are illustrations of ground-truth data-gathering activities for the environmental health and housing quality studies. As a result of the tests done in mission 73, it appears certain that remote sensing from aircraft can provide a large amount of the data now needed for environmental health surveys at a greatly reduced cost compared to present methods of obtaining the same data.

The Barringer Absorption Spectroscopic measurements correlate reasonably well with visual observations (fig. 3-13) and ground monitoring station measurements of nitrogen dioxide and sulfur dioxide (fig. 3-14). The airborne traverse method is greatly superior to ground monitoring for determining geographic extent of these air pollutants. The increased concentrations measured across the northern and eastern portions of the Los Angeles Basin make sense geographically.

Several categories of urban land use can be determined from remote-sensor data alone; thermal infrared scanner imagery shows promise for observations at night or through heavy air pollution. The fact that urbanized areas can be located and appear cold in the passive microwave imagery shows promise for further research; for example, as a possible gross measure of built-up area in regional surveys.

SURFACE ENERGY BALANCE

Studies of the energy balance of the earth surface and its response to land-use changes brought about by man's activities may be among the major long-run applications of spaceborne remote sensors. In addition, knowledge of microclimatic factors gained from energy balance studies will be an aid to interpretation of thermal infrared imagery which is becoming more widely available. The purpose of the portions of mission 73 experiments dealing with surface energy balance was to test remote-sensor techniques for assessing the quantity of reflected shortwave radiation and emitted longwave radiation from the earth surface. Cameras, a radiometer, and a thermal infrared scanner provided airborne sensor data to correlate with ground measurements. Field measurements of reflectance of various surface features were accomplished with a spectroradiometer and a photometer. Surface thermal emission was estimated with the aid of a hand-held radiometer and contact surface

temperature measurement devices. Calibrated reflectance and emission panels (fig. 3-15) set up on a prominent place along the flight line provided reference values against which to compare film density and color measurements.

The infrared scanner (Reconofax IV) used in these tests is inadequate for quantitative temperature measurements that would be needed for energy balance studies. The automatic gain control, lack of calibrated signal, and lack of tape storage precludes serious consideration of this instrument for all but the most cursory observations of outgoing, longwave radiation. For example, two separate thermal wells in the Imperial Valley gave identical brightness returns in the infrared imagery. Field checking revealed that one was inactive at 97° F and the other active and with a surface temperature of 235° F. Until calibrated images can be obtained, an infrared radiometer will be of more value in energy budget studies than the scanner. Where bodies of open water are present, there is excellent indication that the scanning microwave radiometer can record areas of wind disturbance and hence horizontal energy transfer. On June 7, the northern portion of the Salton Sea was relatively calm, while the southern portion was subjected to high winds and was extremely choppy. The distinction was clearly shown on the passive microwave imagery (fig. 3-16). The average microwave brightness temperatures in the northern part were 158° K, while those of the southern part were 174° K. The advantages of magnetic tape storage and computer data-processing capability are illustrated in the three playbacks of the same image of the Salton Sea obtained with the imaging passive microwave radiometer (fig. 3-17).

SOIL MOISTURE

Soil moisture was chosen for special emphasis in these experiments not only because it is an important part of the water resource but also because its presence at and near the surface influences the quality of data returns from a variety of remote sensors. It would, therefore, be of great value not only to determine the distributions and concentration of soil moisture but also to be able to correct for soil moisture effects in remote-sensor data. The passive microwave sensors were expected to provide basic quantitative information on soil moisture assuming that proper calibration of the instruments could be done. Supporting data from the airborne infrared and photographic sensors were expected to aid in soil moisture assessment in a qualitative way. Ground control information was obtained from standard soil moisture sampling, augmented by knowledge of irrigation schedule and procedures.

We were disappointed in the results of the passive microwave radiometers aboard the Convair 240. In future experiments, integration times shorter than 1 second are necessary so that the signal responds to a smaller area on the ground. Also, boresighted cameras or some other means of locating the signal precisely on the ground are essential. Since there is considerable interest in making the measurements at night as well as in the daytime, some innovations in procedures, such as flash photography, are called for in future research efforts. The calibrated scanning microwave radiometer shows promise for soil moisture determination, but considerable research is needed on the problem of correlating the point measurements of soil moisture on the ground with the area measurements obtained by the remote sensor. Ground measurements with passive microwave radiometers show promise of being able to determine small concentrations of soil moisture. Effects of viewing angle and polarization are better understood as a result of the measurements that were conducted during mission 73. (See fig. 3-18.) A healthy field of month-old cotton, that is, one that is not under moisture stress, seems to be a clear indication of at least 10-percent soil moisture concentration. Thus, the large fields in the Imperial Valley suggest themselves as excellent ground-truth areas for testing low-resolution infrared or microwave radiometers and their ability to discriminate soil moisture concentrations. (See fig. 3-19.) The progress of irrigation water in the fields can be clearly seen on the thermal infrared imagery but is almost completely obscured in the panchromatic photograph taken simultaneously (fig. 3-20).

PROGRAM IMPLICATIONS OF MISSION 73

We are now busy applying the results of mission 73 to the planning for the coming year of the Geographic Applications Program. Figure 3-21 shows the matrix of sensors and applications with a preliminary attempt to evaluate the results of each sensor in terms of each of the four major applications in our program. For simplicity, only four gradings were used: excellent, good, poor, and unusable. Each of the numbers assigned to a place on the matrix results from a considerable amount of analysis of the data received thus far and also represents a consensus of a number of the investigators. The chart, however, is not self-explanatory. The absorption spectroscope, for example, was rated unusable in every category except urban problems. Actually, the only purpose of its test in this experiment was to measure the atmospheric pollutants nitrogen dioxide and sulfur dioxide in the Los Angeles area. Some explanation of the less than excellent rating of the RC-8 camera is required. For land-use studies, the use of this camera with the color infrared film does, indeed, produce a sharp, clear image. However, the problem of vignetting results in a great variability in hue and

intensity from the center of the exposure to the edges. Therefore, land-use identification based on comparison of color tones leaves much to be desired. The 12-inch camera used in mission 73 did not have this problem; therefore, it received a higher rating. Also, as a result of these experiments, we found the Hasselblad with color infrared film just as valuable for land-use identification as the RC-8. Owing to the much smaller costs in both operation and film processing, we believe the Hasselblad should be used much more in the future for land-use experiments than the RC-8. Blank squares in the chart represent cases where we do not yet know the answers or have not had time to evaluate the data. Figure 3-22 shows the same matrix of sensors versus applications with our recommendations for future research using the mission 73 sensors. Category 1 represents those applications which are now ready to be tested in space. Note that the Hasselblad cameras and the 12-inch cameras are the only sensors presently in this category, and their use with color infrared film is of the highest priority. The research would be advanced greatly if we could now obtain data from space over geographic test sites in conjunction with simultaneous measurements made on the ground and hopefully also from medium- and high-flying aircraft.

Most of the other sensors require further aircraft testing and are indicated by category 2. Note that for certain applications some of these sensors are recommended to be dropped (category 4). For example, the AAS-5 scanner with ultraviolet detector has not proved to be of sufficient value to our research to warrant further use. Also, the MR-62 and MR-64 passive microwave radiometers, as presently operated, and with their considerable difficulty in data processing, will be in this category based on our preliminary evaluation. We are, however, considerably interested in obtaining data from microwave radiometers, particularly for soil moisture and energy budget applications. Some of the cameras, for example the RC-8 carrying the black and white film, are required for indexing only and are so indicated by category 3. It does not seem to be proper use of the RC-8 camera, however, as an indexing reference for pinpointing the ground locations of data from other sensors. Less expensive cameras could do the job and should, in fact, be boresighted with the radiometers or other sensors for which location is desired. We also require, from means such as flash photography, the obtaining of indexing information at night when the infrared and microwave radiometers are required to be tested.

The many activities which were included in mission 73 could, of course, have been carried out separately. For some purposes, it is valuable to carry out intensive remote-sensing experimentation at a single small highly instrumented site. For other purposes, the requirement is for small-scale, large-area, high-altitude coverage, generally for assessment of regional and seasonal differences in the environment.

There are advantages of including in the remote-sensing program a broad complex mission such as mission 73. Among these advantages are the following: (1) time, one of the most troublesome variables in environmental studies, is held nearly constant where simultaneous measurements are made in several spectral bands over a large area; (2) there is an obvious economy in aircraft time, as well as time spent by ground parties, when several remote-sensor tests are carried out at once using data from the same aircraft passes and the same ground data such as soil temperature, soil moisture, and so forth; and (3) a more rapid exchange of knowledge and techniques is fostered when several diverse groups combine in one remote-sensing mission. For example, the geologists benefited from the film and filter combinations developed by the geographers for land-use analysis. The agriculture specialists learned of new research techniques form the specialists in passive microwave radiometry. The air pollution research people benefited from contact with the people who had developed methods for data collection with remote sensors. And the city and county planning commissions, charged with obtaining data on housing quality and neighborhood environmental health, learned that much of the information they require can be obtained through remote sensing more cheaply and effectively than through their conventional techniques. Each of the examples cited was realized specifically in mission 73. Finally, with a large mission, such as mission 73, there is considerable benefit for educational training and demonstration purposes, and when we are ready to conduct the spacecraft remote-sensing missions with appropriate ground measurements, a region-wide mission of the character of mission 73 may well prove to be the most effective way of calibrating the sensors and evaluating the results of the early spacecraft test site experiments. Medium- and low-flying aircraft will still be needed for correlation with smaller-scale spacecraft imagery.

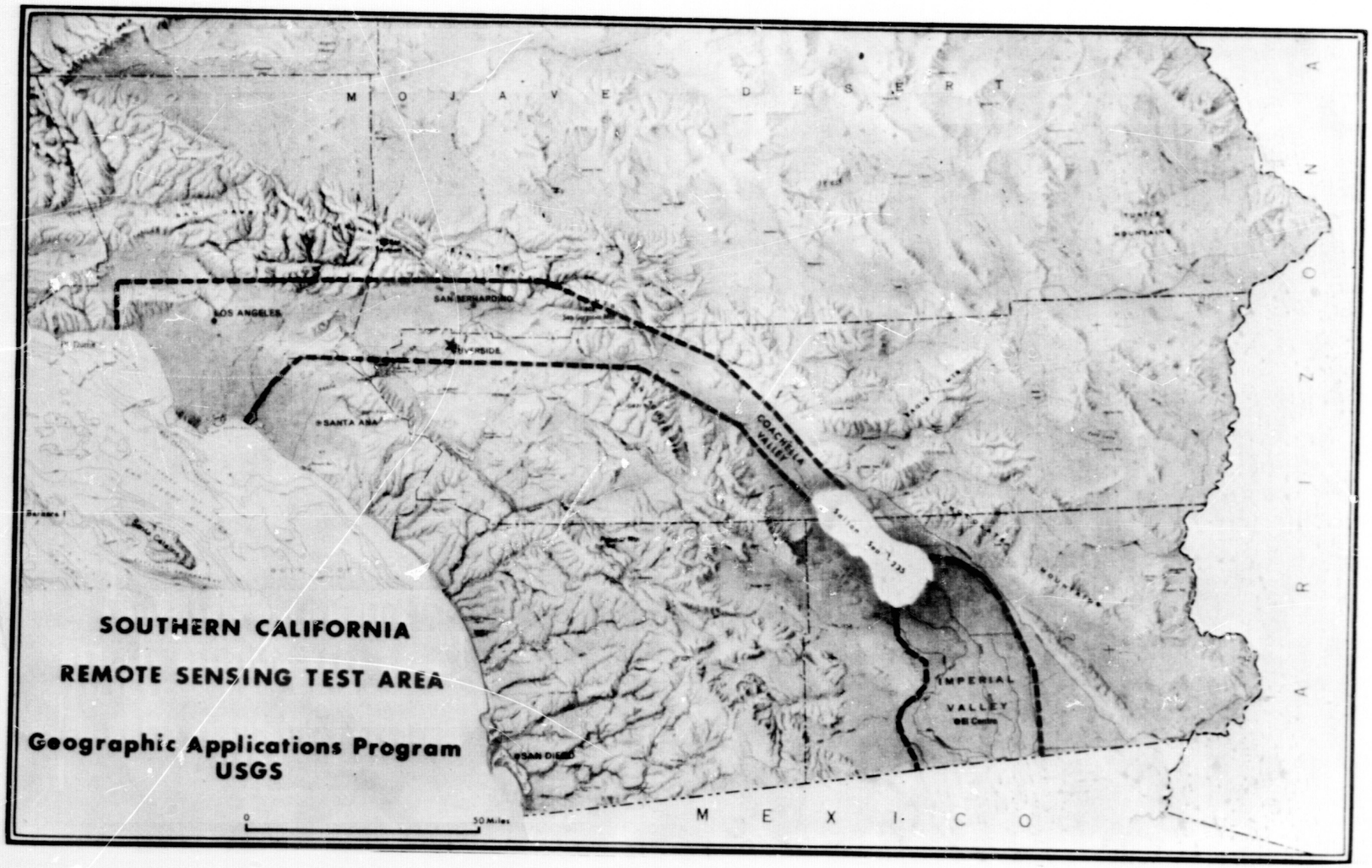

Figure 3-1.- Location of mission 73 geographic experiments.

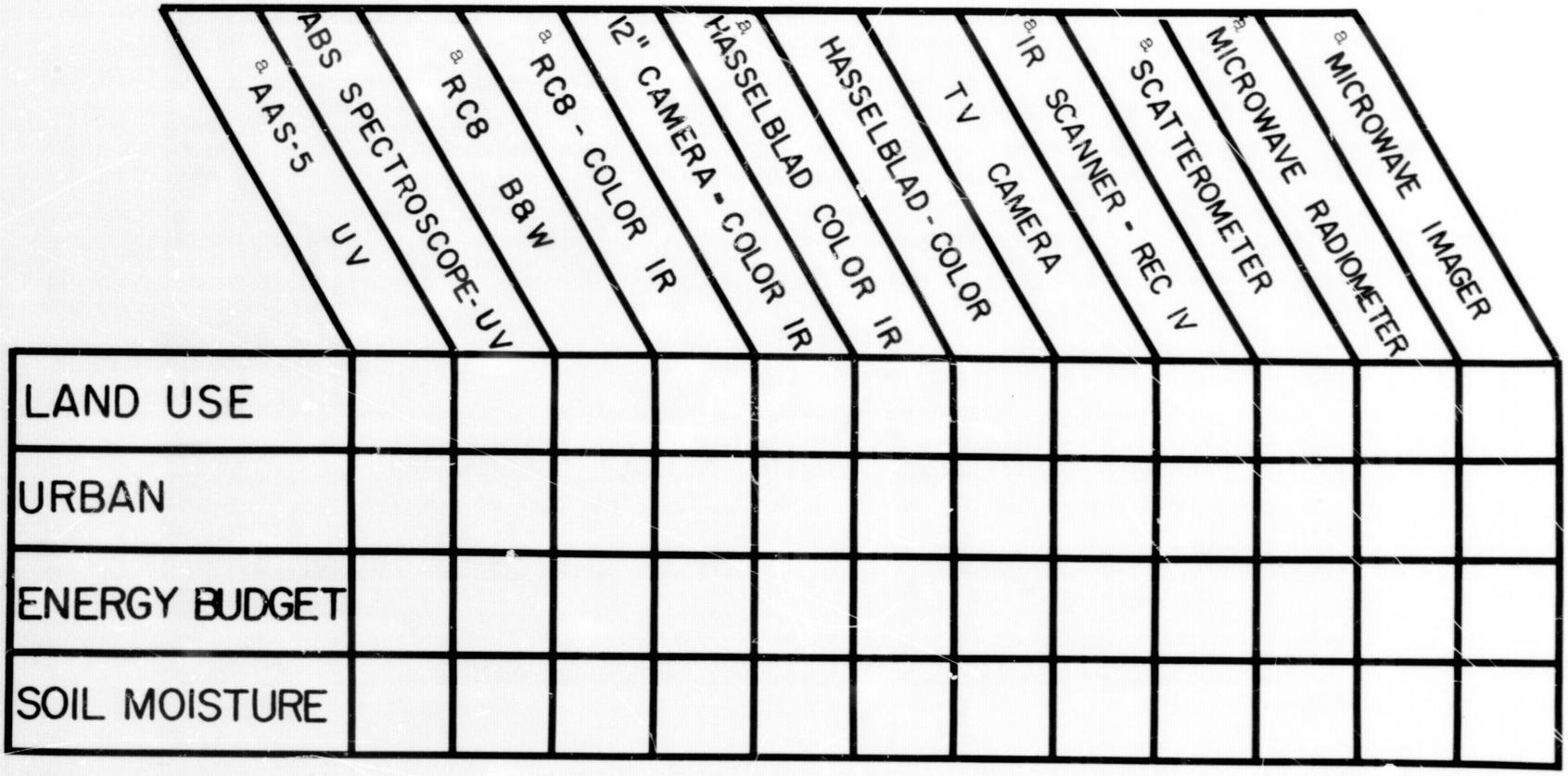

[a] Sensors carried aboard NASA aircraft

USGS/NASA
Geographic Applications Program

Figure 3-2.- Sensors and applications in mission 73.

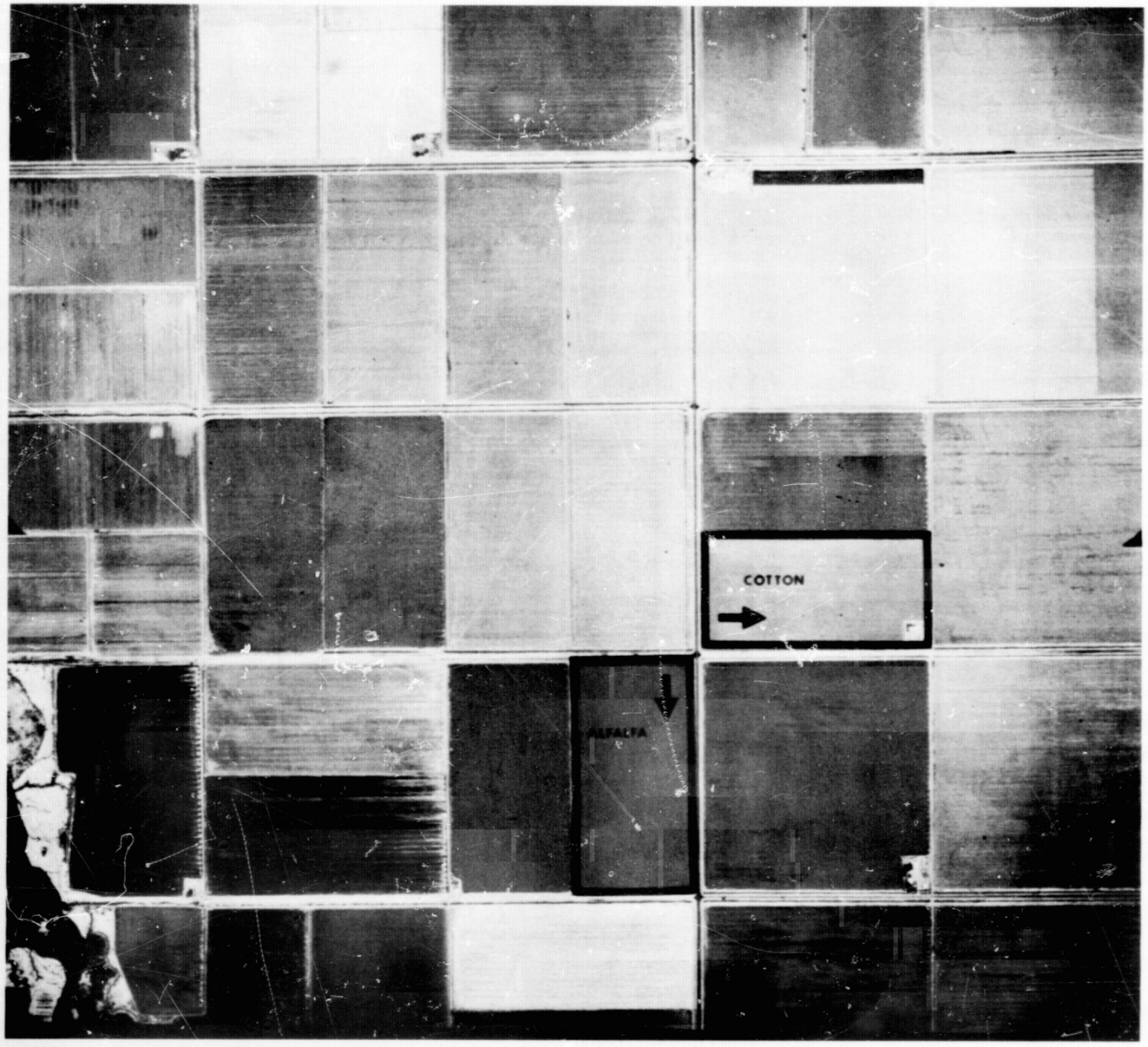

Figure 3-3.- Agricultural land use, Imperial Valley. Black and white print of color infrared photograph taken from 20 000 ft, 12-in. camera. Arrows show location of ground photographs shown in figures 3-4 and 3-5. (Gallaher - June 1968).

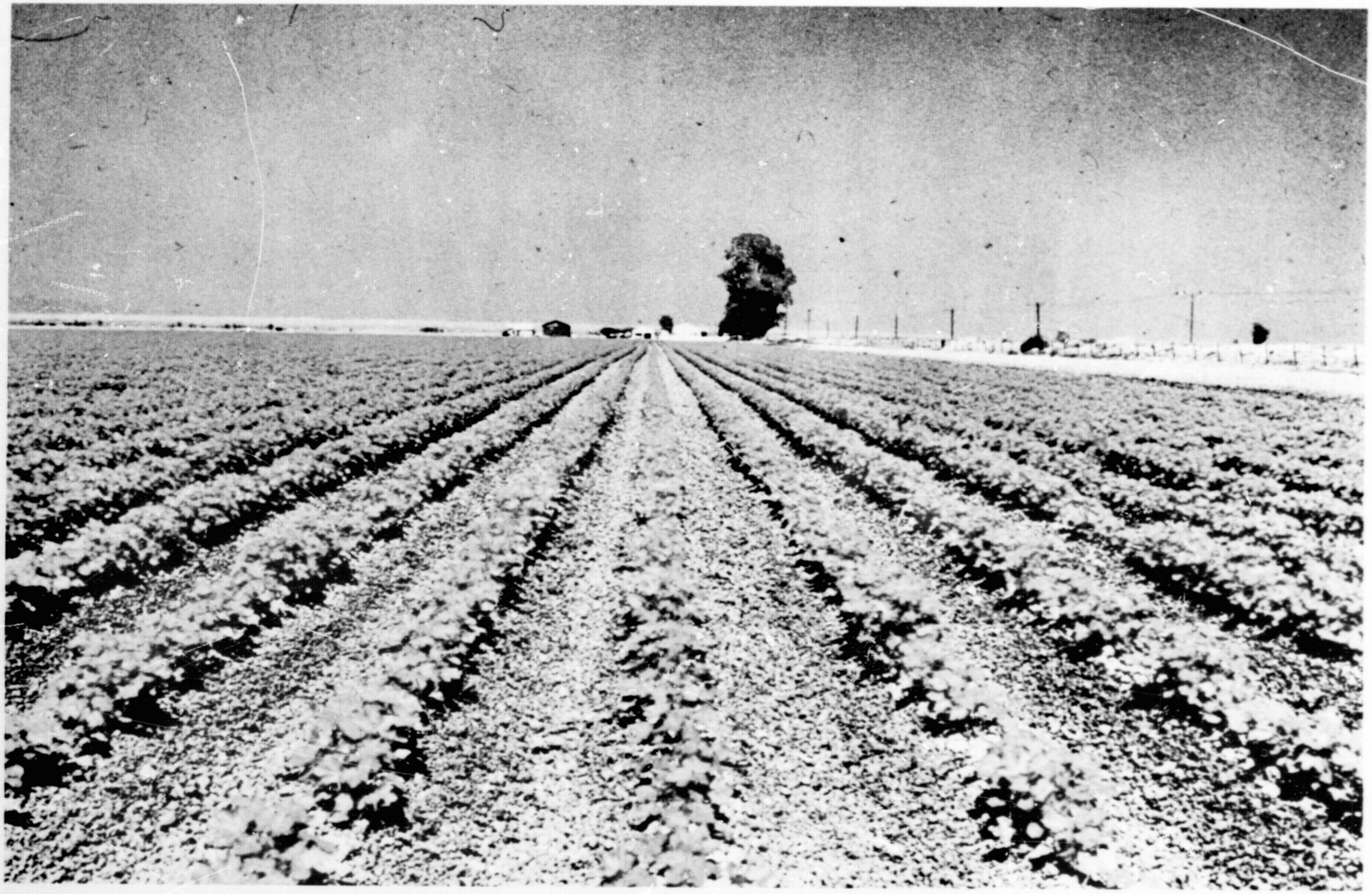

Figure 3-4.- Ground photograph of month-old cotton, taken in Imperial Valley at location of arrow in figure 3-3. Black and white reproduction of color infrared photograph.

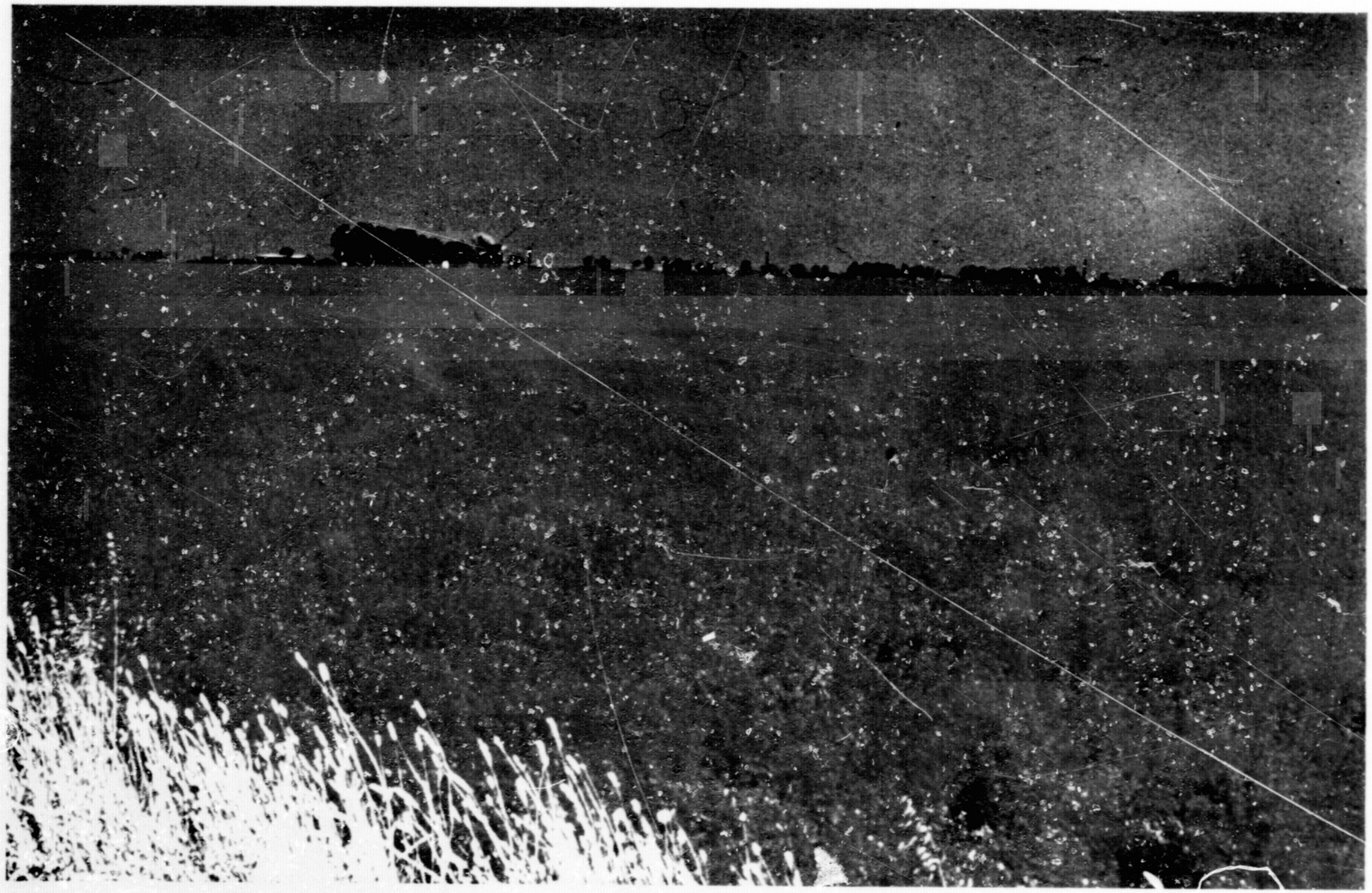

Figure 3-5.- Ground photograph of mature alfalfa, showing 100-percent ground cover, taken in Imperial Valley at location of arrow in figure 3-3. Black and white reproduction of color infrared photograph.

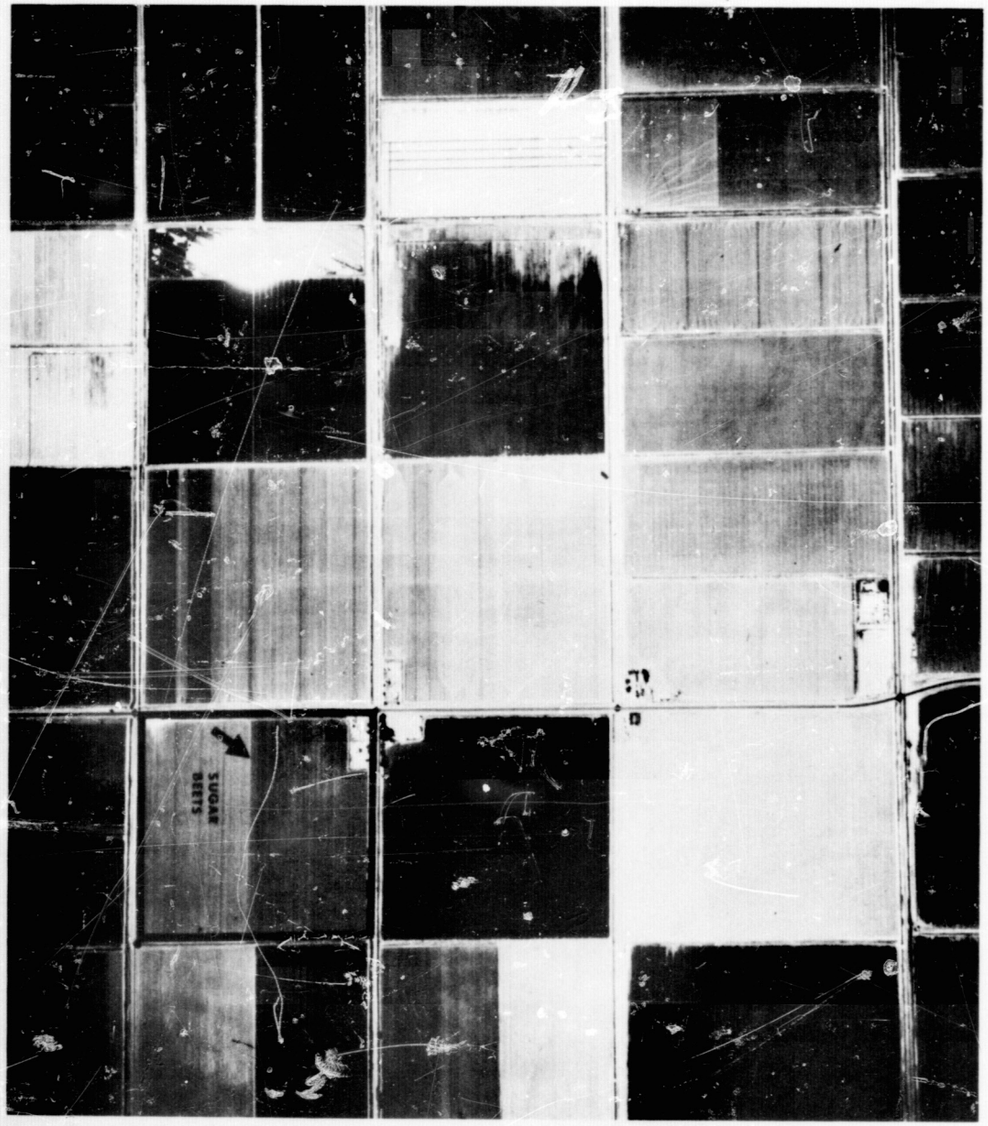

Figure 3-6.- Agricultural land use in the Imperial Valley. Black and white print of color infrared photograph taken from 20 000 ft, 12-in. camera. Arrow shows location of ground photograph verifying sugar beet harvesting. (Gallaher - June 1968).

Figure 3-7.- Sugar beet harvesting operation, Imperial Valley. Ground photograph taken at location of arrow in figure 3-6. Black and white reproduction of color infrared photograph.

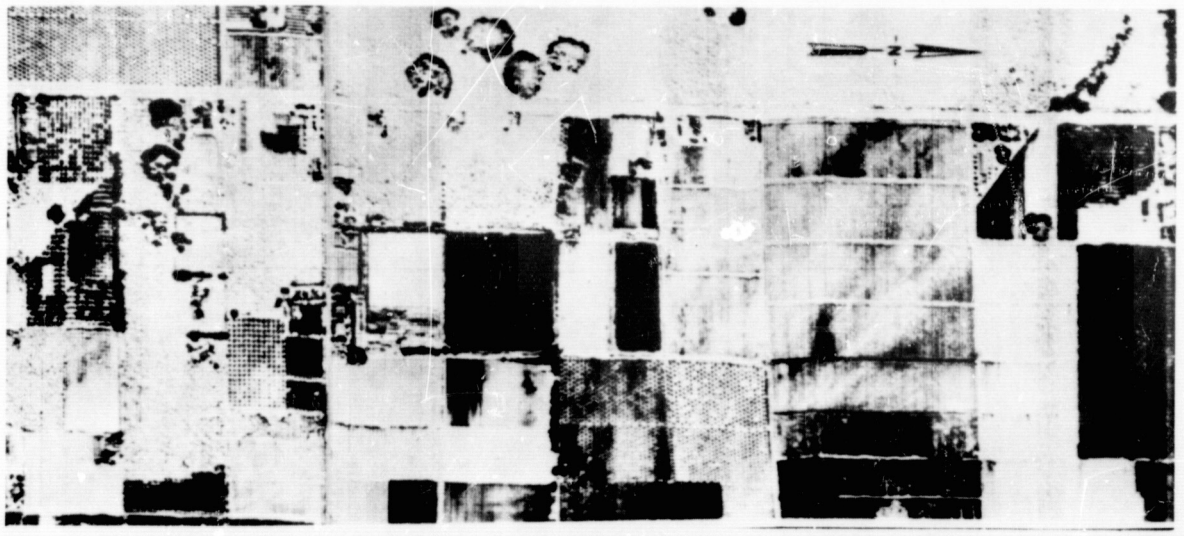

a. Ultraviolet, AN/AAS-5 sensor, flown May 21, 1968.

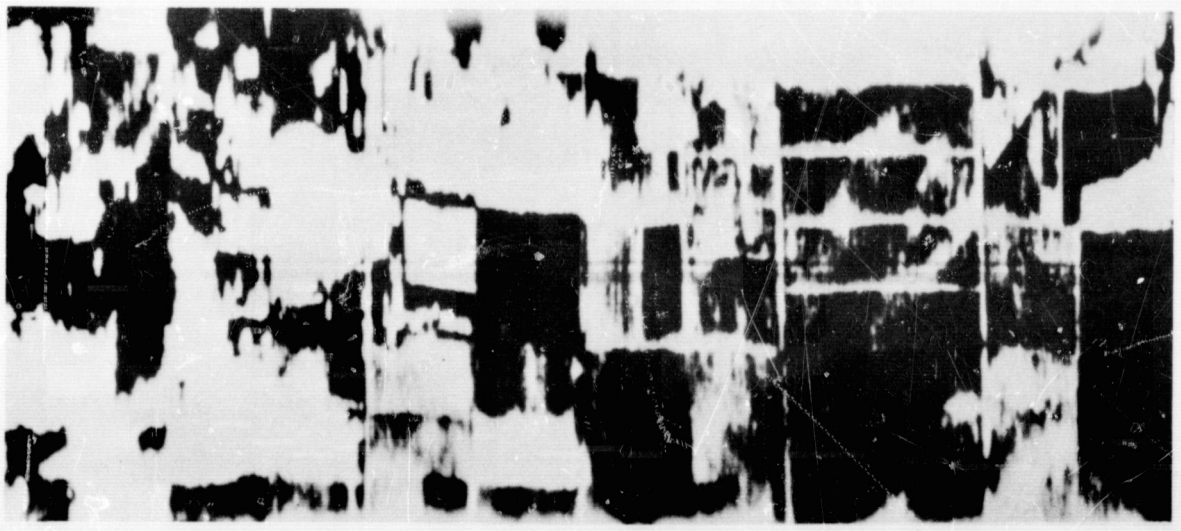

b. Thermal IR, Reconofax IV sensor, flown May 21, 1968.

Figure 3-8.- Comparison of ultraviolet imagery from the AAS-5 scanner with thermal infrared imagery from the Reconofax IV scanner. Portion of Jackson Street, Indio. NASA Convair 240-A.

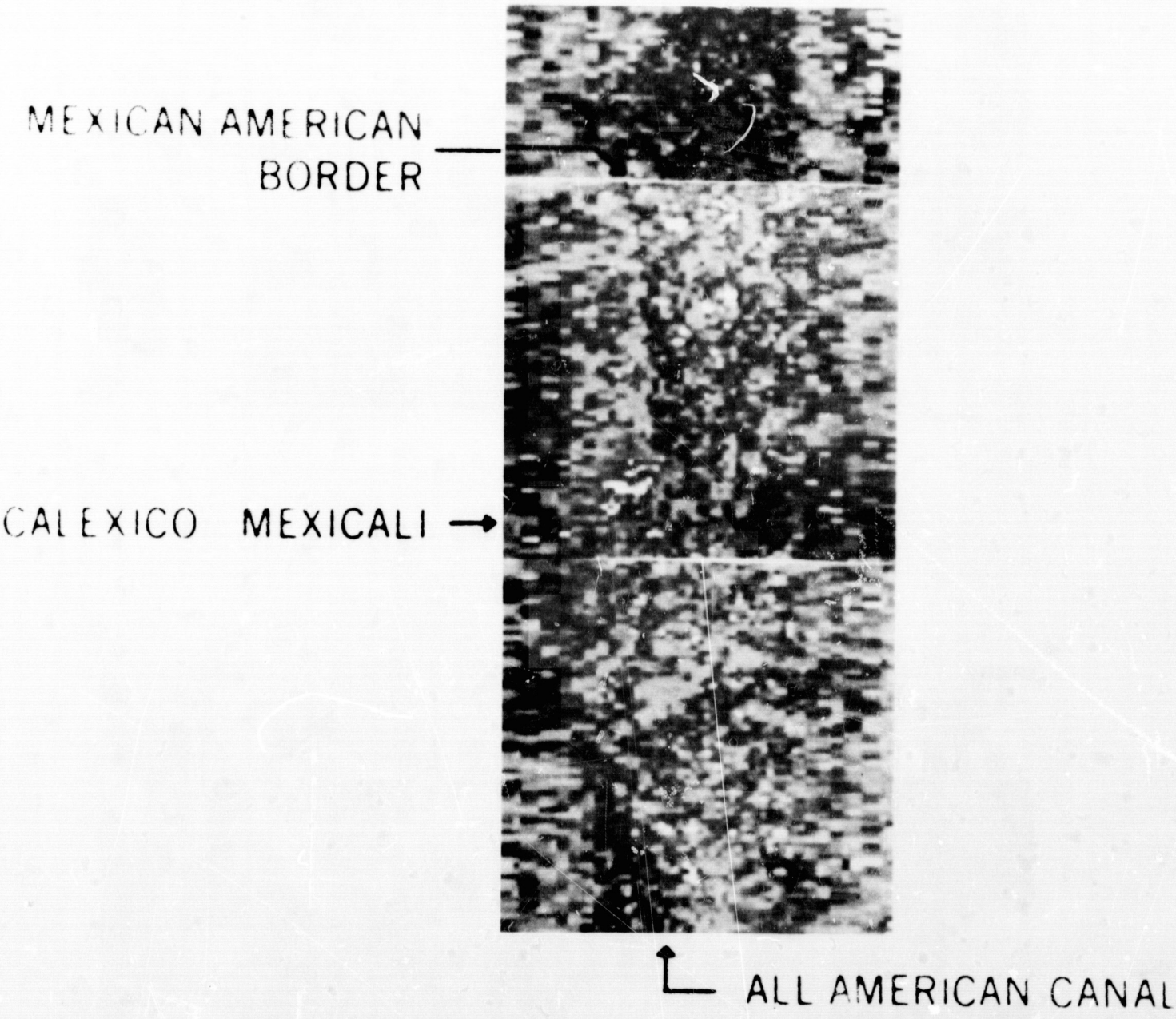

Figure 3-9.- Passive microwave imagery of Mexican-American border area, Imperial Valley. Dark tones on this image represent cool radiometric temperatures; light tones represent warm. Black and white reproduction of color TV display of digital data stored on magnetic tape. North is to the right. NASA Convair 990, approximately 40 000 ft, June 1968.

Figure 3-10.- Portion of the Willowbrook district of Los Angeles, illustrating improving residential environmental conditions with increasing distance from railroad and junkyard at top of photograph. North is toward the left. Black and white reproduction of color infrared photograph. NASA Convair 240, RC-8, mission 73, May 24, 1968.

Figure 3-11.- Obtaining ground truth for urban housing quality and environmental health studies. A portion of Willowbrook-Watts area, Los Angeles. Black and white reproduction of NASA color photograph (Moncrief). May 24, 1968.

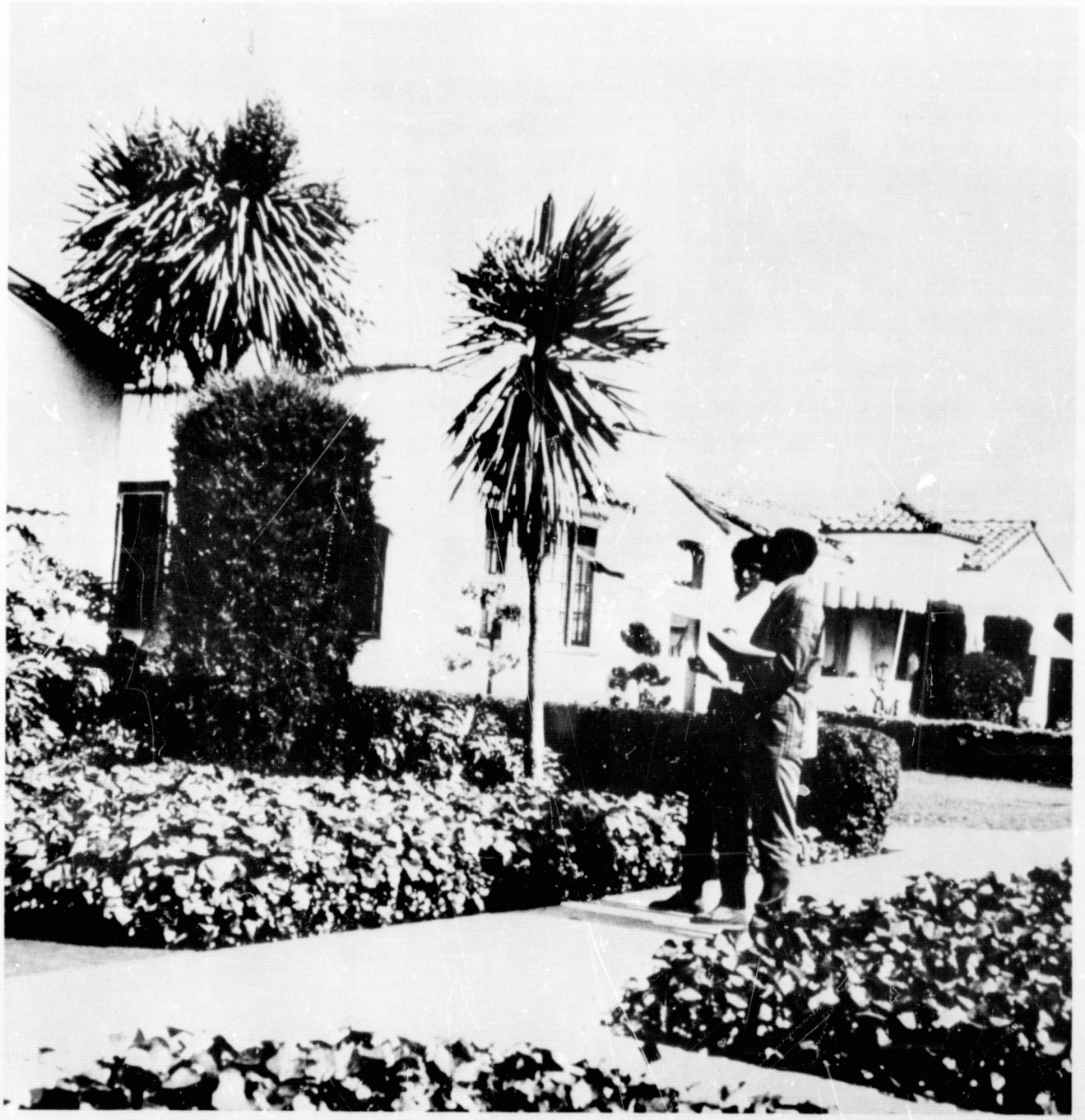

Figure 3-12.- Urban field team obtaining ground-truth observations for Los Angeles area flight line in Santa Monica. Black and white reproduction of NASA color photograph (Moncrief). May 24, 1968.

Figure 3-13.- Aerial view of smog over Los Angeles. Looking north toward San Gabriel Range. NASA photograph (Moncrief) taken from Barringer research aircraft. May 23, 1968.

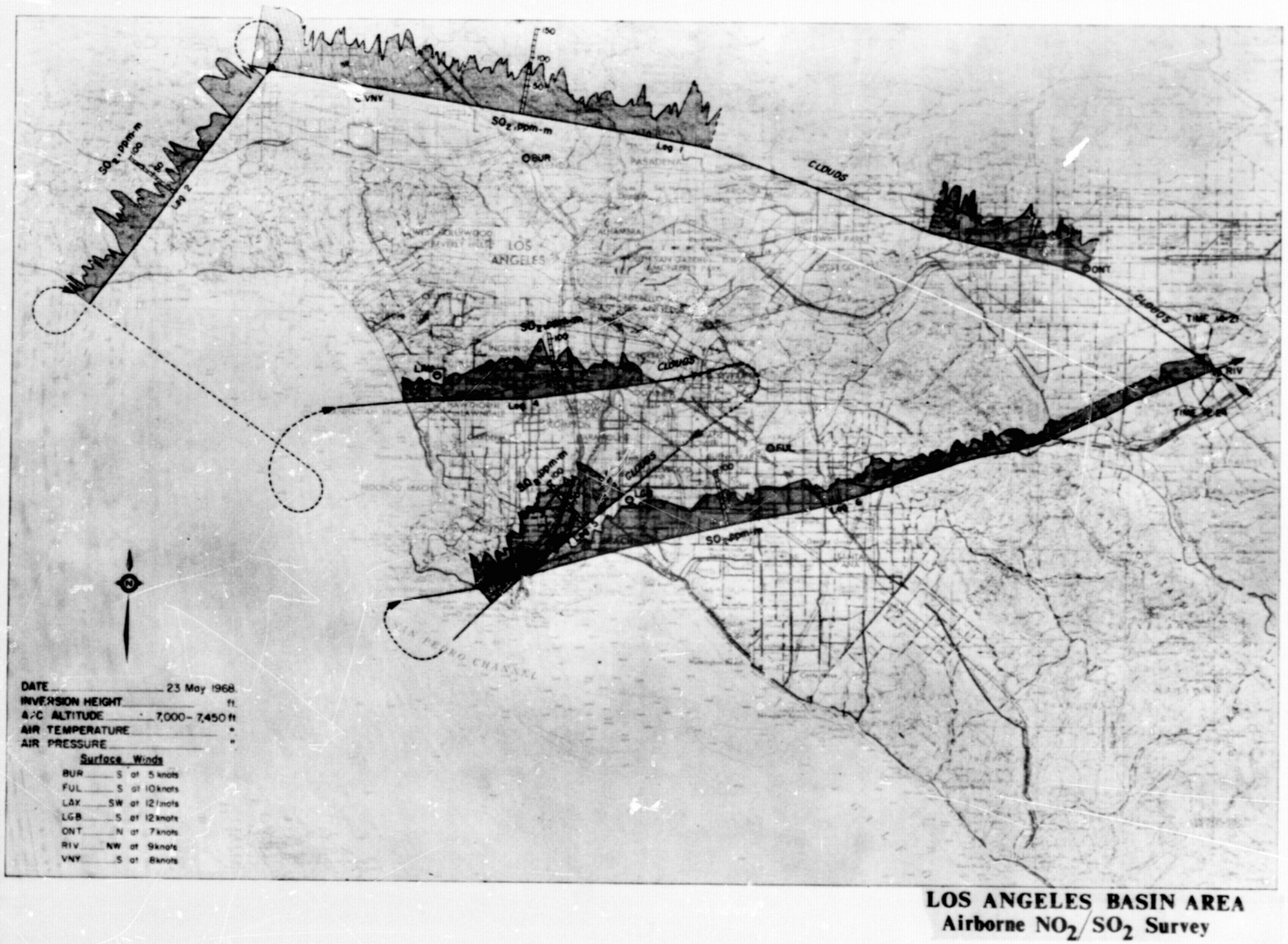

Figure 3-14.- Plots of sulfur dioxide (concentration times path length) measurements obtained with Barringer absorption spectroscope.

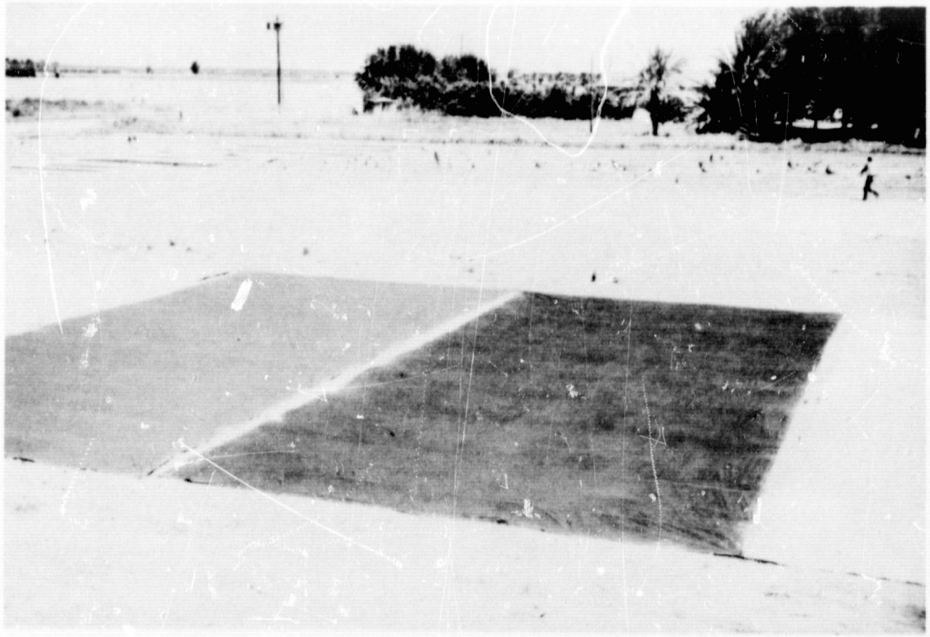

a. Y-2 filter, f/8 at 1/250 (Plus X-1120).

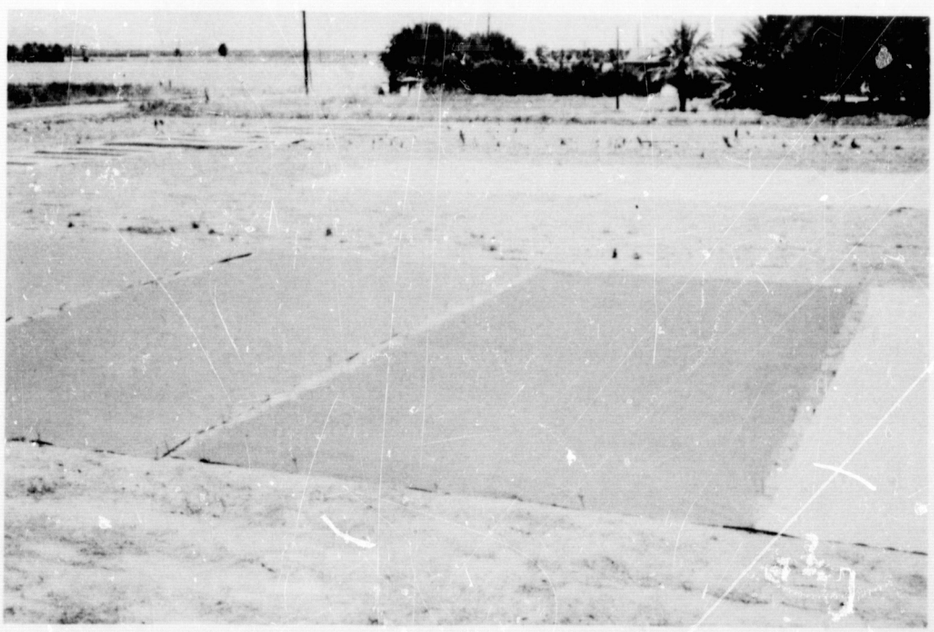

b. 25A filter, f/4 at 1/250 (Plus X-1125).

Figure 3-15.- Multispectral photographs of calibrated color panels. (Left to right: red, blue, green, yellow.) (Photographs by Harry Mallow.)

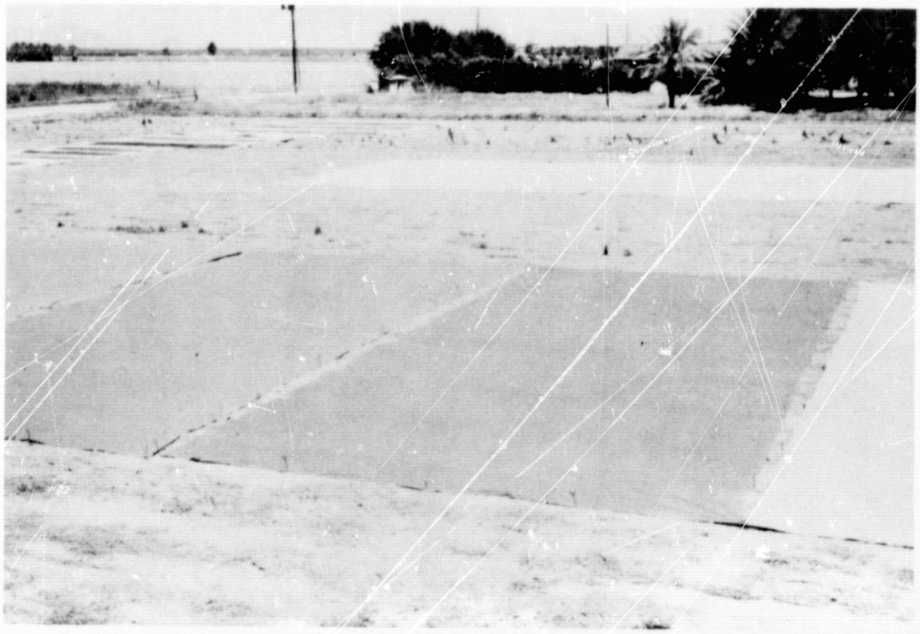

c. 47 filter, f/5 at 1/250 (Plus X-1125).

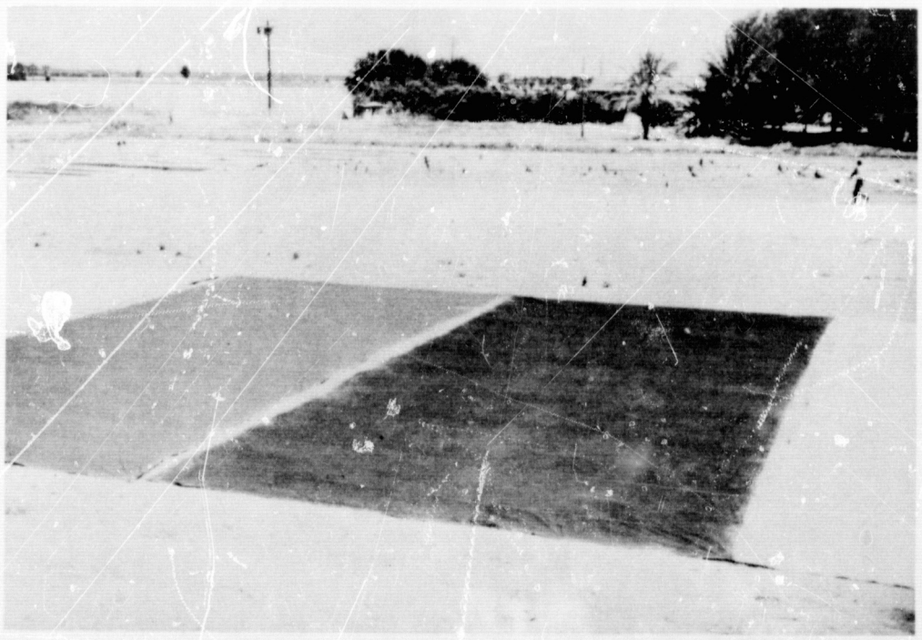

d. 58 filter, f/4 at 1/250 (Plus X-1127).

Figure 3-15.- Concluded.

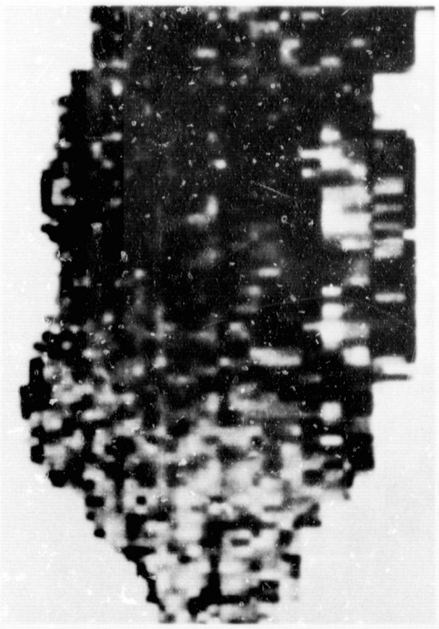

a. Smooth sea.

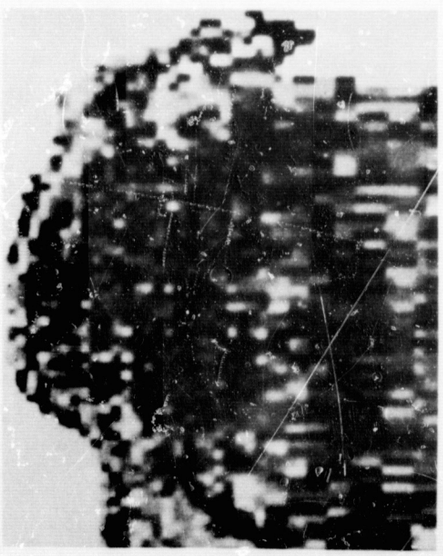

b. Rough sea.

Figure 3-16.- Passive microwave (19.35 GHz) image of Salton Sea. Cooler radiometric temperatures at northern (calm) end; warmer radiometric temperatures at southern (choppy) end. Black and white reproduction of color TV display. NASA Convair 990, 40 000 ft, June 1968.

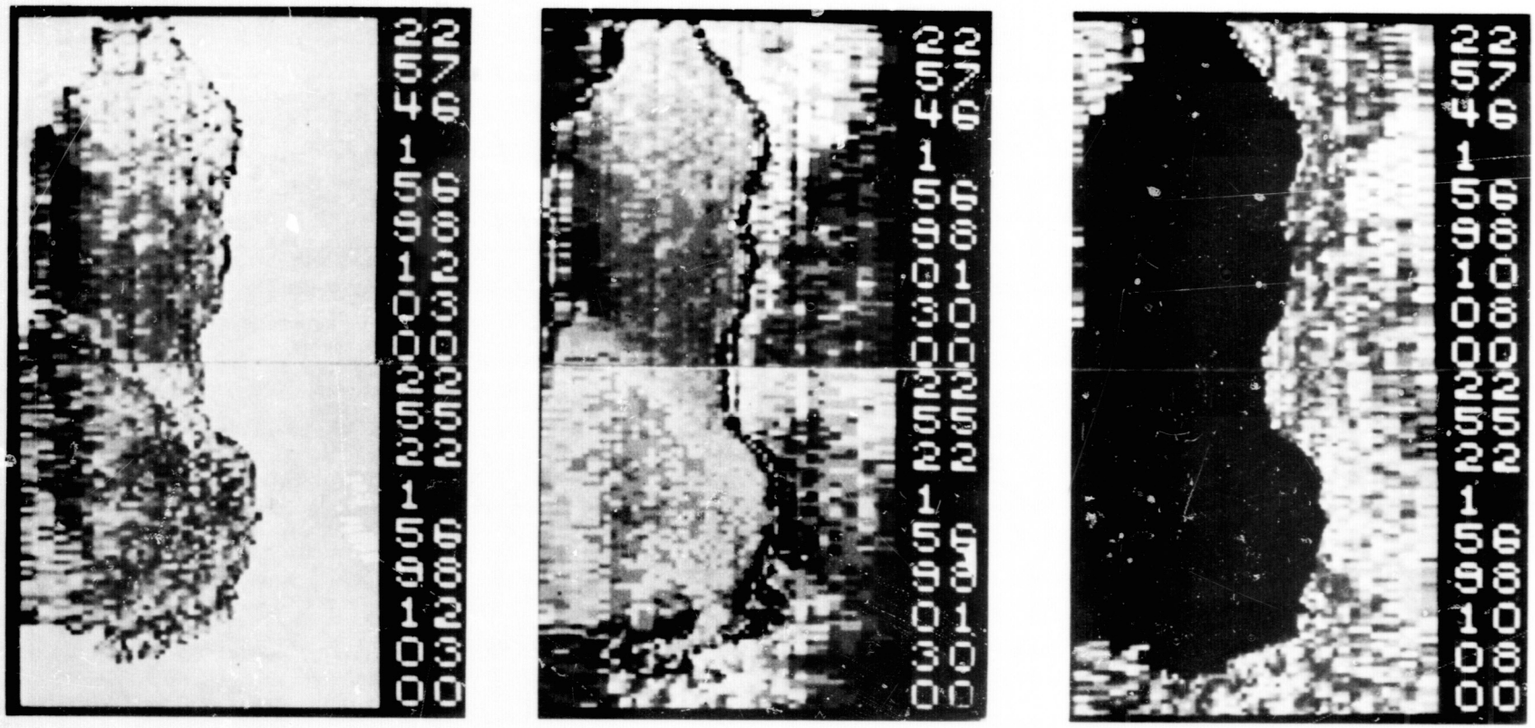

Figure 3-17.- Three playbacks of same passive microwave image of Salton Sea, illustrating advantages of magnetic tape storage and computer data-processing capability. NASA Convair 990, June 1968.

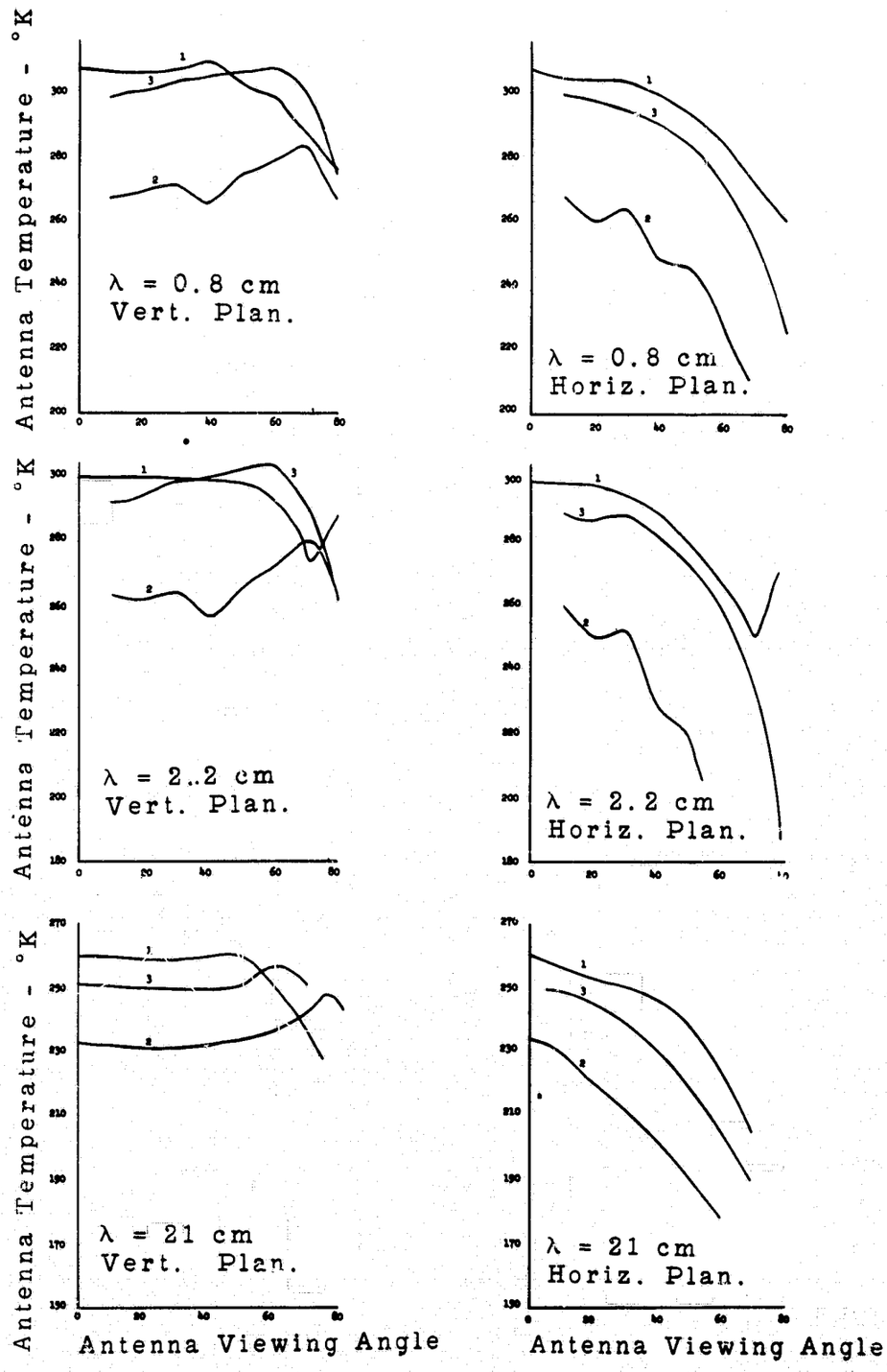

Figure 3-18.- Ground measurements of passive microwave temperature versus viewing angle, Coachella Valley. Site 1, driest soil; site 2, wettest soil; site 3, intermediate moisture content. Aerojet-General Corp

Figure 3-19.- Cotton being irrigated, Imperial Valley. Black and white reproduction of NASA color photograph (Moncrief) May 21, 1968.

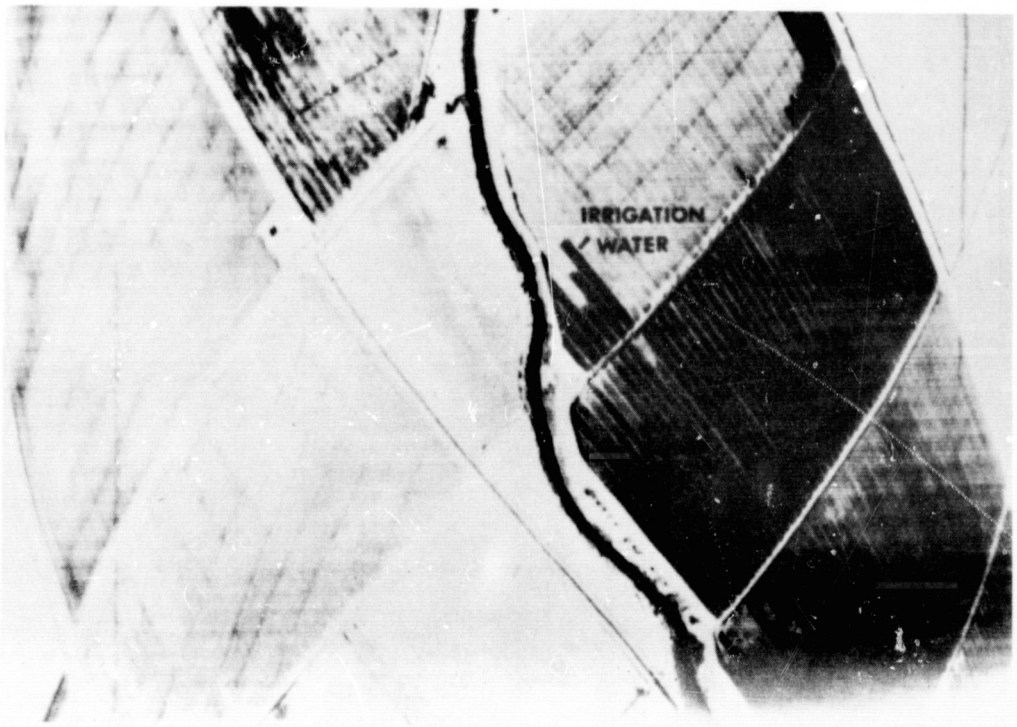

a. Reconofax IV sensor, 8μ to 14μ (date flown: May 21, 1968).

Figure 3-20.- Fields under irrigation, showing advantage of thermal infrared image (Reconofax IV) over panchromatic photograph (RC-8) for identification of moist area. (U.S.G.S./NASA Geographic Applications Program.)

Figure 3-20 (b). RC-8 camera sensor, panchromatic film. (date flown, May 21, 1968)

	[a]AAS-5 UV	ABS SPECTROSCOPE-UV	[a]RC8 B&W	[a]RC8 - COLOR IR	12" CAMERA - COLOR IR	[a]HASSELBLAD COLOR IR	HASSELBLAD - COLOR	TV CAMERA	[a]IR SCANNER - REC IV	[a]SCATTEROMETER	[a]MICROWAVE RADIOMETER	[a]MICROWAVE IMAGER
LAND USE	3	4	2	2	1	1	3	2	2	2	4	3
URBAN	3	2	2	1	1	1	2	2	2	3	4	3
ENERGY BUDGET	4	4	4	4	3	3	4	4	3	4	4	
SOIL MOISTURE	4	4	3	2	2	2	3	4	2		4	

[a]Sensors carried aboard NASA aircraft

USGS/NASA
Geographic Applications Program

Figure 3-21.- Results of use in mission 73 (preliminary): (1) excellent, (2) good, (3) poor, and (4) unusable.

	[a]AAS-5 UV	ABS SPECTROSCOPE-UV	[a]RC8 B&W	[a]RC8 - COLOR IR	12" CAMERA - COLOR IR	[a]HASSELBLAD COLOR IR	HASSELBLAD - COLOR	TV CAMERA	[a]IR SCANNER - REC IV	[a]SCATTEROMETER	[a]MICROWAVE RADIOMETER	[a]MICROWAVE IMAGER
LAND USE	4		3	2	1	1	1	2	4	2	4	2
URBAN	4	2	3	2	1	1	1	2	2	2	4	2
ENERGY BUDGET	4	2	3	3	3	3	2	2	4	4	4	2
SOIL MOISTURE	4		3	2	3	2	2	2	4	2	4	2

[a]Sensors carried aboard NASA aircraft

USGS/NASA
Geographic Applications Program

Figure 3-22.- Recommendations for future research (mission 73 sensors): (1) ready for space, (2) further aircraft testing required, (3) required for indexing only, and (4) drop.

N71-16128

SOUTHERN CALIFORNIA REGIONAL RESOURCES STUDIES

By Leonard W. Bowden
Department of Geography, University of California, Riverside

INTRODUCTION

The Southern California Test Site 130 was established in August 1966 in the Geographic Applications Program as one of a number of test sites for detailed testing of sensor capabilities versus geographic characteristics and data needs. Besides the physical and cultural diversity of the region, encompassing a major coastal metropolitan center and its arid hinterland, advantages of southern California as a remote-sensing test site include more than 300 days of suitable flying weather per year and an excellent road network, enabling ground parties to travel diverse subregions in a reasonably short time. The area is moderately well documented in terms of geologic, hydrologic, land-use, cadastral, topographic, and vegetation data, as well as extensive aerial photographic coverage. There are wilderness and preserved areas adjacent to highly developed urban and recreation areas; there are intensively irrigated lowlands next to deserts, forests, and mountains; and there are old residential areas, modern sprawling suburbs, and diversified commercial, industrial, and transportation activities. Recurring forest fires, flash floods, landslides, and the ever-present danger of earthquakes are additional characteristics of the area. Most recently, there have been conflicts resulting from air pollution, highway traffic congestion, competition for land for urban growth, and social unrest.

TEST SITE OPERATION

The test site was originally operated by the Departments of Geography at the University of California Riverside and Los Angeles campuses, under contract with the Geographic Applications Program, with funds provided by the NASA Earth Resources Program. As of August 1968, the test-site operation is contracted solely to the Department of Geography, University of California, Riverside. The remote-sensing data shown in table 4-I have been obtained from the Convair 240A and the P3A, both of the Manned Spacecraft Center (MSC) Aircraft Program.

TABLE 4-I.- DATA RECEIVED FROM EARTH RESOURCES AIRCRAFT PROGRAM AT TEST SITE 130

Mission	Aircraft	Date flown	Date received	Sensor							
				RC-8	Multiband	Nikon	R-IV/RS-7	AAS-5	Microwave radiometer	Microwave imager	Scatterometer
29	926	8/8/66 to 8/12/66	10/15/66	X			X	X	X		
42	927	3/6/67 to 3/8/67	6/4/67	X							
56	927	9/6/67 to 9/9/67	3/14/68	X			X				
73	926	5/21/68 to 5/28/68	6/3/68	X	X		X	X	X		X

The test site has also benefited from data-gathering flights by a number of other aircraft equipped variously with side-looking airborne radar, a high-altitude telescopic sensor, a four-band multispectral camera along with cameras carrying color and color infrared (IR) film (in association with Edward Yost of Long Island University), and a new commercial thermal IR scanner (Bendix Aerospace Systems Division); by privately flown color IR of several subregions; by passive microwave imagery and matching "color aero neg" from NASA/AMES 990; and by high-altitude military photography and radar. Color photographs taken by the Gemini astronauts over the test site have been obtained and analyzed. Also, gross characteristics of the region are shown by television images from the Nimbus and Advanced Technology Satellite (ATS) spacecraft.

The following five broad characteristics of the regional geography of southern California are being investigated with regard to the potential of aircraft, and eventually spacecraft, sensing feasibility and capability:

1. Land use — pattern, change, and variability

2. Settlement patterns — urban and rural, migration, seasonal variability, and rate of change

3. Problems of the urban environment — transportation, congestion, environmental health, pollution, and fire and flood danger

4. Ecological landscape — vegetation pattern, types of plants and crops, and transitional and altitudinal variations of plant and animal life

5. Physical environmental factors — climatic patterns and change, heat and water balance, soils, vegetation, and landform type and texture

While the overall concept of regional resource analysis has not been abandoned, various missions were more specifically defined. Objectives of recent tests were to correlate multisensor and ground-truth observations and to evaluate the feasibility of sensors and sensor combinations as data-gathering components in aircraft (and eventually spacecraft) in the following areas of emphasis: land use, urban problems, surface energy balance, soil moisture, vegetation mapping, and air pollution analysis.

The following section is a summary evaluation of each sensor listed in table 4-I. However, one crucial point that applies to all the missions (except mission 73) is the time lag between the date flown and the date received of the data. Note particularly the 7-month period that elapsed on mission 56 (table 4-I). As a result, none of the evaluations could be considered timely or quantitative because the ground-truth data and the experiences of the ground teams grew cold during the long waiting period. Often, the researchers moved on into other and different endeavors and were then forced to go back and pick up an almost forgotten mission by the time the data arrived. The opportunity to return to the field and to evaluate the anomalies that appeared in the data was often lost or fruitless.

EVALUATION OF SENSOR DATA RECEIVED

1. Mission 29

a. RC-8 (8443 film with 15 filter). The resolution was poor, and no color contrast or hue was obtained. The data were rated as "not quite as good as if they had flown Plus-X." Land-use mapping was possible (scale 1:20 000), but vegetation, hydrology, urban analysis, or spectral reflectance were impossible to detect. One positive factor of mission 29 was that the inferior color IR film initiated a successful search for filter combinations that have made color IR imagery one of the most successful sensor packages available.

b. Microwave radiometer data. The radiometric profile was uncalibrated and could not be tied to known targets along the flight line. The data were rated as "useless."

c. Reconofax IV, classified confidential at the time of flight. Because of the difficulty of working with classified material in a university environment, the data were never fully analyzed. Overall evaluation came later when additional thermal IR imagery was received from

later missions or other (non-NASA) sensors. The greatest value of Reconofax IV imagery was as a basis of comparison and training for later missions.

d. AAS-5, classified confidential at the time of flight. The data in this mission were originally intended for use in "smog" analysis. Later unclassified AAS-5 imagery has indicated there is little or no potential for this sensor in air pollution research or energy budget studies.

2. Mission 42

a. RC-8 (8442 film and 8443 film with 15 filter). Of all the missions and all the sensors, this package was the most outstanding and most useful received. Flown at high altitude, mission 42 provided small-scale, high-resolution color photography in both the visible and near IR regions over a variety of landscapes. The uses of this film have produced urban and agriculture land-use maps, housing quality studies, vegetation maps, designs for regional planning, hydrologic maps, and "open space" study reports. The 8443 film (color IR) from mission 42 has almost become the standard from which to judge the utility or diversity of other imagery sensors in test site 130.

b. One unfortunate aspect of mission 42 was that no other sensor was operational with which to compare the high-quality photograph for multisensor application.

3. Mission 56

a. RC-8 (2 cameras: 8443 film with 15 filter and 8443 film with 22 filter), almost as good as the color IR imagery from mission 42. Part of the objective was to analyze the utility of the two filters when imaging arid environments. Although not as successful as anticipated, mission 56 paved the way to the research on additive filters that is now part of a technical report (Pease, Robert W.; and Bowden, Leonard W.: Making Color Infrared A More Effective High Altitude Sensor).

b. RS-7, classified confidential. The imagery cannot be described here except to say that it provided the opportunity to examine and evaluate high-altitude thermal IR imagery of the same targets flown daytime and nighttime.

4. Mission 73 — All the sensors and the preliminary findings are evaluated in the previous report by Robert H. Alexander. Overall, the mission was successful and the results encouraging. The amount of work,

effort, and "sweat" that went into mission 73 on the part of the personnel of test site 130, the other user agencies, and the aircraft program was enormous. As principal investigator, I would like to commend and thank the more than 150 people who participated. Mission 73 might well be the initial step in a somewhat more practical operation of multisensor, multiaircraft and spacecraft, and multidiscipline test sites. The idea of combining these aspects rather than proliferating small but diverse test sites, as in the past, is well worth examining for future research and application.

A variety of other data from the aircraft program have been requested to meet specific needs. For example, the panchromatic and color IR imagery flown for test site 27 (Salton Sea) was used in connection with the analysis of the automatic lock-on tracking system imagery taken of the same area. Imagery flown over test site 26 (Scripps Beach) was used in evaluating the Westinghouse side-looking airborne radar (SLAR) (missions 101 and 102) of the coast of southern California, as was the imagery from test site 2 (Pisgah Crater) for evaluating both SLAR and Bendix thermal mapper imagery. The combined photographic coverage from all the missions has contributed significantly to our comparative evaluation of the imaging microwave radiometer flown on the NASA/AMES 990.

From the time of conception of test site 130, we have sought three goals that describe the relationship among NASA, the U.S. Geological Survey (U.S.G.S.), and the University of California, Riverside. One goal has been to define the scientific and economic benefits of remote sensing as a means of examining the resources of a region, the second goal was to make recommendations on the scientific use of sensors in future space experiments, and the third goal was to develop and maintain the proficiency of skilled scientists who can continue in the future with research which uses spacecraft imagery and data for geographic investigation.

Figures 4-1 to 4-9 illustrate some of the imagery obtained over the past 20 months. The figures illustrate some of the accomplishments and point out the need for additional research.

From the experiments and collection of imagery at the Southern California Test Site, the following preliminary judgments are made:

1. Aero Ektachrome IR 8443 is the single most useful sensor package for land use, geomorphology, urban analysis, vegetation mapping, agriculture inventory, and ecological studies when used with the proper filter combinations. The high resolution and clarity of the resultant images are superior to most other film types. Although limited to daylight and cloudless conditions, the ability of the 8443 film to penetrate haze and "smog" is extremely useful.

2. Side-looking airborne radar, multiband photography, thermal IR imagery, telescopic systems, and imaging passive microwave devices are useful as secondary sensors but, for total environmental analysis, are often redundant to color IR imagery and to each other. All seem to have potential for specialized studies such as energy budget but only when closely tied to other sensor combinations and to extensive "on time" ground observations.

3. It is necessary to pay much more attention to ecological and environmental conditions before some of the results of present remote-sensing devices can be understood. In case after case, the sensors produce data or images that cause more questions than they produce answers. The argument for multidisciplinary, multisensor missions (such as mission 73) is justified. However, a point for simple, less complicated missions also needs to be made. For example, under the present program, we were working with camera filters and needed an airborne platform to test the various combinations. A light aircraft with hand-held photography would have sufficed because we wanted to photograph, process, examine, rephotograph, process, and so forth, all within a short time. Using one of the NASA multisensor aircraft was impossible because of scheduling conflicts, slow turnaround on data processing, and nonadaptability of camera-filter systems. The flexibility and control needed for such studies as energy flux, interface conditions, or controlled environment are presently impossible with the available program and aircraft. A more useful and potentially rewarding program might be one where less expensive but more flexible aircraft are contracted for single-sensor tests. The information obtained could then be better fit into an overall multidisciplinary mission of maximum effort using what has been learned as a guide to managing the multisensor aircraft.

Because of our research in land-use mapping, energy budget, urban analysis, and resource inventory, we are now cooperating with the following agencies.

1. San Diego County Planning Agency
2. West Valley Planning Agency
3. San Bernardino County Planning Agency
4. Los Angeles County Planning Agency
5. Los Angeles County Health Department
6. Coachella Valley Soil Conservation District
7. U.S. Wildlife and Game Refuge, Salton Sea

8. United States Geological Survey, Menlo Park

9. United States Geological Survey, Garden Grove

10. TRW Systems, Inc., Redondo Beach

11. Southern California Area Government

12. California Committee on Open Space

13. Aerojet General, Inc.

14. North American Aviation, Downey

15. Western Aerial Survey, Inc.

16. Bureau of Land Management

17. Statewide Air Pollution Control Center, University of California, Riverside

18. California Water Resources Department

19. Department of Geology, University of California, Riverside

20. Chevron Research Labs

21. TRACOR, Inc., San Diego

With each of the preceding, we have operated on a mutual exchange basis with benefit to both parties involved. We have taken the role of advisor and demonstrator in what can and should be done in remote sensing that will benefit these user agencies. For example, through our efforts in remote sensing and the results obtained, we were in a position to recommend to both the San Bernardino and Los Angeles County Planning Agencies that they fly their areas with color IR photography (at their own expense). We are now advising them on interpretation and analysis, and in return, they can furnish us with valuable ideas on user agency needs, benefit-cost, and the ability of remote sensing to replace more conventional and often tedious data gathering necessary to planners. Although it is the role of a university to be both a research and a service agency, often the service is overlooked in such programs as we are now involved. The kind of cooperative ventures just described took place without additional cost or sacrifice to the contract funds and may very well reap as many benefits in the long run as the defined research portion of the Southern California Test Site.

FUTURE NEEDS AND OBJECTIVES

The accumulation of remote-sensing data, while less than ideal, has been adequate enough to evaluate a variety of sensors and capabilities. A matrix of evaluations for each sensor is presented in the paper on mission 73. However, a few points can be added here in reference to the MSC Aircraft Program and the total Earth Resources Program.

1. Aircraft capability

a. The greatest need is for higher altitude performance than has been previously available. High-altitude data from photography need further analysis; in fact, spacecraft altitude is preferred because we believe that the systems and resolution available from photography can yield a wealth of resource information. Other sensors need a variety of altitudes available for complete evaluation.

b. Small-aircraft, single-sensor capability is also desirable (as described elsewhere in this paper).

c. In reference to present aircraft, the opportunity to acquire overflights for a block of time with repeated flights and with the aircraft remaining on station until data are processed is desirable. In the case of newer high-speed long-range aircraft, the possibility of recalling the aircraft for a repeated overflight offers the same merit.

2. Sensors

a. Photography. Overall, the photographic missions have been successful, and the images have been very useful for a variety of studies. The greatest frustration has been the lack of flexibility in camera, film, and filter systems. Very often, we have taken the 9- by 9-inch RC-8 format when a 70-millimeter system would have sufficed. The flying and reflying of the Itek nine-lens system, even though it was established several years ago that the system had limited research and operational capability, was a needless effort. Multiband photography, while still offering potential, is far from a satisfactory sensor. Such items as balanced film, specific spectral wedges, and proper exposure guides for varying altitude and landscape are not yet operational. It is our belief that there presently exists a dichotomy in photographic sensing. On one side is the highly sophisticated mapping camera with high-resolution standardized film that has proved itself many times over; and on the other side is the experimental undeveloped multispectral photography that still needs considerable research and testing before aircraft installation. For example, to take the Yost multiband and color additive system or any of the filter wedges being developed by Slater would be

premature for installation in the new multisensor aircraft. These systems, while potentially useful, need more testing on the ground or in light aircraft before committing them to a large multisensor platform.

b. Infrared scanners and imagers. A more desirable system than presently available would be thermal IR sensors that offer a greater range of the spectrum with more optional band passes available. For example, we have acquired some intriguing but undeciphered results from both 3.5μ to 5.5μ scanners and 8μ to 14μ scanners. A very useful experiment involving dual scanners, sensing at approximately 4.5μ and 10μ simultaneously, would seem to offer regional data on surface energy, atmospheric interfaces, radiation changes, inversion layers, and so forth. Sensors such as the Reconofax IV are too broad in bandwidth to be quantitative and are inflexible to inflight filter changes for varying bandwidth.

c. Passive microwave imager (PMI). At present, the resolution is too poor, but refinement and continued research could develop the PMI into a very useful secondary sensor.

d. Imaging radar. We need imaging radar as soon as possible. From past experience, the K-band side-looking imager is desirable.

e. Other sensors.

(1) AAS-5 ultraviolet — Abandon.

(2) Scatterometer — needs further testing but must be more closely identifiable with position of aircraft. A time tie to a "bore-sighted camera" or connection to such devices as position navigation gear is necessary.

(3) Microwave radiometer — Abandon (in present form).

3. Modifications in Earth Resources Program — The roles and the guidelines of all levels of participation are not clearly defined in the total program. Our experience in working with NASA (both Headquarters and MSC), the U.S. Geological Survey, various other university and line agency researchers, and private industry leads us to believe there is a definite and useful role to be played by each.

The following items, defined by groups, are recommendations for future guidelines and revisions, although they parallel present activities. There is no intent to interfere or to dictate to NASA or Government agencies on how they operate, but to merely make a statement of how we envision a more successful future program.

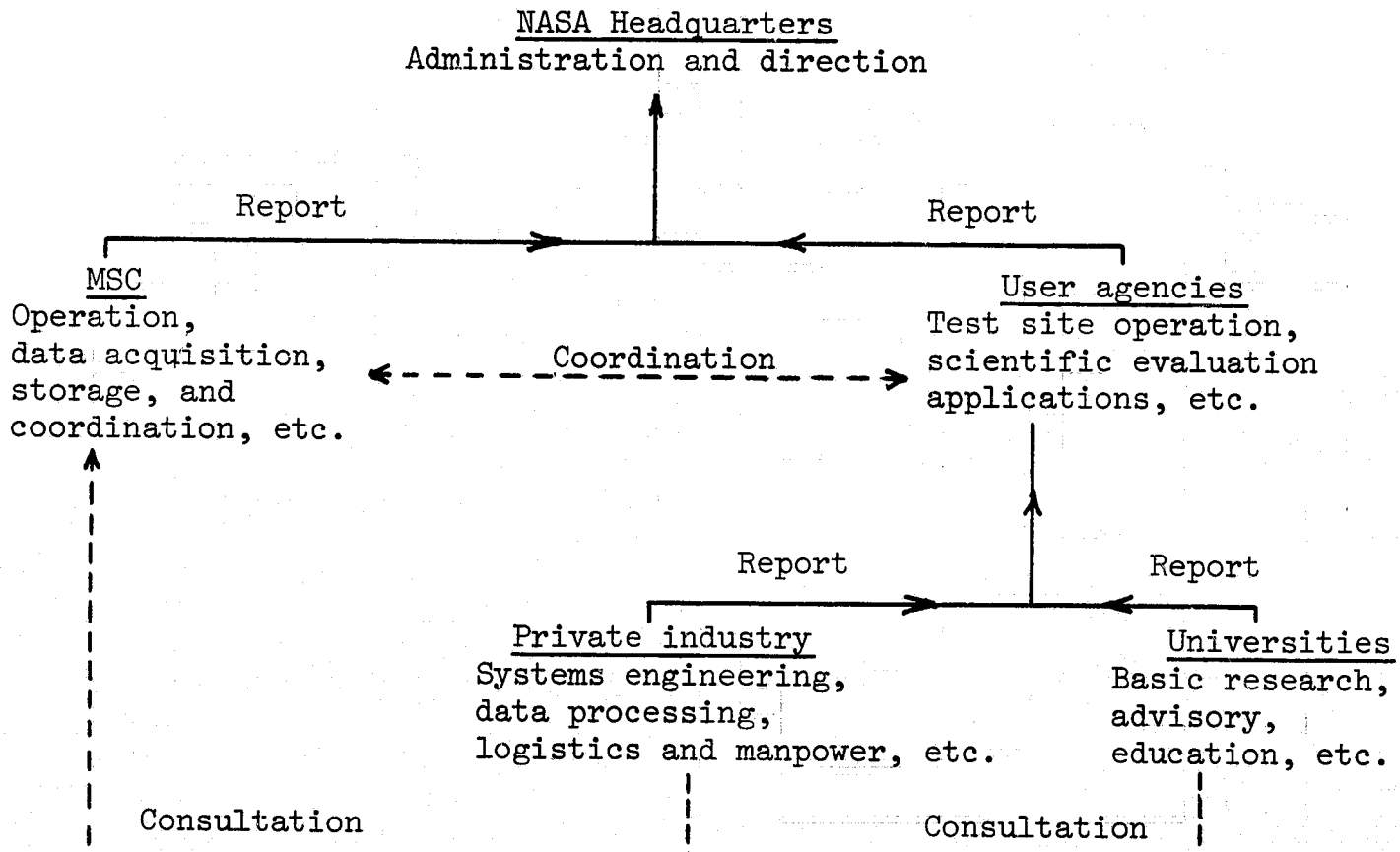

The modifications in t[illegible] foregoing from the present program (whether defined or not) are the following.

1. User agencies (U.S. Geological Survey, U.S. Department of Agriculture, etc.) operate the test sites rather than universities. The user agencies should contract private industry to assist in test operation, and the university should serve as advisor or become involved only when specific research demands it.

2. The role of the aircraft program, under MSC, is to furnish data. The Manned Spacecraft Center acts as a storage and processing center and handles data distribution upon the recommendation of the user agency. The aircraft program is a critical function and should continue to be so for many years. Eventually, the role of present research and development will phase into a role of spacecraft support. The aircraft will someday function with the spacecraft in a manner similar to the way in which ground-truth teams now function in coordination with aircraft.

3. Private industry should play a more significant role than in the past. It is becoming more and more difficult for either the universities or "in-the-field" line agency investigators to handle and operate the test sites. The increase in the industry role is based on three assumptions: (1) that multidisciplinary, firmly established test sites be used

(a necessity long overdue, especially when and if operation moves outside the United States); (2) that a test site be provided with multiaircraft, multisensor data for a specific period (hopefully in connection with spacecraft overflights); and (3) that microscale test-site operation be curtailed or abandoned. If single-sensor, single-purpose testing is needed by a particular researcher, it can be contracted from private industry or similar sources.

BIBLIOGRAPHY

Alexander, Robert H.; Bowden, Leonard W.; Marble, Duane F.; and Moore, Eric G.: Remote Sensing of American Urban Environments. Fifth Symposium on Remote Sensing, University of Michigan, Apr. 1968.

Babcock, Elkanah A.: Annotation of Thermal Infrared Imagery of the Salton Sea Region. Status Report I, U.S. Department of Interior, Contract 14-08-0001-10674, Oct. 1967.

Bowden, Leonard W.: Remote Sensing of the Environment and Its Relation to Geographic Research. Remote Sensing of the Environment, University of California Extension, Los Angeles and TRW Systems Corp, Redondo Beach, California, Aug. 1968.

Bowden, Leonard W.: Multi-Sensor Signatures of Urban Morphology, Function and Evolution. Status Report II, Technical Report 2, U.S. Department of Interior, Contract 14-08-0001-10674, Mar. 1968.

Bowden, Leonard W.: Remote Sensing of the World's Arid Lands. Symposium Sobre Desiertos Costeros, UNESCO/Union Geograficia International, Lima, Peru, Apr. 1967.

Bowden, Leonard W.; Estes, John E.; and Wilson, J. Ellen: ALOTS: Its Relation to Landscape Analysis. Status Report I, U.S. Department of Interior, Contract 14-08-0001-10674, Oct. 1967.

Bowden, Leonard W.; and Pease, Robert W.: Remote Sensing of the Environment and Its Relation to Energy Budget Studies of the Earth. The Eighteenth Technical Conference of the Institute of Geophysics and Planetary Physics, University of California, May 1968.

Francaviglia, Richard V.: Land Use Mapping of Coachella and Imperial Valleys from Gemini Imagery and Land Use and Vegetation Mapping of Indio from Part I - Middle Altitude Ektachrome Infrared Photography, Part II - High Altitude Ektachrome Infrared Photography, and Part III - High Altitude Ektachrome Photography. Status Report I, U.S. Department of Interior, Contract 14-08-0001-10674, Oct. 1967.

Minnich, Richard A.: Identification of San Bernardino Mountains Vegetation on High Altitude Ektachrome Infrared. Status Report I, U.S. Department of Interior, Contract 14-08-0001-10674, Oct. 1967.

Pascucci, Richard; and North, Gary W.: Mission Summary and Data Catalog (Mission 73). USGS/NASA Southern California Remote Sensing Program, Aug. 1968.

Pease, Robert W.; and Bowden, Leonard W.: Making Color Infrared Film A More Effective High Altitude Sensor. Status Report II, Technical Report I, U.S. Department of Interior, Contract 14-08-0001-10674, Oct. 1967.

Pease, Robert W.: Making Color Infrared Film A More Effective High Altitude Sensor. Remote Sensing of the Environment: An Interdisciplinary Journal (in press).

Pease, Robert W.: Color Infrared - A Boon to Geographers Who Fly. Association of American Geographers, Washington, D.C., Aug. 1968.

Zech, Gerald A.: An Attempt to Isolate Saline Soil Tone Signatures on Infrared Ground Truth Photos. Unpublished M.A. Thesis, University of California, Los Angeles, California, June 1967.

Figure 4-1.- Indio Area, Coachella Valley; Aero Ektachrome IR 8443 obtained on mission 42, NASA aircraft 927, March 1968; scale 1:78 000.

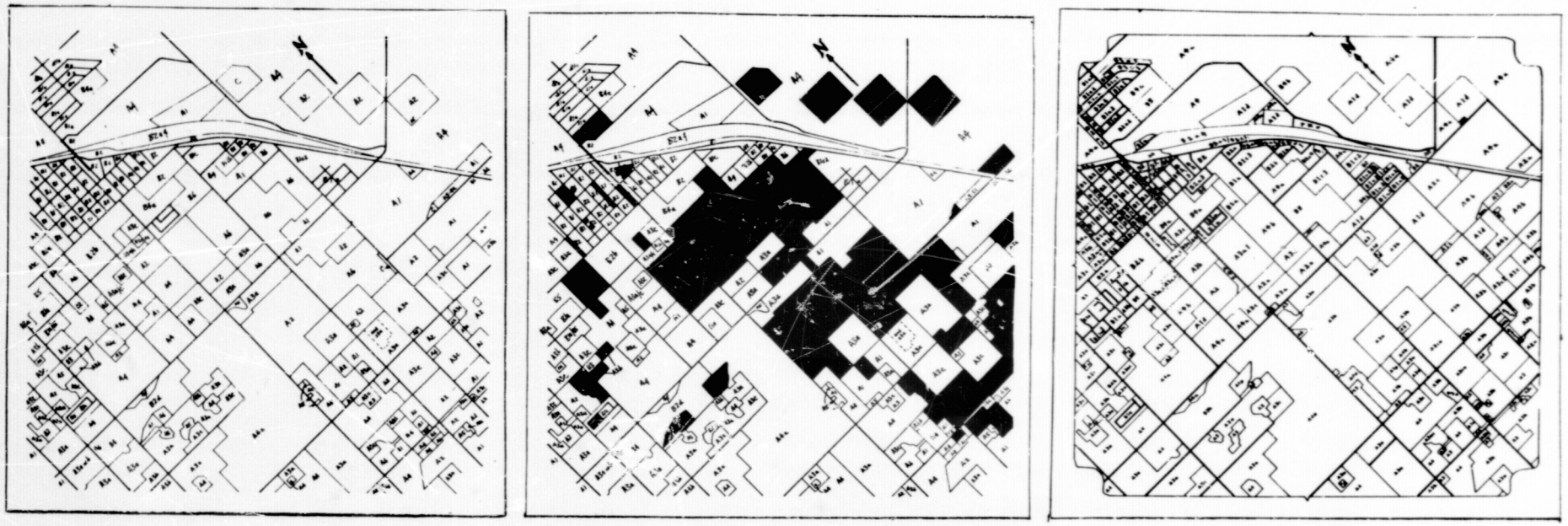

LAND USE EXTRAPOLATED FROM COLOR I.R. PHOTOGRAPH

CLASSIFICATION ERRORS DISCOVERED BY "GROUND SURVEYS"

CORRECTED LAND USE MAP

Figure 4-2.- Land-use map of Indio area. The original map was constructed from imagery taken on mission 29, and the corrections were made prior to mission 42. If the map had been constructed from mission 42 imagery shown in figure 4-1, the errors would have been greatly reduced. As of October 1968, we will have completed a detailed land-use map of the entire Coachella Valley at a scale of 1:62 500. The map has been constructed entirely from information gathered on the various missions, and sample surveys indicate that it contains less than 1 percent error in classification and identification.

a. IR Imagery of west Los Angeles.

Figure 4-3.- A reduced image of west Los Angeles acquired on mission 42. The two maps were constructed entirely from the imagery. Ground checks indicate that they are more accurate than those compiled by the Los Angeles County Planning Agency during the same year, and both were completed in 2 weeks (as compared to several months for the Los Angeles County Planning Agency maps).

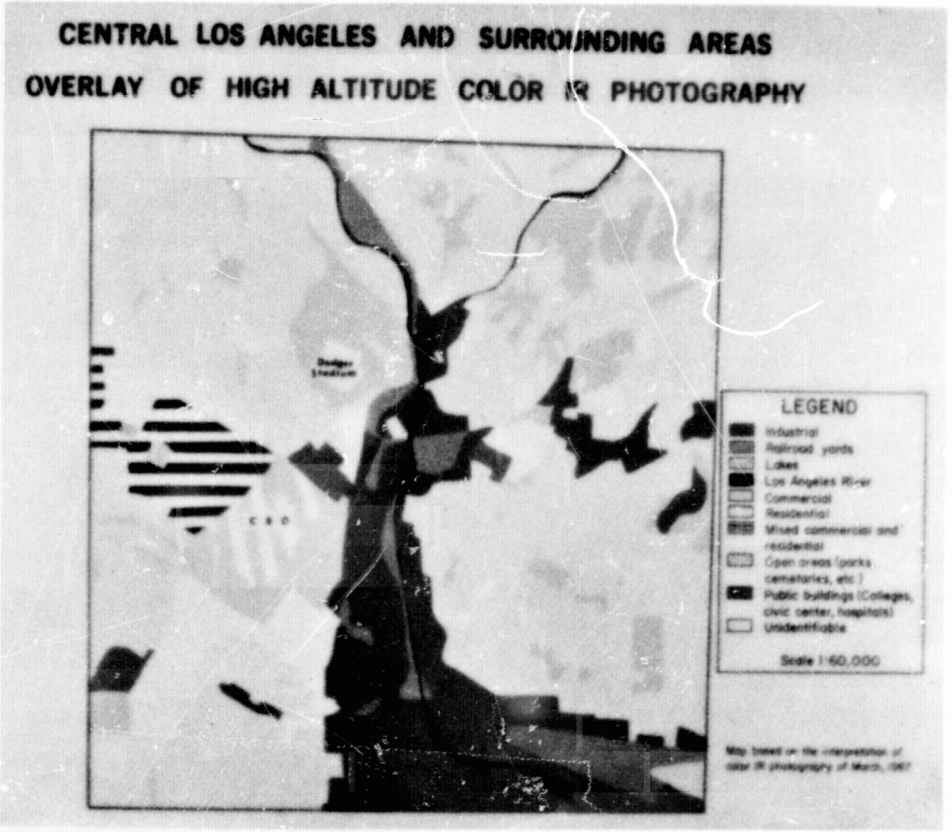

b. Maps constructed from IR imagery.

Figure 4-3.- Concluded.

a. A black and white print made from the same transparencies roll as the copy in figure 4-3. The arrow points to the Century City Plaza photograph. The original roll is scale 1:60 000, imaged from 30 000 feet.

Figure 4-4.- Views of Century City Plaza.

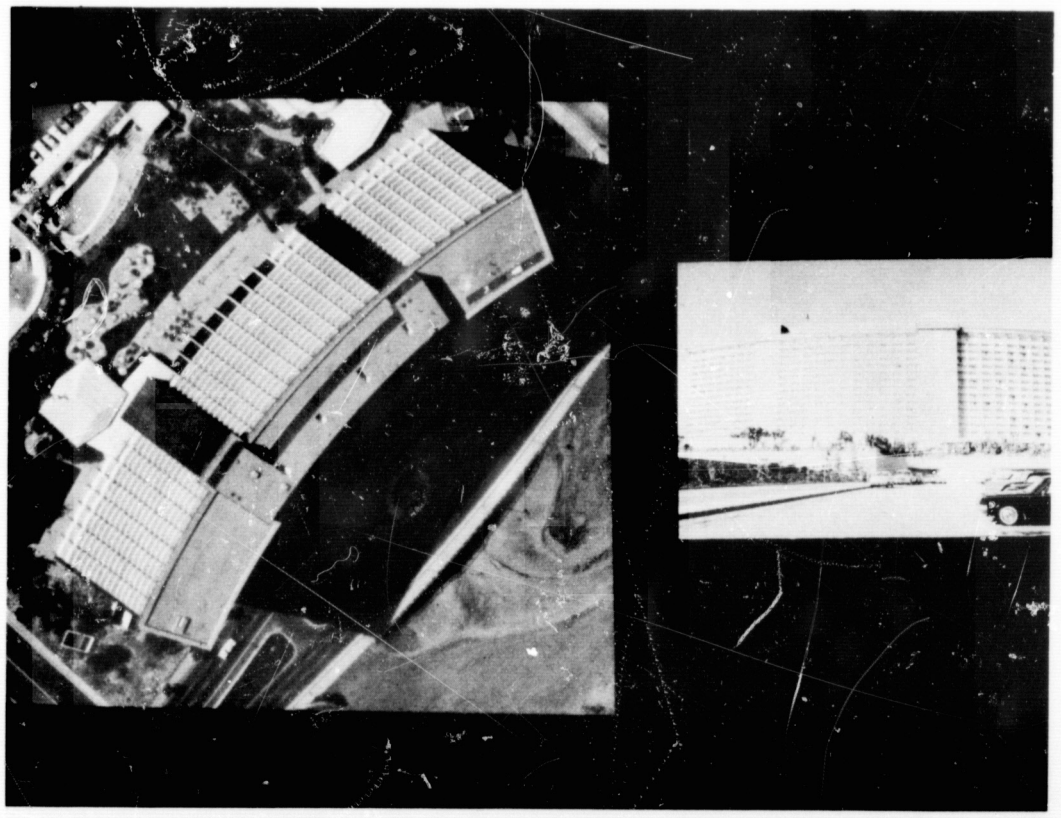

b. Century City Plaza as imaged by the automatic lock-on tracking system from 40 000 feet; scale 1:1500.

Figure 4-4.- Concluded.

a. Black and white print of Alamo River Delta area taken on mission 22 (test site 27), scale 1:20 000 on original; outlines are index frames of images taken by the automatic lock-on tracking system.

Figure 4-5.- Imagery from mission 22, test site 27.

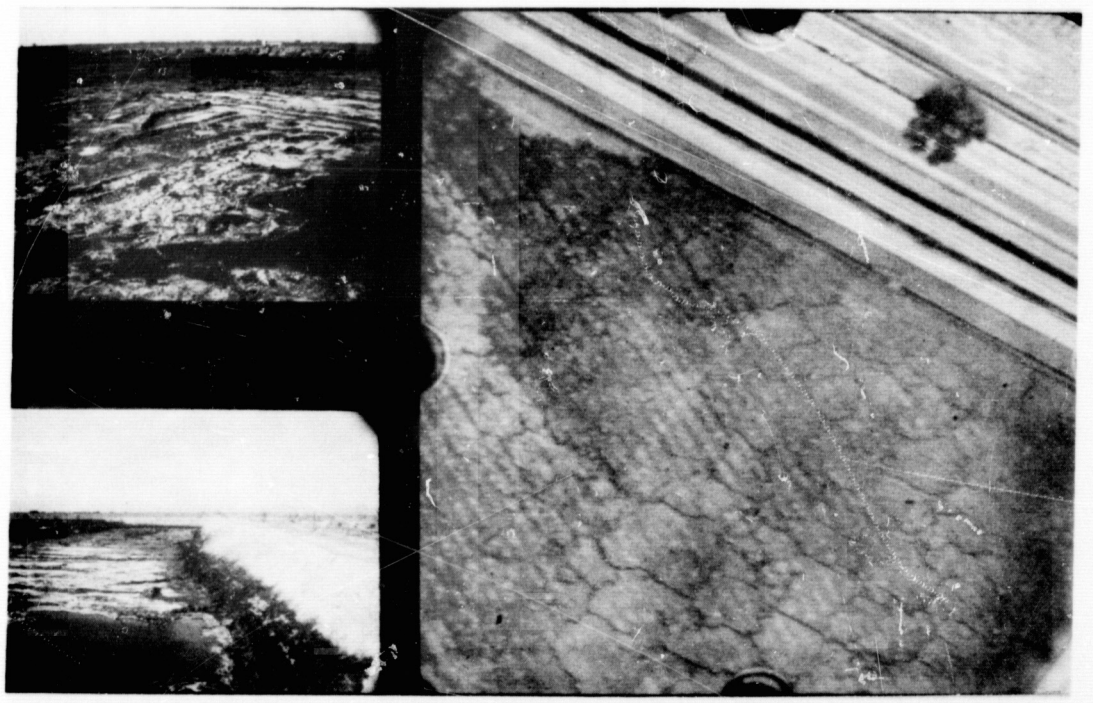

b. Automatic lock-on tracking system 70-millimeter frame of the area shown in the upper outline in figure 4-5a. This print is a copy made from the original Anscochrome transparency. Figures 4-5a and 4-5b demonstrate a level of resolutions obtainable from varying altitudes and scales. The major point is that images of the scale of figure 4-5a can be obtained at spacecraft altitudes if systems such as are in figure 4-5b are used.

Figure 4-5.- Concluded.

a. Photographed from Gemini V. Note the road, railroad, and vegetation pattern on the east (far) shore at the base of the Chocolate Mountains.

Figure 4-6.- Salton Sea area.

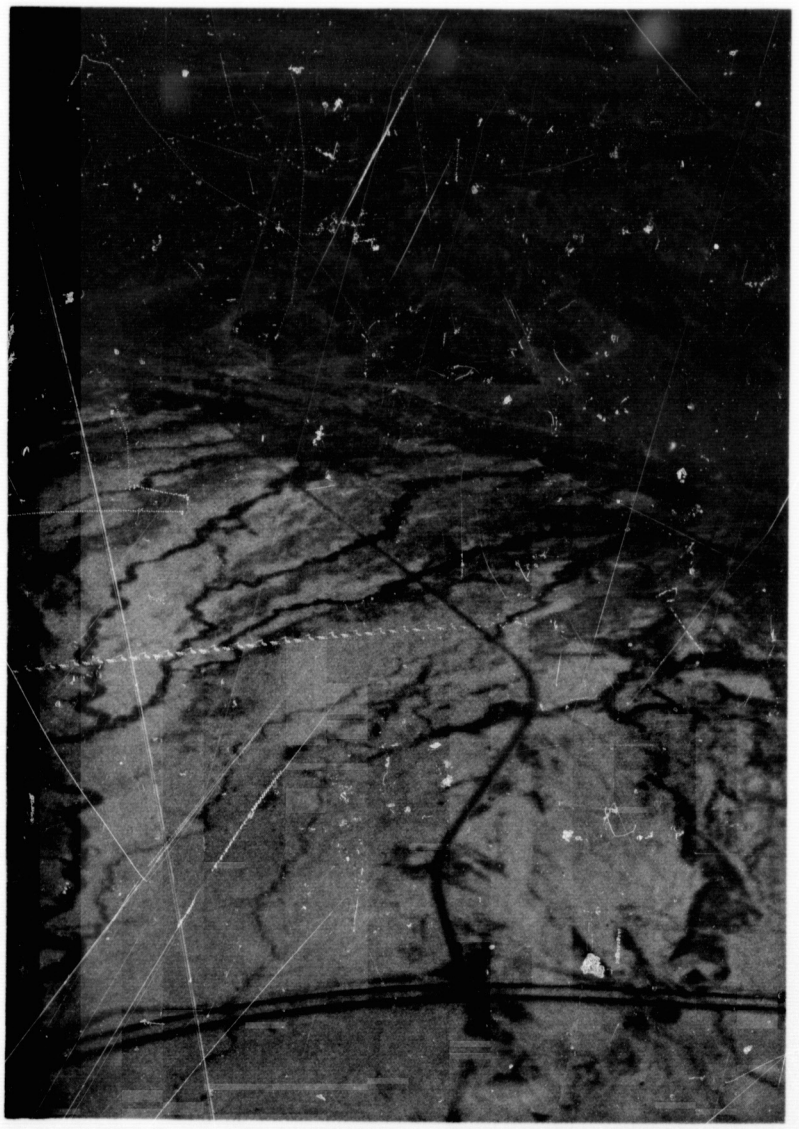

b. Aero Ektachrome IR 8443 taken on 35-mm film with 15 plus 80B filter during mission 73. The IR reflectance through 15 000 feet of atmosphere is enhanced by this filter combination. The riverine vegetation is a surrogate of the seepage from the unlined All-American Canal and a valuable indicator of the water loss resulting from poor construction and management of the distribution system.

Figure 4-6.- Concluded.

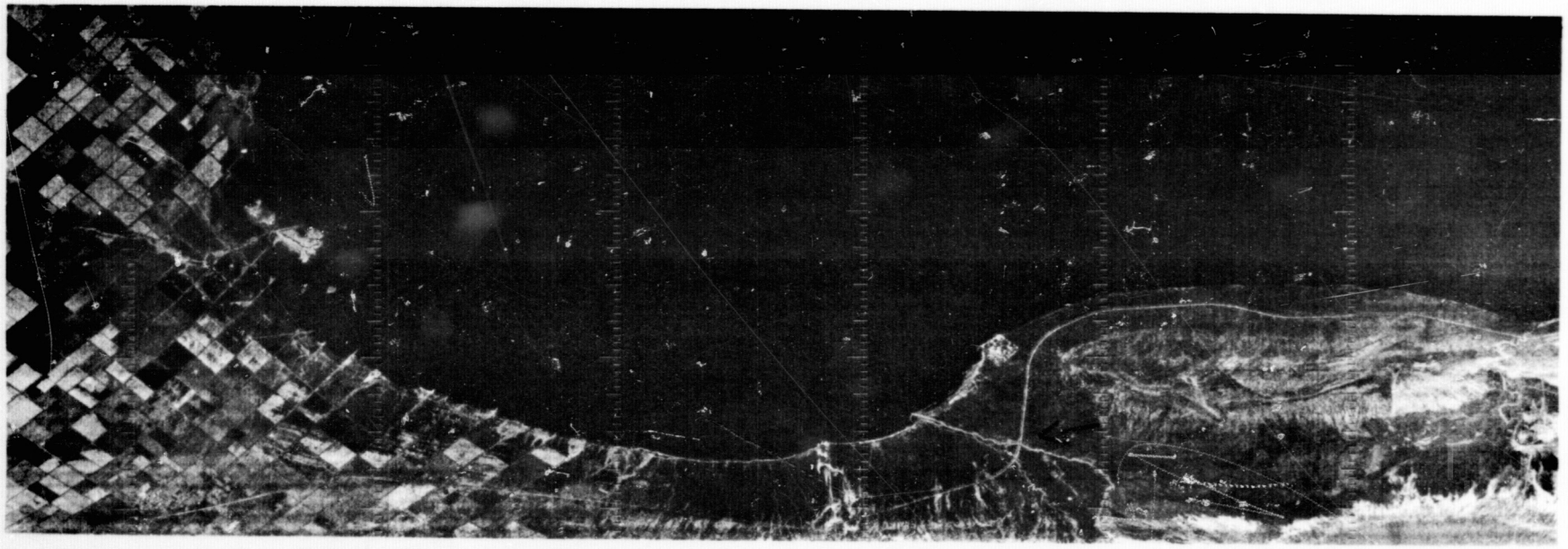

a. Reconofax IV 8μ to 14μ image of the same area as shown in figures 4-6b and 4-7b taken at 23:00 hours on mission 73. Note that the data (arrow) are more informative for resource analysis than figure 4-7b but inferior to figure 4-6b. The broadband width and the noticeable change due to AGC (automatic gain control) as the sensor crossed the shoreline have resulted in a less satisfactory image than figure 4-6b. However, the point must be made that both figures 4-7a and 4-7b are nighttime images and are useful for certain other types of analysis.

Figure 4-7.- Imagery from missions 73 and 102.

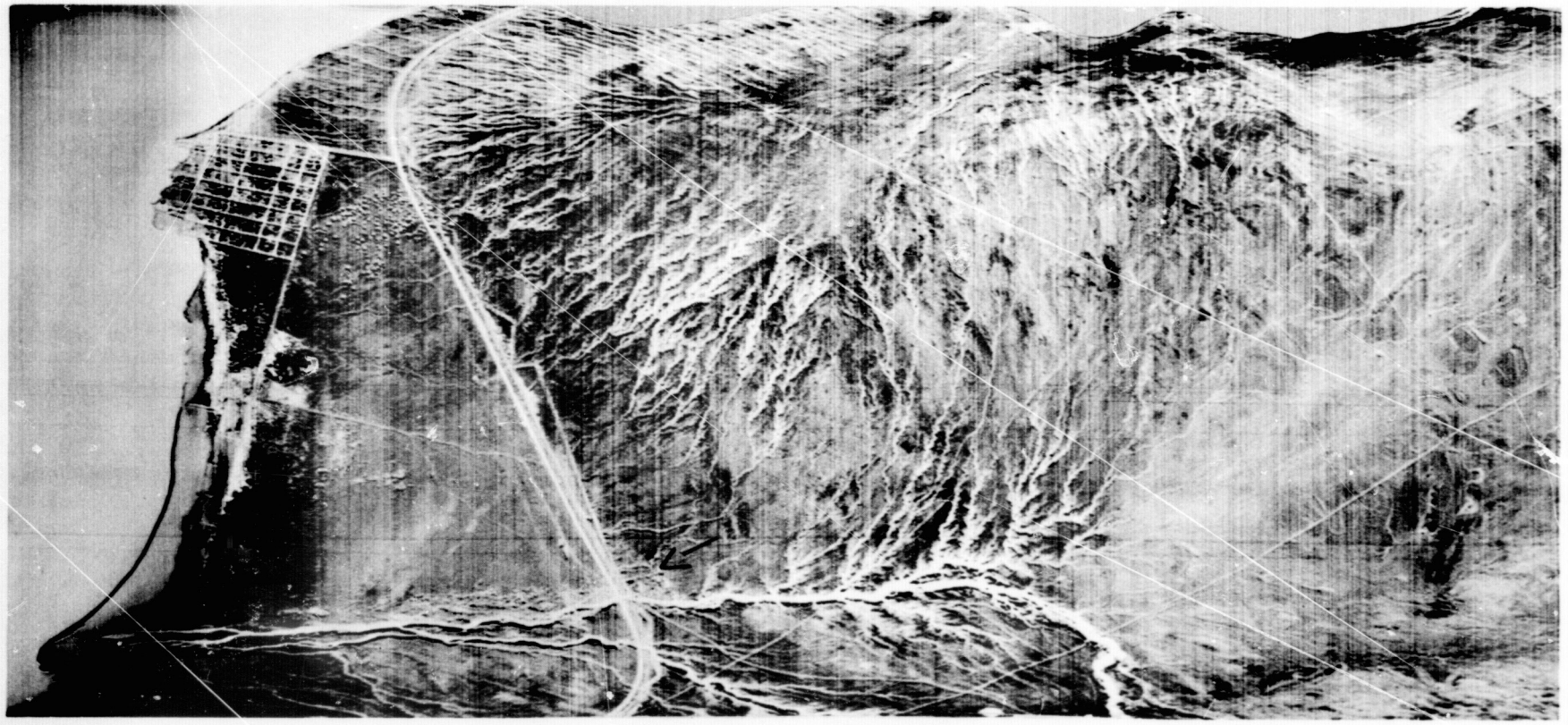

b. AN/APQ-97 side-looking airborne radar of the east shore of the Salton Sea (Westinghouse mission 102). Compare the information obtainable from that shown in figure 4-6b. Note that the railroad and riverine vegetation (arrow) show but cannot be clearly identified or distinguished as in color IR.

Figure 4-7.- Concluded.

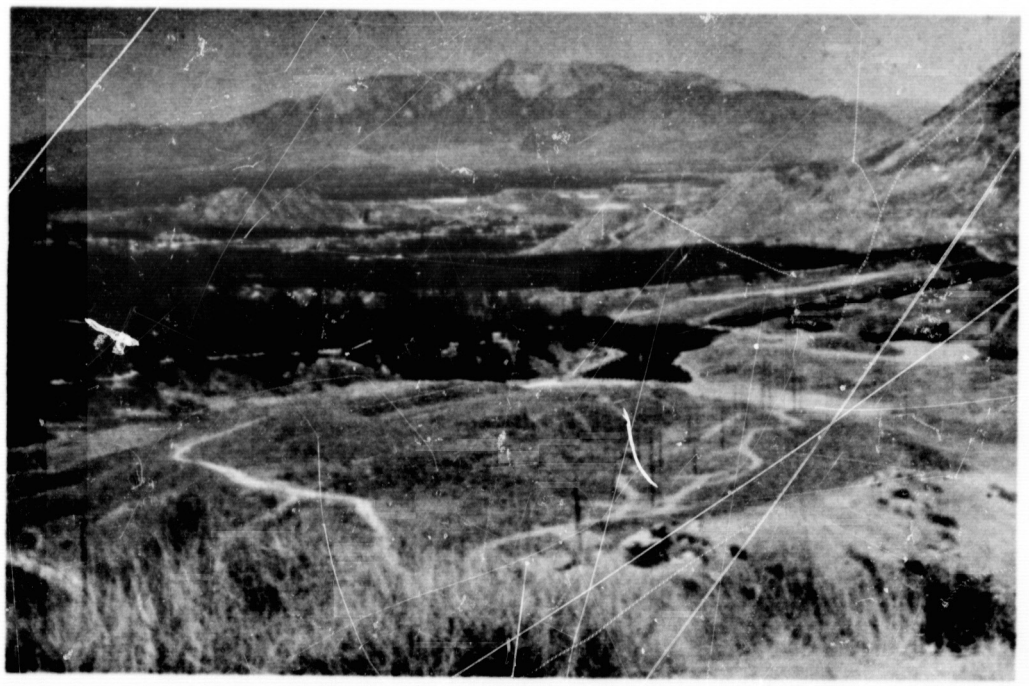

a. A normal color view across the eastern end of the Los Angeles Basin on a moderately clear day. The San Gabriel Mountains are approximately 25 miles distant. The coastal sage vegetation cover in the foreground in this fall season is at a minimal level of vegetative growth.

b. The effect when only minus-blue (Wratten 15) filtration is used. The orange groves in middistance are a deep red. Only a slight hint of color on the distant mountain slopes marks conifer forest. Nearby off-season vegetation shows no IR reflection. Like all the views on this plate, this picture was taken within minutes of the others.

Figure 4-8.- The effects of various additive enhancement filters on type 8443 film, the results of a filter experiment conducted at the test site and reported in Remote Sensing of the Environment: An Interdisciplinary Journal. (A final and successful test of this experiment was conducted with 70-mm Hasselblads aboard NASA aircraft 926 during mission 73.) Time: 1:30 p.m. in early October 1967.

c. The effect when a CC30B additive enhancing filter is used. Mild IR reflection shows on the distant mountains. The orange groves are brighter, more red — a characteristic of this enhancement. A little red shows in the nearby vegetation. The yellow cast is typical of blue color-compensation filters.

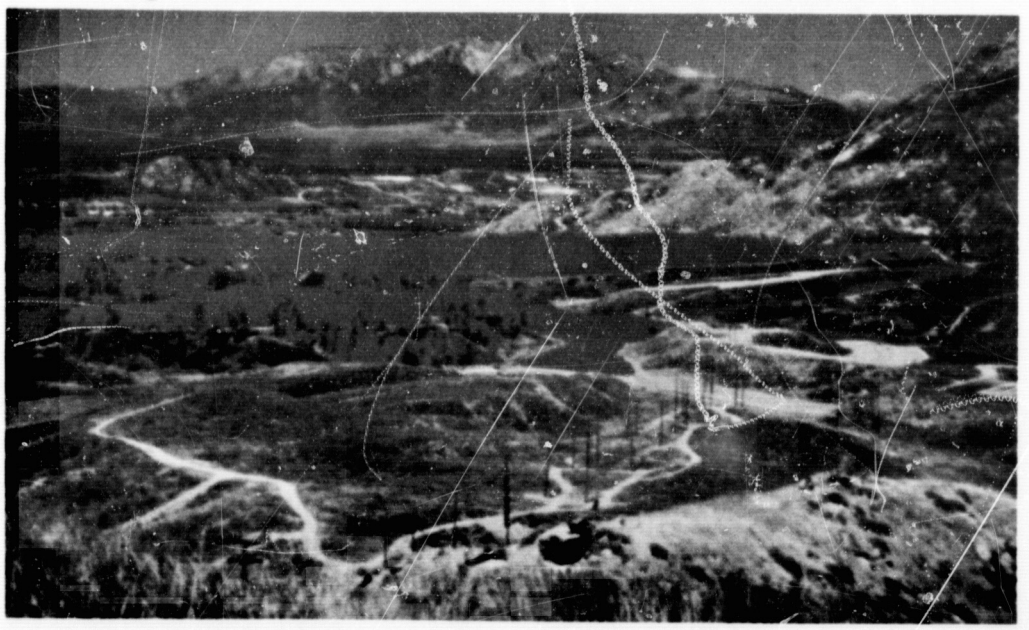

d. The effect when an 80B is used as the additive filter. The conifer forests on the distant mountains are now yielding a strong IR record. The color reproduction fails to show how intense the red of the orange groves has become, and considerable IR record occurs from the nearby off-season vegetation. Note that rocks and soil have become neutral in tone.

Figure 4-8.- Concluded.

a. In this view of the Canadian River of Oklahoma, taken with color IR film from an altitude of 40 000 feet, the false color blushes of newly sprouted winter wheat give a strong IR record. The distant bend in the river flood plain is approximately 50 miles away, yet the red reflection penetrates through this great thickness of atmosphere. This picture was taken from an airliner window with a 35-mm camera, using a CC30B filter in addition to the basic minus-blue Wratten 12 filter recommended for the film. Time: 3:45 p.m. in mid-October 1967.

Figure 4-9.- Color IR imagery of Canadian River of Oklahoma and Pomona-Claremont area of Southern California.

b. Pomona-Claremont area of Southern California taken on 35-mm color IR film at 17 000 feet with additive 80B filter through airliner window in late December. Ozone "smog" count was 18 ppm, and a distinct inversion line is detected about midway up the slopes of the San Gabriel Mountains. Single-family suburban housing patterns can be distinguished, as well as vacant land, orange groves, vineyards, and grazing land. Distinct color differences of the various arteries differentiate freeways from streets and/or empty flood canals. Ribbon commercial developments, industrial sites, shopping centers, and recreation areas also have individual responses. There is a color change between the higher conifers and the upper boundary of chaparral. "Smog," which tends to be yellow in color, is best penetrated by this filter combination. A matching Kodachrome-X with a Tiffen Haze 1 filter revealed little more than the top of the inversion with the mountain peaks showing through.

Figure 4-9.- Concluded.

N71-16129

LAND USE AND REGIONAL ANALYSIS

By Robert W. Peplies
East Tennessee State University

EAST TENNESSEE STATE UNIVERSITY

As a result of the Houston Conference on the "Use of Spacecraft in Geographic Research," the Geography Department at East Tennessee State University (ETSU) decided to become involved in the remote-sensing program in 1965. With a grant from the Office of Naval Research (contract number N00014-67-A-0102-0001), attention was focused on the Asheville Basin in western North Carolina (NASA site 46) and particularly on a flight line across the general "grain" of different geographical features which are typical of the Southern Appalachians (fig. 5-1).

The test site occupies the drainage basin of the Upper French Broad River within the Asheville Basin of western North Carolina, a part of the Blue Ridge physiographic province. The area encompassed in the Upper French Broad River Basin includes four counties of western North Carolina: Buncombe, Henderson, Madison, and Transylvania. The land area of the basin is approximately 1638 square miles. With an orientation of N 35° W and a length of approximately 50 miles, the flight corridor extends across the Upper French Broad Basin from the drainage divide east of Hendersonville in the southeast to a point on the French Broad River northwest of Hot Springs. The type of terrain traversed is variable. It consists of both steep mountains and hill lands and gently undulating relief forms interspersed with floodplains.

Initially, the research theme for studies in remote sensing in the basin was to do regional analysis. This approach, while it provided a great amount of research latitude, was too broad and too inclusive. Two problems prevented achieving the original goal which was to be accomplished: (1) a logistical problem (trained manpower, equipment, and finances) and (2) the fact that remote sensing is not the panacea for discovering all of the answers about a region. In the second phase of the ETSU program, the general regional analysis task was approached from specific problem-oriented viewpoints, especially in terms of the individual investigators' research interests. In general, these interests could be classified in two categories: (1) interests which

resulted from looking at sensor records and seeing "things" which signify significant geographical relationships, and (2) looking at sensor records for specific "things" which were known to exist.

Between November 1965 and the present, five overflights were made of the Asheville Basin test site with the use of the NASA Convair 240 and P3A, and two flights with the use of the Westinghouse radar aircraft (appendix A). The first three overflights (November 1965, May 1966, and October 1966) were at low and medium altitudes (approximately 2000 and 12 000 feet above mean terrain elevations), and the last two flights were at high altitudes (approximately 20 000 feet). During the first overflight, more than 100 people from ETSU and Tennessee Valley Authority (TVA) formed the ground-truth team. Large quantities of ground data were collected, including among other things black and white and color photography, soil and soil moisture samples, air temperature and humidity readings, and radiometric readings (appendix B). The TVA provided hydrologic data and established specific vegetative monitoring sites. In cooperation with the forest service, TVA lit a small forest fire for us, which was not recorded because the aircraft was slightly off the flight path. During subsequent flights, smaller field groups were sent out, and specific ground data were collected, particularly in relation to the problems on which the different investigators were working.

Although the research themes of ETSU investigators focused on different areal and spatial subjects, the different projects are related to land use and regional analysis in varying degrees. Among the various findings that we discovered through these investigations, the more significant with respect to land use are described in the sections immediately following.

Comparison of Color Infrared, Color, and Panchromatic Films for Interpreting Rural Land Use Characteristics

In this experiment, color infrared photographs were compared with color (Ektachrome) and panchromatic photos to determine the relative ease, speed, and certainty with which features associated with rural land use could be identified and studied.[1] Specific features associated with land use in the Asheville Basin (e.g., terrain, drainage, vegetation, farmstead characteristics, farm layout, field movement patterns,

---

[1]Samol, David: Rural Land Use Analysis Via Ektachrome Infrared Photo Interpretation. (Unpublished master's thesis, Department of Geography, ETSU, 1968; contract number N00014-67-A-0102-0001.)

crops and crop emphasis, and farming techniques) were identified on all three types of photographs, and the differences in signatures were noted. The accuracy with which features were identified through photo interpretation techniques was established by field checking. In addition, an attempt was made to delimit agricultural regions directly from the photography.

A general conclusion of this study, on the basis of all available evidence, is that color infrared photographs appear to be superior to Ektachrome and panchromatic photos for interpretation of rural land-use features, and that the most prominent advantage offered by infrared film for use in land-use studies is the unique representation of vegetation. The film provides substantial variation in image colors representing vegetation, thereby allowing the interpreter to distinguish between types of vegetation in terms of physiology, maturity, and health. It is the investigator's opinion that color infrared film can be more effective than either color or panchromatic films in the study of distribution of crops and crop systems, agricultural emphasis and degree of specialization, farm and farmstead morphology, variations in agricultural activity, and distribution of land management practices. This conclusion can be positively stated for the Asheville Basin and for areas with similar environmental traits.

Integrated Landscape Analysis Via Radar Imagery

The general hypothesis of this experiment was that radar provides a means for delimiting varying associations of physical and cultural phenomena through outlining variations in tone, texture, pattern, and shape.[2]

Patterns which were delimited on radar image were visually correlated to data collected via air photos, from the findings of other investigators, and from field investigations. It is admitted that statistically valid sampling techniques and quantitative analysis are more meaningful and will be used eventually. These techniques, however, were beyond our capabilities, especially in terms of equipment and finances (although some small attempts were made in this direction). Nevertheless, it can be shown that enough information can be interpreted from the radar images basically to characterize a number of relatively distinct regions in the Asheville Basin (fig. 5-2). The very thing,

---

[2]Nunnally, Nelson: Integrated Landscape Analysis with Radar Imagery. (Unpublished manuscript, ETSU, 1968; contract number N00014-67-A-0102-0001.)

however, which permits the rapid identification of integrated landscapes, namely the small scale and limited resolution, prohibits interpretation of detailed regional variations.

The interactions of K-band radar with different physical and cultural phenomena, including among other things, fields, vegetation, roads, water bodies, and terrain features, make it possible to differentiate areas which exhibit a more or less homogeneous pattern throughout and which are distinctly different in appearance from other areas. From the radar image of the Asheville Basin, 11 distinct areal patterns were delimited, and some of these could be subdivided on the basis of variations within the main patterns.

In conclusion, the radar regions delimited in this study do appear to correlate with distinctive integrated landscape types. However, there is reason to suspect that rapid, reliable regional delimitation of a similar type can also be carried out by the use of small-scale and hyperaltitude photography.

Radar Study of Linear Features

There are obvious numbers of linear features contained in the radar images of the Asheville area.[3] The ability to map such features aids in locating relatively high-yield water well sources in the crystalline rocks of the southern Appalachian region. At the present time, many low-ordered central places in the Appalachians are associated with these sources, and knowledge of where sources of adequate flows of water exist has stimulated industrial, residential, and certain types of agricultural land-use activities.

The linear features were mapped from radar images, and their orientations were compared with the orientations of joints and shear zones that were previously located and measured by field workers. Stereograms which have been produced of the orientations show remarkable parallelism between the two sets of features (fig. 5-3). It has been concluded that bedrock fractures in the Asheville test site produce linear features at the topographic surface which are emphasized on the radar image owing to the low angle of look.

---

[3]Williams, Lyman O.: Radar: An Aid to Geologic Mapping of Crystalline Rocks at Test Site 46, North Carolina. (Unpublished manuscript, ETSU, 1968; to be published as a NASA technical report, contract number N00014-67-A-0102-0001.)

Trade-Area Analysis

The major thesis of trade-area analysis was to investigate the potential use of remote-sensor imagery for determining trade areas and traffic flow.[4] Dominant directions of traffic flows can be determined from observations of black and white panchromatic, color, and color infrared film. Color infrared film, however, is superior for interpretative purposes (fig. 5-4). Markings (generally blue on infrared color) appear to indicate the major directions of turning movements at intersections and the more heavily traveled routes. The exact cause of these markings is not known, but they appear to be a result of oil droppings, rubber left by vehicles, or moisture in the ruts of roads. Changes in the dominant direction have suggested that such patterns could be used as criteria to supplement the delineation of trade-area boundaries.

Where possible, traffic flow direction at road intersections and driveway connections were interpreted from medium- and low-altitude false color imagery. The traffic flow directions were plotted on standard series topographic maps, 1:24 000 (fig. 5-5). Flow in two opposite directions in the same area was interpreted to mean a transition zone between two trade areas. These data were then field checked and compared to theoretically derived trade regions. In general, the interpreted trade region closely approximated the actual trade patterns in the Asheville Basin.

The investigator has concluded that direction of traffic flows can be more quickly determined from certain types of remote-sensor imagery relative to the time required by field work; and, to a certain degree, trade areas and trading habits can be ascertained from the patterns that traffic flow exhibits in a region. However, any study of this type (especially of trading habits) demands some "ground" knowledge of the economic, cultural, and physical traits of the area.

Farm Pond and Lake Study

Within the study area of the Asheville Basin, there are some 33 farm ponds and lakes. After a cursory inspection of the initial imagery that had been flown over the basin, it was observed that the ponds showed up in different colors on color and color infrared emulsions and with different gray tone values on panchromatic films. The factors responsible for these differences were hypothesized. It is the opinion

---

[4] Honea, Robert: Trade Areas and Traffic Flows Via Remote Sensor Imagery. (Unpublished manuscript, ETSU, 1968; contract number N00014-67-0102-0001.)

of the investigator that certain physical variables of the environment, such as water depth, sediment sizes and concentration, organic content, water mass surface area, and water temperature, interact to determine the color of water bodies on color and color infrared films and the gray tone on panchromatic films.[5] In addition, it was our opinion that the color characteristics of the films (as well as the gray tones) have some relationship to the overall land use and to land-management characteristics of the farm pond and lake drainage areas.

During subsequent flights, water samples and water data were collected from all of the ponds in the Asheville area, and each variable mentioned previously was measured. Pearson's coefficient of correlation and multiple regression analysis techniques were applied to the data. The results indicate that two factors are the most important variables in contributing to water body colors on color and color infrared emulsions — water depth and sediment concentrations. In addition, it is our opinion that certain quantities of organic materials (particularly algae) contribute to the color differences. These differences, however, are not noticed until certain threshold levels of coverage over the surface of a pond are reached. Laboratory experiments to discover these threshold levels have not been successful.

It is the principal investigator's opinion of this particular experiment that if we can control some of the parameters that affect the variations of colors on color and color infrared films for farm ponds, particularly depth of water, we can then get a "handle" on such things as the erosional characteristics, land-use intensity practices, and land-management practices in small (and perhaps large) drainage basins.

Slope Failure Forms Detectable Via Remote Sensing

Another study (actually three parts) with a similar product in mind is being conducted with respect to slope failure.[6] Slope failure forms

---

[5]Williams, Lyman O.: Preliminary Study of Colors on Selected Remote Sensor Photographs of Water Bodies in the Asheville, North Carolina Test Site. (Unpublished manuscript, ETSU, 1968; contract number N00014-67-0102-0001.)

[6]Poole, Donald H.: The Development of Criteria for Recognizing and Identifying Slope Failure Forms as Depicted by Remote Sensor Returns. The Regionalization of Slope Failure Forms in the Area of Overflight as Depicted by Remote Sensor Returns. An Evaluation of the Utility of Available Remote Sensor Returns for a Study of Slope Failure Phenomena. (Unpublished manuscript, ETSU, 1968; contract number N00014-67-0102-0001.)

are a part of landscape, and many of these forms result directly or indirectly from land-use practices.

In the Asheville Basin, slope features were identified with a high degree of accuracy on large-scale infrared and color photographs. These features include sheet wash, rills, gullies, soil creep, earth flows, and slumps. Mapping the locations and distribution of these forms can be readily accomplished at costs far below those of ground surveys of comparable detail. In addition, photo location is a more accurate and thorough method of mapping forms, particularly when many features are obscured to the ground observer by vegetation, or when the areas of study are difficult to traverse with ground transportation.

The most desirable scales for this type of interpretation range from 1:8000 to 1:15 000. Smaller scales obscure some forms to the extent that an interpreter may fail to recognize the form or to err in classification of what one has observed. Slump and earth-flow phenomena are particularly difficult to identify on small-scale photographs. Scales larger than 1:8000, while desirable for ease in interpretation, may not show desired areal associations.

Knowledge of the types of slope forms contained in an area and the ability to predict slope form failures contribute to understanding certain aspects of land use particularly because slope failures tend to limit the use of land, especially agriculture and transportation (routes of communication).

Remote-Sensor Applications to Urban and Regional Transportational and Land-Use Planning

Two research programs were carried out by graduate students from the University of Tennessee in the areas of urban and regional studies.[7] Their task largely focused on the feasibility of utilizing remote-sensing data for transportation and land-use planning purposes. In addition, they described the cost benefits that can be derived from remote-sensing techniques in contrast to conventional methods for the same purposes.

---

[7]Hannah, John: A Feasibility Study for the Application of Remote Sensors to Selected Urban and Regional Land Use Planning Studies. (Unpublished master's thesis, Graduate School of Planning, University of Tennessee, 1967; contract number N00014-67-A-0102-0001.)
Pate, Maynard: A Feasibility Study of Remote Sensor Application to Urban and Regional Transportation Planning. (Unpublished master's thesis, Graduate School of Planning, University of Tennessee, 1967; contract number N00014-67-A-0102-0001.)

In general, the conclusions were that remote sensors are apparently capable of collecting planning data with greater ease, more rapidly and reliably, and with less cost and manpower requirements than by conventional methods.

To provide a base of study, the researcher who investigated the benefits of remote sensing for transportational planning purposes made several assumptions and structured a hypothetical situation. (1) It was assumed that type and extent of data acquired by remote sensing did not differ radically from data needed in transportation planning. (2) The second assumption was that both approaches must seek the same end result. To meet this requirement, attention was centered on the Origin and Destination Survey since it is probably the most important survey in transportation data collection. (3) Finally, it was assumed that a comparable base could exist only if the two approaches utilized the same study area. For this purpose, use was made of a hypothetical city and region, a population of 75 000 and a total area of 50 square miles (the approximate size of Asheville). The investigator proceeded to investigate cost benefits of remote-sensing and conventional techniques in terms of planning the survey, survey initiation, data collection, and data handling. In each of these cases, the benefits favored remote sensing.

In the case of the investigation of application of remote sensors to urban land-use planning (specifically the development of land-use maps, surveys, and analysis), the study was predicated on three basic questions. (1) Can various land uses be identified as well from remote-sensor imagery as from a field survey; (2) can accurate measurements of land use be made from remote-sensor imagery; and (3) would the time, cost, and accuracy of accomplishing studies compare favorably with conventional means? The means of testing these hypotheses were accomplished by comparing the results of imagery analysis of Asheville with the results of a survey analysis carried out by a consultant firm for the same area at approximately the same time that the imagery was made, and by comparing field data against the results obtained from the interpretation of remotely sensed data.

Of 1713 land uses identified via remote-sensing techniques, only 26 were misinterpreted (for an area of 1000 acres). A comparison of measurements revealed that the consultant firm had made some gross errors in calculations. It was estimated that total cost for having imagery flown (particularly color and color infrared) and processed and base maps produced would be approximately $55 000 for a city the size of Asheville. The same results were achieved through conventional field techniques for a cost of $70 000.

Major Problems

The major problems encountered at ETSU were the following. (1) The data received determined the type of research that was carried out, rather than the reverse. (2) Only four types of remote-sensing returns were investigated — black and white, color, and color infrared photography and radar. Three rolls of thermal infrared imagery were received before the beginning of the summer; however, most of the investigators were off campus. (3) The third and final problem involves having more trained manpower and financial resources to buy equipment and to pay for the printing and processing of reports (in addition to those which were mentioned, 20 other investigations have been carried out, 11 of which are somewhere in the publishing phase).

EAST TENNESSEE STATE UNIVERSITY/UNIVERSITY OF TENNESSEE CONSORTIUM FOR REMOTE-SENSING STUDIES

As a result, in part, of the fact that the two graduate students in urban planning from the University of Tennessee worked on their research programs with ETSU materials, a research consortium for remote-sensing studies was developed between the two institutions. Both institutions are pooling equipment and exchanging ideas for an expanded program. The University of Tennessee has acquired an old DC-3 which is being modified with two camera wells. The consortium also has a four-camera Hasselblad system, and an infrared scanning system will be acquired in the next few months. In addition, interpretation laboratories have been set up on both campuses.

The consortium has received a large grant from the Department of Defense (Project Themis), and flights have already been made in several areas of the eastern part of the TVA region (TVA is cooperating in this project).

ASSOCIATION OF AMERICAN GEOGRAPHERS COMMISSION ON GEOGRAPHIC APPLICATIONS OF REMOTE SENSING

The Commission on Geographic Applications of Remote Sensing was formed during the summer of 1967 under a grant from the Geographic Applications Program, United States Geological Survey, contract number 14-08-0001-10921. Under the first grant, the Commission was charged with three tasks which could be classified as administrative, research, and preparation for educational programs (National Science Foundation (NSF))

Institutes in Remote Sensing — University of Michigan, 1968, and University of Tennessee, 1969). Of particular note here is that the research program is to lead to the development of a land-use classification system and a land-use map of the United States that is amenable to spacecraft imagery.

Land-Use Classification System and Mapping

Eighteen consultants (from six areas of the U.S.) were elected by the Commission to recommend and advise the Commission on the procedures that should be followed with respect to land-use mapping and classification problems that are expected to be encountered in each of the areas. A general conclusion reached by the consultants was that an attempt should be made to map the land-use traits of the U.S. at a scale of 1:250 000 because of the level of generalization which can be obtained from expected spacecraft imagery and photography and because of the convenience of being able to utilize these land-use maps with Army Map Service series maps of the same scale. A pilot project is being worked on by Norm Thrower of the Geography Department, UCLA, who is presently developing a land-use map and classification system for selected areas in the southwestern part of the United States from Gemini and Apollo imagery. The classification system that is being developed should be flexible enough for use in other sections of the country. To date, Thrower's group has extracted as much land-use information and locational data as possible from Gemini imagery, including natural features (e.g., playas, sand dunes, mountains, alluvial fans, and vegetation zonation patterns) and cultural features (e.g., agricultural fields, survey lines, grazing zones, urban and central places, and mining activities). These data are being placed on 1:250 000 maps, and plans are to field check the data during December 1968.

Tennessee Valley Authority Test Region Experiment

Another phase of the commission's activities is being directed toward establishing a large area for future spacecraft overflights. Particularly, the geographical experiments are to be of problem-oriented types rather than of inventory and classification types. Initially, the commission recommended that attention be concentrated on the Tennessee Valley region and adjacent areas. In part, this area was selected because of (1) the on-going program in the Asheville area by ETSU; (2) the proposed programs of the ETSU-University of Tennessee Consortium on Remote Sensing Studies; (3) the availability of large quantities of ground-controlled data from the TVA as well as complete index coverage of maps and air photos for the region; and (4) NASA has already designated this region as an area of first priority for future spacecraft overflights. Plans are to utilize the coming year to organize

channels of communications between geographers and appropriate state and federal organizations that wish to participate in the experiment and to formulate specific plans for studies for the experiment among various geographers from different institutions.

National Science Foundation Institute in Remote Sensing

Realizing that one of the main deficiencies of the remote-sensing program in geography is the absence of trained personnel, the commission recommended at one of its early meetings that a summer institute be arranged for the purpose of training college geography teachers in the techniques of remote sensing. Capitalizing on the experience which was gained by the University of Michigan in conducting institutes of this type during 1966 and 1967, the commission submitted a proposal for an NSF supported 5-week institute which was held at the University of Michigan during the summer of 1968. Twenty-five geographers attended the institute, many of whom are now planning to set up courses in remote sensing at their own institutions. A similar program is being planned for 1969 to be held at the University of Tennessee. A proposal has already been submitted, and a schedule of instruction is being worked out.

Bibliography

The commission has published, through the Geographic Applications Program, a bibliography of pertinent references dealing with remote sensing.[8] The bibliography is broken down into four parts: references concerned with the fundamentals of remote sensing, basic remote-sensing references, remote-sensing and land-use references, and references dealing with automatic pattern recognition processes. Copies can be obtained from the Central Office of the Association of American Geographers and from the Geographic Applications Program, United States Geological Survey.

---

[8] Honea, Robert B.; and Prentice, Virginia L.: Selected Bibliography of Remote Sensing. Interagency Report NASA-129, prepared under U.S. Geological Survey Contract No. 14-08-0001-10921.

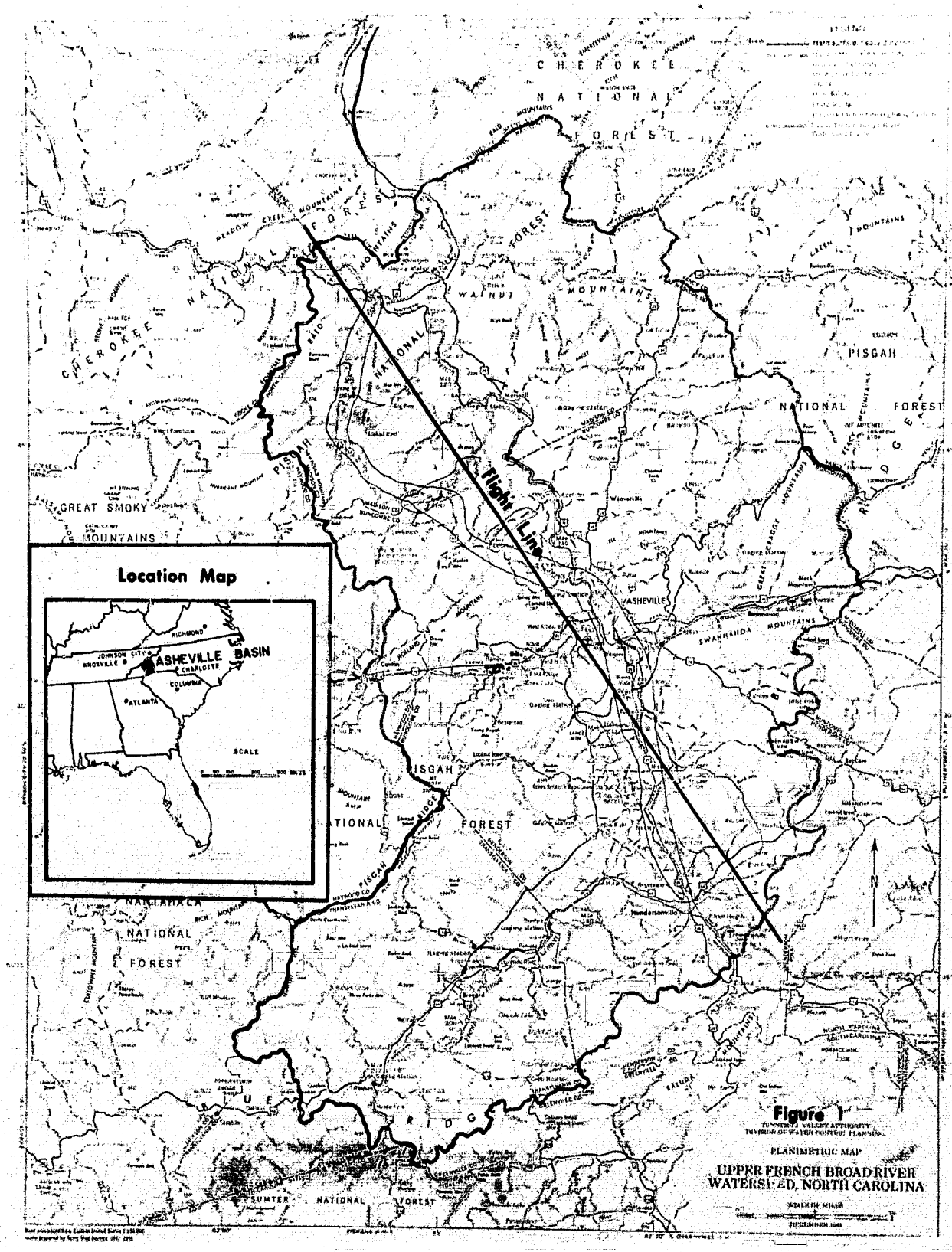

Figure 5.1.- Flight line across the general "grain" of different geographical features which are typical of the Southern Appalachians.

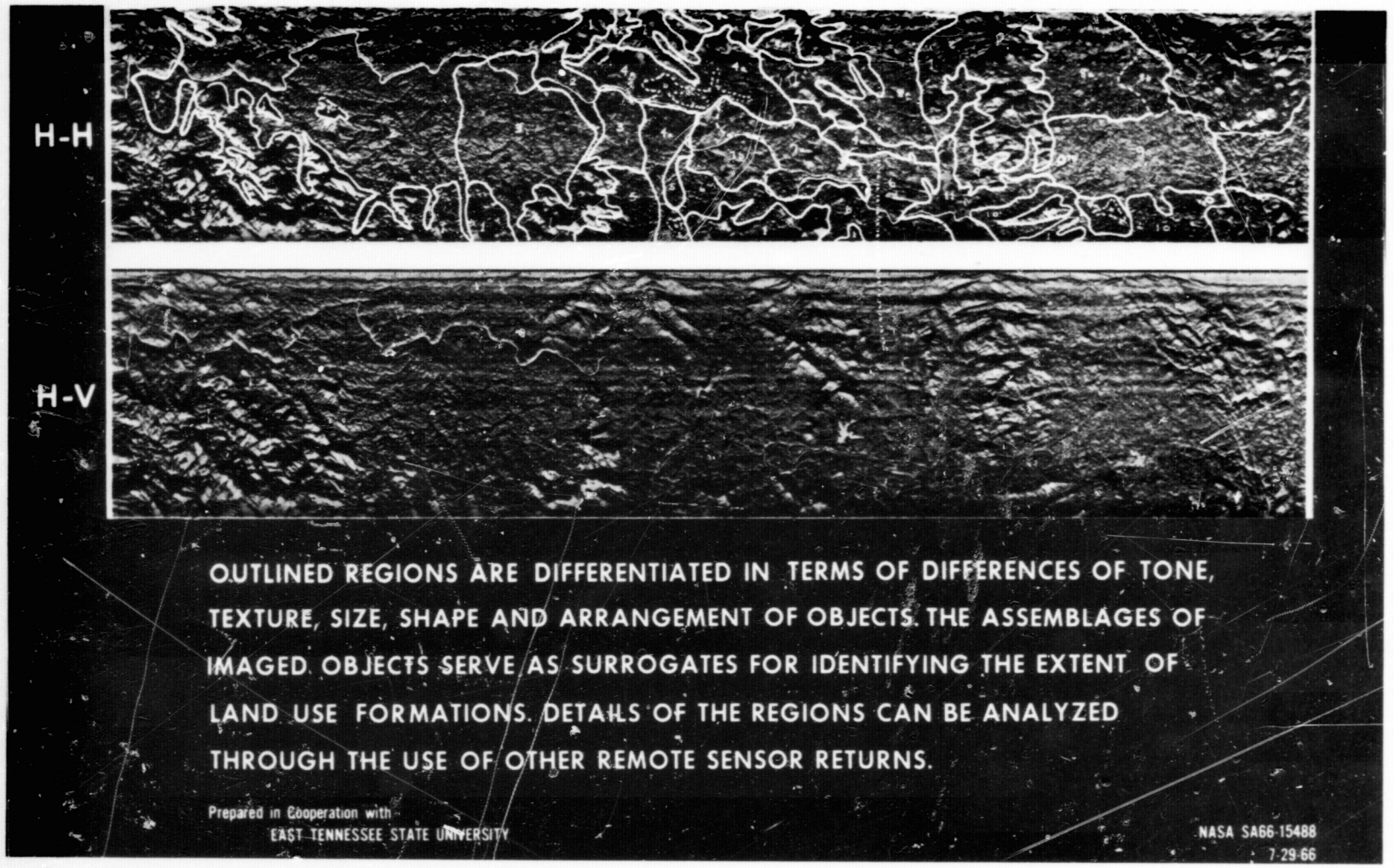

Figure 5-2.- Radar imagery of a number of relatively distinct regions in the Asheville Basin, western North Carolina.

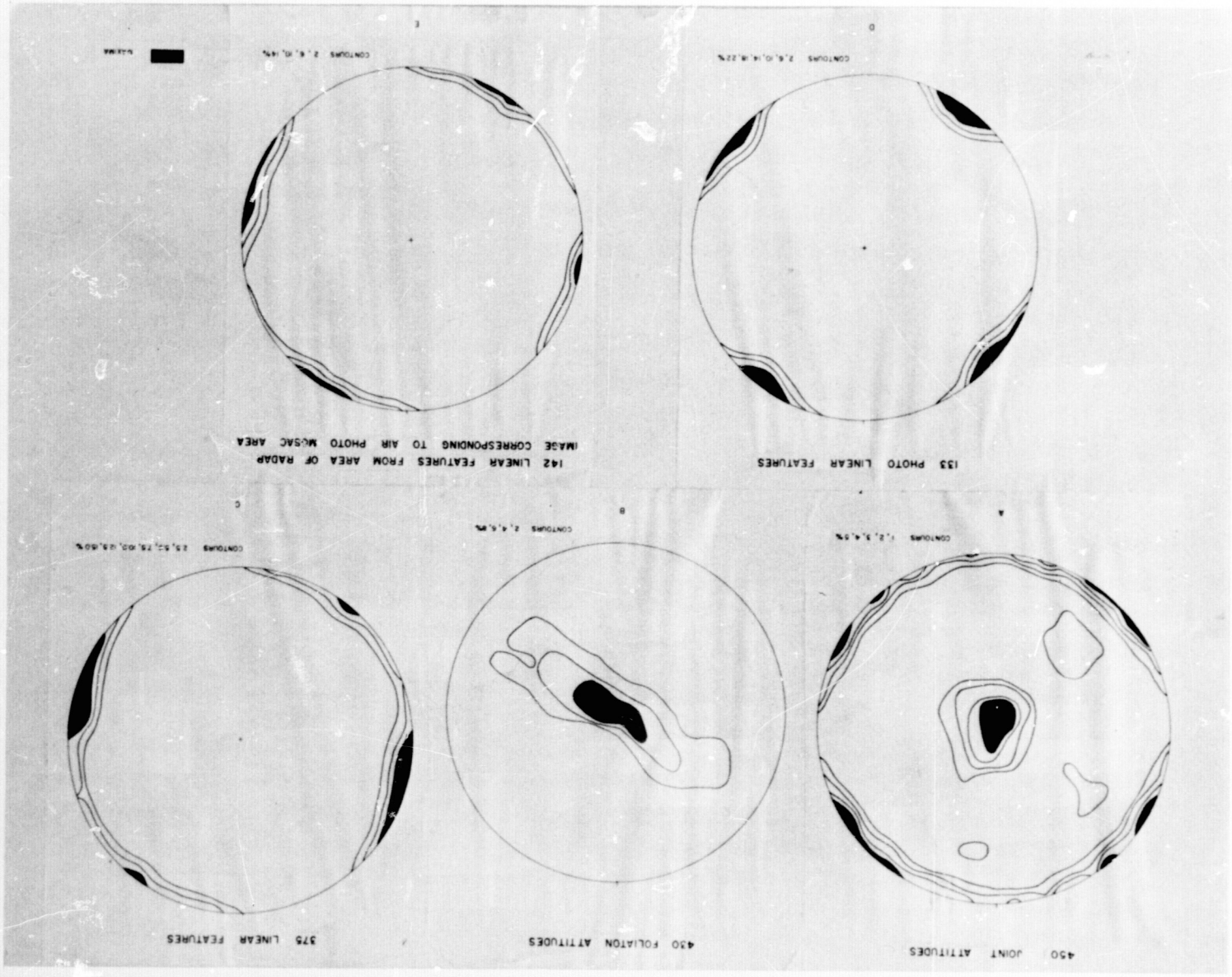

Figure 5-3.- Stereogram of linear features in the Asheville Basin.

Figure 5-4.- Black and white photograph of color infrared photograph showing road markings at road intersections.

Figure 5-5.- Traffic flow directions plotted on standard series topographic map, 1:29 280.

APPENDIX 5A

INFORMATION CONCERNING OVERFLIGHT DATA OVER THE ASHEVILLE BASIN TEST SITE (SITE 46)

Missions

Five missions were flown over the Asheville Basin site by NASA (Convair 240A and P3A) between November 3, 1965, and January 1968 — missions 14 (November 15, 1965), 23 (May 7, 1966), 34 (October 10, 1966), 53 (July 10, 1967), and 65 (January 16, 1968). Two overflights were made with the Westinghouse radar plane during September and November 1965.

Data Received

Most of the materials received from the overflights were from the photographic sensors — RC-8 (color and color infrared) and multiband photography. These data were received between 1 and 6 months after the missions were flown. Infrared thermal imagery was made of the test site by using the AAS-S and RS-7 sets. These data, however, (for all missions) were not received until May 1968. Microwave radiometer traces were made of the Asheville site, but no reference points were indicated on the records; therefore, these remote sensor records were of no value for investigative purposes.

Quality of Data Received

Most of the color and color infrared photography was of good to excellent quality, and these remote-sensing returns formed the data base for most of the on-going or completed investigations. Low-altitude color and color infrared, taken with the 240A, were of marginal value for comparison purposes because the overflight coverage was not simultaneous. Only where the flight paths crossed could the imagery be used for multisensor interpretation purposes. On the other hand, most of the color and color infrared photography made from high altitudes (15 000 and 25 000 feet) was comparable, but these data naturally did not have the higher-resolution qualities of the low-altitude photography. Low-altitude nine-lens multispectral photography was of little value for interpretation purposes because the narrow field of view of the system often missed specific ground-truth stations.

Since none of the thermal infrared materials were received until June of this year, very little investigative work has been carried out with these materials. As mentioned earlier, the microwave traces were of no value because of the absence of reference points.

TABLE 5A-I.- USE OF REMOTE-SENSING DATA

Missions	Remote-sensor record	How used
14 23 34	Low-altitude and high-altitude color and low- and high-altitude infrared	Pond analyses, slope failure studies, urban land-use analyses, transportation studies, historical studies, rural land-use studies, socio-economic surrogates, vegetative analysis, "grassland" balds, and vegetative communities.
	Multispectral (nine-lens camera) (of little value for all studies carried out by ETSU)	Rural land use (differentiate crops and fields).
	Panchromatic	Pond analysis. Slope failure forms.
	Thermal infrared	Not used.
	Microwave	Not used.
53	High-altitude color and color infrared	Because of cloud cover, only selected portions of imagery could be used for rural land-use, ponds and pollution, and slope failure studies.
65	High-altitude color and color infrared	Snow covered landscape. Correlated with imagery from Mission 53 for undercovering difference detectable seasonal landscapes.
	High-altitude thermal infrared	Not used.

APPENDIX 5B

TABLE 5B-I.- ASHEVILLE BASIN GROUND-TRUTH DATA COLLECTED DURING OVERFLIGHT

	Nov. '65	May '66	Oct. '66	June '67	Jan. '68
Color slides and prints	X	X	X	X	X
Black and white prints	X	X	X	X	X
Rock sample and maps	X				
Soil sample and maps	X				
Soil moisture and maps	X				
Soil temperature and maps	X				
Air temperature charts	X		X		
Relative humidity and maps	X		X		
Land-use maps	X	X	X	X	X
Intensive area studies	X	X	X	X	X
Hydrological and climatological observation	X	X	X		
Surface weather observation	X	X	X		
U.S.G.S. hydrologic record	X	X	X		
Radiometric readings (temperatures)	X				

N71-16130

REMOTE SENSING OF FIRE PHENOMENA IN TROPICAL GRASSLANDS: THE FLORIDA TEST SITES, 1967-68

By Merle C. Prunty
University of Georgia

In the current phase of the grassland fire project, test sites employed are in two locales (fig. 6-1). One locale is about 50 miles southeast of Orlando, Florida, near the northern margin of the range cattle region of central Florida. This area also is known as the Florida flatwoods region. The site employed during 1967-68 is part of the K-6 Ranch, one of the holdings of Deseret Farms, Inc. The other locale is along the Georgia-Florida state line, near Tallahassee, Florida, and Thomasville, Georgia. This locale involves four sites, each quite different in physical characteristics, ranging from about 500 to more than 8000 acres in size. Together, these sites are identified as test site 165 in the Mission Summary Reports of the Earth Resources Aircraft Program. Obviously, this project classifies as research in land-use analysis, although it contains some overtones of environmental-impact analysis as well.

The long-range rationale of this research involves the following: tropical savannas are areas in which herbaceous cover, mainly grasses, is areally dominant. Certain species of trees, bush, and brush also are present in varying amounts. These vast tropical grasslands are believed to have evolved largely in response to the annual wet and dry rainfall cycle which typifies savanna grassland regions throughout the world. However, maintenance of the savanna — or grassland — characteristic of these huge areas is believed to be primarily a function of ground fires (refs. 6-1 to 6-3). Recurrent ground fires, frequently annually recurrent, are characteristic of savannas everywhere and apparently have been for thousands of years (refs. 6-4 and 6-5). While most savanna ground fires today are of cultural origin, many also result from lightning strikes. These fires are most frequent near the close of the savanna dry season, though they are not confined to that period (refs. 6-6 to 6-8).

Throughout tropical America, the present rates of population increase portend crises in population-supporting capacities that easily

can lead to political and economic "explosions" of dangerous proportions. The rates of increase in these tropical American nations, as a group, significantly exceed increase rates in any other large segment of the world. Presently, these populations are jammed in the old, classical highland areas of settlement that have been the settled areas since colonial times (ref. 6-9). In contrast, the great Latin American "empty areas," supporting generally low population densities, are the savanna grasslands and the tropical rain forests. Of these two environmental types, savannas generally are regarded as much more favorable for settlement.

Immediate relief of the population crisis in tropical America can come through extensive settlement on the savannas. Permanent settlement of these areas, in contrast to the extensive, low-grade grazing of cattle which now is their main use, involves the ground-fire phenomenon (ref. 6-10). In some instances it will be desirable to exclude fire. In others, fire will be a necessary settlement and management tool. In both instances, a knowledge of the frequency, areal distribution, seasonality, and localization of ground fires clearly will be fundamental to the success of new settlements on the savannas.

However, as things stand, there is simply not enough known about fire in savannas to know where, when, and how to use fire as an aid in settlement or expansion or where, when, and how to protect against fire. Present knowledge comes from a group of empirically derived studies, mostly in small areas, conducted over the past 40 to 50 years by many scholars for many different purposes from many different viewpoints. There is little uniformity, hence comparability, among these studies as to time, areas, or purposes and modes of observation. After about a decade of interest in the subject, I had given up the idea of research on grassland fire because I saw no prospect of going beyond the present sorts of small-area, empirically based studies until the remote-sensing prospect provided by the satellite programs developed. Remote sensing presents the opportunity to produce observations that can be standardized as to observational procedure and quality, that are both areally comprehensive and inclusive, that are temporally uniform and, particularly, that can encompass large regions.

The long-range objectives of this research, then, are development of temporally uniform and areally comprehensive data regarding the occurrence, distribution, type, and effect of fires in savanna grasslands of tropical America and analysis of these data in terms of their implications in the expansion and creation of settlement in these grassland regions.

The immediate objectives — those of the 1967-68 year — have been to identify those remote sensors best fitted to observation of ground-fire phenomena, to develop familiarity with the properties and

limitations of these sensors, to develop experience in interpretation of remote-sensed imagery, and to establish preliminary imagery-interpretation indices. The Florida-Georgia test sites have been used for these purposes (fig. 6-1).

The test sites were selected to fit several criteria. (1) Sites were needed which simulated upland, lowland, marsh or swampland savanna, and wooded as well as open savanna conditions. (2) The sites had to be reasonably accessible at all seasons. (3) Inclusion of at least some cropland or fallow land that could be burned was desired. (4) It was of course essential to employ sites owned by people who would cooperate in terms of access and also in terms of timing and distribution of burnings. (5) It was particularly important to obtain test sites on unimproved range land because cattle ranching is the areally dominant land use in savanna grasslands. Fortunately, all these criteria were met. The Pipeline Road and the K-6 sections of Deseret Farms, Florida, provide "open" and lightly wooded grazing land, plus a diversity of phytomorphic types therein. The Mitchell-Swift unit provides a mixture of lightly and heavily wooded grassland on a mixture of terrain types plus numerous small fields both in cultivation and in fallow. Birdsong Plantation provides a large tract of "improved" grassland occasionally subjected to burning. Cobb Rocks, a segment of the St. Marks U.S. Wildlife Refuge, provides one large tract of marsh grassland. Tall Timbers Plantation is the property of Tall Timbers, Inc., a privately endowed fire ecology research station which contains tracts that are experimentally burned in rotations of up to 80 years in length. Tall Timbers Plantation also contains rather large tracts of upland pine woodland with a savanna understory.

The following are the basic hypotheses under test. (1) The modifications in vegetative cover caused by ground fires could be recorded by remote-sensing instruments at accuracy levels sufficient for production of relatively large-scale maps. (2) These modifications could be recognized, and mapped, in the chronologic order in which various fires occurred. (Hence, on savannas with a satellite in orbit, burnings which occurred between "overhead" stages could be recognized and mapped sequentially.) (3) Two or more sensors might reasonably provide collative, or supporting, data on both ground-fire occurrence and fire chronology.

The first and most fundamental step was detailed mapping, on the ground, of the vegetative cover by phytomorphic classes. The resultant vegetation classes are morphologic and are high in geographical qualities. The classes have been examined by plant ecologists, experts in the areas, who confirmed their validity (refs. 6-8 and 6-11 to 6-13). The maps of existing vegetative cover were completed approximately 2 months before any burnings in the 1967-68 season. These maps became the principal ground control for the entire project. Figure 6-2 is an example map from the Pipeline Road unit, Deseret Farms.

It should be noted that the test sites are small segments of a huge phytomorphic landscape. (Practically all of the south Atlantic and Gulf coastal plain — including all of Florida — has been subjected to recurrent ground fires for literally thousands of years (refs. 6-12 to 6-14).) Thus, the vegetative cover of the area is fire conditioned to the point that plants which cannot tolerate ground fires occur only in very moist locales where fire does not penetrate. Only in recent decades has much of the coastal plain area been protected from recurrent ground fires. Hence, the test sites — which are not fire protected — are covered by phytomorphic plant associations just as are the tropical savannas.

In mapping the preburn vegetative cover, then, we were mapping the plant cover prior to 1967-68 burning, but we also were mapping the cover of a landscape which bears the marks of frequent burns in the recent past.

In order to simulate the precession of an observation satellite, we arranged for burns at monthly intervals for 3 months prior to the first flights (which were in the first week of January 1968). These sequenced burns were located on Deseret Farms in central Florida. All burning in the Tallahassee-Thomasville area (where annual burning is customary) occurred in conjunction with the second overflight, on March 1, 1968. These were the only overflights for this project during the 1967-68 fiscal year.

In addition to ground control provided by the phytomorphic mapping, air temperature, humidity, wind velocity, and soil moisture readings were obtained at representative sites during the overflights. A Barnes infrared thermometer of the PRT-5 type, University-owned, was used on one terrain profile during the March overflights. All phytomorphic classes were ground photographed in Kodachrome and color infrared before burning, during burning, and immediately after burning. Each locale was rephotographed 10 weeks after the last burns in March 1968.

In general, the ground-control data (other than that from the vegetation maps) are of restricted value. Most of the data are nondiscriminatory or apply to such a small segment of the whole test site as to be essentially useless. For example, soil moisture is not particularly critical to the movement of a ground fire. Relative humidity and wind velocity are much more critical (ref. 6-15). One of the largest and most spectacular ground fires was on a marsh grassland on which there actually was standing water. It is nearly impossible to obtain data from the radiation thermometer on the ground that are relevant to radiation readings recorded by aircraft. To do so, the ground instrument would have to be mounted on a gantry, or on a tower on top of a truck, at a height sufficient to clear treetops and at an angle coincident to that of the plane-mounted sensor. A time lag of more than a few minutes

between passage of the remote sensor and the ground-mounted radiation thermometer would negate its usefulness. Even if the problems of angle, height, mobility, and large area-sampling were resolved, the uncontrolled and sometimes unknown variables interposed between ground and airborne instruments by the atmosphere itself place serious constraints on the use of correlation analysis. High levels of areal correspondence in the signatures of two or more airborne sensors (such as the Reconofax IV and color infrared and Ektachrome) appear more useful than the ground-control readings used in this project to date, except for the large-scale maps of phytomorphic units.

After the imagery was obtained, preselected key sites were used to establish interpretation keys. These keys were used to reduce the imagery to large-scale maps. Then, these maps were measured against the ground-control maps of phytomorphic classes. Since the areal limits of the fires put through the vegetation were known from the ground, the tone and textural changes in the imagery could be tested to detect fire effects on the vegetative cover with substantial accuracy. All ground photography (Kodachrome and color infrared) was keyed to the vegetation maps, and was used as a cross-check. The procedure involved working from low-altitude imagery (3000 feet) to higher altitude imagery (15 000 feet or more).

The Reconofax IV imagery is, as a result of resolution, not as reliable at the higher altitude, but produces better results than expected. The value of the Reconofax lies in its ability to record the large cores of areas of uniform vegetative cover that were burned at a given time, hence to corroborate recognition of the same areas on the color infrared imagery. The Reconofax imagery is of restricted value in developing the boundaries of such areas because its image quality degrades with altitude. Boundaries of burned areas have had to come, to date, from the color infrared imagery. The infrared imagery has produced consistently good results at both altitudes, even with some smoke interference from fires underway, and at this stage is our most reliable tool. Its ability to produce precise boundary results at the higher altitude is particularly encouraging. The Ektachrome imagery was exposed in the T-11 camera and generally is a disappointment.

The problems in developing accurate boundaries, when engaged in areal differentiation of almost any phenomena, are recurrent in geographical work. One aspect of the problem is the bias — or lack of it — of the observer. The ground-control mapping of vegetative cover was performed by the three principal investigators, the writer and his two research assistants (with some aid from hourly rate labor). The same three investigators produced the interpretation keys and applied them to the imagery. A test was run to determine the extent of bias in the results, hence to determine the extent to which the investigators

interpreted what they observed as what they should observe because they knew ground conditions fully. The test, conducted by Donald Maxfield, University of Georgia (a man with years of photointelligence experience in the Aeronautical Chart and Information Center, American Meteorological Society), was designed to determine the levels of accuracy in boundary determinations. The results produced a linear boundary correspondence of better than 92 percent, an areal correspondence of more than 95 percent, and the conclusion that the analysis, as mapped, does not contain an interpretation bias.

Results to date are encouraging. Recognition of and mapping of the distribution of ground-fire areas proceeded with accuracy even on sites where forest cover is relatively dense. We can recognize — and delineate accurately — burned areas of different ages; we can approximate the time since the burn occurred; and we can therefore recognize burning sequences.

The sequenced burns that were staged prior to the January 1968 flight thus proved their worth in this test. Both the color infrared and the Reconofax IV imagery recorded tone-and-pattern differences in response to the age differences in these burns. Obviously, both sensors were recording differences in the volume/density of chlorophyll in the regrowth, as well as differences in the height/density of the plant structure residual to the fires.

While the foregoing results were anticipated, some quite unexpected results were also obtained. Figure 6-3 represents the distribution of areas burned in the autumn and early winter of 1967, and these are the areas referred to in the preceding paragraph. Figure 6-3 also represents the distribution of burns which occurred in the autumns of 1965 and 1966. The boundaries of these areas were not recognized when the vegetative cover was control mapped on the ground but appeared on the color infrared imagery. When these areas were first noted, we were unable to determine definitely what they were. It was established that these were old burn distributions by checking the records of the ownership involved. There is, then, recognizable variation in the "chlorophyll response" of burns 1, 2, and 3 years of age. Just what this may mean in terms of rangeland and grassland management and in regard to vegetative mapping and ecologic investigations is not clear. The potentials are intriguing and deserve additional investigation.

The results from 15 000-foot infrared film are virtually identical to those from exposures at 3000 feet; the ability of the color infrared imagery to "hold" its powers of boundary resolution at the higher altitude is quite promising. The higher altitude results from the Reconofax IV are influenced by its low resolution levels, but still provide corroborative data. We now need to see what results can be obtained from sensors at much higher altitudes and from an infrared thermal

sensor with greater powers of resolution than those of the Reconofax IV, and we need to experiment with radar signatures from burned areas. We would like to obtain Ektachrome imagery of quality, flown at 15 000 feet, or higher, to examine closely before discarding the Ektachrome imagery for this project. We also wish to expand the size of the central Florida test site to include a greater number of variables in grassland conditions.

During this year, imagery was obtained from two overflights, one in winter and one in early spring. We now wish to expand the coverage to include all seasons so that the ability of the sensors to detect fire modifications during periods of rapid vegetative regrowth can be examined.

REFERENCES

6-1. Hills, Theo L.: Amazon Savanna Landscapes - Their Nature and Origin. Paper presented at 64th Annual Meeting, Assoc. of Am. Geographers (Washington, D.C.), Aug. 18-22, 1968.

6-2. Johannessen, Carl: Savannas of Interior Honduras. Ibero Americana, vol. 46, 1963, p. 98.

6-3. Denevan, W. M.: The Upland Pine Forest of Nicaragua. Univ. of California Pub. in Geography, vol. 12, no. 4, 1961, pp. 278-285.

6-4. Sauer, Carl: Early Relations of Man to Plants. Land and Life, A Selection from the Writings of Carl Ortwin Sauer. John Leighly, ed. Univ. of California Press (Berkeley), 1965, p. 160.

6-5. Budowski, Gerardo: The Ecological Status of Fire in Tropical American Lowlands, Actas del XXXIII Congreso Interamericano de Americanistas. (San Jose, Costa Rica) vol. 1, 1958, pp. 265-267.

6-6. Blydenstein, John: Burning and Tropical Savannas. Paper presented at the Seventh Annual Tall Timbers Fire Ecology Conference (Tallahassee, Fla.), Mar. 1968.

6-7. Komarek, E. V., Sr.: Lightning and Fire Ecology. Paper presented at the Seventh Annual Tall Timbers Fire Ecology Conference (Tallahassee, Fla.), Mar. 1968.

6-8. Robertson, W. B., Jr.: A Survey of the Effects of Fire in Everglades National Park. Unpublished report to U.S.D.I. National Park Service, 1953, pp. 11, 16-17, 20-33.

6-9. James, P. E.: Trends in Brazilian Agricultural Development. Geographical Rev., vol. 43, 1953, pp. 301-328.

6-10. Jones, C. F.; and Darkenwald, G. G.: Economic Geography. The Macmillan Company, 1954, pp. 124-125.

6-11. Edmisten, Joe A., Assist. Prof. of Botany, Univ. of Georgia: personal communication.

6-12. Edmisten, Joe A.: The Ecology of The Florida Pine Flatwoods. Unpublished Ph.D. dissertation, Univ. of Florida, 1963, pp. 1-4.

6-13. Garren, K. H.: Effects of Fire on Vegetation of The Southeastern United States. Botanical Rev., vol. 9, 1943, pp. 631-633.

6-14. Harper, Roland M.: The Geography and Vegetation of Northern Florida. Fla. Geol. Survey Rep., no. 6, 1914.

6-15. Batchelder, R. B; and Hirt, H. F.: Fire in Tropical Forests and Grasslands. U.S. Army Natick Lab. (Natick, Mass.), 1966, pp. 48-50.

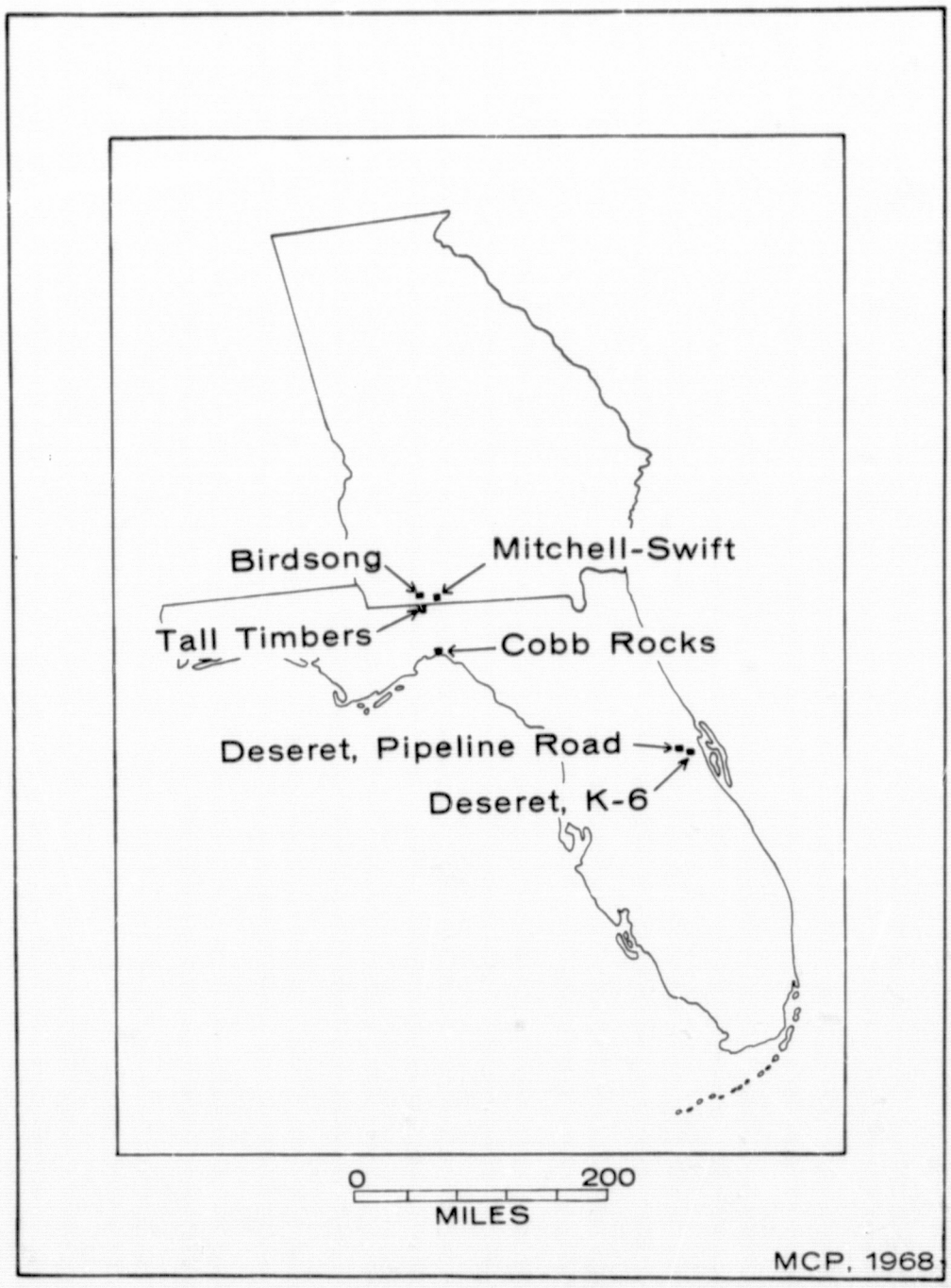

Figure 6-1.- Location of test sites.

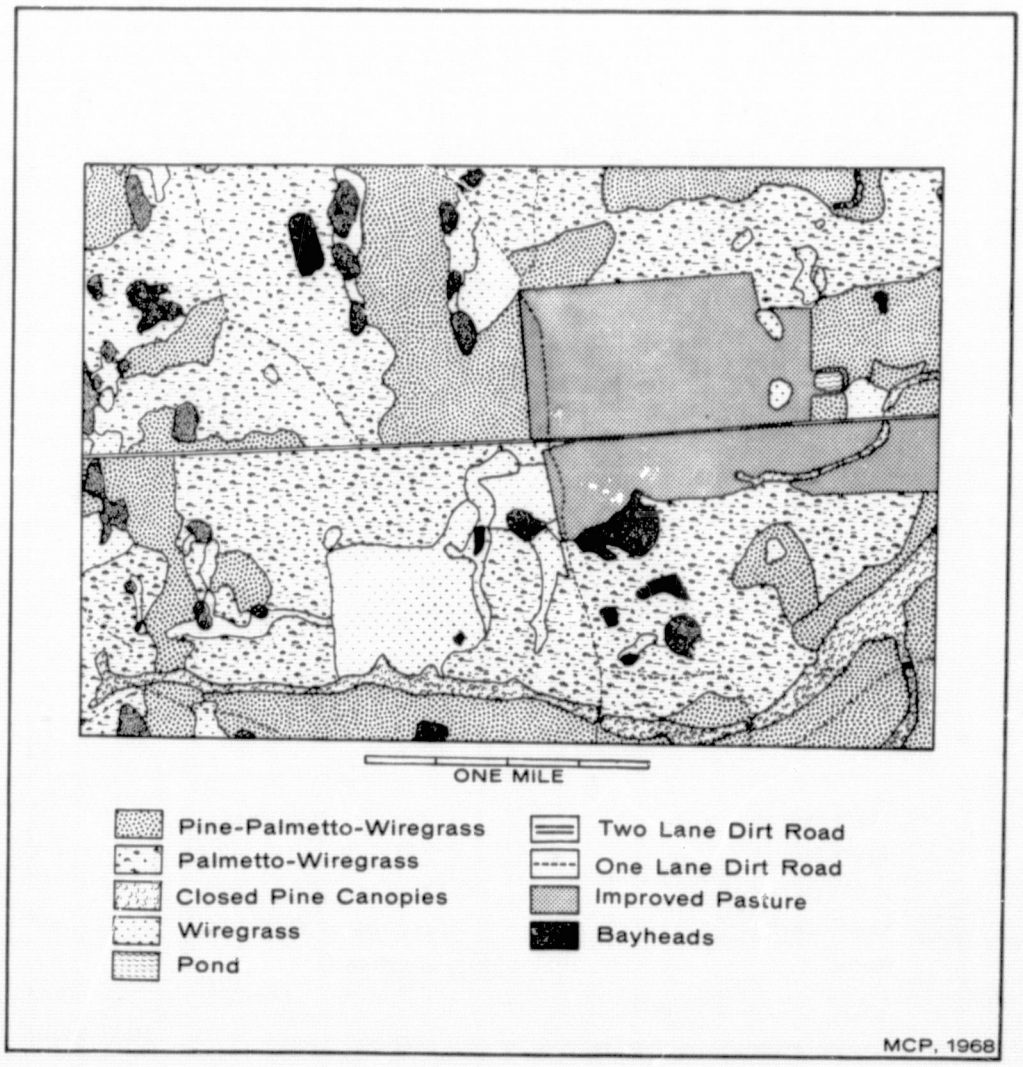

Figure 6-2.- Distribution of vegetation types, Pipeline Road.

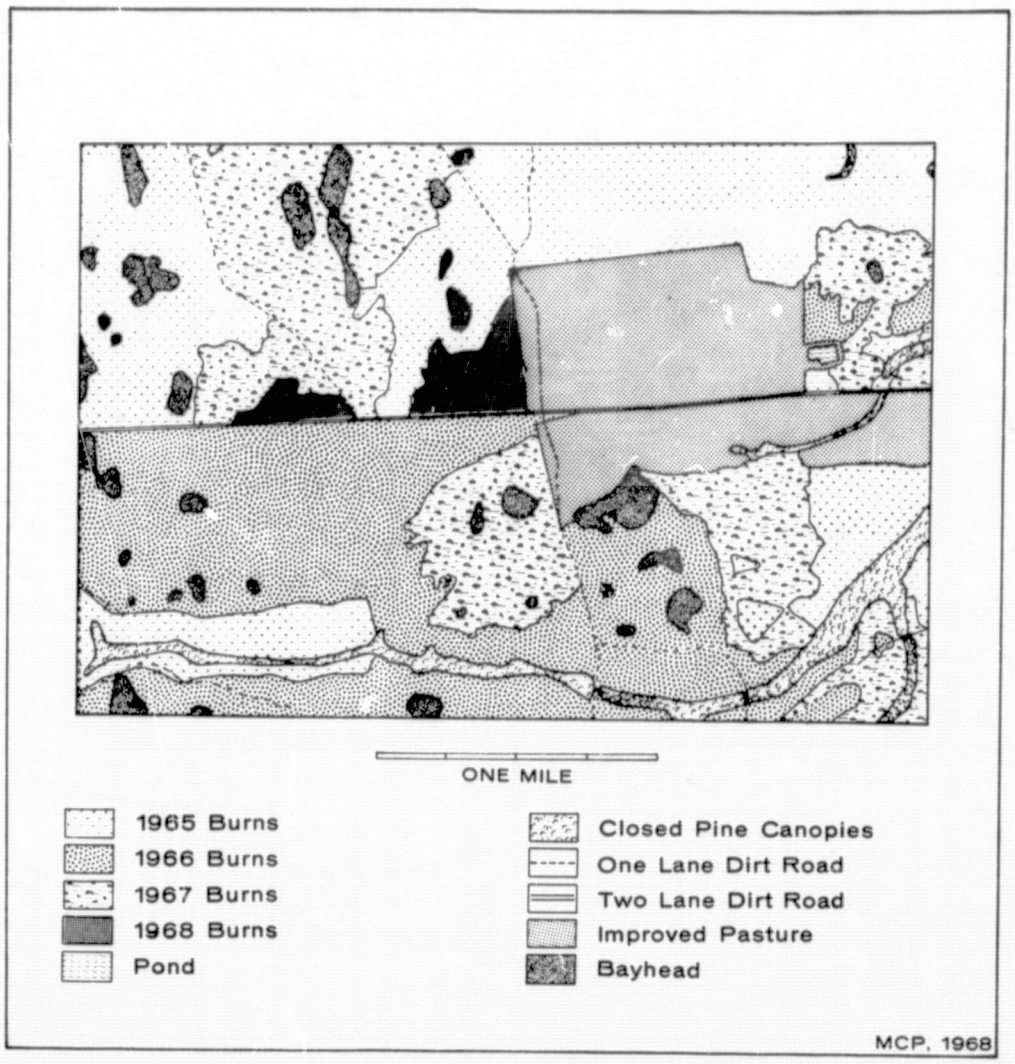

Figure 6-3.- Distribution and age of burns, Pipeline Road.

ERRATA

SECTION 6

REMOTE SENSING OF FIRE PHENOMENA IN TROPICAL GRASSLANDS:
THE FLORIDA TEST SITES, 1967-68

By Merle C. Prunty
Sept. 1968

Page 6-6, line 4: American Meteorological Society should be changed to Army Map Service.

Page 6-6, line 24: The sentence should be changed to read "... results also were obtained" instead of "... results were also obtained."

Page 6-6, line 27: The sentence should be changed to read "... which occurred in 1965 and 1966" instead of "... which occurred in the autumns of 1965 and 1966."

Issue date: 9-1-69

N71-16131

REMOTE SENSING AND THE STUDY AND PLANNING OF URBAN AREAS

By Duane F. Marble
Department of Geography, Northwestern University

and Frank E. Norton
Department of Geography, University of Iowa

Today, there are as many people in the urban areas of our country as there were in the total population less than two decades ago, and in the next 40 years our urban areas will double in size, growing as much in that time as all of our urban growth since the first settlement of North America. The basic question we face as a nation is not one of our capability to provide for this massive and complex growth, since we can and will do so, but rather if we can mount such an effort without including disasterous shifts in the quality of urban life. This problem arises at a time when there is already grave concern about the serious pathological state of our cities. President Johnson made the following note last year on the occasion of certain demonstrations of this condition (ref. 7-1):

"The only genuine, long-range solution for what has happened lies in an attack — mounted at every level — upon the conditions that breed despair and violence. All of us know what those conditions are: ignorance, discrimination, slums, poverty, disease, not enough jobs. We should attack these conditions — not because we are frightened by conflict, but because we are fired by conscience. We should attack them because there is simply no other way to achieve a decent and orderly society in America."

The future of our cities will be shaped to an important degree by the choices we make today. The problems of the cities are being actively attacked at all levels of Government, and it has become apparent that correction of present pathological conditions, while simultaneously attempting to provide for substantial new growth, will constitute one of the major demands upon the resources of our society in the decades to come. (To illustrate, one recent estimate of the urgent funding needs for urban transportation alone calls for expenditures of at least $5 billion a year over the next decade.) The city is an exceedingly

complex organism, and while we have some feeling for the way we would like it to be, we are severely handicapped by our general lack of knowledge of how it operates. Several weeks ago, Secretary Weaver of the Department of Housing and Urban Development of the Presidental Cabinet pointed this out to a select committee of the Congress when he said the following (ref. 7-2):

"There is no simplistic formula under which we can ensure the development of a viable and valid national environmental policy for urban America, not today and not for a good many days to come. There are too many things we do not know, basic matters such as how we define quality in the urban environment, how we measure it, and how we strike a balance among competing values."

Coupled with the action programs that are so urgently needed by our cities, there must be an intensive program of research and planning which will enable us to carry out these change programs with the highest efficiency possible. Without viable supporting programs in these areas, we stand in grave danger of dissipating our scarce national resources without attaining our desired ends.

The phenomena we call a city are the complex sum of a host of human and physical subsystems which both generate and respond to a wide variety of stimuli. Research studies designed to define and analyze the stimuli-response relationships between and within urban subsystems are being actively pursued by researchers in many disciplines. For example, in the last two decades, geographers have developed a significant body of knowledge dealing with those spatial relationships which play a major role in establishing the physical structure of the city. The complex interactions which characterize the maze of urban subsystems force the researcher away from the formulation of broad definitive statements and into a posture where results are acquired only in minute increments in a manner resembling the construction of a large jigsaw puzzle. This framework, unfortunately, tends to operate within an accomplishment time frame of years or even decades.

Interacting with these research efforts are the activities of the planners who are attempting, on the basis of the limited knowledge currently in hand, to guide our growing urban areas in directions which hopefully reflect at least some of the goal structures of the individuals inhabiting them. The relationship between the planners and the researchers is, of necessity, a close one. In its most effective form, the relationship is a strong, two-directional relationship, since the planners, in the course of their daily operations, have access to experiences which assist the researchers in structuring their investigations of the urban system.

One of the major stumbling blocks to the efforts of both urban researchers and planners has been the lack of pertinent and reliable data. Data perform a vital, two-fold task: (1) to provide a basis for testing research hypotheses relating to urban subsystems and subsystem elements and (2) to provide a basis for current decision making, as well as a means of monitoring the outcome of past decisions. Hence, the acquisition and maintenance of large quantities of data represent a basic link in the attempts to attack our massive urban problems.

Data used in urban studies should ideally meet a variety of criteria such as timeliness, flexibility, compatibility, and reliability. In present circumstances, the researcher or planner usually feels fortunate indeed if his data set satisfies even one of these criteria — let alone all four. It is quite clear to workers in this area that something must be done to improve significantly both the quality and quantity of urban data, or we will be unable to get on with our main task of improving the urban environment.

In 1963, the National Aeronautics and Space Administration, in cooperation with several other groups, convened a Conference on Space, Science, and Urban Life. The following was the basic question posed for the participants:

"Can a national program of space exploration be applicable to the daily tasks of the men and women who live and work in our cities?"

The conference answered the question in what could best be described as a series of guarded affirmatives based largely upon technological spillover effects and upon secondary and tertiary economic impacts (ref. 7-3). This appears, in our opinion, to represent far too limited a view, since it is our contention that the space program is now moving toward a position in which it can be of direct assistance to those planners and researchers who are deeply involved with our urban problems. This direct involvement can grow out of the studies which are currently being conducted as part of the Earth Resources Survey Program on the evaluation of remote sensors as data sources for urban and transportation studies. The remote sensors appear to have a place as one of several data sources incorporated into a larger urban information system (fig. 7-1).

In our investigations at Northwestern, we have pursued two parallel approaches to this evaluation problem, first, by focusing upon recent advances in sensor technology and moving from there to the identification of possible urban applications and second, by beginning with the identification of critical urban problems and their specific data needs and then examining the capability of remote-sensor systems to provide the required data. The first approach is exemplified by the reports we

have prepared on side-looking radar, thermal infrared (IR) scanners, and hyperaltitude photography as potential urban data sources (appendix 7A). The second approach is represented by our studies relating to the measurement of quality of the residential environment from photographic imagery. The latter approach is, by far, the most desirable one, but since the exotic sensors were almost unknown to us, as well as to most other urban researchers, it appeared necessary to develop some basic understanding of their gross capabilities before pressing for more detailed inquiries arising out of perceived urban data needs.

Our studies have shown that, in the limited cases examined, remote sensors possess certain comparative advantages as urban data sources, but only when considered within the general urban information system context mentioned earlier. An appropriate query at this point is "Where do we stand? What has been accomplished, and what remains to be done?"

At the start of this program, remote sensors, other than conventional black and white photography, were neither widely used nor generally considered as urban data sources. Based upon imagery provided by the Earth Resources Aircraft Program, we have demonstrated that the efficiency with which the photographic sensors are used can be significantly increased and that in one critical urban problem area, measurement of the quality of the residential environment, the photographic sensors can quickly and efficiently supply many of the classes of data which are currently collected by relatively slow and inefficient ground surveys. (Appendix 7B contains a more detailed discussion of the relationship of our research to the aircraft support program provided by the Manned Spacecraft Center, Houston, Texas.) Studies of the more exotic sensors have confirmed earlier impressions that they can provide valuable supplements to, or perhaps even replacements for, photographic studies. However, we have not examined the sensors in the context of the data needs of many other vital urban problems, nor have we come to grips with the question of cost effectiveness.

Investigations of other critical urban problem areas are necessary in order to clearly establish the potential of remote sensors as viable urban data sources. An evaluation of all available data-collection methods with a view to determining which method comes closest to achieving predefined levels of acceptability for the requirements of timeliness, flexibility, compatibility, and reliability within the constraints of a specified budget is a necessity. One major difficulty in undertaking any study of the cost effectiveness of remote sensors vis-a-vis other scurces of urban data lies in the unfortunate fact that very little cost documentation is available for the data-collection methods currently in use. We are in the process of obtaining detailed cost information for one large ground survey conducted in Los Angeles immediately before mission 73, but the existence of such information must be considered highly unusual.

Currently, it appears that useful cost-effectiveness data can be produced only through the actual operation of current data-collection methods within a strict cost-accounting framework. Aside from a rather unattractive and expensive decision to undertake the development of this information entirely within the Earth Resources Survey Program, the only viable alternative appears to be to persuade the relevant action agencies to embed one or more of their future data-collection efforts within an appropriate cost-accounting framework. This latter course of action would undoubtedly require coordination and persuasion on a fairly high administrative level. Any effort directed at cost-effectiveness studies implies, of course, that comparable accounting records will be developed for all phases of the existing aircraft program and that viable estimates of the costs of spacecraft programs will become available. The exceedingly complex problem of joint costs and benefits between the various sensing systems must also be successfully untangled.

Probably, the most promising area for immediate investigation is that of data inputs for the urban transportation planning process. This process, diagramed in figure 7-2, utilizes data relating to existing land-use and movement patterns within the city to forecast future movement patterns. Included in this forecasting process is the development of land-use forecasting models which are utilized by both urban planners and transportation planners. These models are critical to decision makers in that they specify probable outcomes of alternative action programs. The testing of urban models of this type has been seriously hampered by the lack of a sound data base and particularly longitudinal data sets. These forecasts then form the basis for major investment decisions in freeways, mass transit, et cetera. All major urban areas in the United States are required to participate in this process on a continuing basis in order to qualify for Federal participation in the funding of the resulting construction schemes. Our current research has already demonstrated the ability of airborne sensors to provide the required data on residential land use, and it appears likely that techniques to provide the desired data on commercial and industrial uses can be developed. The question of the necessary movement inventories is quite another matter. For several years, we have urged without success that experiments in this critical area be incorporated into the program. One major difficulty appears to be that experiments in movement dynamics are unique to this portion of the Earth Resources Survey Program. The demands of such experiments in terms of aircraft flight time and related ground studies would be heavy, and newly specialized sensors (e.g., moving target indicator radars, plus appropriate transponders mounted on a sample of vehicles) would be required. The failure to develop experimentation in this area represents one of our major disappointments with the Earth Resources Survey Program. Significant, if not as comprehensive, results can still be obtained through demonstrations that remote sensors can supply the data necessary for the static inventories (e.g., land-use inventories for small areas within

the city). Studies of the data requirements for the urban transportation planning process are also attractive in that this problem area would appear to be one of the best for the collection of cost data.

So far, nothing has been said about the remote sensing of urban areas from earth-orbital platforms. There is a good reason for this omission. At the present time, we have only low-altitude thermal IR imagery and a few scattered radar images. The radar appears somewhat more attractive than the thermal scanners, but we need to experiment with a much larger quantity of urban imagery more representative of the broad spectrum of available radars before more definitive statements can be made. In the photographic area, the low-altitude aircraft flights have demonstrated that high- to ultrahigh-resolution imagery, from an orbital standpoint, can be a valuable source of urban data. Our studies of the limited Gemini urban imagery show that useful information on the size, location, and — by implication — functional structure of the system of cities can be obtained at relatively low-resolution levels.

Based upon our investigations, there is no question in our minds that images obtained from remote sensors in earth orbit can be a useful source of urban data in this country and particularly in the rest of the world. However, detailed interpolation between the two extreme cases mentioned previously is quite difficult. The situation would be clarified considerably by the generation of additional data points, and as a consequence, we would suggest that a very high priority be assigned to placing a standard, long-focal-length mapping camera in a short-term earth orbit as soon as possible. Imagery obtained from aircraft operating at altitudes of at least 15 to 20 miles would also be useful. When additional information of the type discussed here becomes available, more specific comments on potential urban uses of imagery obtained from sensors in earth orbit will be possible.

REFERENCES

7-1. Anon.: Address of July 27, 1967, quoted in Appendix C of Report of the National Advisory Commission on Civil Disorders. U.S. Govt. Printing Office, Washington, D.C., 1968.

7-2. Anon.: Joint House-Senate Colloquium to Discuss a National Policy for the Environment. Hearing before the Committee on Interior and Insular Affairs, United States Senate, and the Committee on Science and Astronautics, U.S. House of Representatives, July 17, 1968.

7-3. Anon.: Conference on Space, Science and Urban Life. NASA SP-37. U.S. Govt. Printing Office, Washington, D.C., 1963.

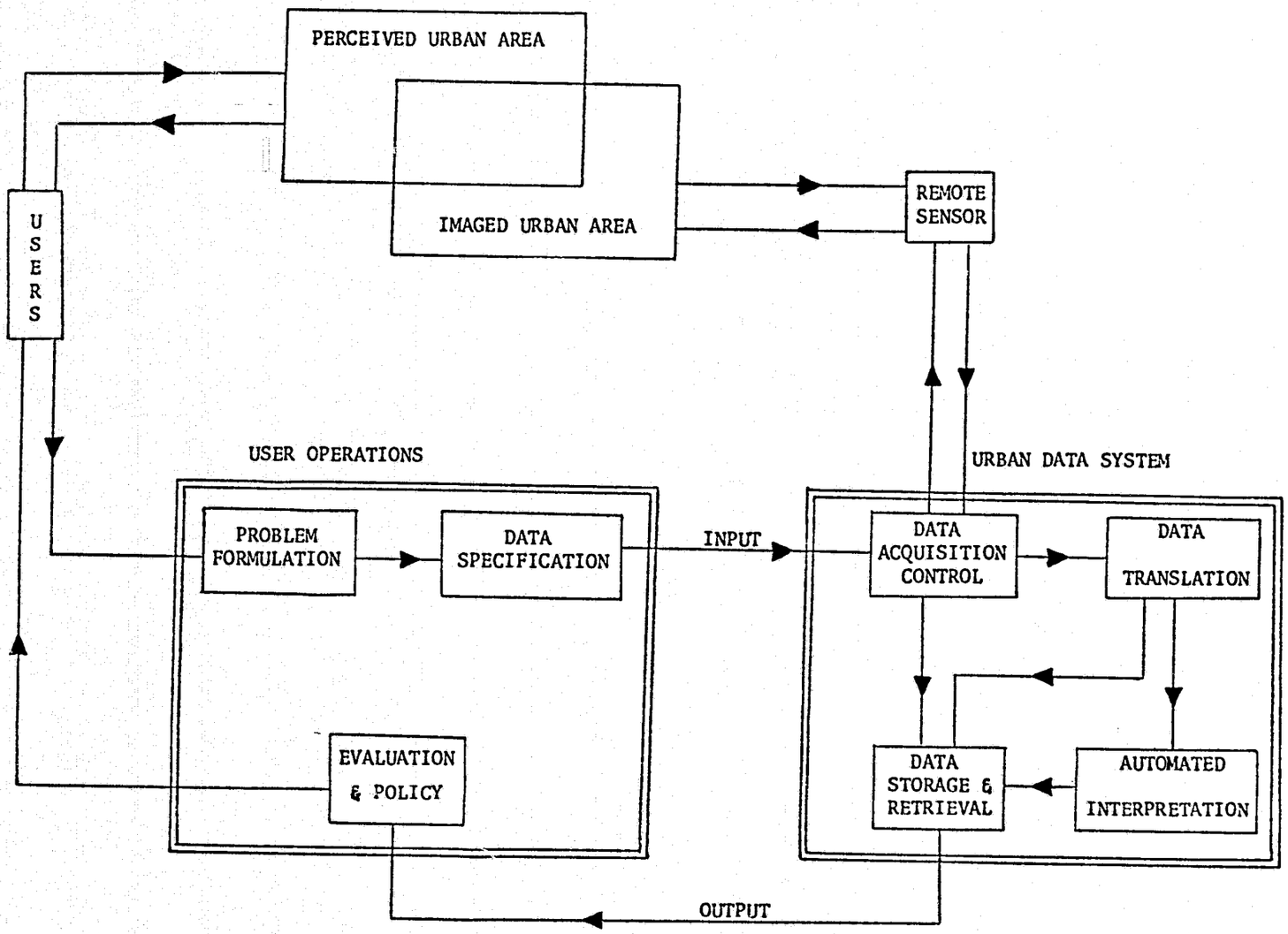

Figure 7-1.- A framework for the collection and processing of urban data using remote sensor imagery.

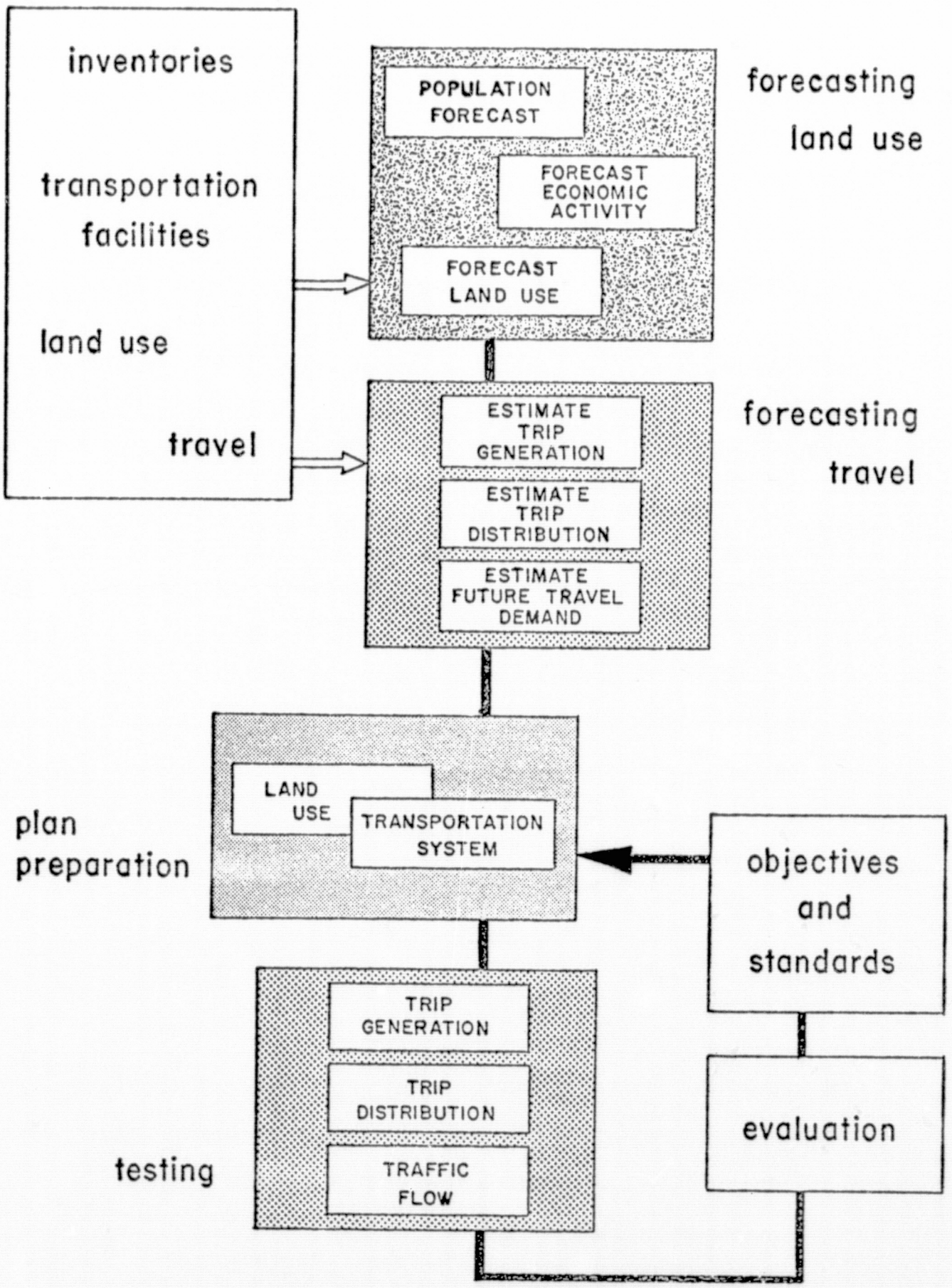

Figure 7-2.- The planning process.

APPENDIX 7A

SELECTED REPORTS PREPARED BY THE REMOTE SENSING LABORATORY, DEPARTMENT OF GEOGRAPHY, NORTHWESTERN UNIVERSITY

Betak, John F.: Object Identification in Aerial Photographs: A Preliminary Report. April 1967.

Binsell, Ronald: Dwelling Unit Estimation from Aerial Photography. June 1967.

Dacey, Michael F.: A Model for the Areal Pattern of Retail and Service Establishments Within an Urban Area. April 1966.

Dacey, Michael F.: Some Observations on a Two-Dimensional Language. December, 1965.

Dacey, Michael F.; and Marble, Duane F.: Some Comments on Certain Technical Aspects of Geographic Information Systems. December 1965.

Dueker, Kenneth J.: Spatial Data Systems: Organization of Spatial Data. December 1966.

Dueker, Kenneth J.: Spatial Data Systems: Systems Considerations. December 1966.

Dueker, Kenneth J.: Spatial Data Systems: Special Topics. December 1966.

Garrison, William L.; et al.: Data Systems Requirements for Geographic Research. April 1965.

Garrison, William L.; et al.: Five Papers on Remote Sensing and Urban Information Systems. April 1966.

Manji, Ashraf S.: Uses of Conventional Aerial Photography in Urban Areas: Review and Bibliography. July 1968.

Moore, Eric G.: Side-looking Radar in Urban Research: A Case Study. June 1968.

Moore, Eric G.; and Wellar, Barry S.: Experimental Applications of Multiband Photography in Urban Research. February 1968.

Moore, Eric G.: Remote Sensor Imagery in Urban Research: Some Potentialities and Problems. December 1967. (Also issued as NASA Technical Letter 118, May 1968).

Schneider, Clarke H. P.: Material Identification in Urban Areas from Gray Tone Variations in Multispectral Photography. June 1967.

Thomas, Edwin N.; and Marble, Duane F.: The Use of Remote Sensors in Urban Information Systems. April 1966.

Wellar, Barry: Generation of Housing Quality Data from Multiband Aerial Photographs. April 1967.

Wellar, Barry: Thermal Infrared Imagery in Urban Studies. September 1968.

APPENDIX 7B

RESULTS ACQUIRED FROM THE USE OF DATA FROM NASA AIRCRAFT

Introduction

The Remote Sensing Laboratory, Department of Geography, Northwestern University, has been involved in flight operations on four urban test sites: Chicago, Illinois (43); Phoenix, Arizona (29); Los Angeles, California (130); and New Orleans, Louisiana (132). Involvement with test sites 130 and 132 has been quite recent, and generally the comments which follow will apply to investigations based upon imagery obtained over test sites 43 and 29.

Imagery Available

Test site 29 was flown by NASA Convair 240A aircraft in July 1965, February 1966, and March 1967. In addition, a small quantity of thermal IR imagery was obtained from the HRB-Singer flight in August 1966. Little useful color photography was obtained on missions 12 and 19 as the result of exposure problems. The multiband black and white photography was generally good and formed the basis for much of the early work.

Test site 43 was flown by NASA aircraft in November 1965, July 1966, and November 1966. Mission 14 imagery covered a limited portion of the site, and utility of the imagery was reduced through double exposure of a signigicant portion of the multiband film. Mission 25 covered more of the test site, but several equipment failures occurred. Mission 31 attempted to pick up flight lines that were skipped on mission 25, but was only partially successful because of weather conditions. Two sets of radar imagery were obtained in October 1965 and July 1966 by the Westinghouse Corporation acting under contract to the NASA Earth Resources Program.

Results Obtained

Since a large number of technical reports have been prepared which were based upon analyses of the imagery (appendix 7A), this section will serve mainly as a guide. Most of the imagery available consisted of conventional color and multiband black and white. The range of current

applications of this type of imagery is pointed out by Manji (1968). Early works, primarily with the multiband imagery, lead to reports dealing with the place of remote sensors in urban information systems (Dueker, 1966; Garrison, 1966; and Thomas and Marble, 1966). More detailed studies on object identification and signatures in urban areas followed (Betak, 1967; and Schneider, 1967) in an attempt to develop data on problems of signature versus pattern analysis in urban areas. A heavy concentration on nonresidential land use produced reports by Wellar (1967) and by Moore and Wellar (1968) which demonstrated the utility of multiband photography in this area.

Reports dealing with the thermal scanner (Wellar, 1968) and imaging radar (Moore, 1968) were prepared, but their release was held up for several months because of security considerations. In addition, a report has been prepared on the subject of urban data which can be extracted from Gemini photography.

Instrument Evaluation

Studies to date have had available standard color photography, color IR photography, and multiband photography in large quantities plus smaller amounts of imagery from scanners operating in the thermal IR and in the ultraviolet regions. In general, photographic sensors have been found to be the most useful with color IR photography which is superior to regular color because of increased contrast and haze penetration. A bank of medium- to high-resolution mapping cameras operating in a multiband mode would appear to be highly useful in an earth-orbital situation, but only if combined with appropriate data-handling equipment. Imaging radars also appear to be highly useful. Returns from scanners operating in the thermal IR region do not currently seem as promising, and no positive results have been obtained from examination of the ultraviolet scanner imagery.

It should be realized that the previous statements reflect the availability of various types of imagery. Neither imaging radars nor the thermal scanners have been studied in appropriate detail (text of this report), and a thorough instrument evaluation must wait until a broader capability is available in these areas.

ERRATA

SECTION 7

REMOTE SENSING AND THE STUDY AND PLANNING
OF URBAN AREAS

By Duane F. Marble and Frank E. Horton
Sept. 1968

Page 7-1, byline: The name of the second author should be Frank E. Horton instead of Frank E. Norton. This correction should also be made on page iii in the Contents.

Issue date: 9-1-69

N71-16132

THEMATIC LAND-USE MAPPING WITH SPACECRAFT PHOTOGRAPHY AND RADAR

By David S. Simonett
Department of Geography and Center for Research in Engineering Science
University of Kansas, Lawrence, Kansas 66044

ABSTRACT

Construction of thematic maps with spacecraft-derived photographs and with radar images obtained from aircraft with resolutions comparable to those anticipated from spacecraft is in progress, supported by funding from the Geography Applications Program, U.S. Geological Survey, for the National Aeronautics and Space Administration. Preliminary studies are reported in a discussion of (1) whether existing thematic land-use maps could be constructed with space data, (2) problems of constructing thematic land-use maps using space data, (3) information in Gemini photographs and in aircraft radar images, and (4) some aspects of the roles of photography and radar as complementary and supplementary sensors.

INTRODUCTION

The interest of geographers in the possibility of spacecraft thematic mapping arises because most thematic maps have scales between 1:100 000 and 1:2 000 000 and are laboriously pieced together with data which vary markedly in quality, quantity, and date of collection. It is rarely possible to obtain a single synoptic view with existing methods of data collection, except in single countries at the time of their national censuses. However, for many parts of the world, national censuses are infrequent and are of only modest accuracy. For most underdeveloped nations, thematic maps which are useful for planning and for various levels of policy decisions are inadequate.

It has been suggested or implied by a number of geographers, including the writer, that multisensor space systems may well constitute the best source of contemporaneous data acquisition for construction of some existing types of thematic maps and for the construction of new types of thematic maps. It has been argued, for example, that instead

of widely scattered point information, which is variable in both quantity and quality, spacecraft will give us broad-perspective, small-scale, repetitive areal observations which have not hitherto been obtainable. It has also been suggested that spacecraft repetitive and multisensor observation may offer new opportunities both to reduce the degree of our dependence on ground study and to improve the quality of our inferences in the areas between field study sites.

To test these suggestions, it is appropriate to consider various thematic maps in regard to their data base and uses and with regard to the feasibility of constructing the maps with spacecraft-derived imagery.

POSSIBILITY OF EXISTING LAND-USE MAPS BEING CONSTRUCTED USING SPACE DATA

The following preliminary conclusions have been reached on the basis of inspecting a great variety of land-use maps at scales ranging from 1:20 000 to 1:1 000 000:

1. Very few existing land-use maps at any scale could be exactly duplicated from spacecraft data. This arises because practically every map inspected mixes some categories which would be observable using space data with others which are nonobservable. The nonobservable categories may require (a) too high a spatial resolution (allotment gardens shown on a number of British maps), (b) information which is not obtainable from space, being obtained from statistical sources, (c) inferences only (not precise information) which could be obtained from space, or (d) a synthesis of material usually from statistical sources. Examples of statistical sources would include such categories as unirrigated vineyards, irrigated vineyards, improved pasture, grazed desert shrubland, fine wool raising, et cetera.

2. Spacecraft-derived data may be used to bridge existing thematic land-use maps, but with varying degrees of "accuracy," depending on the problem at hand.

3. Spacecraft data derived from Gemini photographs may be used to produce thematic maps with differing levels of error, depending on the need at hand. This, it is suspected, will apply even with finer resolution photographs. Thus, it may be necessary to delineate all small villages and small highways, and the Gemini photographs may be found to be unsuitable for such a purpose. Alternatively, some loss function (perhaps 20 percent in this case) may be found to be acceptable.

PROBLEMS OF CONSTRUCTING THEMATIC LAND-USE MAPS USING SPACE DATA

In June and July of 1968, a study was begun on the problems which would be involved in producing a simple eight-category thematic land-use map, employing the following categories, to be compiled initially at a scale of 1:250 000:

1. Settlement
2. Cultivation
3. Grass
4. Forest
5. Water
6. Brush
7. Barrenness
8. Ice and snow

Two parallel studies were carried out on the cell size for decision-making and the cell size for resolution. In the first study, the cell size for decisionmaking took cells in steps of 100, 200, 400, and 1000 ft^2 in Kansas, Panama, southeast Asia, and Puerto Rico. In a major study in eastern Kansas involving four adjacent counties (4000 square miles) the cell size for decisionmaking was 40 acres. One subsample in the eastern Kansas study was tested with six operators individually making decisions to obtain some idea as to the types of decision differences which could later be compared with machine decisions. These studies lead to the following preliminary conclusions:

1. The degree to which a given spatial resolution effects information transfer is a function of the spatial and temporal distribution of objects in each given geographic area. In short, no single resolution will convey the same information in all environments. A given resolution has, in effect, an information transfer function accompanying it which is environmentally modulated. Much further work is needed on this problem.

2. The infinite variety of possible combinations of different objects within large-resolution cells makes it infeasible, except on an

occasional basis, to carry out within-cell multispectral discrimination techniques. In short, gross-resolution multispectral data cannot substitute across the board for higher resolution information.

3. Tests begun on several Gemini and Apollo photographs, including those of the Dallas-Fort Worth area, to compare transportation routes with routes delineated on radar indicate that the Apollo photographs have a very high potential for accurate delineation of transportation routes in that environment, though it may not be easy to discriminate between route types. In particular, roads under construction are the most readily detected and indicate a valuable potential for change detection. The radar images of the same area have yet to be evaluated.

4. Color-separation plates prepared with Gemini photographs to determine the information available in the different wavelengths indicate considerable differences in information in each channel, depending on the environment.

5. Studies on a Gemini photograph of the MacDonnell Ranges of central Australia, supplementing those already carried out under Australian sponsorship by R. N. Colwell (Berkeley, California) and R. A. Perry (CSIRO, Australia), have been made on the cut-off effect in vegetation and soil boundary discrimination evident with an approximately 300-foot resolution on the Gemini photograph. These studies indicate, as Colwell has already determined, that boundaries of significant vegetation communities (determined by Perry and others from field work) were easier to delineate on space photographs than on air photomosaics and that a number of subtle boundaries were easier to detect on the space photography than on air photographs and photomosaics. In other instances, however, now being documented in detail, significantly different vegetation communities are displayed in comparable color tones because of the presence of the fine mixture of vegetation, soil, bare rock, et cetera. Thus, light-toned areas on the Gemini photograph include complex dissected laterite areas, bare red soil, dry kerosene grass and red soil, dry mitchell grass and red soil, and some salt pans. On the basis of color tone or texture alone, these areas cannot be separated on the space photograph. Similarly, dark-toned objects including dense Mulga (Acacia aneura), Melaleuca, Eucalyptus camaldulenis, and Collitris sp. cannot be acceptably separated on color or multispectral tone value alone. To enable these communities to be distinguished, higher resolution is necessary, perhaps on the order of 100 feet, in order for distinctions to be made employing spatial associations in context. A modest amount of light-aircraft aerial oblique photography coupled with spot ground checks could usefully be employed with Gemini space photographs to produce rapid-reconnaissance vegetation-type maps. As suggested also by Colwell and Poulton at this meeting, there would, of course, be errors in such maps, but all maps compiled by man contain

errors. The only question of relevance is of the nature of the errors and the degree to which they are intolerable for the purpose at hand.

INFORMATION ON GEMINI PHOTOGRAPHS

The 120 space photographs have been color separated and arranged by the moisture in the atmospheric mass. These are being inspected to determine the relative amount of noise in the blue, green, red, and infrared (IR) layers as a function of atmosphere-contained moisture. It will be 6 to 8 months before this work is sufficiently far advanced for definitive information to be given. Experiments were also carried out in central Australia using film-filter combinations in false color involving the Wratten 12 and the Wratten 15 plus 80B filters which Pease and Bowden of the University of California at Riverside have used in experiments. Color-separation plates in central Australia have been edge enhanced for detection of fine structure within the images. It is now clear that color-separation plates, used in conjunction with the color photography, convey more information than the color photography alone.

INFORMATION ON RADAR IMAGES

1. In order to determine the degree to which radar images and space photography may usefully complement and supplement one another, Gemini and Apollo space photographs in the Houston and Dallas-Fort Worth areas are being compared with radar imagery of different resolutions in the same areas. This study is at an early stage, and it is not feasible yet to report on the results, except that detection of urban and transportation areas in four Gemini photographs were made in the Gila Bend, El Paso-Juarez, Midland-Odessa, and Houston-Gulf Coast areas. Comparisons also were made of radar images with 17 interpreters, and the quality of the results are now being compared.

2. The information available on radar imagery is discussed in a number of preliminary reports. The report by A. J. Lewis, "Evaluation of Multiple Polarized Imagery for the Detection of Selected Cultural Features," is summarized in appendix 8A. It employs an analysis of the imagery from nine areas scattered widely throughout the United States and tests statistically the differences between like-polarized (HH) radar imagery and cross-polarized (HV) radar imagery in the detection and delineation of point and line cultural targets. The report employed some 70 interpreters to provide adequate statistics.

3. A preliminary study has also been made by Joseph Sabol outlining the steps necessary to calculate the relationship among areas of small communities to correlate with population. This will be necessary to define the types of errors present in simple population-area model predictions. It is already known that Stig Nordbeck's Law of Allometric Growth, which implies an orderly relationship between size of an area and population of the area, does not hold at all well when Gemini space photographs are used (personal communication, Duane Marble, Northwestern University). A preliminary study by Sabol is reported in the first annual report of U.S. Geological Survey contract 14-08-0001-10848 (ref. 8-1). Sabol's study is entitled "The Relationship Between Population and Radar Derived Area of Urban Places." This and related studies at Northwestern University are fundamental to possible thematic population mapping. However, since each culture is unique, the relationship will also be unique for each culture. Twenty-one interpreters were used in the study to define the nature of the errors in measurement.

4. Landform studies using radar imagery have been carried out employing NASA-funded AN/APQ-97 imagery of the Wasatch Range reported on by Rex Peterson. This was supported mostly by project THEMIS (U.S. Army Engineer Topographic Laboratories DAAK02-68-C-0089), though some support was also received from U.S. Geological Survey contract 14-08-0001-10848. This study is reported in the annual report on U.S. Geological Survey contract 14-08-0001-10848. In addition, a landform class identification study was carried out by David Schwarz and Roland Mower utilizing non-NASA-funded imagery in Puerto Rico. Comparisons were made of this type of landform class maps with landform maps prepared by other investigators employing detailed topographic maps as their information source.

5. Radar natural-vegetation studies have been carried out extensively at Horsefly Mountain. These studies were funded under a number of NASA grants including U.S. Geological Survey contract 14-08-0001-10848. Other studies with multiband and color photographs have been employed at the Horsefly Mountain Test Site to see what combinations of radar and photography may usefully be employed in plant community discrimination, using the image discrimination enhancement and combination system (IDECS).

6. A study on the type of soil reconnaissance information available in radar imagery in north-central Oklahoma has also been prepared under the U.S. Geological Survey contract.

7. A series of studies at Garden City, Kansas, on the relation between radar return and crop type, cover, state, et cetera, have also been funded under a variety of NASA contracts, including U.S. Geological Survey contract 14-08-0001-10848 for the Geography Applications Program.

COMPLEMENTARY AND SUPPLEMENTARY ROLES FOR RADAR AND PHOTOGRAPHY

As a portion of this phase of the study, computer-derived maps comparing the time available to radar and photography by month and season for selected stations in the United States have been generated. These are now under study.

FIGURES

Twelve illustrations were used in the presentation. These included a number of color photographs of central Australia in an area covered by a Gemini photograph. This photograph has been studied by R. N. Colwell (Berkeley, California) and Ray Perry (CSIRO, Australia) during the last year, as well as more recently, for different purposes, by the writer. Since the central Australian photographs are still under active study, they are not included in this selection. The figures given here are confined to illustrations of cultural target discrimination, urban land use, and soil association studies with K-band radar.

Figure 8-1 summarizes for the Woodsboro, Maryland, area the improvement of K-band radar detection of point cultural targets (such as farm buildings) through the use of multiple polarization. With a monochromatic radar source, scintillation is a handicap in the detection of point (though not area-extensive) cultural objects. As is demonstrated in this figure, the addition of several polarizations materially improves the chance of detection of such objects. As has been demonstrated earlier in studies at Garden City, Kansas, at Horsefly Mountain, and elsewhere, multiple polarization materially aids the differentiation of various area-extensive targets such as natural and cultivated plant communities. This figure also demonstrates that the addition of multiple-polarization aids in detection of small targets as well. In the paper by A. J. Lewis, referred to previously, there are approximately 40 tables involving statistical comparisons on detection of bridges, farm houses, oil fields, and so forth. This figure illustrates one such comparison.

Figures 8-2 and 8-3, showing the Lawrence, Kansas, area as displayed in a K-band radar image, also indicate the transportation network and land-use interpretation derived from the radar image, together with the areas misinterpreted in the land-use interpretation. The figures illustrate, on a small scale, the utility of K-band radar imagery on the Westinghouse AN/APQ-97 system in the delineation of transportation and internal land use in cities. Comparable studies within the Chicago

metropolitan area have also been carried out by geographers at Northwestern University. In addition, studies in the Los Angeles urbanized region are being made by groups at the University of California, Riverside, and at the University of California, Los Angeles. All these studies have indicated, as Eric G. Moore (ref. 8-2) notes,

"A considerable amount of data relating to patterns of land use within the urban area can be obtained utilizing a K-band side-looking radar. It is evident that different degrees of accuracy are associated with the identification of different components of urban structure: (1) The linear elements of the transportation network are clearly defined with the HV polarization proving to be more useful than the HH, as high returns from adjacent buildings on the latter prevent accurate interpretation. (2) The gross patterns of industrial, residential, and open space land use are capable identification, although it is not possible to map the local boundaries of different land uses in detail. The main criterion for distinguishing between these land-use categories is the variation in image texture. The HH polarization provides the main basis for interpretation. (3) Attempts to identify commercial land proves to be surprisingly unsuccessful, the cardinal affect introducing considerable problems in the recognition process."

These conclusions indicate that aircraft radar may usefully supplement space photography for intraurban studies and that moderate-resolution radar imagery obtained in space will aid in studies on transportation and city structure.

Figure 8-4 is a K-band radar image of a portion of Woods County, Oklahoma. Through interpretation of this image, the two soil association maps given in figures 8-5 and 8-6 were produced.

Figure 8-5 shows soil associations normally distinguishable on K-band imagery in Woods County, Oklahoma. Comparison between this and the preceding illustration shows that of the four soil associations shown, three — the Vernon Badlands, salt plains, and Lincoln-Yahola (flood plains) — are distinguishable with relative ease on the radar imagery, but item four — river terraces — is distinguishable only with some difficulty. The Vernon Badlands association typically has a steeply convex valley side plunging into a narrow, almost flat-floored, valley. The rough valley walls, clad variously in small trees, grass, sagebrush, and exposed gypsum, are easily delineated on the radar imagery. The salt plains association is a bare soil on river wash with a distinctive light tone on the radar image. The flat Lincoln-Yahola flood plains association is covered with mixed grass, sagebrush, and occasional trees. While the association as a whole is easily mapped, its component soil

series cannot be detected. The river terraces association usually can be separated from the flood plains, but, again, several soil series cannot be noted. In other regions, we have found it more difficult to distinguish terraces from flood plains, for example, in the Kansas and Wakarusa valleys near Lawrence, Kansas. The ability to distinguish river terraces on radar imagery varies in relation to the environment; the radar look angle, the easiest being at low angles of elimination; and the location at which the vegetation differs on the terrace and flood plains.

Figure 8-6 shows four additional soil associations in Woods County, Oklahoma, which could not be distinguished from one another, although collectively they could be separated from the associations mapped in the preceding figure. Associations shown in this illustration include soils which would be classified as Udic Argustools, Typic Ustochrupts, and Haplic Calciustolls. The inability to discriminate between these soil associations on the radar image is in many ways to be expected in an area so completely given over to cultivation. Studies by Lundien and Simonett have already indicated that radar is much less sensitive to soil texture variations within a field than it is to between-field differences in crops. Field patterns are dominant on this radar imagery and mask any weakly expressed soil information. Long-wavelength radar systems, of course, remain to be studied. There are some preliminary indications from studies by L. F. Dellwig that radar imagery of C-, L-, and P-bands may aid in making distinctions between different soil types.

SUMMARY OF OBJECTIVES AT LAWRENCE, KANSAS, TEST SITE 85 IN RELATION TO THE NASA EARTH RESOURCES AIRCRAFT PROGRAM

Imagery obtained by NASA, or with NASA funds, is being used as input data in an experimental investigation of real-time image-processing devices known as the IDECS multi-image correlation system (ref. 8-3). This system was developed under NASA contract NGR 17-004-003 and USAETL contract DAAK 02-C-67-0089, and work currently being performed is under the USAETL contract. With adequate ground-truth data collected at the time of each imaging flight, multispectral photographic and K-band radar imagery have been color combined and have been used to measure the ability of the multi-image correlation system to make a map based on single factor or multifactor stratifications. Such maps include those showing boundaries of soils, natural vegetation, agricultural land use, and trafficability.

In addition to the preceding, the following objectives also apply at this test site to assess the geoscience value of imaging and scatterometer radars.

1. Imaging radar. Identification and/or detection of (a) natural and cultural features, (b) land-use patterns, and (c) agricultural and natural vegetation

2. Radar scatterometer. Correlation of agricultural and natural vegetation patterns with scatterometer returns to determine to what degree crops can be differentiated and to what degree natural vegetation classes and bare ground can be discriminated

The other remote-sensing instruments include the metric mapping cameras, the IR scanner, and the ultraviolet (UV) scanner. These are requested to be operational during each mission as ancillary instruments and are generally given a third priority. Evaluation of data from these systems is limited to qualitative determination of land use. However, one metric mapping camera is necessary to provide indexing photography for scatterometer data. Data from a multiband camera are desirable for use in conjunction with a multi-image correlation study currently in progress.

SUMMARY OF SCIENTIFIC ANALYSES PERFORMED TO DATE

Multiband photography and multipolarizations of K-band radar have been used as input data for the multi-image correlation system to produce color-combined images for analyses in several areas within the Lawrence, Kansas, Test Site. Several areas in and near Baldwin, Kansas (located within the test site), have been investigated and analyzed for the purpose of discriminating agricultural land uses and urban versus rural areas. Color-combined multiband images of an area along the Wakarusa Area indicated areas of high soil moisture content resulting from recent flooding. These same images, combined with a K-band radar image of comparable scale from a flight approximately 2 years before the multiband imaging, resulted in a color-combined image which indicated a change in the river meander pattern. To date, only qualitative analyses have been made of these color-combined images.

Radar land-use and transportation maps of Lawrence and vicinity have been prepared by several interpreters, and the nature of the areas misinterpreted has been discussed in Simonett, et al. (ref. 8-1).

SUMMARY OF SCIENTIFIC ANALYSIS TO BE PERFORMED

Current investigations using NASA-funded multiband photography and NASA-funded radar are being concentrated on land-use mapping of the

Lawrence urban area. Manipulation of the color-combined images that form these maps to approximate boundaries on land-use maps prepared by the Office of the Lawrence City Manager will allow quantitative measurements of the degree of correlation between the land-use maps of Lawrence City and the land-use maps made from color-combined multiband photography and color-combined multipolarization K-band radar.

In anticipation of receiving 13.3-gigahertz scatterometer data from mission 74, a black and white flight-line aerial photomosaic has been prepared from color transparencies, and a land-use and crop overlay has been prepared from ground-truth data collected during the mission. The area of concentrated study is primarily an agricultural area, although there are some natural vegetation areas located within the flight path, and a city-farmland boundary is present. Similar overlays have been prepared for IR and UV data made simultaneously with the photography and scatterometry. A qualitative examination of the UV and IR imagery has been prepared, and tabular comparisons have been made with color photography. These will be evaluated quantitatively in due course.

For mission 61 data, land-use, vegetation (agriculture and natural), geology, and soils overlays are being prepared from detailed ground-truth data collected by the Kansas Geological Survey for the color photography, thermal IR imagery, and UV imagery. This information will be used in a correlation study with 13.3-gigahertz radar data for one area within the test site. Also, it is anticipated that a brief qualitative comparison of the photography, IR imagery, and UV imagery will be performed.

Since no scatterometry was obtained during mission 54, any analysis performed on the data received (color IR photography, IR imagery, UV imagery, and multiband photography) will be limited to qualitative analysis of the imagery. The IR imagery is poor and unusable because of scanning distortions, and the UV imagery is poor and unusable because of limited dynamic range. The color IR photography is not of good quality because it is out of focus along one edge, but it is anticipated that various overlays and comparisons can be prepared.

REFERENCES

8-1. Simonett, D. S.; et al.: The Utility of Radar and Other Remote Sensors in Thematic Land-Use Mapping from Spacecraft. Annual Report (U.S.G.S. 14-08-001-10848), Geographic Applications Program, U.S.G.S., 1968.

8-2. Moore, E. G.: Side-Looking Radar in Urban Research: A Case Study. (U.S.G.S. 14-08-0001-10654), Geographic Applications Program, U.S.G.S., June 1968.

8-3. Dalke, G. W.; et al.: Multi-Image Correlations Systems Study for MGI, Phase II Technical Report (U). (USAETL contract DAAK 02-67-C-0435), June 1968.

8-4. Moore, R. K.; and Simonett, D. S.: Potential Research and Earth Resources Studies with Orbiting Radars: Results of Recent Studies. AIAA Paper No. 67-767, 1967.

TABLE 8-I.- SUMMARY OF DATA COLLECTED AND OF WORK AT LAWRENCE, KANSAS, TEST SITE 85

[NASA MSC MISSIONS, PRINCIPAL INVESTIGATOR, D. S. SIMONETT]

Mission number	Date flown	Data	Date received	Quality	Results
54/1	August 7, 1967	Scatterometer	Not available for this mission		
		Reconofax IV (IR)	August 17, 1967	Poor	No results because of too much distortion from poor image quality
		AN/AAS-5	August 17, 1967	Poor	No results because imagery was too dark
		RC-8 (color IR film)	January 11, 1968	Fair	Only limited use because one side of film was out of focus
		Multiband	August 17, 1967	Fair	Lens 2 out of focus; other frames used for selected areas of multi-image color-combined mapping experiments on the IDECS
61/4	November 15, 1967	Scatterometer	N/R		
		Reconofax IV (IR)	December 1, 1967	Good	Use awaits receipt of scatterometry data
		AN/AAS-5	December 1, 1967	Good	
		RC-8 (color)	December 11, 1967	Excellent	
		Multiband	December 1, 1967	Good	Has been used for multi-image color-combined studies of soil moisture and agricultural land use along selected areas of the Wakarusa River with the IDECS
74/2	June 18, 1968	Scatterometer	N/R		
		Reconofax IV (IR)	July 9, 1968	Good	Use awaits receipt of scatterometry data
		AN/AAS-5	July 9, 1968	Good	
		RC-8 (color)	July 3, 1968	Excellent	Will be used for indexing and comparison
		Multiband	Camera unavailable		
Westinghouse AN/APQ-97 radar missions	September 14, 1965	AN/APQ-97 imaging radar	October 2, 1965	Very good	These data used to prepare radar land-use maps of Lawrence and vicinity
	September 15, 1965	AN/APQ-97 imaging radar	October 2, 1965	Very good	

TABLE 8-II.- SUMMARY OF DATA OBTAINED AND USED FROM MSC MISSIONS ALONG THE OREGON COAST (TEST SITE 7)[a]

Mission number	Date flown	Data	Date received	Quality
13	September 24, 1965	Black and white, duplicate positive transparency	September 1967	Good, out doesn't cover entire coast because of clouds south of Umpqua River
42	March 7, 1967	Black and white, duplicate positive transparencies	July 1967	Fair, however, coverage is spotty because of cloud cover

[a]The photographic transparencies from missions 13 and 42 were used to supplement the radar image coverage of the Oregon Coast flown by Westinghouse in 1965. It was used in preliminary field studies on coastal geomorphology by A. J. Lewis of the Center for Research in Engineering Science (CRES). CRES was not on the original recipient list for either mission 13 or mission 42, test site 7. The data received for test site 7 were requested after the mission was completed, although CRES did support mission 42 at the scheduling meeting. In both cases, the films were from trial or experimental overflights (ref. 8-4).

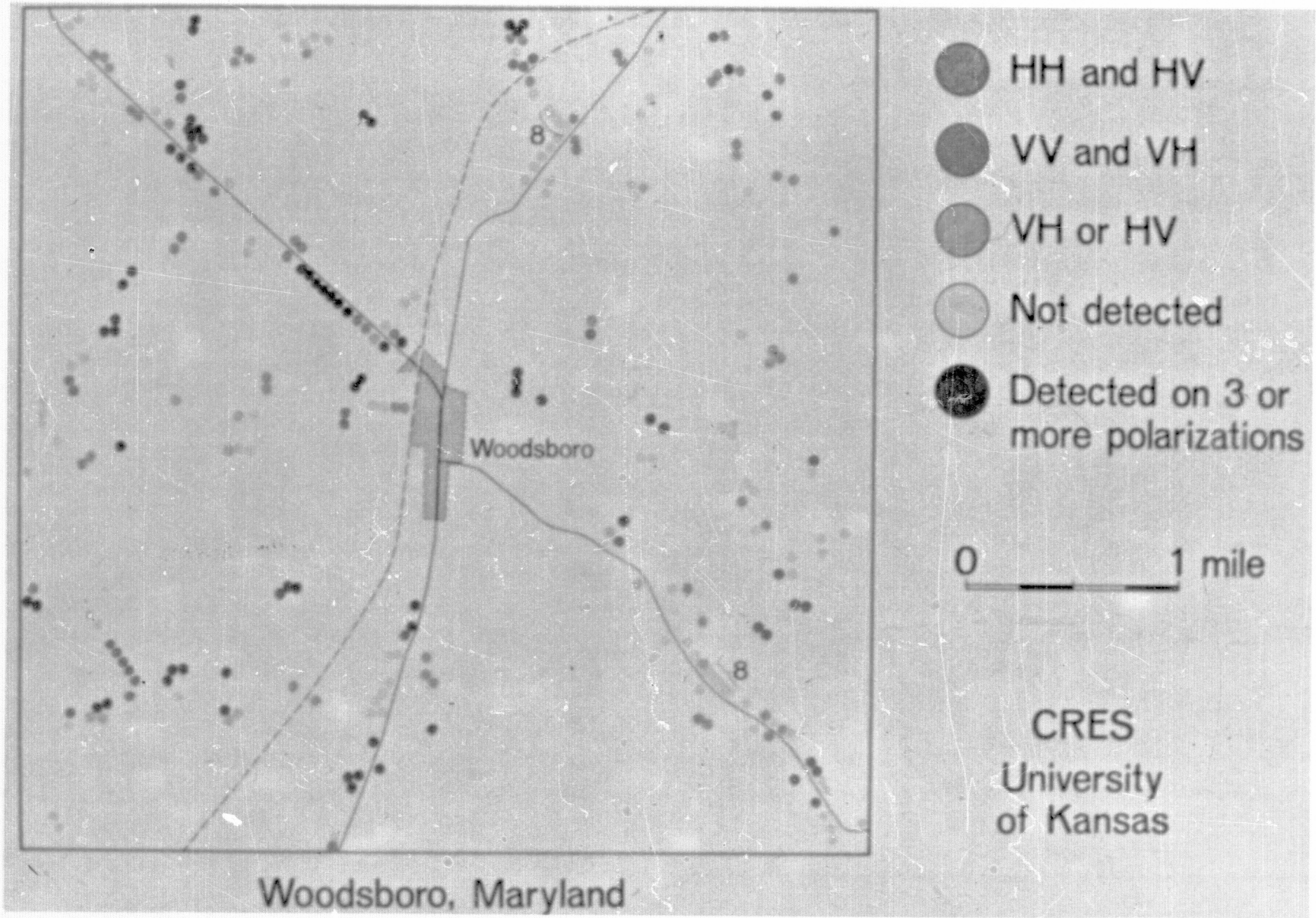

Figure 8-1.- Multiple-polarization identification of farm buildings on radar images.

K-BAND RADAR IMAGE

LAWRENCE, KANSAS SEPTEMBER, 1965

TRANSPORTATION NETWORK

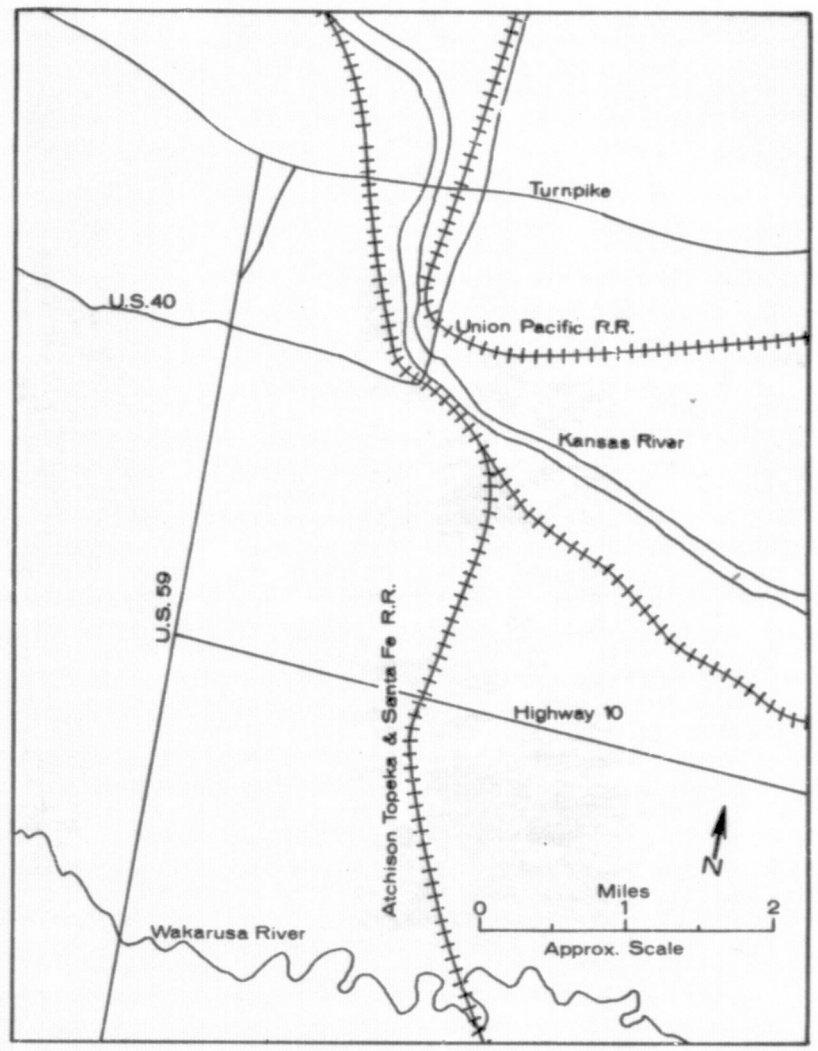

Figure 8-2.- K-band radar image and transportation network of Lawrence, Kansas, in September 1965.

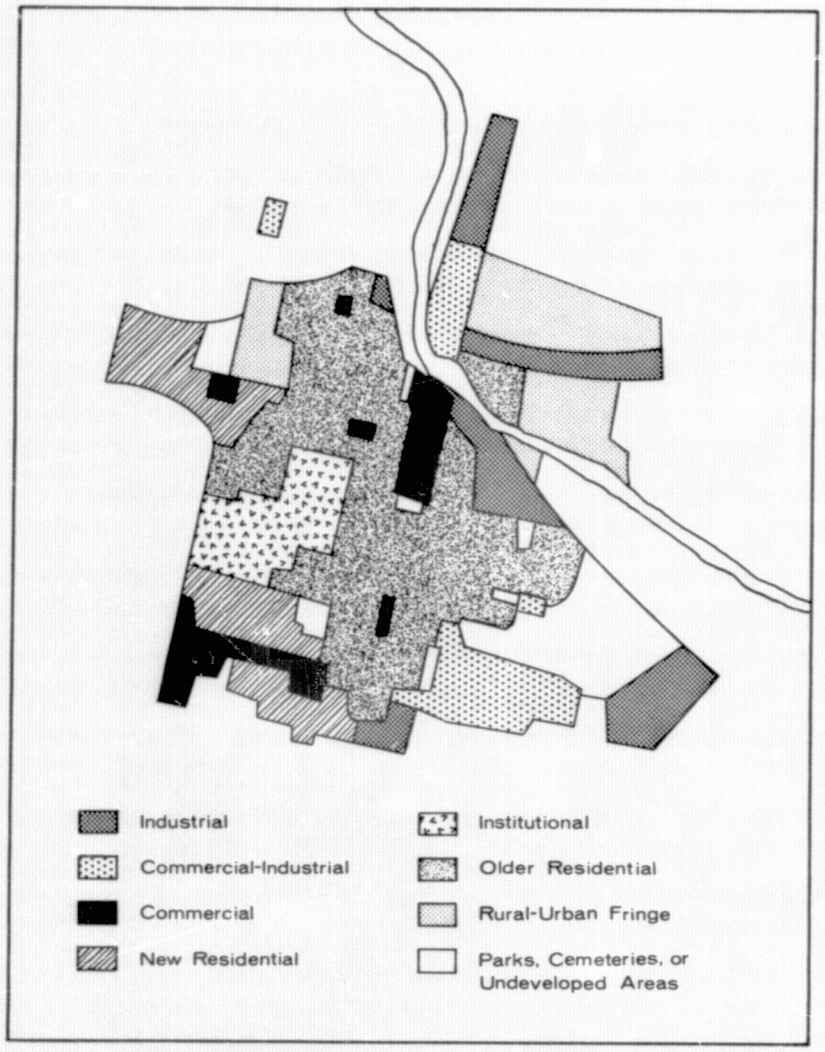

a. Urban land use as determined from the radar image. Thirty-three areas have been separated on the basis of tone, texture, and proximity to transport facilities and other relative location aspects. Six areas are misinterpreted (fig. 8-3b).

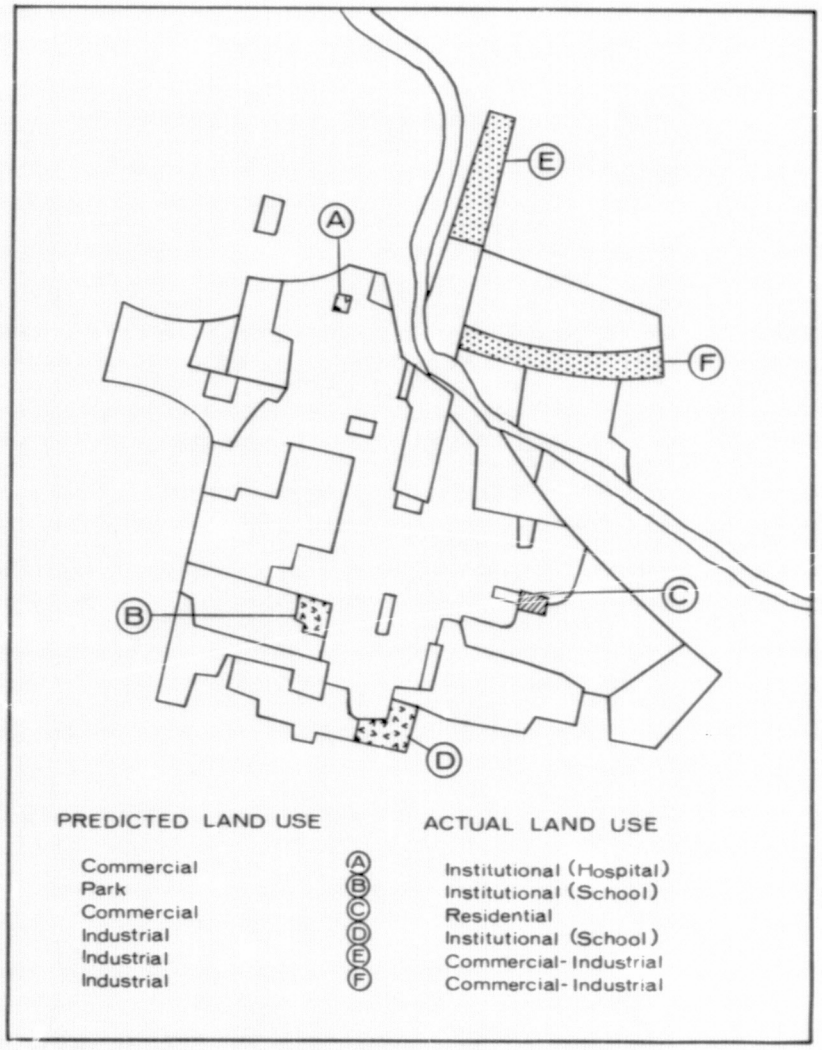

b. These six land-use regions had been improperly interpreted from radar (fig. 8-3a). They tend to be small areas or areas where the commercial and industrial distinction is not quite clear.

Figure 8-3.- Land-use map of Lawrence, Kansas.

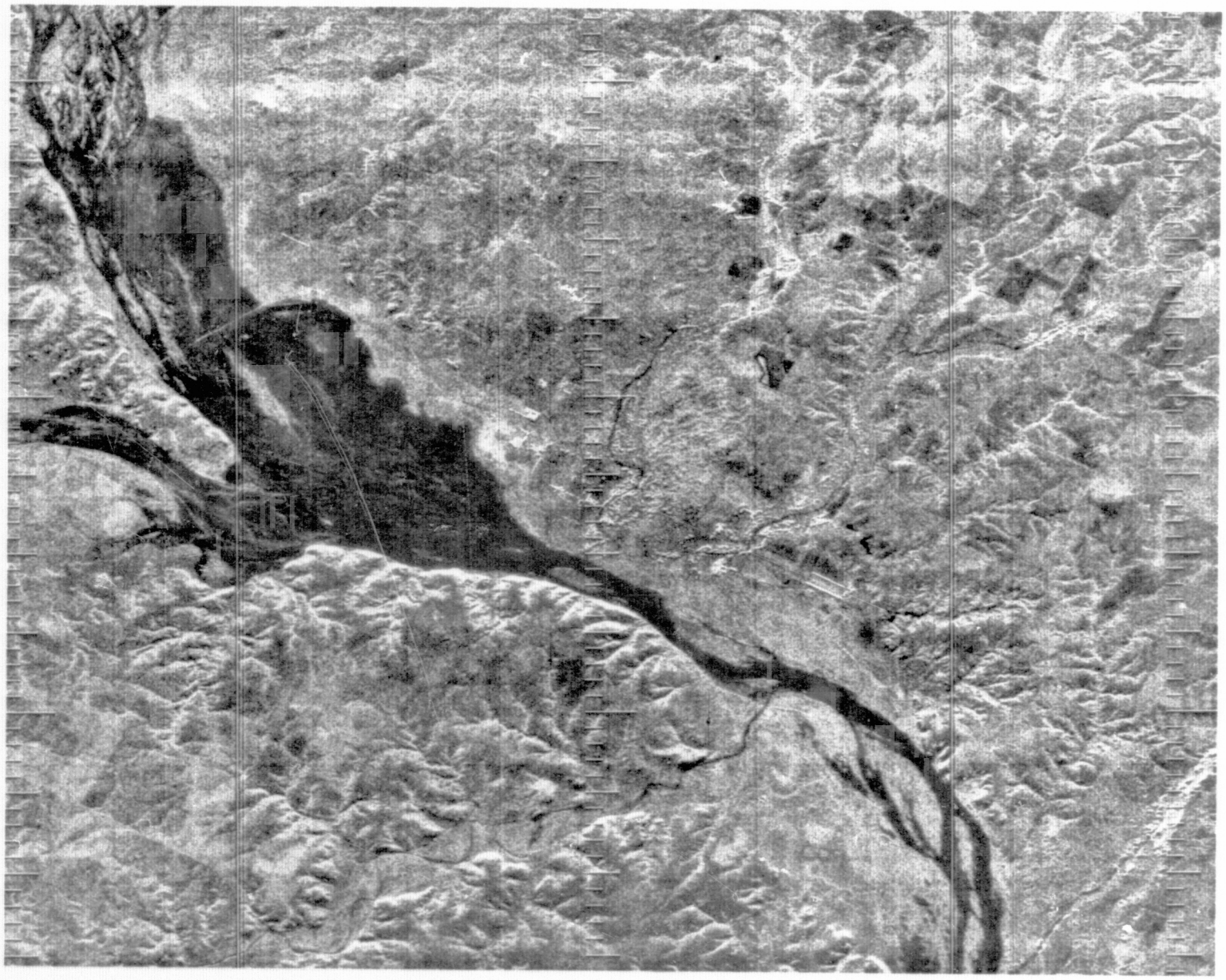

Figure 8-4.- K-band radar image of a portion of Woods County, Oklahoma.

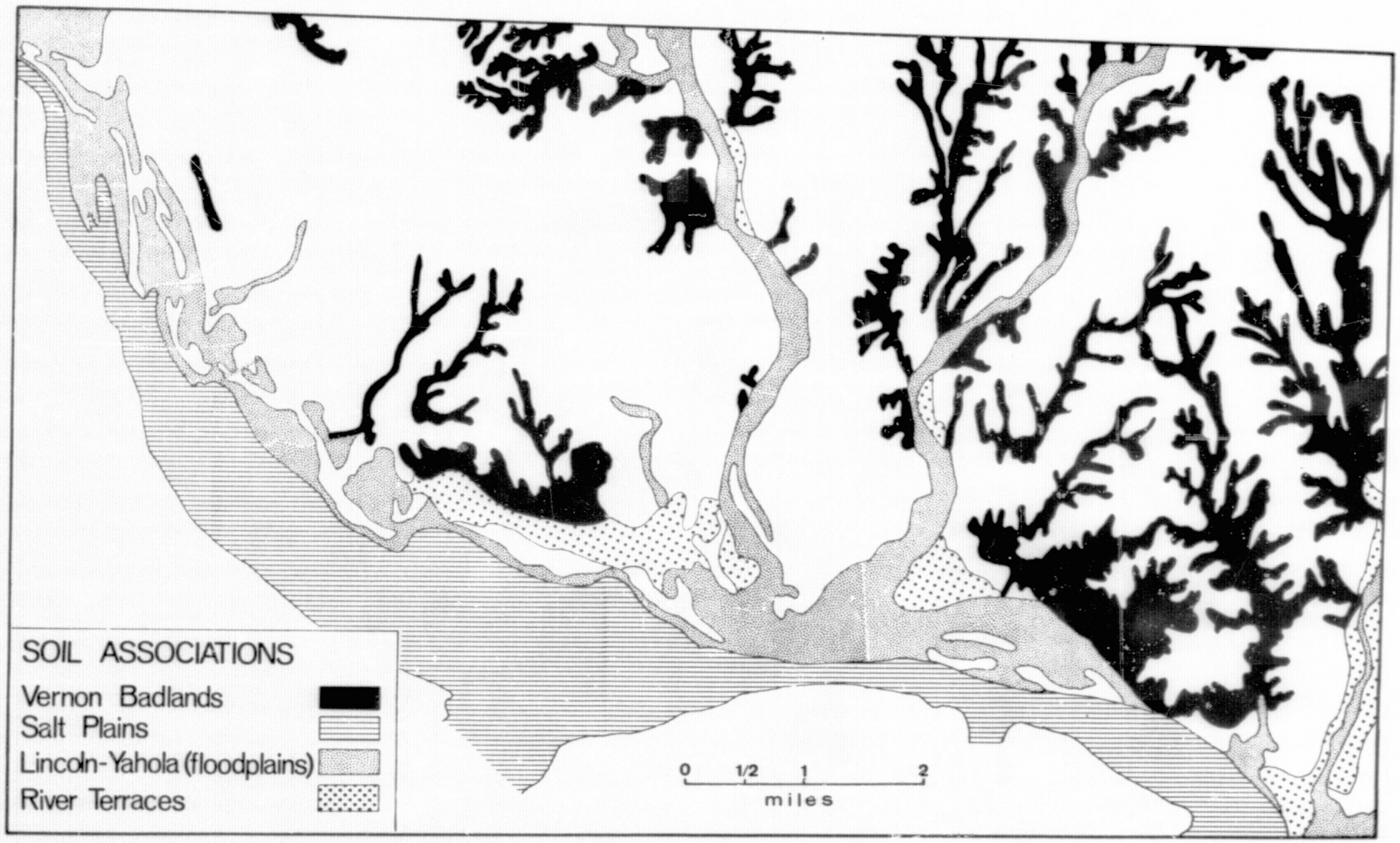

Figure 8-5.- Soil associations normally distinguishable on K-band imagery, Woods County, Oklahoma.

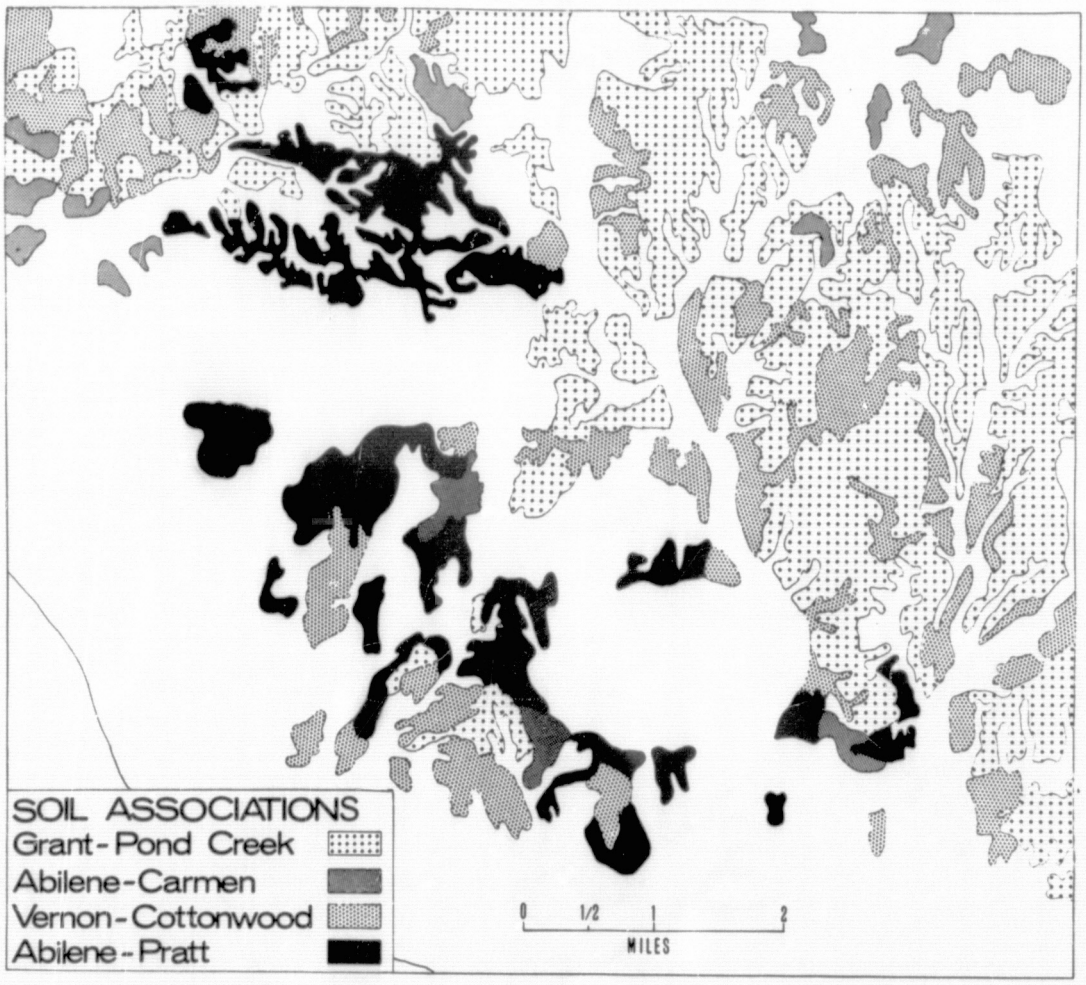

Figure 8-6.- Soil associations which cannot be separated on K-band imagery, Woods County, Oklahoma.

APPENDIX 8A

MULTISITE STUDY OF THE UTILITY OF POLYPOLARIZATION RADAR IN THE DETECTION AND IDENTIFICATION OF SELECTED CULTURAL FEATURES

SUMMARY OF DATA USED IN THE STUDY

NASA-funded Westinghouse K-band radar imagery of nine different geographic areas was used in the study. The areas studied are as follows:

1. Frederick County, Maryland
2. Rural area outside of Dayton, Ohio
3. Lawrence, Kansas
4. San Diego, California
5. Bountiful, Utah
6. Superior, Wisconsin
7. Wichita, Kansas
8. Banida, Idaho
9. Monticello, Utah

SUMMARY OF CRES OBJECTIVES IN RELATION TO NASA EARTH RESOURCES AIRCRAFT PROGRAM

The purpose of this study was to evaluate empirically and statistically the polarization components of K-band radar imagery for the detection of selected cultural features, especially rural, urban, and agricultural patterns, and transportation and communication nets. The study was funded under NASA contract NSR 17-004-003, and U.S. Geological Survey contract 14-08-0001-10848.

SUMMARY OF SCIENTIFIC ANALYSES PERFORMED TO DATE

Methodology

Both quantitative and qualitative methods were used in the study. Quantitative evaluations were made on the basis of data collected in experiments with over 70 interpreters, as well as through the comparison of field data and the radar imagery. Qualitative evaluations were made, based on personal experience, maps, and field work.

Evaluation of various polarization schemes for discriminating agricultural patterns was qualitative. However, previous quantitative work by CRES personnel in Garden City provided the basis for evaluation.

Detection of spots of high-intensity return (taken to be cultural targets, primarily buildings and powerlines) in selected geographical areas was evaluated by several experienced radar interpreters who located and counted these point high returns on radar imagery of the same area with different polarizations. The total and average count point high return for each polarization was used for tentative evaluation of the four polarizations. Standard deviations were computed to test the variation around the mean. Roof-construction material and orientation was correlated with radar return of different polarization schemes, and the results were tabulated.

The bulk of the study was based on the observations of 68 interpreters using radar imagery of four geographic areas and two different polarizations. Results of the experiment were compiled, and an analysis of variance was computed to test for significant differences in the detection of cultural features between two polarizations (HH and HV).

Results

Visible variations between polarizations in agricultural areas suggest that differences in crop types and/or field conditions not available on any one polarization may, in some instances, be discriminated using multiple-polarized imagery. In regions devoted mainly to grazing, the cross-polarized imagery was judged better for detecting pasture and field boundaries.

The studies involving the high-intensity spot detection and comparison of roof material and orientation with polarization both revealed that the cross-polarized imagery (HV) was best for the total detection of buildings; however, buildings not detected on the cross-polarized imagery

were frequently detected on the other polarizations used. Tentatively, the polarization was categorized as follows:

1. HV — highest detection capability

2. HH and VH — intermediate detection capability

3. VV — lowest detection capability.

Statistical analysis of the student interpretation employing HH and HV imagery revealed the following:

1. At the 99.9-percent confidence level, the like-polarized (HH) imagery was better for detecting (a) vegetated residential areas and parks versus nonvegetated urban areas, (b) powerlines and railroads when alined parallel to the flight path or crossing water bodies, and (c) bridges and channel markers.

2. At the 99.9-percent confidence level, the cross-polarized (HV) imagery was better for detecting powerlines and railroads when at an angle (other than parallel) to the flight path or traversing land.

3. At the 95-percent confidence level, the like-polarized imagery was better for detecting the central business district.

4. Detection of airports and roads did not prove to be significantly different on either the HH or HV polarizations.

5. Cross-polarized radar imagery was better for detecting railroad nets. However, the degree of confidence varied from 99.9-percent to less than 95-percent, depending on the area studied.

Conclusion

Multiple-polarized radar imagery provides the geoscientist with information relating to the complex physical properties of the target which may not be otherwise available with a single-polarized system. More specifically, several of the applications in the sensing of cultural features are (1) helping to discriminate between residential and business or industrial districts, (2) increasing the ability to plot more complete transportation and communication nets, (3) providing the observer with additional information concerning the rural setting or location and number of farmsteads, and (4) separating fields of different crops or crop states.

SUMMARY OF SCIENTIFIC ANALYSIS TO BE PERFORMED

More testing remains to be done with other cultural targets not studied in this report, as well as with several in this report for which the sample size was small. Variations among geographical areas and among radar frequencies in polarization sensitivity also need to be tested.

Rapid data acquisition from spacecraft, in both time and space, all but necessitates the use of target-enhancement methods that will facilitate interpretation of targets either by automatic recognition or by visual inspection. Level selection, photographically or electronically, lends itself to detection of cultural features which are characteristically high-energy returns. A logical extension of this study is, therefore, level slicing in order to effectively eliminate all but the high-energy return, then testing the use of automatic recognition and the accuracy of cultural target discrimination. Optical and electronic combining of radar imagery of different frequencies and polarizations is also planned. The technique of image combination provides a means of discriminating the similarities and differences on several images without a time-consuming point-by-point comparison.

N71-16133

INSTRUMENTATION OF IMAGE ANALYSIS AND TELEVISION SIMULATION TECHNIQUES

By James P. Latham
Department of Geography, Florida Atlantic University

INTRODUCTION

The Remote Sensing Laboratory of the Department of Geography at Florida Atlantic University is investigating concepts and electronic systems which discriminate and analyze geographic phenomena in imagery resulting from aerial and space sensor operations. Present activities are generally focused on one of three principal objectives:

1. The acquisition, evaluation, and interpretation of multisensor imagery which by time-series observations record the dynamic seasonal changes of the physical and cultural adaptations within the tropical and monsoonal test site extending from Boca Raton to Belle Glade, Florida

2. The further development and testing of electronic instrumentation techniques that discriminate and sample or measure the geographic distribution of phenomena recorded in imagery and that can thereby provide some techniques for the automatic interpretation which must be part of a complete geographic information system

3. The simulation of orbital television observation of the surface of the earth, in order to study how scale and scan-line rate changes affect the interpretation of geographic patterns in scan-line imagery

RESULTS ACQUIRED FROM THE USE OF DATA FROM NASA AIRCRAFT

Test site 164: Boca Raton to Belle Glade, Florida
Investigator: James P. Latham, Remote Sensing Laboratories, Florida Atlantic University, Boca Raton, Florida
Missions:
1. Mission 66, February 5-6, 1968
2. Mission 79, September 11, 1968

Objectives:

1. Evaluation and interpretation of multisensor imagery, which by seasonally differentiated observations records the significant changes in the geographic patterns of resources and land use in a tropical and monsoonal environment in order to establish interpretation techniques and sensor choices that increase efficiency and effectiveness in collection and analysis of aerial or space imagery in such regions

2. To develop and evaluate instrumentation concepts and techniques for detecting, measuring, and integrating the data in photographic or scan-line imagery of an area in order to categorize land use and otherwise contribute to the possibilities of automatic interpretation

Results: Since mission 79 (the second mission) has just been flown, its data are not yet available to provide the investigator's first opportunity for comparison of seasonal variations. It is expected to illustrate one problem of collection in this tropical environment, since cloud cover provided sensor restraints. Investigation of the color, color infrared (IR), and thermal imagery will evaluate effectiveness and limitations of this imagery in relation to previous mission imagery, as well as evaluating seasonal changes in land use and resources.

Imagery secured from mission 66 (winter season mission) on February 5-6, 1968, varies in quality from excellent to fair, with climate restraints providing expected limitations, since Convair aircraft could not complete the mission in favorable hours. Hence, typical afternoon convectional clouds of tropical environment caused "spotty" variations in imagery, particularly for light-sensitive color IR. However, very useful data were obtained for most of the test site, particularly at the 5000-foot altitude. Only partial coverage was secured at 15 000 feet because of developing cloud cover and operational time constraints. Imagery includes color, color IR, Plus-X, and thermal modes.

In combination, color and color IR imagery proved most useful for discriminating land-use patterns. Color was very useful for detecting general patterms and most cultural phenomena, but color IR was especially helpful in revealing waterway and coastal features so significant in this environment. Color IR imagery was also valuable in revealing vegetative boundaries in both agricultural and undeveloped surfaces. Plus-X imagery was principally used to provide better definition in shaded areas and to provide land-use patterns for experiments in the instrumented land-use categorization experiments.

As the cloud cover in figure 9-1 suggests, the Boca Raton to Belle Glade Test Site includes a variety of landscape types in the most humid tropical and monsoonal region of the continental United States. The

flight path from Fort Lauderdale to Palm Beach contains two ports, the Intracoastal Waterway and its frequent inlet connections to the Atlantic, the adjacent waterway or beach homes and resort facilities, some industry and institutional land use, railroads and highways, and still prevailing patches of undeveloped marshlands or palmetto-pine vegetation, as suggested by the view of the northern half of the flight path seen in figure 9-2. Boca Raton is a rapidly expanding city with a population of 25 000, economically based on affluent seasonal residents and visitors, middle-income retirement, educational institutions, IBM manufacturing, and abandoned winter vegetable farms which have become speculative urban lands.

The flight path from Boca Raton to Belle Glade, illustrated by figure 9-3, centers on the Hillsboro Canal, a part of the Central and South Florida Flood Control District, and passes over some undeveloped pine flatwoods and everglades terrain. The interior Belle Glade area, pointed out in the map sheet in figure 9-4, contains one of our four ground survey sampling areas, as partially illustrated by the color IR photograph in figure 9-5. The cooperating Belle Glade Agricultural Experiment Station also provides a zone of precise "ground truth" data, and the sketch map in figure 9-6 illustrates with some field notes the nature of the Belle Glade ground survey sampling area which includes the photographed land-use patterns.

We have completed the second of an initial series of four overflights that are required to adequately sample this seasonally changing environment, which can follow 90 days of drought with 90 days of rain and vary from frantic agricultural harvesting and processing to closed cane mills and packing sheds and from empty hurricane-shuttered buildings to packed homes and hotels. Land use, vegetative conditions, and transportation flows all vary with these changes, and so do some factors affecting remote-sensing and interpretation requirements. As seasonally spaced overflights continue, they will provide the data for analyzing remote-sensing and interpretation requirements in such humid tropical regions of monsoonal character.

With a growing data bank of multisensor coverage from aerial and space imagery, the Florida Atlantic Investigators are selecting examples of the surface patterns for evaluation by electronic scanning and computer-assisted imagery-analysis systems. As illustrated by figure 9-7, scan-line traverses across images are converted by waveform analysis to signals which indicate, by amplitude fluctuations, the gray-tone value of the densities in the image along the traverse. The analyzer is adjusted to express the value in terms of a percentage, by adjusting the gain to yield a peak value of 100 for the brightest spot in the image and a value of zero for the blackest spot. Details of the waveform fluctuations are measurable from 5× or 25× magnifications.

With gray-tone values measured as percentages by the amplitude fluctuations, two advantages are present:

1. When photoimages of different density qualities (because of variations in such factors as processing procedures or lens settings) are being analyzed, the fact that values are being determined by their percentage of the density range in each particular image (rather than an absolute density or gray-tone value) tends to provide a common denominator between images which reduces the significance of the quality differences in images. A phenomenon does not have to produce an absolute density value for comparability. It only must retain its relative tonal value.

2. When images from different sensor systems are compared, and consequently the gray tones of each image represent very different portions of the spectrum, the fact that we are measuring the values as percentages of return for the particular parameters of the sensor provides a possible basis for comparing and integrating the data.

The effectiveness of this percentage-value method for analyzing imagery has been tested in an initial experiment in the applicability of waveform analysis and computer systems for land-use categorization. Wendell Beckwith, a geography student and a computer expert, was challenged to utilize the percentage values as quantified samples from land-use categories observed in imagery.

As figure 9-8 illustrates, 16 photographic examples of land-use types in the Boca Raton Test Site were selected. A systematic matrix of 11-by-11 density percentage values was then extracted by waveform analysis from a block of area in the approximate center of the photograph, as indicated in the three last examples. Figure 9-9 shows the matrix of values for catalog types as placed in the computer and shows how each line was computed to yield four measures: average, range, oscillation, and texture. The array was also rotated and the second set of measures calculated.

With the 16 catalog types now stored in the computer, three other photographed areas were selected as "unknowns" to test the ability of the computer to classify areas. Figure 9-10 illustrates these unknowns and shows that a 19-by-19 array is sampled from the center of the unknown. The manner in which the gray-tone percentage values are directly related to location of general features can be seen in the outlined values for schematic 3 shown below the photo. To the right, one sees how movement of the 11-by-11 matrix of catalog types within the 19-by-19 array from the unknown yielded probable identifications with similar catalog types and correctly included catalog 5 as the best match for the center area of the unknown. The flow chart in figure 9-11

illustrates the method of unknown identification, which has proved significantly useful in this preliminary experiment.

Simulation of orbital television observation of the surface of the earth in order to study interpretation of geographic patterns in scan-line imagery has been achieved with the equipment illustrated in figures 9-12 and 9-13. Gemini color photography is projected upon a specially designed rear-projection polacoat screen and is scanned by a COHU 3200 series television camera which utilizes a choice of signal generation boards to change the scan-line rates to yield 525-, 729-, 873-, or 945-line resolution. As illustrated, the television camera used opens at the back and is converted from one scan-line rate to another by changing one or more of the modular plug-in panels which contain the appropriate electronic circuits. When calibrating the camera to maximize pattern detail and resolution at the new scan-line rate, additional refinement is achieved by manual adjustments of such parameters as gain, blanking, target threshold, and aperture. Although this multiscan rate camera does not yield the complete scan-line resolution improvements that are achievable in instruments specifically designed for higher scan-line rates (e.g., the RCA 5000 Line Return Beam Vidicon system which requires laser printing of its high-resolution television scan lines), this laboratory tool does yield monitor images which improve resolution in geographic patterns as scan-line rates are increased, for interpretation studies. Curtis Norling, Chief Television Engineer of the University, provides technical control and supervision.

It is also possible to simulate other observation variations, such as those that could result from optical or orbital altitude alternatives, by changing the size of the projected image or the distance from which it is viewed by the camera. Of course, this does not change the original resolution of the Gemini transparency being projected, but such film resolution is much greater than that achievable in our scan-line rates and hence provides little limitation on our experiments. Alternate lens sytems are also available for both our projector and our television camera.

Figure 9-13 indicates that signals from the camera are directed through a modified Tektronix 529 Waveform Analyzer which can be adjusted to handle any of the scan-line rates and to then pass to the proper monitor for the line rate. The image resulting is photographed for interpretation.

Over 40 interpretation experiments have been carried out to establish changes in the interpretability of geographic patterns which occur when different orbital television sensing systems are simulated. To minimize and test interpretation bias resulting from the differences among interpreters, three interpreters were used. The following two

interpreters were geographers: Clark Cross who is particularly experienced with forestry photointerpretation, and Richard Witmer, a physical geographer with interest in remote sensing. The third interpreter, our research associate William Kuyper, has completed 23 years of photointerpretation and research with the Air Force. Each interpreter was expected to have a general knowledge of the nature of the region but was also expected to avoid applying any specific knowledge not clearly discernible in the image. In each experiment, the smaller scale or grosser scan-line pattern was interpreted before viewing the next higher level of image refinement.

The patterns separately interpreted included transportation routes, land use, and physical regions. Areas, imagery scale, and scan-line patterns were varied. As an example of the results obtained, two sets of variable-scale experiments are herewith illustrated.

Figure 9-14 displays transportation patterns observable for east-central Florida with 525 scan lines in a device orbiting with an altitude and optical system combination which yields an image scale of 1:1 000 000 on the 14-inch television monitor. The test area at this scale is of course a small part of the monitor image. The improvement resulting in figure 9-15 when the simulated orbital-optical combination yields a scale of 1:500 000 is then seen. Please note that the "reference scale" is approximate for only the central image area as displayed on the monitor. At a scale of 1:250 000 in figure 9-16, little detail seems to be added, but there is an increase in agreement among the interpreters. When orbital-optical combination yields an image scale of 1:131 250 on the 525-line system, as in figure 9-17, there is a substantial increase in the routes observed by interpreters, and all interpreters now agree on some routes not previously seen by anyone.

At this same reference scale of 1:131 250, figure 9-18 demonstrates that some improvement in the detection of transportation routes results from increasing the scan-line rate to 945 lines. The significant increase, however, seems to be the revealing of routes which are at some distance from the image center and which are consequently of smaller size because of distance perspective. Apparently the 525 rate was adequate at this scale for locating most transport routes in the central area directly below and closest to the sensor. There is also a definite detailing now by all interpreters of the broad path of the major construction project.

Land use in the east-central Florida area was interpreted by a similar set of experiments. This particular set illustrates the patterns delineated by one interpreter at each of the four scales resulting from simulated orbital-optical combinations when a 945 scan-line system is used. Figure 9-19 indicates that, since at this small scale the test area spans only a few scan lines on the monitor, the generalization of

surface-pattern changes causes the high returns of urban areas and major route construction to look alike and contribute some confusion. This distortion is reduced in figure 9-20, and the scale of 1:500 000 yields meaningful but limited patterns. At the scale of 1:250 000 used in figure 9-21, additional categories of land use are delineated in an interpretation that generalizes zonal shapes and size, but also reveals greater aspects of the orientation of land-use patterns. At the reference scale of 1:125 000, figure 9-22 presents an effectively delineated and quite detailed pattern of land-use categories. Various levels of both urban and rural use can be mapped. The orientation aspects of the patterns are clearly discernible, and the spatial interrelationships of areas are seen.

After the land-use patterns observable in this simulated orbital television image had been finalized in the map shown in figure 9-22, land-use maps of the same region compiled from detailed land surveys by the East Central Florida Planning Council were secured and compared with the results we obtained. When maps comparable in scale with our television image "reference scale" were studied, they were very similar, even though they had been compiled from larger scaled detailed maps based on ground surveys and large-scale aerial photography. Differences in urban patterns were sometimes resolved in favor of the space television interpretation, but boundaries between classes of rural land use were not as firm in our imagery, probably because of the lesser contrast in border zones.

Future investigations of the Florida Atlantic Remote Sensing Laboratories will study the interpretation of geographic patterns in images simulating observation of the earth with the new 5000 or better line scanning systems, as they are made available by the U.S. Geological Survey/NASA program. Instrumentation techniques for analyzing both aerial and space imagery of the test site will continue to be refined. Detailed studies of the multispectral imagery of test site 164 will be directed toward establishing the significant environmental changes in a monsoonal tropical area that can be observed, measured, and perhaps predicted with the help of multispectral imagery. Higher altitude and space imagery will be utilized as it becomes available.

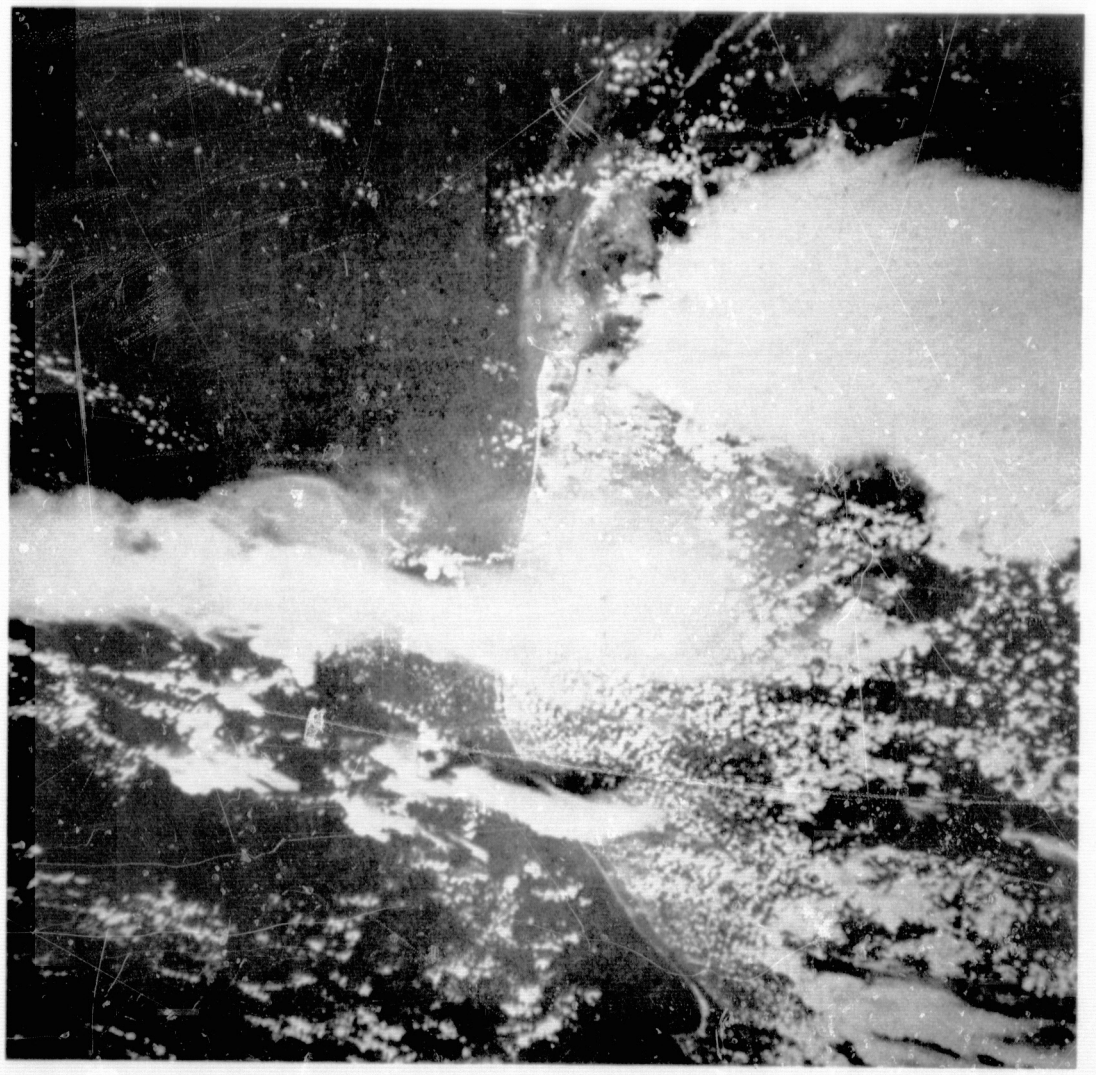

Figure 9-1.- Test site 164 located at Boca Raton to Belle Glade is in central area of this image taken by Gemini mission.

Figure 9-2.- Coastal flight path from northern Boca Raton to Palm Beach, Florida, as printed from color IR transparency.

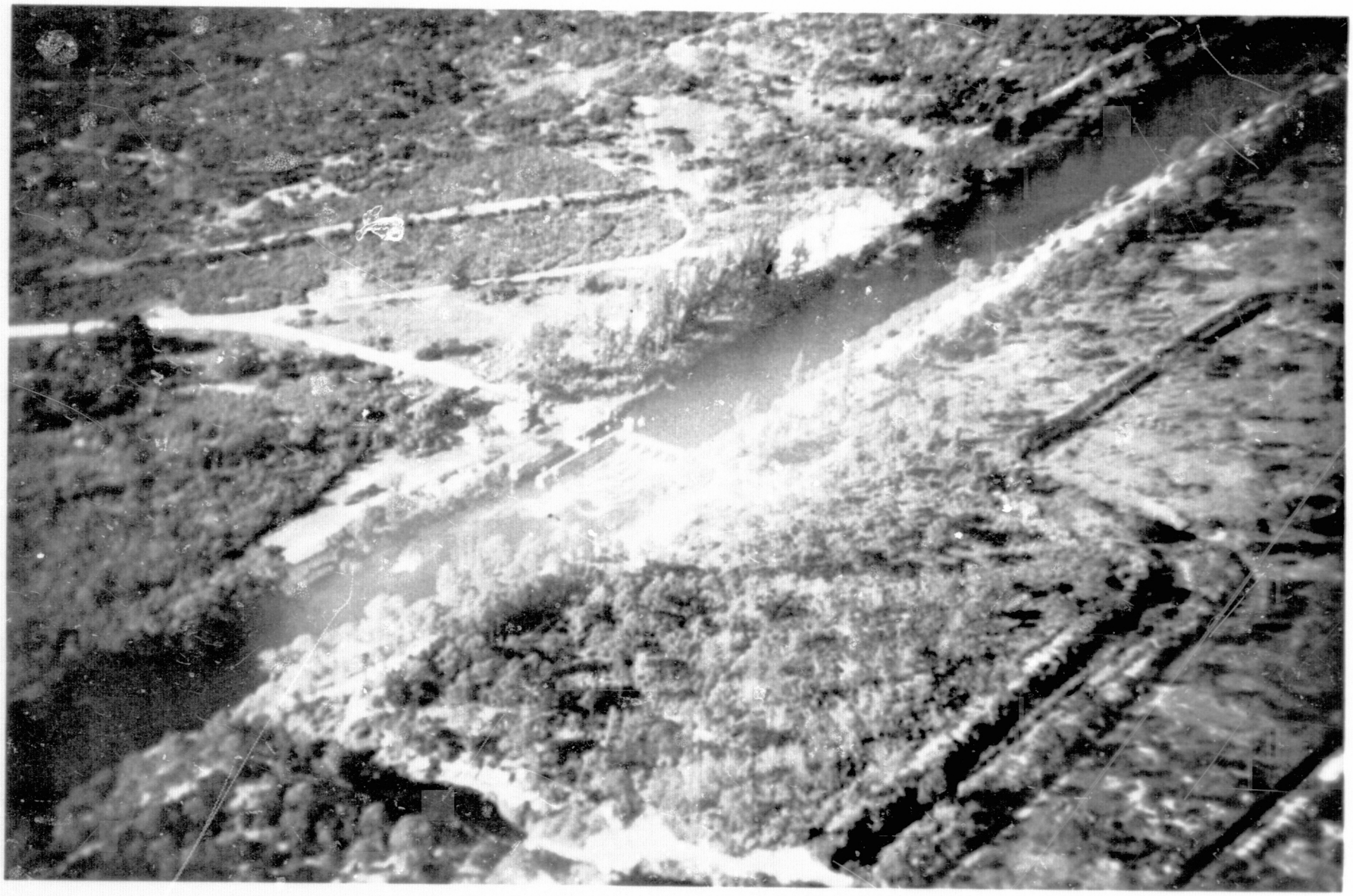

Figure 9-3.- Hillsboro canal and flood control dam along flight path over underdeveloped terrain between Boca Raton and Belle Glade, Florida.

Figure 9-4.- Test site 164 located on West Palm Beach map sheet, with interior Belle Glade and coastal Boca Raton indicated.

Figure 9-5.- Sugar cane, cattle grazing, and settlement patterns recorded originally by color IR in Belle Glade Field Survey Site of test site 164.

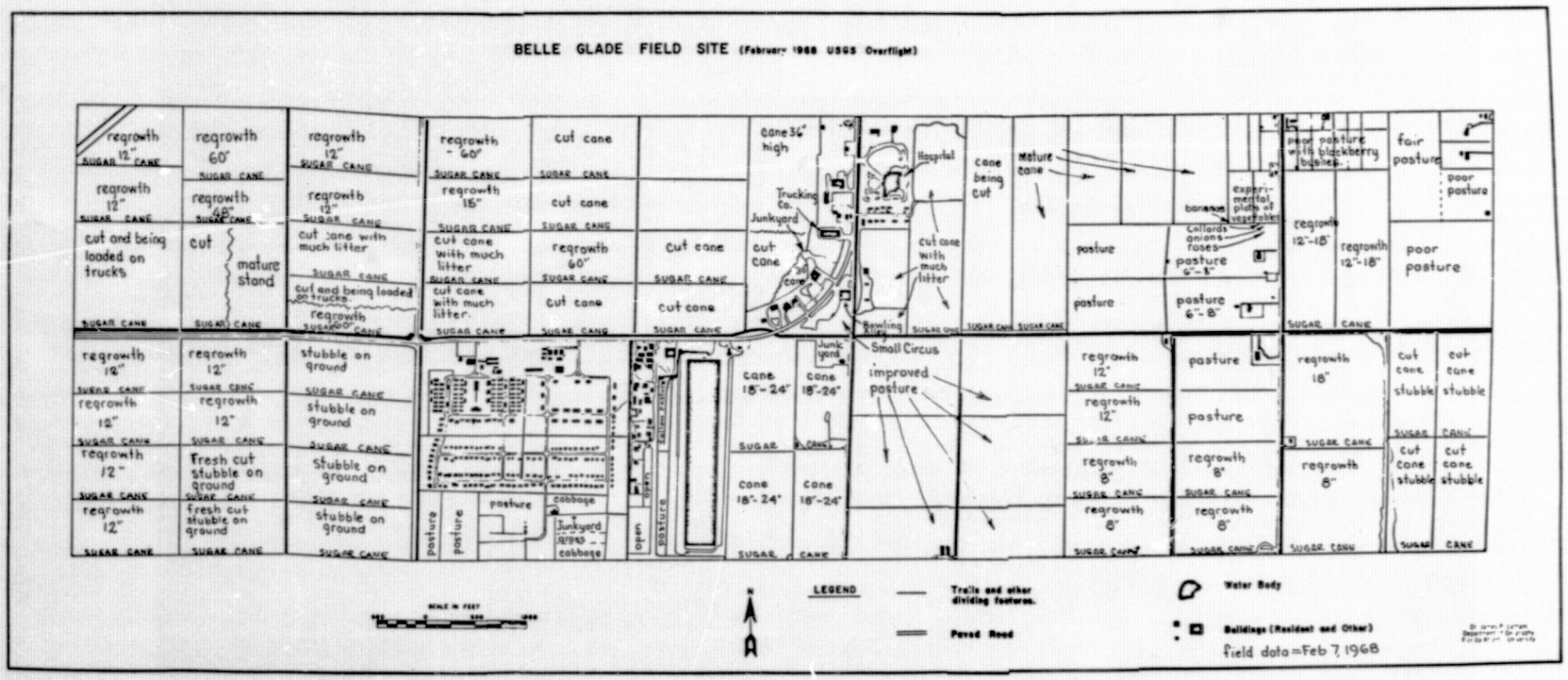

Figure 9-6.- Belle Glade Field Survey Site with some field annotations indicated.

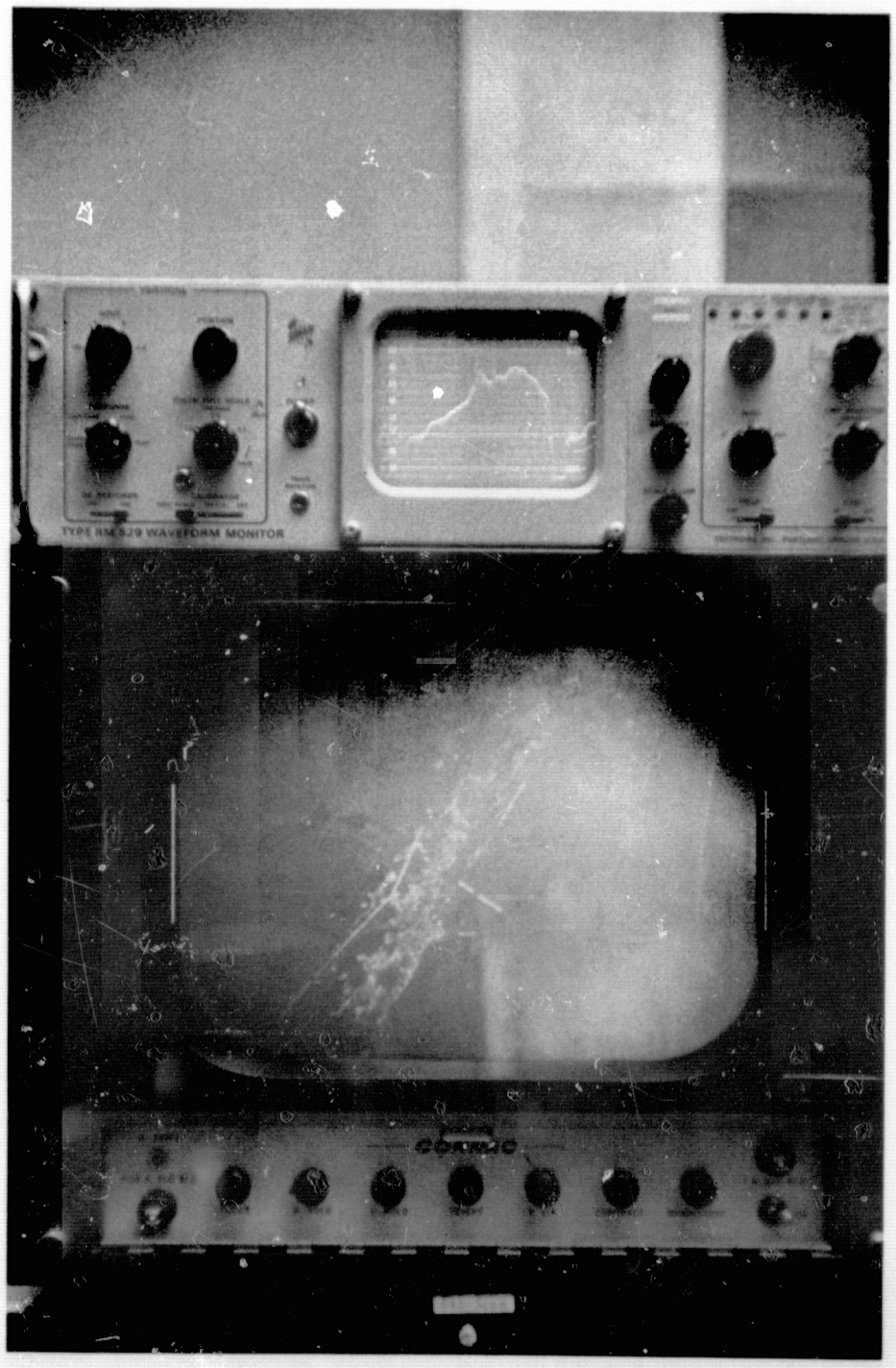

Figure 9-7.- Monitor and waveform analyzer equipment utilized for image control and for sampling image density or gray-tone percentage values used in land-use categorization.

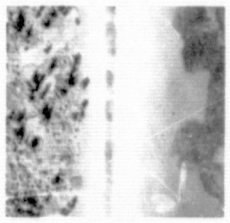

Catalog 1

BEACH AREA

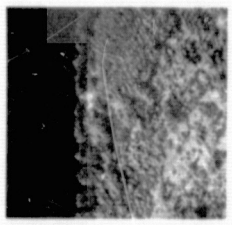

Catalog 2

AUSTRALIAN PINE

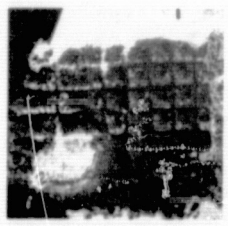

Catalog 3

MANGROVE

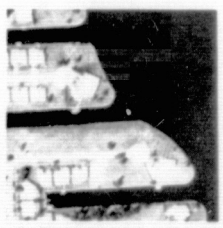

Catalog 4

INTRA-COASTAL WATER

Catalog 5

INTRA-COASTAL HOUSING

Catalog 6

RESIDENTIAL HOUSING

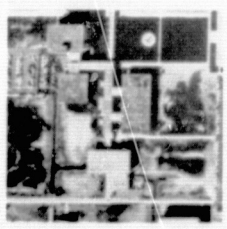

Catalog 7

LARGE BUILDINGS

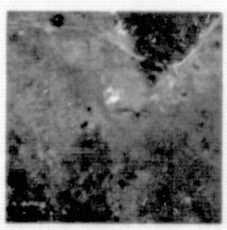

Catalog 8

OPEN GRASSLAND

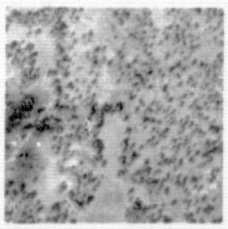

Catalog 9

PINE-PALMETTO (SPARSE)

Catalog 10

CANAL-INLAND WATER AREA

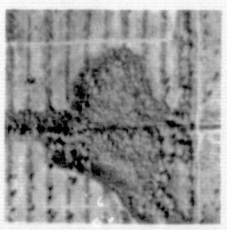

Catalog 11

PALM-PALMETTO BRUSH

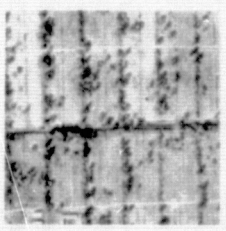

Catalog 12

MIXED CROPLAND (ROWED)

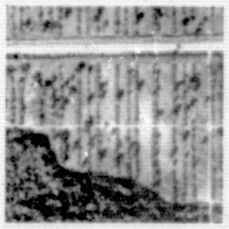

Catalog 13

UNUSED CROPLAND

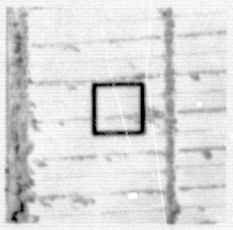

Catalog 14

FRESHLY PLOWED CROPLAND

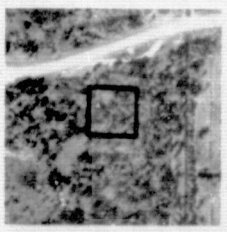

Catalog 15

PINE-PALMETTO (DENSE)

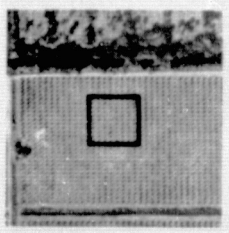

Catalog 16

ORANGE GROVE

Figure 9-8.- Selected land-use categories as cataloged for computer identification experiment.

CATALOG 1

80	90	39	71	94	94	92	93	50	55	49
89	90	60	57	94	95	95	90	58	52	50
88	91	82	62	95	97	95	90	56	52	49
87	92	55	58	97	97	95	91	55	50	47
85	94	50	70	95	98	93	87	55	51	48
86	92	46	70	93	99	93	86	55	52	48
81	90	40	78	96	99	93	84	50	52	46
85	89	45	87	99	99	95	87	49	55	49
88	95	60	87	99	99	96	85	46	54	50
87	94	59	85	99	99	95	82	45	54	51
88	91	60	90	99	99	90	78	45	52	51

CALCULATIONS ON INITIAL ARRAY

AVERAGE	RANGE	OSCIL.	TEXTURE
73	55	6	17
75	45	2	11
77	48	3	11
74	50	2	13
75	50	3	15
74	53	3	15
73	59	5	17
76	54	4	16
78	53	4	14
77	54	4	14
76	54	4	13

CALCULATIONS ON ROTATED ARRAY

AVERAGE	RANGE	OSCIL.	TEXT.
85	9	6	2
91	6	4	1
54	43	4	10
74	33	5	5
96	6	3	1
97	5	1	0
93	6	2	1
86	15	4	2
51	13	1	2
52	5	3	1
48	5	3	1

CATALOG 2

10	22	12	18	10	10	12	17	12	15	20
8	9	11	12	8	5	6	20	18	28	13
4	3	8	21	15	8	8	10	8	22	15
7	3	13	31	17	18	10	8	10	18	11
11	6	9	26	17	20	10	9	15	9	9
12	8	7	11	17	12	13	18	11	12	15
16	17	9	17	10	17	18	22	11	13	14
10	11	16	11	4	5	16	21	10	12	20
11	5	17	14	7	17	24	22	10	29	26
11	10	10	12	6	12	24	11	14	20	23
17	12	9	15	10	13	15	5	8	20	20

CALCULATIONS ON INITIAL ARRAY

AVERAGE	RANGE	OSCIL.	TEXTURE
14	12	6	5
12	23	5	5
11	19	6	5
13	28	6	7
11	20	4	5
12	11	5	3
14	13	6	5
12	17	4	5
16	24	6	8
13	18	5	5
13	15	5	4

CALCULATIONS ON ROTATED ARRAY

AVERAGE	RANGE	OSCIL.	TEXT.
10	13	4	3
9	19	3	5
11	10	4	3
17	20	7	6
11	13	4	3
11	11	7	6
14	18	4	3
14	17	5	4
11	10	5	3
18	20	5	6
16	17	6	4

CATALOG 3

5	6	9	8	15	9	15	9	8	10	18
11	9	10	10	10	6	16	17	10	10	22
2	3	3	2	2	3	4	2	4	8	8
1	6	7	5	5	8	7	3	6	10	9
3	9	9	4	7	5	6	5	6	8	9
9	4	11	9	7	8	9	9	7	8	8
11	9	10	10	12	7	12	10	7	10	14
3	2	2	2	2	2	2	1	3	9	9
3	2	9	4	8	9	6	4	5	9	10
4	2	9	3	8	9	4	3	4	9	9
8	3	12	5	4	9	8	6	6	5	5

CALCULATIONS ON INITIAL ARRAY

AVERAGE	RANGE	OSCIL.	TEXTURE
10	13	6	4
11	16	4	3
3	6	3	1
6	9	5	2
6	6	5	2
8	7	4	2
10	7	6	2
3	8	1	2
5	8	5	2
5	7	5	3
6	9	4	3

CALCULATIONS ON ROTATED ARRAY

AVERAGE	RANGE	OSCIL.	TEXT.
5	10	4	3
5	7	6	3
8	10	5	3
5	8	8	3
7	13	4	4
6	7	5	3
8	14	8	4
6	16	6	4
6	7	6	2
8	5	4	1
11	17	6	3

CATALOG 4

75	91	92	40	10	2	1	1	1	1	1
79	93	75	40	35	4	1	1	1	1	1
91	91	59	35	30	10	2	1	1	1	1
80	80	39	29	25	20	2	1	1	1	1
61	42	22	17	36	15	3	2	1	1	1
40	33	35	32	38	4	2	1	1	1	1
35	28	21	16	3	2	2	1	1	1	1
3	2	1	1	1	1	1	1	1	1	1
1	1	1	1	1	1	1	1	1	1	1
1	2	2	3	4	5	6	7	8	9	1
26	28	30	29	27	26	28	29	29	30	17

CALCULATIONS ON INITIAL ARRAY

AVERAGE	RANGE	OSCIL.	TEXTURE
28	91	1	10
30	92	1	10
29	90	0	9
25	79	0	7
18	60	2	9
17	39	4	5
10	34	0	3
1	2	0	0
1	0	0	0
4	7	2	1
27	13	4	2

CALCULATIONS ON ROTATED ARRAY

AVERAGE	RANGE	OSCIL.	TEXT.
44	90	2	13
44	92	2	12
34	91	3	14
22	39	3	9
19	37	4	11
8	25	2	6
4	27	4	3
4	28	3	3
4	28	1	2
4	29	1	2
2	16	1	1

CATALOG 5

44	58	74	62	57	72	59	45	52	45	33
45	42	40	48	53	67	53	52	36	42	59
55	82	55	54	57	18	43	48	48	48	45
68	90	79	50	27	12	15	44	32	33	47
75	90	85	60	18	11	10	44	38	49	50
65	88	80	62	46	11	10	25	50	49	38
50	62	67	45	38	10	8	17	50	49	50
53	87	85	63	21	9	8	9	55	51	57
69	88	85	62	19	10	8	8	19	50	55
51	84	83	44	13	9	8	7	9	26	52
58	60	57	50	13	10	9	8	9	9	17

CALCULATIONS ON INITIAL ARRAY

AVERAGE	RANGE	OSCIL.	TEXTURE
54	41	5	11
48	31	3	8
50	64	4	13
45	78	4	15
48	80	4	14
47	78	3	15
40	59	4	12
45	79	4	17
43	80	2	14
35	77	2	15
27	52	3	6

CALCULATIONS ON ROTATED ARRAY

AVERAGE	RANGE	OSCIL.	TEXT.
57	31	4	10
75	48	3	14
71	45	3	14
54	19	7	9
32	44	4	10
21	63	3	6
21	51	1	5
27	45	2	5
36	46	5	11
41	42	5	8
45	42	5	11

CATALOG 6

36	37	28	22	26	27	22	19	29	20	25
32	30	30	42	40	31	63	72	45	75	70
66	81	47	81	86	48	82	82	47	68	75
82	80	48	71	74	47	65	58	42	35	30
58	55	38	43	32	35	40	53	43	50	53
20	35	31	52	48	57	56	62	69	70	72
59	73	74	58	41	42	51	50	26	40	46
75	43	49	37	39	30	28	28	24	18	31
55	35	25	20	45	36	55	75	57	65	58
22	29	23	56	73	55	60	79	47	78	70
42	45	60	70	65	33	42	28	28	51	37

CALCULATIONS ON INITIAL ARRAY

AVERAGE	RANGE	OSCIL.	TEXTURE
26	18	6	5
48	45	6	12
69	39	5	22
57	52	4	14
45	26	5	7
52	52	6	7
50	48	4	10
36	57	5	8
47	55	6	14
53	57	7	17
45	42	5	12

CALCULATIONS ON ROTATED ARRAY

AVERAGE	RANGE	OSCIL.	TEXT.
49	62	5	24
49	52	5	20
41	51	4	16
50	61	4	20
51	60	5	18
40	30	5	13
51	60	5	19
55	63	5	23
41	45	5	15
51	60	5	26
51	50	5	25

CATALOG 7

62	11	19	46	67	9	50	58	47	55	40
58	25	11	73	72	11	35	61	56	52	48
61	20	16	56	70	71	64	62	62	59	52
55	25	15	40	75	84	72	61	61	59	50
52	20	34	55	74	31	45	60	57	55	45
49	35	28	70	68	15	39	55	58	57	50
30	39	22	68	65	15	48	52	60	54	40
30	36	40	65	70	10	43	54	55	52	45
63	58	45	71	72	82	70	63	60	58	45
86	85	32	56	71	80	68	56	57	58	42
88	80	21	71	72	13	42	52	55	51	42

CALCULATIONS ON INITIAL ARRAY

AVERAGE	RANGE	OSCIL.	TEXTURE
42	58	6	24
45	62	4	23
54	55	2	11
54	69	2	14
48	54	4	17
47	55	4	16
44	53	5	19
45	60	3	15
62	37	2	9
62	54	4	14
53	75	4	23

CALCULATIONS ON ROTATED ARRAY

AVERAGE	RANGE	OSCIL.	TEXT.
57	58	3	9
39	74	7	10
25	34	6	9
61	33	6	13
70	10	6	3
38	75	3	29
52	37	6	15
57	11	3	3
57	15	5	3
55	8	4	3
45	12	4	4

CATALOG 8

37	36	35	36	37	41	41	42	41	40	39
37	38	37	37	37	40	44	43	42	41	40
37	37	37	37	37	45	67	53	47	42	43
39	37	38	38	38	45	50	58	46	43	42
39	37	37	37	37	40	73	66	47	45	43
40	37	38	40	36	46	50	40	43	42	42
41	40	37	37	40	38	41	37	37	38	39
40	42	40	39	40	38	39	37	38	35	29
43	43	41	41	42	40	40	41	40	35	30
43	42	35	40	40	41	39	38	39	38	37
44	40	25	44	37	40	40	40	40	39	38

CALCULATIONS ON INITIAL ARRAY

AVERAGE	RANGE	OSCIL.	TEXTURE
38	7	3	1
39	7	3	1
43	30	3	5
43	21	3	3
45	36	2	6
41	14	6	3
38	4	5	1
37	13	7	2
39	13	4	1
39	8	5	2
38	19	3	5

CALCULATIONS ON ROTATED ARRAY

AVERAGE	RANGE	OSCIL.	TEXT.
40	7	5	0
39	7	3	1
36	16	6	2
38	8	7	1
38	6	5	1
41	8	5	2
47	34	6	10
45	29	4	6
41	10	6	2
39	10	2	1
38	14	4	2

Figure 9-9.- Sampled percentage values in matrix form for computer processing and values calculated for identification of each category.

UNKNOWN 3

GRAY TONE SCHEMATIC 3

19 X 19 UNKNOWN

2	1	1	1	1	1	1	1	1	1	1	1	1	1	1	2	4	5	5
2	2	2	2	2	3	23	30	6	9	10	17	9	5	9	17	8	8	7
20	20	20	22	30	28	80	95	82	80	41	32	30	28	65	60	25	10	9
35	37	38	37	34	35	72	90	97	97	40	35	40	40	80	95	75	9	7
36	33	33	35	36	37	35	70	95	95	40	40	40	40	90	95	70	8	6
43	41	51	49	55	45	58	80	72	70	41	62	66	52	90	90	20	6	5
40	62	64	61	65	50	50	90	82	65	72	90	90	60	70	70	15	6	5
70	78	78	75	78	76	82	92	82	91	92	90	91	70	65	50	9	4	3
60	60	73	52	57	51	41	53	70	57	65	70	86	52	75	30	4	3	2
49	48	48	32	29	41	50	41	58	61	54	45	42	82	98	30	4	3	2
47	65	60	78	83	60	55	86	75	95	95	48	33	95	90	12	4	3	2
87	92	70	91	95	70	94	88	83	95	95	57	93	80	65	7	4	3	2
90	90	62	91	88	52	91	80	80	91	78	57	80	62	20	4	3	2	1
78	68	50	65	52	40	65	60	61	74	62	49	47	33	7	5	4	2	1
42	45	25	35	65	20	18	12	11	11	11	10	9	7	6	5	4	2	1
11	10	8	10	10	8	8	8	8	8	9	8	8	7	5	4	3	2	1
10	10	8	8	8	8	8	9	9	14	10	10	9	8	6	4	3	2	1
11	10	9	20	30	30	38	35	45	55	42	46	13	9	7	6	5	3	2
12	12	30	44	42	55	92	75	55	62	92	72	40	10	9	7	5	4	3

GENERAL FEATURES

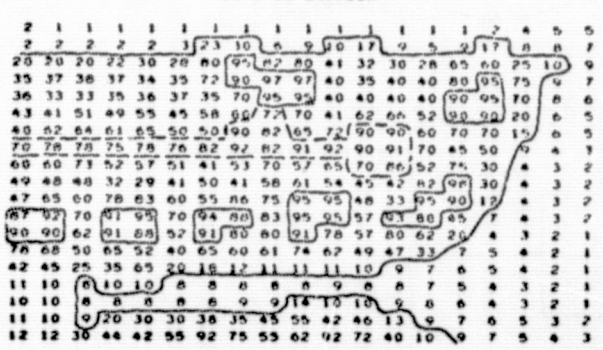

PROBABLE CATALOGS IDENTIFIED

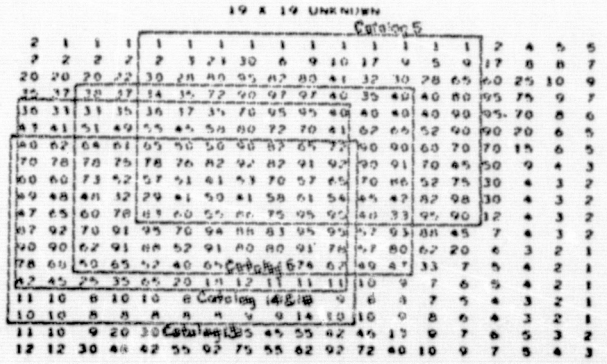

UNKNOWN 1

UNKNOWN 2

Figure 9-10.- Land-use types selected as "unknowns" for computer identification and schematic illustrations of relation to terrain features and matrix matching process.

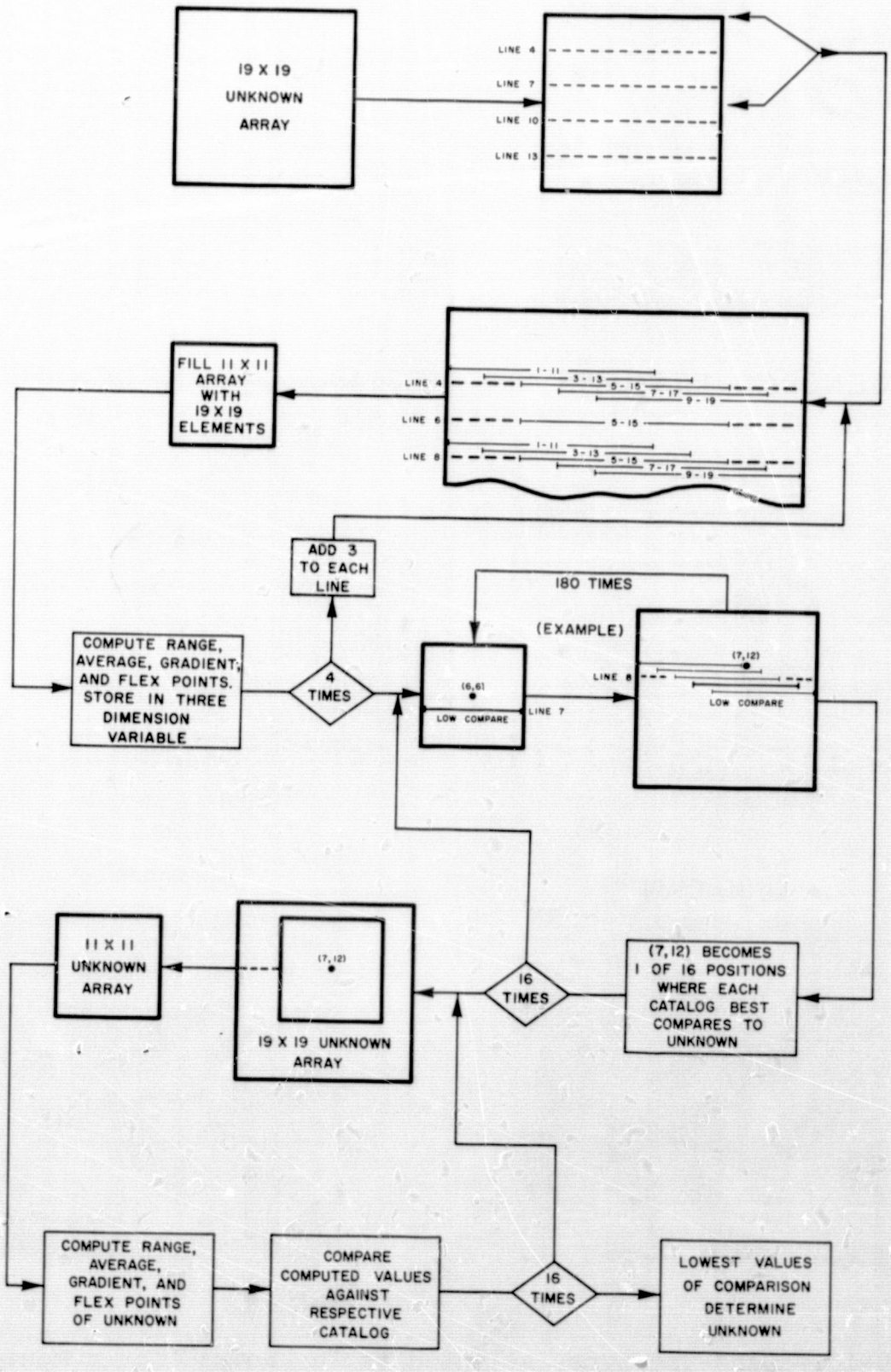

Figure 9-11.- Flow chart for computer processing to identify unknowns.

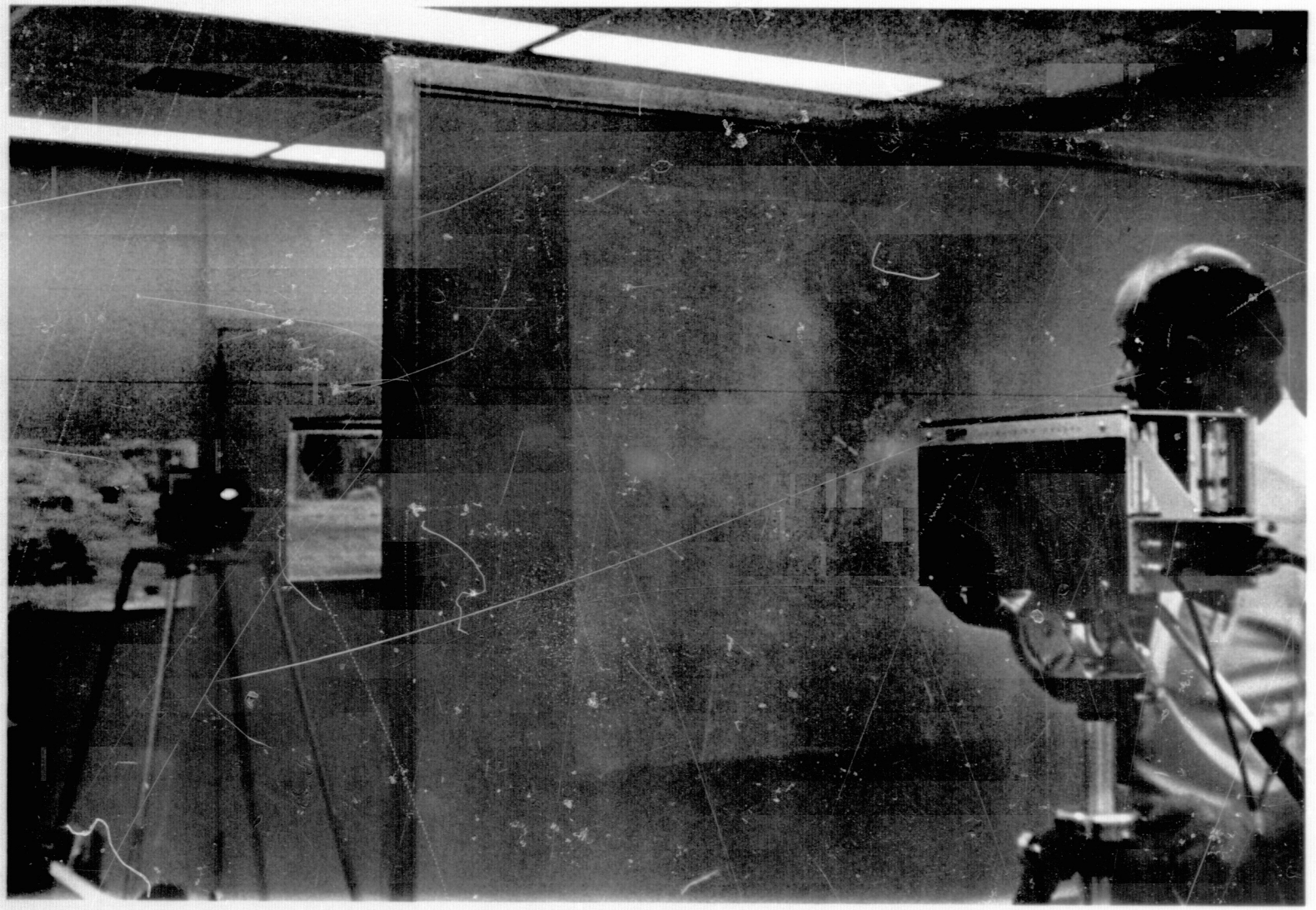

Figure 9-12.- Equipment system for simulating a television observation from space altitudes.

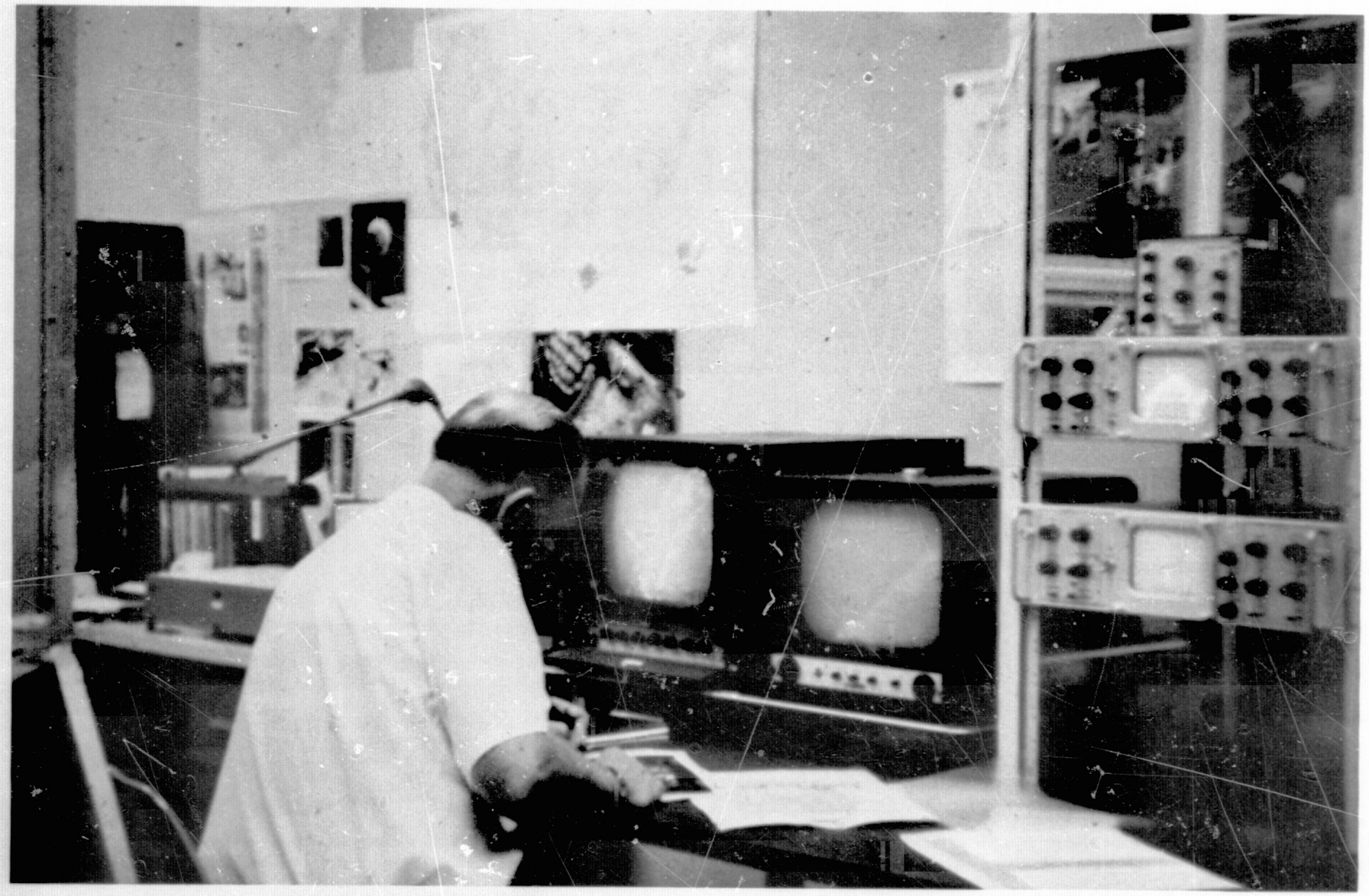

Figure 9-13.- Monitors and waveform analyzers used to control and display image.

INTERPRETED AS TRANSPORTATION ROUTE BY:

..... Some 1 Analyst
– – – 2 Of The Analysts
——— All 3 Analysts

TV MONITOR IMAGE

525 Scan Line System

PHOTO= GEMINI VII (NASA No. 65-63806)
Altitude 120NM Dec 6, 1965
Lens 250mm, Film Scale=1:2,000,000
Projected Image Scale= 1:250,000
Aspect Azimuth 300° GT 1750Z

0 5 10 15 30
scale in statue miles

Geog. Dept., Florida Atlantic Univ.

Figure 9-14.- East-central Florida transportation patterns, reference scale of 1:1 000 000.

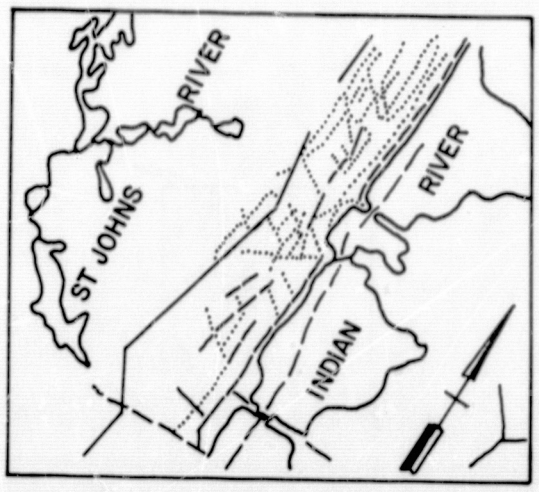

INTERPRETED AS TRANSPORTATION ROUTE BY

..... Some 1 Analyst
— — — 2 Of The Analysts
——— All 3 Analysts

TV MONITOR IMAGE

525 Scan Line System

PHOTO = GEMINI VII (NASA No. 65-63806)
Altitude 120 NM Dec 6, 1965
Lens 250mm, Film Scale 1:2,000,000
Projected Image Scale 1: 250,000
Aspect Azimuth 300° GT 1750 Z

0 5 10 15 20 25

scale in statute miles

Geog. Dept., Florida Atlantic University

Figure 9-15.- East-central Florida transportation patterns, reference scale of 1:500 000.

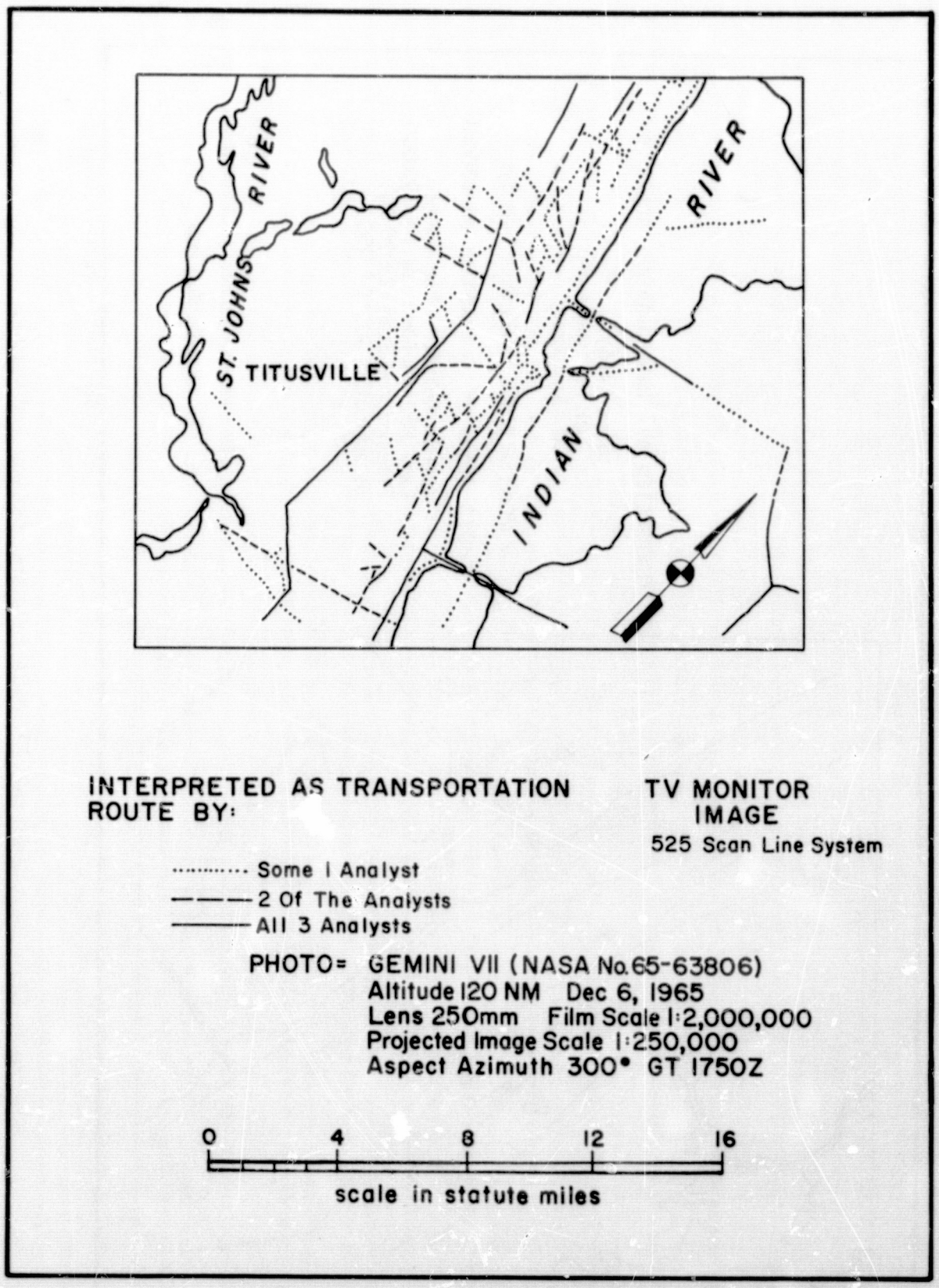

Figure 9-16.- East-central Florida transportation patterns, reference scale of 1:250 000.

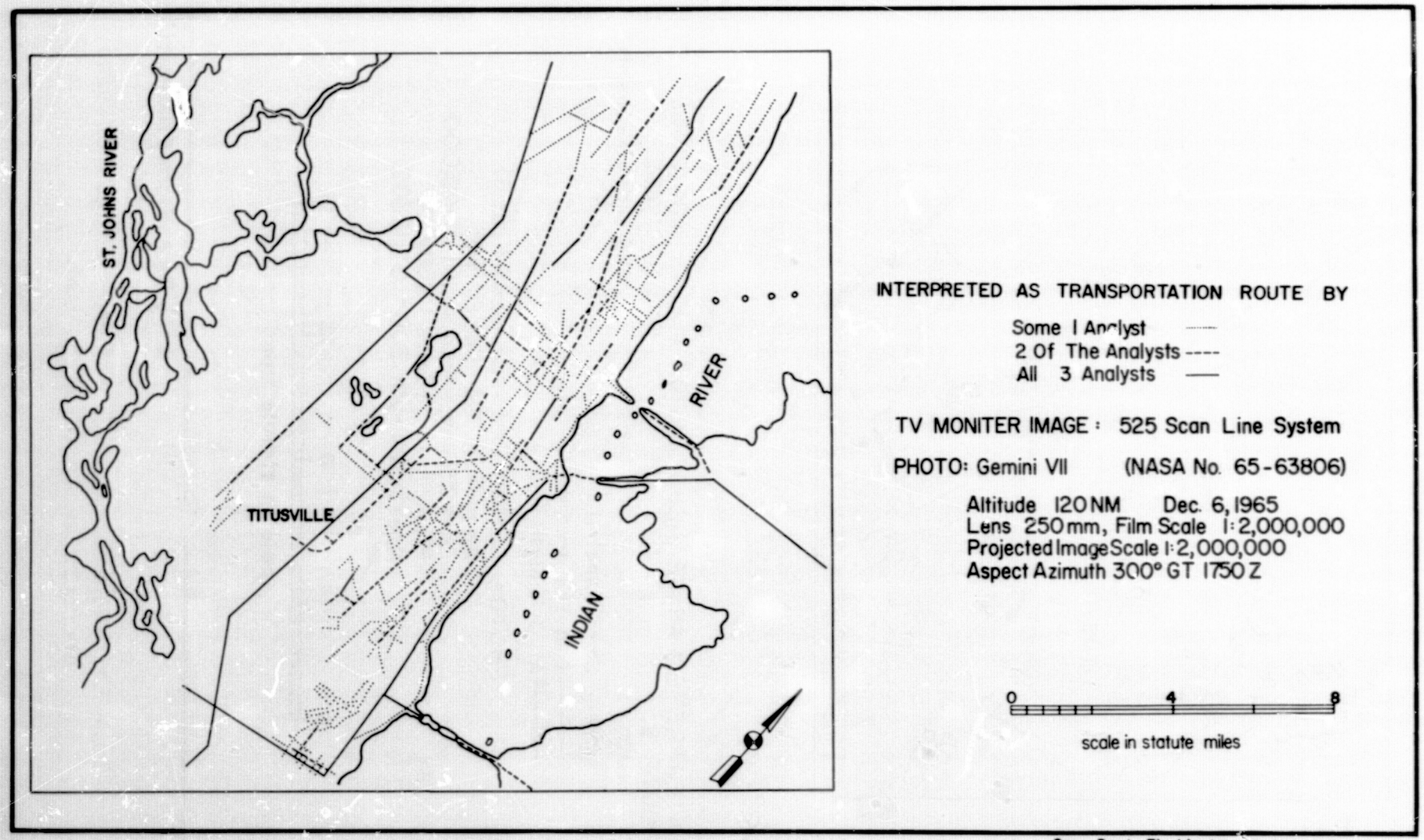

Figure 9-17.- East-central Florida transportation patterns, reference scale of 1:131 250.

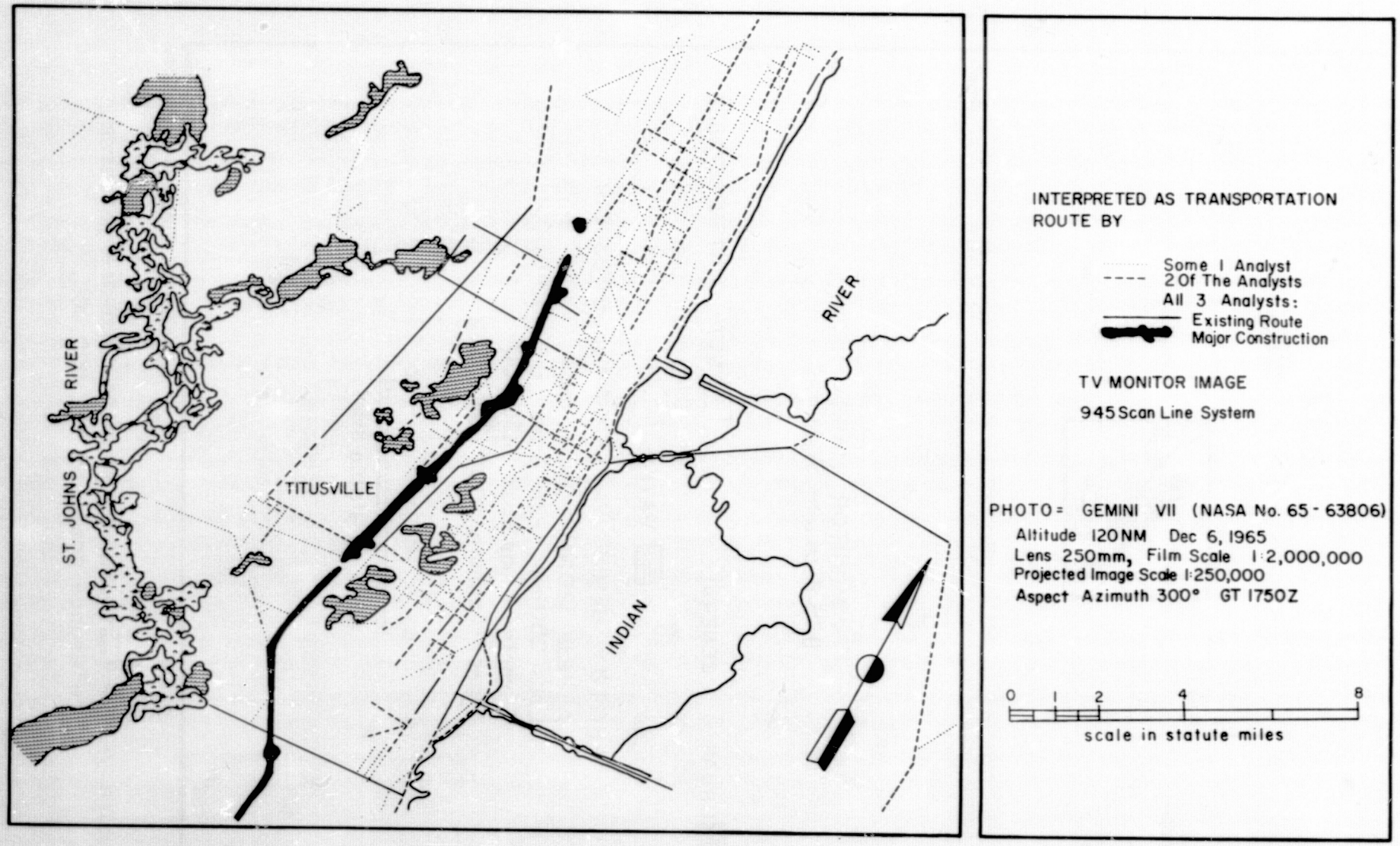

Figure 9-18.- East-central Florida transportation patterns, reference scale of 1:131 250.

TV MONITOR IMAGE
945 Scan Line System

URBAN GENERAL

NOT INTERPRETABLE

WATER

PHOTO = GEMINI VII (NASA No. 65- 63806)
Altitude 120 NM Dec 6, 1965
Lens 250 mm, Film Scale 1:2,000,000
Projected Image Scale 1:250,000
Aspect Azimuth 300° GT 1750Z

0 5 10 15 30
scale in statue miles

Geog. Dept., Florida Atlantic Univ.

Figure 9-19.- East-central Florida land-use patterns, reference scale of 1:1 000 000.

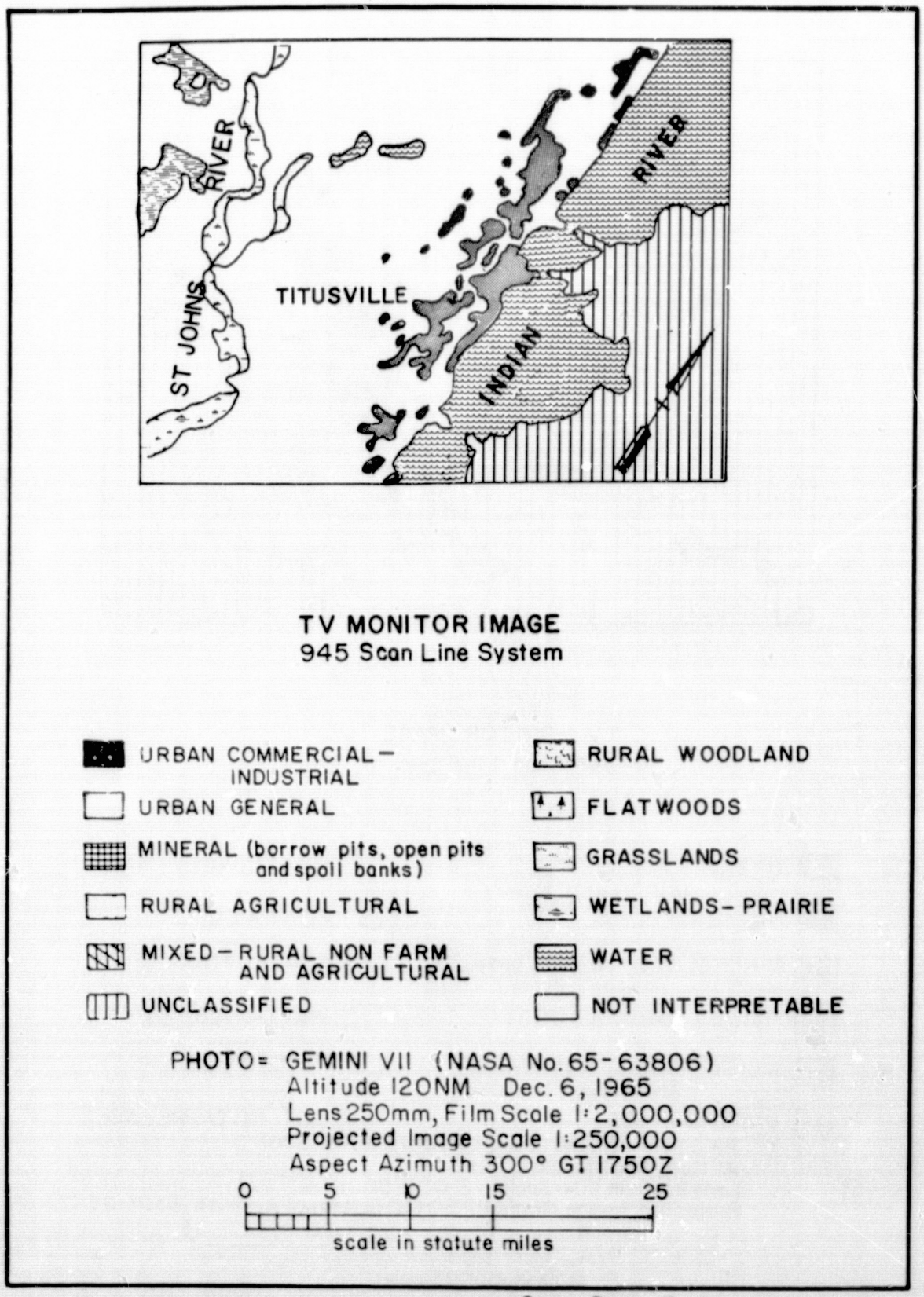

Figure 9-20.- East-central Florida land-use patterns, reference scale of 1:500 000.

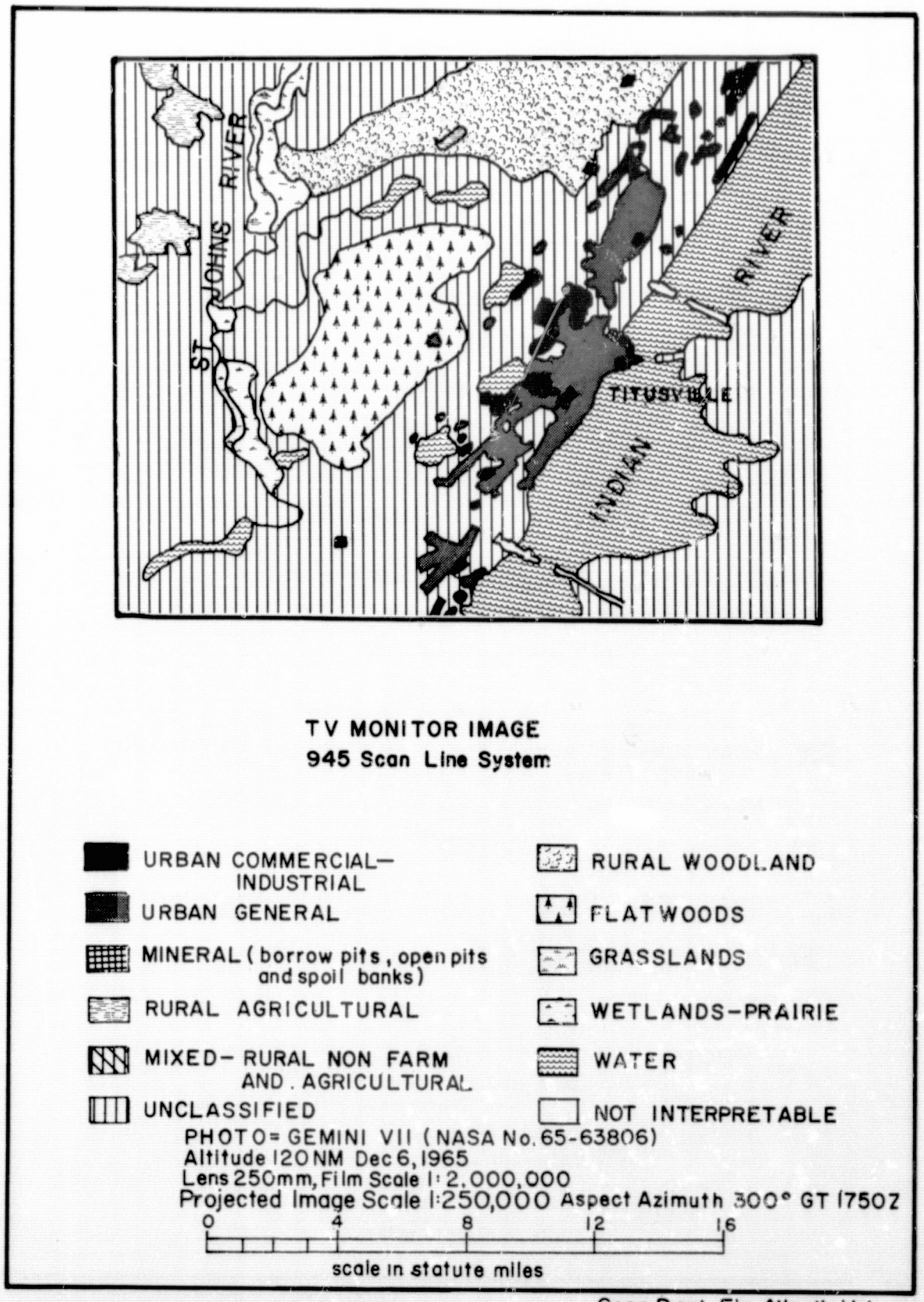

Figure 9-21.- East-central Florida land-use patterns, reference scale of 1:250 000.

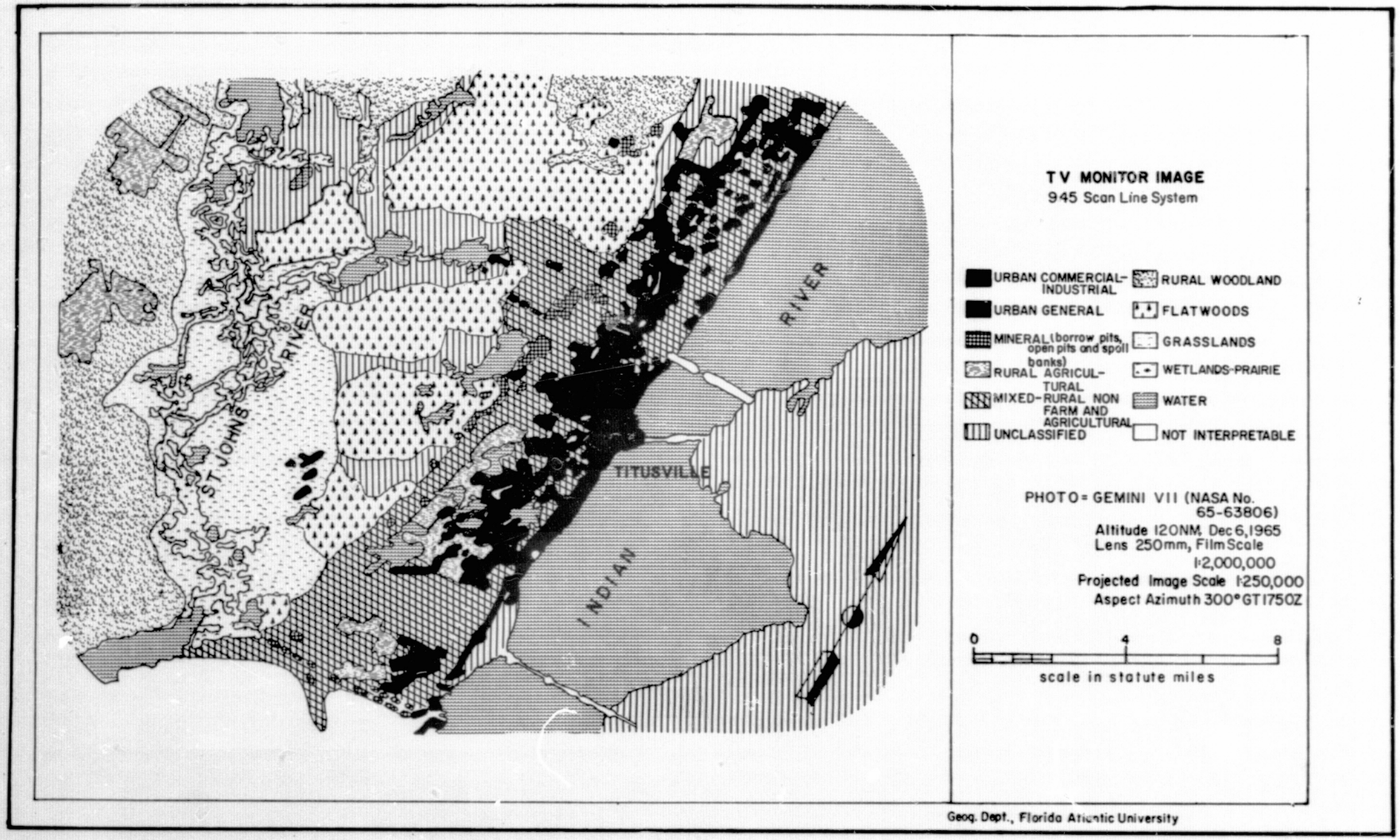

Figure 9-22.- East-central Florida land-use patterns, reference scale of 1:141 250.

N71-16134

INFRARED SURVEY OF THE PISGAH CRATER AREA, SAN BERNARDINO COUNTY, CALIFORNIA: A GEOLOGIC INTERPRETATION*

By Stephen J. Gawarecki
U.S. Geological Survey, Washington, D.C.

ABSTRACT

Infrared imagery in the 8μ to 14μ band of the Pisgah Crater area, California, has provided useful geologic information to complement data obtained from ground studies and from aerial photography. Thermal contrasts representative of those found through the diurnal cycle were acquired during three of six flight periods: at about 20:00 hours (post-sunset), 04:00 hours (presunrise), and 12:00 hours (midday). The largest amount of information on geologic thermal parameters from a single imaging period was obtained from the imagery flown shortly after sunset.

Among the geologic features shown on the imagery of one or more flight periods were basalt flow contacts where the adjacent flows differed in surface character, distribution of pyroclastics and their alluvial derivatives on the flows, collapsed lava tubes, fissured areas, detail of the Pisgah fault, zonation within Lavic Dry Lake, active drainage on an alluvial fan, and moist areas suggestive of ground-water conditions. Most of these features are either unique in infrared imagery or are superior in infrared presentation to images obtained from other remote-sensing systems.

The integration of data from infrared-scanning systems with data acquired simultaneously with other sensors should greatly expand the interpreter's capability by providing many unique physical-property combinations for the identification of geologic features.

*Work performed under NASA Contract No. R-146.

INTRODUCTION

General Statement

The infrared (IR) survey of the Pisgah Crater area, San Bernardino County, California, was undertaken primarily to establish parameters by which rock types, structures, and textures peculiar to this locale could be recognized or differentiated. A secondary purpose was to provide an adequate evaluation and calibration of airborne and ground-based instruments used in the survey.

Pisgah Crater and its vicinity were chosen as one of the fundamental test sites for the NASA Remote-Sensing Program because of the relatively fresh basaltic flows and pyroclastics. The typical exposure of basalt in the area also made it a possible lunar analog. A fundamental test site for the purpose of the program is defined as a readily accessible area for which the topography, geology, hydrology, soils, vegetation, and other features are relatively well known. All remote-sensor instrument teams (that is, IR, radar, microwave, and photography teams) were obligated to use the fundamental test sites for instrument evaluation and to establish terrain-identification procedures.

Pisgah Crater, nearby Sunshine Cone, and their associated lava flows are in the southern Mojave Desert about 40 miles east-southeast of Barstow, California (fig. 10-1). U.S. Highway 66 skirts the northern part of the area and provides access to the Crater and the perimeters of the flows via asphalt-paved and dirt roads.

Pisgah Crater, which is a pumiceous cone, is owned and occasionally quarried by the Atchison, Topeka, and Santa Fe Railroad. The remaining part of the area to the south is within the boundary of the Marine Corps Base, Twentynine Palms, California, and is currently being used as a gunnery and bombing range. The proximate area to the east, west, and north of Pisgah Crater is public domain.

Originally, an area totaling 10 square miles was outlined for detailed study (fig. 10-2). This included an 8-mile-long strip extending southeast from and including Pisgah Crater to Lavic Dry Lake and a 2-mile strip alined to include a portion of the Sunshine lava flow and Lavic Dry Lake. Additional aerial IR imagery of the Sunshine and Pisgah flows along the Pisgah fault proved so interesting and informative that the Pisgah fault area is included in the discussion.

Infrared surveys were flown February 11 to 13, 1965, and August 4 and 5, 1966. The initial survey was flown by NASA personnel aboard the NASA 926 Convair 240 aircraft. Because of technical problems with the IR scanners (4.5μ to 5.5μ and 8μ to 14μ bands) and with certain ground

instruments, most of the imagery and ground temperature data obtained during the initial survey period were of little value. However, excellent IR imagery in the 8μ to 14μ region of the spectrum was acquired by the U.S. Geological Survey during the August 1966 survey. The scanner was mounted in a Beech D-18 aircraft provided by the U.S. Geological Survey Water Resources Division. Likewise, more reliable ground data were obtained at this time because of improved instrumentation and technique.

Ground data were taken by U.S. Geological Survey personnel including W. A. Fischer, J. D. Friedman, W. R. Hemphill, D. L. Daniels, G. R. Boynton, P. W. Philbin, and the author of this report. C. R. Fross operated the IR scanner during the August 1966 survey, and R. M. Turner was responsible for photoprocessing of the IR imagery. Their assistance is gratefully acknowledged.

Previous Studies

The geology of the Pisgah Crater area has been previously mapped in whole or part by several geologists. Highly generalized reconnaissance maps were made by Darton (ref. 10-1), Gardner (ref. 10-2), and Kupfer and Bassett (ref. 10-3) at the respective scales of 1:500 000, 1:250 000, and 1:125 000. Dibblee (ref. 10-4) and Dibblee and Bassett (ref. 10-5) mapped the Lavic and Cady Mountains quadrangles, respectively, at a scale of 1:62 500, covering the area of the present study. In conjunction with the present study, W. S. Wise (ref. 10-6) mapped the Pisgah and Sunshine Cone lava fields in detail. Figure 10-3 is a compilation of these sources, of personal observations in the field, and of geology taken from large-scale aerial photographs of the area. The author assumes responsibility for the resulting geologic interpretation of the mappable units as presented in this report.

Several NASA technical letters on the Pisgah Crater area were distributed by the U.S. Geological Survey. These included reports and/or preliminary maps by Gawarecki (ref. 10-7), Dibblee (ref. 10-8), Fischer and others (ref. 10-9), Altenhofen (ref. 10-10), Daniels (ref. 10-11), and Friedman (ref. 10-12).

GEOLOGY

Geomorphic Setting

The Pisgah Test Site is within the Basin and Range physiographic province and is one of the many centers of recent volcanic activity which lie on broadly alluviated valleys and playas across the central

part of San Bernardino County. Pisgah Test Site also lies within the southern Mojave Desert, a part of the Mojave structural block, which is characterized by generally northwest-trending fault block mountains and intermontane basins.

Elevations in the Pisgah Test Site range from 1886 feet above sea level at Lavic Dry Lake in sec. 27, T 7 N, R 6 E to 4421 feet at Sunshine Peak, which is 4 miles distant in NW1/4, sec. 1, T 6 N, R 5 E. The maximum elevation in the area of detailed study is 3121 feet above sea level at Sunshine Cone, but the average is close to 2100 feet.

The drainage is internal, to Lavic Dry Lake playa on the south, and to Troy Dry Lake on the northwest. The two areas are believed to have been connected by northward drainage during Pleistocene time (ref. 10-13), prior to damming by the flood of Pisgah basalt and the subsequent development of the playas during the pluvial stages. The lake beds have been augered to a depth of 160 feet in the northeast part of Lavic Dry Lake without reaching lava (ref. 10-14), indicating that a considerable amount of deposition has taken place. A dry 10-foot-deep bomb crater observed in the lake bed shows that the water table is not near the surface.

The surface of the playa is extremely flat and has widely developed giant desiccation polygons, the sides of which are outlined by moist sediments and, in many cases, by vegetation. Inside the southern and western margins of the playa, phreatophyte mounds have been formed by the aeolian deposition of sand and silt around the base of the brushy vegetation. The moisture for this and other vegetation is probably derived from coarser intercalated detrital beds below the surface related to the alluvial fans bordering the playa.

Recent deposition appears to be minor. The playa may contain shallow standing water for brief periods after a rare desert cloudburst. During the August 1966 period of investigation, only the eastern margin of the lake showed evidence of moisture. Rainfall in this part of the Mojave Desert is only 1 to 2 inches annually.

The effects of wind are especially noticeable on the north side of the area where a long fetch enables the prevailing westerlies to deposit sand and silt across the northern reach of the Pisgah flows and the area immediately north of the Pisgah Cone.

Lithology

General comments.- The lithologic units found in the area are shown on the geologic map (fig. 10-3). In addition to the sources of the geologic data described earlier, geologic units discovered on the IR imagery are included on the map. A later section of this report on the interpretation of the imagery will discuss properties of the various units insofar as the properties affect the thermal behavior and contrast of the units.

The rocks range in age from probable Mesozoic to Recent. Their exact ages are unknown for the most part because there is little stratigraphic and no paleontologic control available for these units of limited lateral extent.

The following description of the lithologic units is necessary for an understanding of their thermal behavior as shown on the imagery.

Biotite quartz monzonite (bgm).- The oldest rock recognized is a biotite quartz monzonite that is found on Peter's Mountain as a few small inliers near the center and in NW1/4 sec. 19, T 7 N, R 6 E. Dibblee (ref. 10-4) describes the rock as a gray, massive, medium-grained, commonly porphyritic granitic rock composed of from 10 to 30 percent quartz; 35 to 50 percent plagioclase (andesine); 15 to 30 percent potassic feldspar, in many places as orthoclase phenocrysts up to 2 centimeters long; 3 to 20 percent biotite, in part altered to iron oxides; 0 to 5 percent hornblende; and a total of about 1 percent sphene, zircon, and magnetite. Field relations west of the Lavic quadrangle lead Dibblee (ref. 10-4) to consider the monzonite to be of Mesozoic age.

Dacite porphyry (Tdp).- Dacite porphyry of the Lava Bed Mountains borders the western part of the study area. It is in intrusive contact with the biotite quartz monzonite and has been the primary source of the gravels on the west side of the area. It is a gray-white to light-greenish-gray massive prophyry composed of euhedral and subhedral phenocrysts as large as 4 millimeters. In a microcrystalline groundmass, the phenocrysts, which make up 40 to 60 percent of the rock mass, are mostly plagioclase (oligoclase-andesine) with minor amounts of biotite, hornblende, and quartz (ref. 10-4). The gray-white groundmass is composed of plagioclase and potassic feldspar and traces of iron oxides. Emplacement of the porphyry as a large intrusive mass probably occurred during an early stage of Tertiary volcanic activity. Dibblee (ref. 10-4) suggests that the dacite porphyry is most likely of Oligocene or early Miocene age or possibly older.

Andesite breccia (Tab).- In the Peter's Mountain area, a sequence of volcanic and sedimentary rocks, probably as old as middle Tertiary, overlies the eroded biotite quartz monzonite. The descriptions of rocks within this sequence are largely those of Dibblee (ref. 10-4), with additional comments by the author of this report.

The oldest rock unit in this sequence is an andesite breccia, estimated to be about 250 feet thick. Gardner (ref. 10-2) tentatively correlated it with the Red Mountain andesite. The unit is a flow breccia, massive to very crudely bedded, composed of light-pinkish to very-dark-reddish-brown, unsorted angular fragments of andesite in andesite matrix. The andesite proper has phenocrysts as large as 4 millimeters which make up from 20 to 50 percent of the rock and which are set in a microcrystalline to subvitreous groundmass. Most of the phenocrysts are white

plagioclase (andesine?), but some are small plates of biotite, needles of hornblende (or, rarely, quartz). The groundmass is mostly plagioclase with little or no potassic feldspar and minor specks of iron oxide.

Tuff breccia (Tt).- Unconformably overlying the andesite breccia, in the NE1/4 sec. 19, T 7 N, R 6 E, is a pinkish-tan to gray-white tuff breccia composed of small white fragments of devitrified pumice and small-to-large angular fragments of porphyritic-to-felstic andesitic rocks of Tertiary age in a matrix of fine- to coarse-grained tuff. The unit also contains some intercalated beds of tuffaceous sandstone and conglomerate with andesite and dacite porphyry detritus.

Fanglomerate of granitic detritus (Tfg).- A fanglomerate of granitic detritus covers the andesite and tuff breccias on the north, in secs. 17 and 18, T 7 N, R 6 E. On the eastern side of Peter's Mountain, the fanglomerate is medium-tannish-gray, and is composed of unsorted, subangular boulders of quartz monzonite in an arkosic matrix. Desert varnish is common. The age of this fanglomerate is believed to be Oligocene or Miocene.

Basalt (Tb).- Above the fanglomerate stratigraphically, and perhaps also intercalated with and intruded into it, is a massive to thickly layered basalt that caps Peter's Mountain and occurs as scattered outliers as far north as sec. 7, T 7 N, R 6 E. Sizable basalt outcrops found east of the Pisgah flow are similar lithologically and stratigraphically to those on Peter's Mountain. Dibblee (ref. 10-4) considers the eastern basalt flow to be slightly younger than the flows to the west; but because of their similarities, the author believes all the flows to be of the same unit. The basalt in both eastern and western flows is olivine-bearing, dark-gray to black, vesicular, with differences that are common to any large flow or sequence of related flows. These flows differ from the younger Sunshine and Pisgah flows in being finely crystalline rather than significantly glassy in character.

The surface of basalt is generally devoid of sharp outcroppings and is commonly mantled by large angular blocks. The outcrops east of Lavic Dry Lake appear to support more brushy vegetation than do those on the west.

Gardner (ref. 10-2) tentatively correlated this basalt unit with the Black Mountain Basalt of Pliocene (?) and Pleistocene age. Dibblee (ref. 10-4) believes that the western occurrences are probably either Oligocene or Miocene. There is no definite evidence for either opinion. However, the relationships of the later basalts with the Lavic Dry Lake beds, which may in part represent Pleistocene pluvial deposits, suggest that the so-called Black Mountain Basalt correlative is significantly older than Pleistocene, probably Pliocene, in age.

Claystone (QTc).- A light-reddish-brown to greenish-gray massive to bedded claystone is described by Dibblee and Bassett (ref. 10-5) as outcropping about 3 miles west-northwest of Pisgah Crater. Interbedded with the clay is a 10-foot-thick cream-white, massive limestone and associated white bentonitic tuff. Dibblee and Bassett (ref. 10-5) indicate a probable lacustrine origin for the beds which grade upward into an older gravel and fanglomerate unit. The age of the claystone is believed to be of late Tertiary or Pleistocene age.

Older fanglomerate and gravel (Qof).- A light-tannish-gray fanglomerate and gravel overlies the fanglomerate of granitic detritus (Tfg) on the north side of Peter's Mountain and also the Tertiary basalt to the south. A similar unit is found to the north and east of the Pisgah lava field. In both occurrences, the unit is mostly unstratified fanglomerate of poorly sorted cobbles and boulders in a coarse sandy matrix. In the western occurrence, it differs from the underlying fanglomerate (Tgf) primarily by being lighter in color and more easily eroded. At the other occurrences to the north and east, the source was to the east, and the unit contains more fragments of volcanic rocks, including felsites (also Tertiary chert and jasper and Mesozoic granitic rocks).

In all occurrences, the unit is undergoing erosion. North of Pisgah Crater, sections of the surface have been stripped of the fines by wind, leaving behind boulders and cobbles with surfaces coated with desert varnish. The varnish causes the surface to appear darker than most of the fresh rock surfaces.

The age of this unit is considered as Pleistocene by Dibblee (ref. 10-4), but may be as old as Pliocene.

Sunshine basalt flows (Qbs_1, Qbs_2, and Qps).- The Sunshine lava field, a major unit in the southwestern part of the study area, resulted from at least two periods of eruption. Flows related to each period are distinguishable (fig. 10-4). An older series of flows (Qbs_1) in the north end of the field were primarily erupted from a vent represented by a now faulted and eroded pumice cone in the center of sec. 30, T 7 N, 6 E. The younger flows (Qbs_2) to the south issued from at least two vents: a partially buried cone in the NW1/4 sec. 30, T 7 N, R 6 E, and the other (the slightly eroded Sunshine Cone) in sec. 31 of the same township. Some fissure flows from the Pisgah fault may also have occurred at this time. The younger Sunshine basalt is found as far south as sec. 21, T 6 N, R 6 E. Much of the intervening area of flow, as in the northeast margin, is buried deeply by recent fanglomerate. The eastern edge of the lava field is buried under the Lavic Dry Lake beds and fanglomerate, and the western margin is covered by fanglomerate from the Lava Bed Mountains.

The older basalt, which is dark-gray to black on a fresh surface, is described by Wise (ref. 10-6) as a porphyritic alkali-olivine basalt. Single phenocrysts, as well as glomeroporphyritic clots of plagioclase and olivine, occur in a groundmass of plagioclase, titanaugite, olivine, magnetite, ilmenite, and anorthoclase. Minor, but consistently present, dark-brown phenocrysts of titanaugite set these lavas apart from all others in the Pisgah Test Site. Table 10-I shows the modal analysis of this flow.

The original surface of the flow has been almost entirely removed by weathering and erosion, and drainage is integrated. The flow surface is rubbly, and the angular blocks of basalt have developed a smooth desert varnish. A product of weathering is a ubiquitous coating of calcium carbonate on joint planes and in local minor depressions. This appears to account, in part at least, for the relatively lighter tone of the unit on aerial photographs.

The younger basalt is also a dark-gray-to-black vesicular alkali-olivine basalt. Wise (ref. 10-6) states that "scattered phenocrysts (3 to 5 mm) occur in a groundmass of plagioclase, titanaugite, olivine, magnetite, ilmenite, and anorthoclase." He notes that plagioclase phenocrysts are rare to absent in the area of the test strip, although they are abundant in a later flow on the southern end of the lava field. Modes are shown in table 10-I.

The original surface features of the younger series of flows are only partially dulled by weathering and erosion. Numerous depressions still exist that have developed into small carbonate and silt playas as large as 100 feet across. Calcium carbonate is also prominent along joint planes, as in the older Sunshine flows.

The difference in surface erosion between the two units that make up the Sunshine lava field appears to indicate that a significant amount of time had elapsed between the two major eruptive periods.

The three recognized pumice cones associated with the Sunshine flows are all similar in their character and are considered as one lithologic map unit of basaltic pumice (Qps). The pumice cones are described by Dibblee (ref. 10-4) as brownish-black scoriaceous basalt composed of basaltic glass. The faulted cone related to the earlier flow period has been noticeably dissected by erosion, and the pumiceous materials have been carried downslope to form an epiclastic alluvium of pebble-cobble scoria and basaltic detritus (Qpa) in the NE1/4 sec. 30, T 7 N, R 6 E. The cone to the west of the fault is partially buried by fanglomerate from the Lava Bed Mountains and by a flow that possibly emanated from its vent. The Sunshine Cone is cut by drainage rills 2 to 15 feet deep, but the cone essentially retains its original shape. The topography suggests that an earlier pyroclastic stage may have occurred. Gardner (ref. 10-2)

notes that a small playa about 80 feet in diameter occurs in the center of the crater. In this respect, it is similar to most other cones that characteristically contain substantial amounts of silt and weathering products, especially calcium carbonate, sifted down just below the surfaces of the cones.

Dibblee (ref. 10-4) presumes a Pleistocene age for the Sunshine basalt eruption.

Pisgah basalt flows (Qb_1, Qb_2, Qb_3, and Qpb).- The Pisgah lava eruption, as described by Wise (ref. 10-6), took place in at least three distinct phases. His thesis is based solely upon the texture of the phenocryst minerals in each phase.

The first eruptive phase of the basalt (Qb_1) is believed to have begun with the building of a cinder cone in the low hill area north of the main cone and with the issuance of lava from vents near the cone. Flows extended as far as the Lavic basin, about 0.5 mile to the north and 7 miles to the west-northwest in the present vicinity of U.S. Route 66.

The flow is cut by the Pisgah fault at the highway, where small tumuli are spaced quite regularly along the fault (fig. 10-5). The uniformly limited development of the tumuli suggests that their source was from below a congealed lava crust that ruptured during fault movement and not from along fault conduits below the effusive. The relations indicate that the Pisgah fault was active at this time, as does the topography, which controlled the movement of all the Pisgah flows.

There is a possibility that the younger Sunshine flow was nearly contemporaneous with the initial Pisgah eruption, since the younger Sunshine flow has the same preserved surface appearance; and its direction of flow was controlled by the fault and the developing Lavic basin. The older Sunshine flow is too eroded and weathered to be considered anything but older than the first Pisgah phase.

The lavas of the first eruptive phase are composed of blocky pahoehoe-type, and less commonly, aa-type flows (figs. 10-6 and 10-7). Wise (ref. 10-6) finds the flows to be a microporphyritic alkali-olivine basalt. Microphenocrysts of olivine (less than 2 mm) are scattered and rare. The groundmass minerals are olivine plagioclase, titanaugite, magnetite, and ilmenite. Basic glass is also a common constituent in the groundmass (table 10-I). The surfaces of the flows commonly have the slight lustre of desert varnish that forms a tan-colored material which is a noticeable coating on fractures and at the bases of spall sheets common on the pahoehoe. All types of flows are highly vesicular, indicating a substantial volatile or gas content during the magmatic stage. The vesicles, which make up to one-third of the volume, now contain a mixture of weathered products such as clay, carbonate, and ferrous oxides.

The second eruptive phase (Qb_2) began after a long period of quiescence; lava issued from at least two separate conduits. One conduit built a cinder cone close to the present cone, and a second conduit domed the earlier flow unit about 2500 feet south-southeast of the Pisgah Crater and poured forth a voluminous amount of lava from around the dome base. Several small possible conduits are found scattered to the east and south of the Pisgah Cone (fig. 10-3). However, the conduits may represent breaches in the solidified crust that allowed lava to be issued under a magmatostatic head from a subcrustal lava passage.

Lava from the second phase reached into the Lavic basin and again flowed northwestward toward the highway along drainage developed west of the first flow. The lava first overflowed the drainage, then settled as it continued downstream, leaving prominent ridges of solidified lava crust along its margins. These and other levee-like pressure ridges formed by the pulsating flood crests of lava are accentuated by alluvial fan detrital deposited later in the troughs. A considerable part of this flow is believed to be buried by the alluvial fan in this area.

The lava of this phase is largely aa (fig. 10-8), but pahoehoe surfaces are found on most of the long westward part of the flow.

Lava tubes developed near the south end of the dome conduit close to the end of the flow period. Subsequent partial collapse of the roof occurred after drainage of the subcrustal lava.

The second flow is a black porphyritic alkali-olivine basalt with larger olivine (2 to 3 mm) and plagioclase (2 to 5 mm) phenocrysts than the first flow. The groundmass minerals with modes shown in table 10-I are the same as those found in the earlier phase. Basic glass makes up more than 40 percent of the flow near the cone and only 24 percent in the Lavic Dry Lake area.

The third and probably final period of basalt flow (Qb_3) occurred from two separate points. The present Pisgah cinder cone in NW1/4 sec. 32, T 8 N, R 6 E formed at this time, and lava issued from a vent or vents at its base on the southeast side. The lavas from the vents, restricted by the previous flows, moved westward about 4 miles, southeastward 3 miles, and northward only 2 miles.

Pahoehoe-type lava covers almost the entire surface of the flow, but pressure ridges and resulting blocky surfaces are quite common. The flow is cut on the west by the Pisgah fault, with tumuli again developed along the fault in the same manner as in the first flow. The southwest margin has several ridges thrust up and accentuated by fan material, as in the second flow. Lava tubes developed on the margins of Pisgah Crater, which subsequently collapsed over much of their lengths (fig. 10-9). One tube on the eastern side of the crater is over 2000 feet long where exposed by roof collapse.

The alkali-olivine basalt has plagioclase phenocrysts generally larger than 10 millimeters in length and clots of olivine crystals about 5 to 6 millimeters across, which serve to distinguish these flows from the earlier one. However, the overall groundmass mineralogy is similar. Table 10-I gives modal analyses for grid samples taken 1300 feet southwest of Pisgah Crater.

All Pisgah lavas on the northern and western sides of the area are covered with substantial amounts of windblown sand and silt carried by prevailing westerlies from the alluvial fans and Troy Dry Lake to the east. The smoother pahoehoe basalts are covered by greater amounts because saltation is easier across its surface.

The Pisgah Cone (Qbp), which crowns the highest part of the lava field, is built up of fragments and lapilli of brownish-black to dark-reddish-gray scoriaceous basaltic glass or pumice (fig. 10-10). Older cinder cones, probably related to the earlier eruptions on the north side of the crater, are dark-reddish-gray, have been covered in greater part by the last eruption, and are strongly eroded where exposed. However, the most recent cone has a relatively fresh appearance. Road cuts in the flank of the crater expose thin silty horizons, both buried and near the surface, that may be the result of windblown material and of in situ weathering (fig. 10-11). The center of the crater is floored with typical pahoehoe-type basalt (fig. 10-10). There are no indications that the basalt ever reached the rim of the crater during eruption.

The top edge of the crater has loose scoria and pumice ranging in size from pebbles to small boulders. The average size is about that of small cobbles (64 mm). The flanks of the cone are covered with larger fragments, mostly in the small boulder size (256 mm). Volcanic bombs with the typical spindle shape are rare. The interior slope of the crater has the same size and type of material as the rim, but also has occasional small boulders and vesicular basalt.

The surface of the cone, which slopes from 25° to 30°, is free of vegetation. The pahoehoe surfaces generally have scattered sage and other brushy vegetation.

The ages of the Pisgah flows and pyroclastics are believed by Dibblee (ref. 10-4) to be of Pleistocene and/or Recent age.

Alluvium of basaltic pumice and/or detritus (Qpa).- Minor erosion of the pumice cones associated with the Sunshine and Pisgah flows caused the local transport and deposition of pyroclastics and other basaltic detritus. Because of their similar characteristics and continuing minor movement, they are recognized as a single formation. The age of this alluvium ranges from Pleistocene to Recent.

Playa deposits (Qc).- The most extensive playa deposits are those of Lavic Dry Lake. Other deposits of limited extent are found on the surface and along the margins of the Sunshine and Pisgah flows.

The Lavic playa surface is classified as a hard, dry, compact-floor type, composed essentially of densely packed, fine-grained argillic materials that are ordinarily only slightly penetrated by precipitation (ref. 10-13). Kerr and Langer (ref. 10-13) give the following estimates of the gross mineralogic character: 79 percent clay, 21 percent granular components, 0.2 percent accessory minerals, and a trace of saline minerals. The clays are montmorillonite and illite. The granular components are predominantly quartz and feldspar, but also include hornblende, chlorite, epidote, clinopyroxene, actinolite, biotite, muscovite, sericite, vermiculite (?), zircon, magnetite, tourmaline, and rock fragments. Saline minerals, surprisingly meager in amount, are halite, sylvite, and carbonate. Although halite is considered dominant by Kerr and Langer (ref. 10-13) calcium carbonate is obvious by its effervescence when specimens of the lake surface are treated with dilute acid.

The lakebed has a characteristic development of giant polygonal desiccation cracks over most of its surface. These cracks are measurable in hundreds of feet. Because of infilling, the cracks show very little depth and are not noticeable everywhere on the ground because of their variable degree of development. Near the margins of the lakebed, brushy vegetation has taken root in the moisture afforded at depth by many of the cracks. However, a younger, unvegetated set of cracks appears to have developed; these cracks are outlined by moist stripes of sediment (fig. 10-12). Typical mudcrack polygons are ubiquitous but are not as permanent as the giant polygons, which owe their existence to desiccation at depth over a long period of time.

Development of small, ephemeral polygons is variable over the lakebed. Adjacent to the south margin of the Pisgah flow, the silty clay appears more desiccated, forming major irregular polygons averaging 10 inches across and cracks at least 6 inches deep (fig. 10-13). Small subordinate polygons are developed within these major polygons. A flat mosaic of weakly developed polygons up to 6 inches across, with edges somewhat wind eroded, were found toward the center of the lakebed during one early visit to the area. An extremely flaky crust, affecting several layers and producing potterylike shards was also found on the northwest margin of the lakebed during an early visit.

Three days prior to the August 1966 survey, the eastern margin of Lavic Dry Lake had been moistened by rainfall running off the Bullion Mountains. The rain produced a few small puddles in vehicle tracks and softened the playa. The open water disappeared before the aerial survey was made, but the eastern margin of the playa remained moist.

Lavic Dry Lake was, in its lower part at least, contemporaneous with the Pisgah flows. A basin toward which the lavas flowed was in existence in this area. A lava dam apparently formed at that time, which has continued through present time and provided a closed depositional basin. The age of beds in this basin probably ranges from late Pleistocene through Recent.

Older alluvium (Qoa).- An earlier phase of Quaternary alluvium is exposed and has eroded and in some places re-covered by recent detritus. The Quaternary alluvium consists mostly of massive to crudely bedded fanglomerate and of gravel of unsorted fragments from preexisting detritus and from volcanics on Peter's Mountain. This Quaternary alluvium differs from other Quaternary alluvium in the vicinity by being very weakly consolidated, by having a light desert varnish that gives it a darker tone, and by supporting slightly more vegetation.

Basaltic gravel mosaic (Qbg).- At the north end of the Lavic lakebed, a mosaic of angular aa and blocky basalt cobbles and pebbles is found on the lake sediments. The limited size of the fragments and their location above a buried flow suggest that they originated by vertical ice rafting during periods of winter flooding in the lake. The surface of the mosaic is quite variable in development. The age of the mosaic is probably Recent.

Alluvium (Qa).- The most recent sediments are widespread detrital materials at lower elevations that range in size from cobble gravel through pebbly coarse sand to sand and silt. The heterogeneity of the sediments is a function of its multiple sources. However, local extremes in detrital composition result in nearly distinct alluvium subunits.

Structure

Faults.- The Pisgah fault, a major fracture zone, is the dominant structural feature of the area. The fault extends along the western boundary of the area and strikes N 22° W near Sunshine Cone, but gradually curves to about N 40° W near U.S. Route 66 on the northwest where it passes under alluvium (fig. 10-3). The fault continues south-southeast from the Sunshine flows, where the fault is covered by a large alluvium fan and then reappears in the Bullion Mountains where the fault becomes an echelon with the Bullion Mountain fault before dying out. A dextral en echelon discontinuity appears also to be developed near U.S. Route 66, with a 0.2-mile offset of the fault trace.

Near the north end of the Sunshine lava field in the center of sec. 30, T 7 N, R 6 E, the fault was observed to be essentially vertical without any local indication of relative movement direction. To the south-southeast where the fault cuts the main body of lava, the fault is

splayed and highly irregular. The east wall is downdropped about 250 feet, and the structure appears to be a faulted monocline. The fault at depth here is probably vertical, but the fractures in the flows tended to splay and propagate upward in the direction of the downthrown block (ref. 10-15). There is a possibility that the lava flowed over the developing fault at an early stage, but the relatively steep repose angle of the original second lava-flow surface strongly suggests that deformation was primarily responsible for the present topographic situation. In this vicinity, an apparent right lateral displacement of the contact between the older and younger Sunshine flows and of the drainage across the younger flow suggests that the same stresses were present as in the San Andreas fault system far to the west. A postearly Sunshine eruption dextral movement of 0.5 mile is indicated by displacement of the faulted cone. This vector is also implied by the fracture pattern on the younger flow (fig. 10-3).

At the southern end of Peter's Mountain, a small graben is associated with the fault, and the southwestern side of the fault becomes displaced relatively downward. Where the fault cuts the Pisgah flows to the northwest, the relative displacement is reversed twice more.

The Pisgah fault was active during part of the periods of eruption, at least, of the Sunshine and Pisgah flows. This is indicated by marked faulting of a cone and associated lavas of the first sequence of Sunshine flows and by minor faulting of the first and third Pisgah flows with the development of tumuli before final cooling of both flows. The deflection of the first and second Pisgah flows around the base of Peter's Mountain on the southeastern margin of the lava field indicates that most of the deformation had occurred prior to Pisgah time.

On the east side of Peter's Mountain, a topographic scarp and associated slickensides denote a vertical, generally north-trending fault, the Peter's Mountain fault, that probably extends from under the north margin of the Sunshine basalt northward to beneath the Pisgah flows. Slickensides on the fault plunge 50° due north, indicating both lateral and vertical components of displacement during the last movement.

Between the Peter's Mountain fault and the Pisgah fault, the Tertiary volcanics and gravels are severely cut by numerous short faults of generally high angle and limited displacement. One of these faults, which intercepts the Pisgah fault, also cuts the older Sunshine flow. Many more faults exist in this area than are shown on the map.

Two noticeable faults are found north of the Pisgah lavas. These strike about N 10° W, appear to be relatively downthrown on the east side, and probably dip east at a moderately steep angle. Other minor faults in this vicinity have been found in clay quarries by Dibblee (ref. 10-4).

Wise (ref. 10-6) has mapped a fissurelike fault, approximately 1 mile in length in the southern part of the youngest Pisgah flow that strikes north-northwestward and has a downthrown southwest wall (fig. 10-3). Dextral en echelon offsets suggest that a weak right lateral component of strain was present. Movement along the fault, as expressed in the basalt, has been negligible, and it could represent cauldron subsidence governed in its direction by regional stress or, more likely, differential movement of lava below a solidified crust.

Folds.- Aside from the monoclinal fold on the Sunshine lava, described in the foregoing section, there is little other folding present. Dibblee (ref. 10-4) has mapped dips that suggest the presence of a gentle northwest-trending closed anticline underneath a mask of alluvium in secs. 23 and 26, T 8 N, R 5 E which would be about 1 mile long in surface expression (ref. 10-4, map). Other dips in the area suggest that other minor fold structures are present, but incomplete outcrops and scale considerations prevent their delineation on figure 10-3. This deformation in the older Quaternary sediments is not reflected in the Pisgah flows.

INSTRUMENTATION

Aerial IR surveys were flown using airborne scanning radiometers which, with appropriate bandpass filters, were sensitive to the 4.5μ to 5.5μ and 8μ to 14μ regions of the electromagnetic spectrum. Both wavelength bands coincide with transmission "windows" in the atmosphere. The latter band corresponds with the region of maximum earth emission for normal surface temperatures. Fischer and others (ref. 10-9) summarize the basic IR scanning technique as used in the Pisgah study.

An AN/AAS-5 IR scanner was used with a dielectric filter to obtain imagery in the 4.5μ to 5.5μ band during the February 1965 survey. The detector, an InSb intrinsic photoconductor, was cooled with liquid nitrogen. The field of view of the scanner was limited to 80° because of a two-channel scanning-mirror-system conf guration. The second channel recorded the visible spectrum by means of a photomultiplier.

Imagery in the 8μ to 14μ band was obtained with an HRB-Singer scanning radiometer during the February 1965 and the August 1966 surveys. The detector used in this instrument was a GE:Hg extrinsic photoconductor cooled by a helium-charged, closed-cycle refrigeration system and filtered to receive only the 8μ to 14μ radiation.

Infrared imagery was acquired at 4-hour intervals to observe the changes in the relative apparent temperature of the various terrain units in a diurnal cycle. Because of detector problems in both scanners and because of a noisy power supply during the initial February 1965 survey by NASA aircraft, the imagery from that flight for the most part was unusable. However, the 8μ to 14μ imagery obtained during the August 1966

mission by the U.S. Geological Survey was, in general, satisfactory. Noticeable distortion because of incorrect vertical-to-horizontal ratio setting was insufficient to detract from the value of the imagery.

Ideally, it would have been preferable to record the detector signal on tape for later printing on film. The tape-recording technique preserves a dynamic range approximately seven times that directly printed on film (W. A. Fischer, oral communication, 1965). Under normal terrain temperature ranges, as at Pisgah, all contrasts could have been recovered through the laboratory print-out of the tape signal, although the complete range may not have been within the gray scale of the film on which the imagery was printed. Also, direct recording on film is susceptible to exposure variations during the survey and in film processing.

INTERPRETATION OF THE INFRARED IMAGERY

Infrared imagery in the 8μ to 14μ band was flown August 4 and 5, 1966, over three flight lines (fig. 10-2), commencing about 20:00, August 4 and at approximately 4-hour intervals thereafter, covering a complete diurnal cycle. The vertical-to-horizontal setting of the scanner was set too low for all flights, but the error does not significantly affect the geological interpretation. One result is an exaggerated longitudinal scale in relation to the lateral scale. Because of this distortion, no attempt was made to provide a general scale. Geographic locations can be obtained by viewing the geologic map photomosaic (fig. 10-3) and/or the location map (fig. 10-2).

An examination of the imagery shown on figures 10-14 to 10-16 shows that the midnight and presunrise images are essentially the same with slightly more contrast available on the midnight image. The midday images, obtained under maximum solar heating conditions, show the most textural contrast within the basalt flows, while the postsunset images provide the greatest contrast between basalt bedrock and the alluvial formations. Differential heating of eastern and western slopes because of low sun angles is noticeable on the postsunrise morning and presunset afternoon images, respectively.

Imagery of flight line 1 which covered the main area of study, including Pisgah Crater, its flows to the south, and Lavic Dry Lake, is shown on figure 10-14. Boundaries between the different types of basalt surfaces, which correspond in places to the separately mapped flow units, are noticeable to some degree on all of the flights. Examples of the contrasts between the first, second, and third Pisgah flows are best shown on the 20:10, 08:27, and 12:02 flight images. These flows are labeled 1, 2, and 3, respectively, on figure 10-14. On the 20:10 image, the contrast is caused by textural rather than by tonal (thermal) differences between the flows with small playa pockets in the third flow providing the texture. The term "texture" is used here in its photointerpretation sense, and as defined by Colwell (ref. 10-16, p. 538), is

"the frequency of tone change within the images." Flow 2 is slightly warmer than flow 3 at 20:10, but the reverse is true at 08:27 and 12:02, for which thermal contrast is dominant. A probable explanation of this phenomenon is that solar radiation during the day is not reflected from the aa to the extent that it is on the pahoehoe because of its roughness and somewhat darker color, thus causing the absorption of more solar photons and consequently greater heating. The cavernous structure of the rough aa also makes it behave more like a blackbody, but this structure also causes heating of the rock to a greater depth because of the structure's larger integral surface area. The pahoehoe, however, has a smoother, lighter, and consequently more reflective surface which would tend to absorb less radiation and restrict that heat absorbed to a shallower depth. This would account for the higher radiant temperature of the pahoehoe during periods of illumination, as shown during the 08:27, 12:02, and 16:16 flights (fig. 10-14).

Because the aa and pahoehoe textures are not restricted entirely to individual flow units and because blocky intergradations are common between the two types of textures, the units cannot be entirely delineated. Where two different flow units are adjacent and have the same surface texture, it is not possible to differentiate them on the imagery. The minor differences in mineral composition and degree of crystallinity between the units are alone insufficient to produce significant variations in thermal parameters. Surface texture of the lava, which is primarily a function of the temperature of extrusion, would cause changes that would override or mask any changes brought about by differences in composition. The large-scale secondary texture resulting from the presence of detrital-filled collapse structures on the dominantly pahoehoe crust of the first flow is a strong differentiating feature, especially on imagery that shows the greatest contrast between bedrock and detritus.

The Pisgah Cone (p in fig. 10-14), which is composed of scoriaceous basaltic glass and pumice, shows to advantage on the 20:10 image soon after sunset. The fragmented, porous pyroclastic material acts as an insulator and cannot conduct the solar heat input much below the immediate surface. As a consequence, the thermal input is concentrated at the surface, and its radiant temperature is the highest of all the terrain units, as seen in the midday (12:02) image. As soon as the solar illumination is removed at sunset, the high radiance disequilibrium between the pumice and the cold sky causes the pumice to cool rapidly. The insulating property of the material and its small mass prevented it from becoming a heat sink of any consequence in comparison with the surrounding basalt flows, which have a decidedly higher thermal inertia. The diurnal radiant-temperature variation relationship between the scoriaceous pumice and the pahoehoe, as shown on the imagery, coincides with the relationships established with ground-based radiometers. At 12:02, the radiant temperature of the pumice was recorded at 61° C, and the nearby pahoehoe of flow 3 was recorded at 54° C — a difference of 7° C. Prior to sunrise at 04:18, the radiant temperature of the pumice was 23° C, and the basalt was warmer at 26° C — a difference of only 3° C.

The thin alluvial wash of pumice immediately southeast of the Pisgah Cone (Qpa on fig. 10-3 and a on fig. 10-14) reacts thermally in the same manner as its source material. The presence of thin alluvial wash is not readily apparent on conventional photography, but its thermal contrast is easily seen on the imagery.

The partially collapsed lava tube located immediately east of the Pisgah Cone (t in fig. 10-14 and fig. 10-9) remains warm and is noticeable on the imagery flown between sunset and sunrise (20:10, 00:46, and 04:18). The depressions formed by the collapsed roof act somewhat as a blackbody cavity where radiation is exchanged between the walls, retaining the heat longer before ultimately radiating it out to the cold sky. The alinement of the partially exposed tube is easily delineated on the IR image, whereas it is unnoticeable on conventional photography of the same scale. During the daytime flights (08:27, 12:02, and 16:16), the collapsed portions are observable because of their cool rim shadows. The same diurnal relationships hold for the deeply fissured area about 0.5 mile south-southeast of the cone (f on fig. 10-14).

A roughly circular area, distorted to an oval-shape, is centered at c on the images of figure 10-14. Its outline is best seen on the 20:10, 08:27, and 12:02 flights, and it is characterized by a cooler rim on the first flight and a warmer rim on the latter two flights. The northwest margin is defined by several small vents, and the remaining margin is defined by pressure ridges and surface differences in the basalt. These features, which are not noticeable on conventional photography, may represent a minor subsidence area over an abnormally thick portion of the second Pisgah flow.

The effects of windblown sand and silt on the basalt north of Pisgah Crater are noticeable only on the nocturnal imagery (s on fig. 10-14; 20:10, 00:46, and 04:18 flights). Enough windblown material mantled the basalt to significantly raise its albedo during the period of solar heating. As a result, the area is much cooler than the surrounding unmantled basalt. A wind-scoured area on the older fanglomerate and gravel to the northwest of this area (v on the 20:10 image, fig. 10-14) shows up warmer on the nocturnal imagery because the residual coarser material left behind as a result of deflation has a higher thermal inertia, that is, a better capability to store solar heat. The darker color of the area, caused by a slight desert varnish in comparison to the normal fanglomerate surface, lowered the albedo of the area during the day, which also resulted in greater heating during the day. On the midday image (v on the 12:02 image, fig. 10-14), this same area is slightly cooler than the normal surface, presumably because of the ability of the area to absorb solar heat in the coarser residual fractions of the gravel.

The Tertiary basalt on the east side of the Pisgah lava field (b on the 20:10 image, fig. 10-14) reacts thermally in generally the same manner as the Pisgah basalt throughout the diurnal cycle. The original

surface has been eroded, and the present surface is smoothed as a result of weathering rubble which serves to distinguish this formation from the Pisgah lavas. As with the Pisgah flows, the Tertiary basalt is best differentiated from the enclosing gravel formation and recent alluvium on the 20:10 image (fig. 10-14).

Lavic Dry Lake (L on fig. 10-14) exhibits much more detail on the IR imagery than on conventional photography, especially when the latter is optimally exposed for all terrain features. All images show evidence of crude zoning in the lakebed. There is a cool, fairly well defined margin that extends discontinuously northward along the basalt-fan contrast to the neck of the Pisgah lava field. A slightly warmer interior zone, which is restricted to the lakebed proper, includes an ill-defined area characterized by a warm reticulate pattern.

The east side of the lakebed, which is especially cool, was muddy and moist from a recent desert rainstorm. Because of the remoteness of the Pisgah area, no local data are available on the occurrence of precipitation. However, it appears that a heavy rain fell about 3 days prior to the survey to the east of the Pisgah area in the Bullion Mountains. The moist, braided channels on the fan carried the run-off to the Lavic basin, and the lakebed margin with its high silt and fine sand content appears to have absorbed this run-off before it encroached on the less permeable clay-rich interior.

The extremely cool nature of the eastern lake margin is a function of many conditions, including the recency of the rainfall that provided the moisture, the high degree of saturation which resulted in a high-heat capacity and conductivity, and the dissipation of solar heat by the latent heat of vaporization of the water. The high saturation and darker color therefrom causes the eastern margin to become a heat sink, but the latent heat of vaporization of the moisture prevents the surface from heating as much as the drier parts of the playa during the period of insolation. As a result, it remains the coolest terrain in the area throughout the diurnal cycle. The other margins of the playa are only slightly warmer than the eastern margin, but are generally cooler than the interior zone. This remaining portion of the perimeter zone may be thermally affected by groundwater entering the playa beds from the bordering alluvial fans. The general absence of a cooler margin along the Pisgah flows appears to support this hypothesis.

The slightly warm reticulate pattern (d on fig. 10-14) is visible against a cooler background to a highly varying degree in all images from flight lines 1 (fig. 10-14) and 2 (fig. 10-15). The relatively warm lines that make up the netlike pattern are slightly moist stripes that form the boundaries of giant desiccation polygons (fig. 10-12). The darker color of the lines resulting from their slightly moist condition provides a lower albedo for greater heating during the day. The minor

moisture, which may be in whole or part hygroscopic and/or intermolecular, is probably insufficient and/or too inefficient to reduce solar heating by vaporization. The low-moisture effect of lowering the albedo therefore appears dominant in this case. Near the southern margin (v on the 12:02 image, fig. 10-14), dry brushy vegetation and associated dry phreatophyte mounds are alined along many of the polygon boundaries. The dark color of the vegetation and dryness of the underlying mounds combine to produce a target warmer than the background at midday (12:02 image, fig. 10-14).

The cool background to the polygonal pattern appears anomalous, but the playa in this area consists primarily of tannish-white, well-compacted clay which would be expected, from albedo and moisture considerations, to be cooler than the stripes. The other warmer portions of the interior zone may reflect the thermal behavior of a puffy and/or shardlike, mud-cracked surface found on much of the playa bed.

It might be expected that thermal behavior of the lake sediments would change radically with a significant change in the amount and distribution of contained moisture on the surface and with depth and that thermal behavior of the lake sediments would change with the mineralogy, grain size, and distribution of the medium holding the moisture, which in turn would control the albedo, the manner in which the moisture is held, and the rate of release. The presence of salts concentrated by evaporation and the retention of intermolecular water in certain clay minerals would have a further modifying effect. With all of these possible physical variables, it is not surprising to find complex thermal patterns on the imagery of Lavic Dry Lake through the diurnal cycle. It would also hold that seasonal variations in these patterns would be commonplace because of these factors and the changes of the surface by the development of mud crack plates in extreme desiccation. The effects of moisture require further detailed study because the degree of saturation governs the heat capacity and thermal conductivity, and saturation affects the albedo of porous terrain.

On the north side of the Lavic lakebed, the basaltic gravel mosaic (g on the 00:46 image, fig. 10-14) stands out on the nocturnal images with a warm rim surrounding a generally cooler interior. During the day, the mosaic acts thermally in the same manner as the Pisgah basalt to the north. The gravel, which consists of angular to subangular cobbles and pebbles of vesicular basalt, is spread unevenly on the playa surface and appears to overlie a buried flow a few inches to several feet below the surface. The gravel is buried in or covered slightly at the margin which coincides with the thermally anomalous rim. The high temperature of the basaltic gravel is expected during the day because of its low albedo, but the intimate association of basaltic gravel with the playa sediments prevents significant development of thermal inertia of the unit; and like the cone material where thermal content is limited to the surface, the

basaltic gravel cools rapidly after sunset. The warm rim on the night images appears to be the result of a higher thermal inertia of that portion of the unit. The buried gravel at the margin presumably would give off its heat more slowly because it has to pass through a finite amount of playa sediment.

Flight line 2 imagery (fig. 10-15), which covers a short segment of the area originally outlined for detailed study (fig. 10-2), duplicates some of the area previously discussed and contains some features better viewed on flight line 3 imagery (fig. 10-16). However, flight line 2 imagery offers a good comparison of the alluvial fans on the east and west sides of the Lavic playa and a reiteration of some features discussed under flight lines 1 and 3.

The alluvial fan on the east side of the Lavic playa (f on the 12:10 image, fig. 10-15) exhibits on all images of flight line 2 the braided channels that were active during the recent precipitation in the Bullion Mountains. The strongest contrast of the moist channels against the dry-fan background is seen, as expected, on the 12:10 image. While these channels are also visible on conventional photography, it is believed that the contrast would remain longer on the IR imagery as the channels slowly dried up.

The fan between the Pisgah and Sunshine flows to the west of the playa shows no evidence of recent run-off, as the eastern alluvial fan shows. However, on daytime images (08:36, 12:10, and 16:24 images, fig. 10-15), there is an apparent thermal contrast between the segment of the fan that borders the Sunshine flow and the segment bordering the Pisgah flow. The southern segment of the fan, which appears slightly darker from the air, derives most of its detritus from the nearby outcrops of basalt, andesite, and other bedrock on the south side of Peter's Mountain (figs. 10-2 and 10-3). The remaining northern segment of the fan has as its predominant source the older fanglomerate gravels on the northeastern part of Peter's Mountain. These gravels provided finer detritus for the northern part of the fan than the bedrock source provided for the southern part. This difference is manifested by thermal contrast on the imagery, with the slightly coarser southern segment of the fan appearing a little cooler during the day because the larger average gravel size enables the coarser segment to absorb the solar heat to a slightly greater depth. That this effect is minor is shown by the lack of reverse contrast on the nighttime images. Apparently, the slightly darker color of the southern fan segment did not sufficiently lower its albedo to override the thermal effect brought about by the difference in gravel size.

Along the contact between the Pisgah lava field and the alluvial fan, a cool drainage channel is visible on the daytime images (m on the 12:10 image, fig. 10-15). The channel appears to have its origin where

the foot of the fan meets the lava field isthmus. This suggests that groundwater may be dammed at this point and that enough moisture is present just below the surface to provide a daytime thermal contrast.

Flight line 3 is centered on the Pisgah fault, about 3 miles to the southwest and parallel to flight line 1 (fig. 10-2). Imagery from flight line 3, shown on figure 10-16, covers a small part of the area on the east flank of the Sunshine lava field that was originally chosen for detailed study. The line was flown to obtain information on the expression of the fault on the imagery and on the thermal behavior of rock types in this part of the area. With the exception of the last flight at 16:09, which had shadows of a few scattered clouds (c on the 16:09 image, fig. 10-16), the imagery is free of such natural detractions. The electronic deficiencies present on the north ends of the 08:15 and 11:55 images (fig. 10-16) necessitated a shortening of the interpreted portion of the flight line.

The Sunshine lava flow sequences, shown as 1 and 2 on the flight line 3 imagery of figure 10-16, may be differentiated to some degree on most of the images. However, the best contrast, resulting from the differences in the degree of surface uniformity between the flows, is seen on the midday imagery (11:55 image, fig. 10-16). This effect is slightly noticeable on the 08:15 image also. On the nocturnal imagery, the main difference between the first and second flow sequences appears to be that a warm veining of drainage is noticeable on the first sequence, but is somewhat obscured by background in the second sequence.

The basaltic pumice of Sunshine Cone (the southernmost p on the 20:03 image, fig. 10-16) and of the other cones associated with the Sunshine flows behaves thermally in the same manner as the pumice of Pisgah Crater. The alluvial pumice from these cones and other basaltic detritus (a on the images of fig. 10-16) are easily delineated on the nocturnal imagery, as similar materials are on flight line 1 (fig. 10-14).

The northernmost pumice found in place in the Sunshine lava field (p on the west side of the 20:03 image, fig. 10-16) was found to be the western half of the faulted cone found displaced 0.5 mile to the south on the east side of the Pisgah fault. This outcrop is difficult to determine on aerial photographs, but is easily discerned on the nocturnal imagery.

The Pisgah fault (Pf on the 20:03 image, fig. 10-16) shows on the early morning imagery (00:41 and 04:14 images, fig. 10:16) as a relatively warm network of fine lines in detail not observable on photography. The warm nature of the fault zone appears to be caused by large rubble-lined crevices and, in many places, by blocky scree where voids act much

like blackbody cavities. The cavity walls lose their radiant heat more slowly than the surrounding basalt after sundown because of sustained radiation interchange between the walls before ultimate cooling to the sky. This is the same effect that causes the warm streaks shown in collapse depressions of lava tubes and fissures near Pisgah Crater.

The best distinction between the basaltic rocks and the surrounding alluvium is on the 20:03 (fig. 10-16) postsunset image, as was the case in flight line 1 (20:10 image, fig. 10-14). The Tertiary basalt (b on the 20:03 image, fig. 10-16) on top of Peter's Mountain and along its northeast flank behaves in the same way as its eastern correlative shown on flight line 1 (b on the 20:10 image, fig. 10-14). This older basalt has a physically weathered surface, and the float hides the exact contact with the enclosing gravels. Other bedrock features on the south end of Peter's Mountain do not show well enough to be differentiated.

The warmer ill-defined gravel unit on the east side of the mountain seen in the nocturnal imagery is the fanglomerate of granitic detritus. This fanglomerate is older, darker, and more compact than the gravels bordering it to the west and can absorb slightly more heat during the day (Cf on fig. 10-3). The northwestern tip of the dissected gravel of Peter's Mountain is as warm as the older gravel unit on the east side and may be either the same material or a facies difference in the main mass of younger gravel that makes up the mountain.

On the small bajada just west of Peter's Mountain a thin cool area is noticeable along one drainage (m on the 20:03 and 11:55 images, fig. 10-16). This thin cool area occurs at the lower end of a long drainage from the mountain and may be either the result of higher moisture in the immediate subsurface or of its fresh, unvegetated nature, or of both factors. The cool area shows on older photographs of the area, but does not differ here from drainages nearby. This suggests that moisture may be the main cause.

CONCLUSIONS

The aerial infrared survey of the Pisgah Crater area resulted in 8μ to 14μ band infrared imagery that provided useful geologic information to complement data obtained from ground studies and aerial photography.

A series of thermal contrasts representative of those found through the diurnal cycle was acquired during three of the six flight periods: at about 20:00 (postsunset), 04:00 (presunrise), and 12:00 (midday). No single imaging period provided or can provide all of the relative thermal contrasts potentially present in the area. However, the largest

amount of information on geologic thermal parameters from a single imaging period was obtained from imagery flown shortly after sunset, when optimum thermal contrast occurred between the terrain materials. At this time, thermal contrasts are best seen between bedrock and alluvium and between basalt flows and pyroclastics and their derivatives.

Midnight and presunrise images are similar, and one flight period within this time period would, in most cases, satisfy the requirement for both periods. These nocturnal images show more detail of the Pisgah fault where it cuts the Sunshine flows than is normally seen on aerial photographs of the area. The discovery of a faulted outcrop of pumice on imagery of the Sunshine flow was instrumental in determining a lateral displacement of 0.5 mile on the Pisgah fault.

Distinction of the Pisgah flows, which depends primarily on a difference in surface character between adjacent flow units, is made on the basis of thermal (tonal) contrast on the daytime images, and the distinction is best seen on the late-morning and midday images. The postsunset image shows this distinction of flows to a lesser degree with a difference in image texture, that is, with the frequency of tone change within the image.

Collapsed lava tubes and fissured areas in the Pisgah flows are distinguished as relatively warm streaks on the nighttime images because of a blackbody cavity effect, but appear as relatively cool areas during the day.

The imagery of Lavic Dry Lake reveals crude zoning and other features in more detail than can be found with other imaging sensors. Moisture appears to be the primary factor that controls the thermal behavior of this and some of the surrounding alluvial environment. The presence of moisture outlined active drainage channels on an alluvial fan and indicated other areas of near surface drainage. The complex role of moisture in these environments is incompletely known at present and requires further detailed study because the degree of saturation governs the best capacity and thermal conductivity and affects the albedo of porous alluvial terrain.

The empirical interpretation as presented in this report indicates that infrared imagery should prove to be a useful tool in geologic field mapping. The data can bring the geologist's attention to anomalous features not readily apparent in the visible spectrum, and many valid conclusions can be reached with a minimum of field verification. When the infrared scanning technique is eventually used in conjunction with other remote-sensing systems, the integration of the resulting data should greatly expand the capability of the interpreter by providing many unique property combinations for the identification of terrain.

REFERENCES

10-1. Darton, N. H.: Guidebook of the Western United States, Part C. The Santa Fe Route. U.S. Geol. Survey Bull. 613, 1915.

10-2. Gardner, D. L.: Geology of the Newberry and Ord Mountains, San Bernardino County, California. Calif. Jour. Mines and Geology, vol. 36, no. 3, 1940, pp. 257-292.

10-3. Kupfer, D. H.; and Bassett, A. M.: Geologic Reconnaissance Map of Part of the Southeastern Mojave Desert, California. U.S. Geol. Survey Mineral Inv. Field Studies Map MF-205, 1962.

10-4. Dibblee, T. W., Jr.: Geologic Map of the Lavic Quadrangle, San Bernardino County, California. U.S. Geol. Survey Misc. Geol. Inv. Map I-472, 1966.

10-5. Dibblee, T. W., Jr.; and Bassett, A. M.: Geologic Map of the Cady Mountains Quadrangle, San Bernardino County, California. U.S. Geol. Survey Misc. Geol. Inv. Map I-467, 1966.

10-6. Wise, W. S.: Geologic Map of the Pisgah and Sunshine Cove Lava Fields. U.S. Geol. Survey Tech. Letter NASA-11, 1966.

10-7. Gawarecki, S. J.: Geologic Reconnaissance Report of the Pisgah Crater, California Area. U.S. Geol. Survey Tech. Letter NASA-2, 1964.

10-8. Dibblee, T. W., Jr.: Preliminary Geologic Map - Pisgah Crater and Vicinity, California. U.S. Geol. Survey Tech. Letter NASA-4, 1965.

10-9. Fischer, W. A.; Friedman, J. D.; and Sousa, T. M.: Preliminary Results of Aerial Infrared Surveys at Pisgah Crater, California. U.S. Geol. Survey Tech. Letter NASA-5, 1965.

10-10. Altenhofen, R. E.; Oman, J. K.; and Sousa, T. M.: Topographic Studies of Pisgah Crater, California. U.S. Geol. Survey Tech. Letter NASA-7, 1965.

10-11. Daniels, D. L.: Infrared Spectral Emittance of Rocks from the Pisgah Crater and Mono Craters Areas, California. U.S. Geol. Survey Technical Letter NASA-13, 1966.

10-12. Friedman, J. D.: Composition of Basalt Flows at Pisgah Crater, California: Preliminary data. U.S. Geol. Survey Tech. Letter NASA-11, 1966.

10-13. Kerr, P. F.; and Langer, A. M.: Mineralogical Features of Mojave Desert Playa Crusts. Geology, Mineralogy, and Hydrology of U.S. Playas: Environmental Res. Papers, No. 96, Neal, J. T., ed., A. F. Cambridge Research Laboratories (Bedford, Mass.), 1965, pp. 31-72.

10-14. Dellwig, L. F.; Bickford, M. E.; Kirk, N.; and Walters, R.: Remote Sensor Studies of the Pisgah Crater Area, California: A Preliminary Report. Center for Research in Engineering Science Tech. Memorandum 61-18, Univ. of Kansas (Lawrence), 1966.

10-15. Hills, E. S.: Elements of Structural Geology. John Wiley and Sons, (New York), 1963.

10-16. Colwell, R. N.: Photographic Interpretation for Civil Purposes. Am. Soc. Photogrammetry, Manual of Photogrammetry, 2nd ed. (Washington, D.C.), 1952, pp. 535-602.

TABLE 10-I. - MODAL ANALYSIS OF SUNSHINE AND PISGAH BASALTS[a]

[W. S. Wise (ref. 10-6)]

Mineral	Sunshine lavas		Pisgah lavas			
	First flows (b)	Second flows (b)	First flows (c)	Second flows (c), (d)		Third flows (d)
Olivine					p-2	p-1
Phenocrysts	5.0	4.3	7.0	6.1	3.5	1.5
Groundmass	5.7	5.4	5.7	5.2	2.2	2.8
Plagioclase						
Phenocrysts	7.2	1.1	1.5	3.0	2.8	4.4
Groundmass	17.9	22.7	22.6	16.9	11.9	12.2
Clinopyroxene						
Phenocrysts	.3	.0	.1	.0	.0	.2
Groundmass	19.2	14.3	20.5	15.2	3.7	.6
Alkali feldspar	10.6	4.1	4.0	2.3	.7	12.2
Opaques	15.0	14.3	11.7	11.6	Trace	Trace
Apatite	4.1	1.5	3.6	2.1	Trace	Trace
Glass	Trace	10.1	4.6	24.0	41.9	48.4
Voids	14.7	22.2	18.6	13.3	34.0	30.0

[a]Note the importance of the degree of crystallization in comparing these modal analyses. The two samples from near the cinder cones are at least 75 percent glass and bubbles, while those collected from the end of the flows at Lavic Dry Lake are more completely crystallized.

[b]Both samples are from flows in the center of the test strip near the shore of Lavic Dry Lake, NE1/4 sec. 29. Each is an average of seven 2000-point counts.

[c]These two samples were collected in the center of the main test strip, also near Lavic Dry Lake, west side of sec. 20. Each is an average of four 2000-point counts.

[d]These two samples are from 0.25 mile south of Pisgah Cone. Each is an average of eight 2000-point counts.

Figure 10-1.- Index map showing location of Pisgah Crater area.

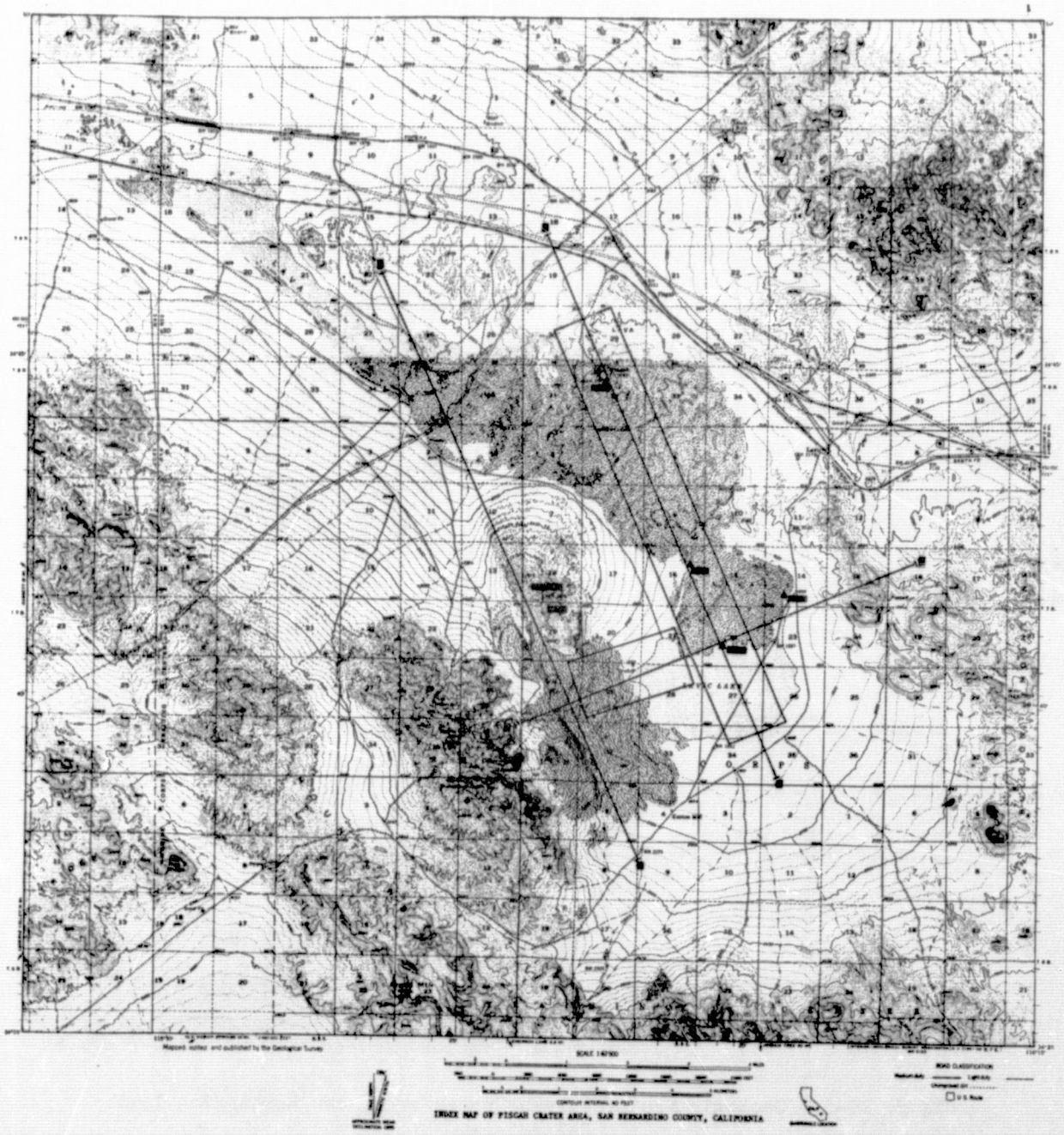

NASA
S-69-17322

Figure 10-2.- Index Map of Pisgah Crater area, San Bernardino County, California.

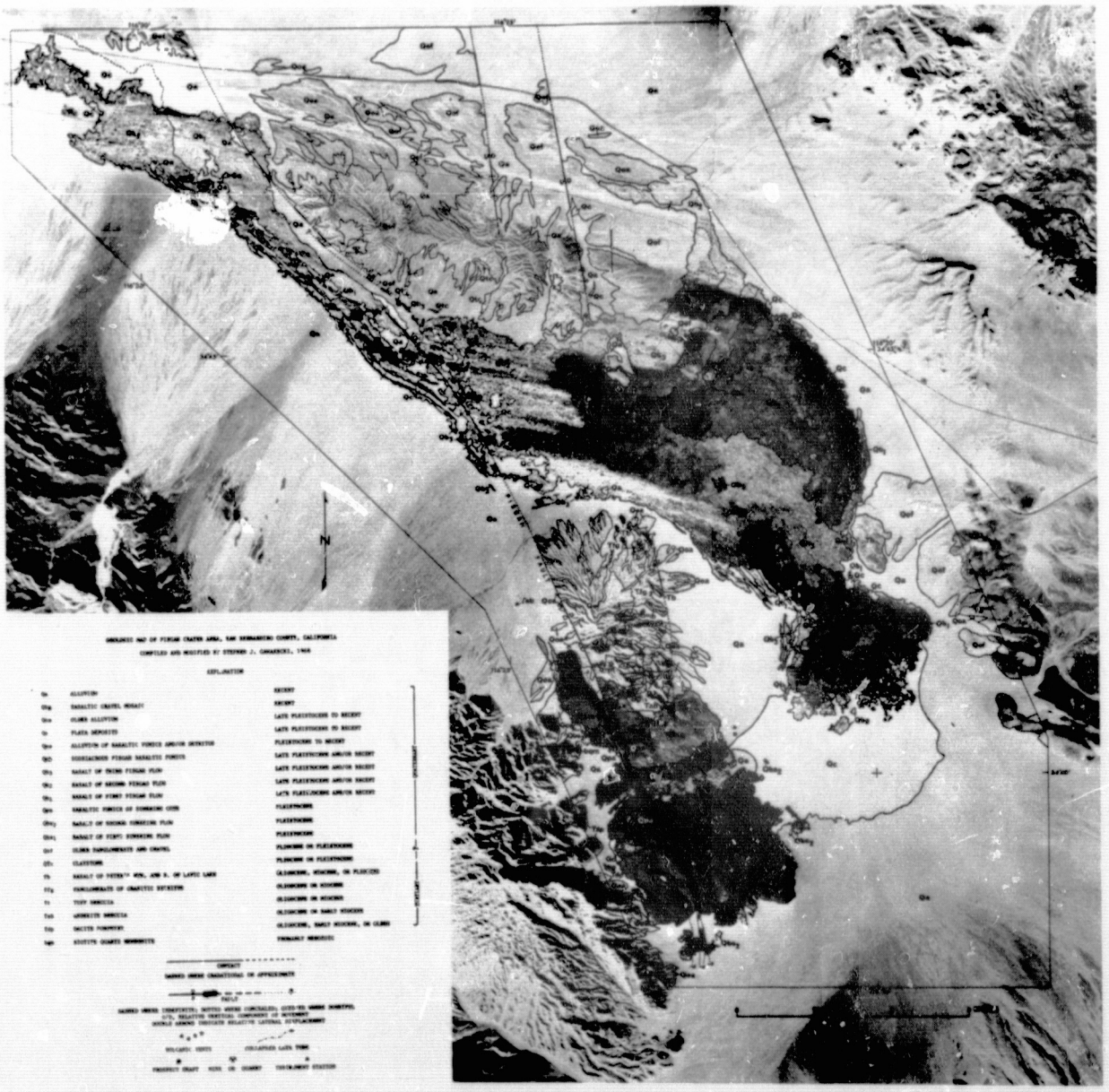

Figure 10-3.- Geologic Map of Pisgah Crater area, San Bernardino County, California.

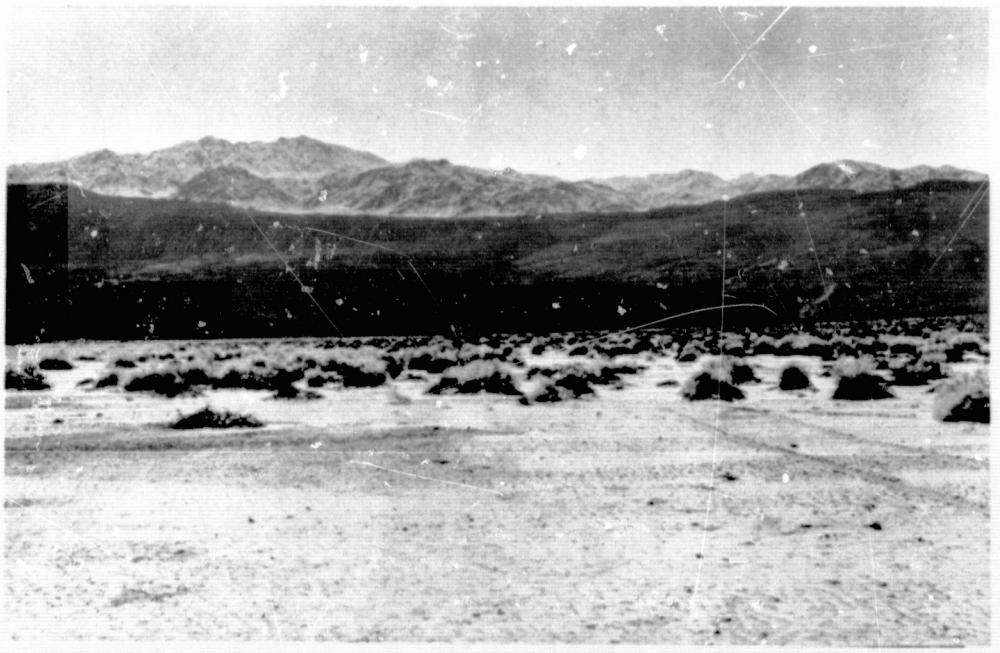

Figure 10-4.- Sunshine lava field viewed from Lavic Dry Lake.

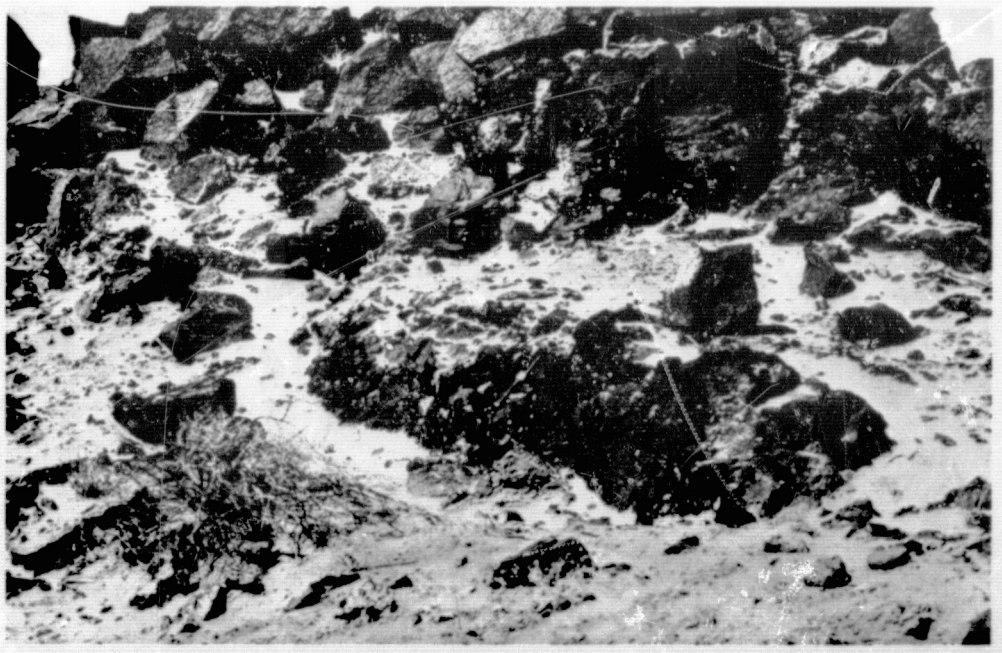

Figure 10-5.- Pisgah fault scarp with tumulus development.

Figure 10-6.- Typical pahoehoe surface of first Pisgah basalt flow (Qb_1) at station 66-2 near Lavic Dry Lake.

Figure 10-7.- Fissured aa dome in first Pisgah flow (Qb_1).

Figure 10-8.- Typical aa surface of second Pisgah basalt flow (Qb_2) at station 66-3 near Lavic Dry Lake.

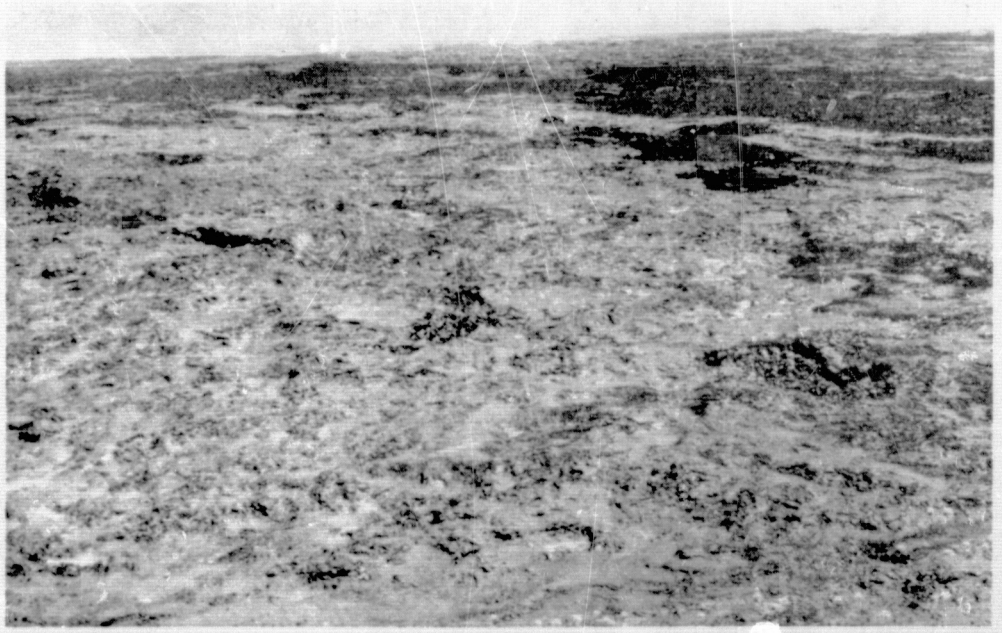

Figure 10-9.- View of collapsed lava tubes in pahoehoe basalt of third Pisgah flow (Qb_3).

Figure 10-10.- Interior view of Pisgah Cone.

Figure 10-11.- Road cut in slope of Pisgah Cone showing surface and buried silty horizons.

Figure 10-12.- Typical moisture stripe boundary of giant desiccation polygon in Lavic Lake near center, section 27.

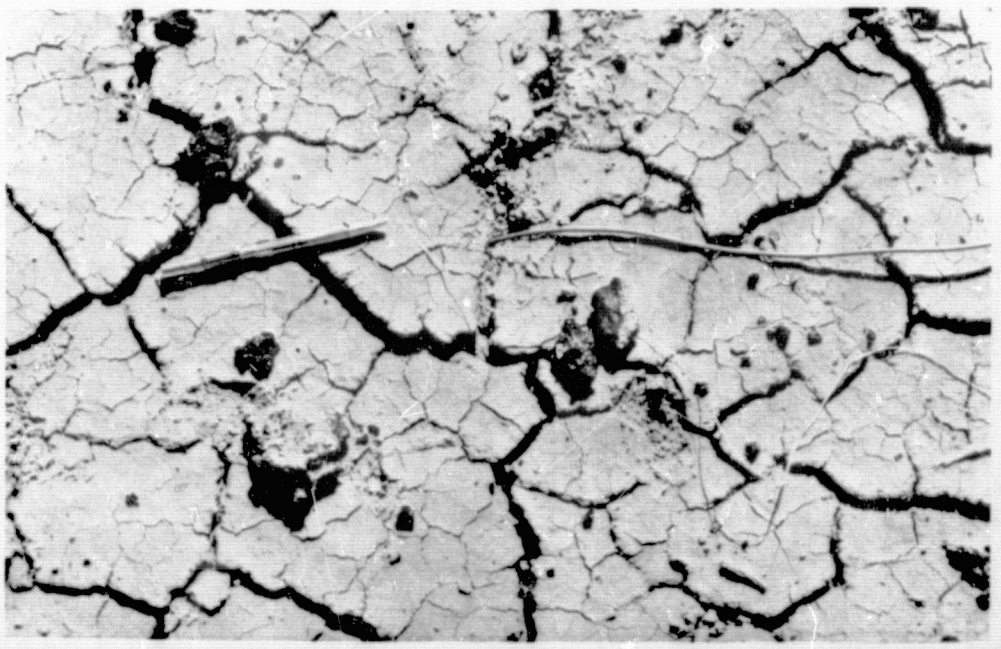

Figure 10-13.- Desiccation cracks in Lavic playa next to Pisgah flow at station 66-2.

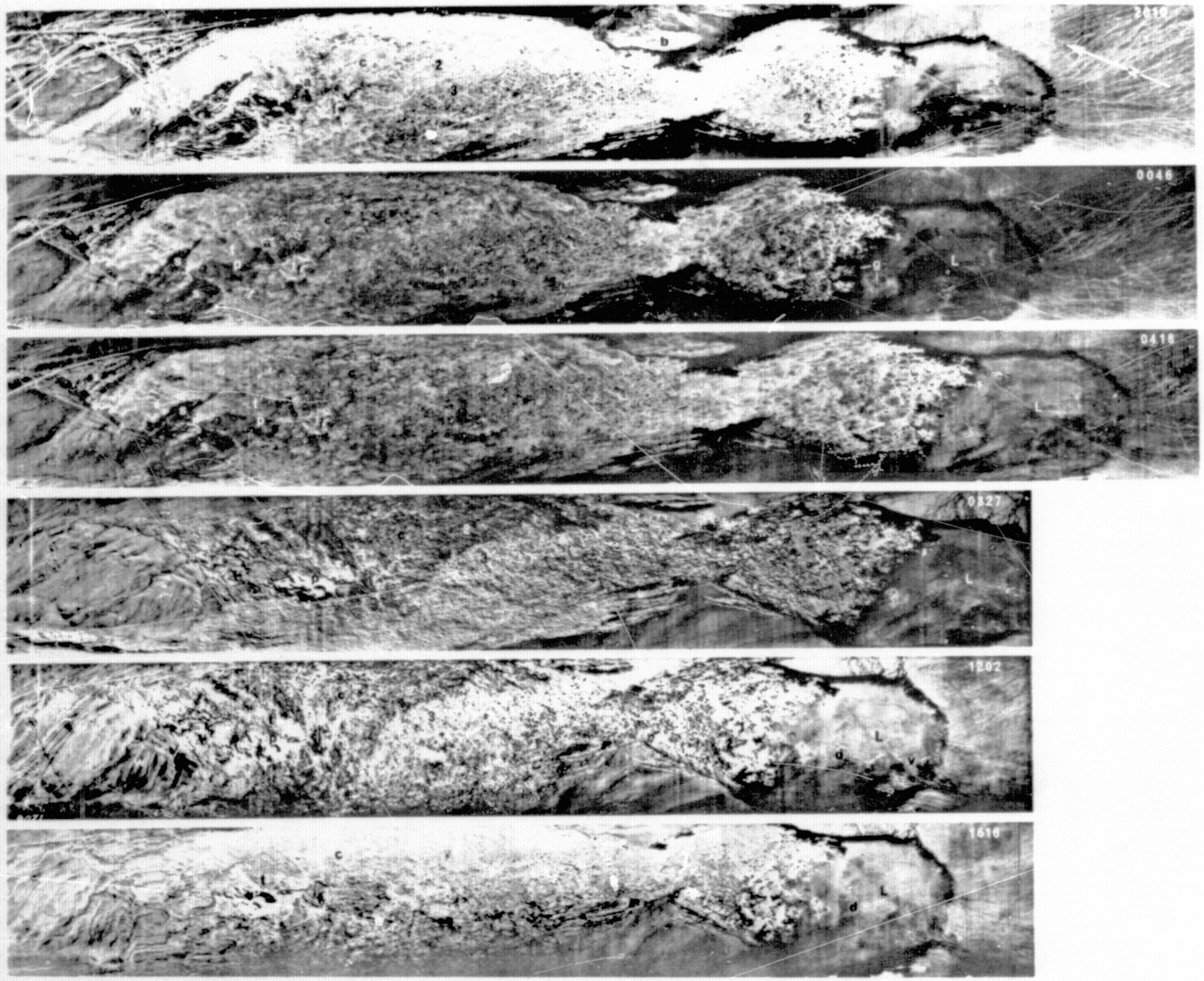

Figure 10-14.- Infrared images along flight line 1, showing changes in thermal response of rock materials throughout a diurnal cycle.

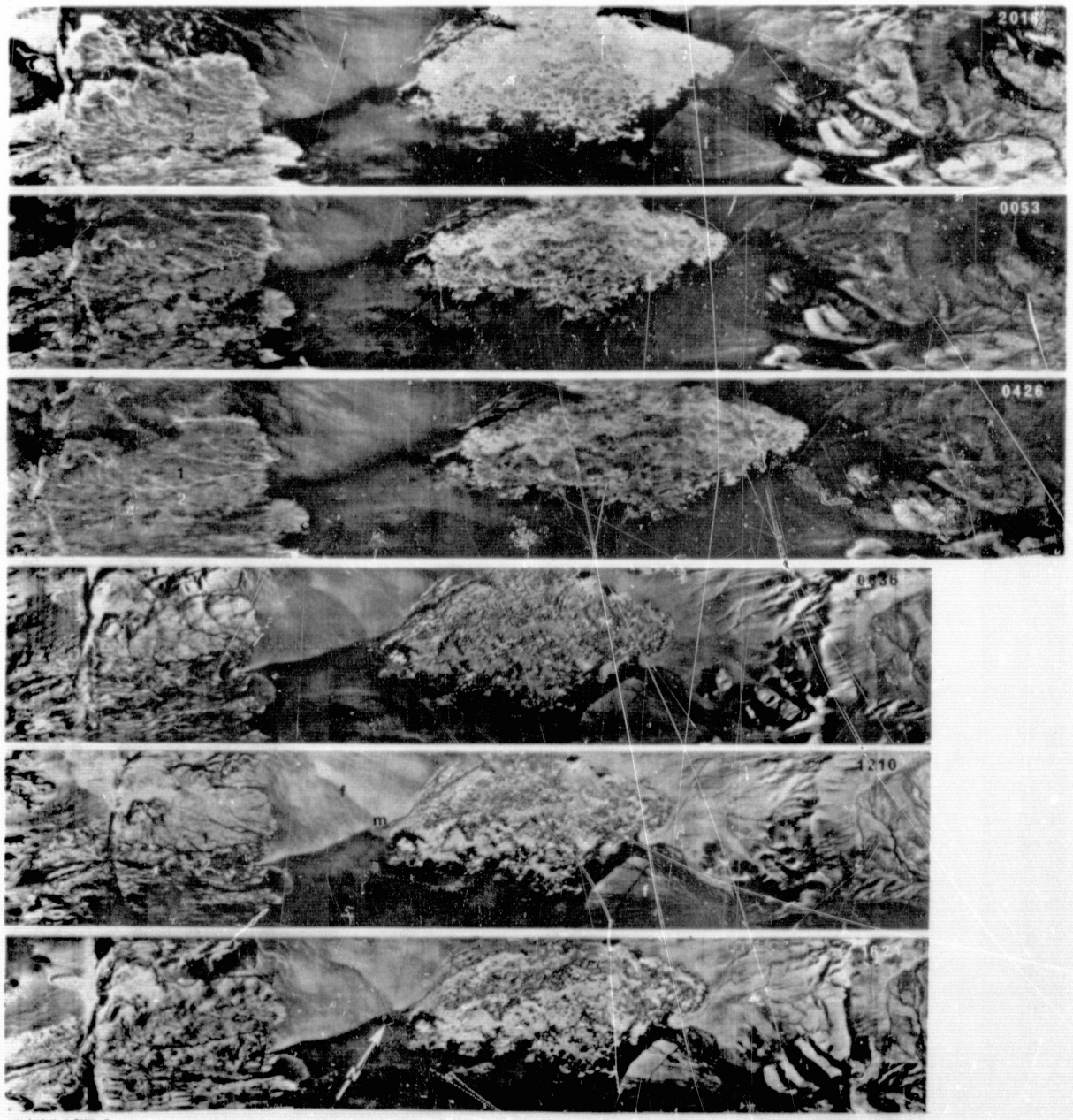

Figure 10-15.- Infrared images along flight line 2, showing changes in thermal response of rock materials throughout a diurnal cycle.

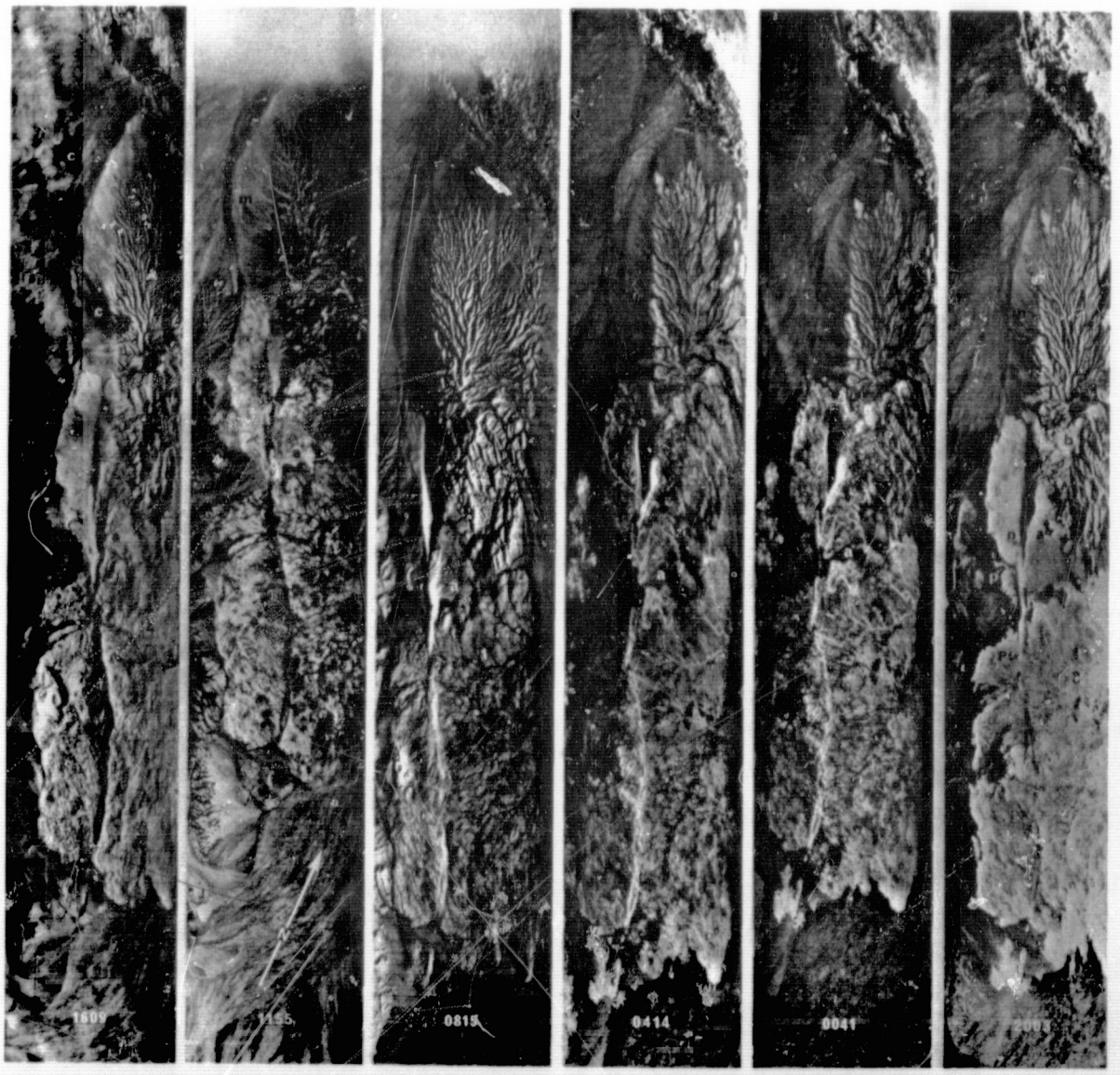

Figure 10-16.- Infrared images along flight line 3, showing changes in thermal response of rock materials throughout a diurnal cycle.

N71-16135

THERMAL ANOMALIES AND GEOLOGIC FEATURES OF THE MONO LAKE AREA, CALIFORNIA, AS REVEALED BY INFRARED IMAGERY

By Jules D. Friedman
U.S. Geological Survey, Washington, D.C.

ABSTRACT

The Mono Lake area, California, was selected for airborne infrared scanning radiometer experiments because of the exposure in this area of a variety of lithologies having different physical and thermal properties, as well as a diversity of textural and morphologic features. Infrared surveys were undertaken in 1965 and 1966 to measure variations in infrared emission from the surface in the 4.5μ to 5.5μ and 8μ to 14μ bands. Areal variations in emission from the surface were registered on film as differences in image tonal density. In addition, variations of surface radiant temperature with time during the diurnal cycle were recorded at several selected localities. The contrasting thermal patterns observed can be grouped as follows:

1. Thermal anomalies caused by convective heat loss detected when the temperature difference between the heat source and surrounding terrain was maximal, for example, hot springs and a warm effluent at Black Point

2. Daytime radiant-temperature differences resulting from variations in the incident radiant solar flux as a function of microrelief and morphology of the surface

3. Nighttime radiant-temperature differences resulting from contrasts in physical and thermal properties of various lithologic units and water expressed as different rates of change in emission, for example, among olivine basalt lapilli-ash beach deposits, lacustrine carbonate deposits, and water along the north shore of Mono Lake at Black Point

The detectability of the third group of thermal patterns in the Mono Lake area is of great experimental interest. Nighttime radiative heat loss is dependent upon the $(1 - r_o/\beta)$ ratio as a property of

materials, the total radiant energy incident on the surface during daytime J_o as a function of topography, and integrated emissivity ε as a function of surface roughness and blackbody cone effects (and, to a lesser extent, of composition).

INTRODUCTION

Infrared (IR) airborne surveys of the Mono Lake area were undertaken in 1965 and 1966 with a NASA Convair 240 airplane and a U.S. Geological Survey twin-engine Beechcraft airplane to study natural thermal anomalies related to structure and to analyze emittance characteristics of several lithologies as represented on IR imagery. Imagery taken in 1965, using a detector sensitive to radiation in the 4.5μ to 5.5μ wavelength band, is not analyzed in detail in the present report, but was used to plan the 1966 surveys. Variations in radiant emission from the terrestrial surface in the 8μ to 14μ wavelength interval were registered during a diurnal cycle as image tonal density differences on conventional photographic film by an airborne scanning radiometer on July 27 and 28, 1966. In addition to earlier overflights and several test runs, three north-south flight lines (fig. 11-1) with a total flight length of 54 miles were flown during a sequence of six surveys (table 11-I) during a 24-hour period in the Mono Lake area on July 26 to 28, 1966. Ground monitoring stations at Black Point, South Beach, Mono Lake, and Aeolian Buttes, by utilizing automatic-recording, variable-sequencer thermistor and IR radiometer systems, recorded ground-surface temperatures in a variety of materials simultaneously with overflights. This report is primarily a summary of the data obtained from the July 27 and 28, 1966, experiment. At an earlier stage in the project, a geologic map (fig. 11-2) was compiled at a scale of 1:31 680 on a rectified orthophotomosaic base to provide geologic control for location of ground monitoring stations, collection of samples, and interpretation of the IR imagery acquired.

This study was carried out with the support of the staff of the Infrared Laboratory, U.S. Geological Survey, under the supervision of Robert M. Moxham, and with the cooperation of pilots Raymond Rote and Howard Chapman, flying the U.S. Geological Survey, Water Resources Division, aircraft in which an IR scanning radiometer and supporting equipment were mounted. Charles R. Fross operated the scanning radiometer with the assistance of Robert M. Turner. Philip W. Philbin and George R. Boynton set up ground monitoring instruments, including an Eppley pyrheliometer, variable-sequencer thermistor systems, and Barnes IT-2 and IT-3 radiometers. Robert M. Turner processed the imagery. Joanne K. Oman and Philip W. Philbin operated the isodensitometer in the laboratory. David L. Daniels made laboratory emissivity determinations on rock samples

collected from the Mono Lake area, and Gordon W. Greene provided data on thermal parameters of many of these same rocks. Roger Bowen, Branch of Computations, Geological Survey, Menlo Park, programed the function given by Jaegar and Johnson for diurnal temperature variations. Alonzo E. Stoddard provided notes on IR radiation theory, emissivity, and absorptivity. G. G. Dalrymple, C. W. Chesterman, C. H. Gray, and Clyde Wahrhaftig contributed useful geologic information on the Mono Lake area; and David L. Daniels, Stephen J. Gawarecki, Gordon W. Greene, and R. J. P. Lyon accompanied the author in the field on several occasions. Stephen J. Gawarecki kindly made available several photographs of Paoha Island for use in this report.

The unusual variety of lithologic, volcanic, and tectonic features of Mono Lake basin, the locus of the most intense and complex volcanism of the Owens Valley region, influenced selection of the Mono Lake area for the IR survey experiment. Lithologies surveyed include late Pleistocene olivine-basalt pyroclastics of the sublacustrine Black Point volcano; recent andesite-basalt[1] volcanics and carapace of lacustrine deposits of Negit and Paoha Islands; the largely recent rhyolite-obsidian complex of brecciated youthful tholoids, coulees, and block craters; rhyolitic tephra rings, ramparts, and basin-floor layers of the main crater complex south of the lake; and the older Pleistocene Bishop tuff of Aeolian Buttes.

SYMBOLS

$B(\lambda,T)$ amount of energy radiated in all directions from a 1-cm^2 blackbody surface at temperature T per second and per unit wavelength interval

C specific heat, cal-gm-$^oC^{-1}$

F_o net radiant solar flux, measured as the diurnal maximum incident radiant flux J_o minus the reflected radiant flux R_o

F_o/β net radiant solar flux — thermal inertia ratio that controls the initial temperature rise of a point on the terrestrial surface (approximately proportional to the maximum-minimum amplitude of a diurnal surface-temperature curve)

---

[1]Petrographic studies by Kenneth LaJoie, University of California, Berkeley, reported since completion of this paper, indicate that the volcanics of Paoha and Negit Islands are of rhyodacitic composition.

I_{BB} intensity of radiation emitted by 1 cm^2 of a natural surface within a specific wavelength range, per second, at blackbody-equivalent temperature T

I_N radiation emitted by 1 cm^2 of a natural surface within a specific wavelength range, per second, at temperature T

J_o incident radiant flux at the terrestrial surface

k thermal conductivity, $cal\text{-}cm^{-1}\text{-}sec^{-1}\text{-}{}^{\circ}C^{-1}$

L latitude

N radiance, $W\text{-}cm^{-2}\text{-}ster^{-1}$

R_o reflected radiant solar flux

r_o total reflectivity of a surface for the incident radiation J_o; $r_o = R_o/J_o$; $(1 - r_o/\beta)$ = ratio of total absorptivity to thermal inertia of a specific material (characteristic of specific lithologies)

T temperature, °C or °K

T_{md} mean daily surface temperature of a specific point on the terrestrial surface

T_o surface temperature of a specific point on the terrestrial surface at a given instant in time

t time measured from local noon, equation (11-5)

V/H ratio of velocity of survey aircraft to altitude (V/H settings of scanning radiometer possibly cause of geometric distortion of IR imagery if aircraft velocity and film transport are improperly synchronized)

α thermal diffusivity, $cm^2\text{-}sec^{-1}$

β thermal inertia — the measure of the rate of heat transfer at the interface between two dissimilar media, $cal\text{-}cm^{-2}\text{-}{}^{\circ}C^{-1}\text{-}sec^{-1/2}$

γ	film emulsion density, as measured by a double-beam recording isodensitometer
$\nabla\gamma$	increment in film density — in a specific frame of IR imagery, a function of IR emission from the terrestrial surface
ε	integrated emissivity, the ratio I_N/I_{BB} determined in the laboratory for a flat surface for the 8μ to 14μ wavelength interval
ε_c	apparent emissivity dependent upon cavity shape
ε_λ	spectral emissivity
λ	wavelength, measured in microns in the IR region of the electromagnetic spectrum
ρ	bulk density, $gm\text{-}cm^{-3}$
δ	solar declination
ω	angular velocity of the earth, 7.27×10^{-5} $rad\text{-}sec^{-1}$

PREVIOUS INVESTIGATIONS

The Mono Lake/Mono Craters area has been studied extensively during the past 80 years, with attention focused primarily on the geology of the Mono Lake basin and the volcanic rhyolite-obsidian complex. For a list of selected reports on the geology of the area through 1965, see reference 11-1. The geologic map compilation prepared for reference 11-1 is a summation of much of the literature for the specific area of IR radiometry surveys reported in reference 11-1. The most recently published geologic map of a large part of the Mono Craters area is reference 11-2.

Previous studies of the Mono Craters area carried out by the Infrared Laboratory, U.S. Geological Survey, include reference 11-3, in which the spectral emittance of selected rock types from the Mono Craters area in the 8μ to 14μ wavelength band is reported. Daniels concluded that the emittance spectra of acidic igneous rocks of the area are very

similar, are recognizable in spite of their rough and weathered surfaces, but are different from the spectra of basaltic rocks from the area.[2]

OBJECTIVES

The purpose of the Mono Lake area IR imagery experiment reported in this document is to determine the degree to which it is possible to distinguish lithologic and other natural materials of different thermal properties or different emissivity ε by means of IR emission variations resulting from varying rates of cooling or warming at sunset and dawn. The IR emission variations are registered as tonal density differences on photographic film by an airborne scanning radiometer that senses radiation in the 8μ to 14μ wavelength band from the terrestrial surface.

PROCEDURES

Three north-south flight lines (fig. 11-1) were used to control the IR surveys made with a Reconofax IV scanner mounted in the U.S. Geological Survey twin-engine Beechcraft on July 27 and 28, 1966. Rotating high-intensity beacons marked the flight lines during night surveys. Several ground instrument-monitoring stations were set up along or close to the flight lines at geologic contacts between selected lithologic map units (table 11-I). The ground stations were designed to obtain observations on diurnal temperature variations of selected natural lithologic surfaces. The following two types of instrument systems were operated simultaneously with survey overflights: (1) Barnes IT-3 and IT-2 fixed-field radiometers, recording continuously on an Esterline-Angus strip-chart recorder, and (2) Sprinkle variable-sequencer thermistor-probe systems, recording on Esterline-Angus recorders. Other equipment included automatic-recording tempscribe thermographs and a recording Eppley pyrheliometer to determine variations in the incident radiant flux at the terrestrial surface,[3] recording thermographs for

---

[2]Recent work by R. J. P. Lyon, Stanford University, suggests that careful computer programing of the infrared emittance spectra of acidic igneous rocks of the Mono Lake area permits identification of several more rock types.

[3]The majority of the incident-radiant solar flux is recorded by the Eppley pyrheliometer. The transmission capability of the glass bulb is above 50 percent for wavelengths from 305 Å to 4.4μ and is above 90 percent for wavelengths between 360 Å and 2.6μ.

determining ambient temperature variations, and a velometer for near-surface wind variations. Diurnal surface-temperature curves were established from these ground measurements.

Infrared survey overflights were made at 4-hour intervals during a 24-hour cycle. Selected frames of IR imagery obtained by this method were scanned in the laboratory at magnifications of ×5 and ×10 by a double-beam recording isodensitometer to obtain color print-outs of film-emulsion density increments. These print-outs are roughly equivalent to form-line isoradiance maps with a variable contour interval. Density profiles were also obtained. A comparison between image tonal density differences and diurnal surface-temperature curves for various materials, established from ground observations (figs. 11-2 to 11-6), was the next step. Thermal properties and IR integrated-bandpass emissivity determinations on rocks of the Mono Lake area were compiled to aid in construction of theoretical diurnal surface-temperature curves, by using equations for a physical model. The theoretical warming and cooling curves obtained were compared with those obtained by ground observation to estimate the degree to which surface-temperature variations and IR emission variations are influenced by differences in the thermal inertia β of natural materials. Finally, anomalous thermal patterns recorded on the IR imagery, but not attributable to insolation variations or to thermal-parameter or emissivity differences of materials, were interpreted geologically.

ACCURACY OF SURFACE-TEMPERATURE MEASUREMENTS AT GROUND MONITORING STATIONS

1. Barnes IT-3 IR thermometer (fixed-field radiometer). The thermometer integrates temperatures over the entire area subtended by its optical system. Absolute accuracy is attainable within 1.2° C for a target of unity emissivity. Average emissivity of surfaces studied is 0.9±. An additional error of <1° C is inherent in the Esterline-Angus recording system.

2. Sprinkle variable-sequencer multiprobe thermistor system. The error is <1° C, but is subject to additional error of <1° C inherent in the Esterline-Angus recording system.

3. Tempscribe recording thermograph. The calibration error is <1° C, but additional error is introduced in positioning the needle arm.

GEOLOGY OF MONO LAKE AND CRATERS AREA

The volcanotectonic depression containing Mono Lake has been the locus of the greatest concentration of volcanic activity in the upper Owens Valley since the mid-Pliocene age. The oldest manifestations of volcanism in the area are the Tertiary volcanic rocks of the Bodie area north of Mono Lake. Rhyolitic ignimbrite of the Bishop tuff of Pleistocene age is exposed in the Aeolian Buttes area several miles south of the lake. The volcanotectonic basin has undergone continued subsidence throughout Quaternary time. It is bounded by near-vertical faults on the basis of recent geophysical studies (ref. 11-4) and probably contains about 300 cubic miles of Cenozoic sediments and volcanics to a depth of approximately 18 000 feet. Mono Lake itself presently occupies the lowest part of the basin. The surface of the remainder of the basin is underlain by lacustrine deposits covered in part by ashfall tephra deposits. Studies of the lake bottom topography (ref. 11-5) indicate that its eastern half is a smooth plain, but that the western half has two deep basins with irregular topography attributed to faulting, volcanism, glaciation and submarine slumping. Paoha and Negit Islands in Mono Lake are of volcanic origin and represent some of the most recent volcanic activity in the area. A gravity low with a Bouguer gravity value of approximately -260 milligals is centered on Paoha Island (ref. 11-4). Slump features in recent marl deposits exposed on Paoha Island may be the surface expression of sublacustrine uplift or volcanism. East of Negit Island is an archipelago of eight small islands composed of lacustrine sediments; some of these islands are diked and silled with andesitic lava (ref. 11-5). Black Point, on the northwest shore of Mono Lake, is an accumulation of almost flat-lying tephra resulting from a sublacustrine pyroclastic eruption (ref. 11-6) during the high stand of Mono Lake (= Tioga time?).

The Mono Crater rhyolite obsidian and pumice complex south of Mono Lake extends southward in a broad arc which is convex to the east. The Inyo Craters continue this volcanic lineament farther south. The main complex of the Mono Craters represents considerably more than 50 volcanic events, perhaps separated by only short intervals of time. Recent potassium-argon age determinations by Dalrymple (1967) suggest ages of 5000 to 6000 B.P. for much of the complex. The lack of lakeshore features on most landforms of the main complex also indicates a post-Tioga age for this multiple volcanic event. A possible exception is an older andesite crater remnant near the northwestern end of the chain which may have a wavecut bench on its western face. The pattern of evolution of individual volcanos within the complex is recognizable. Pyroclastic eruptions of rhyolitic pumice from a central crater formed tephra rings, ramparts, and cones. In most cases, these formations were followed by emergence of tholoids or endogenous domes, for example, North (Panum)

Crater where the tephra ring is still intact.[4] Elsewhere, as at North and South Coulees, the viscous rhyolite-obsidian flows overran the tephra rim, obliterating most of the initial-stage tephra features. In the northernmost rhyolite-obsidian coulee, and possibly elsewhere, a viscous second-stage tholoid emerged and expanded as a flow above the lower stage flow. Partially emergent tholoids, blowout craters, and rhyolite-block pyroclastic craters are also identifiable. At a late volcanic stage, very recent pyroclastic eruptions covered much of the volcanic complex and surrounding lacustrine plain with ashfall tephra.

LUNAR ANALOGS

Features of the area which might be regarded as analogous to certain features of the lunar surface include the subcircular volcanotectonic depression of the Mono Lake basin itself, small blowout craters throughout the area, circular tephra rims, and pumice plains of ashfall tephra. No proven examples of impact features are present.

GEOLOGIC FACTORS AFFECTING INFRARED IMAGE TONAL DENSITY

Radiative Heat Transfer

To analyze the geologic factors affecting image tonal density for the Mono Lake area (figs. 11-7 to 11-23) on July 27 and 28, 1966, we note that image tonal density obtained in the 8μ to 14μ wavelength region is related to electromagnetic emission from the terrestrial surface in such a way that image tonal density, as measured by a recording isodensitometer, is a nonlinear function of the blackbody-equivalent temperature of the surface (figs. 11-24 and 11-25; table 11-II), as modified by instrumental and photographic processing factors. Thus, IR image tonal density is largely controlled by those factors affecting the surface temperature of the image. Stated theoretically, I_N is the intensity of radiation emitted by 1 cm^2 of a natural surface within a specific wavelength range, per second, at temperature T. The following discussion demonstrates the role of emissivity ε of the natural surface in affecting I_N.

---

[4] Recent absolute age dating by Irving Friedman, U.S.G.S., suggests an age of less than 2000 years for this endogenous dome.

Radiation emitted in all directions by a blackbody within the wavelength interval λ_1 to λ_2, on the basis of Planck's law, is given by

$$I_{BB} = \int_{\lambda_1}^{\lambda_2} B(\lambda,T)d\lambda \qquad (11\text{-}1)$$

where $B(\lambda,T)$ is the amount of energy radiated from 1 cm^2 of a "black" surface at temperature T per second and per unit wavelength interval. Radiance N from a natural surface is modified by the spectral emissivity $\varepsilon(\lambda)$, as follows.

$$I_N = \int_{\lambda_1}^{\lambda_2} N(\lambda,T)d\lambda = \int_{\lambda_1}^{\lambda_2} \varepsilon(\lambda)B(\lambda,T)d\lambda \qquad (11\text{-}2)$$

If $\varepsilon(\lambda)$ is known in the wavelength interval λ_1 to λ_2, I_N may be calculated from equation (11-2). Alternatively, I_N and I_{BB} may be measured directly in the laboratory. Their relationship is then given in terms of the integrated bandpass emissivity ε, as follows.

$$I_N = I_{BB} = \varepsilon \int_{\lambda_1}^{\lambda_2} B(\lambda,T)d\lambda \qquad (11\text{-}3)$$

The relationship between spectral emissivity ε_λ (emittance in ref. 11-3) in the 8μ to 14μ wavelength region and integrated bandpass emissivity ε may be stated as follows.

$$\varepsilon = \frac{I_N}{I_{BB}} = \frac{\int_{8\mu}^{14\mu} \varepsilon(\lambda)B(\lambda,T)d\lambda}{\int_{8\mu}^{14\mu} B(\lambda,T)d\lambda} \qquad (11\text{-}4)$$

The ratio I_N/I_{BB} or ε, integrated bandpass emissivity, for the 8μ to 14μ wavelength region has been determined by Daniels (ref. 11-3) in the laboratory for representative lithologies of the Mono Lake area (table 11-III), using a Kern-Buettner-type emissivity box (ref. 11-7) and Barnes IT-3 IR thermometer. The results are reported in average digital values for the entire 8μ to 14μ band. Spectral emissivity (emittance) ε_λ for the 8μ to 14μ band was determined by Daniels (ref. 11-3) in the laboratory by comparison of continuous analog traces of the sample surface in contrast to a laboratory blackbody reference by means of a Black I-4T spectrometer (interferometer type). The results are reported in continuous analog curves giving emissivity variations over narrower spectral bands within the 8μ to 14μ wavelength region than is possible with the Kern-Buettner emissivity box method of determining ε. The following generalizations can be made from the results of these laboratory emissivity studies.

The emittance spectra of acidic igneous rocks of the Mono Lake area (rhyolite obsidian and pumice, rhyolitic ignimbrite of the Bishop tuff, and quartz monzonite) are very similar and are spectrometrically difficult to distinguish from one another. However, the spectra of acidic igneous rocks of the Mono Lake area do differ from the spectra of basalt. The spectra of weathered surfaces, in general, are still recognizable as the spectra of the underlying rock. The integrated emissivity ε determinations lead to a similar conclusion that the averaged emissivity over the 8μ to 14μ wavelength region is between 0.868 and 0.969 for these same rock types (table 11-III). The effect of topographic irregularities in enhancing the apparent emissivity beyond even these values and in causing apparent emissivity differences greater than 0.1 (fig. 11-26) is discussed in a later paragraph of this report.

Wide differences in IR emission from different materials were, however, recorded by the Reconofax IV scanner, suggesting that differences in surface temperature (figs. 11-24 and 11-25) are of considerable importance in affecting total emission and, consequently, image tonal density (table 11-II).

The following discussion demonstrates the significance of thermal properties β of rock and soil materials, of total reflectivity of the surface r_o, and of the diurnal maximum radiant flux J_o in controlling the temperature of the terrestrial surface.

The temperature of a specific point on the terrestrial surface varies in a periodic way with the diurnal cycle. The dependence of the diurnal variation upon properties of the terrestrial surface has been

calculated by Jaeger and Johnson (ref. 11-8), using a simplified model for the thermal flux across the surface. The result is given by

$$\theta_o = \frac{F_o}{\beta}\left[\frac{\cos\lambda\cos\delta}{\omega^{1/2}}\sum_{n=1}^{\infty}\frac{2(\sin nh\cos h - n\cos nh\sin h)}{\pi n^{3/2}\left(n^2-1\right)}\cos\left(n\omega t - \frac{\pi}{4}\right)\right]$$

$$= \frac{F_o}{\beta} f(L,\delta,\omega,t) \qquad (11\text{-}5)$$

where T_s = surface temperature

F_o = net radiant solar flux across the solid terrestrial surface, that is, the diurnal maximum radiant flux J_o incident upon the surface minus the reflected radiant flux R_o

β = thermal inertia

$\cos h = -\tan\lambda\tan\delta$

ω = angular velocity of the earth, 7.27×10^{-5} rad-sec^{-1}

δ = solar declination: 19.3° for July 27 and 28, 1966; 23.5° for summer solstice; 0.0° for autumnal equinox

L = latitude (38° N)

The function $f(L,\delta,\omega,t)$ is graphed for the summer solstice, the autumnal equinox, and July 27 and 28, 1966, at the latitude (38° N) of Paoha Island (fig. 11-27).

To compare these theoretical warming and cooling curves with surface-temperature records, a mean daily surface temperature for a given point must be introduced into the theoretical curves such that

$$T_s = T_{md} + \frac{F_o}{\beta} f(L,\delta,\omega,t) \qquad (11\text{-}6)$$

where T_{md} equals the mean daily surface temperature at a specific point. For the purpose of experimental comparison of theoretical diurnal temperature curves with recorded curves, the mean daily surface temperatures for two lithologies (lacustrine marl[5] (Qm) and basalt lapilli-ash beach deposits (QVb) at Black Point) have been assumed to be equal. A similar assumption has been made for two lithologies at Aeolian Buttes (Bishop tuff (Qbt) and quartz monzonite (Ka)).

Net radiant solar flux F_o in equation (11-5) is a measure of the peak thermal flux into the solid terrestrial surface. In terms of the peak radiant flux incident upon the surface J_o and the amount of flux which is reflected r_o, we have

$$F_o = J_o(1 - r_o) \tag{11-7}$$

The peak radiant flux J_o is given for the south beach of Mono Lake for July 27 and 28 (upper curve, Eppley pyrheliometer records, fig. 11-2). Total reflectivity r_o is dependent upon lithology and other factors and has been estimated from published absorption coefficients of solar radiation of various terrestrial materials and from recorded surface-temperature curves (table 11-IV). In terms of J_o and the estimated reflectivity r_o, the theoretical expression (eq. (11-5)) for the diurnal temperature variations becomes

$$T_o = \frac{J_o(1 - r_o)}{\beta} f(L,\delta,\omega,t) \tag{11-8}$$

In actuality, the recorded temperature curves for two lithologies at Black Point and two lithologies at Aeolian Buttes resemble the theoretical curves and have the expected differences in amplitude (figs. 11-28 to 11-31). The theoretical curves were constructed, using the best estimates and determinations for J_o, r_o (hence, F_o), and β. Thus, the recorded diurnal curves reasonably confirm that the F_o/β ratio does

---

[5]Reported by LaJoie to be highly diatomaceous.

indeed control the amplitude (table 11-IV) of the Black Point and Aeolian Buttes surface-temperature curves. Comparison of the Black Point and Aeolian Buttes theoretical curves with recorded temperature curves also significantly confirms the role of r_o in estimating F_o and J_o.

The mean daily surface temperatures T_{md} (eq. (11-6)) are assumed to be the same for the pairs of lithologies in the construction of figures 11-28 and 11-29. However, where r_o varies considerably, as at Black Point, this assumption yields theoretical curves which are too closely spaced in comparison to the recorded curves.

The recorded curve suggests a significantly lower mean daily surface temperature for marl (Qm) than for basalt lapilli-ash beach deposits (Qvb). This distinct surface-temperature difference between Qm and Qvb throughout much of the diurnal cycle gives rise to one of the most outstanding features of the imagery (fig. 11-7) and isodensitracer scans (figs. 11-2 to 11-7) derived from the imagery of Black Point, that is, the contrast between lacustrine carbonates and basalt pyroclastics.

A second point of difference is that the recorded surface temperatures between 10:00 p.m. and 7:00 a.m. (for Qm, Qvb, Ka, and Qbt) are higher than would be expected from the theoretical curves (figs. 11-30 and 11-31). An explanation of this disparity lies in the boundary condition at the surface that leads to equations (11-5) and (11-7). The loss of heat from the surface is assumed constant throughout the day in this calculation. A more realistic assumption is that the loss of heat from the surface is dependent upon temperature. As the temperature decreases during the night, the loss would also decrease, yielding a lowered nighttime cooling rate in accordance with the recorded temperature curves.

The denominator β in the F_o/β ratio, the thermal inertia characteristic of specific lithologies, is given by

$$\beta = \sqrt{k\rho C} \qquad (11\text{-}9)$$

where k = thermal conductivity, $cal\text{-}cm^{-1}\text{-}{}^{\circ}C^{-1}\text{-}sec^{-1}$

ρ = bulk density, $gm\text{-}cm^{-3}$

C = specific heat, $cal\text{-}gm^{-1}\text{-}{}^{\circ}C^{-1}$

and

$$k = \alpha C \rho \qquad (11\text{-}10)$$

where k equals the thermal diffusivity in $cm^2\text{-}sec^{-1}$. Thus, β is a measure of the rate of heat transfer at the interface between two dissimilar media. Literature data and U.S. Geological Survey laboratory determinations by Greene of thermal parameters of several lithologies sampled and imaged in the Mono Lake area are given in table 11-IV. A direct logarithmic relationship between k and ρ for certain rock types (e.g., basalt) has been suggested in reference 11-9.

From the foregoing discussion, it is suggested that low bulk densities and/or low total reflectivity yield high F_o/β ratios and high-amplitude surface-temperature curves. If IR image tonal density is a function of blackbody-equivalent temperatures of the surface, as suggested by analysis of isodensitracer scans of the Mono Lake imagery (figs. 11-2 to 11-24 and table 11-II), it may be concluded that lithologies of low bulk density and/or low total reflectivity will be registered on IR imagery, in contrast to lithologies of high bulk density and/or high total reflectivity if all other factors are equal. The contrast between lacustrine carbonates (Qm) and basalt pyroclastics (Qvb) of Black Point and Paoha Island represent wide differences in total reflectivity (table 11-IV). Moreover, differential solar heating of the terrestrial surface during daylight hours occurs across uneven topographic surfaces because J_o, the incident radiant flux on the surface, is dependent upon the inclination of the solar rays to the topographic surface. Such variations in J_o influence emission in the 8μ to 14μ interval, particularly during daylight hours, but also continue to affect 8μ to 14μ range emission to a lesser extent at night (figs. 11-10e and 11-10f), producing thermographic imagery of topography and microrelief. An extreme case occurs in which thermal shadows in early morning and late afternoon imagery enhance surface textures (figs. 11-7a, 11-8a, 11-9a, 11-10a, 11-11a, and 11-11b).

One additional type of radiative heat transfer to the atmosphere, dependent on topography, affected image tonal density during the July 27 and 28, 1966, survey period in the Mono Lake area. Apparent emissivity ε_c, which is dependent on surface roughness, is more effective in influencing emission than is ε, simply as a function of rock type (table 11-III). This is demonstrated by graphs of change in apparent emissivity ε_c as a function of cavity shape (fig. 11-26). A surface composed of rock of uniform emissivity ε may exhibit variations in

apparent emissivity ε_c as a result of topographic relief. Figure 11-26 shows the dependence of apparent emissivity on the dimensions of a cylindrical cavity, forming a depression in a surface of emissivity ε (ref. 11-10). Examples of situations intermediate between the latter two effects are common.

Radiative heat loss from the terrestrial surface in the Mono Lake area during the period July 27 and 28, 1966, was affected by the following interrelationship, which consists of four parameters characteristic of specific lithologies, a fifth parameter dependent on topography and microrelief, and a sixth parameter dependent on surface texture:

1. Thermal diffusivity α

2. Specific heat C

3. Bulk density ρ

4. Total reflectivity r_o

5. Total radiant energy incident on the surface J_o as a function of topography

6. Apparent emissivity ε_c as a function of surface roughness and blackbody cone effects

Convective Heat Transfer

Convective heat loss from fractures heated by the movement of epithermal solutions or gases, which has been detected on night and predawn imagery, provides a means for outlining the surface configuration and estimating the intensity of thermal anomalies associated with hot springs and fumaroles at Paoha Island (figs. 11-8a, 11-8d, 11-8e, and 11-8f) and Deschambeau Ranch at Black Point (figs. 11-7a, 11-7d, 11-7e, and 11-7f).

Hot spring activity in the Mono Basin, and specifically on Paoha Island, has long been known and was first reported by Russell in 1889 (ref. 11-11); the present status, distribution, and structural control of hot springs and fumaroles continues to be a subject of interest. A decline in the level of Mono Lake since 1955 made possible the detection of an array of distinct points of convective heat loss ringing the

southeastern peninsula of Paoha Island, where remnants of a recent andesite-basalt volcano are exposed through a carapace of lacustrine deposits (figs. 11-32, 11-33a, and 11-33b).

Surface temperature at the apertures of hot springs ranged up to 85° C at several points, based on measurement with a bimetallic thermometer on July 25, 1966. This thermal activity bears a superficial resemblance to thermal activity on several other active volcanic areas, including the classic andesite caldera of Santorin (Thíra) volcano in the Cyclades archipelago (fig. 11-32). Santorin is now known to have had two Krakatoan eruptions in 25 000 and 1400 B.C. More than 1000 years after the second eruption, Néa Kaïmeni, the Santorin analog of Paoha, emerged as a central island crater in the subsided caldera. Since then, recurrent volcanic activity has occurred in the area of Néa Kaïmeni. Recent Russian reports (ref. 11-12) indicate continued hot spring and fumarolic activity around the periphery of Néa Kaïmeni.

Other possibly analogous volcanotectonic depressions in the Philippines and Indonesia have similar morphology and distribution of thermal points around a resurgent central crater island which has been the locus of the most recent activity. The analogy should not be pressed too far, yet if the evidence of differential uplift involving deformation of the carapace of lacustrine deposits of Paoha (fig. 11-33c), the gravity low centered on the island (ref. 11-4), the volcanic morphology (fig. 11-33d) of Paoha (as well as of its neighbor Negit), and the greatest concentration of thermal points in Mono caldera around Paoha are considered, it seems likely that the Paoha-Negit Islands area was indeed the most recent locus of volcanism in the Mono Lake basin, that the fumaroles and hot springs may represent late-volcanic activity, and that Mono caldera as suggested by Pakiser and others (ref. 11-4) should indeed be regarded as one of the areas of active, albeit late-stage volcanism in the United States.

Other Anomalies

Two additional types of anomalies were noted on imagery of the Mono Lake area: The first type is associated with thermal currents in the Mono Lake, where hot springs discharge into effluent ponds at Black Point (figs. 11-7a, 11-7d, 11-7e, and 11-7f) and into Mono Lake from points along the north shore and peripheral to Paoha Island (figs. 11-8a, 11-8d, 11-8e, and 11-8f). The second type is negative daytime anomalies in saturated unconsolidated materials (e.g., a playa surface on Paoha Island (fig. 11-8d)) which suggest that evaporation and lateral heat-transfer change in specific small areas where a thermal near-equilibrium has been established.

SUMMARY

Field and laboratory studies of infrared imagery of the terrestrial surface of the Mono Lake area, California, during July 27 and 28, 1966, confirm that interplay between several physical and thermal parameters of surface materials controls radiant emission from the surface in the 8μ to 14μ wavelength interval. The following physical properties and processes, in addition to meteorologic factors, probably have the greatest influence.

1. Emissivity of the surface as a function of surface roughness and topographic blackbody cone effects and, to a considerably lesser extent, as a function of lithology

2. Radiative heat loss dependent on the following properties of the surface

   a. Thermal diffusivity α

   b. Specific heat C

   c. Bulk density ρ

   d. Total absorptivity $1 - r_o$, integrated over the entire solar spectrum

   e. Radiant flux intensity J_o as a function of inclination of solar rays to the topographic surface

3. Convective heat loss from the following

   a. Structures heated by circulating epithermal solutions

   b. Actual surface discharge of hot springs and fumaroles representing late-volcanic activity mostly on or near Paoha Island

   c. Thermal currents in Mono Lake associated with cold and hot spring discharge

4. Evaporative cooling and lateral heat transfer by conductive and convective mechanisms in saturated unconsolidated materials and by air movement or entrapment in and around talus slopes and surfaces having complicated microrelief

To determine the relative importance of these physical properties and heat-transfer processes, ground surface-temperature and radiant flux-intensity monitoring were found to be useful as meteorologic records. Field measurement of thermal parameters and total solar reflectivity should also be carried out in future surveys, preferably as part of the ground-monitoring procedures simultaneously with infrared imaging overflights. A sequence of overflights during the 24-hour diurnal cycle at Mono Lake provided data for diurnal surface-temperature curves. Construction of theoretical warming and cooling curves for the same surface materials permitted comparison with observations and estimation of either the thermal inertia β or total reflectivity r_o, where other parameters plus the radiant flux intensity J_o were known.

Comparison of recorded temperature curves with theoretical curves confirmed that the F_o/β ratio does indeed control amplitude of the surface-temperature curves and that this ratio is a function of the parameter $(1 - r_o)/\beta$, a characteristic property of specific lithologies. Comparison of image tonal densities by means of an isodensitometer scanning technique indicates that variations in amplitude (or variations in time rate of change) of diurnal temperature curves are detectable by means of IR imagery, provided radiant flux intensity is known, that meteorologic and hydrologic factors do not interfere, and that topography and microrelief are simple. Where topography, vegetation, saturation, and meteorologic factors do not affect the F_o/β ratios, many rock types having characteristic F_o/β ratios are distinguishable though not categorically identifiable. Because β generally increases with bulk density and because F_o is related to absorptivity $(1 - r_o)$ so that $T_o \sim f[J_o(1 - r_o)/\beta]$, lithologies of high density and/or high albedo contrast sharply with lithologies of low density and/or low albedo. Thus, with sufficient ground-monitoring data to support IR imagery surveys, the geologic contacts, if exposed, among bedrock and unconsolidated materials, among volcanic flows and low-density pyroclastics, and among iron-rich volcanic rocks and light-colored carbonates, and similar contrasting lithologies can be distinguished.

The best time of day in California in July and August for detection of thermal anomalies involving convective heat loss is 8:00 p.m. to 6:00 a.m. Maximum distinctions between surface materials, arising from differences in the F_o/β ratio, occur between 3:00 p.m. and 7:30 p.m., but thermographic effects from the surface mask these distinctions. The thermographic effects diminish after sunset faster than the decline in

emission related to the F_o/β ratio as a property of materials. The time between 8:00 to 10:00 p.m. is thus a good period for maximum distinction of lithologies, but a sequence of surveys from 8:00 p.m. to 4:00 a.m., showing different rates of cooling, is best for delineating lithologic units.

REFERENCES

11-1. Friedman, J. D.: Geologic Map of the Mono Craters Area, California. Tech. Letter NASA-12, Geological Survey for the National Aeronautics and Space Administration, 1967.

11-2. Kistler: Geological Map of the Mono Craters Quadrangle, Mono and Toulumne Counties, California. U.S. Geological Survey Geological Quadrangle Map CQ-462, 1966.

11-3. Daniels: Infrared Spectral Emittance of Rocks from the Pisgah Crater and Mono Craters Areas, California. U.S. Geological Survey Tech. Letter NASA-13, 1966.

11-4. Pakiser, L. C.; Press, F.; and Kane, M. F.: Geophysical Investigation of Mono Basin, California: Geol. Soc. Amer. Bull., vol. 71, no. 2, 1960, pp. 153-160.

11-5. Scholl, D. W.; von Huene, Roland; and St.-Amand, Pierre: Geology of Mono Lake. Geol. Soc. Sacramento, Guidebook along the East-Central Front of the Sierra Nevada, Ann. Field Trip, June 18-19, 1966.

11-6. Christensen, N. H.; and Gilbert, V. M.: Basaltic Cone Suggests Constructional Origin of Some Guyots. Science, vol. 143, no. 3603, 1964, pp. 240-243.

11-7. Buettner, K. J. K.; and Kern, C. D.: The Determination of Infrared Emissivities of Terrestrial Surfaces. Jour. Geophys. Res., vol. 70, no. 6, 1965, pp. 1329-1337.

11-8. Jaeger, J. C.; and Johnson, C. H.: Note On Diurnal Temperature Variation: Geofisica Pura e Applicata, vol. 24, Milano, 1953.

11-9. Robertson and Greene: Monthly Progress Reports, Branch of Theoretical Geophysics, U.S. Geological Survey, Dec. 1965 and Dec. 1966.

11-10. Gouffé, Andre: Corrections D'ouverture des Corpsnoirs Artificiels Compte Tenu des Diffusions Multiples Internes: Rev. 'Optique, 24, no. 1-3, 1945, pp. 1-10.

11-11. Russell, Issac: Quaternary History of Mono Valley, California. U.S. Geol. Survey, 8th Ann. Rept., 1887-1889, pt. 1, 1889, pp. 261-394.

11-12. Butuzova, G. Yu.: Iron-ore Sediments of the Fumarole Field of Santorin Volcano, Their Composition and Origin. Doklady Akademii Nauk SSSR, vol. 168, no. 6, 1966, pp. 1400-1404.

BIBLIOGRAPHY

Brunt, D., 1932, Quart. Jour. Royal Met. Soc., 58, 389.

Carslaw, H. S.; and Jaeger, J. C.: Conduction of Heat in Solids. Oxford, Clarendon Press, 2 ed., SIOP, 1959.

TABLE 11-I.- TIME RATE OF CHANGE OF IMAGE TONAL DENSITY DURING DIURNAL CYCLE, MONO CRATERS AREA, JULY 27 AND 28, 1966

Ground instrument station	Flight-line number	Geologic map units	Observations (a)	Instruments	Figure number (this report)
Number 1 Wilson Creek Delta, Black Point	1	Qrb Qb (=Qal + Qm)	Diurnal surface-temperature variations (contact temperature)	Multiple thermistor-probe variable sequencer (Sprinkle)	11-14
Number 1A Thermal Ponds, Black Point	1	- -	Thermal spring and effluent temperature	Tempscribe	-
Number 2, Aeolian Buttes	1	Ka Qbt Surficial pumice tephra	Diurnal radiometric surface-temperature variations	IT-2 IT-3 Barnes IR thermometers	11-15
Number 3 South Beach, Mono Lake	2	Qb (includes pumice and sand)	Diurnal surface-temperature variations Diurnal temperature variations at depth (contact temperature)	Multiple thermistor-probe variable sequencer (Sprinkle)	11-17
Mono Lake surface	2	- -	Correct surface temperature (contact temperature)	Tempscribe	11-18
Number 4 East Pumice Sand Flat	3	QpA (includes pumice and sand)	Solar flux density (diurnal variations)	Eppley pyrheliometer	11-14
Airborne radiometry	2	Mono Lake	Radiometric surface temperature of Mono Lake	IT-3 Barnes IR thermometer	11-18

[a]Observers — S. J. Gawarecki, George Boynton, Philip Philbin, J. D. Friedman.

TABLE 11-II.- INFRARED FLIGHT LOG DATA, MONO CRATERS AREA, JULY 27 AND 28, 1966[a]

Run	Mark	Heading	Line number	Time		Filter, 8μ to 14μ	AGC	Altitude (msl)	Remarks
				On	Off				
July 27: take-off, 07:25; landing, 09:24; pilot, Chapman; copilot, Simpson; IR crew, Fross/Turner									
1	5	N	1	- -	- -	x	Minimum	10.5M	
2	4	S	1	07:58	08:05	x	Minimum	10.5M	
3	3	N	2	08:11	08:18	x	Minimum	10.5M	
4	2	S	3	08:22	08:29	x	Minimum	10.5M	Dry sun
5	5	N	1	08:33	08:38	x	Minimum	10.5M	
6	4	S	2	08:40	08:48	x	Minimum	10.5M	
7	3	N	3	08:50	08:57	x	Minimum	10.5M	
July 27: take-off, 11:28; landing, 13:22; pilot, Chapman; copilot, Simpson; IR crew, Fross/Turner									
1	5	S	1	11:57	12:04	x	Minimum	10.5M	Signal excessive; reduced bias five complete turns; improvement but still bottoming. Scope shows some noise in water, weather clear, air rough, some clouds over lake.
2	4	N	2	12:07	12:15	x	Minimum	10.5M	
3	3	S	3	12:17	12:25	x	Minimum	10.5M	
4	2	N	1	12:28	12:34	x	Minimum	10.5M	
5	5	S	2	12:36	12:44	x	Minimum	10.5M	
6	4	N	3	12:46	12:53	x	Minimum	10.5M	
	3					- -	- -	- -	Finish - printed - warmup
July 27: take-off, 15:30; landing, 17:22; pilot, Chapman; copilot, Simpson; IR crew, Fross/Turner									
1	5	S	1	16:03	16:10	x	Minimum	10.5M	
2	4	N	2	16:12	16:19	x	Minimum	10.5M	Signal excessive; reduced bias; still bottoming. Light clouds over lake, clear visibility, a rough ride.
3	3	S	3	16:20	16:29	x	Minimum	10.5M	
4	2	N	1	16:31	16:38	x	Minimum	10.5M	
5	5	S	2	16:41	16:46	x	Minimum	10.5M	
6	4	N	3	16:47	16:55	x	Minimum	10.5M	
	3								Finish and warmup

[a]Bishop, California; Reconofax IV scanner.

TABLE 11-II.- INFRARED FLIGHT LOG DATA, MONO CRATERS AREA, JULY 27 AND 28, 1966[a] - Concluded

Run	Mark	Heading	Line number	Time		Filter, 8μ to 14μ	AGC	Altitude (msl)	Remarks
				On	Off				
July 27: take-off, 09:36; landing, unrecorded; pilot, Rote; copilot, Hegel; IR crew, Fross/Turner									
1	5	N	1	20:03	20:08	x	3	10.5M	
2	4	S	2	20:10	20:17	x	3	10.5M	
3	3	N	3	- -	20:27	x	3	10.5M	
4	2	S	1	20:29	20:36	x	3	10.5M	AGC/3/bias, 2
5	5	N	2	20:38	20:45	x	3	10.5M	
6	4	S	3	20:46	20:53	x	3	10.5M	
	3								Finish - printed - warmup
July 27: take-off, 23:37; landing, unrecorded; pilot, Rote; copilot, Hegel; IR crew, Fross									
1	5	N	1	23:59	00:05	x	3	10.5M	
2	4	S	2	00:07	00:14	x	3	10.5M	
3	3	N	3	00:15	00:23	x	3	10.5M	
4	2	S	1	00:25	00:31	x	3	10.5M	
5	5	N	2	00:33	00:40	x	3	10.5M	
6	4	S	3	00:42	00:48	x	3	10.5M	
	3								Finish - printed - warmup
July 28: take-off, 03:38; landing, unrecorded; pilot, Rote; copilot, Hegel; IR crew, Fross									
1	5	N	1	04:00	04:05	x	4	10.5M	
2	4	S	2	04:07	04:14	x	4	10.5M	
3	3	N	3	04:15	04:22	x	4	10.5M	
4	2	S	1	04:25	04:30	x	4	10.5M	
5	5	N	2	04:35	04:43	x	4	10.5M	
6	4	S	3	04:44	04:50	x	4	10.5M	
	3								Finish - printed - warmup

[a]Bishop, California; Reconofax IV scanner.

TABLE 11-III.- INTEGRATED 8μ TO 14μ EMISSIVITIES OF ROCKS FROM MONO CRATERS AREA[a]

$$\left[\varepsilon = \frac{I_N}{I_{BB}} = \frac{\int_{8\mu}^{14\mu} \varepsilon(\lambda)B(\lambda,T)d\lambda}{\int_{8\mu}^{14\mu} B(\lambda,T)d\lambda}\right]$$

Field number	Unit	Rock description	Location	1	2	3	4	Average
G-66-11	Qvb	Basaltic lapilli with lacustrine silt; unconsolidated	Delta Channel, Black Point	0.986	0.982	0.986	0.984	0.985
SF-66-18	Qm	Lacustrine silt encrusted with evaporite salts; playa in crater	South Crater on Paoha Island	.973	.977	.978	.974	.976
G-66-12	Qal	Fragile crust of basaltic sand and lacustrine silt; unconsolidated deposit	Delta Channel, Black Point	.976	.972	.972	.976	.974
328	Qjlb	Red, oxidized, basalt cinder; from rim of low splatter cones; June Lake Basalt unit	1 mile NE June Lake Junction	.967	.974	.973	.976	.973
F-66-13	Qm	Unconsolidated marl; fragile crust of lacustrine silt	SE Paoha Island	.967	.972	.972	.970	.970
F-66-16	Qb	Fragile, calcareous, crust of lacustrine silt; unconsolidated beach deposit	Black Point (station 1)	.968	.969	.975	.968	.970
G-66-4B	Qbt	Bishop tuff, uppermost unit; tan, crystal lithic rhyolite tuff, surface rough, moderate weathering	Aeolian Buttes	.963	.984	.966	.964	.969
339	Qyrp	Rhyolitic lapilli; rhyolite pumice and obsidian fragments and assorted basement rocks; from pyroclastic rim	East rim of crater, 9138 ft	.968	.967	.971	.968	.969
F-66-14A	Qm	Fragile crust of lacustrine silt and basaltic pyroclastics; unconsolidated	NE Paoha Island	.968	.962	.965	.969	.968

[a]Kern-Buettner-style "Emissivity Box" — Barnes IT-3 IR thermometer (measurements made at Infrared Laboratory, U.S.G.S., Arlington, Virginia, by David L. Daniels).

TABLE 11-III.- INTEGRATED 8μ TO 14μ EMISSIVITIES OF ROCKS FROM MONO CRATERS AREA[a] - Continued

$$\left[\varepsilon = \frac{I_N}{I_{BB}} = \frac{\int_{8\mu}^{14\mu} \varepsilon(\lambda)B(\lambda,T)d\lambda}{\int_{8\mu}^{14\mu} B(\lambda,T)d\lambda}\right]$$

Field number	Unit	Rock description	Location	1	2	3	4	Average
338	Qyrc	Rhyolite pumice; low-density pumice with large vesicles and dark-colored glass	South Coulee	0.959	0.981	0.959	0.966	0.966
SF-66-19	QpA	Sand flat unconsolidated pyroclastics; rhyolite lapilli; ash deposit	East craters sand flat	.969	.968	.961	.962	.965
S-66-5	Qb	Calcareous lake deposit; white carbonate coating on cemented rhyolite beach sand	South shore beach of Mono Lake	.964	.966	.962	.966	.965
F-66-3	Qbt	Bishop tuff; upper unit; tan, crystal-lithic rhyolite tuff; rough, heavily weathered	1 mile SE of Aeolian Buttes	.960	.962	.960	.960	.961
340	Qyrp	Rhyolite lapilli; rhyolite pumice and obsidian with basement rocks; same as number 339 except higher obsidian content	East rim of crater, 9138 ft	.958	.953	.963	.961	.959
335	Qb	Rhyolite beach sand; sorted rhyolitic glass fragments	Beach-South shore Mono Lake	.954	.961	.964	.958	.958
F-66-17	Qb	Fragile crust of lacustrine silt; unconsolidated beach deposit	Black Point (station 1)	.959	.957	.958	.953	.957
F-66-14B	Qm	Greenish tuffaceous sandstone	Eastern Paoha Island	.952	.957	.954	.954	.954

[a]Kern-Buettner-style "Emissivity Box" — Barnes IT-3 IR thermometer (measurements made at Infrared Laboratory, U.S.G.S., Arlington, Virginia, by David L. Daniels).

TABLE 11-III.- INTEGRATED 8μ TO 14μ EMISSIVITIES OF ROCKS FROM MONO CRATERS AREA[a] - Continued

$$\left[\varepsilon = \frac{I_N}{I_{BB}} = \frac{\int_{8\mu}^{14\mu} \varepsilon(\lambda)B(\lambda,T)d\lambda}{\int_{8\mu}^{14\mu} B(\lambda,T)d\lambda}\right]$$

Field number	Unit	Rock description	Location	1	2	3	4	Average
X-66-1	Qyrc	Rhyolite; medium density; surface flat, smooth, lightly weathered	South side North Crater	0.953	0.948	0.949	0.953	0.951
F-66-7	Qjlb	Olivine basalt; abundant plagioclase phenocrysts; red-black, dull, rough, weathered surface	1 mile NW of June Lake Junction	.948	.950	.952	.955	.951
F-66-1	Qbt	Bishop tuff; upper unit; tan-violet, crystal lithic rhyolite tuff; rough, light weathering	1/2 mile NW of Aeolian Buttes	.945	.949	.953	.951	.950
F-66-4	Qbt	Bishop tuff; lower welded unit; dense, tan, crystal-lithic, rhyolite tuff; rough, heavily weathered	1 mile south of Aeolian Buttes	.946	.946	.946	.950	.947
S-66-6	Qm	Greenish tuffaceous sandstone	East side Paoha Island	.943	.943	.938	.947	.943
F-66-9	Qor	Rhyolite; vitrophyric (feldspar phenocrysts) gray-brown, heavily weathered surface	2000 ft NE of Punch Bowl	.953	.938	.943	.944	.943
F-66-8	Qor	Rhyolite; vitrophyric (abundant 1/8-inch feldspar phenocrysts); gray-brown, moderate weathering	2000 ft NE of Punch Bowl	.940	.942	.942	.942	.942
F-66-15	QpvA	Basalt; fine-grained, finely vesicular; black, fairly fresh surface	NE quarter Paoha Island	.938	.939	.959	.932	.942

[a]Kern-Buettner-style "Emissivity Box" — Barnes IT-3 IR thermometer (measurements made at Infrared Laboratory, U.S.G.S., Arlington, Virginia, by David L. Daniels).

TABLE 11-III.- INTEGRATED 8μ TO 14μ EMISSIVITIES OF ROCKS FROM MONO CRATERS AREA[a] - Continued

$$\left[\varepsilon = \frac{I_N}{I_{BB}} = \frac{\int_{8\mu}^{14\mu} \varepsilon(\lambda)B(\lambda,T)d\lambda}{\int_{8\mu}^{14\mu} B(\lambda,T)d\lambda}\right]$$

Field number	Unit	Rock description	Location	1	2	3	4	Average
S-66-3B	Qam	Andesite; large plagioclase phenocrysts, lithic inclusions, layered fine-grained ground mass; dull surface	2 miles NW of Crater Mountain	0.936	0.942	0.940	0.949	0.942
S-66-1B	Qyrc	Rhyolite; medium density; surface flat, rough, moderate weathering	South side North Crater	.939	.938	.938	.940	.939
F-66-5	Qjlb	Olivine basalt; abundant plagioclase phenocrysts, rough, dull-black surface	1 mile NW of June Lake Junction	.940	.938	.940	.935	.938
S-66-1A	Qyrc	Rhyolite; dense flow material; surface flat, rough, dark weathering	South side North Crater	.939	.944	.930	.934	.937
S-66-3A	Qam	Andesite; plagioclase phenocrysts; lithic inclusions, layered fine-grained ground mass; smooth surface coating	2 miles NW of Crater Mountain	.929	.936	.935	.947	.937
G-66-15	Qrb	Rhyolite pumice; finely vesicular, medium density, blocky ejecta; flat, rough, weathered surface	Satellite cone, 1 mile SE of North Crater	.933	.934	.936	.934	.934
333	Ka	Medium-grained, biotite quartz monzonite	Aeolian Buttes	.931	.928	.933	.932	.931
F-66-11	Qjlb	Olivine basalt; abundant plagioclase phenocrysts, rough, black, dull glossy surface	1 mile NW June Lake Junction	.926	.926	.933	.927	.928

[a]Kern-Buettner-style "Emissivity Box" — Barnes IT-3 IR thermometer (measurements made at Infrared Laboratory, U.S.G.S., Arlington, Virginia, by David L. Daniels).

TABLE 11-III.- INTEGRATED 8μ TO 14μ EMISSIVITIES OF ROCKS FROM MONO CRATERS AREA[a] - Concluded

$$\left[\varepsilon = \frac{I_N}{I_{BB}} = \frac{\int_{8\mu}^{14\mu} \varepsilon(\lambda)B(\lambda,T)d\lambda}{\int_{8\mu}^{14\mu} B(\lambda,T)d\lambda}\right]$$

Field number	Unit	Rock description	Location	1	2	3	4	Average
G-66-27A	Qyrc	Rhyolite; dense, grades into obsidian; flat smooth surface, relatively unweathered	North Coulee	0.902	0.913	0.927	0.913	0.914
S-66-3C	Qam	Andesite; large plagioclase phenocrysts, lithic inclusions, aphanitic ground mass; gray, dull, glossy surface	2 miles NW of Crater Mountain	.916	.920	.895	.918	.912
G-66-2C	Qyrt	Dark rhyolitic obsidian; dull, frosted fracture surface	Talus slope North Crater	.891	.890	.900	.904	.896
G-66-2A	Qyrt	Gray-black rhyolite obsidian; smooth, glassy fracture surface	Talus slope North Crater	.868	.867	.870	.871	.869
G-66-2B	Qyrt	Gray-black rhyolite obsidian; smooth, glassy fracture surface	Talus slope North Crater	.864	.868	.870	.870	.868

[a]Kern-Buettner-style "Emissivity Box" — Barnes IT-3 IR thermometer (measurements made at Infrared Laboratory, U.S.G.S., Arlington, Virginia, by David L. Daniels).

TABLE 11-IV.- RELATIONSHIP BETWEEN AMPLITUDE OF DIURNAL SURFACE-TEMPERATURE CURVES AND THERMAL PARAMETERS FOR SELECTED LITHOLOGIES OF THE MONO LAKE AREA, JULY 27 AND 28, 1966

Lithology	Amplitude of diurnal surface temperature curve, °C (a)	F_o/β (b)	Net radiant solar flux, $F_o = J_o(1 - r_o)$ (c)	Incident radiant flux, J_o (d)	Total reflectivity expressed in terms of absorption of solar radiation, $1 - r_o$ (e)	Thermal inertia ($\beta = \sqrt{k\rho C}$), cgs units	Thermal conductivity, k	Bulk density, ρ	Thermal diffusivity, α	Specific heat, C	Integrated emissivity, $\varepsilon\lambda$, 8μ - 14μ
Qvb, basalt, lapilli ash of Black Point	57 ± 2	0.462	0.017	0.0250	0.75	[f]0.037	[h]0.004	[h]1.9	[h]0.011	[h]0.2	0.985 ± 0.003
QpA, Qb, rhyolite pumiceous sand of South Beach and pumice sand flats	51 ± 1	0.439	0.004	0.0250	0.2	[g]0.009	[i]0.0006	[i]1.0	[i]0.004	[i]0.16	0.958 ± 0.006
Qbt, Bishop tuff (upper unit) of Aeolian Buttes	50 ± 2	0.375	0.015	0.0250	0.6	[g]0.040	[i]0.0028	[i]1.8	[illegible].0086	[i]0.18	0.947 ± 0.003
Qal, silty playa crust and deltaic deposits of Black Point	48 ± 1	0.427	0.010	0.0250	0.4	[g]0.024	[i]0.0014	[i]1.8	[i]0.003	[i]0.24	0.957 ± 0.004
Qm, lacustrine carbonate crust of Black Point	47 ± 2	0.423	0.005	0.0250	0.2	[f]0.012	[h]0.0011	[h]1.8	[i]0.003	[h]0.2	0.974 ± 0.002

[a] From recorded surface-temperature curves.

[b] Calculated from $T_o = T_{md} + F_o f$

[c] Calculated from $F_o = J_o (1 - r_o)$.

[d] From recorded Eppley pyrheliometer curve.

[e] Estimated from diurnal temperature curve.

[f] Estimated from diurnal temperature curves.

[g] Approximately equal to U.S.G.S. laboratory determinations by data cited in Clark, S. J., 1966, Handbook of Geophysical Constants.

[h] Estimated.

[i] Laboratory determinations.

TABLE 11-IV.- RELATIONSHIP BETWEEN AMPLITUDE OF DIURNAL SURFACE-TEMPERATURE CURVES AND THERMAL PARAMETERS FOR SELECTED LITHOLOGIES OF THE MONO LAKE AREA, JULY 27 AND 28, 1966 - Concluded

Lithology	Amplitude of diurnal surface temperature curve, °C (a)	F_o/β (b)	Net radiant solar flux, $F_o = J_o(1 - r_o)$ (c)	Incident radiant flux, J_o (d)	Total reflectivity expressed in terms of absorption of solar radiation, $1 - r_o$ (e)	Thermal inertia ($\beta = \sqrt{k\rho C}$), cgs units	Thermal conductivity, k	Bulk density, ρ	Thermal diffusivity, α	Specific heat, C	Integrated emissivity, $\varepsilon\lambda$, 8μ - 14μ
Qb, lacustrine carbonate cementing pebbles of South Beach	36 ± 1	0.263	0.010	0.0250	0.4	[f]0.038	[h]0.004	[h]2.0	[h]0.011	[h]0.18	0.965 ± 0.003
Ka, quartz monzonite of Aeolian Buttes	28 ± 2	0.250	0.015	0.0250	0.6	[g]0.060	[i]0.0075	[i]2.8	[i]0.017	[i]0.16	0.931 ± 0.003

[a] From recorded surface-temperature curves.

[b] Calculated from $T_o = T_{md} + F_o f$.

[c] Calculated from $F_o = J_o (1 - r_o)$.

[d] From recorded Eppley pyrheliometer curve.

[e] Estimated from diurnal temperature curve.

[f] Estimated from diurnal temperature curves.

[g] Approximately equal to U.S.G.S. laboratory determinations by data cited in Clark, S. J., 1966, Handbook of Geophysical Constants.

[h] Estimated.

[i] Laboratory determinations.

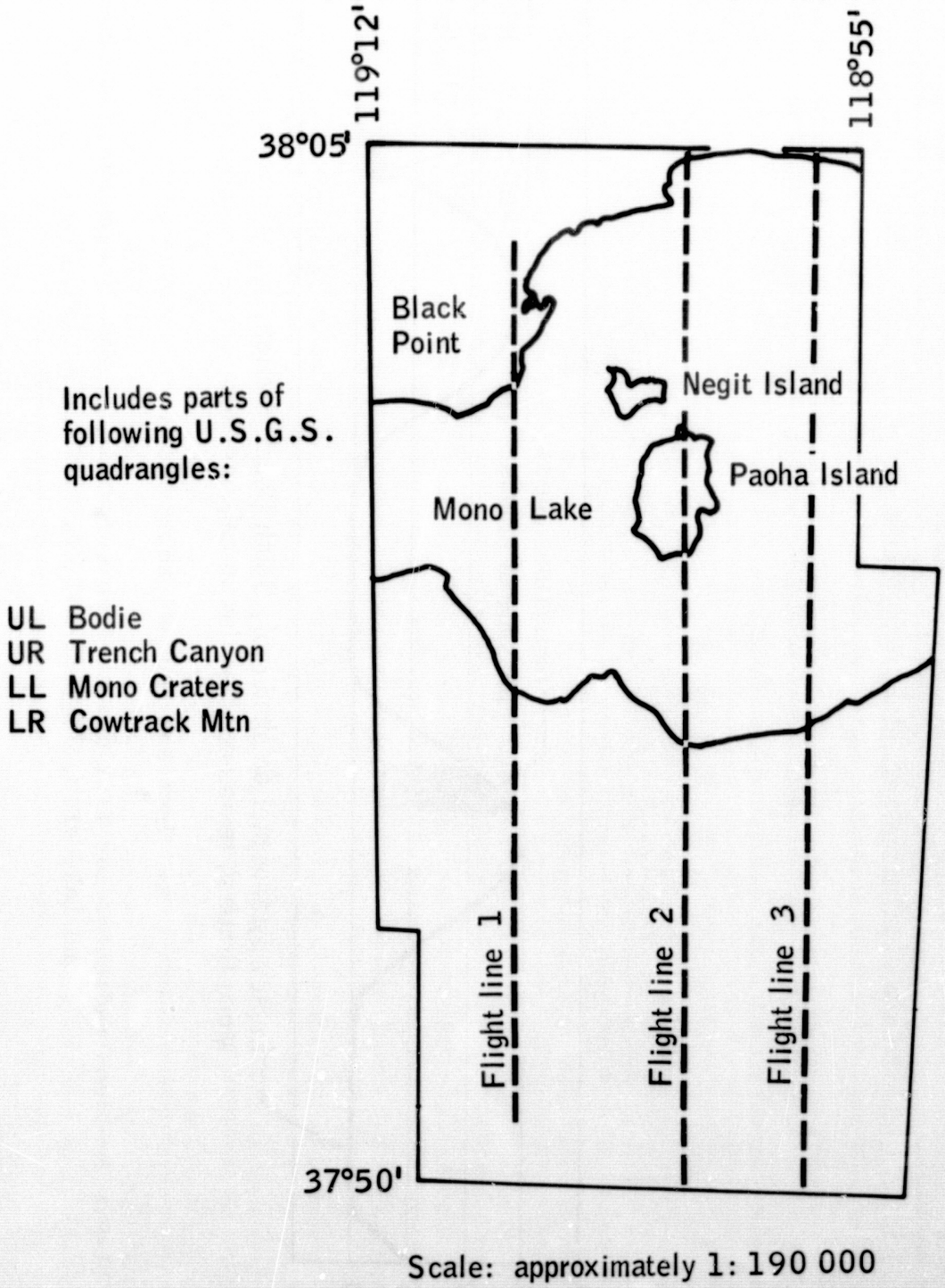

Figure 11-1.- Flight lines, IR imagery surveys, July 27 and 28, 1966, Mono Craters area, California.

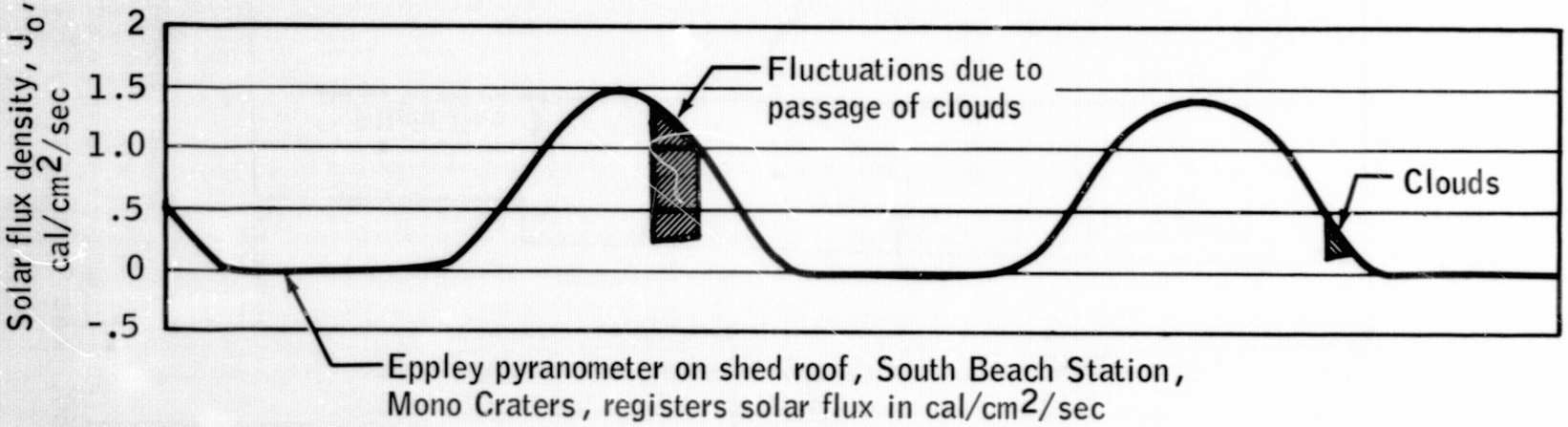

a. Incident radiant solar flux.

Figure 11-2.- Incident radiant solar flux and surface temperature, Mono Instrument Stations, Mono Lake area, July 27 and 28, 1966.

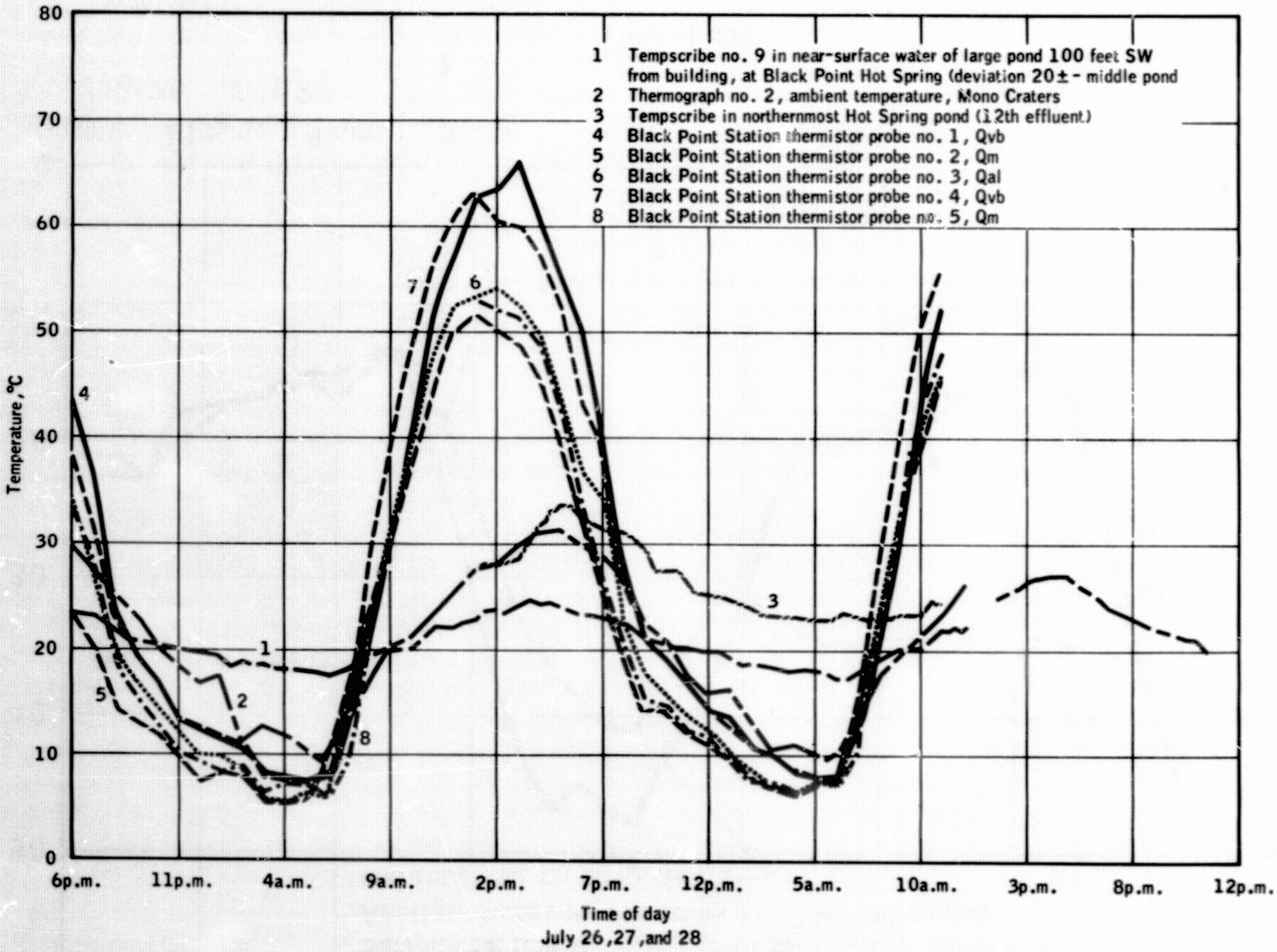

b. Surface temperature.

Figure 11-2.- Concluded.

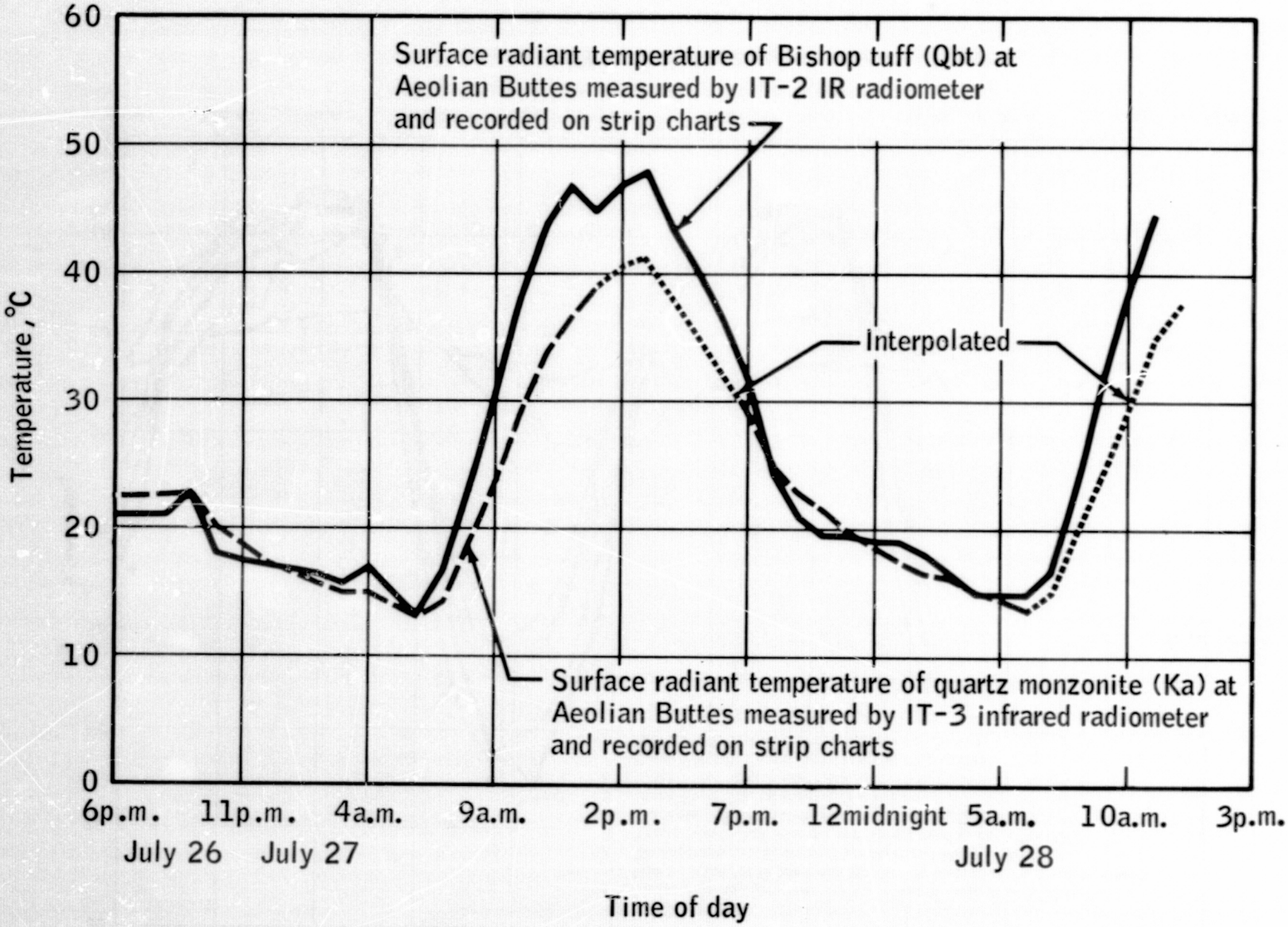

Figure 11-3.- Surface radiant temperatures, Aeolian Buttes, Mono Lake area, July 27 and 28, 1966.

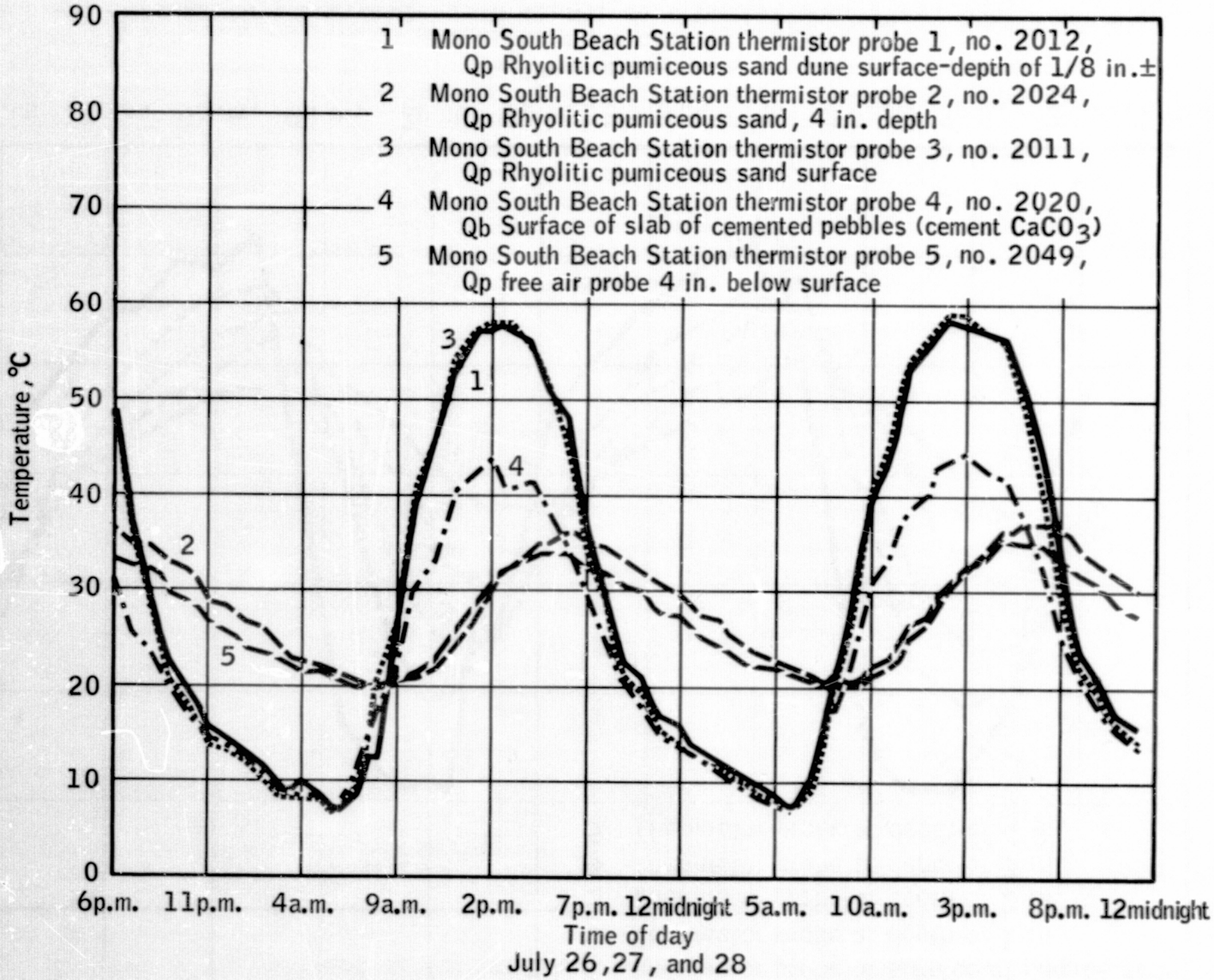

Figure 11-4.- Surface and near-surface temperatures determined by thermistor probe, Mono South Beach station, July 27 and 28, 1966.

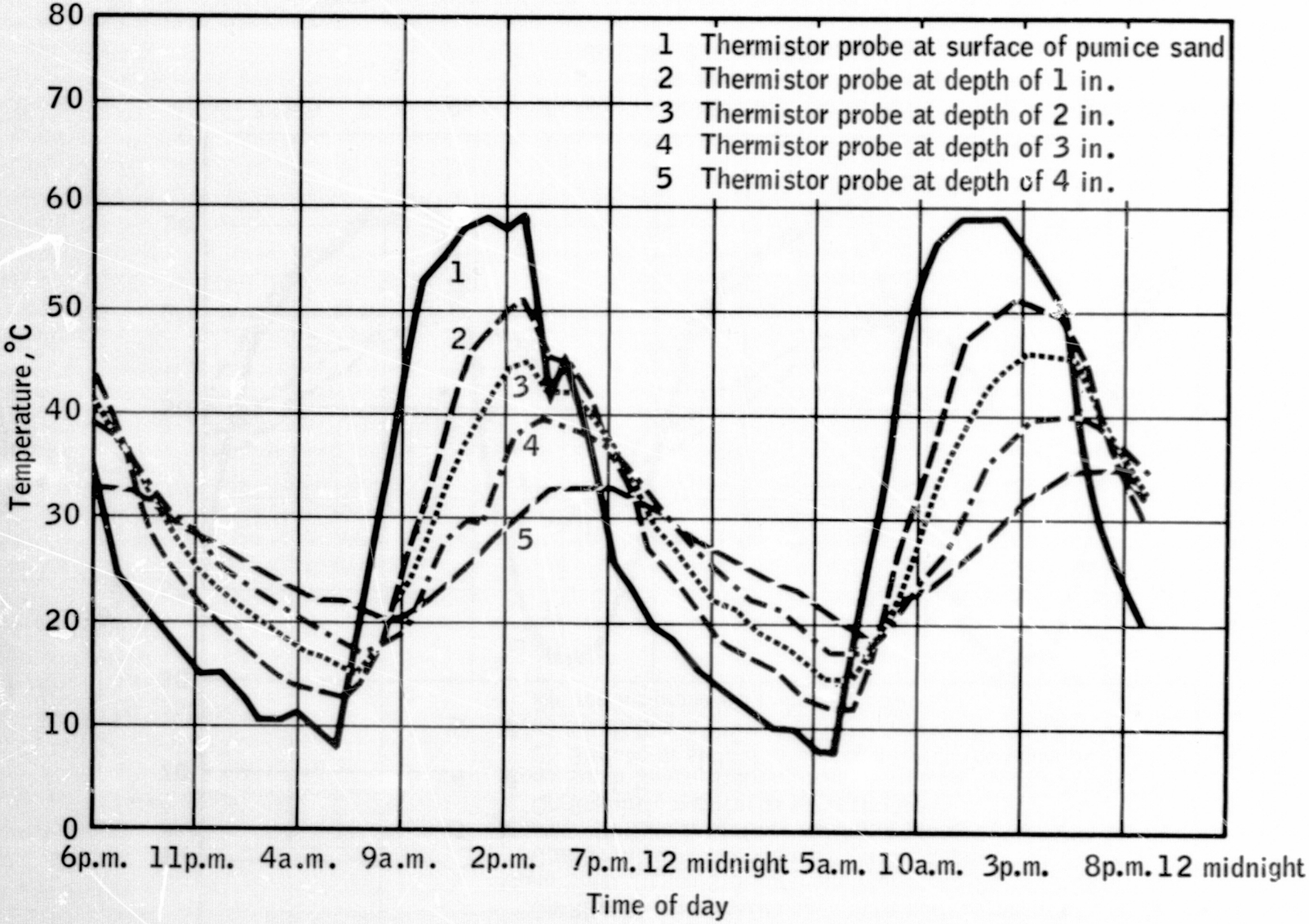

Figure 11-5.- Change in temperature with depth, east pumice sand flat, Mono Lake area, July 27 and 28, 1966. (Instrument station 3, variable sequencer G258931.)

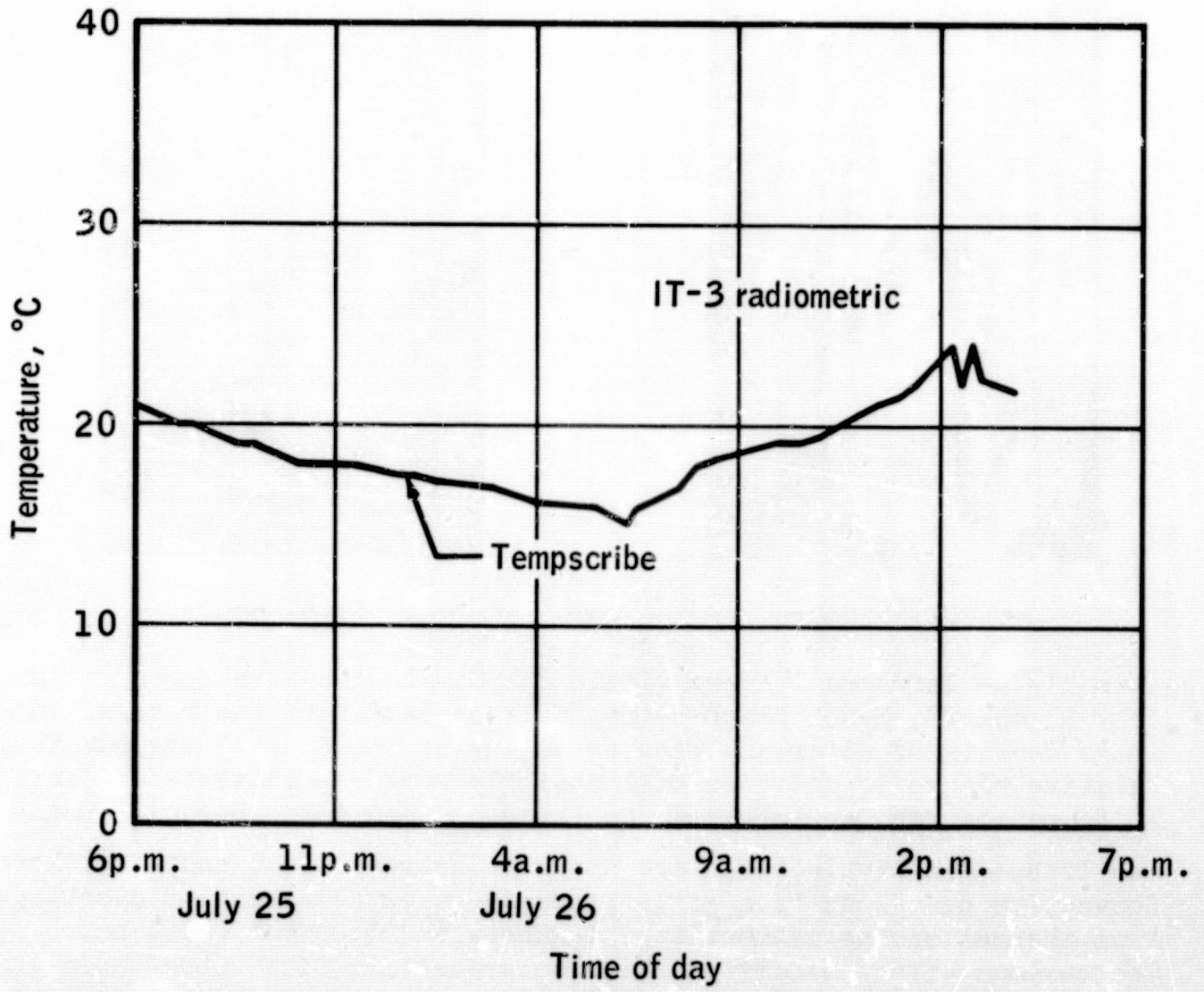

Figure 11-6.- Surface temperature of Mono Lake, South Beach area, 120 feet out in 3-foot depth at 6 inches below surface (tempscribe), July 27 and 28, 1966.

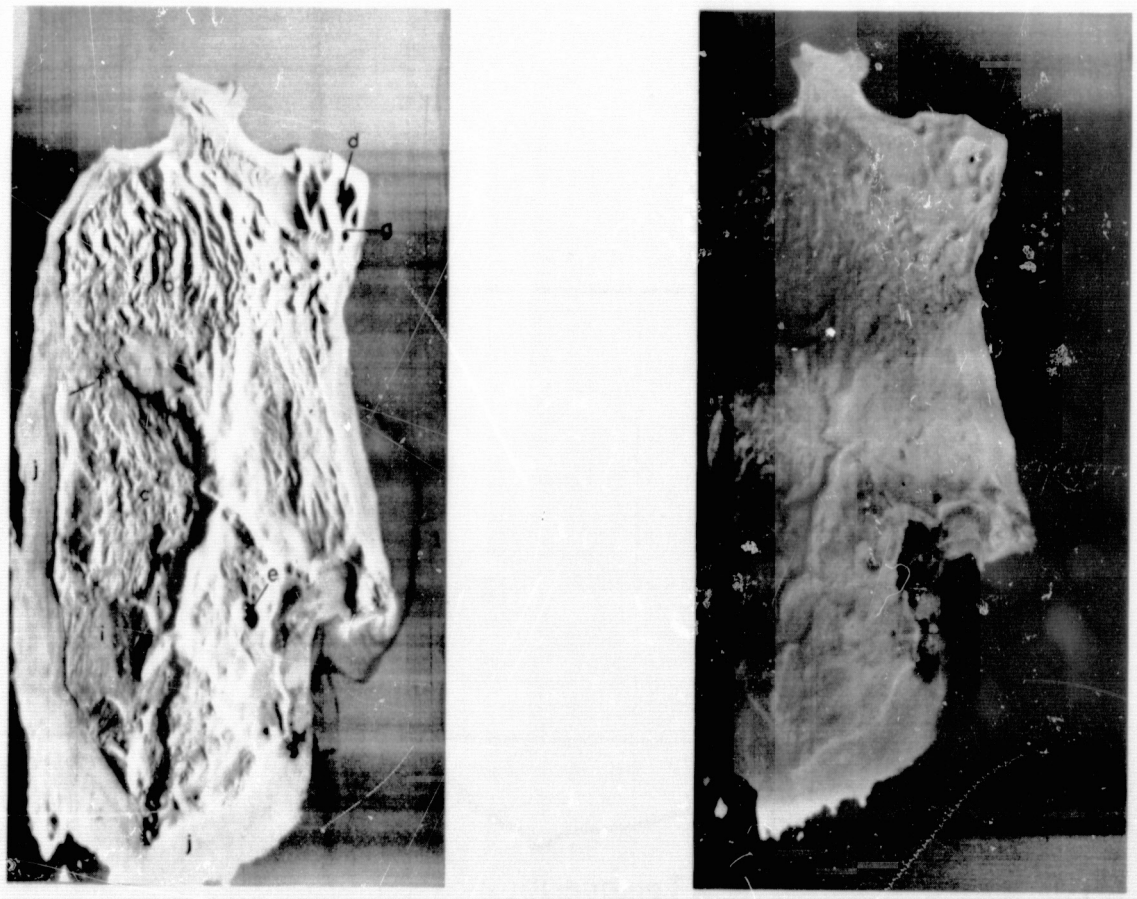

a. 07:25 hours. b. 11:57 hours.

Figure 11-7.- Infrared imagery within the 8μ- to 14μ-wavelength region, July 27 and 28, 1966, Black Point, California. Note the reversal of image density of water and land areas during the diurnal cycle. The relative change in radiance of lithologic surfaces indicates different F_o/β ratios for Qvb (area a), Qm (area b), and Qal (area c). Maximum lithologic distinctions are apparent between 20:00 and 24:00 hours. Convective heat loss from effluent ponds (area d) retaining discharge from thermal spring is most striking between 20:00 and 04:00 hours. The maximum effect of differential solar heating of a topographic surface appears at 07:25 hours. Thermal currents in the lake (area e) are probably the result of cold spring discharge. The area of isodensitracer scans shown by areas f; approximately the same areas were scanned for all the photographs. Ground monitoring station g, located near geologic contacts between Qvb, Qm, and Qal, was instrumented with an automatic-recording multiple thermistor-probe/variable-sequencer system to establish diurnal surface-temperature variation of several lithologies; a similar thermistor-probe telethermometer system was operated at area h; Tempscribes, a recording thermograph, and bulb thermometers were utilized to determine surface and thermal spring effluent temperatures at area i.

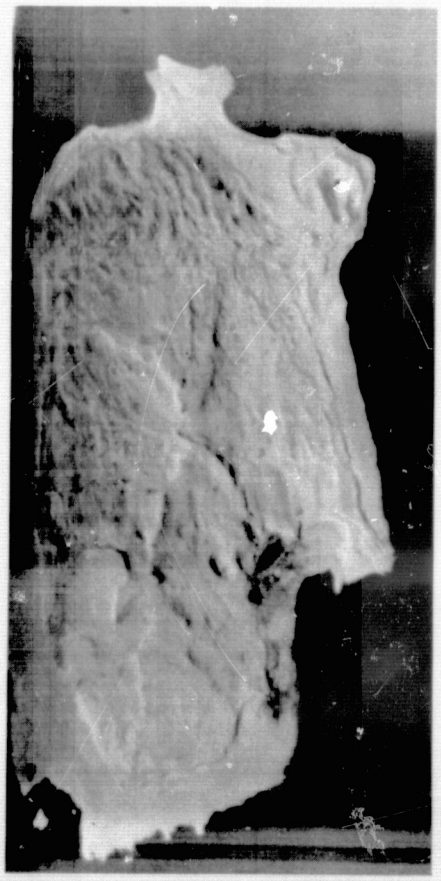

c. 16:31 hours.

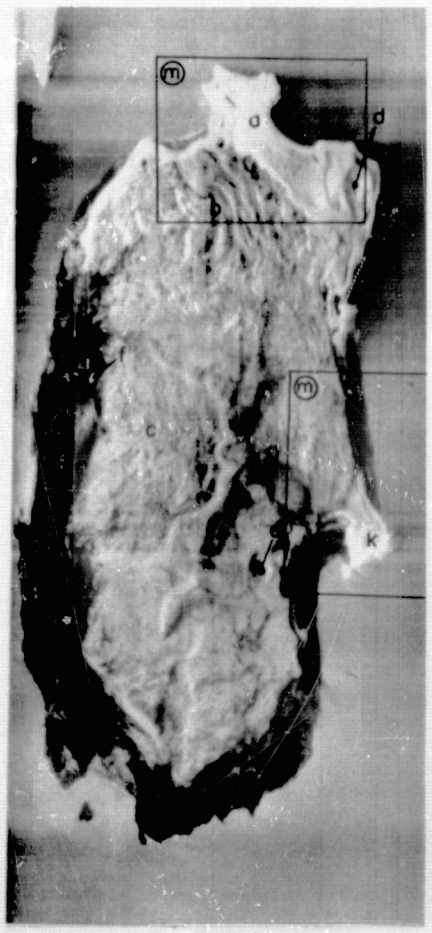

d. 20:29 hours.

Figure 11-7.- Continued.

e. 23:59 hours.

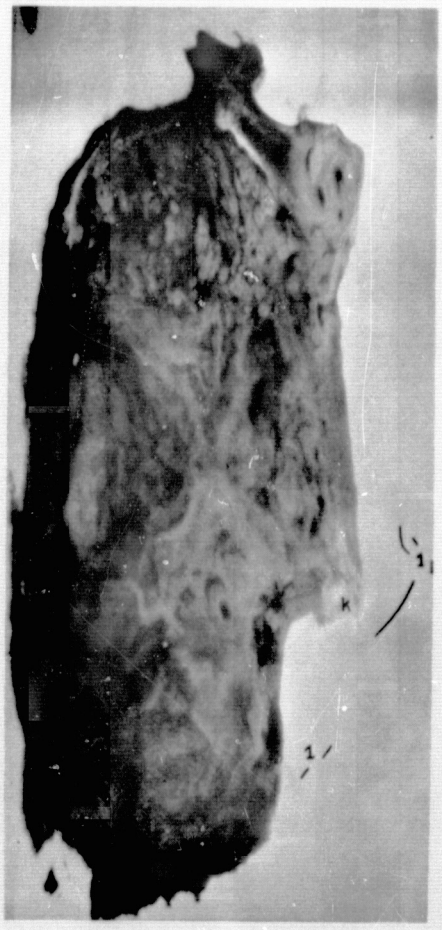

f. 04:00 hours.

Figure 11-7.- Concluded.

a. 08:11 hours.

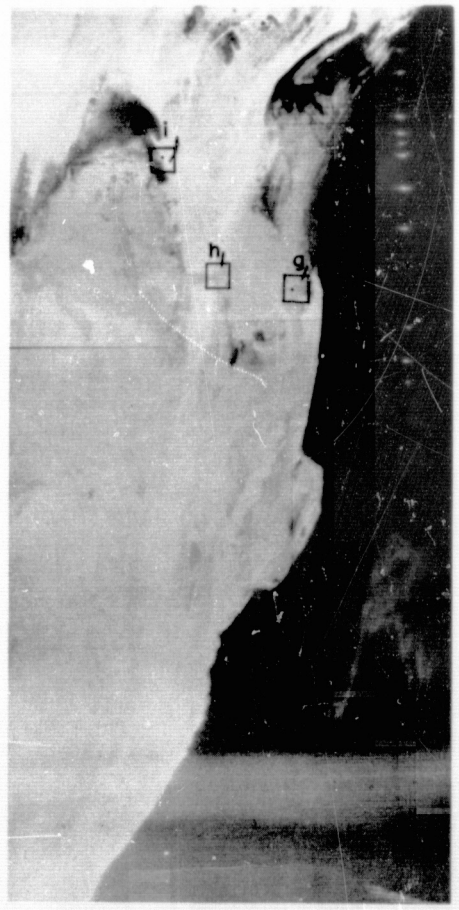

b. 12:07 hours.

Figure 11-8.- Infrared imagery within the 8μ- to 14μ-wavelength region, Poaha Island, Mono Lake, California, July 27 and 28, 1966. Lithologic distinctions arising from the F_o/β parameter are most definitive at 20:10 hours. Note that emission from QpvA (area a) is greater to the northwest where pyroclastics grade into a basaltic lava flow. Emission from thickest part of the lava flow remains highest through 04:07 hours. The northern part of Qm (area b), rich in ashfall components, shows greater emission than the southern three-quarters of the Qm (area c). The lowest emission throughout the diurnal cycle is from salt-pan evaporites in the pit of the pyroclastic crater (area d) and in the blowout crater (area e). On the western side of the island (area f), wet evaporating pan or playa surface exhibits high radiance from its center during nighttime surveys, but the darker color resembles dry evaporites in tonal density. Morning imagery (08:11 hours) shows the best topographic detail. Note the transecting pyroclastic craters (area g), the lava flow ridges (area h), the landslip topography, (area i), the wavecut bench and remnants of former shoreline (area j). Thermal anomalies (area k) representing convective heat loss from thermal springs and fumaroles and related thermal currents in the lake are distinct from the 20:10- to 08:11-hour surveys. Cold currents (area l) representing discharge from springs are most clearly delineated at 08:11 hours, but are partially visible (area l_1) on nighttime imagery. The areas of isodensitracer scans are shown by areas m; approximately the same areas were scanned for all the photographs.

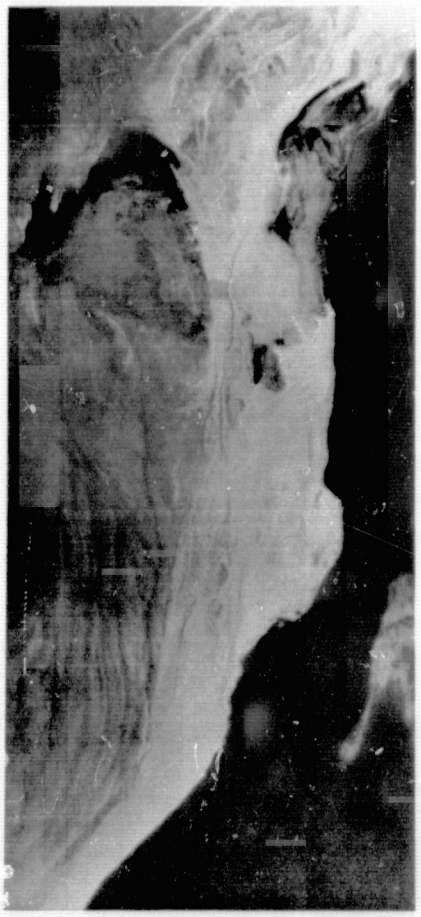

c. 16:12 hours.

d. 20:10 hours.

Figure 11-8.- Continued.

e. 00:07 hours.

f. 04:07 hours.

Figure 11-8.- Concluded.

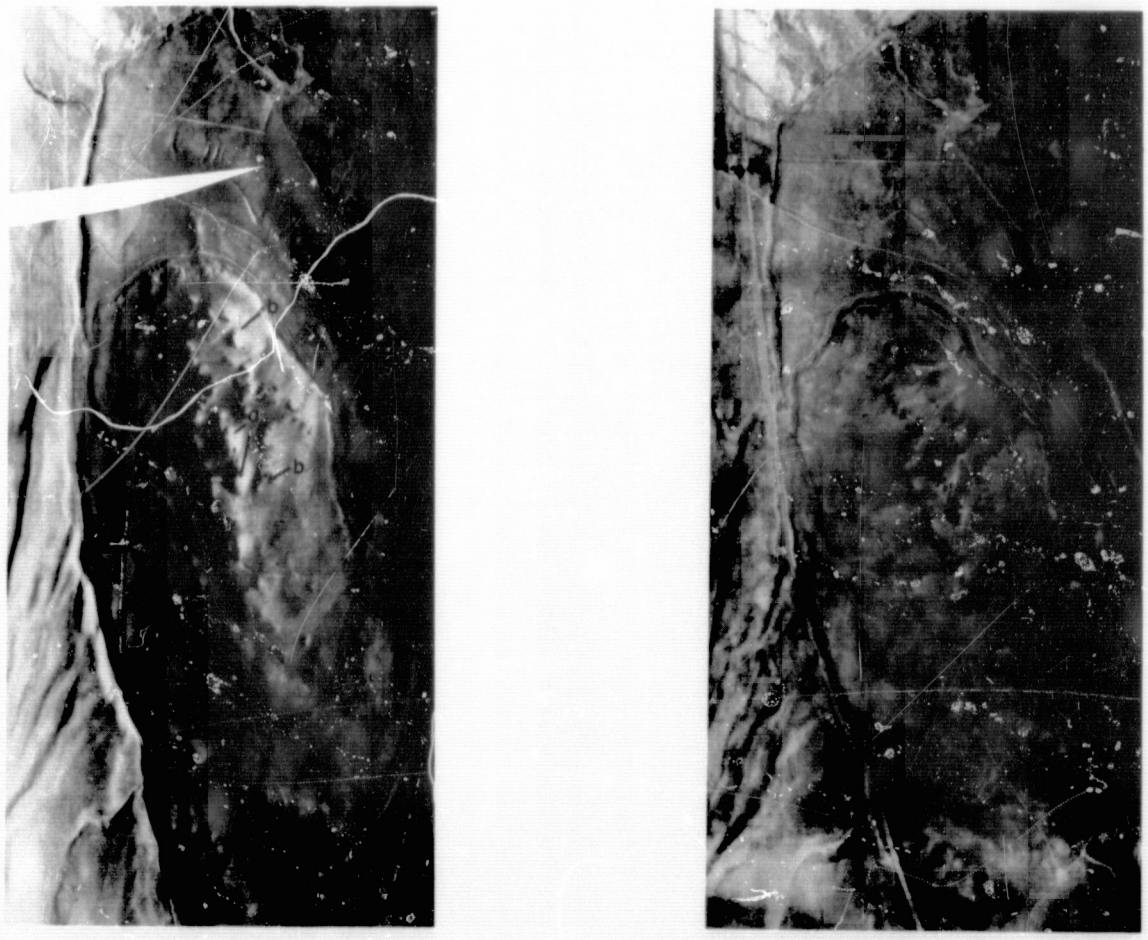

a. 07:58 hours. b. 12:04 hours.

Figure 11-9.- Infrared imagery of Aeolian Buttes, 3 miles west of Mono Craters complex, California, 8μ- to 14μ-wavelength region, July 27 and 28, 1966. Bedrock outcrops of Aeolian Buttes inlier exhibit lower amplitude diurnal surface-temperature change than surrounding unconsolidated material. Note the reversal in comparative image tonal density. The innermost outcrops in the Aeolian Buttes area (area a) are quartz monzonite (Ka); the outer ring (area b) represents exposures of upper units of Bishop tuff (Qbt); unconsolidated materials (area c) are largely lucustrine deposits (Ql_1) overlain by a recent tephra layer of pumiceous rhyolite lapilli and ash (Qyrp). Slightly greater nighttime emission from quartz monzonite (Ka) than from Bishop tuff (Qbt) outcrops can be attributed to the higher thermal inertia of quartz monzonite. The unconsolidated tephra layer (Qyrp) has a lower thermal inertia and a higher total reflectivity than either type of bedrock. The ground monitoring station (area d) located on the geologic contact between the quartz monzonite and the upper units of Bishop tuff was instrumented with automatic-recording Barnes IT-2 and IT-2 fixed-field radiometers and with meteorologic equipment during the period of the survey.

c. 16:03 hours.

d. 20:29 hours.

Figure 11-9.- Continued.

e. 23:59 hours.

f. 04:00 hours.

Figure 11-9.- Concluded.

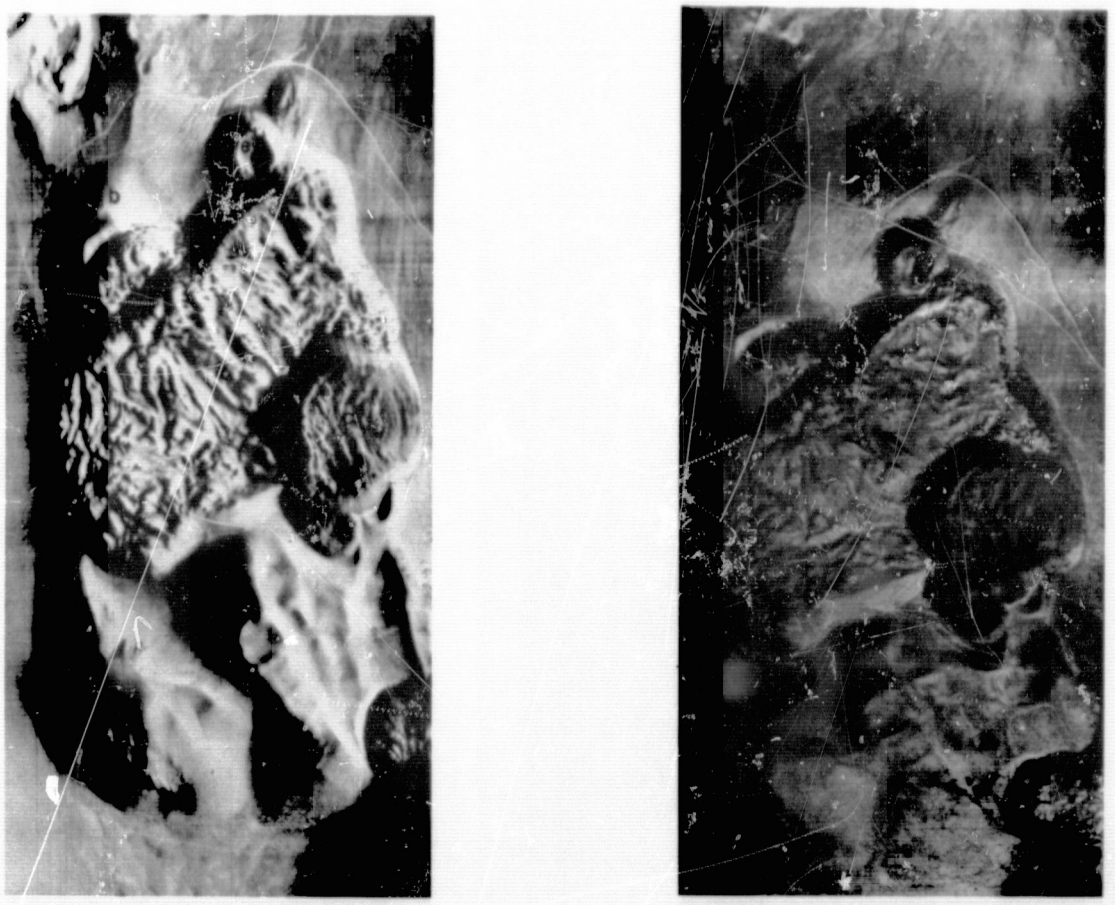

a. 08:11 hours. b. 12:07 hours.

Figure 11-10.- Infrared imagery within the 8μ- to 14μ-wavelength region, July 27 and 28, 1966, North Coulee, Mono Craters rhyolite-obsidian complex. The maximum topographic effect appears at 08:11 hours. The relative change in radiance during the diurnal cycle reflects different F_o/β ratios for unconsolidated material and bedrock. Area a is Qp, rhyolite pumice tephra (ash and lapilli); area b is Qyrp, rhyolite pumice tephra rings and cones; area c is Qyrt, rhyolite and obsidian of tholoids with overlying Qyrp in places; and area d is Qam, andesite. The upper stage of tholoid (area c) shows relatively different radiance during the diurnal cycle than the lower stage, suggesting that the upper stage is composed of blocky rhyolite and obsidian, devoid of fine pyroclastics, as is the small subsidiary cone at area e. The ashfall tephra coating much of the lower stage may indicate pyroclastic eruptions from the volcanic complex immediately to the south between the time of formation of the lower and upper stages of the North Coulee tholoid. The low nighttime emission from troughs (area f) between the flow ridges of lower stage may be the result of interplay of several factors: the concentrations in the troughs of fine pyroclastics having low thermal inertia, the blackbody cone effect of troughs causing increased emissivity and thus entailing greater heat loss at night, and the topographic effect on incident solar radiation during the day, causing the thermal shadows and lower surface temperatures of the walls of the troughs. The movement of denser cool air troughs may also contribute to lower temperatures in troughs.

c. 16:41 hours.

d. 20:38 hours.

Figure 11-10.- Continued.

e. 00:33 hours.

f. 04:07 hours.

Figure 11-10.- Concluded.

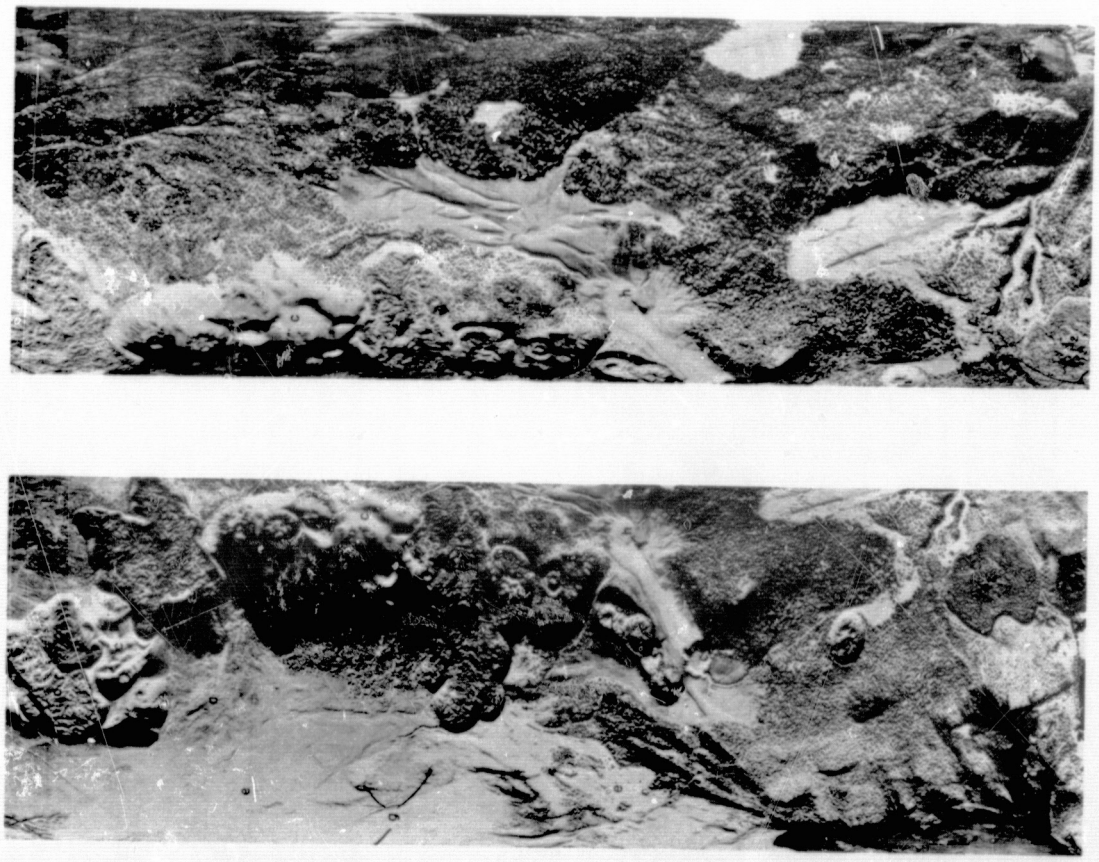

Figure 11-11.- Infrared imagery of the main rhyolite-obsidian complex at Mono Craters within the 8μ- to 14μ-wavelength region, 08:00 hours, June 4, 1965. The major effect in early daytime imagery is the enhancement of topographic and microrelief features subject to the most direct solar heating. The intensity of the incident radiant flux is dependent upon the inclination of the solar rays to the topographic surfaces; emission in the 8μ to 14μ interval from the surface is a function of this insolation. Thermal shadows are the result of relatively low emission from cooler shaded areas. These effects in early morning imagery accentuate textural patterns, microrelief, low-order relief features and other geomorphic details. Note the outlines and texture of slope-wash and fan deposits west of the crater complex (area a), the texture and lineaments in pumiceous tephra east of the crater complex (area b), the details of crater morphology (area c) — particularly in the dissected pyroclastic cones and explosion pits of the main range, the late-stage explosion pit (area c_1) in the bedrock of Punchbowl, the tholoid completely enclosed by older tephra ring (area c_2), the flow ridges and outflow centers in the rhyolite-obsidian tholoids and coulees (area d), the vertical turreted tholoid of Wilson Butte (area d_1), the biscuit-shaped obsidian-rich Glass Mountain tholoid and flow with prominent flow ridges and outflow centers (area d_2), the outcrop pattern of the June Lake basalt sheet west of the crater complex (area e), the configuration of the Tahoe-age morainic ridges near Aeolian Buttes and South Coulee (area f), the Aeolian Buttes inliers of quartz monzonite ringed by the upper units of Bishop tuff (area g), the wet spot (dark) in the center of the pumiceous sand flat east of Punchbowl (area h), suggestive of playa conditions.

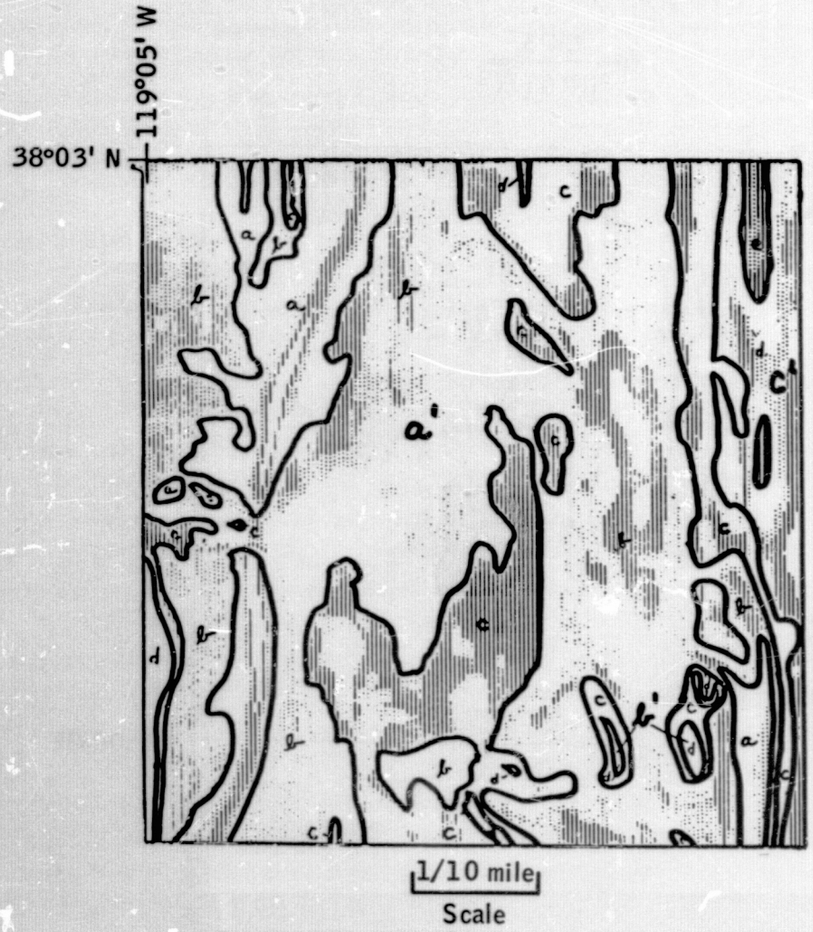

LEGEND

Map unit			Relative film density
Color		Pattern	Hot
			0.60
a	Red	Dash	.56
		Dot	.52
		Space	.48
b	Blue	Dash	.44
		Dot	.40
		Space	.36
c	Brown	Dash	.32
		Dot	.28
		Space	.24
d	Green	Dash	.20
		Dot	.16
		Space	.12
e	Black	Dash	.08
		Dot	.04
		Space	.00
			Cold

a' Generally silty surface (Qb) of Wilson Creek delta

b' Evaporating pans of lacustrine carbonates (Qb)

c' Mono Lake

Figure 11-12.- Isodensity scan used in correlating surface temperatures with the image emulsion density scale (figs. 11-24 and 11-25). IR imagery, Wilson Creek delta, Black Point, Mono Lake, 07:50 hours, July 27, 1966.

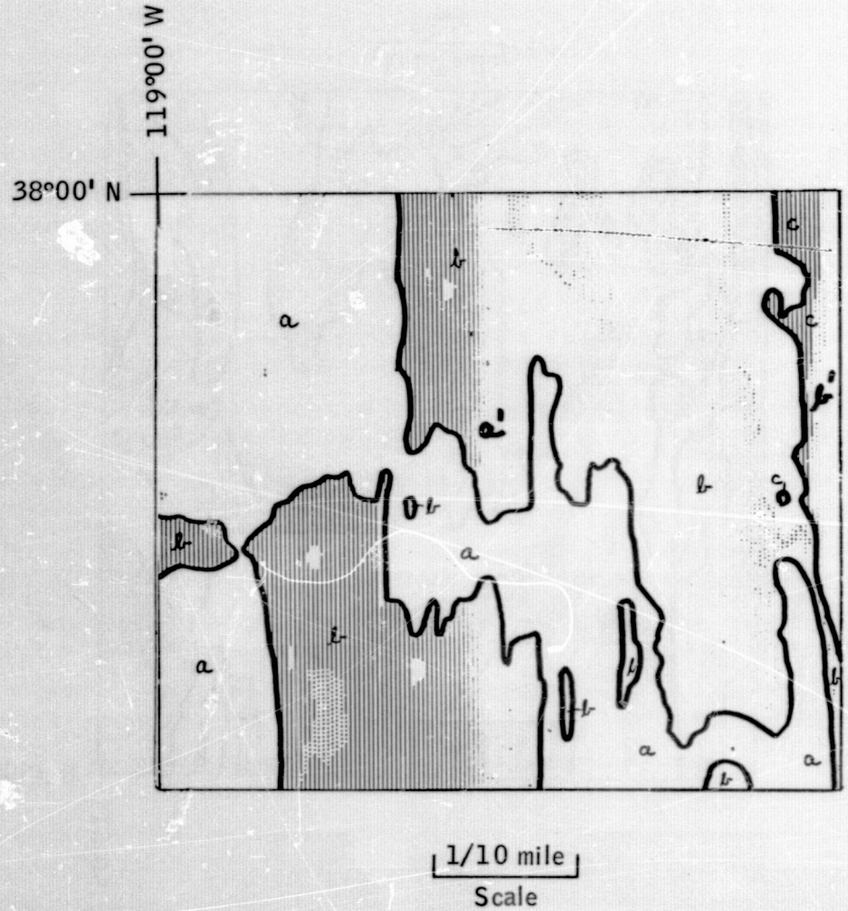

LEGEND

Map unit			Relative film density
	Color	Pattern	
a	Red	Dash	0.96D
		Dot	.84
		Space	.72
b	Blue	Dash	.60
		Dot	.48
		Space	.36
c	Brown	Dash	.24
		Dot	.12
		Space	.00D

Hot ↑ ↓ Cold

a' Lacustrine silt (Qb) of Wilson Creek delta
b' Mono Lake

Figure 11-13.- Isodensity scan used in correlating surface temperatures with image emulsion density scale (figs. 11-24 and 11-25). IR imagery, Wilson Creek, Black Point, Mono Lake, 12:33 hours, July 27, 1966.

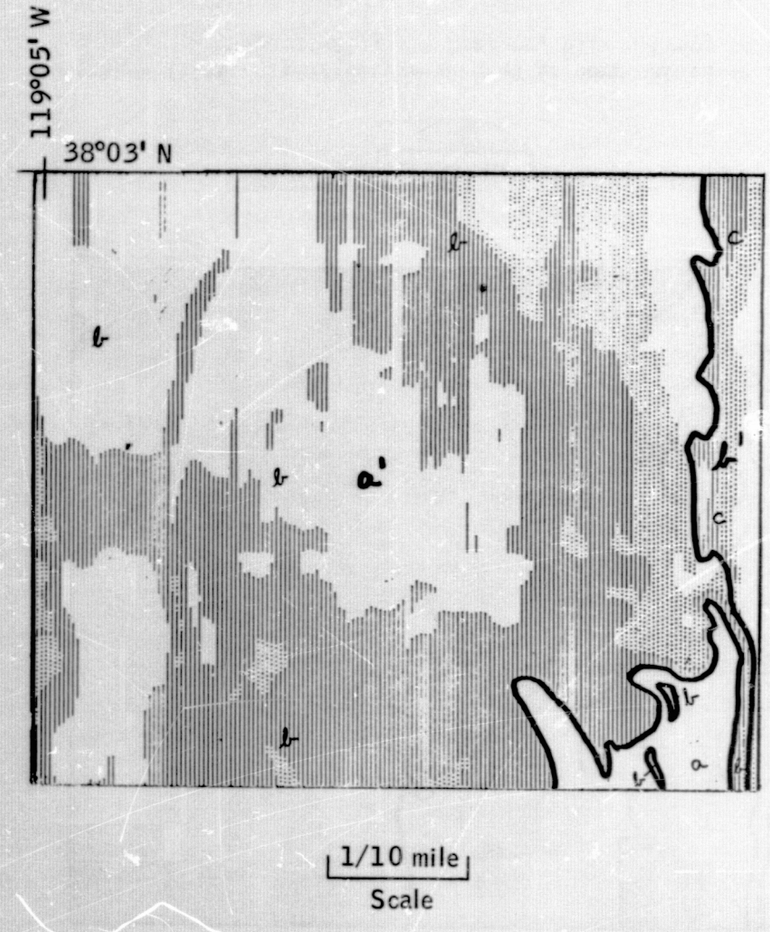

LEGEND

Map unit			Relative film density
Color		Pattern	
a	Lavender	Dash	0.96
		Dot	.84
		Space	.72
b	Red	Dash	.60
		Dot	.48
		Space	.36
c	Blue	Dash	.24
		Dot	.12
		Space	.00D

Hot ↑ ↓ Cold

a' Lacustrine silt (Qb) of Wilson Creek delta
b' Mono Lake

Figure 11-14.- Isodensity scan used in correlating surface temperatures with image emulsion density scale (figs. 11-24 and 11-25). IR imagery, Wilson Creek, Black Point, Mono Lake, 16:31 hours, July 27, 1966.

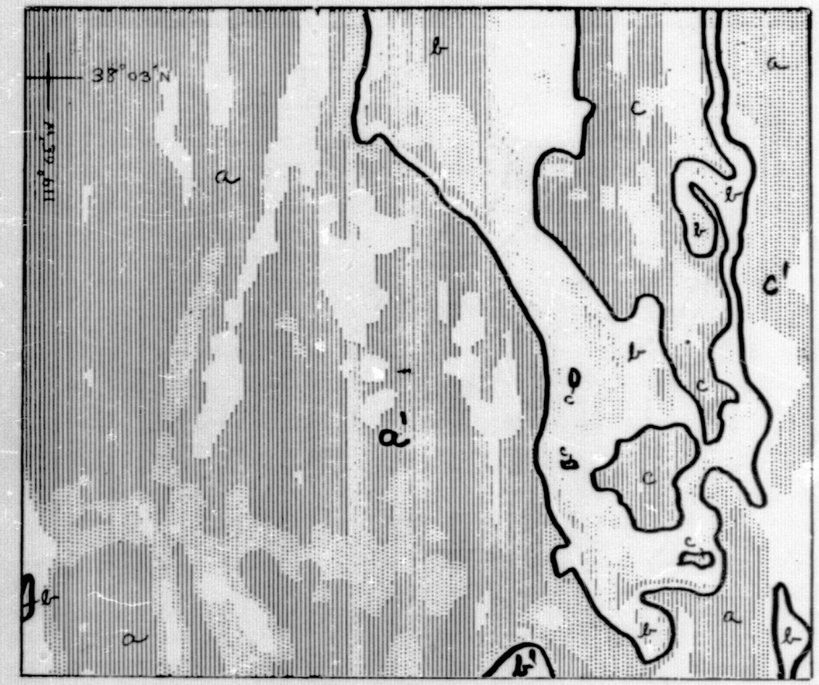

1/10 mile
Scale

LEGEND

Map unit			Relative film density
Color		Pattern	
a	Red	Dash	0.96
		Dot	.84
		Space	.72
b	Blue	Dash	.60
		Dot	.48
		Space	.36
c	Brown	Dash	.24
		Dot	.12
		Space	.00

Hot ↑ ↓ Cold

a' Lacustrine silt (Qb) of Wilson Creek delta
b' Highly reflective evaporites (Qb)
c' Mono Lake

Figure 11-15.- Isodensity scan used in correlation of surface temperatures with the image emulsion density (figs. 11-24 and 11-25). IR imagery, Wilson Creek delta, Black Point, Mono Lake, 20:00 hours, July 27, 1966.

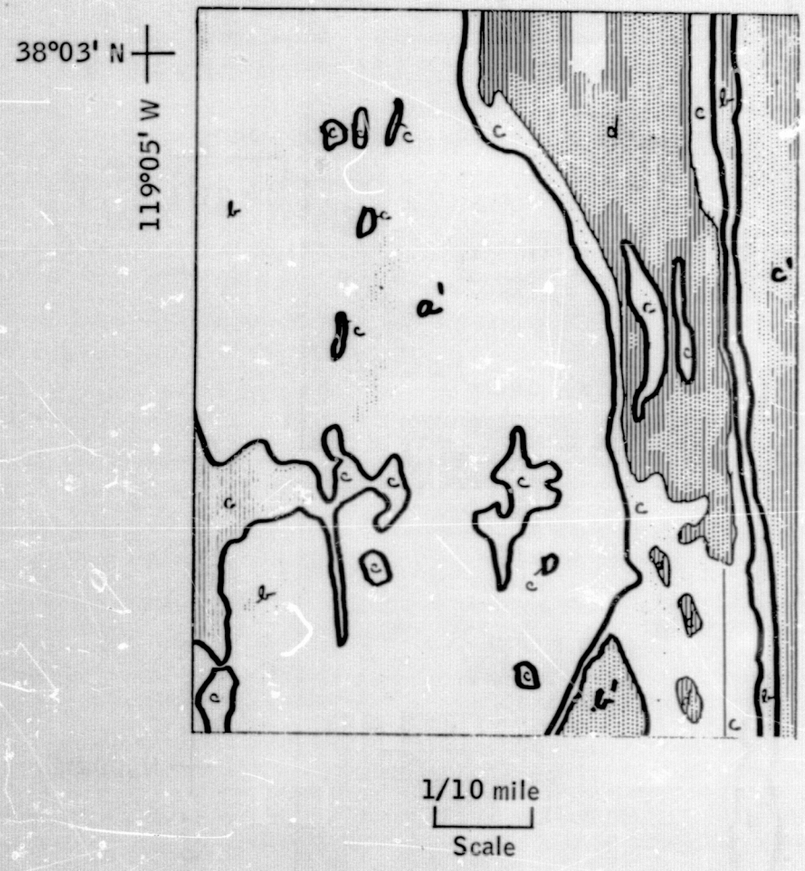

LEGEND

Map unit			Relative film density
	Color	Pattern	
a	Blue	Dash Dot Space	Hot
b	Brown	Dash Dot Space	
c	Green	Dash Dot Space	
d	Black	Dash Dot Space	Cold

a' Lacustrine silt (Qb) of Wilson Creek delta
b' Highly reflective evaporites (Qb)
c' Mono Lake

Figure 11-16.- Isodensity scan used in correlation of surface temperatures with the image emulsion density (figs. 11-24 and 11-25). IR imagery, Wilson Creek delta, Black Point, Mono Lake, 04:04 hours, July 28, 1966.

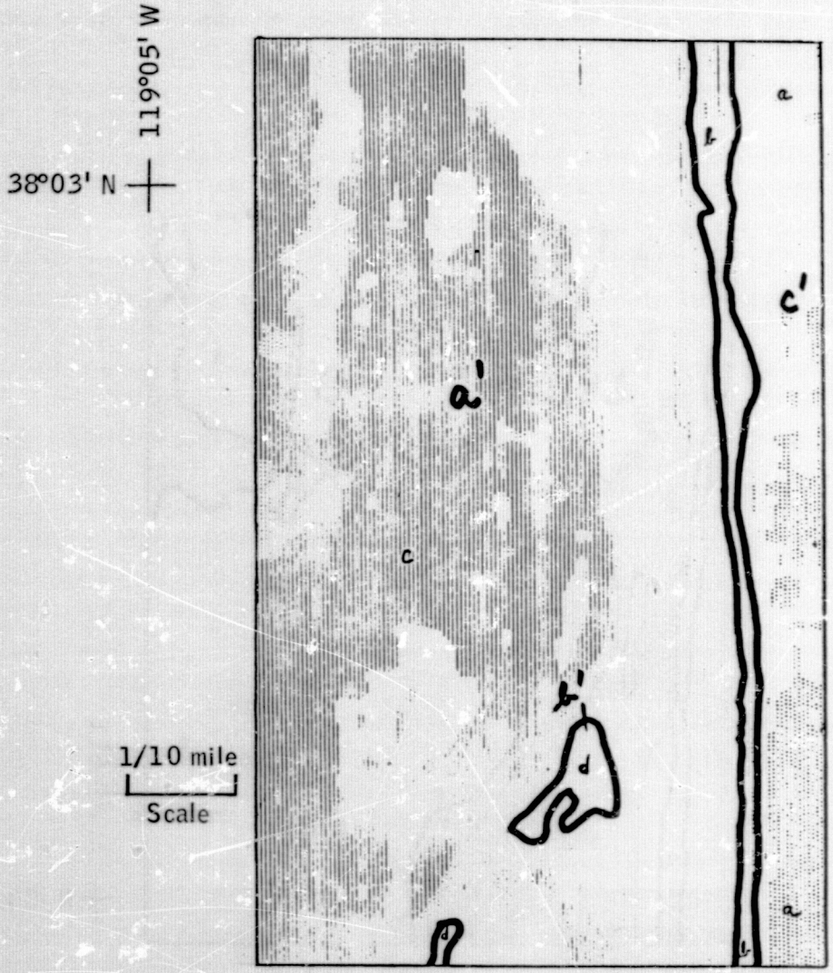

LEGEND

Map unit		Relative film density
Pattern		Hot ↑
a	Dash	1.20
	Dot	1.00
	Space	.96
b	Dash	.84
	Dot	.72
	Space	.60
c	Dash	.48
	Dot	.36
	Space	.24
d	Dash	.12
	Dot	.00D
	Space	↓ Cold

a' Lacustrine silt (Qb) of Wilson Creek delta
b' Highly reflective evaporites (Qb)
c' Mono Lake

Figure 11-17.- Isodensity scan used in correlating surface temperatures and the image emulsion density scale (figs. 11-24 and 11-25). IR imagery of Wilson Creek delta, Black Point, Mono Lake, 04:00 hours, July 28, 1966.

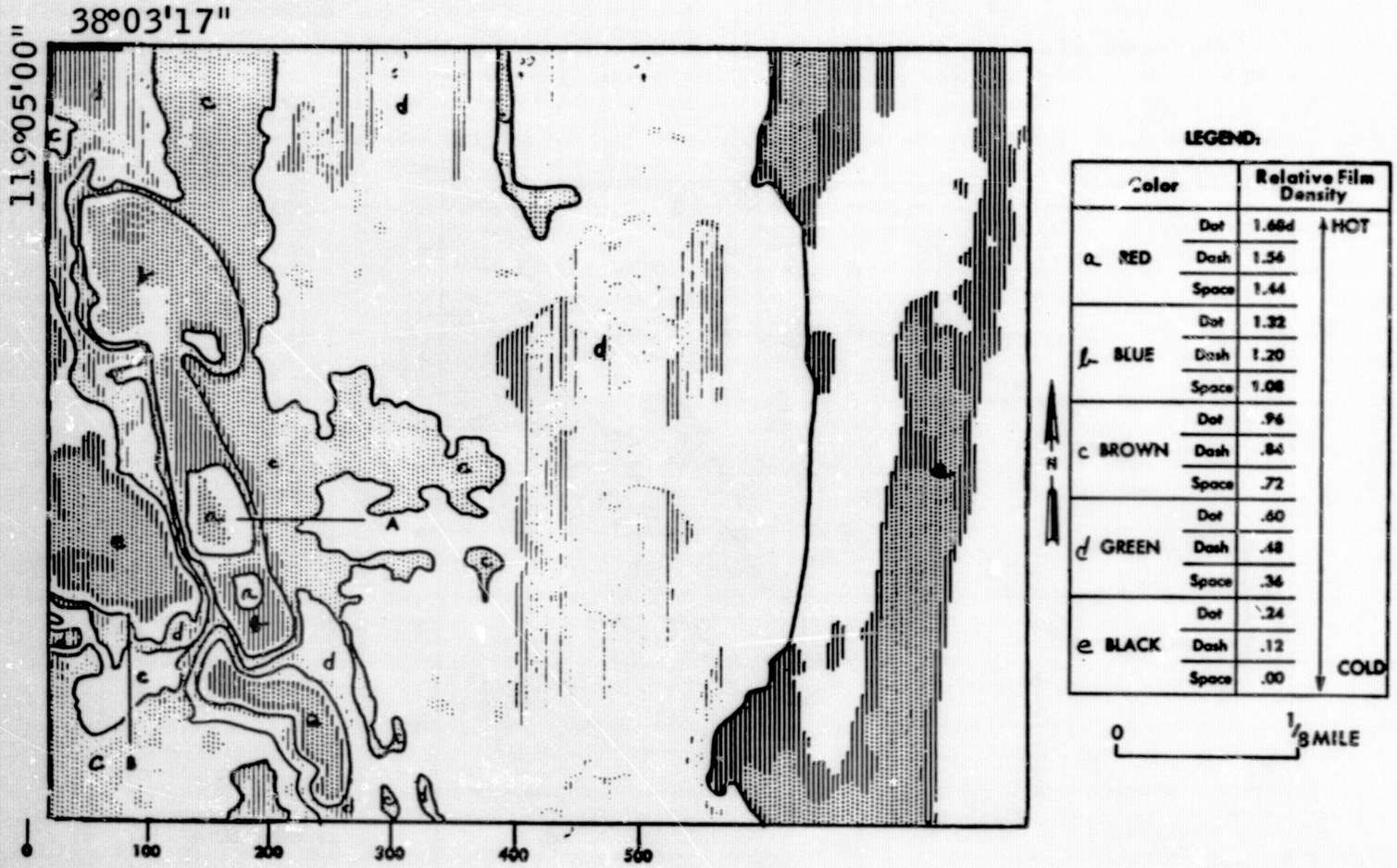

Figure 11-18.- Isodensity scan of IR imagery, 23:59 hours, July 27, 1966, effluent from a hot spring near Deschambeau Ranch, Black Point, California. Ground temperature measurements confirm that the middle point (area a') is warmer than the southeastern-most pond. Note the contrast in radiance between the ponds and adjacent marshy vegetation at area b'.

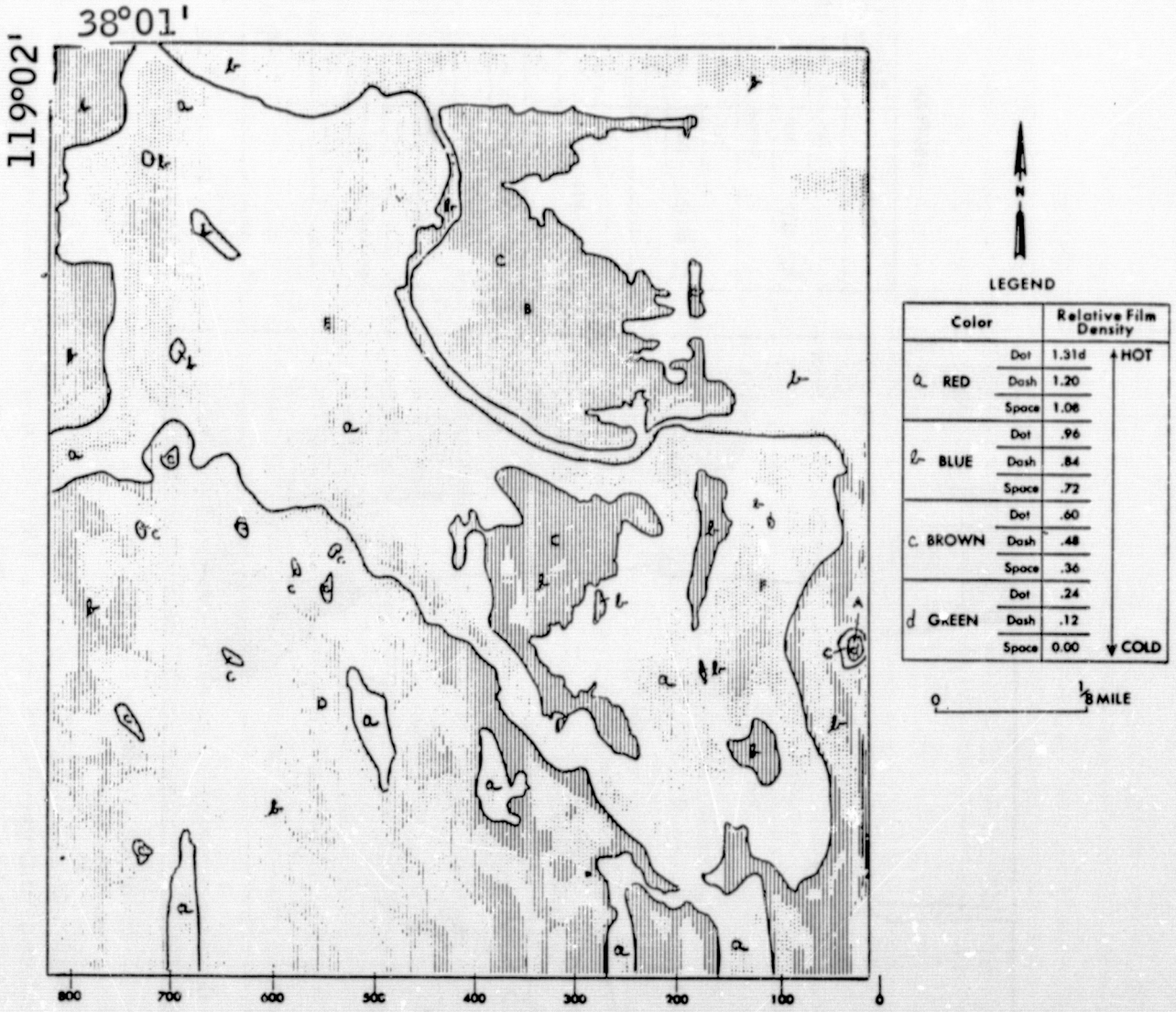

a' Salt pan in the pit of a pyroclastic crater
b' Mono Lake water
c' Unconsolidated material and vegetation
d' Lacustrine tuffaceous marl
e' Andesite-basalt flow
f' Andesite-basalt pyroclastics

Figure 11-19.- Isodensity scan of IR imagery, northeastern Paoha Island, Mono Lake, 20:10, July 27, 1966.

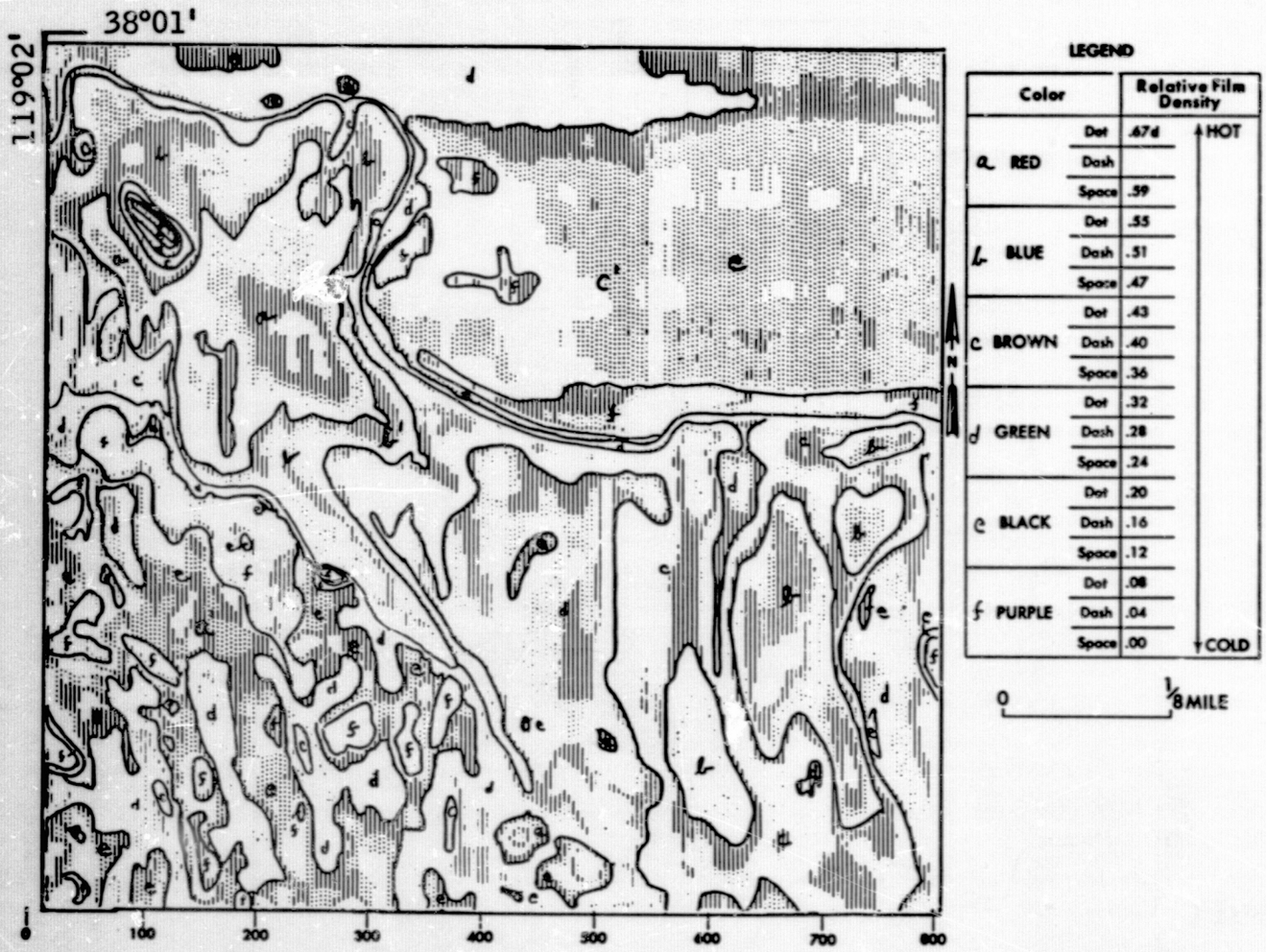

a' Marl (Qm)
b' Andesite-basalt flows (QPva)
c' Mono Lake

Figure 11-20.- Isodensity scan of post-sunset IR imagery, northeastern Paoha Island, Mono Lake, 20:38, July 27, 1966.

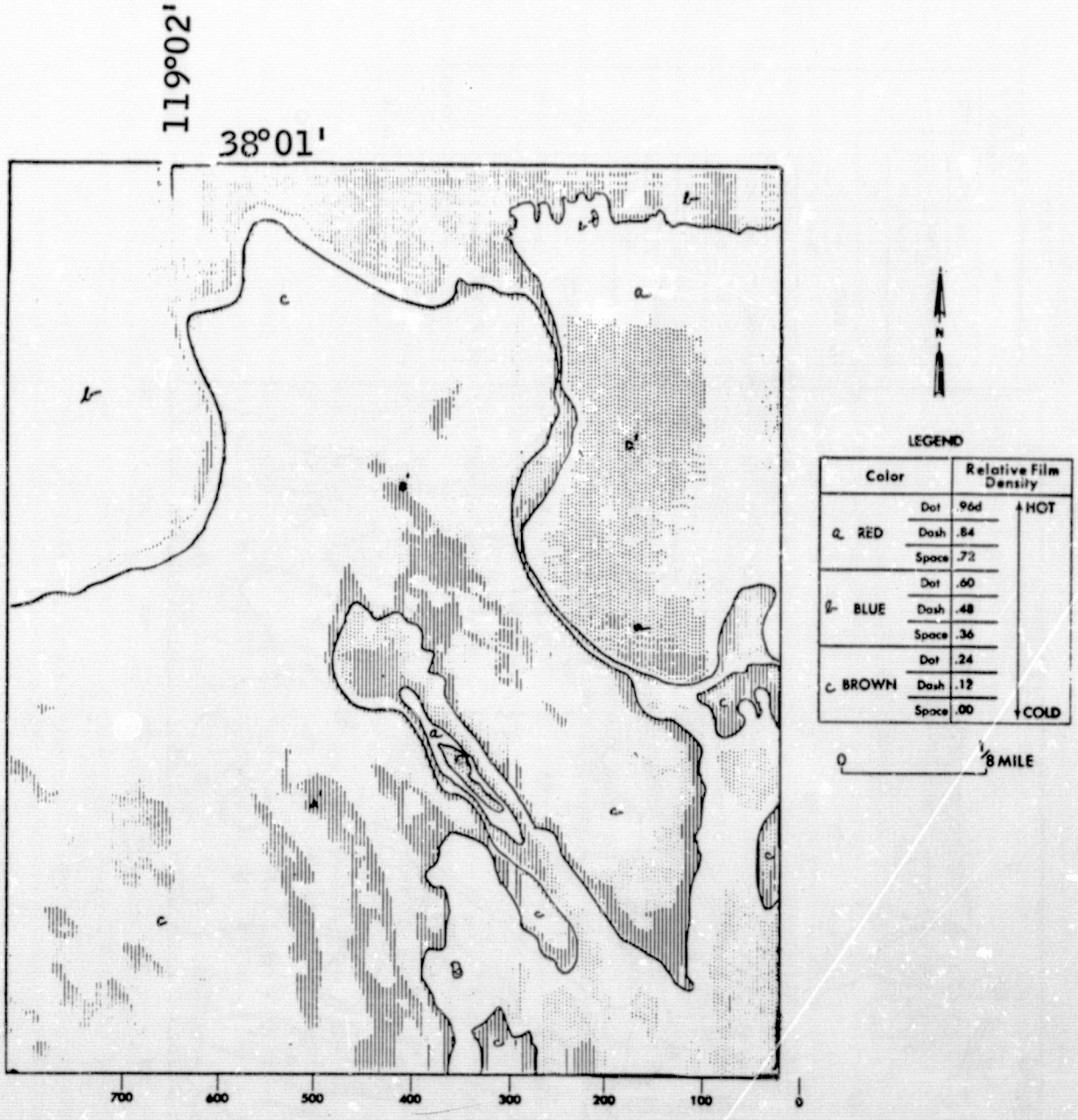

Figure 11-21.- Isodensity scan, Northeastern Paoha Island, Mono Lake, showing virtual disappearance of radiant-temperature distinctions between most lithologic units (e.g., areas a' and b') by 4:07 a.m., July 28, 1966, compared to 8:00 p.m. imagery, with the exception of the residual anomaly at area c' correlated with the position of the andesite-basalt flow ridge. Note the reversal in the comparative temperature position of Mono Lake (area d'): Lake water exhibits higher radiance at this predawn hour than bedrock or unconsolidated materials.

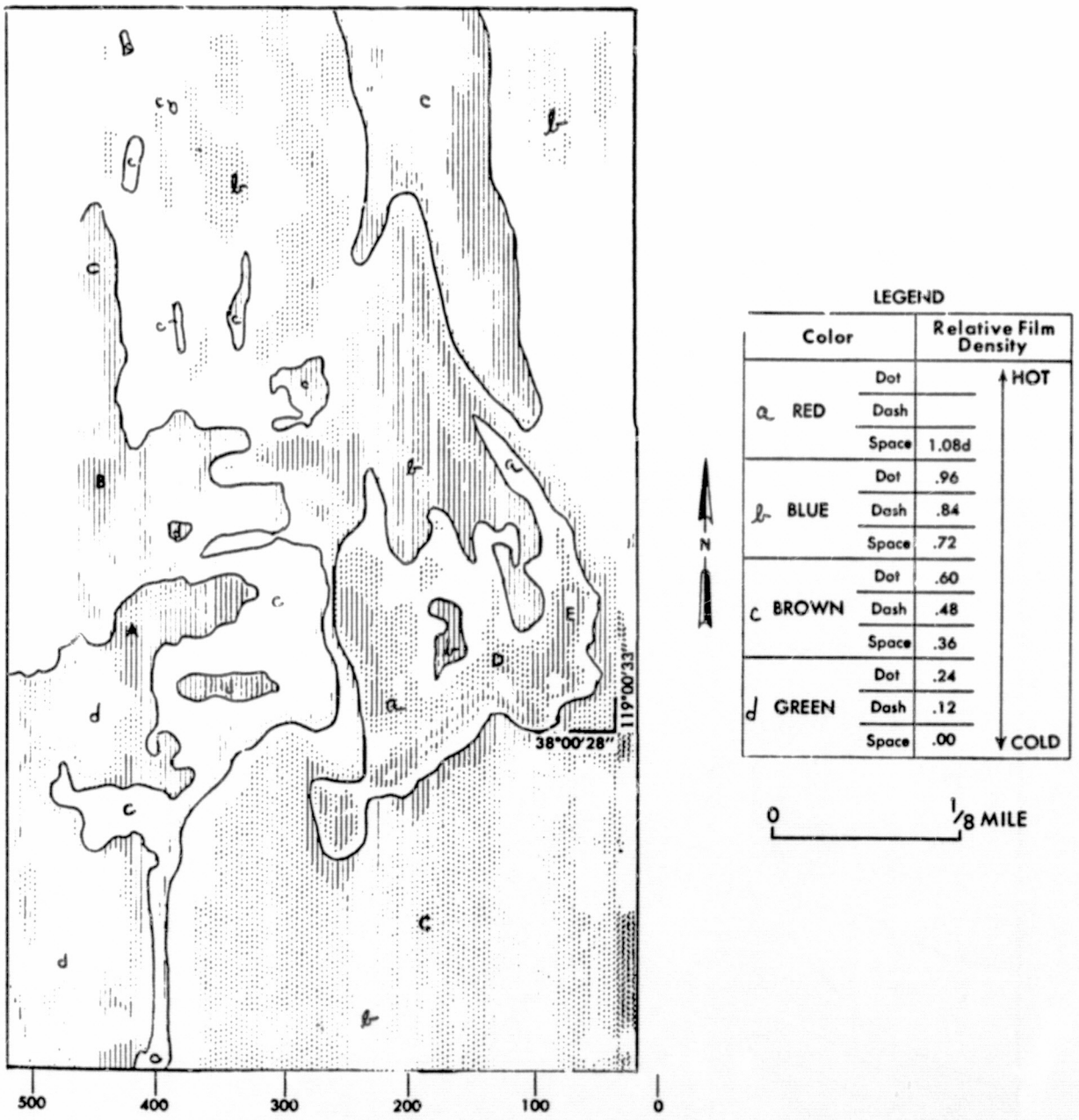

a' Thickly vegetated beach deposit
b' Hummocky area of lacustrine marl (Qm)
c' Mono Lake
d' Andesite-basalt volcanics (Qpva)
e' Thermal spring area

Figure 11-22.- Isodensity scan of IR imagery showing area of thermal anomalies, eastern Paoha Island, Mono Lake, 20:10, July 27, 1966. (Only 12 isodensity units used.)

VI

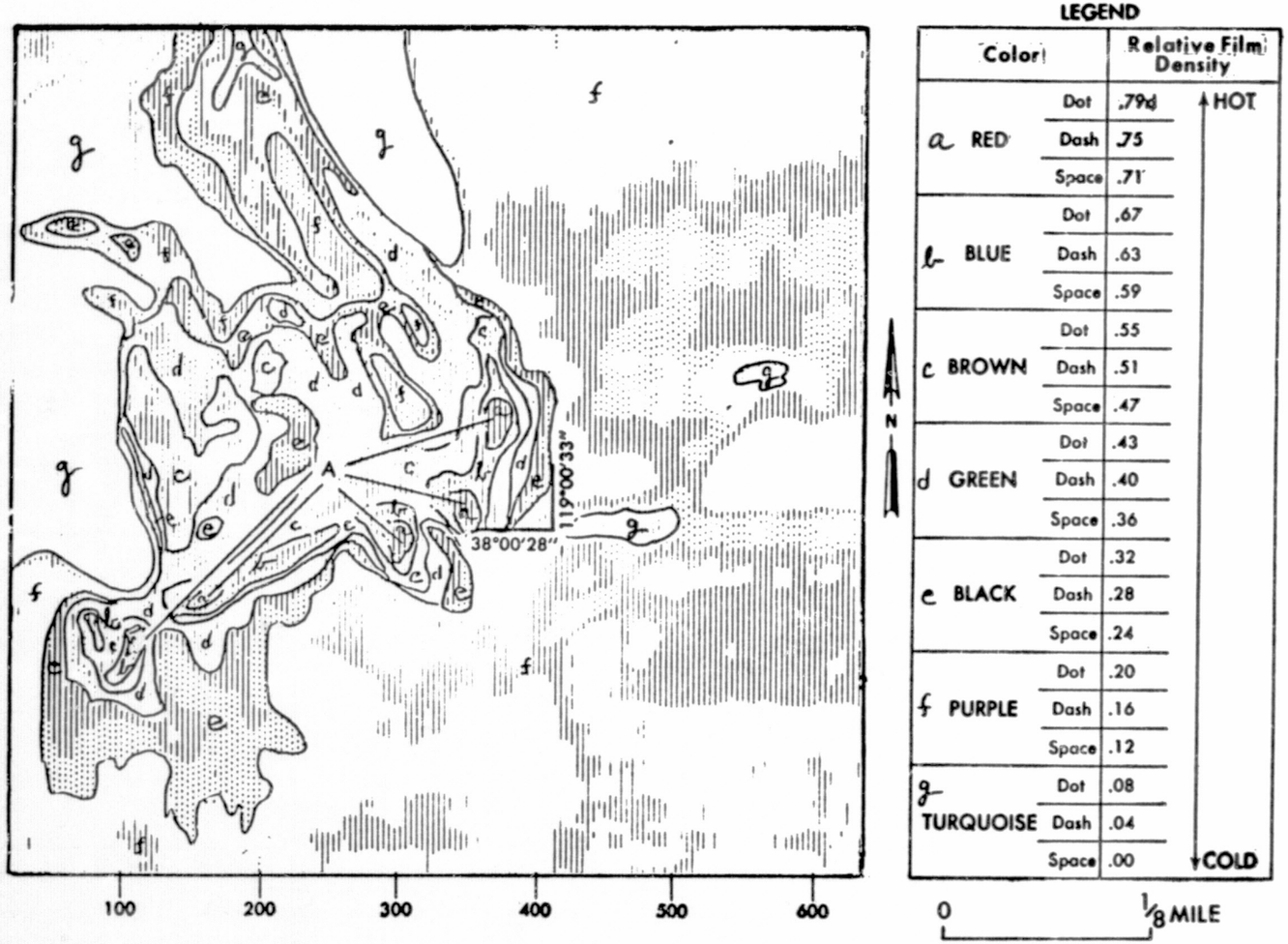

Figure 11-23.- Isodensity scan of IR imagery showing area of thermal anomalies in detail, eastern Paoha Island, Mono Lake, 20:38, July 27, 1966. (Twenty-one isodensity units permits delineation of five thermal anomalies as distinct from normally warm andesite-basalts which appear as units of lower density.)

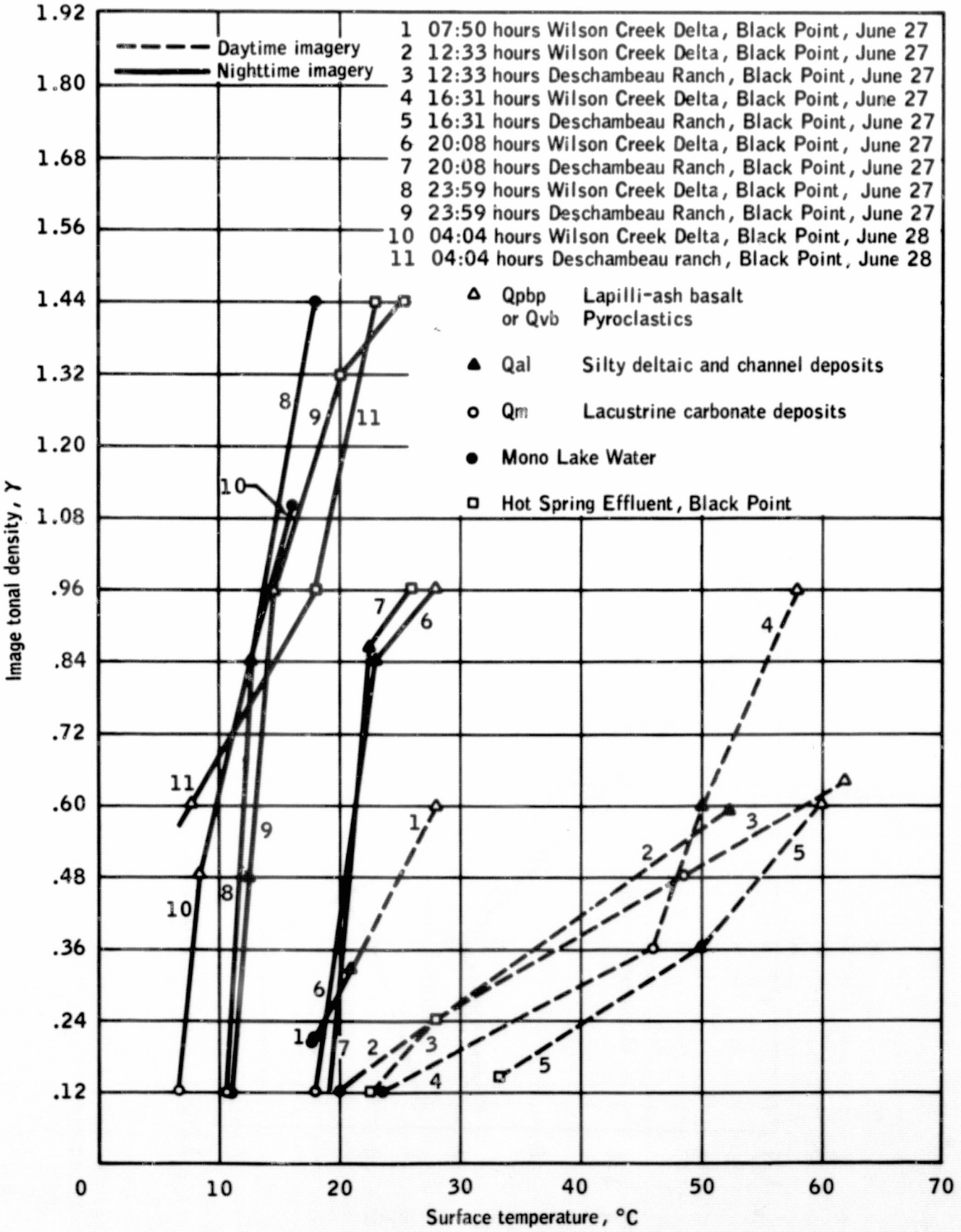

Figure 11-24.- Infrared image density in relation to surface temperature, Black Point, Mono Lake, California, July 27 and 28, 1966. Determined from isodensity scans of IR imagery.

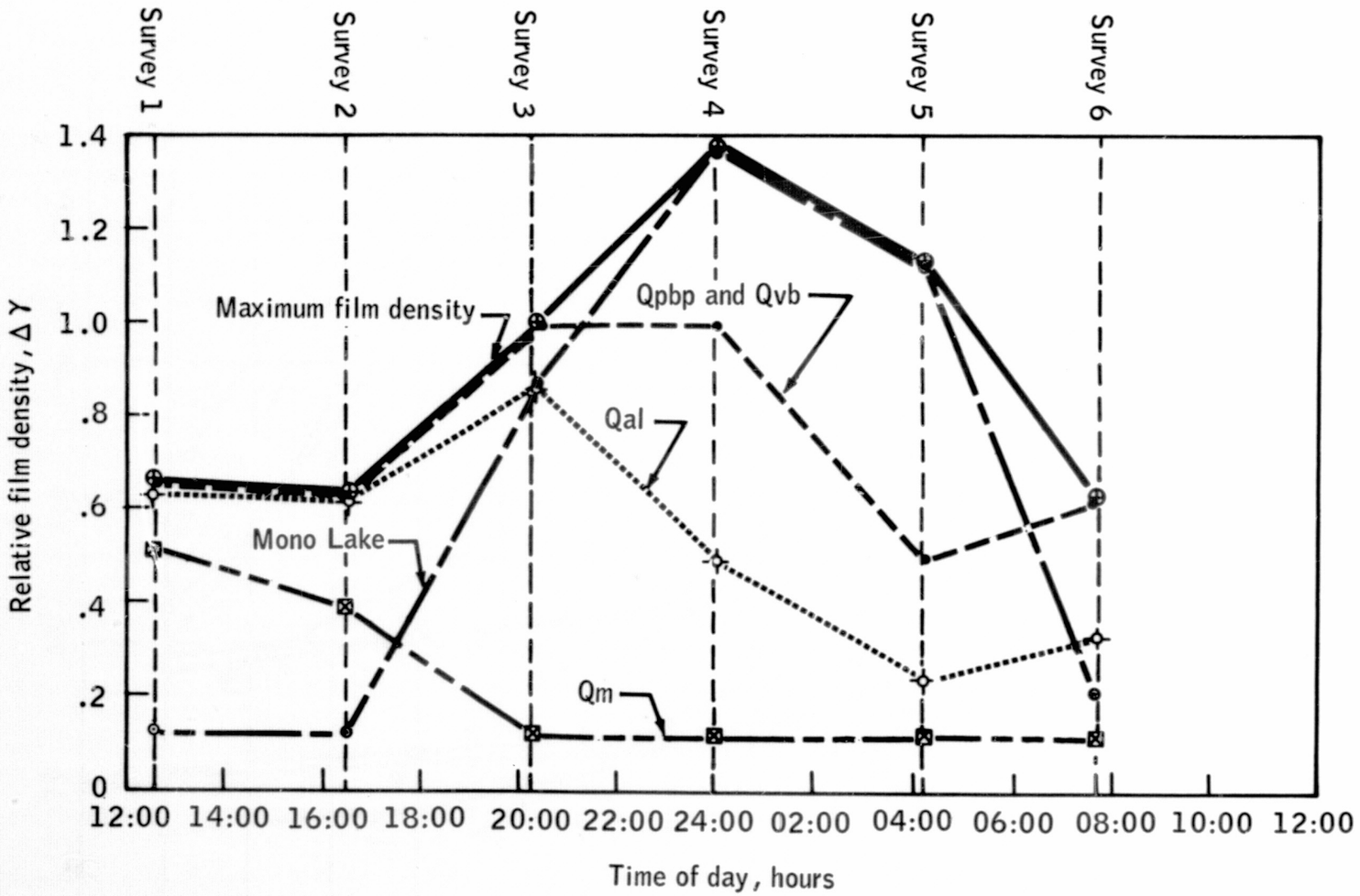

Figure 11-25.- Change in relative film density with time during a diurnal cycle for three lithologies and water. The film density of each material is plotted in relation to the maximum film density for each of six sequences of imagery. Maximum film density is a function of changes in radiance and amplifier gain setting and to a lesser extent of film processing and isodensitometer settings. Film densities at the maximum film density line or at the 0.12 line suggest that the amplifier signal may have been near or beyond the latitude of the film. Black Point, July 27 and 28, 1966.

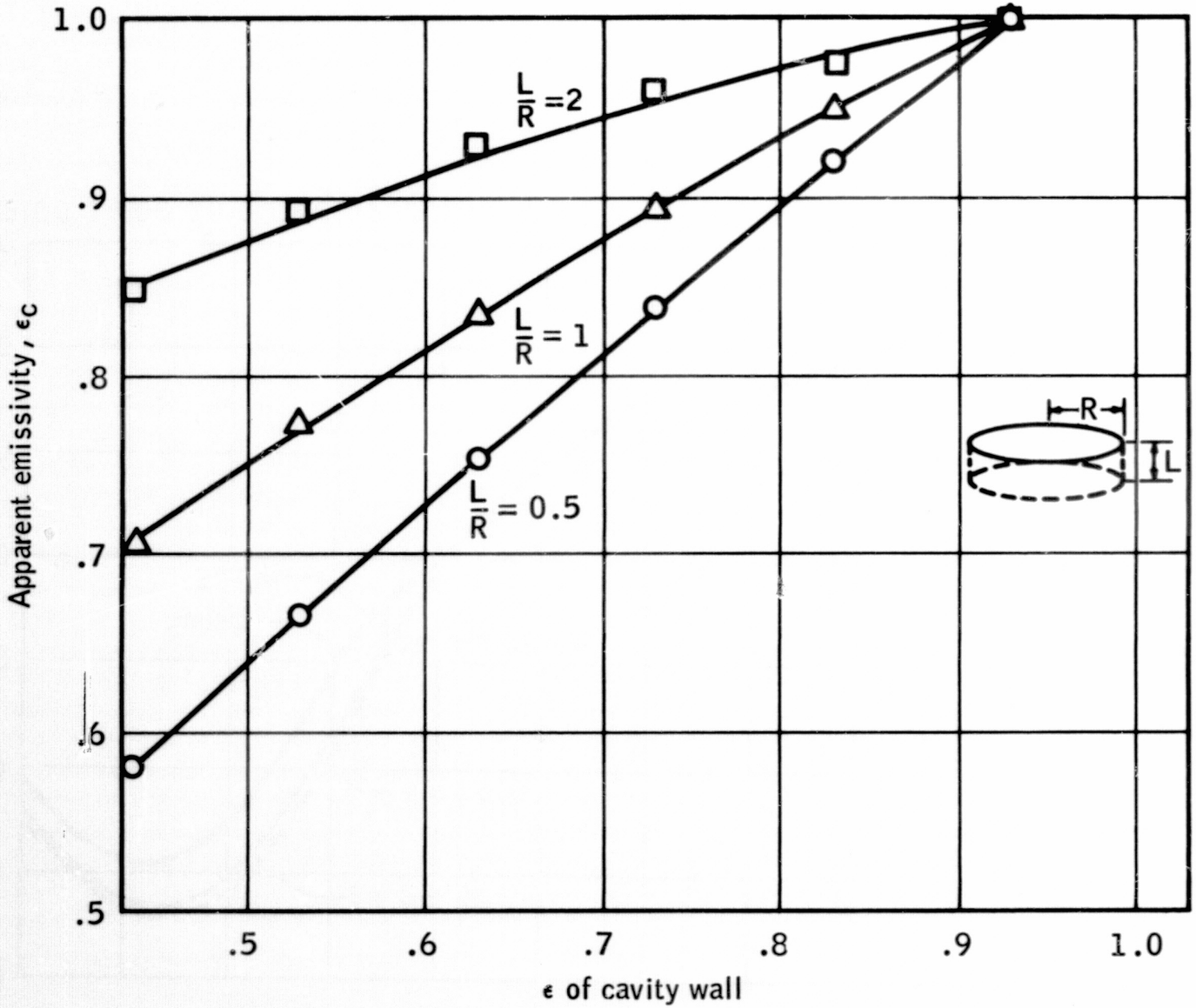

Figure 11-26.- Change in apparent emissivity ε_c as a function of cavity shape and integrated emissivity $\varepsilon_{\lambda,8\mu-14\mu}$ of cavity wall (ref. 11-6).

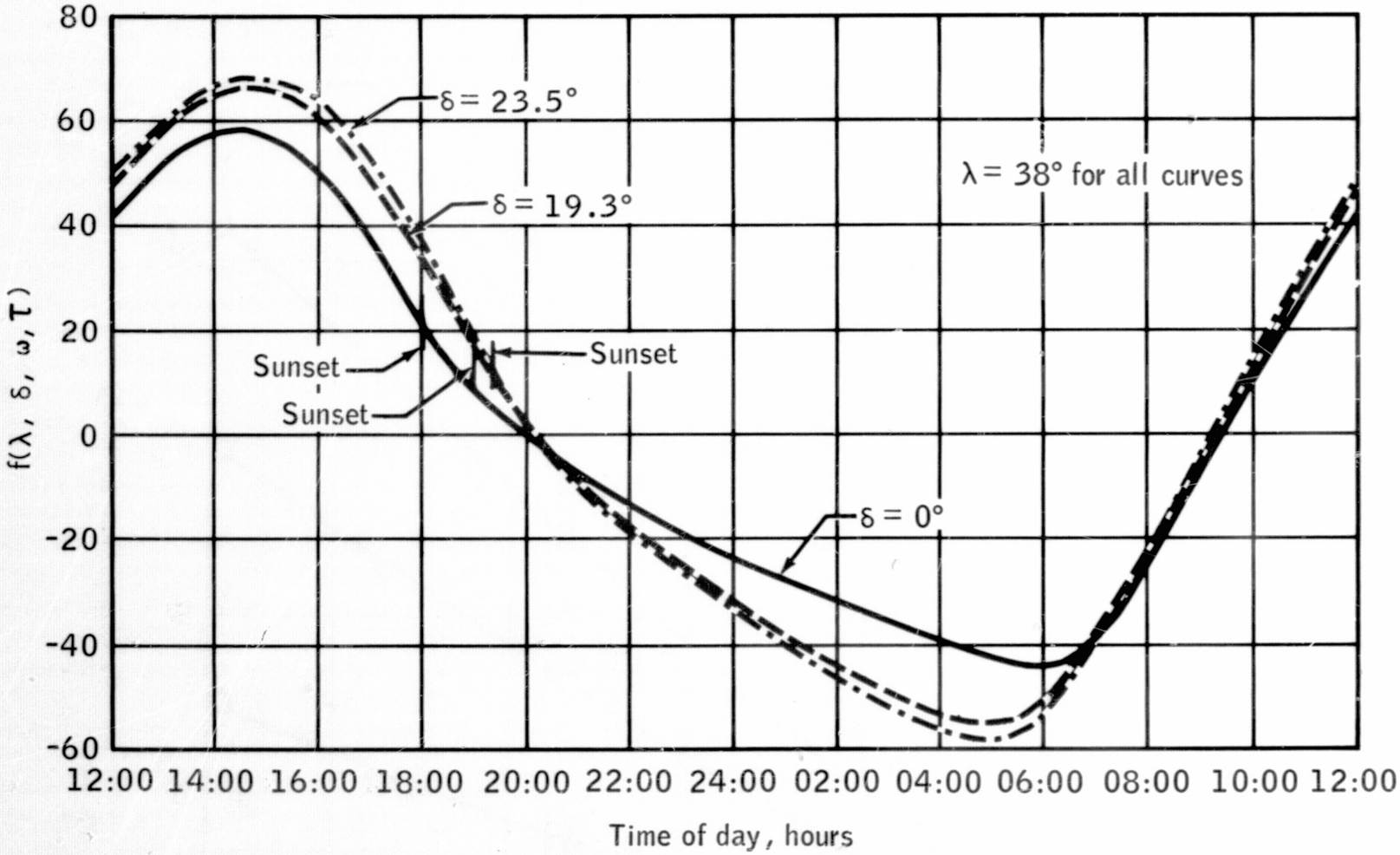

Figure 11-27.- Graph of $f(\lambda,\delta,\omega,\tau)$ for a diurnal cycle at the summer solstice, autumnal equinox, and July 27 and 28, 1966, for latitude 38° N.

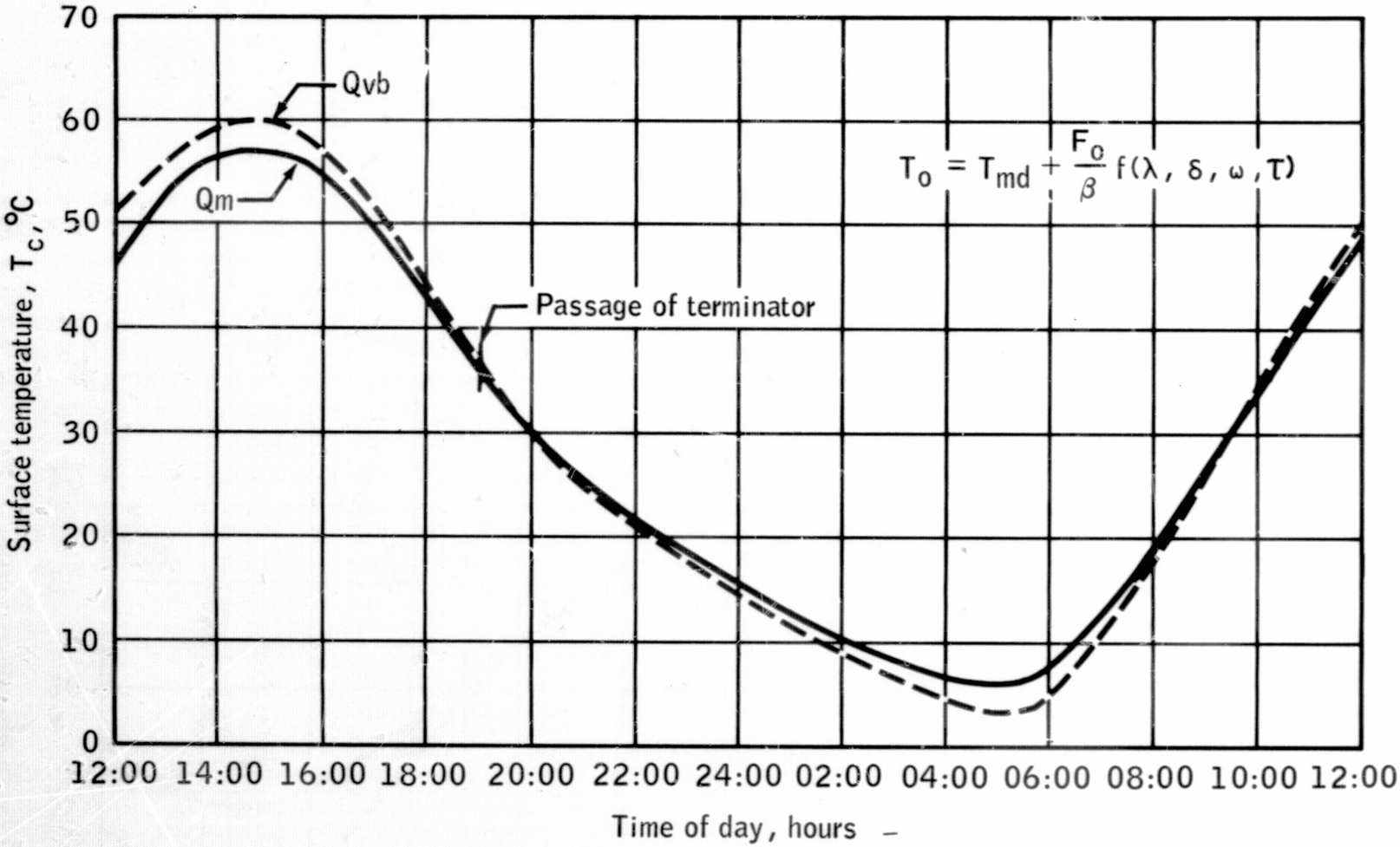

Figure 11-28.- Theoretical diurnal surface temperature variations for lacustrine carbonate deposits (Qm) of Black Point and for olivine basalt lapilli-ash (Qvb) of Black Point, July 27 and 28, 1966. T_{md} = 29° C, estimated coefficient of absorption of solar radiation for Qm ≅ 0.2 and for Qvb ≅ 0.75 and $F_{o,Qm} \cong 0.005$ cal-cm^{-2}-sec^{-1}; $F_{o,Qpbp} \cong$ 0.17 cal-cm^{-2}-sec^{-1}; λ = 38° N; δ = 19°20'; and $\omega = 2\pi/P$, where P = 86.400 seconds. Values of β in c.g.s. units are β_{Qm} = 0.011 and β_{Qvb} = 0.040.

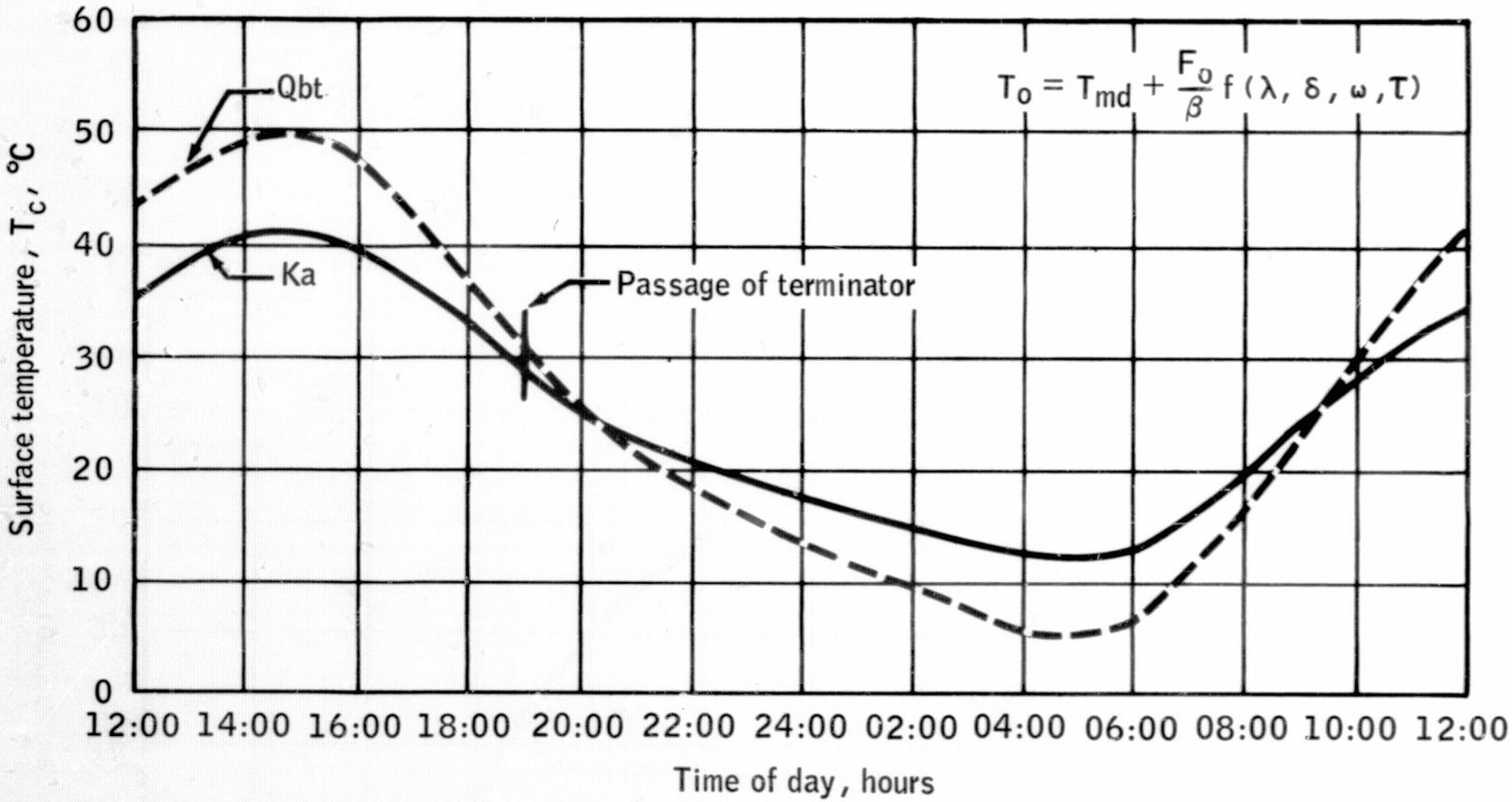

Figure 11-29.- Theoretical variation in surface temperatures of upper unit of Bishop tuff (Qbt) and quartz monzonite (Ka) of Aeolian Buttes, July 27 and 28, 1966. T_{md} = 25° C. The estimated coefficient of absorption of solar radiation for both Qbt and Ka $\cong$ 0.6; $F_{o,Qbt} \cong$ 0.015 cal-cm^{-2}-sec^{-1}; $F_{o,Ka} \cong$ 0.015 cal-cm^{-2}-sec^{-1}; λ = 38° N; δ = 19°20'; and $\omega = 2\pi/P$, where P = 86.400 seconds. Values of β in c.g.s. units are β_{Qbt} = 0.040 and β_{Ka} = 0.060.

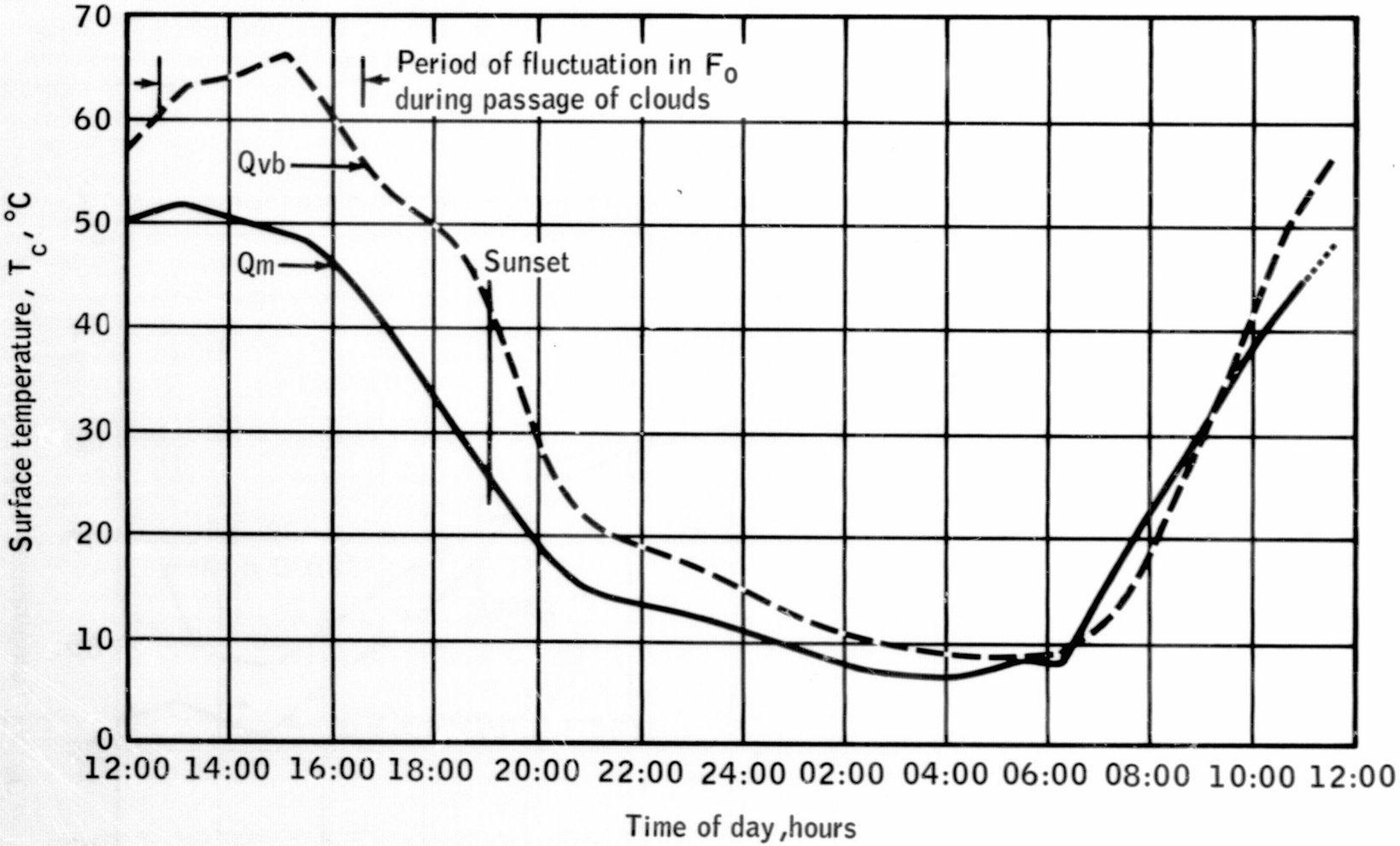

Figure 11-30.- Recorded variations in apparent surface temperature with time during a period of IR survey, Black Point, California, for two lithologies, July 27 and 28, 1966. Determined by variable-sequencer/thermistor-probe system. Qm is lacustrine carbonate crust, and Qvb is olivine basalt lapilli-ash of Black Point. The emissivity (8μ to 14μ) of Qm = 0.974 ± 0.002; the emissivity of Qvb = 0.985 ± 0.003.

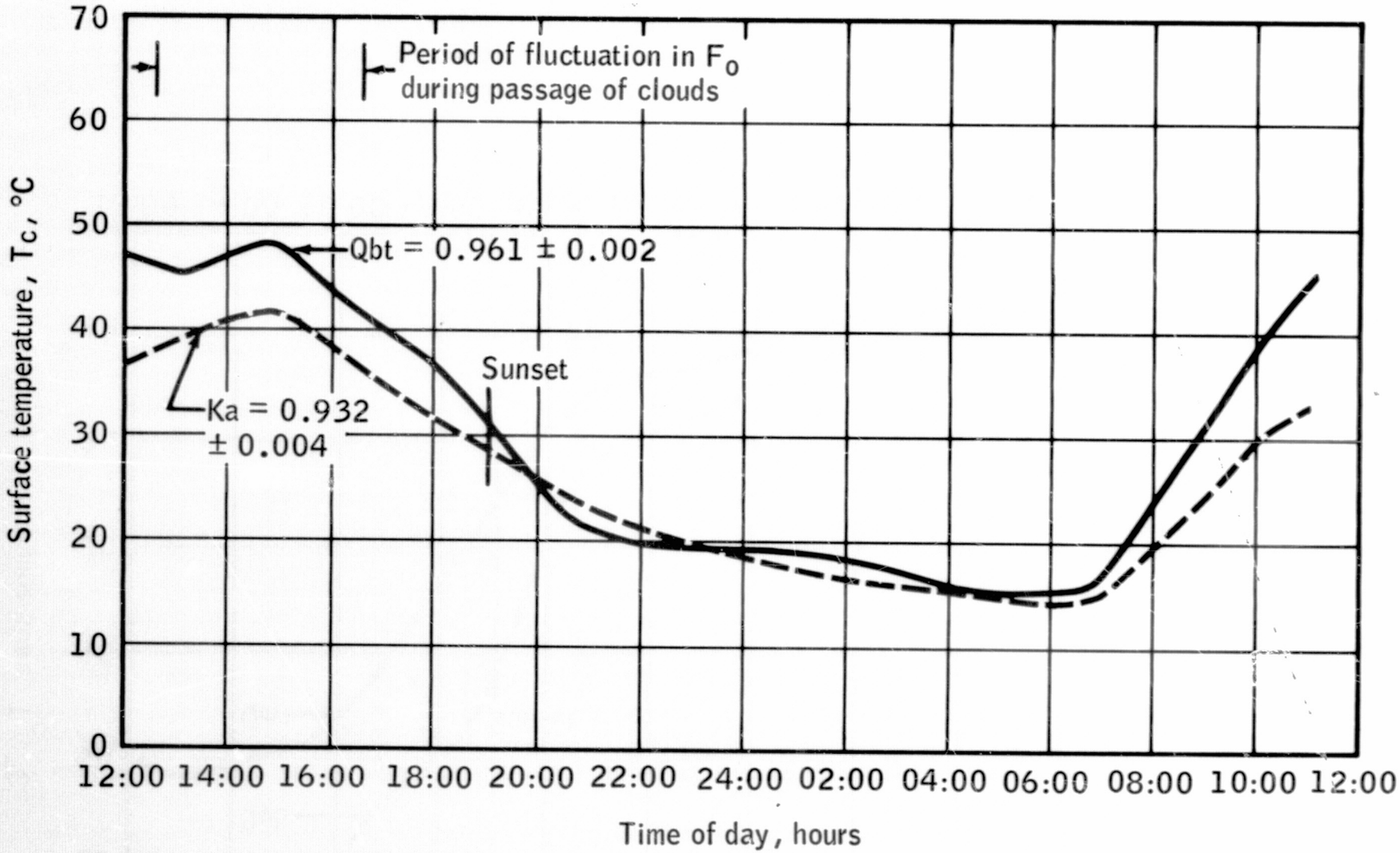

Figure 11-31.- Recorded variations in blackbody-equivalent surface temperature with time during period of IR survey, Aeolian Buttes, California, July 27 and 28, 1966. Determined by IT-3 Barnes IR radiometers. Ka is quartz monzonite, and Qbt is upper low-density unit of Bishop tuff. The emissivity (8μ to 14μ) of Ka = 0.932 ± 0.004; the emissivity of Qbt = 0.961 ± 0.002.

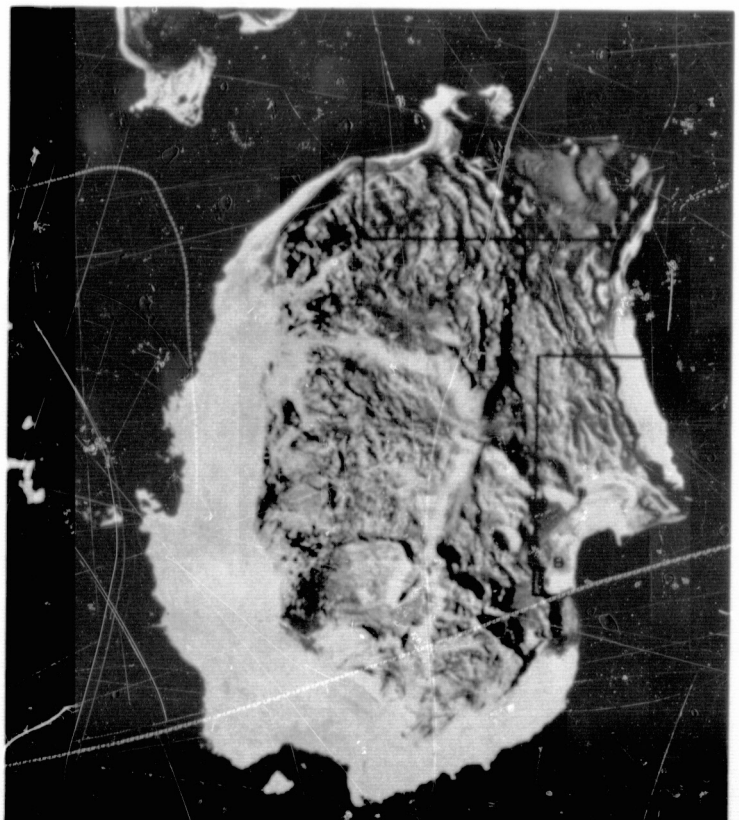

Figure 11-32.- Aerial photograph of Paoha Island showing areas scanned by isodensitracer technique. Arrows on east side indicate points of thermal emission.

a. Thermal spring and fumarolic deposits forming a southward-jutting peninsula along the probable extension of a fracture zone, eastern Paoha Island.

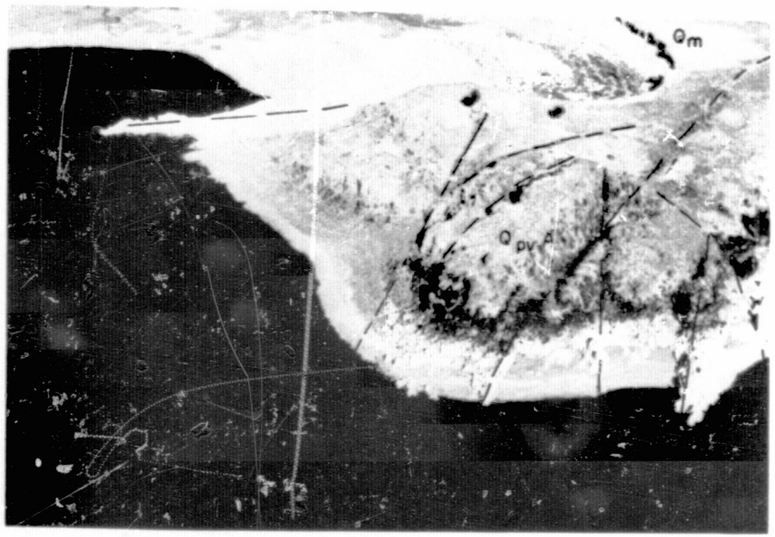

b. Recent andesite-basalt volcanics (QpvA) cut by fracture zones containing epithermal or thermal-spring deposits. Hot springs are concentrated along the lakeward extension of fracture zones.

Figure 11-33.- Photographs of thermal-spring deposits, recent andesite-basalt volcanics, structural deformation of wavecut bench, and the water morphology of Paoha and Negit Islands.

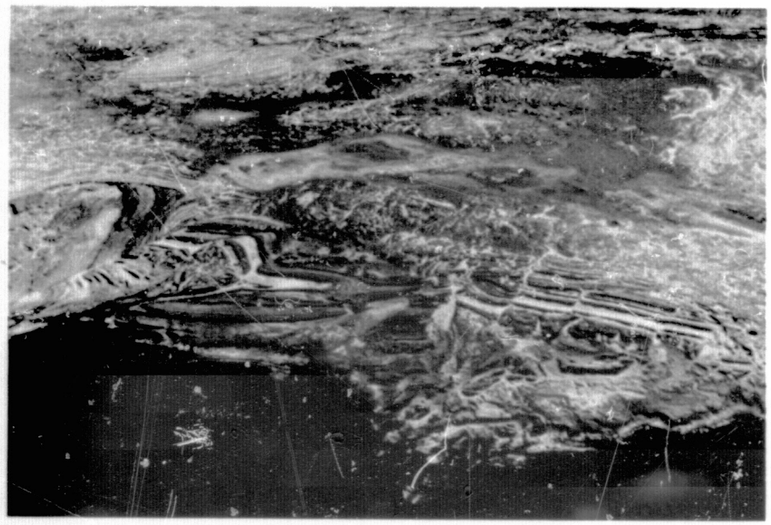

c. Structural deformation of lacustrine deposits (Qm) of wavecut bench, western Paoha Island.

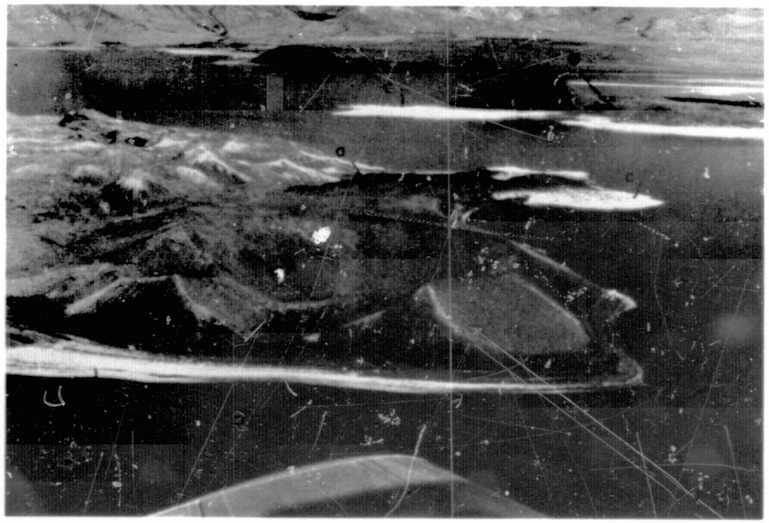

d. Northern Paoha and Negit Islands (view west). Note transecting pyroclastic craters in foreground and rough-surfaced flow forming ridge (area a) in the right middleground. The andesite-basalt crater and flows (area b) of Negit Island appear in the right background. Highly reflective diatomaceous lacustrine deposits (area c) form a rim around the volcanics of both Paoha and Negit Islands.

Figure 11-33.- Concluded.

Figure 11-34.- Subsided Santorin (Thíra) caldera in the Cyclades archipelago, Aegean Sea. Geologic features similar to Mono Lake basin include comparable scale, comparable recency of caldera subsidence, and late-volcanic stage emergence of central island craters with Néa and Palaiá Kaïméni analogous to Paoha and Negit Islands. There have also been parallel inward shifts of focus of volcanic activity with time toward Néa Kaïméni and Paoha, somewhat similar lithologies (Néa Kaïméni, andesitic volcanic products, Paoha, andesitic-basaltic volcanic products), similar widespread tephra layers resulting from earlier pyroclastic eruptions, and similar late-stage distribution of convective thermal anomalies peripheral to the central islands.

N71-16136

GEOLOGIC EVALUATION OF THERMAL INFRARED IMAGERY, CALIENTE AND TEMBLOR RANGES, SOUTHERN CALIFORNIA

By Edward W. Wolfe
U.S. Geological Survey

ABSTRACT

Thermal infrared (8μ to 13μ) imagery was obtained in the Caliente and Temblor Ranges and Carrizo Plain, southern California, in the predawn and postsunrise hours of June 18, 1965. Field observations, measurements of moisture and specific gravity of the regolith and radiation temperatures, and comparison with geologic maps and aerial photographs lead to the following conclusions:

1. The specific gravities of surficial materials (usually not bedrock) influence tonal densities in the predawn infrared imagery.

2. Geologic interpretation of tonal density patterns is complicated by topographic, atmospheric, and vegetative effects on predawn radiation.

3. Geologic features, such as outcrop patterns and some faults, are recognizable in the infrared imagery, as well as in aerial photographs. The sensitivity of the system to microclimatic anomalies may be valuable in aiding recognition of some geologic features with subtle topographic expression.

4. Local radiative anomalies, previously suggested to be caused by the occurrence of groundwater at shallow depths, may be caused by nighttime entrapment of cold air in poorly drained, topographically low areas.

5. Postsunrise infrared imagery is dominated by the preferential warming of slopes exposed to the early morning sun and resembles low-sun-angle photographs.

INTRODUCTION

Thermal infrared (IR) imagery, recording radiation from 8μ to 13μ in wavelength, was taken by NASA on June 18, 1965, in the Carrizo Plain of southern California. A line approximately normal to the regional geologic structure was selected for detailed analysis and is shown in figure 12-1. Localities at which supplemental observations were made are also shown in figure 12-1. A preliminary report on IR imagery from the Carrizo Plain was made by Wallace and Moxham (ref. 12-1). A published geologic map (ref. 12-2) was extensively used in the Caliente Range, and unpublished maps by T. W. Dibblee and J. G. Vedder were used to evaluate the IR imagery in the Temblor Range.

Figure 12-2 is a generalized geologic map of the area in which IR imagery was studied in detail. The stratigraphic nomenclature used on the map and in this report is that of Dibblee (ref. 12-3).

In the image area, the Caliente and Temblor Ranges are underlain by steeply dipping clastic rocks of late Tertiary age. In addition, three basalt flows occur within the Caliente Range sequence. The Caliente and Temblor Ranges in the image area are largely mantled by soil or debris derived from the underlying strata, and extensive outcrops of bare bedrock are rare.

INFRARED IMAGERY

The IR images (figs. 12-3 and 12-4) are line-scan displays of the areal distribution of radiation intensities in the 8μ- to 13μ-wavelength band. Areas of intense radiation are relatively light in tone; those of relatively weak radiation are dark in tone in the IR images. Radiation intensity varies directly with emissivity and with the fourth power of absolute surface temperature. Curvature near the IR image margins is a distortion inherent in the scanning technique.

Figure 12-3 is an IR image made shortly before dawn (05:06 to 05:10 Pacific daylight time) so that the effects of differential solar heating related to slope orientation are minimized. Figure 12-4 is an IR image made shortly after sunrise (06:35 to 06:38 Pacific daylight time). In this IR image, surfaces warmed by the sun appear relatively bright — much as they would in early morning photographs. Figure 12-5, an aerial photograph of the northeastern part of the imaged strip, was taken from approximately 35 000 feet on a midsummer day.

To facilitate comparison and discussion, observation points (localities) are numbered on the predawn and postsunrise IR images

(figs. 12-3 and 12-4) as well as on the aerial photograph (fig. 12-5). The following tabulated annotations are numbered to correspond to the numbers on figures 12-3 to 12-5. Unless specifically noted otherwise, the annotations refer to the predawn IR image (fig. 12-3).

1. The subparallel white lines coincide at least in part with local strike ridges on which bare sandstone beds and basalt flows are exposed. The pebbly texture is chaparral.

2. The white line coincides with a sharp break in slope at the outer edge of a terrace mantled by old alluvium.

3. Flat to slightly concave remnants of an old alluviated surface appear dark, as do portions of nearby stream canyons.

4. The white line coincides with a strike ridge on which the uppermost of three basalt flows forms a bold outcrop of bare rock.

5. This is the same strike ridge as item 2, but here, where the white line is indistinct, the basalt is mantled by soil and rubble.

6. The white line corresponds to a bare outcrop of hard, light-colored mudstone to sandy mudstone. The adjacent bedrock is mantled by soil.

7. The dark band corresponds to the outcrop of the Quatal Formation, a mudstone consisting largely of expanding clay in contact with sandstones of the Caliente and Morales Formations.

8. The small dark patches correspond to outcrops of reddish-brown expanding clay in the Morales Formation. The bordering materials giving brighter tones are sandy soils developed on the Morales Formation and deposits of sandy and gravelly alluvium that veneer all but the small areas represented by the dark spots.

9. This area is a low hill underlain by claystone, sandstone, and conglomerate of the Morales Formation. The hill is bounded by broad alluviated areas. In postsunrise IR imagery, the hill is more distinctly outlined because of preferential heating of slopes exposed to the sun.

10. This area is a small hill a few feet high and relatively bright. The hill lies within a dark region that corresponds approximately with the lowest part of the Carrizo Plain in the IR image area. The IR images show agricultural-field patterns and fan patterns where intermittent streams debouch onto the broad, alluviated Carrizo Plain. Because the Carrizo Plain is nearly flat, there is almost no preferential solar heating, and the postsunrise IR image closely resembles the predawn IR image.

11. The dark spots represent accumulations of tumbleweed against a fence at the northeast edge of the Carrizo Plain.

12. This is a northwest-trending trench along a recently active trace of the San Andreas fault. Well-drained gully bottoms, including the trench along the fault and the fine gullies forming a filigree pattern on the low ridge southwest of the fault, appear bright.

13. These are two elongate hills underlain by Bitterwater Creek Shale. The hills project through the alluvial apron that underlies the Elkhorn Plain at the foot of the Temblor Range. The Bitterwater Creek Shale is dark in the IR imagery, but the shale is bright in the aerial photograph.

14. This area is Bitterwater Creek Shale in contact to the northeast with very coarse conglomerate of the Santa Margarita Formation. The conglomerate and alluvial aprons that bound it on the southwest are bright and contrast sharply with the darkly imaged Bitterwater Creek Shale. In the aerial photograph (fig. 12-5), the contact between Santa Margarita conglomerate and alluvium is readily apparent.

15. Outcrops of downfolded Bitterwater Creek Shale are dark; the same outcrops are bright in the aerial photograph. The geologic map (fig. 12-2) portrays the distribution of sandstone and shale mapped together as Bitterwater Creek Shale. The IR imagery and the aerial photograph, however, display shale facies in sharp contrast to surrounding rocks, whether they be Santa Margarita Formation, a sandstone facies of the Bitterwater Creek, or the alluvium of the Elkhorn Plain.

16. The sharp radiation contact coincides with a fault separating Monterey Shale to the northeast from Santa Margarita conglomerate and a sandstone mapped with the Bitterwater Creek Shale. The conglomerate and the Bitterwater Creek sandstone, inseparable in the IR imagery as well as in the aerial photograph, contrast sharply with the Monterey Shale, which is dark in the predawn image and light in the aerial photograph.

17. The broad dark band occurs in an area underlain by Monterey Shale, shale and sandstone of the Temblor or Vaqueros Formation, and a sandstone unit at the base of the Santa Margarita Formation. Within the band, shale is the predominant lithology.

18. This is a contact between Monterey Shale (dark in the IR image, light in the aerial photograph) and an overlying Santa Margarita Formation (light in the IR image, dark in the aerial photograph).

19. This is a radiation boundary at the northwestern limit of a conglomerate facies (light in the IR image) of the Santa Margarita

Formation within the IR image area. Farther northwest within the IR image area, the Santa Margarita Formation consists predominantly of friable sandstone (dark in the IR image) with rare granitic or metamorphic boulders. In the aerial photograph, the conglomerate facies is darker than the sandstone facies.

20. This sharp radiation boundary coincides with the crest of the Temblor Range. Immediately northeast of the range crest, the Santa Margarita conglomerate, the Media Shale, and the Temblor or Vaqueros Formations all appear bright. Most of the slope for approximately a mile and a half northeast of the range crest in the IR image area is underlain by grass-covered Monterey Shale colluvium that appears relatively bright.

21. The dark band coincides with a prominent, steep, southwest-facing slope nearly devoid of vegetation. The slope is underlain in part by diatomite (mapped by Dibblee (ref. 12-3) as Reef Ridge Formation (fig. 12-2)) and in part by Monterey Shale.

22. This is a sharp radiation contact between Reef Ridge diatomite (dark in the IR image, bright in the aerial photograph) and overlying Santa Margarita conglomerate (bright in the image, dark in the aerial photograph).

23. The small dark spots coincide with windows in a gravel colluvium, through which Reef Ridge diatomite is exposed in the Fellows oil field.

24. The dark band coincides with a steep, barren, southwest-facing slope on which Reef Ridge diatomite is exposed. The Santa Margarita conglomerate southwest of the diatomite and the gravels of the Tulare Formation northeast of the diatomite appear bright. Near the northeast end of the IR image, the community of Fellows stands on undeformed younger alluvial deposits.

The intensity of predawn IR radiation in the Temblor Range is apparently related in part to slope orientation. In the predawn IR imagery (fig. 12-3), north-facing slopes tend to be relatively bright, and south-facing slopes tend to be dark. The largest topographic feature showing this tendency is the crest of the Temblor Range. Near locality 20, a well-defined radiative boundary separates similar lithologic types at the range crest. While the northeast flank of the range is relatively bright, the southwest flank is relatively dark. A few other examples of this tendency, denoted by letters in figures 12-3 to 12-5, are as follows:

a. The steep north-northeast-facing hill in Monterey Shale is bright in the predawn IR imagery (fig. 12-3). The hill is strikingly warmed by the early morning sun (fig. 12-4).

b. The hill underlain by basal sandstone of the Santa Margarita Formation is dark on the south side and bright on the north side in figure 12-3.

c. In the gullied area, just southwest of the range crest, the southeast-facing slopes are dark.

d. Three small ridge crests are on the northeast flank of the range. All three crests are dark on the south side and bright on the north side in the predawn IR image.

e. The steep northeast-facing canyon walls within the dark band at locality 21 are brighter than the nearby southwest-facing slopes. All of these walls and slopes are underlain by diatomaceous Monterey Shale.

GROUND MEASUREMENTS

In an attempt to find systematic relationships between ground conditions and tonal densities in the predawn IR image, radiation temperature, specific gravity, and moisture data were collected late in May 1967. According to U.S. Weather Bureau records, no rain fell in the area in May or June prior to the IR flight on June 18, 1965. Rainfall in April 1965 was approximately 2 inches, both east of the area at Maricopa and west of the area at Cuyama. In April 1967, 1.85 inches of rain fell at Maricopa, and 2.82 inches fell at Cuyama. During May 1967, 0.02 inch of rain fell at both Cuyama and Maricopa approximately 2 weeks before the ground data were collected. In spite of the slightly wetter weather in the spring of 1967, the ground in late May in the area of figures 12-3 to 12-5 seemed thoroughly dry, and the grass cover was brown.

Radiation temperatures were measured with a hand-held Barnes IT-3 radiometer over a period of 2 days and 3 nights from May 22 to 25, 1967, at two different sites near contacts between Bitterwater Creek Shale and alluvium (locality 13). Infrared radiation, the quantity measured by the radiometer, varies as emissivity and as the fourth power of the absolute temperature.

$$W = \varepsilon\sigma T^4$$

where W = total radiation per unit area (8μ to 13μ radiation in this case)

ε = emissivity

T = absolute temperature (°K)

σ = a constant

The emissivity of an object is the ratio of its emittance (radiant energy emitted per unit area) to the emittance of a perfect radiator (blackbody) at the same temperature. Blackbodies exist in theory only; real substances have emissivities smaller than 1. The radiometer measures emittance, but indicates a temperature scale based on an emissivity of 1. Because natural materials have emissivities smaller than 1, radiation temperatures are lower than true temperatures. In the temperature range in which this study was made, a change of 0.05 in emissivity for high emissivities produces a change of approximately 4° C in apparent temperature. Greater distortion occurs with low emissivities.

Laboratory radiometer measurements of large samples of surficial material collected from Bitterwater Creek Shale, Santa Margarita conglomerate (cobbles and boulders excluded), Monterey Shale, Reef Ridge diatomite, Quatal Formation, Morales Formation, and alluvium of the Elkhorn Plain suggest that differences in radiant emittance are not caused by emissivity differences related to the compositions of the soils. Radiation temperatures of the samples, which stood for several weeks in a normally heated room, were all within 1° C of each other, with a systematic variation that was apparently related to position in the room rather than to lithology. The apparent temperatures (near 72° F) approximated room temperature and suggested that all of the samples had high emissivities.

Figure 12-6 displays radiation-temperature data collected on typical grass-covered sandy alluvium and on barren soil developed on Bitterwater Creek Shale. The same relationship, with Bitterwater Creek Shale appearing colder both day and night, was later repeated at a second site. Radiation from alluvium with relatively sparse grass cover and from Bitterwater Creek Shale with sparse grass cover was intermediate between the extremes of barren Bitterwater Creek Shale and typically grassy alluvium both day and night. Single boulders in the alluvium were slightly more radiant in the predawn hours than the deposits that included them. The radiometer measurements show that the radiation patterns recorded in the IR imagery are reproducible, and the measurements suggest that physical properties, such as specific gravity and moisture content, that may have affected radiance when the IR images were made, were also effective in May 1967, when field observations were made.

Densities and moisture contents of representative surficial materials were determined. Approximately 1000 cubic centimeters of soil

from the uppermost 2 inches were carefully collected and immediately weighed. Volume was determined by filling the excavation with a measured quantity of sand, and density was computed. Moisture content was determined by comparing the sample weight after several days of drying at 110° C with the sample weight at the time of collection. Surficial materials developed on sandy alluvium, sandstone units, and Santa Margarita conglomerate (cobbles and boulders excluded from measurements) range in density from approximately 1.3 to 1.5 and in moisture content from 1.6 to 2.8 percent. Surface materials representing shale units range in density from approximately 1.0 to 1.1, and their moisture contents range from 5.3 to 8.4 percent. The specific gravity of diatomite surficial debris from the east side of the Temblor Range (locality 18) is approximately 0.9. From X-ray data, it is seen that much of the shale and mudstone is montmorillonitic; the high moisture contents may represent water driven from the clay mineral structure by heating rather than high accumulations of pore water. In late May, soils in the area of figures 12-3 to 12-5 looked and felt thoroughly dry.

SYNTHESIS

Comparison of the predawn IR image, the aerial photograph, and the ground data suggest that intensity of predawn radiance may be related to specific gravity of soil, vegetative cover, reflectivity, slope orientation, and microclimatic effects as summarized in the following table.

Low predawn radiance	High predawn radiance
Low specific gravity (approximately 1.0)	High specific gravity (approximately 1.3)
Little or no grass cover	Relatively thick grass cover
Bright appearance in aerial photograph (high reflectivity)	Dark appearance in aerial photograph (low reflectivity)
Slope facing south	Slope facing north
Entrapment of cold air	

Soils developed on shale, mudstone, and diatomite have low specific gravities (approximately 1.0) and ordinarily are dark in the predawn IR

image (localities 7, 8, 13, 14, 15, 16, 17, 18, 21, 23, and 24). The same soils generally support little or no grass cover, and the sunlight reflected is relatively intense, as shown by the aerial photograph. In contrast, soils developed on Santa Margarita conglomerate, most sandstone units, and sandy alluvium have higher specific gravities (approximately 1.3) and tend to be bright in the predawn IR image (localities 8, 14, 15, 16, 18, and 22). These soils support more vegetation than the shales and reflect less sunlight, as shown by their darkness in the aerial photograph. In addition, south-facing slopes tend to be less radiant in the predawn IR image than north-facing slopes. Hence, the intensity of predawn radiance from any surface may be controlled by several factors. Microclimatic effects related to nocturnal density-stratification of air apparently produce additional local radiative anomalies that are discussed later.

Specific Gravity

Specific gravity of surficial material plays an important role in determining the thermal inertia of the material, which is a measure of the resistance of the surface of the material to temperature change.

$$\text{thermal inertia} = K\rho C$$

where K = thermal conductivity

ρ = specific gravity

C = specific heat

Surface materials with high thermal inertia react slowly to external temperature changes and, other factors being equal, should be warmer in the predawn hours than surficial materials with low thermal inertia.

Materials with high thermal conductivity transmit heat relatively easily, and changes in surface temperature occur relatively slowly in response to a change in external temperature. Air, water, and solid rock increase in thermal conductivity in the ratio of approximately 1:25:90. Hence, dry porous material has relatively low thermal conductivity, and the surface temperature changes quickly in response to external temperature changes. Specific heat, a measure of heat input necessary to produce a given temperature increase, is approximately five times as high for water as for air or mineral grains. Insofar as an inverse relation exists between specific gravity and porosity in the surficial materials of the IR image area, thermal conductivity, thermal inertia, and, hence, predawn radiance increase with specific gravity.

In addition to the relationship previously noted between soil of low specific gravity and low predawn radiance, the following observations support the correlation between specific gravity and predawn radiance:

1. Outcrops of bare bedrock (localities 1, 4, and 6) with specific gravities much higher than those of the surrounding soils are displayed in the IR imagery as bands of high predawn radiance. It should be noted that a similar band (locality 2) apparently coincides only with a sharp break in slope.

2. As indicated by radiometer measurements in the predawn hours, single boulders were slightly more radiant than the unconsolidated alluvium that surrounded them.

3. Tumbleweed piled along a fence at locality 11 forms a surficial material that, because of its extremely low specific gravity and high porosity, has low thermal inertia and appears dark in the predawn image.

4. Wallace and Moxham (ref. 12-1) showed that unplowed fields in other Carrizo Plain IR images were brighter in the predawn hours than plowed fields. Plowing, by increasing the porosity and lowering the specific gravity of soil, lowers thermal inertia of the soil.

Grass Cover and Reflectivity

Radiometer measurements (fig. 12-6) in late May showed that Bitterwater Creek Shale at locality 13 was less radiant than the adjacent alluvium during both day and night — an unlikely situation if thermal inertia were the sole controlling influence. Perhaps vegetative cover and/or reflectivity influence radiance in one of the following ways:

1. Figure 12-6 shows radiometer measurements on typically barren shale and on typically grassy alluvium. Radiant temperatures on slightly grassy shale and on alluvium with relatively thin grass cover were intermediate between the extremes shown in figure 12-6. Gates (ref. 12-4) states that all plant surfaces have emissivities of 0.95 or greater, and most leaf emissivities are 0.97 to 0.98. It may be that the grass-covered surfaces are slightly higher in emissivity than the barren surfaces. Under the existing conditions, an increase in emissivity of 0.05 would produce a radiant temperature increase of approximately 4° C, a temperature difference consistent with the radiometer results.

2. Possibly, the Bitterwater Creek Shale, bright in the aerial photograph, absorbs less heat than the surrounding alluvium in the daytime because of its relatively intense reflection of solar radiation. Elsewhere in the study area, south slopes underlain by shale tend to be

relatively barren and to reflect solar radiation more intensely than adjacent areas underlain by sandstone, conglomerate, and alluvium.

The barren shales, in addition to absorbing less energy from incoming solar radiation, may cool more rapidly at night because of relatively low thermal inertia. Probably, thermal inertia, vegetative cover, and reflectivity interact complexly in controlling predawn radiance throughout the IR image area.

Slope Orientation

North slopes in the Temblor Range are more radiant in the predawn IR image than nearby south slopes underlain by similar lithologies. In some places, vegetation is more lush on north slopes than on south slopes, but the relationship is not consistent. Untested hypotheses include the possibility that slightly higher moisture content in soils on north slopes may have caused slightly higher thermal inertia or that atmospheric interference such as high clouds to the north at the time of the flight could have impeded radiation to space from the north slopes.

Microclimatic Effects

In addition to the influences of specific gravity, vegetative cover, and slope orientation on IR image tonal densities, microclimatic effects related to local topographic features apparently influence predawn ground temperature and cause radiative anomalies. Low predawn radiance at localities 3 and 10 is attributed to nocturnal accumulation of cold air on poorly drained ground surfaces, a phenomenon extensively documented by Geiger (ref. 12-5). The diamond-shaped dark area at locality 3 in figure 12-3 is a flat surface, or possibly even a shallow, closed depression, partially enclosed by surrounding hills. The surface is underlain by old alluvium, which is sandy and closely resembles in both texture and vegetative cover other alluvial deposits that appear bright in figure 12-3. The suggested interpretation of the diamond-shaped area is that it represents an area in which cold air accumulates preferentially at night, and the surface beneath the colder air becomes slightly cooler than nearby surfaces. A similar interpretation is suggested at locality 10, where the dark region in the IR image coincides approximately with the lowest part of the valley floor in the image area. A small hill projecting through the colder air strata is slightly warmer and appears brighter in figure 12-3.

Gullies at locality 12 appear bright in the predawn IR image, and surface temperatures were no doubt warmer than on the adjacent interfluves. Although the gullies are local topographic lows, the gullies

may be well drained relative to airflow so that development of the stagnation, by which a thick cold-air layer accumulates, cannot occur.

The hypothesis that entrapment of cold air causes radiative anomalies was documented in an effort to test the suggestion that some dark anomalies in predawn IR imagery represent high soil moisture (refs. 12-1 and 12-6). Two areas cited by Wallace and Moxham (ref. 12-1) as places where low radiation might reflect high soil-moisture content were selected for study.

Figure 12-7 is a predawn IR image of a site located along the San Andreas fault east of Soda Lake. The rectangular pattern is a network of subdivision roads. A recently active trace of the San Andreas fault is bounded on the southwest by a scarp, the crest of which is bright in the IR image. The ground surface to the northeast slopes toward the scarp, and the area represented by the dark band is the topographically lowest area northeast of the scarp. Tumbleweed, which has accumulated against the scarp, is imaged as a thin, very dark band bounding the bright scarp on the northeast. In late May 1967, the grass was green, and the soil was visibly damp in places at the foot of the scarp. Moisture measurements in late October 1967 showed 3-percent soil moisture at the top of the scarp and 7-percent soil moisture at the base. Radiometer readings in late October showed an apparent temperature of 8° C on the scarp crest and 5° C at the base.

Predawn air temperature was measured at 1, 16, and 31 inches above the ground at the scarp crest, scarp base, and in between. The data, summarized in table I, show that at any point along the scarp, stratification of the air is strongly developed and that the air becomes appreciably colder as one moves down the scarp. The low area is a trap for cold air, which lowers the local ground temperature. The high radiant temperature (5° C) at the base of the scarp may indicate that the relatively tall grass projected through the coldest air layers into the overlying warmer air.

Figure 12-8 is a predawn IR image of a second site near the southeast end of the Carrizo Plain. The dark roughly triangular area in the center of the IR image is a flat, partly closed alluvial surface bounded on the northwest and southeast by low gravel hills that are bright in the IR image. The semicircular bright feature overlapping the southwest flank of the dark triangular area is an alluvial fan. The flat bottom of the depression and the surrounding hills appear extremely dry. Much of the depression floor is barren of grass, and there are no visible signs of moisture. Soil moisture measurements show 2 percent of moisture at the crest of one of the gravel hills and 4 percent of moisture on the flat surface below. However, the flat surface is floored by fine-grained clay-rich sediment, and the slightly higher moisture content can probably be accounted for as water driven out of clay minerals by heating.

Predawn temperature measurements showed well-developed air stratification with air temperatures from 2° to 4° C lower at ground level on the flat than at ground level on the low gravel hills. The low flat area is poorly drained relative to air flow and permits the accumulation of a layer of dense, cold air.

TABLE 12-I.- AIR AND GROUND TEMPERATURES[a] MEASURED ALONG SAN ANDREAS FAULT EAST OF SODA LAKE, 4:30 a.m. OCTOBER 25, 1967

Height above ground, in.	Top-of-scarp temperature, °C	Middle-of-scarp temperature, °C	Base-of-scarp temperature, °C
31	9.5	7.5	5.5
16	9	7	4
1	7	6	1
Ground	8	--	5

[a]Air temperatures are measured by thermometer; ground temperatures are radiation temperatures measured by Barnes IT-3 radiometer.

Measurements made by A. O. Waananen and C. T. Snyder (unpublished data) indicate that predawn evaporation of water in arid regions is vanishingly small, and the measurements cast doubt on hypotheses that radiative anomalies, such as the anomaly shown in figure 12-8, reflect high soil moisture content. Evaporation from an open water surface in a 4-foot-diameter evaporating pan was measured continuously for several days in late July 1963. The pan was set on a playa surface near Coaldale, Nevada. Air temperature taken at 5 feet above the playa surface ranged from approximately 14° C at night to 38° C in the daytime. Relative humidity, also measured at an altitude of 5 feet, was extremely low, ranging from approximately 0 percent in the daytime to 25 percent at night. Total daily evaporation averaged approximately 0.4 inch, but evaporation from the open pan between midnight and 6 a.m. totaled less than 0.05 inch.

In view of the very low predawn evaporation from an open water surface in the extremely dry atmosphere of the Nevada playa, it seems doubtful that the radiative anomaly of figure 12-8, for which surface moisture content was, at most, a few percent, was a product of evaporative cooling. In addition, the effect of high soil moisture on thermal inertia would act to inhibit nocturnal cooling, and, in the absence of significant evaporative cooling, moist soils might be warmer than dry soils in the predawn hours. It seems most likely that the radiative anomalies of figures 12-7 and 12-8 are predominantly responses to microclimatic effects created by preferential accumulation of cold air.

CONCLUSIONS

Tonal densities in thermal IR imagery may reflect, in part, the specific gravities of surficial materials. Surficial materials with relatively high specific gravities tend to be bright in the predawn IR image. However, effects related to atmospheric conditions, topographic setting, and vegetation may also produce marked anomalies in the imagery. Furthermore, even in the relatively well-exposed geology of the Caliente and Temblor Ranges, the IR imagery was largely controlled by properties of soil — not by bedrock. Lithologic inferences based on qualitative comparisons of radiation from soils, with the radiation complexly modified by topographic, atmospheric, and vegetative effects, are difficult.

The predawn IR imagery shows many geologic features, such as outcrop patterns and faults, that are also discernible in aerial photographs. Because of the potential of IR imagery to display microclimatic anomalies, it might be a valuable adjunct to other types of imagery in mapping geologic features, such as recently active faults that have very subtle topographic expression.

It has been suggested that anomalously weak predawn radiation might indicate soil moisture concentrations related to shallow groundwater in low areas between landslide lobes or in areas where faults might act as barriers to groundwater (refs. 12-1 and 12-6). Two anomalies of this type were investigated and may have been produced largely, if not entirely, by density stratification of air.

Postsunrise IR imagery shows the strong influence of solar warming of surfaces exposed to the sun. Topography is the dominant control of tonal densities in the IR image, which resembles a low-sun-angle photograph.

REFERENCES

12-1. Wallace, R. E.; and Moxham, R. M.: Use of Infrared Imagery in Study of the San Andreas Fault System, California. U.S. Geol. Survey Tech. Letter NASA-42, 1966. Also in Geological Survey Research 1967, U.S. Geol. Survey Prof. Paper 575-D, 1967, pp. D147-D156. Abs. in Symposium Remote Sensing of Environment, 4th (Michigan Univ., Ann Arbor), Infrared Physics Lab., Abstracts, p. 24.

12-2. Vedder, J. G.; and Repenning, C. A.: Geologic Map of the Southeastern Caliente Range, San Luis Obispo County, California. U.S. Geol. Survey Oil and Gas Inv. Map OM-217, 1965.

12-3. Dibblee, T. W., Jr.: Displacements on the San Andreas Rift Zone and Related Structures in Carrizo Plain and Vicinity [California]. Guidebook, Geology of Carrizo Plains and San Andreas Fault. San Joaquin Geol. Soc. and Am. Assoc. Petroleum Geologists, Soc. Econ. Paleontologists and Mineralogists, Pacific Sec. [field trip], 1962, pp. 5-12.

12-4. Gates, D. M.: Characteristics of Soil and Vegetated Surfaces to Reflected and Emitted Radiation. Paper Presented at Symposium Remote Sensing of Environment, 3d (Michigan Univ., Ann Arbor), Infrared Physics Lab., Proc., 1964, pp. 573-600.

12-5. Geiger, R. E.: The Climate Near the Ground. Harvard Univ. Press (Cambridge, Mass.), 1957.

12-6. Sabins, F. F., Jr.: Infrared Imagery and Geologic aspects. Photogrammetric Engineering, vol. 33, no. 7, July 1967, pp. 743-750.

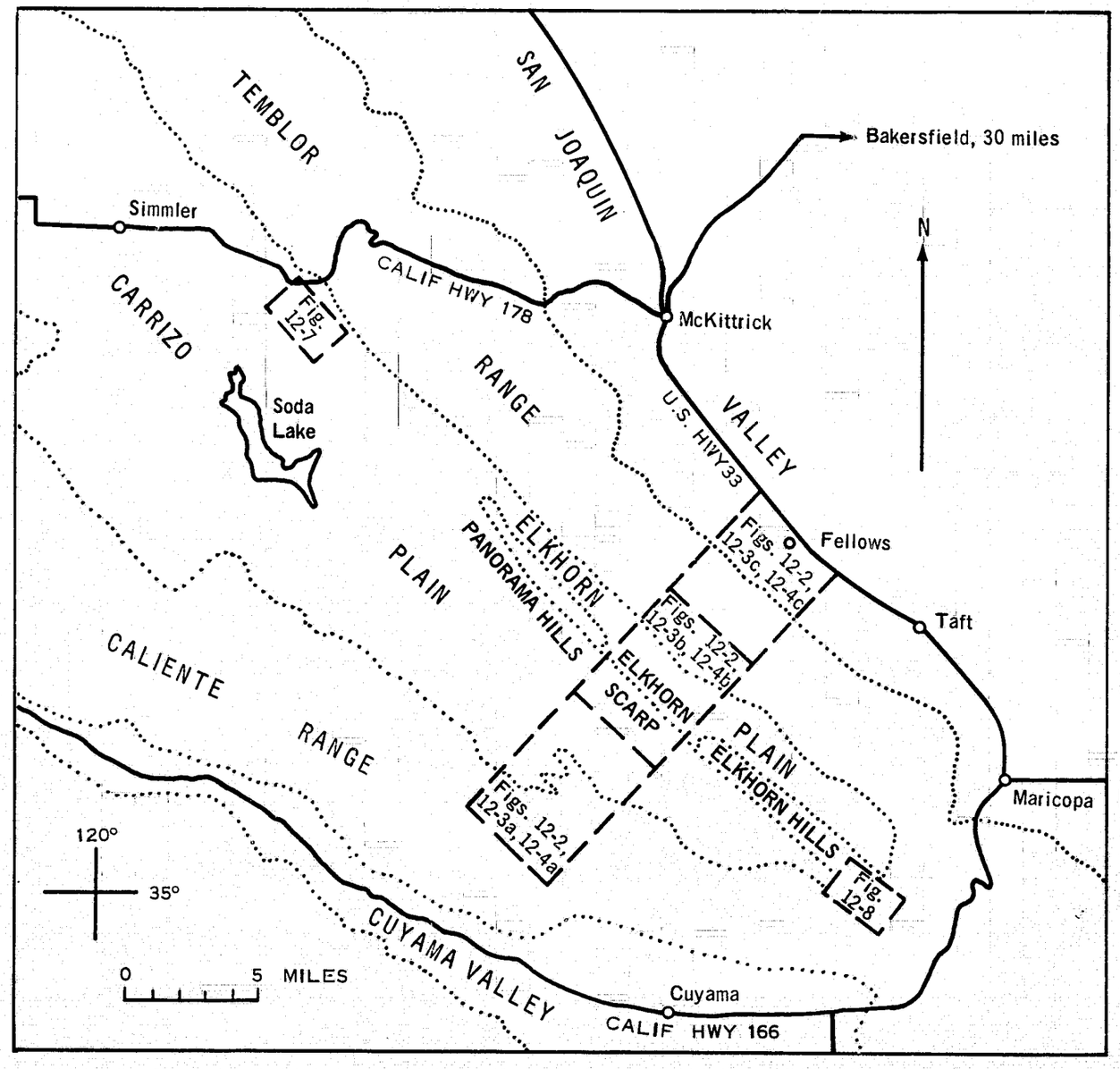

Figure 12-1.- Index map showing major physiographic features and approximate locations of areas described and illustrated in this report.

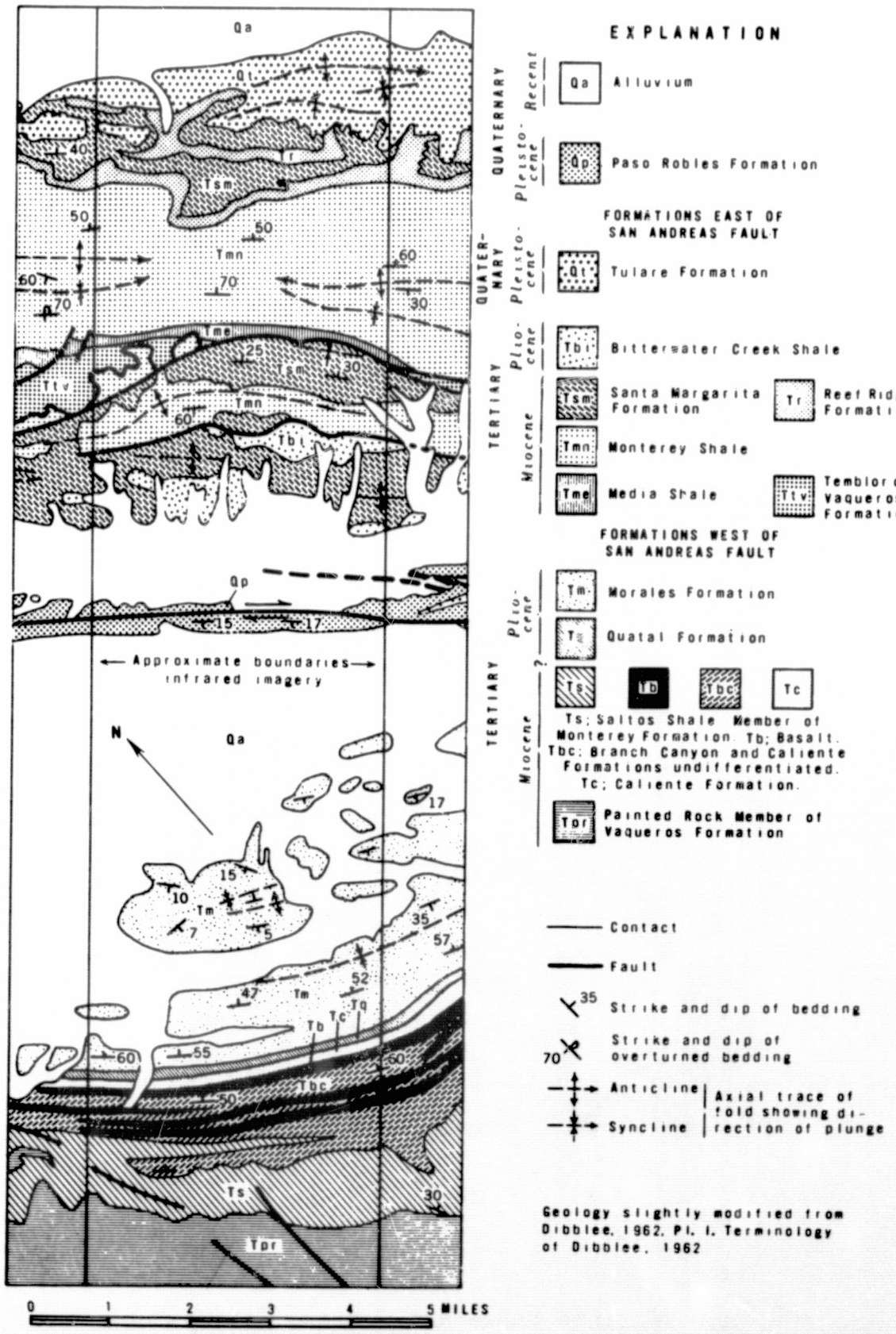

Figure 12-2.- Generalized geologic map of study area.

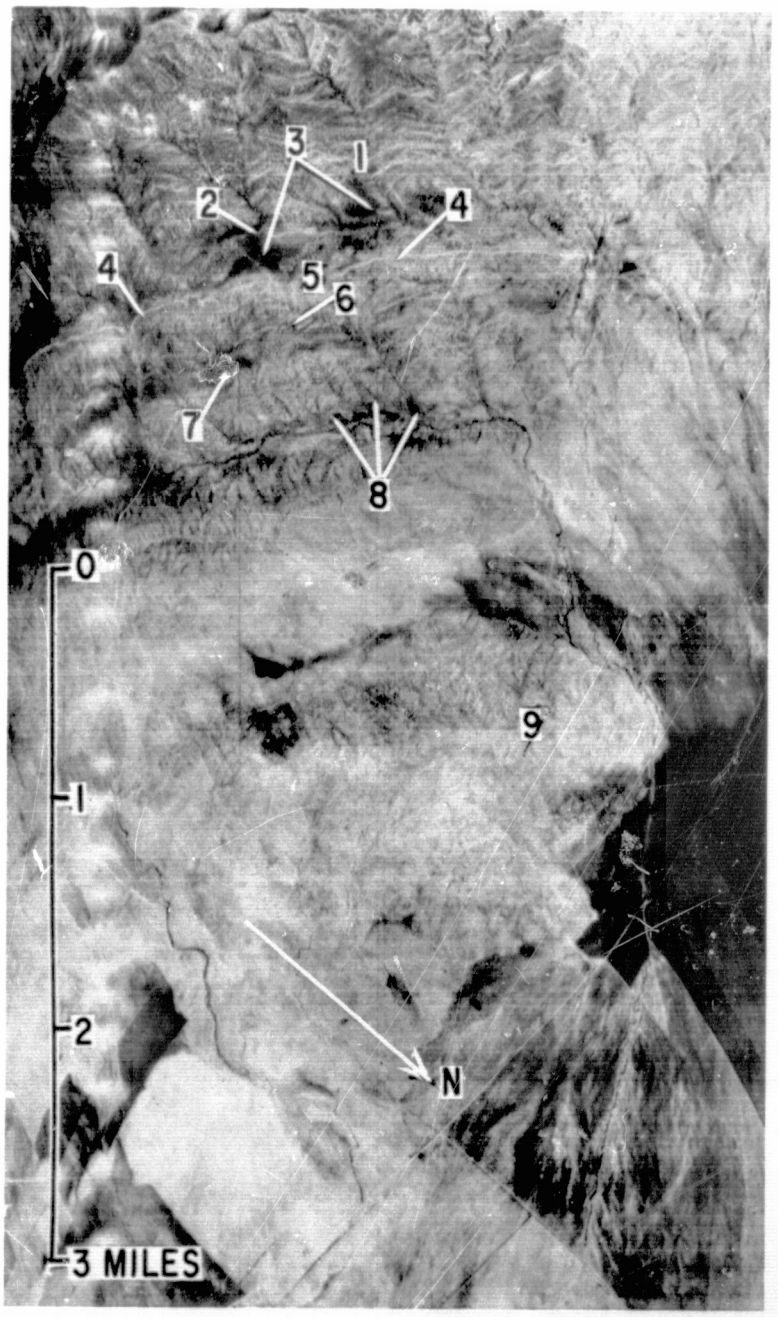

a. Caliente Range and Carrizo Plain.

Figure 12-3.- Predawn IR image.

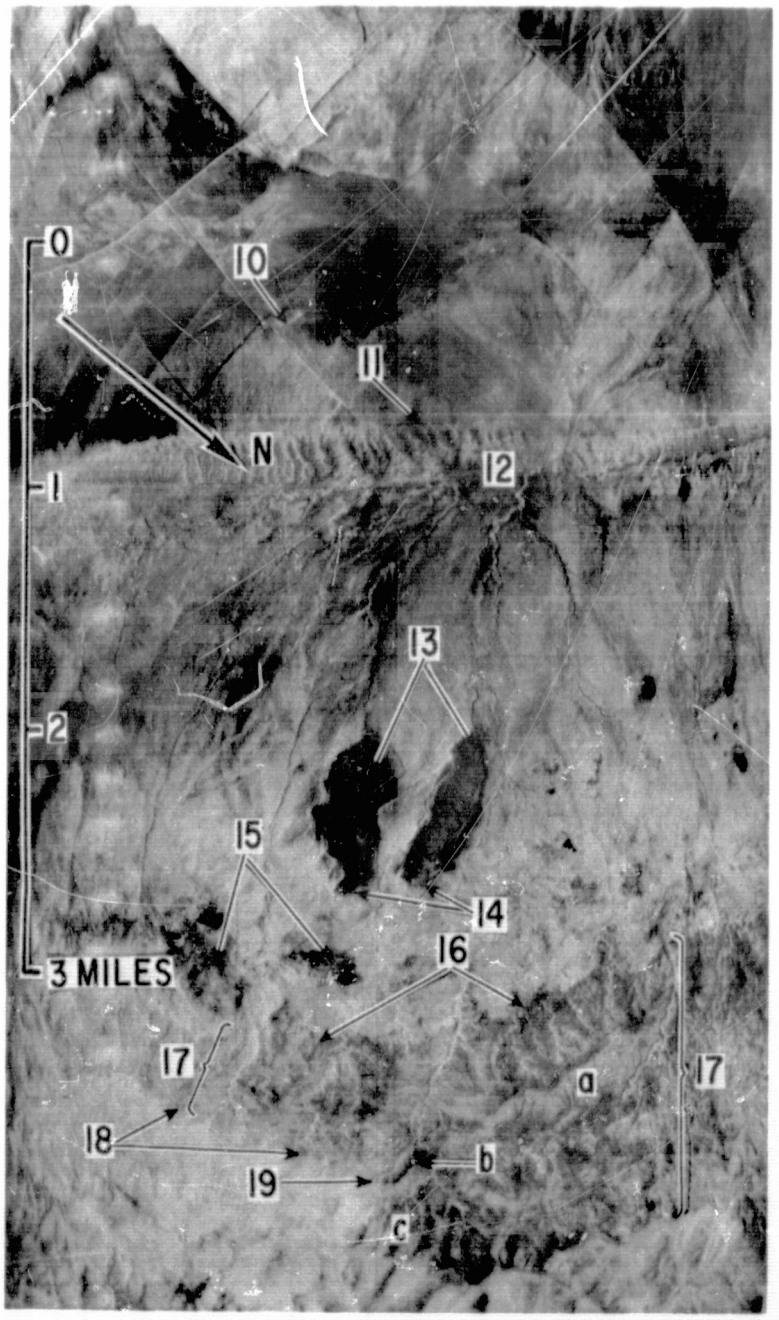

b. Carrizo Plain, Elkhorn Plain, and Temblor Range.

Figure 12-3.- Continued.

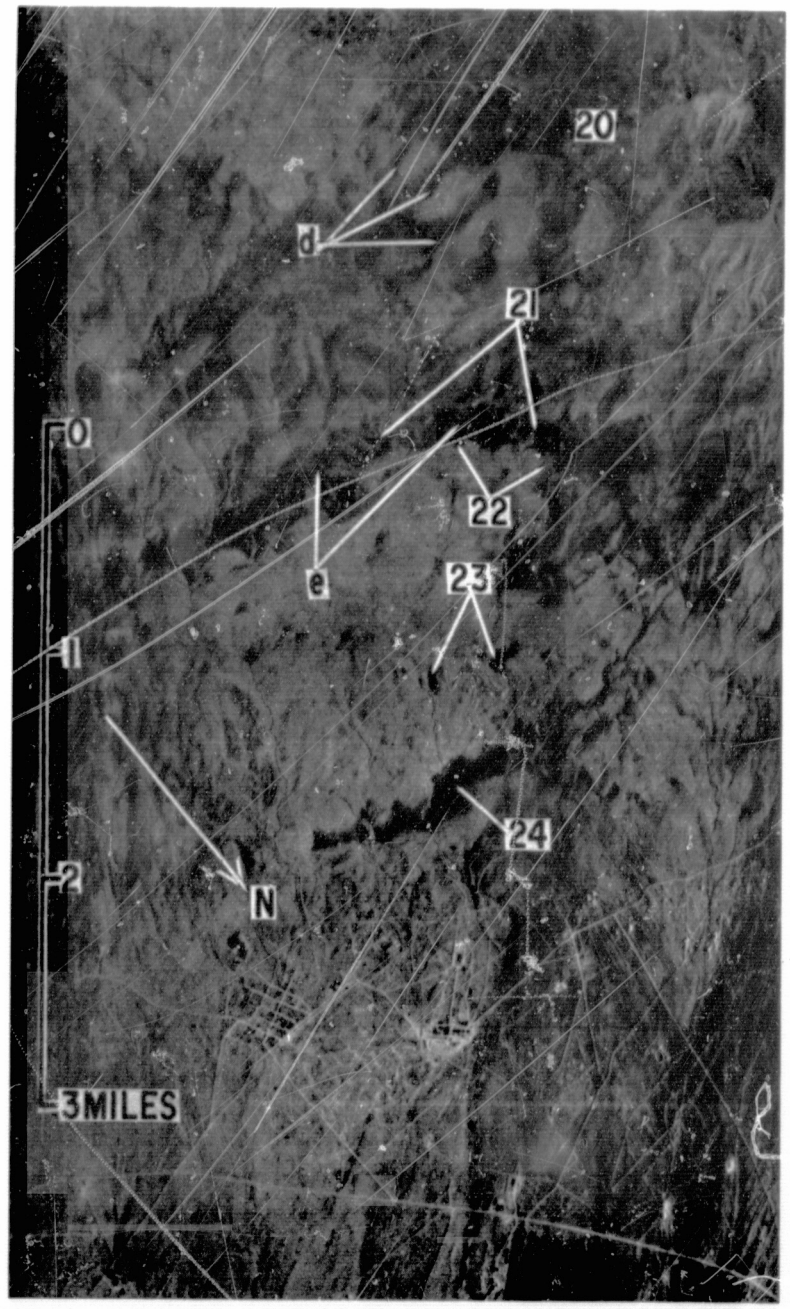

c. Temblor Range.

Figure 12-3.- Concluded.

a. Caliente Range and Carrizo Plain.

Figure 12-4.- Postsunrise IR image.

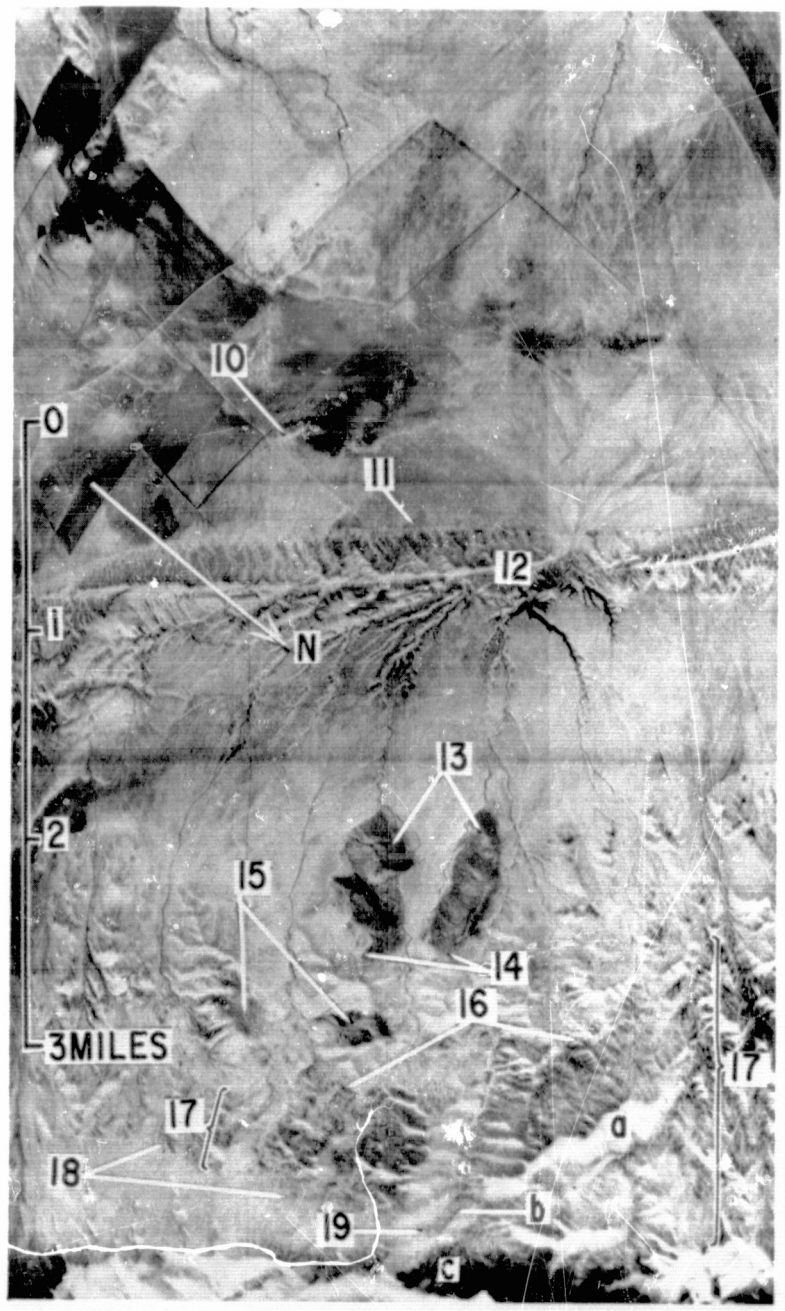

b. Carrizo Plain, Elkhorn Plain, and Temblor Range.

Figure 12-4.- Continued.

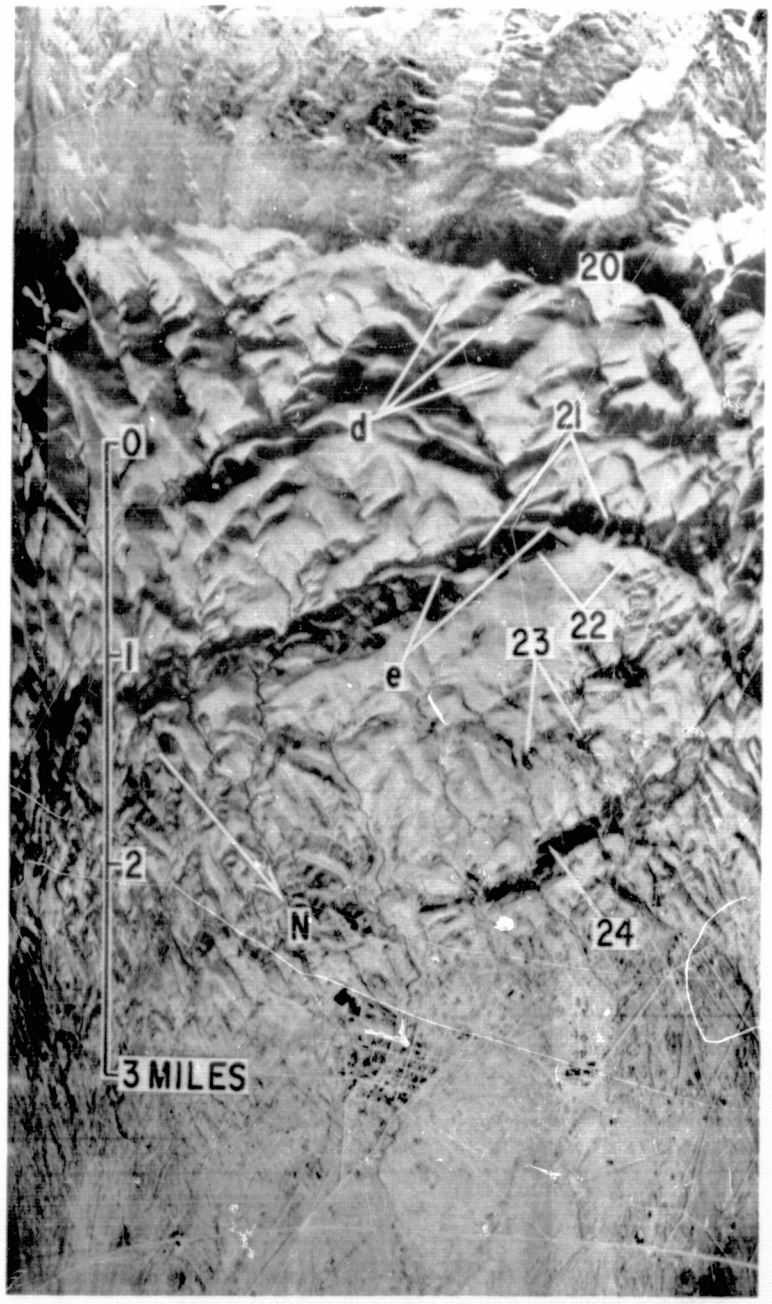

c. Temblor Range.

Figure 12-4.- Concluded.

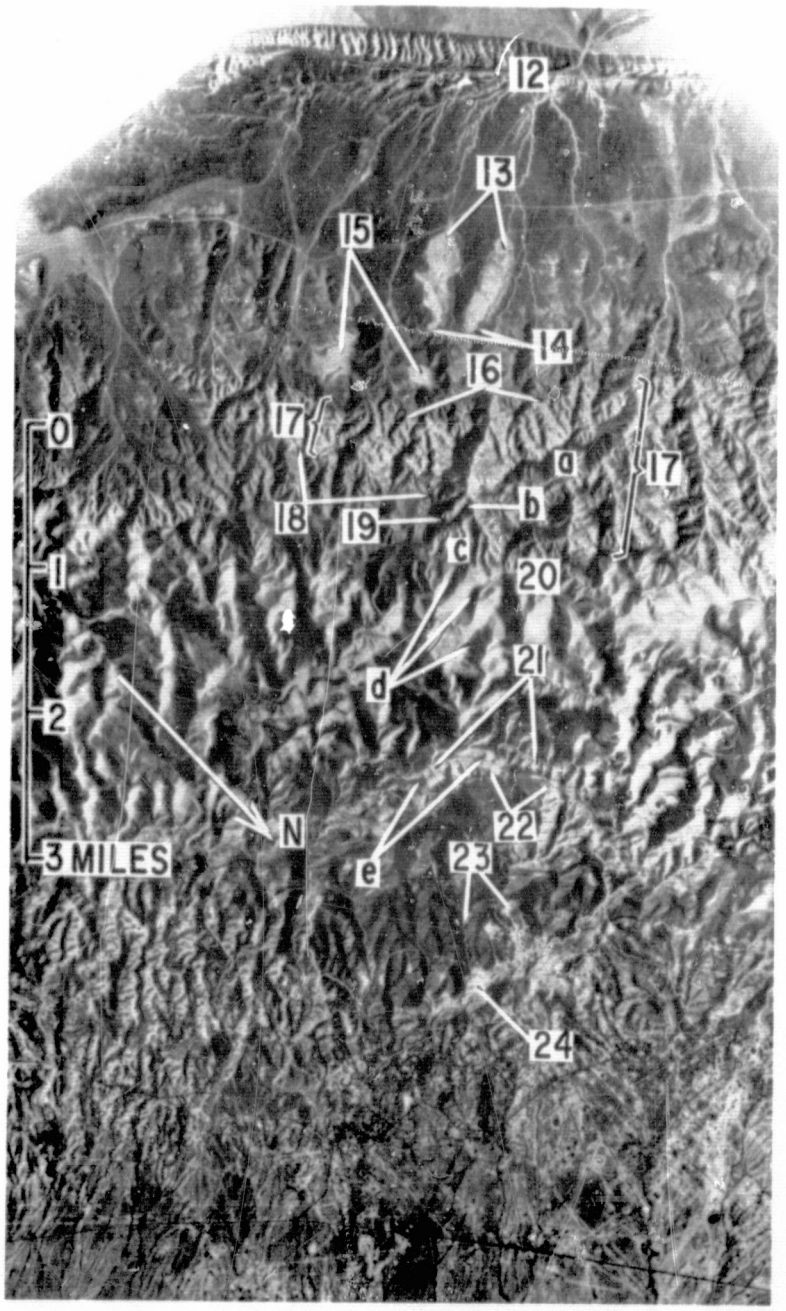

Figure 12-5.- Small-scale aerial photograph of Temblor Range southwest of Fellows.

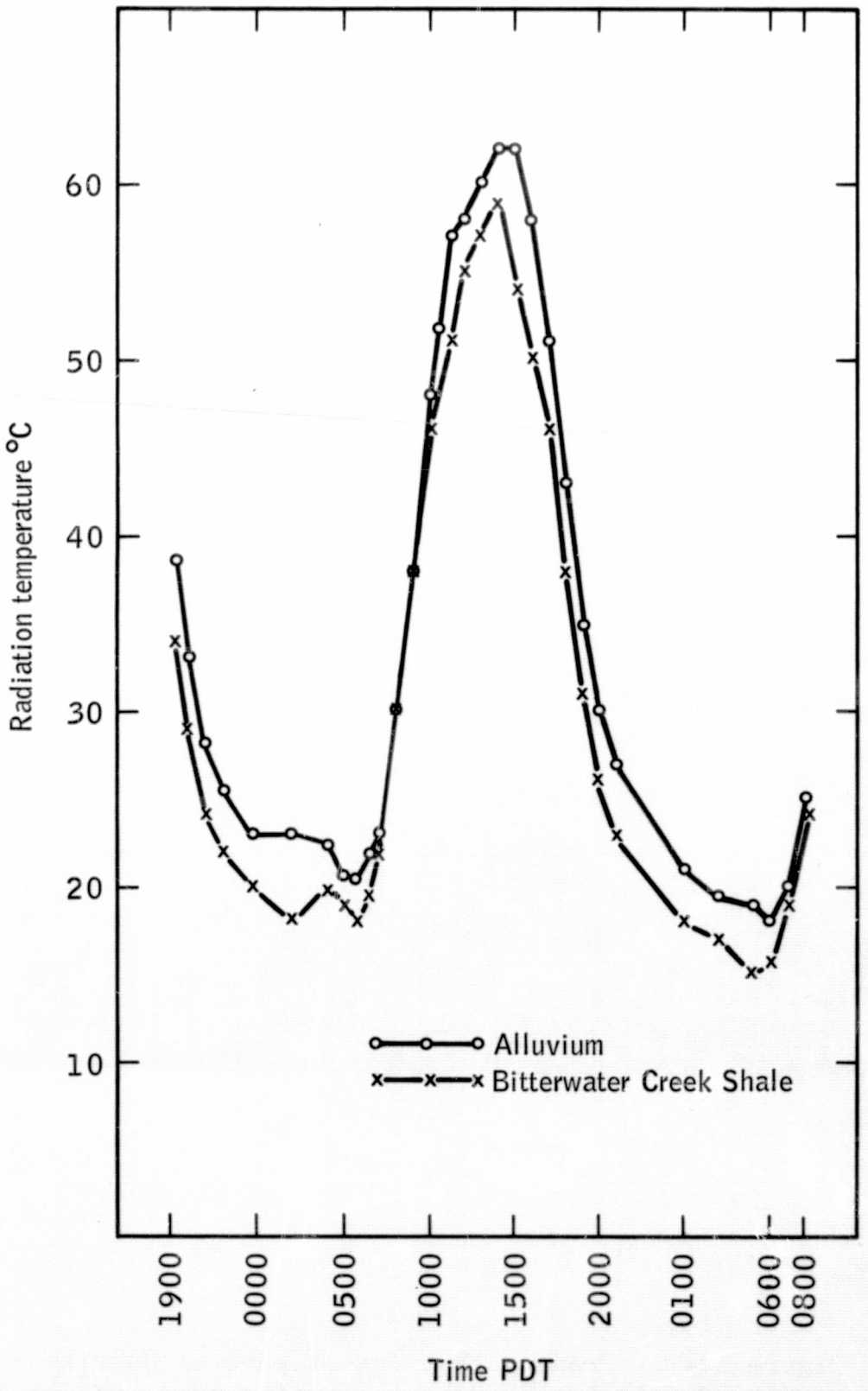

Figure 12-6.- Radiation temperatures measured by Barnes IT-3 radiometer at locality 13, Temblor Range, May 22 to 24, 1967.

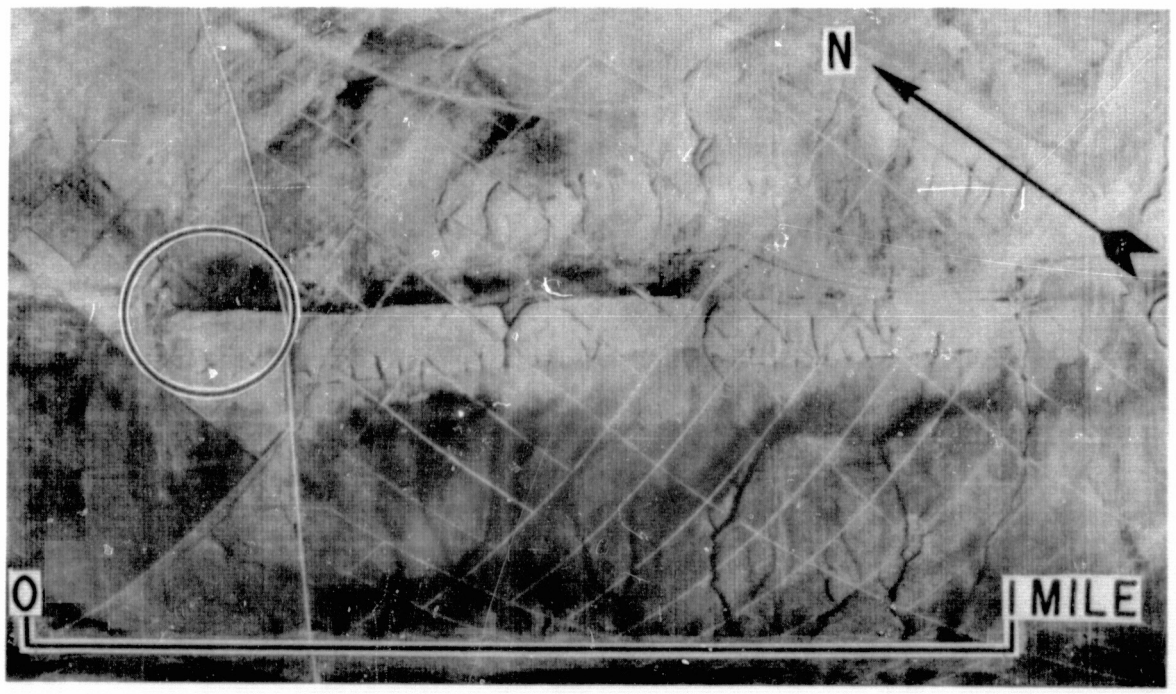

Figure 12-7.- Predawn IR image of part of Carrizo Plain east of Soda Lake. Recently active trace of San Andreas fault across middle of image area. Observations described in the text were made within the circled area.

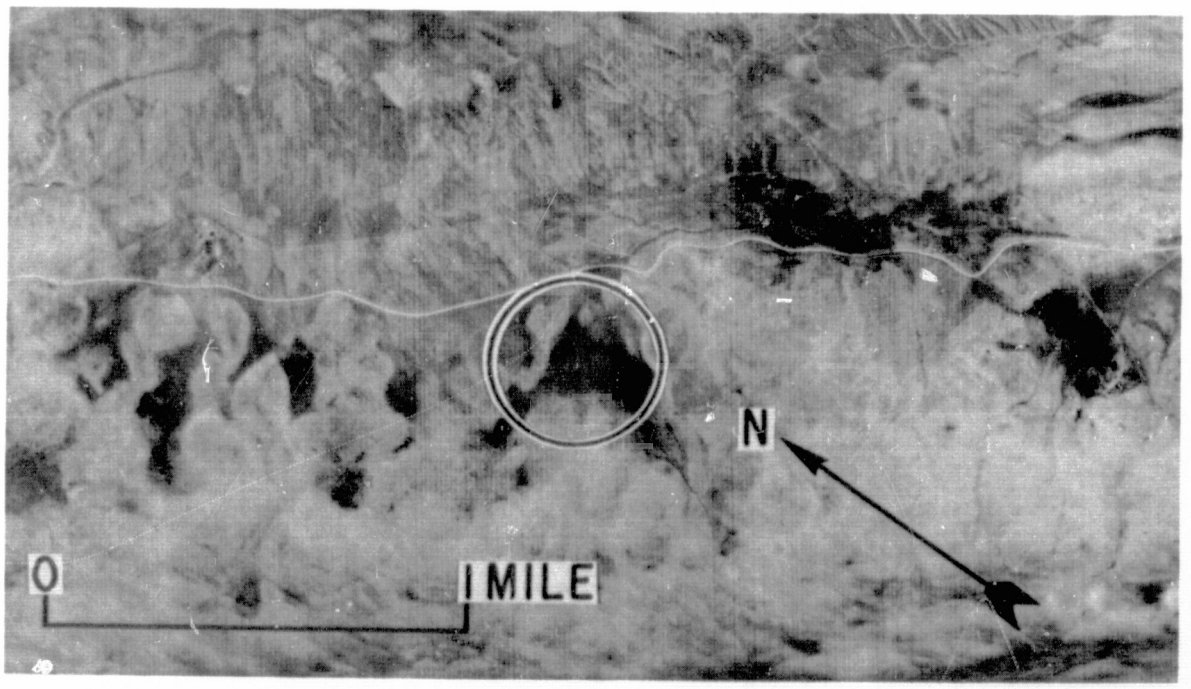

Figure 12-8.- Predawn IR image near the southeast end of Carrizo Plain. Observations described in the text were made within the circled area.

ERRATA

SECTION 12

GEOLOGIC EVALUATION OF THERMAL INFRARED IMAGERY,
CALIENTE AND TEMBLOR RANGES, SOUTHERN CALIFORNIA

By Edward W. Wolfe
Sept. 1968

Page 12-6, line 7: The sentence beginning "All three crests ..." should be changed to read "All three ridges ..."

Page 12-6, line 11: The sentence should read "All of these surfaces ..." instead of "All of these walls and slopes ..."

Issue date: 9-1-69

NASA — MSC

N71-16137

RADAR AND INFRARED IN GEOLOGICAL STUDIES OF NORTHERN ARIZONA

by Gerald G. Schaber
U.S. Geological Survey, Flagstaff, Arizona

INTRODUCTION

During the past 3 years, several types of airborne remote-sensing data were obtained over northern Arizona by NASA and by other organizations under contract to the U.S. Geological Survey (U.S.G.S.) as part of the NASA Earth Resources Aircraft Program. The data include infrared (IR) and ultraviolet scanner data, IR color, conventional color, and black and white aerial film, as well as K-band multipolarization side-looking radar data (refs. 13-1 and 13-2).

The purpose of this report is to summarize briefly the evaluation of the radar and IR data and to emphasize only those features of the imagery which are considered of significant scientific interest and of possible application to future aircraft and earth-orbiting spacecraft use.

The four geologic overflight areas to be discussed include (1) the San Francisco Volcanic Field (test site 101), (2) Meteor Crater (test site 28), (3) Hopi Buttes (test site 71), and (4) Grand Canyon (no designated site number), all located in the vicinity of Flagstaff, Arizona, in the northern part of the state (fig. 13-1).

SAN FRANCISCO VOLCANIC FIELD (TEST SITE 101)

The San Francisco Volcanic Field, named for the San Francisco Peak (the largest extinct volcano in the group), covers 3000 square miles in north-central Arizona. The center of the field lies about 50 miles south of the Grand Canyon of the Colorado, and the southern boundary is in part coterminous with the boundary of the San Francisco Plateau which forms the southwestern division of the Colorado Plateau (figs. 13-1 and 13-2).

This region was selected for remote-sensing investigation because of its extensive cinder-cone morphology and its abundant and varied

dacitic to basaltic flows (as recent as 900 years ago) representing four major periods of activity (ref. 13-3).

The San Francisco Volcanic Field covers quite a range in altitude (5500 to 12 700 feet) and, therefore, represents a wide range of climatic and vegetative types which are useful for evaluation of remote-sensing data.

A remarkable similarity of the San Francisco Field cinder-cone morphology to the morphology of recognized volcanic complexes on the lunar surface has also stimulated interest in the area (ref. 13-4).

Side-Looking Radar Data

Radar imagery covering a total of 1685 square miles was obtained over test site 101 on November 5, 1965, as part of a special contract flight (103) for the NASA-U.S.G.S. Earth Resources Program (fig. 13-2). A preliminary discussion of the multipolarization radar images of this site has been presented earlier (ref. 13-2); therefore, only pertinent conclusions and a brief discussion of the data will be presented here.

It was found that the most useful attributes of the K-band side-looking radar data of the volcanic field were its topographic enhancement and synoptic coverage capabilities which allowed recognition of even very subdued ash-covered basalt flow fronts and permitted a useful investigation of large-scale tectonic features such as cinder-cone alinement and faulting in the volcanic field and its surrounding sedimentary areas.

The S.P. cinder-cone and basalt flow (fig. 13-3), a rather young feature in the volcanic field (1300 years B.P.), was found to return distinctly different radar signatures with regard to the plane-polarized (HH) and depolarized (HV) images which were taken simultaneously. The plane-polarized response from the flow is rather intense, while the depolarized like image is notably darker than even the older ash-covered basalt flows which underlie and surround the flow. This unique response was attributed to the extreme blocky nature of the S.P. flow. The basalt blocks, averaging 1 to 2 feet in their long dimension, presented numerous dihedral and trihedral reflection surfaces to the side-looking radar signal and, in return, reflected most of the radiation back to the receiver in the same polarization mode as transmitted.

The S.P. flow is almost completely devoid of vegetation except for some light grasses growing in ash which has blown along the flow perimeter.

Older basalt flows which are covered by various depths of cinders and ash are most difficult to trace back to parent cinder cones, even from conventional aerial photography at much lower altitudes. However, the enhancement by the radar system of minute topographic changes and delineation of moisture concentrated in washes that tend to outline the flow boundaries seems to provide a workable method for mapping flow units.

Linear and arcuate grabens and other evidence of normal faulting in the vicinity of the S.P. flow (fig. 13-3) are easily recognized on the radar image. These features are enhanced both by their topographic relief and by moisture which is invariably present in the topographically low areas created by tectonics.

Moisture-rich areas are revealed as darker tones on the radar image resulting from the extreme attenuation of electromagnetic radiation by the highly dipolar water molecule. The washes contain slightly more vegetation than the normal terrain surfaces, but do, however, concentrate more silt-sized material which retains moisture well.

Foliation in the northern two-thirds of the area covered by figure 13-3 is extremely sparse, consisting of a few scattered, scrubby Juniper, sage, and Upper Sonoran desert grasses. Vegetation was found to cause no recognizable signature differences in the low areas below 6000 feet in this region.

Recognition of diverse rock types from all three strips of radar imagery in the San Francisco Volcanic Field was somewhat disappointing. A slight but noticeable tonal difference is evident between the Kaibab sandy dolomite and ash-covered basalt flows in figure 13-3, especially on the depolarized image. At area A in figure 13-3, a somewhat isolated outlier of Kaibab dolomite capped by Moenkopi sandstone is rather distinctly visible on the depolarized image but is much less defined on the plane-polarized like image. This tonal difference is greater than that between similar contacts farther from the flight line in the look direction. This has been attributed (ref. 13-2) to a loss in signal strength to the receiver with distance from the flight line.

A triangular array of flight lines over an area with a look direction toward the center of the triangle would be optimum by furnishing both enhancement of linears and topographic scarps in all azimuthal directions, as well as to furnish maximum and more uniform signal-strength returns from areas of interest.

Runs 7 and 15 (figs. 13-4 and 13-5) were flown over the higher country (7000 to 10 600 feet) near Flagstaff, and the imagery is dominated by a light mottled pattern caused by the reflection of the radar signal off the top of the large Ponderosa pine forest. A very sharp,

altitude-dependent boundary between the Ponderosa and Juniper growth zones (approximately 6500 feet) can be located on all three radar strips.

The lobate flows emanating from Mount Elden, a rather unique dacite dome, are easily distinguished on figure 13-4, and a previously unnoticed southeast-northwest set of lineaments can be readily seen passing through Mount Elden and the adjacent Dry Lake Hills to the northwest.

The Woody Mountain fault and Rogers Lake (area A on fig. 13-4) is a very distinct region of moisture concentration, as indicated by the dark tone. Note the more defined moisture boundary within Rogers Lake on the depolarized (HV) image.

An area underlain by Kaibab sandy dolomite is readily distinguished on the extreme western side of figure 13-5 as a lighter tone on both the plane-polarized and depolarized images.

The Kana-a basalt flow, related chronologically to the Sunset Crater eruption in 1064 A.D., is conspicuous on figure 13-6 as a well-defined dark tone on the depolarized image and a less well-defined, lighter signature on the plane-polarized image. Unlike the blocky S.P. basalt flow, however, the Kana-a flow is of the AA type.

Infrared Scanner Data (8μ to 14μ)

Three flights covering a total area of 162 square miles were flown by NASA over a portion of the San Francisco Volcanic Field (fig. 13-2) during mission 21 on April 2, 1966, with simultaneous black and white aerial photography (T-11 camera). The mission was flown during the daylight hours (4:00 p.m.) and, therefore, consists of combined reflection and emission data with a preferred sun-slope heating direction.

It was found that the black cinders and ash distributed by the wind from several young cinder cones in the region can be readily distinguished from earlier ash on the scanner data as very light (warm) tones resulting from the black-body emission characteristics of such a dark material and its ability to retain moisture.

The black ash was found to be generally less vegetated than the surrounding materials (red cinders with fine, light-buff ash), depending on its depth and the slope on which it was deposited. However, in some areas, the black ash tends to concentrate the sage and other bushy-type plants to the near exclusion of the lighter Upper Sonoran desert grasses. In still other areas of the San Francisco Volcanic Field where the dark ash is thin and limited in aerial extent, it tends to support abundant grasses to the exclusion of the larger bushy plants.

The type of vegetation cover on the black ash is apparent on the aerial photographs but was not found to alter the light tone (warm) signal response on the IR scanner data.

The lowest altitude IR scanner flight line covering a total area of 23.28 square miles revealed a series of remarkably straight and well-defined light and dark bands up to several hundred feet in length on top of an old ash-covered flow (fig. 13-7). The aerial-photography coverage of the bands flown simultaneously with the IR scanner shows some of them as very subtle light lines, while others are not visible at all (fig. 13-8).

Aerial and field investigation of the bands revealed an almost indistinguishable subdued and intermittent banding of black ash dunes covered with light desert grasses separated by topographically lower (3 to 5 inches average; 12 inches maximum) areas of red cinders and light-buff ash. This material tends to concentrate the larger sage and bush-type vegetation in at least some parts of the linear bands.

This author, puzzled as to the origin of the features, field checked the local drainage patterns, Moenkopi sandstone joint directions under the flow, and possible surface flowline directions. None of these appeared to satisfactorily answer the question as to the origin of bands. Upon finding abundant prehistoric Indian pottery shards in the area of the linear features and having located Indian campsite ruins associated with each linear set, a local expert on Indian archaeology in northern Arizona (George Gumerman, Prescott College) was called in to aid in the investigation. A fieldtrip to the region confirmed our suspicions that the linear features were a 12th-century Indian agricultural site where the black ash was used as a mulch over crops to retain moisture (ref. 13-5). The Hopi Indians of northern Arizona continue to follow this practice today.

A search was made for the prehistorical agricultural sites on high-altitude (20 000 feet) Army Map Service aerial photography of the region. They were found to be clearly visible with the aid of a low-power hand lens.

The results of this totally unexpected investigation of the Indian agricultural site has aroused much interest among anthropologists and archaeologists in northern Arizona over such remote-sensing techniques.

Soil samples were taken for nitrogen and potassium depletion analysis from both the light and dark agricultural bands, and a systematic collection of pottery and other artifacts were taken for a detailed study by G. G. Schaber and G. J. Gumerman (ref. 13-6).

METEOR CRATER, ARIZONA (TEST SITE 28)

Meteor Crater has been, in recent years, the focal point for many scientific investigations dealing with impact mechanics (ref. 13-7), geophysics (ref. 13-8), and remote sensing (refs. 13-1 and 13-9).

The obvious similarity of the Arizona feature with other, more eroded terrestrial phenomena, as well as with those on the lunar and Martian surface, has prompted its use as a geologic test site for remote-sensing investigations.

Two overlapping strips of radar imagery, covering a total area of 460 square miles and centered on Meteor Crater, were obtained during the special contract flight (103) on November 5, 1965 (ref. 13-1).

Four separate combinations of transmit-and-receive polarizations were used for the two flights over the Crater. In run 8 (fig. 13-9), the upper image was produced from the horizontal component of a horizontally transmitted wave (HH), and the lower cross-polarized image was produced from the vertical component of the same horizontally transmitted wave (HV). In run 14 (ref. 13-1), one image was produced from the vertical component of a vertically transmitted wave (VV); the other image resulted from the horizontal component of the same vertically transmitted signal (VH).

The depolarized images of both radar strips exhibit less tonal contrast than the plane-polarized like images. However, moisture enhancement and delineation of rock types was found to be superior on the cross-polarized images; and for this reason, they contributed considerably more to the geologic interpretation.

At the scale of the imagery (approximately 1:190 000), Meteor Crater was too small to allow any detailed geologic interpretation of the crater walls, rim, or ejecta blanket materials. Evaluation of the crater rim materials with the surrounding geology, however, was attempted.

The most striking feature of both radar images was found to be the excellent detail in which moisture-rich areas were defined (figs. 13-9 and 13-10). These areas were found to relate to alluvium-filled washes and to sandstone bedrock and debris from the Coconino, Toroweap, and Moenkopi formations (fig. 13-11). Many of the washes so well defined on the radar imagery have topographic relief measured in inches.

Ground detail, emphasized by moisture content, was found to decrease appreciably with lateral distance from the aircraft as previously discussed in regard to the test site 101 radar data.

The high radar backscatter seen in all meanders of Canyon Diablo (fig. 13-9), regardless of the flight path of the radar aircraft, is evidence that a blocky, well-jointed rock (Kaibab sandy dolomite) is holding up the canyon walls (ref. 13-10). The limestone blocks, like the blocky basalt of the S.P. flow mentioned earlier (fig. 13-3), are acting like many dihedral and trihedral reflectors to return a strong signal to the receiving antenna.

Widely spaced, northwest-trending, normal faults disrupt the nearly flat-lying Permian and Triassic strata 3 miles east and 7 miles west of the crater (fig. 13-9). These faults are seen remarkably well on the radar imagery (especially on the cross-polarized images) as a result of backscatter from the aircraft-facing scarp, as well as from concentration of moisture in sandy alluvium along the scarp.

The area outlined on figure 13-10 illustrates the best correspondence of the radar data with the geologic map (fig. 13-11). The dark-gray zone running parallel to Canyon Diablo at area A of the figure can be seen to relate the recent alluvium at the contact of the Kaibab sandy dolomite (area B) with the massive lower sandstone of the Moenkopi formation (area C).

Although little of geologic significance could be abstracted from the crater itself on the radar imagery, several features of interest could be seen. (1) A halo of light-gray tone can be seen surrounding the crater (fig. 13-9) and probably represents the present limit of fine ejecta. (2) Many small spots of high radar backscatter on the outer rim slope of the crater are known to be caused by large angular debris (sandstone and dolomite blocks) thrown out of the crater. These are especially noticeable on the vertically polarized (VV) image (ref. 13-1).

The negative features of the radar data are the usual poor resolution of stratigraphic units and the innate image and scale distortions which preclude the use of standard photogrammetric techniques.

GRAND CANYON, ARIZONA

Side-looking multipolarization radar imagery was obtained over Grand Canyon during the same NASA-U.S.G.S. special contract mission that covered test sites 101 (San Francisco Volcanic Field), 29 (Meteor Crater), and 71 (Hopi Buttes) in northern Arizona on November 5, 1965. The plane-polarized (HH) and depolarized (HV) like images (1:177 000 mean scale) of the Grand Canyon are of excellent quality and provide a rather remarkable synoptic view of the complex fault system of the feature (fig. 13-12). This author prepared a lineament map overlay from the data

in approximately 15 minutes, and the map was then compared to a recently published geologic map of the eastern section of the Grand Canyon (ref. 13-11) (fig. 13-13). The percentage of inferred faults that corresponded exactly with the mapped displacements was found to be quite encouraging. The radar data, however, created a preferred orientation as a result of the side-looking enhancement of topographic scarps in the look direction. This problem could, of course, be eliminated by making several passes over such a feature at divergent flight paths.

Stratigraphy in the south rim of the Canyon can be easily seen (area A in fig. 13-12) as alternating light and dark tones. This phenomena is created by the radar shadowing effect on resistant (ledge-forming) and nonresistant (slope-forming) beds and is probably not due, for the most part, to surface texture or composition. It is, however, a feature of side-looking radar data that can be utilized for geologic interpretations. The red wall limestone (Mississippian Age), for example, can be clearly traced throughout the entire length of the south side of the Canyon (area B in fig. 13-12) as a result of its cliff-like ledges which contribute to the radar shadowing.

Distinction of rock types and location of rather sharp geologic contacts is very difficult, if not impossible, and is certainly a disappointing feature of the imagery. The major value, then, of the Grand Canyon data lies in its synoptic coverage and excellent enhancement of tectonic features.

Cultural features surrounding Grand Canyon Village are fairly well defined, as are portions of the south rim drive road. Drainage details on top of the south rim are also well portrayed on the eastern side of the Grand Canyon (area C in fig. 13-12).

HOPI BUTTES, ARIZONA

The Hopi Buttes, located approximately 50 miles east of the San Francisco Volcanic Field (test site 101), are strikingly different from the latter, consisting of monchiquitic basalt-capped buttes, monchiquitic dikes, acid tuffs, agglomerate, and numerous diatremes of a presumed explosive origin (fig. 13-1). Sedimentary sandstones, siltstones, and claystones, ranging in age from Triassic to Jurassic, comprise the local bedrock, and these are overlain by a rather complete record of the Quaternary Period. Vegetation in this area consists of sparse Juniper, sage, and Upper Sonoran desert grasses.

The Hopi Buttes were imaged with five flight lines during the November 5, 1966, special mission (flight 103) covering a total area of 3263 square miles.

The most interesting feature of the data was found to be the delineation of many complex Quaternary soil units which have been enhanced primarily by differential moisture retention (and vegetation changes). A cursory field investigation of the soil units has been completed, and a more comprehensive study is planned.

The diatremes are seen on the radar data as highly reflective circular "rings" which are created by radar backscatter from very rough, dolomitized travertine beds associated with most of the collapsed, lopolith-shaped structures (area A in fig. 13-14).

As was the case with the San Francisco Field data, the large-scale imagery of this site permitted a quick scan of possible diatreme or other tectonic alinement features.

CONCLUSIONS AND SUGGESTIONS

Both the IR and radar data of the northern Arizona sites were found to contribute at least something of unique geologic value. The radar imagery contributed mainly because of its synoptic scale, moisture delineation, and topographic enhancement capabilities. All of these furnish data useful in interpretation of tectonics, surface moisture, and overlapping sequences of lava flows. Evaluation of the IR scanner data in this study provided several new suggested uses for the system: (1) location of prehistorical Indian agricultural sites and (2) furnishing a means of discriminating between recent, dark (unweathered) volcanic ash and lighter, older (weathered) ash-fall deposits as a function of radiant temperature and possible moisture content.

Both the radar and IR scanner imagery provided rather disappointing distinction between rock types in the study area. Part of this problem, however, lies in the fact that the relationships between surface conditions and atmospheric attenuation with signal response are still not well defined or understood for radar IR scanners, as well as the other sensors currently being investigated. Basic spectral research in the laboratory and under simple field conditions is the most urgent direction to proceed at the present time.

Although the gathering, interpreting, and field checking of images from these devices is of great importance and should be continued, the users are becoming more and more aware of the complexities which arise from diverse surface textures, moisture content, and changing atmospheric conditions. As long as such parameters as these are misunderstood, scientifically useful evaluations of image data will be almost impossible.

It has become obvious that the laboratory spectral research and image evaluation programs must become more balanced and that the results from each study more easily disseminated to the users. Hopefully then, in the next few years, these programs will enjoy a fruitful union that will be to the advantage of the earth resources remote-sensing technology.

REFERENCES

13-1. Schaber, Gerald G.: Radar Images - Meteor Crater, Arizona. Technical Letter NASA-62; Natural Resources Program, U.S. Geological Survey, 1966.

13-2. Schaber, Gerald G.: Radar Images - San Francisco Volcanic Field, Arizona - A Preliminary Evaluation. Technical Letter NASA-84; Natural Resources Program, U.S. Geological Survey Open File Report, 1967.

13-3. Robinson, H. H.: The San Francisco Volcanic Field. U.S. Geological Survey, Prof. Paper 76, 1913.

13-4. McCauley, J. F.: The Marius Hills Volcanic Complex. Astrogeologic Studies Ann. Prog. Rept., U.S. Geological Survey Open File Report, 1965, pp. 115-122.

13-5. Colton, Harold S.: Sunset Crater - The Effect of a Volcanic Eruption of an Ancient Pueblo People. The Geographical Review, 1932, pp. 588-589.

13-6. Schaber, Gerald G.; and Gumerman, G. J.: Report on the Use of the Airborne IR Scan Technique for Locating Pre-Historical Indian Agricultural Sites in the Southwest. (In preparation for submission to "Science.")

13-7. Shoemaker, E. M.: Impact Mechanics at Meteor Crater, Arizona. U.S. Geological Survey, Open File Report, Menlo Park, California, 1959.

13-8. Godson, R. H.; Ackermann, H.; and Watkins, J. S.: Seismic Survey of Meteor Crater, Arizona, in Investigations of In Situ Physical Properties of Surface and Subsurface Site Materials by Engineering Techniques. Project Quarterly Report (October 1, 1965 to December 31, 1965), U.S. Geological Survey, Branch of Astrogeology, Flagstaff, Arizona, 1966.

13-9. Hemphill, W. R.; and Vickers, R.: Geological Studies of the Earth and Planetary Surfaces by Ultraviolet Absorption and Stimulated Luminescence. Technical Letter NASA-33 and 33A, U.S. Geological Survey, 1966.

13-10. Rydstrom, Hubert O.: Interpretating Local Geology from Radar Imagery; Proceedings of the Fourth Symposium on Remote Sensing of Environment; April 12-14, 1966. Willow Run Laboratories, Institute of Science and Technology, Ann Arbor, Michigan, pp. 193-201.

13-11. Maxson, J. H.: Preliminary Geologic Map of the Grand Canyon and Vicinity, Arizona. Grand Canyon Natural History Association, Williams and Heintz Map Corporation, Washington, D.C., 1967.

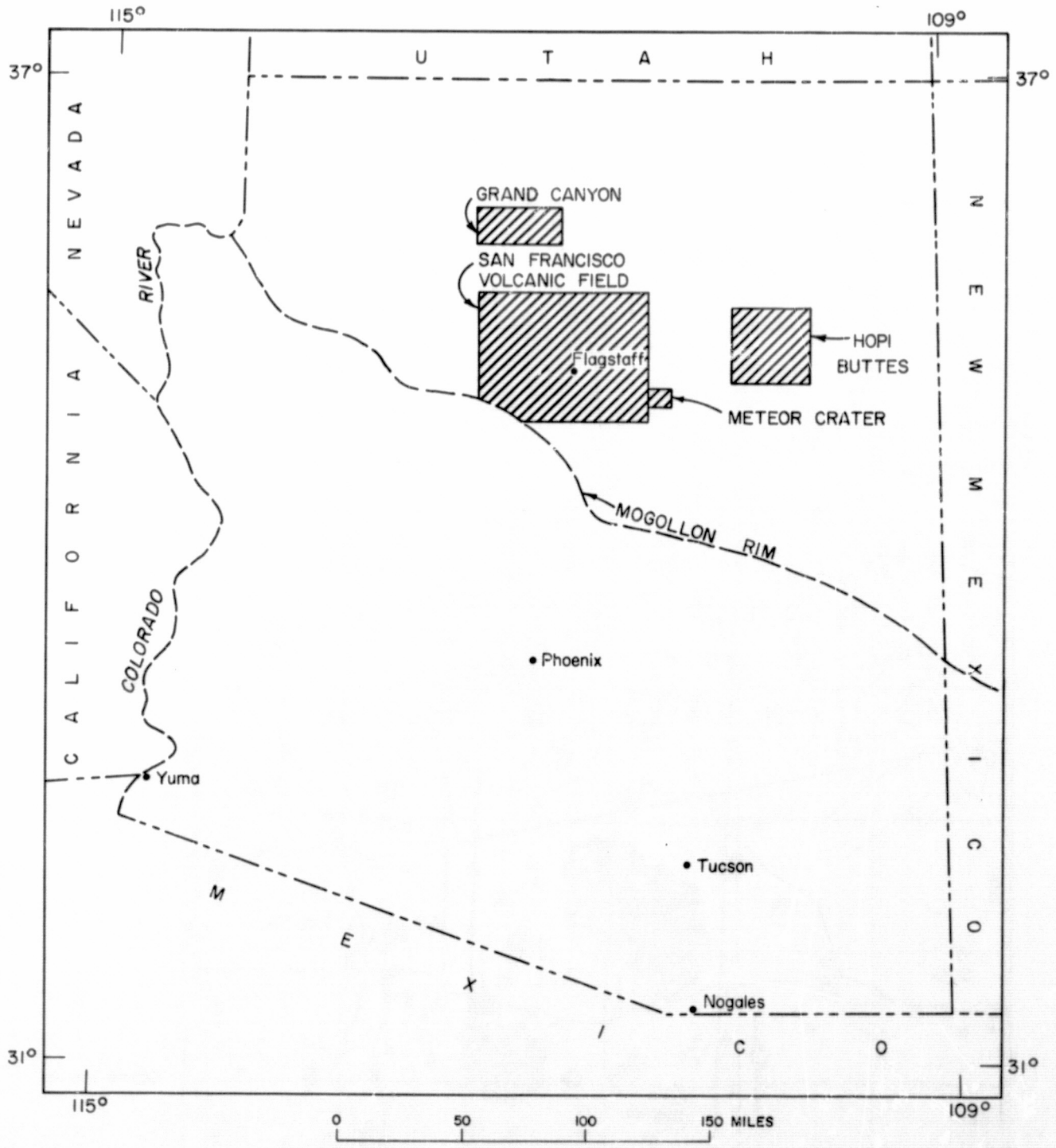

Figure 13-1.- Location map showing geologic test sites 101 (San Francisco Volcanic Field), 28 (Meteor Crater), 71 (Hopi Buttes), and Grand Canyon, Arizona.

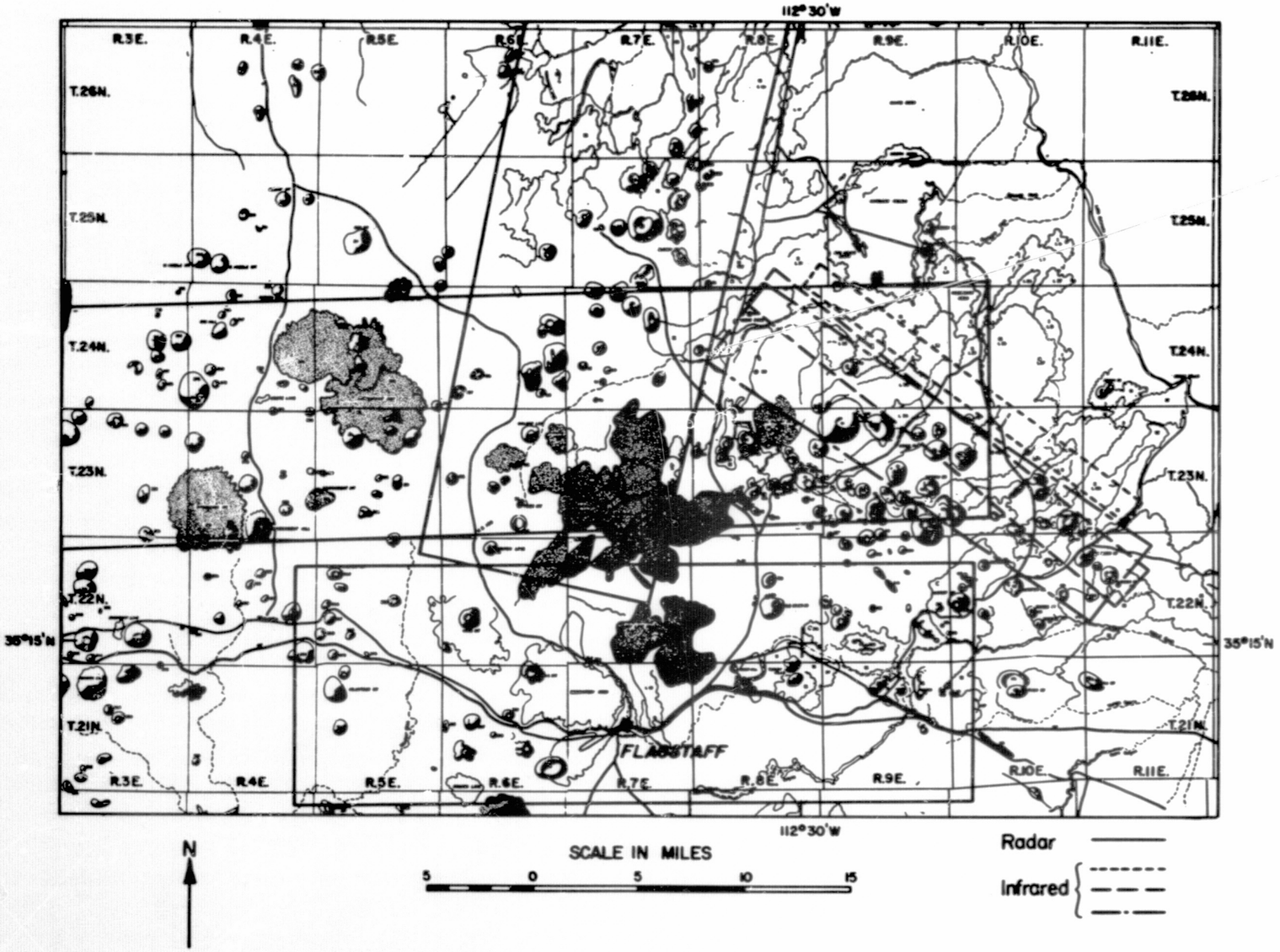

Figure 13-2.- Location map of San Francisco Volcanic Field showing radar and IR scanner coverage.

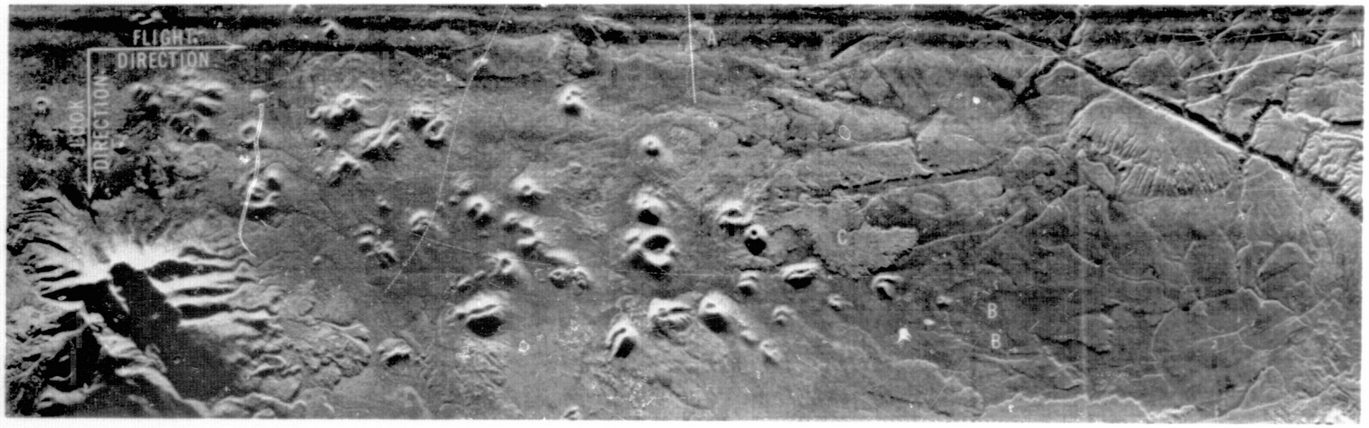

a. Plane-polarized (HH) image.

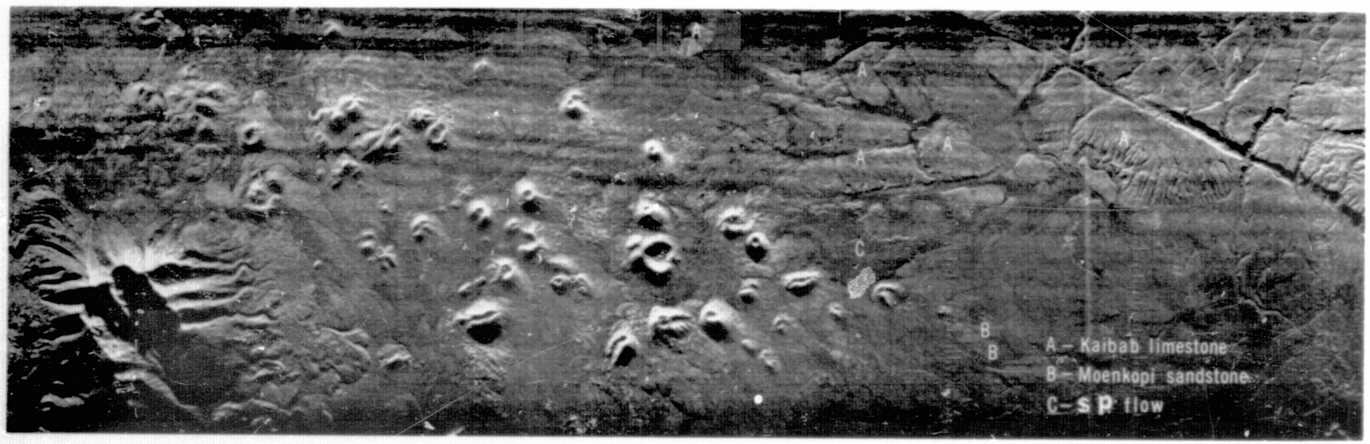

Depolarized (HV) image.

Figure 13-3.- Flight 103 run 16; north-northeast from the San Francisco Peaks. Original scale approximately 1:200 000.

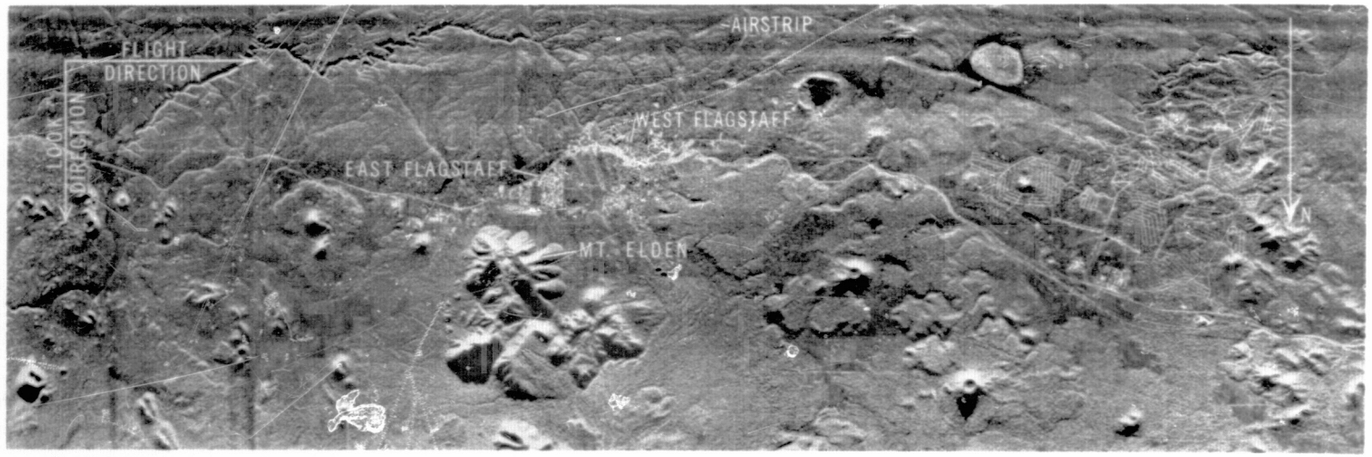

a. Plane-polarized (HH) image.

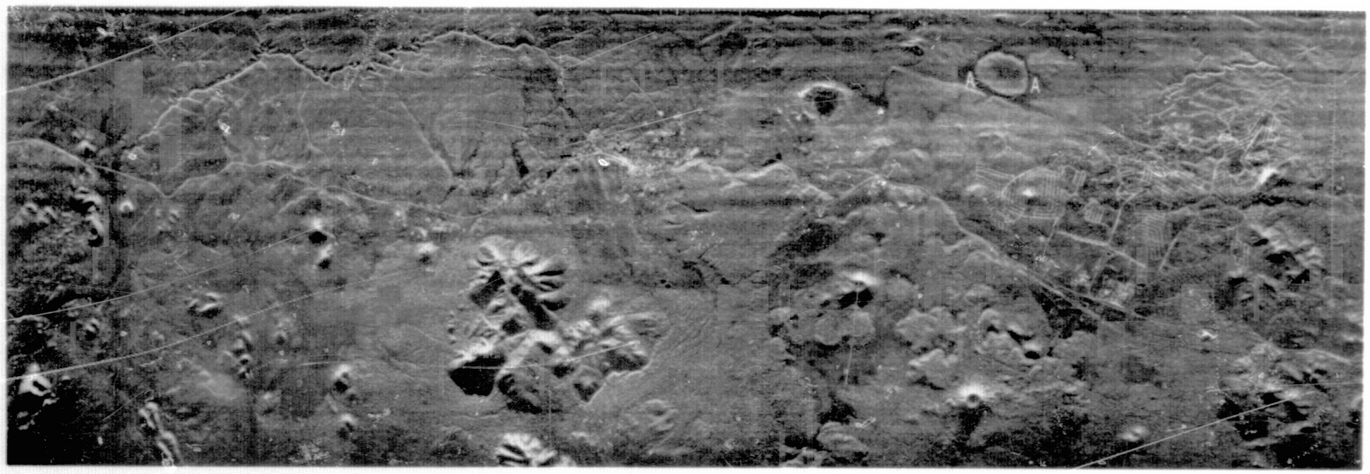

b. Depolarized (HV) image.

Figure 13-4.- Flight run 15; east-west flight over Flagstaff, Arizona.
Original scale approximately 1:220 000.

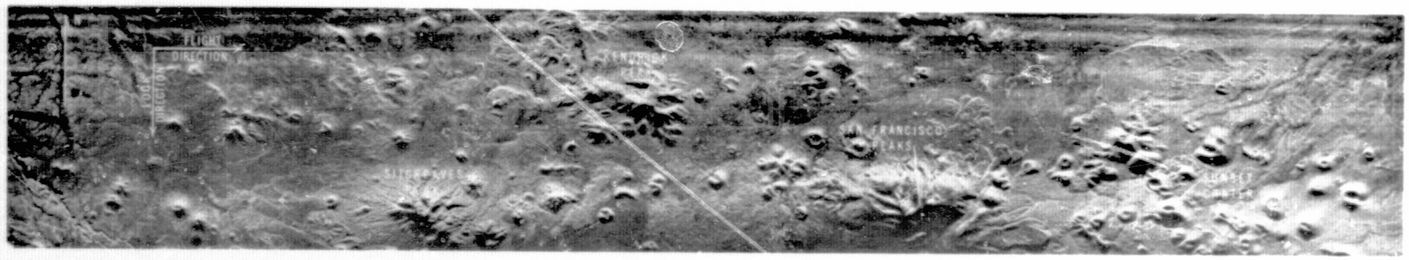

a. Plane-polarized (HH) image.

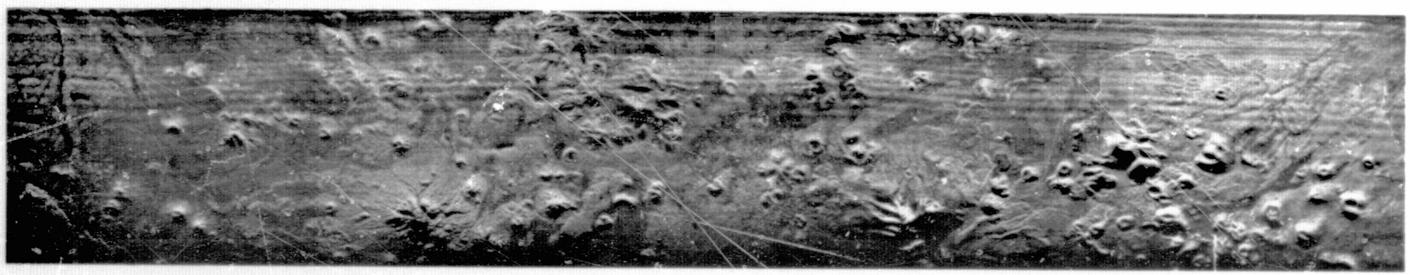

b. Depolarized (HV) image.

Figure 13-5.- Flight 103 run 7; east-west flight north of the San Francisco Peaks. Scale approximately 1:179 750.

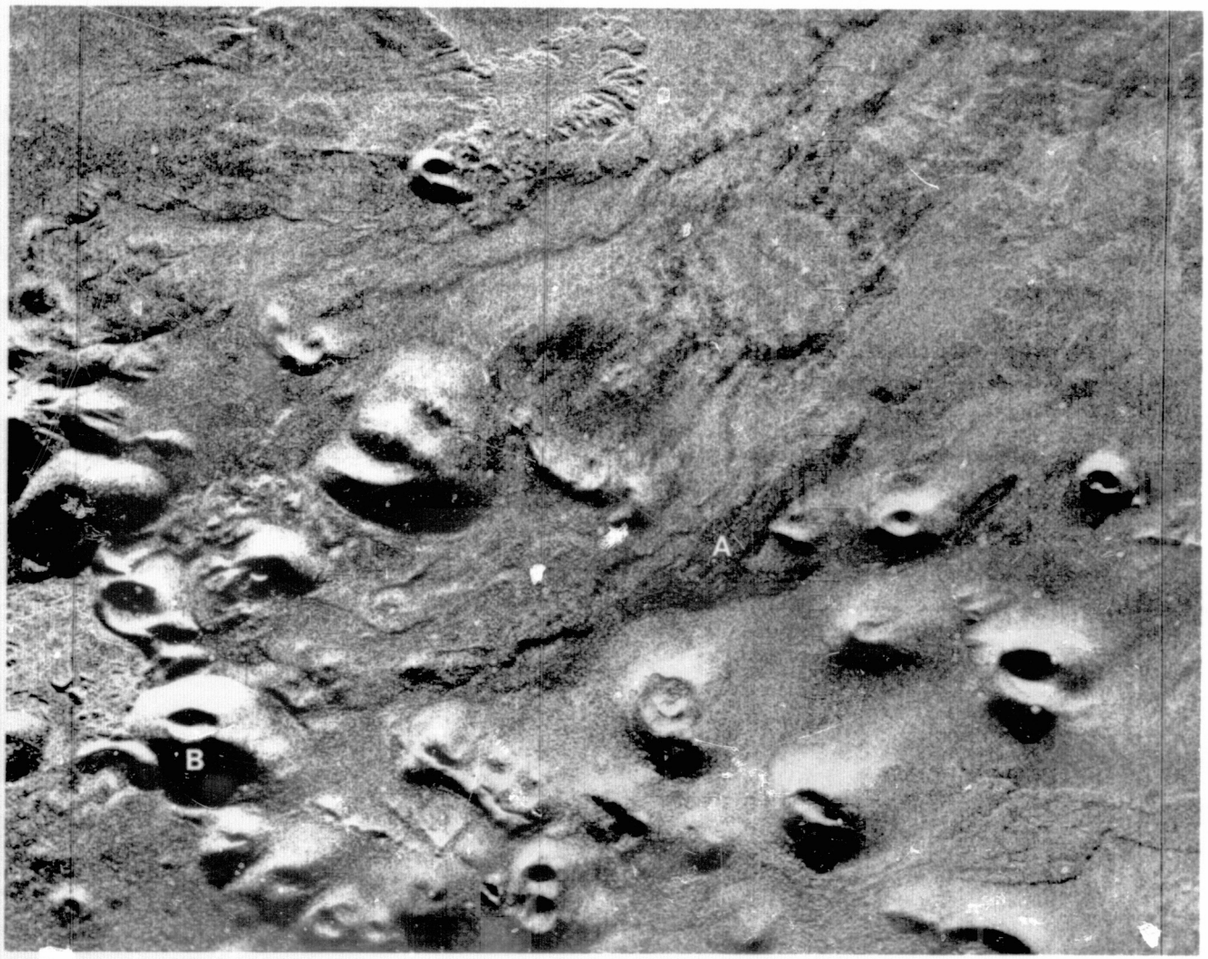

a. Enlarged portion of figure 13-5a (scale 1:124 500) showing Kana-a basalt flow (area A) emanating from 900-year-old Sunset Crater (area B). Plane-polarized (HH) image.

Figure 13-6.- Enlargement of figure 13-5.

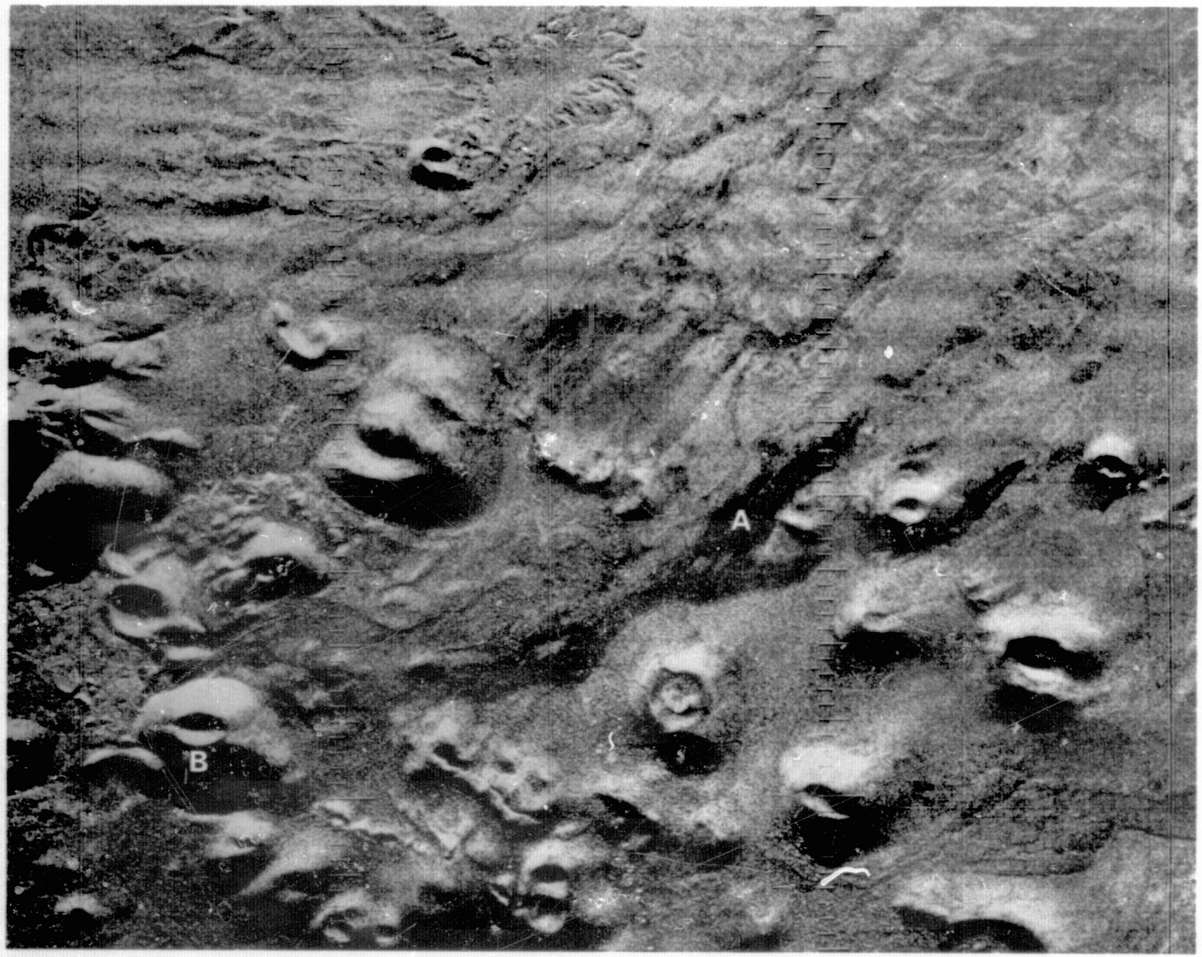

b. Enlarged portion of figure 13-5b (scale 1:124 500) showing Kana-a basalt flow (area A) emanating from 900-year-old Sunset Crater (area B). Depolarized (HV) image.

Figure 13-6.- Concluded.

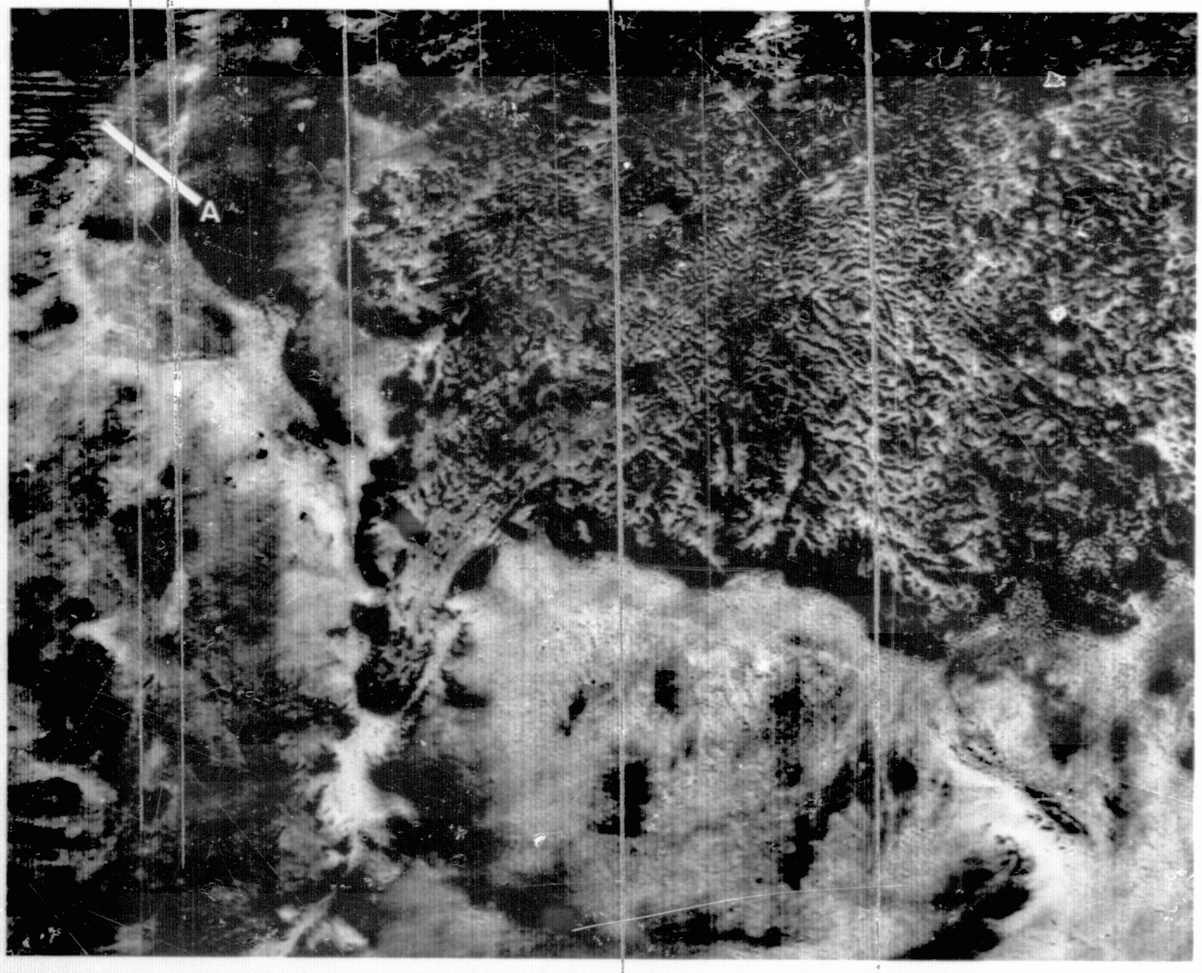

a. Enlarged portion (scale 1:10 800) of low-altitude (under 3000 ft) Reconofax IV run over an area of the San Francisco Volcanic Field northeast of Flagstaff, Arizona. Linear banded features (area A) represent a 12th-century prehistoric Indian agricultural site.

Figure 13-7.- Enlargement of figure 13-2.

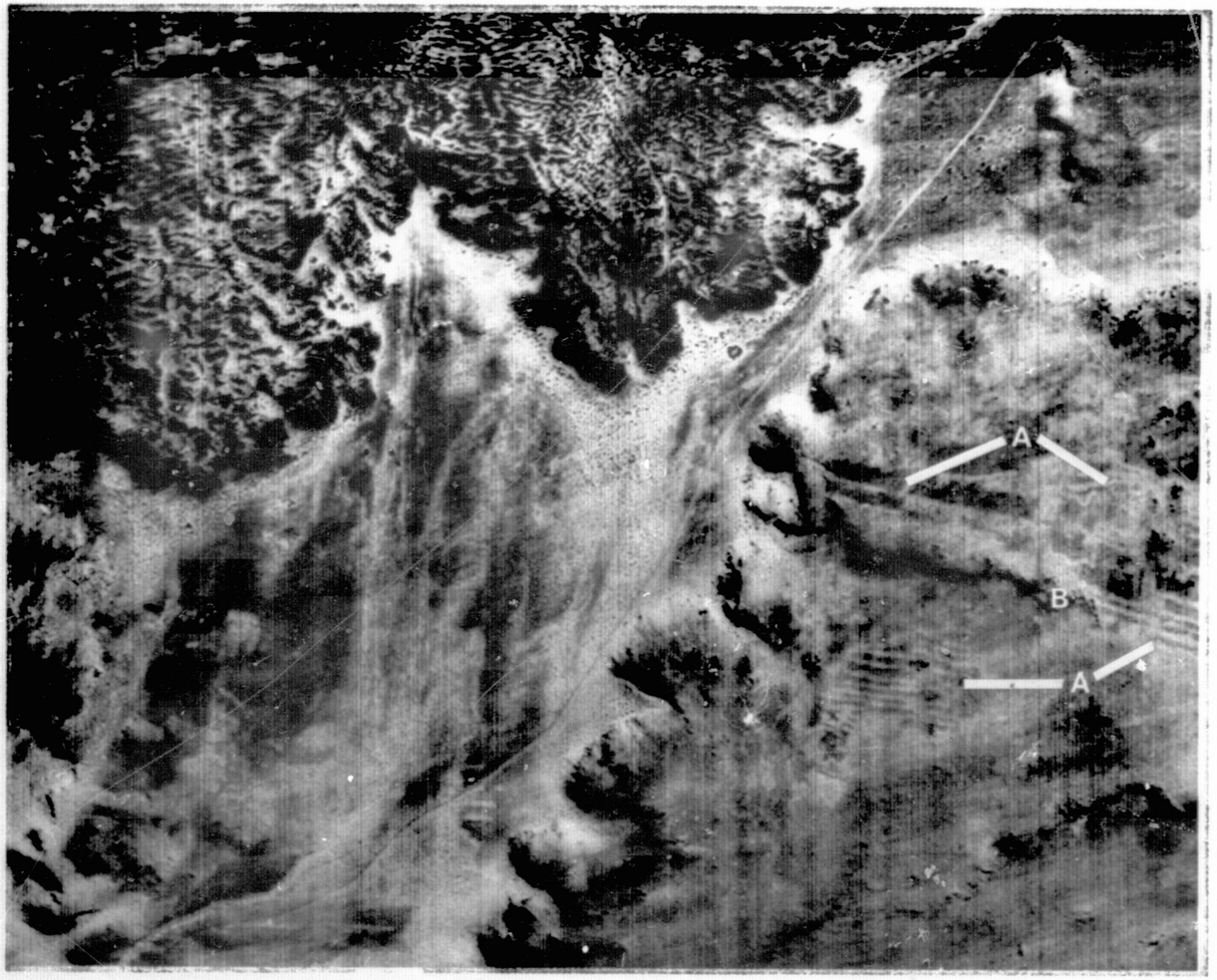

b. Enlarged portion (scale 1:10 800) of low-altitude (under 3000 ft) Reconofax IV run covering the same general region shown in figure 13-7a. Linear features are 12th-century agricultural fields (area A); remains of the Indian living site were found at area B.

Figure 13-7.- Concluded.

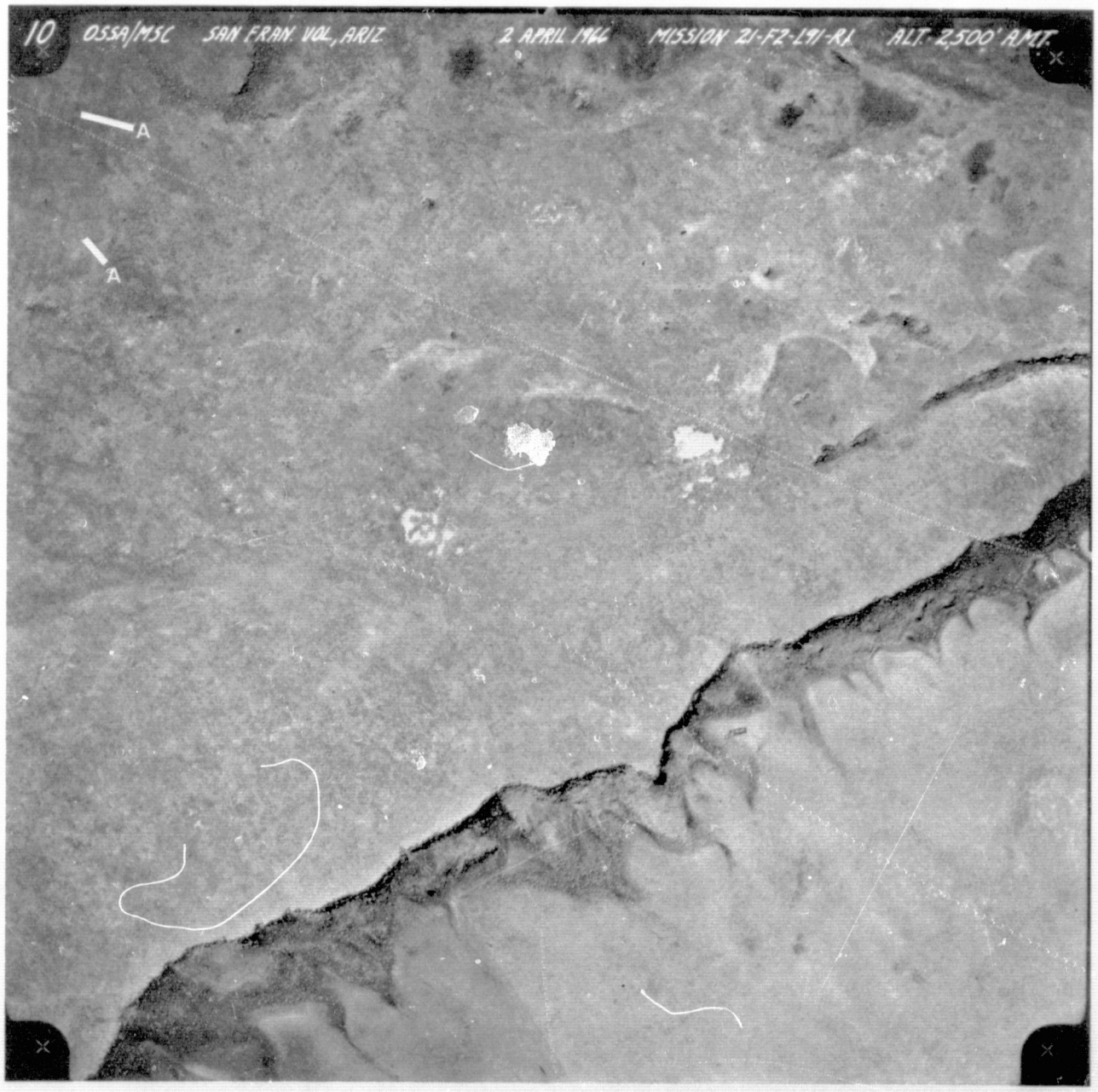

a. Area A indicates the presence of the prehistoric Indian agricultural plots.

Figure 13-8.- Aerial photograph (2500 ft) taken simultaneously with IR scan image shown in figure 13-7.

b. Area A indicates the presence of prehistoric Indian agricultural plots; area B indicates the site of Indian ruins.

Figure 13-8.- Concluded.

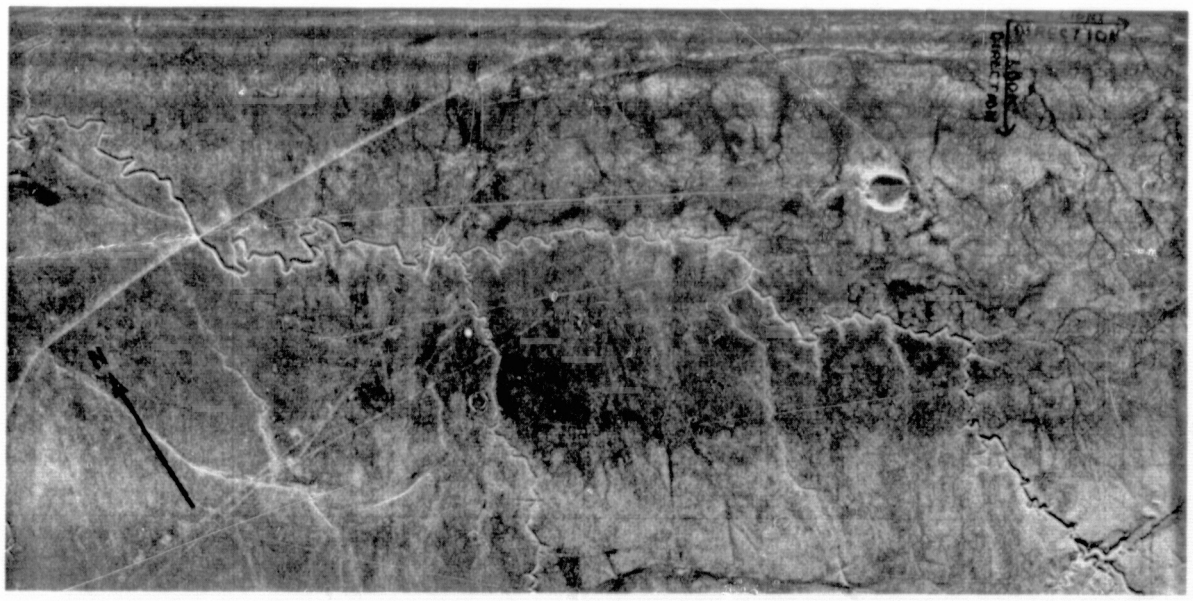

a. Plane-polarized (HH) image of Meteor Crater and vicinity, Arizona.

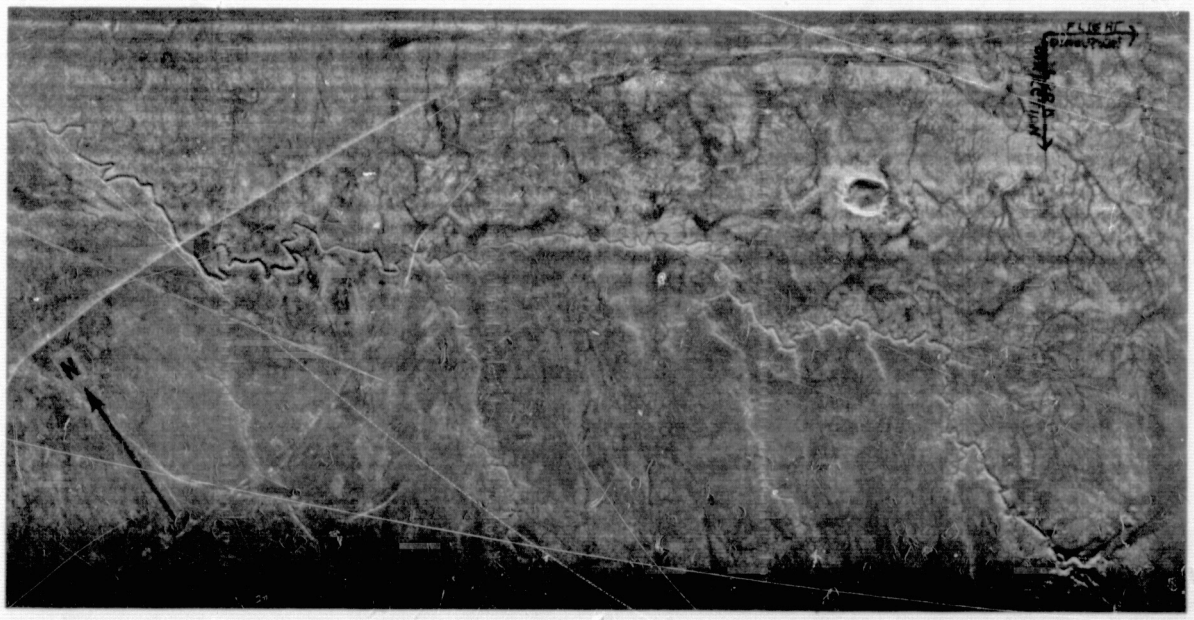

b. Cross-polarized (HV) image of Meteor Crater and vicinity, Arizona.

Figure 13-9.- Radar image run 8.

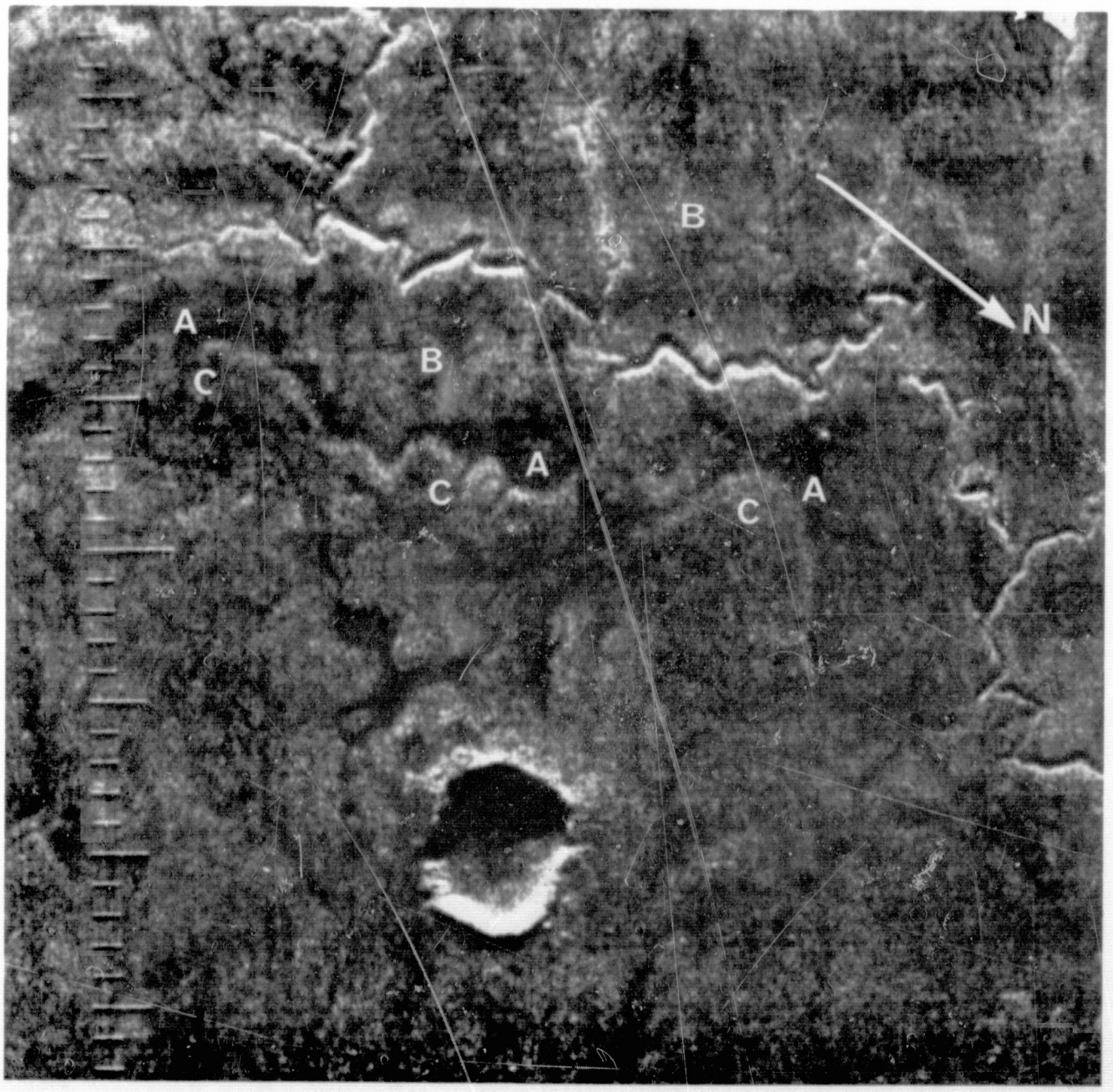

Figure 13-10.- Radar image enlargement (scale 1:55 000) from flight 103 run 14; depolarized (HV) image showing moisture enhancement along stratigraphic contact west of Meteor Crater, Arizona. Recent alluvium along contact between Kaibab (area A), sandy dolomite (area B), and massive lower sandstone of the Moenkopi formation (area C).

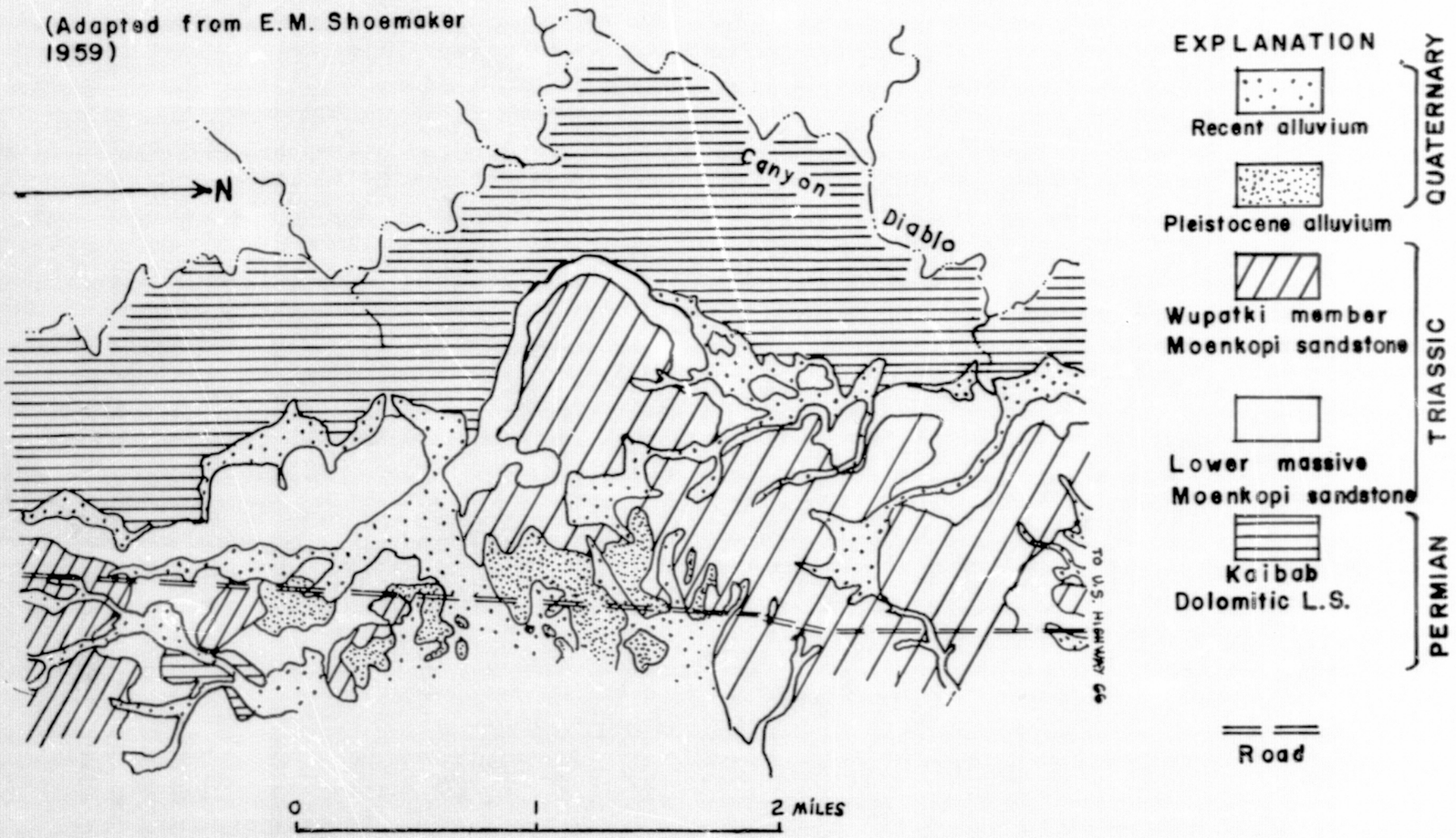

Figure 13-11.- Geologic map showing correlation between geology and radar image.

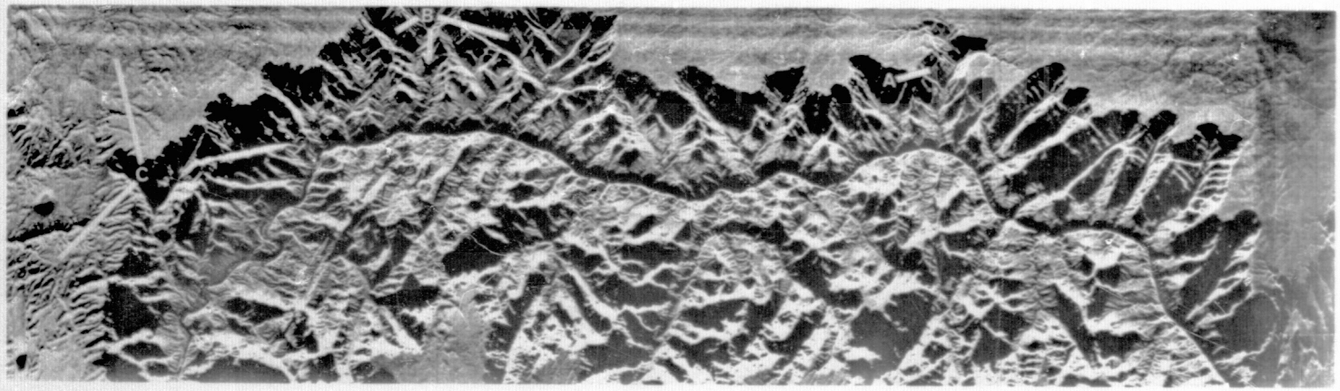

Figure 13-12.- Side-looking radar image of Grand Canyon, Arizona; plane-polarized (HH) image. Original scale 1:177 000. Area A indicates area of distinct stratigraphy in the upper portions of the south rim; area B indicates outcrops of the red wall limestone (Mississippian age); area C indicates an area of detailed drainage patterns.

a. Comparison of mapped, inferred lineaments with actual plotted faults.

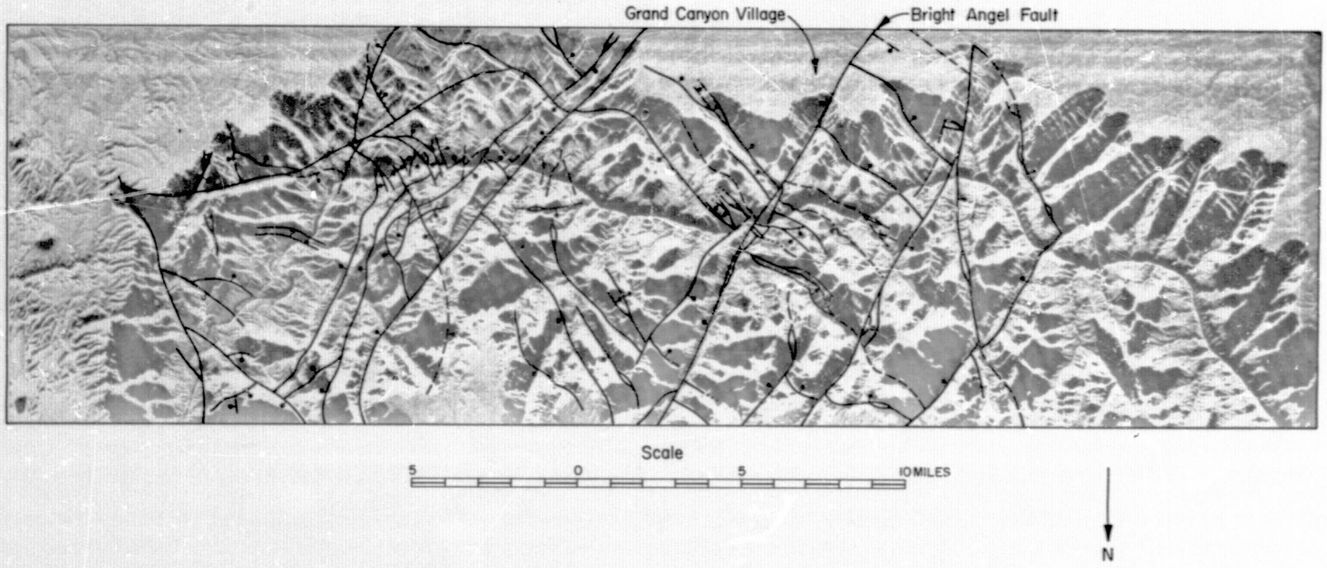

b. Comparison of mapped, inferred lineaments as transferred from ref. 13-11.

Figure 13-13.- Radar image of the Grand Canyon.

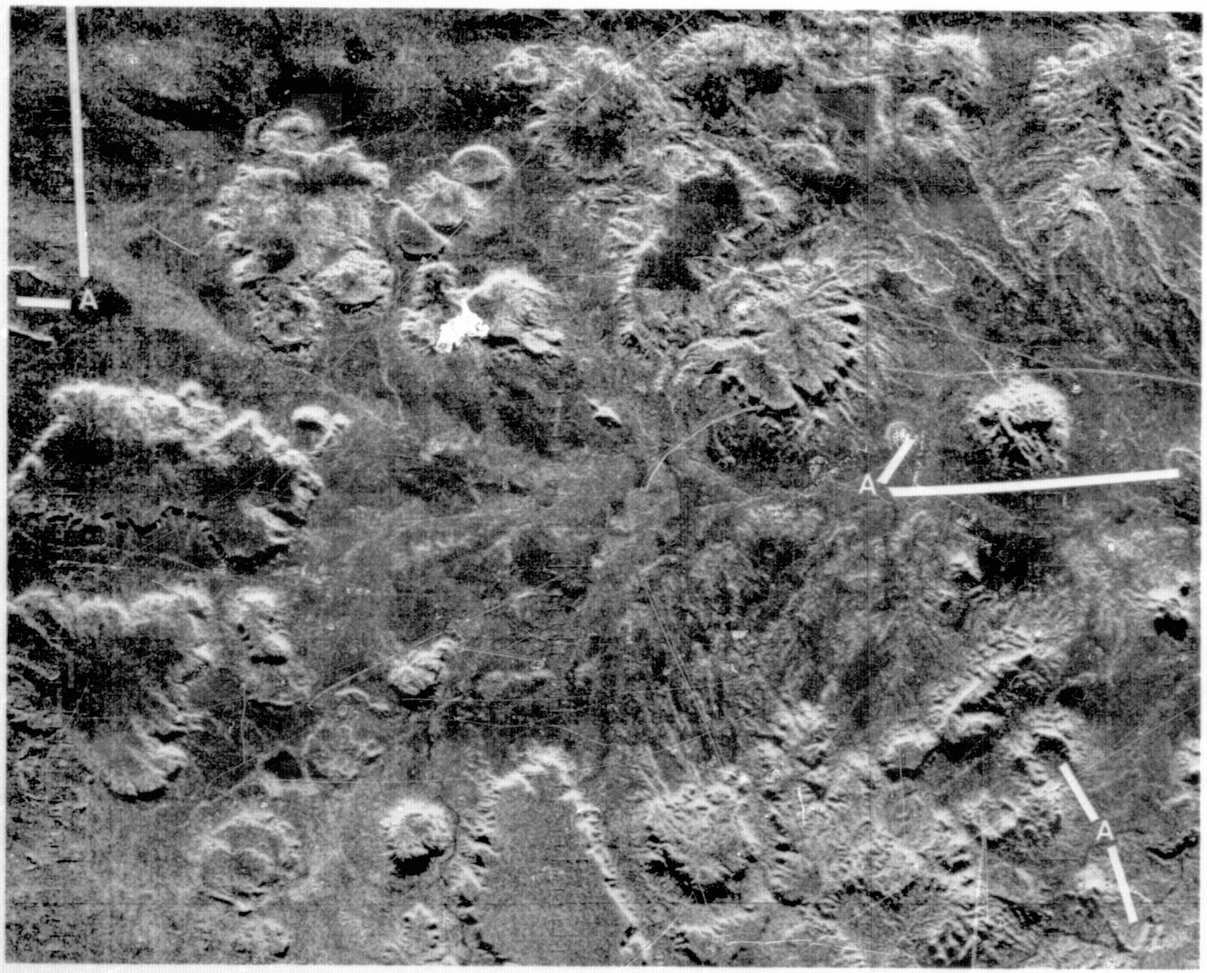

Figure 13-14.- Radar image of Hopi Buttes, Arizona; flight 103 run 12. Plane-polarized (HH) image. Area A indicates explosive volcanic vents (diatremes) which are distinctly visible on the imagery. Mesas are basalt capped with thin (2 to 6 inches) soil cover. Bedrock in region is Triassic and Jurassic sandstones with Pliocene claystones. Scale approximately 1:150 000.

N71-16138

PLUSES AND MINUSES OF RADAR IN GEOLOGICAL EXPLORATION

By L. F. Dellwig
Center for Research in Engineering Science,
University of Kansas

INTRODUCTION

Radar as a sensor has been introduced to the geological community — perhaps oversold. We have reached the point where as responsible scientists we must present an honest evaluation. We must qualify when qualification is necessary, we must make realistic comparisons, and we must project with caution. The purpose of this presentation is to do just that — to outline the unique contribution of radar in geological investigations, to point out weaknesses, and suggest needs for further investigation.

In general, the unique contribution of radar, regardless of environment, purpose, or scope of the study, most likely will be at a maximum in remote and poorly mapped areas of the world, where a regional rather than a detailed picture is desired, and where climatic conditions are adverse to ground and aerial photographic investigation.

Experience has indicated that in regional geologic studies and geological reconnaissance surveys, radar should be one of the primary sensors of any multisensor combination. In such investigations, side-scanning systems can obtain imagery totally independent of daylight conditions or most weather conditions. From radar imagery of one currently operational system, a topographic presentation can be prepared when it is not feasible or possible to collect aerial photography for mapping purposes. Because of the broad areal coverage of side-scan systems, gross structural and topographic relationships are presented in such a fashion that individual and seemingly independent features can be integrated into a regional format. In most terrain environments, radar is the best sensor for detection, integration, and analysis of lineaments.

The value of radar may decrease but is not lost in small-scale studies. In detailed studies, patterns of weathering, soil formation, topography, vegetation, and fracture-texture patterns are enhanced and facilitate separation of rock types; and lineament detection may be facilitated. Polarization and wavelength appear to be of greater significance in detailed geologic studies than in regional studies. In

studies which have been conducted where both the polarized and depolarized components are available for analysis, the depolarized component has made a significant contribution in lithologic differentiation.

RADAR IN REGIONAL STUDIES

In January and February 1967, the AN/APQ-97 system covered Darien Province, Panama, an area of approximately 6500 square miles (fig. 14-1). In 6 days of operation, which included only 6 hours flying time, at least four passes were made over most points. From this imagery was produced the first "photo mosaic" (actually a radar mosaic) of the area. In the previous 15 years, continuous effort had resulted in coverage of only about 40 percent of this province by aerial photographs because of the nearly continuous cloud cover.

This coverage also provided the raw data from which a topographic map has been produced. It cannot be overemphasized that in the absence of aerial photography, particularly in an area in which it is extremely difficult to obtain ground data, such a system is essential for the construction of a base map, as well as for the presentation of geologic data which are normally provided by conventional aerial photography.

One of the greatest values of radar is its capability to display large areas in a small format, which permits the observer to integrate seemingly isolated features into a regional picture. In this image from the Boston Mountains and Arkansas River Valley (fig. 14-2), produced by the AN/APQ-69 system, a strip approximately 40 miles wide was covered on each side of the aircraft. It was on this radar imagery that a pronounced north-south lineament pattern was first recognized (ref. 14-1). This lineament pattern was also well defined on AN/APQ-73 and AN/APQ-97 (fig. 14-3) imagery. The display of lineaments on radar imagery in this environment is primarily a function of large-scale coverage and low-resolution capability, which results in the suppression of normally distracting cultural and topographic details.

To the north of the Boston Mountains, on the south flank of the Ozark Dome in a similar terrain, a relatively narrow zone of long lineaments trends northwestward (fig. 14-4), a zone which has not been previously recorded in the literature but which on radar imagery could be traced for approximately 110 miles.

This zone can be traced northwestward in southern Missouri and southeastward into the Mississippi Embayment, in the latter of which Fisk (ref. 14-2) has noted the existence of the northwest-trending White River fault zone. That this fracture zone maintains a consistent directional trend for 450 miles across two distinct geologic provinces

(Ozark Uplift and Mississippi Embayment) with periods of development widely separated in geologic time suggests that the mechanism responsible for the development of this fracture zone was of a fundamental, deep-seated, and recurring nature. The revelation of such extensive regional shears which are not conducive to identification through more conventional mapping techniques may contribute significantly to our knowledge and understanding of rhegmatic shear systems and orogenic and epeirogenic forces.

A geomorphic evaluation of radar imagery (fig. 14-5) of a portion of the Wasatch Range east of Salt Lake City (an area from which considerable data have previously been assembled) revealed a great deal of information hitherto not presented (ref. 14-3). Although the capture of the drainage of Upper Provo Canyon and of the Provo River (fig. 14-6) has been known since 1915 (ref. 14-4), changes in the drainage pattern of the headwaters of Mill and Big Cottonwood Creeks had not been reported. Radar imagery revealed the earlier, well-developed dendritic drainage pattern, the upper part of which has been transected by the present stream divide to result in an abnormal appearance of the drainage pattern east of the present headwaters of Mill and Big Cottonwood Creeks. However, on the photo mosaic, ground clutter obscured the ancestral drainage.

RADAR IN DETAILED STUDIES

At the Cane Springs, Arizona, test site (fig. 14-7), the capability of radar in the detection of subtle changes of lithology is well demonstrated (ref. 5). Although this capability is not fully understood, the potential of radar in this environment is well documented. Areas a and e contrast with each other and with the more extensive alluvial surface, apparently because of differences in surface roughness and dielectric properties. Area a consists of fine-grained dune sand; area e is characterized by sand mixed with rock fragments with an upper 2-inch zone that is porous and puffy in texture, and the general alluvial surface consists of rock fragments of varied lithology. Neither unit was isolated during field mapping. Although the resolution of radar may be somewhat less than that of the aerial camera, the sensing of different properties permits the detection by radar of features not revealed by vertical photography. Another feature that is more pronounced on the radar imagery than on the photograph is the fault (areas d to d') which bisects the area. The enhancement of this feature on imagery is believed to be partly the result of the absence of signal scattering by the dry, sparse vegetation (an effect apparent also in areas a and e) and of the consequent domination of the return signal by terrain characteristics.

Undoubtedly, the effect of poor resolution and the suppression of distracting detail also contribute to the clarity of the presentation of the fault.

A striking example of the value of radar in detailed lineament studies is seen along the South Fork, Cottonwood River, Chase County, Kansas (fig. 14-8) (ref. 14-6). The long linear features (areas A to A' and B to B') traverse the cross-polarized return of this area of farmland and pasture land, features which are not revealed in the like polarized return or in aerial photographs. Cursory field checking has revealed drainage deflections along portions of the linear features, and it has been established that they are not fence-line controlled. It may be significant that the trend of areas B to B' closely approximates the trend of a basement fault.

MULTIFREQUENCY RADAR

Casual examination of multifrequency radar during the course of previous investigations has suggested that simultaneous imaging of a target area with several frequencies of radar might provide a great deal of data for the bioscientist. Unfortunately, there is only a minimum of multifrequency radar imagery available for systematic evaluation for geoscience content. To evaluate long-wavelength imagery, it becomes necessary to compare long-wavelength imagery of one system with short-wavelength imagery of other systems recorded at different times, so that system and target parameters show a minimum of similarity. In spite of the drawbacks of comparison of imagery from different systems, sufficient data can be obtained from a variety of K-, C-, and P-band images of the Pisgah Crater area (fig. 14-9) to justify additional multiband radar imaging over this or other geologic test sites. Although sufficient data for a thorough evaluation of polarization, resolution, aspect angle, and so forth, are not available, evaluation of existing imagery has demonstrated strong wavelength dependency.

Two particularly significant observations emerged from the study. (1) Windblown silts and sands overlying the northwestern corner of Pisgah flow were penetrated by the long-wavelength radar (P-band), the return signal being essentially from the partly buried lava. (2) The alluvial fan on the southwestern side of Lavic Lake, although well defined on K-band radar imagery, was not delineated on the P-band image. The surface of the fan was composed of fragmental material, 85 percent of which was less than 5 centimeters in diameter. This surface appeared as a dark tone (smooth) to P-band radar, as did the adjacent lake surface.

Although surface roughness appears to be the most strongly influencing parameter on radar return, under some conditions at least, the penetrative capability of long-wavelength radar has been a significant factor in determining the magnitude of the return signal. The real value of long-wavelength radar, judging from the evaluation of only a limited amount of imagery, is not its penetrative capability or any other single factor per se, but its unique total response to terrain characteristics, as compared to a shorter wavelength radar system. Maximum value will be derived only when multiband imagery is recorded.

THE MINUSES OF RADAR

No sensor yet developed is perfect. Many of the drawbacks of radar will assuredly be reduced in magnitude, and some will be eliminated. The following are major weaknesses which we face at present:

1. Look-direction dependency
2. Impracticality of mosaicking slant-range imagery
3. Radar shadowing in areas of high relief
4. Distortion caused by slant-range presentation
5. Displacement of elevated features caused by layover

The minuses to some degree point to avenues for research by engineers and geoscientists. In addition to these problems, the influences of such factors as polarization, wavelength, aspect angle, and dielectric properties need careful evaluation. Some progress has been made, but a quick look at what has been done will emphasize the need for careful consideration and evaluation of such factors in order to present a balanced evaluation and dispel the aurora of skepticism which in part developed as a result of overselling the system.

Cursory examination of the Darien mosaic (fig. 14-1) reveals a very effective three-dimensional presentation of an area about which little was previously known. Careful examination, however, presents a somewhat different picture. Comparison of the original imagery with the mosaic reveals areas where omissions, repetitions, and additions or deletions were necessary to insure matching of coastline and major river segments. Such problems develop in part when attempting to match a near-range segment with a far-range segment (slant-range display) and are in part the result of improper synchronization of film and air speed. Examination of this imagery also revealed that the interpreted drainage direction often varied with look direction. The effect of look direction was of

particular interest because a detailed evaluation of imagery of eight flights over the Boston Mountains (ref. 14-7) led to the conclusion that for this particular terrain environment and the gross topographic expression of the lineaments involved, look direction affected the interpretation, but not to a degree sufficiently significant to justify multiple passes over the area. It is apparent that we have only scratched the surface with regard to the effect of look direction on radar return signal. The Boston Mountains study also pointed up the variations in drainage pattern configuration (fig. 14-10) resulting from changes in look direction. Quite obviously, generalizations cannot be based on analysis of a single terrain environment.

Many other examples could be cited, but elaboration is not necessary. Both suggest the same thing — there is a need for carefully planned experiments for purposes of evaluation of radar as a sensor. I am certain that in the long run the scientific community will benefit if a greater percentage of the effort of the geoscientist is directed toward evaluation of the systems. Certainly, this is not meant to imply that the solution of practical problems should not continue; both approaches are needed.

Supporting data for the material presented herein are included in appendix 14A.

REFERENCES

14-1. Dellwig, L. F.; Kirk, J. M.; and Walters, R. L.: The Potential of Low Resolution Radar Imagery in Regional Geologic Studies. Jour. Geophys. Res., vol. 71, 1966, pp. 4995-4998.

14-2. Fisk, H. M.: Geologic Investigations of the Alluvial Valley of the Lower Mississippi Valley: Vicksburg, Miss. Miss. River Comm., 1944, pp. 66-67.

14-3. Peterson, R. M.: Observations on the Geomorphology and Land Use of Part of the Wasatch Range, Utah. CRES Technical Report 133-4, University of Kansas, 1968.

14-4. Anderson, G. E.: Stream Piracy of the Provo and Weber Rivers, Utah. Am. Jour. Sci., 4th Ser., vol. 40, 1915, pp. 314-316.

14-5. MacDonald, H. C.; Brennen, P. A.; and Dellwig, L. F.: Geologic Evaluation by Radar of NASA Sedimentary Test Site. IEEE Trans. Geosci. Electronics, vol. GE-5, no. 3, 1967, pp. 72-78.

14-6. Dellwig, L. F.; MacDonald, H. C.; and Kirk, J. M.: The Potential of Radar in Geological Exploration, (in press), 1968.

14-7. Kirk, J. M.; Dellwig, L. F.; and Jefferis, L. H.: The Influence of Radar Look-Direction on the Recording of Geologic Lineaments — A Study in the Boston Mountains, Arkansas, (in press), 1968.

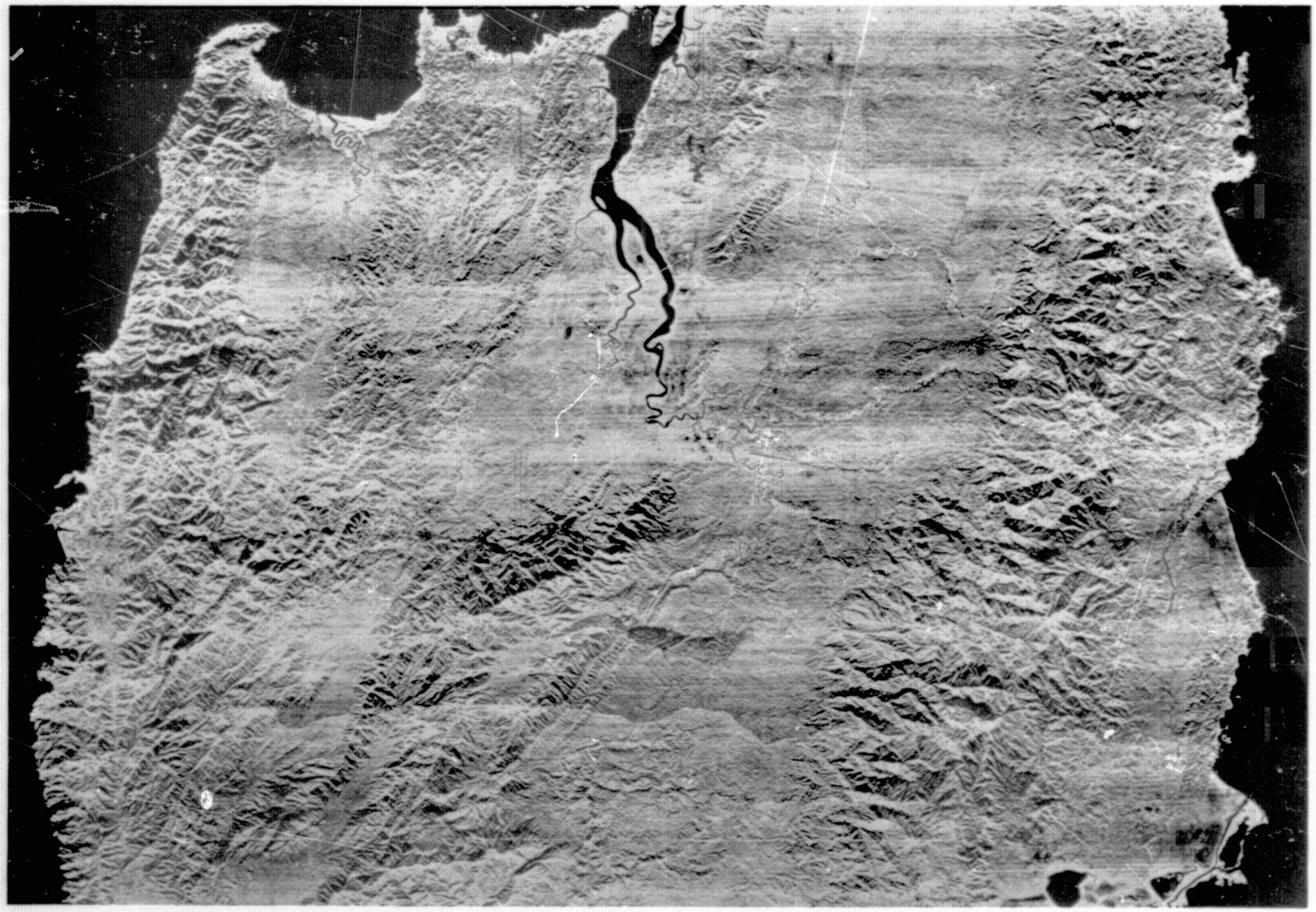

Figure 14-1.- Darien Province, Republic of Panama, and Northwest Colombia.

Figure 14-2.- Radar imagery (AN/APQ-69) in the vicinity of Ozark, Arkansas.

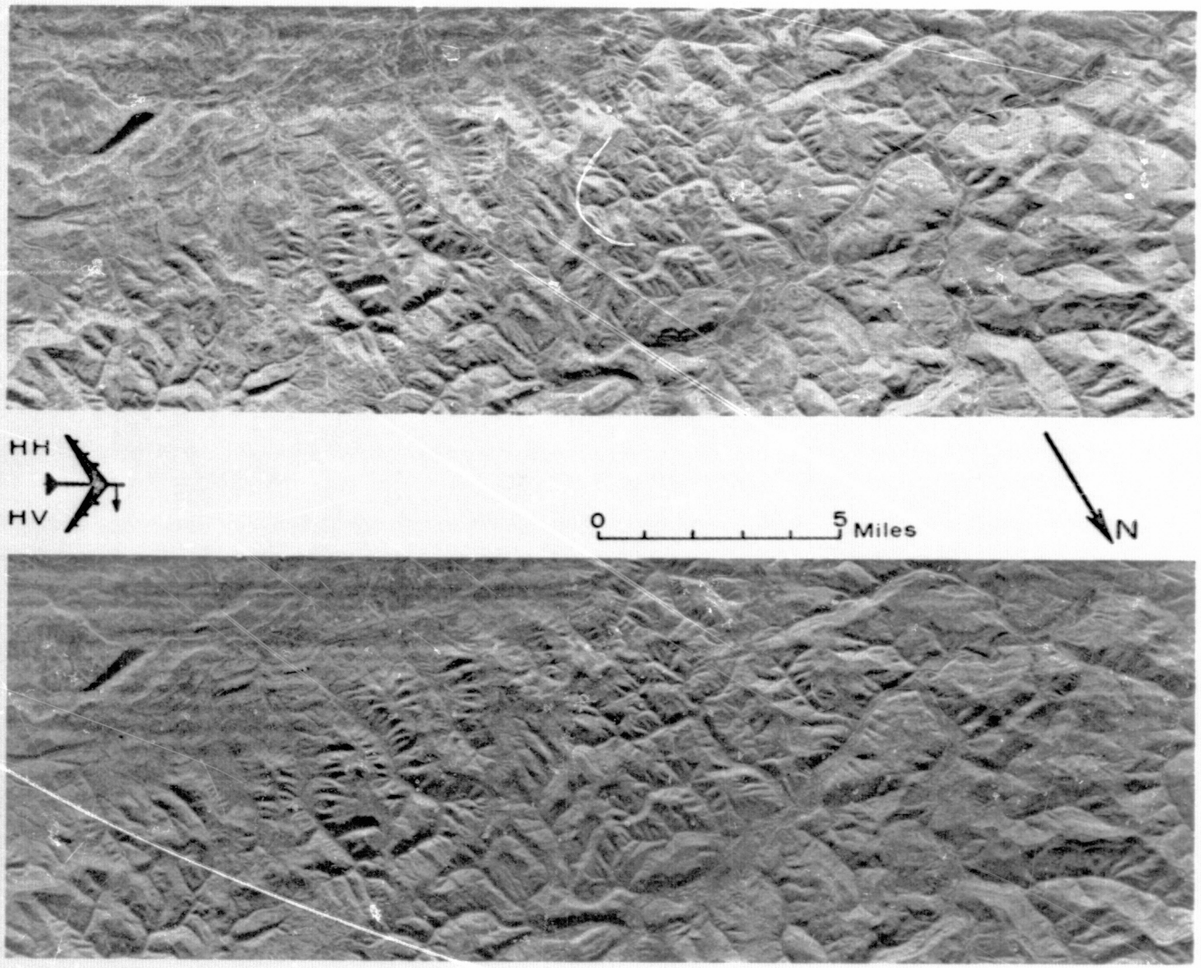

Figure 14-3.- Boston Mountains-Arkansas River Valley, Franklin and Johnson Counties, Arkansas.

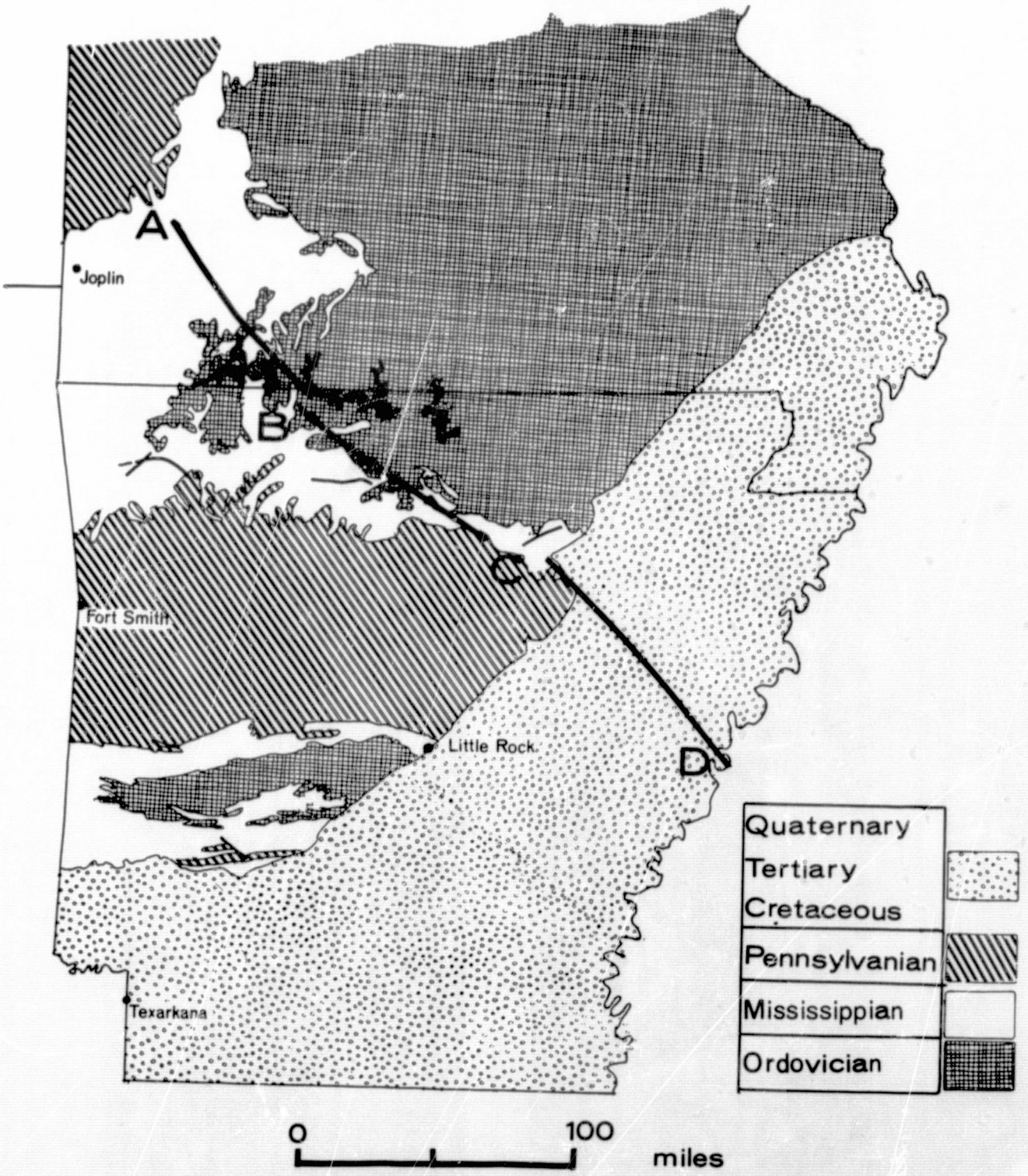

Figure 14-4.- Radar lineament zone (areas B to C) on south flank of Ozark Dome, Arkansas. The lineament zone ties a mapped fault (areas A to B) in southwestern Missouri to the White River fault zone (areas C to D), as mapped by Fisk (ref. 14-2) and represents a concept of a single fracture zone approximately 450 miles in length.

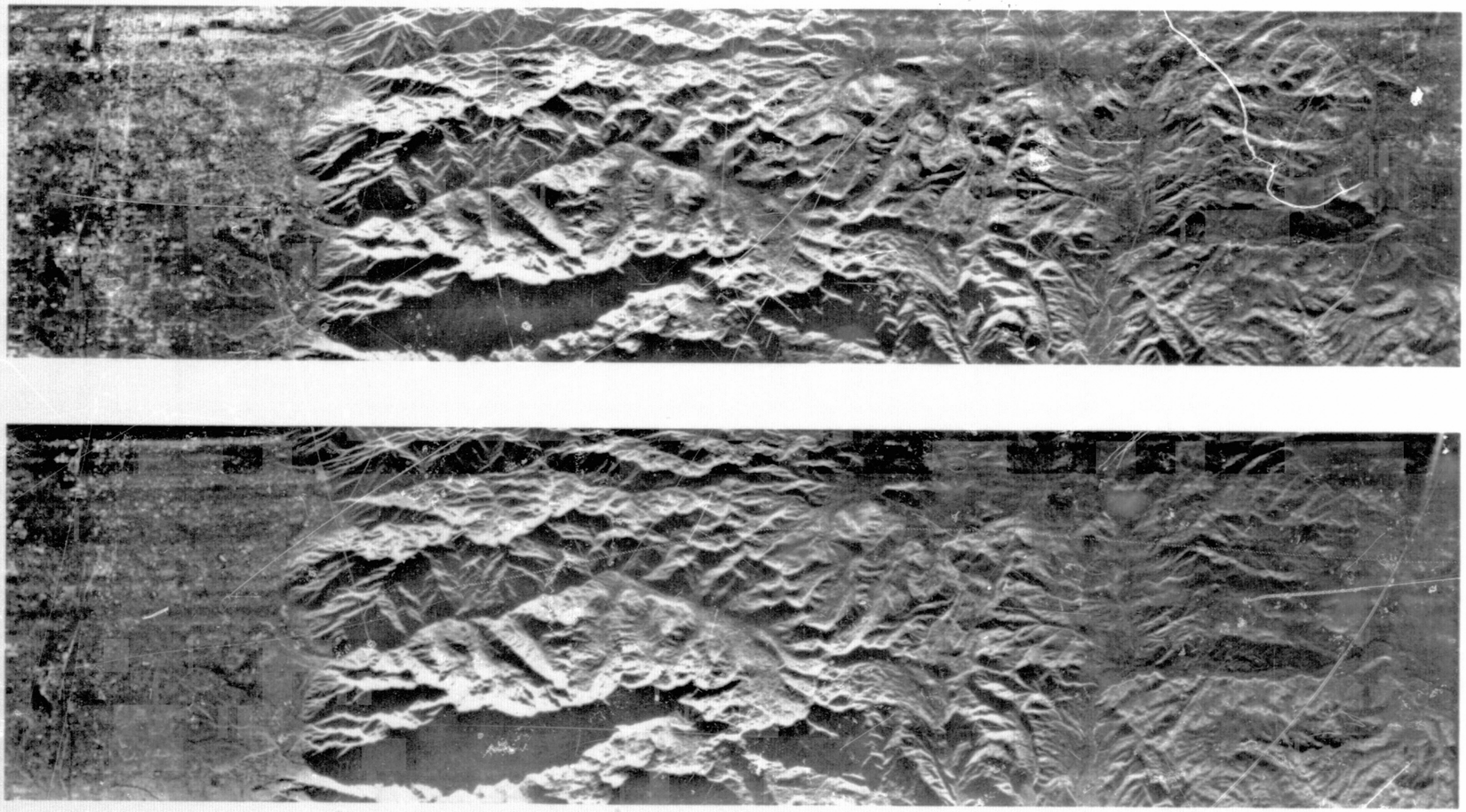

Figure 14-5.- Wasatch Range.

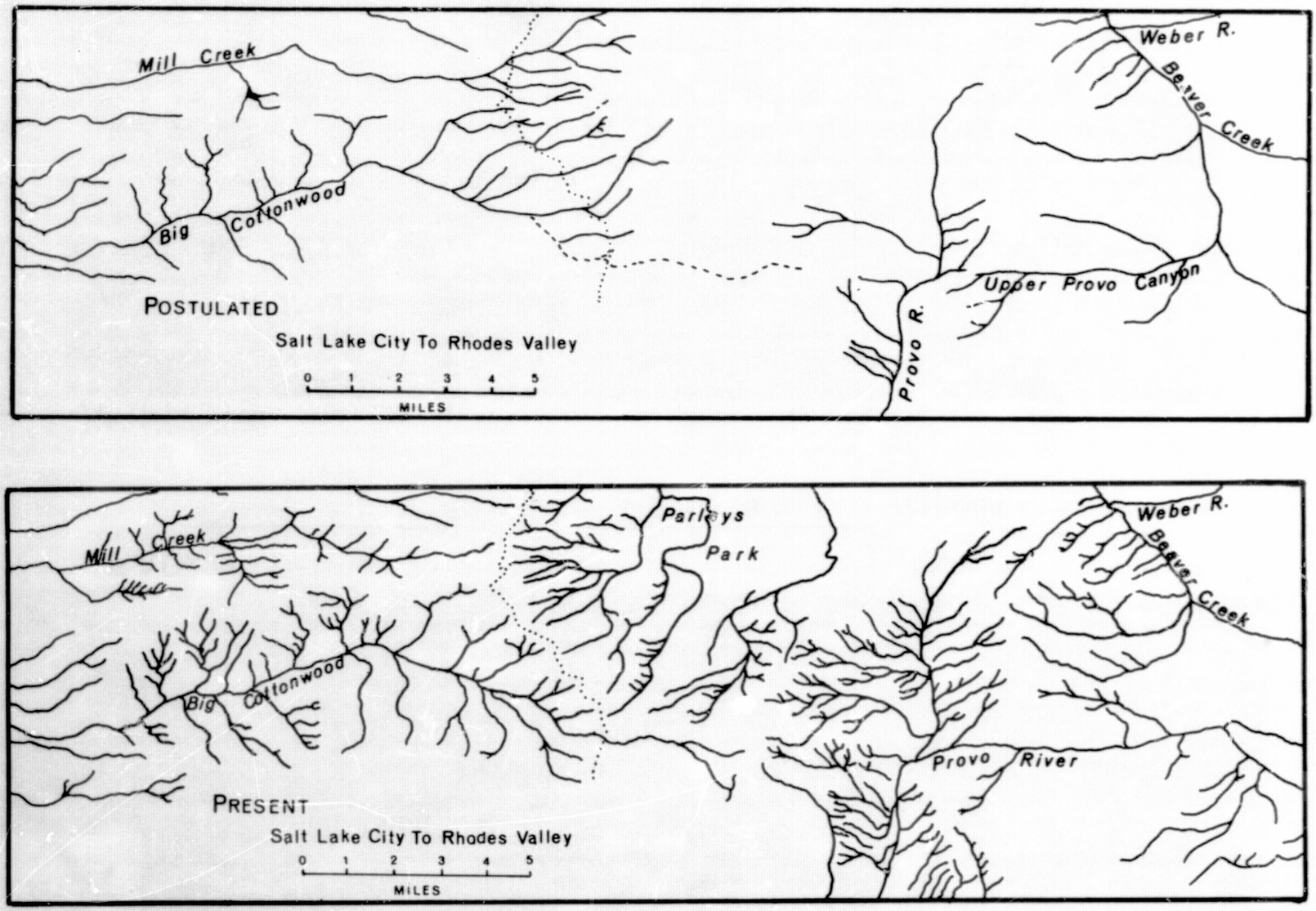

Figure 14-6.- Postulated ancestral drainage and present drainage, Wasatch Range.

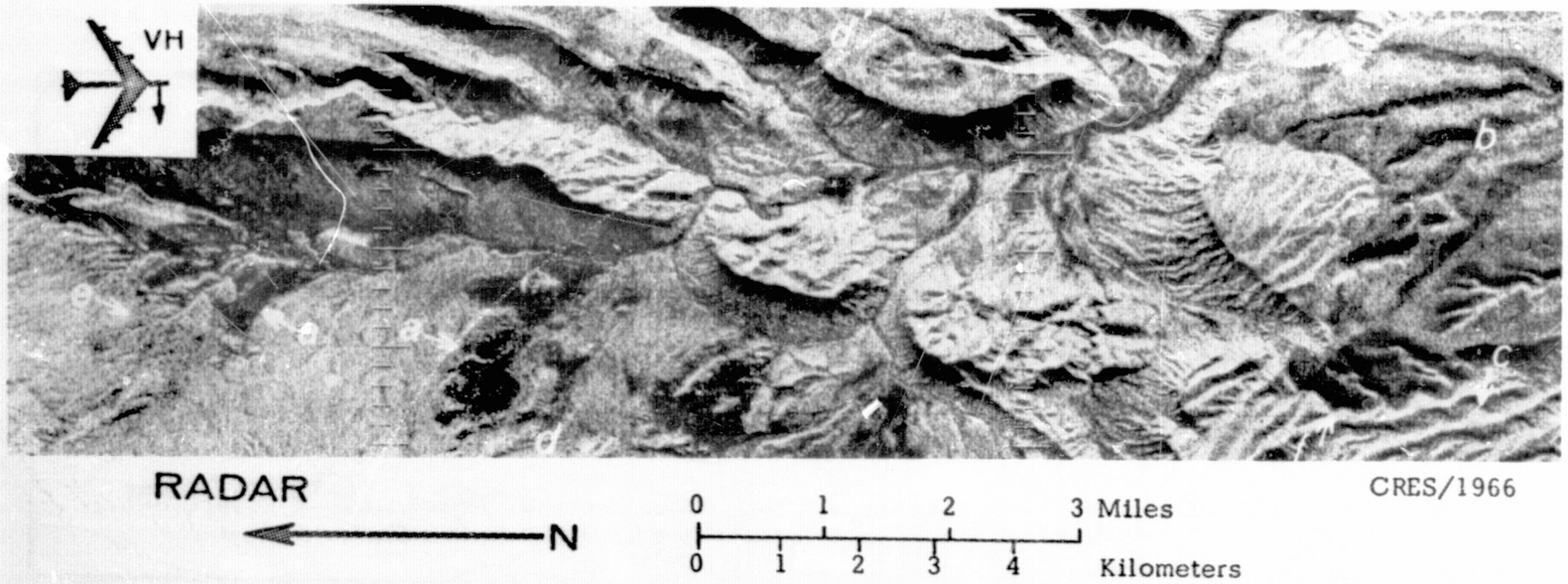

Figure 14-7.- Comparison of radar imagery and aerial photography, Cane Springs Area, Arizona.

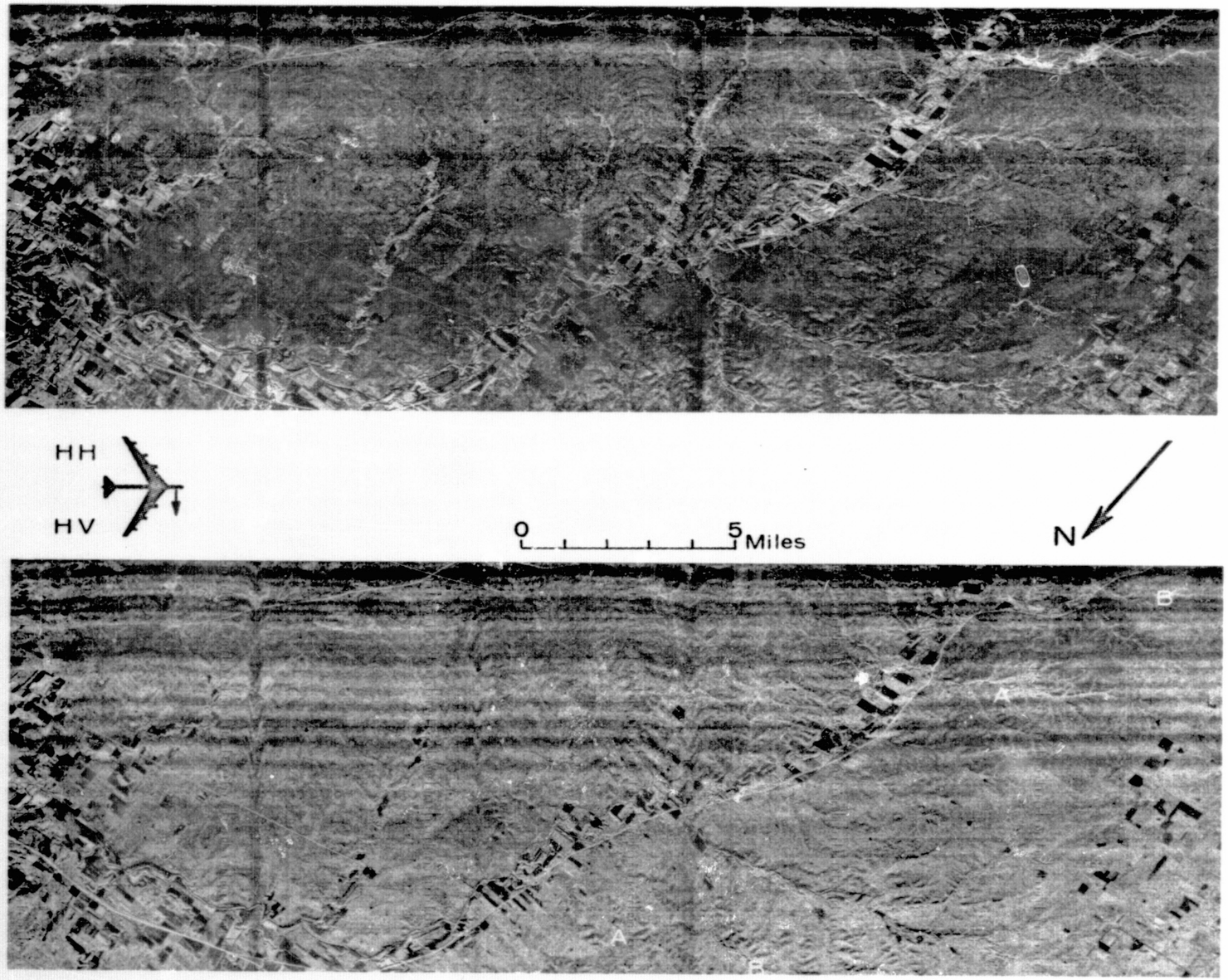

Figure 14-8.- South Fork Cottonwood River, Plymouth to Matfield Green, Chase County, Kansas.

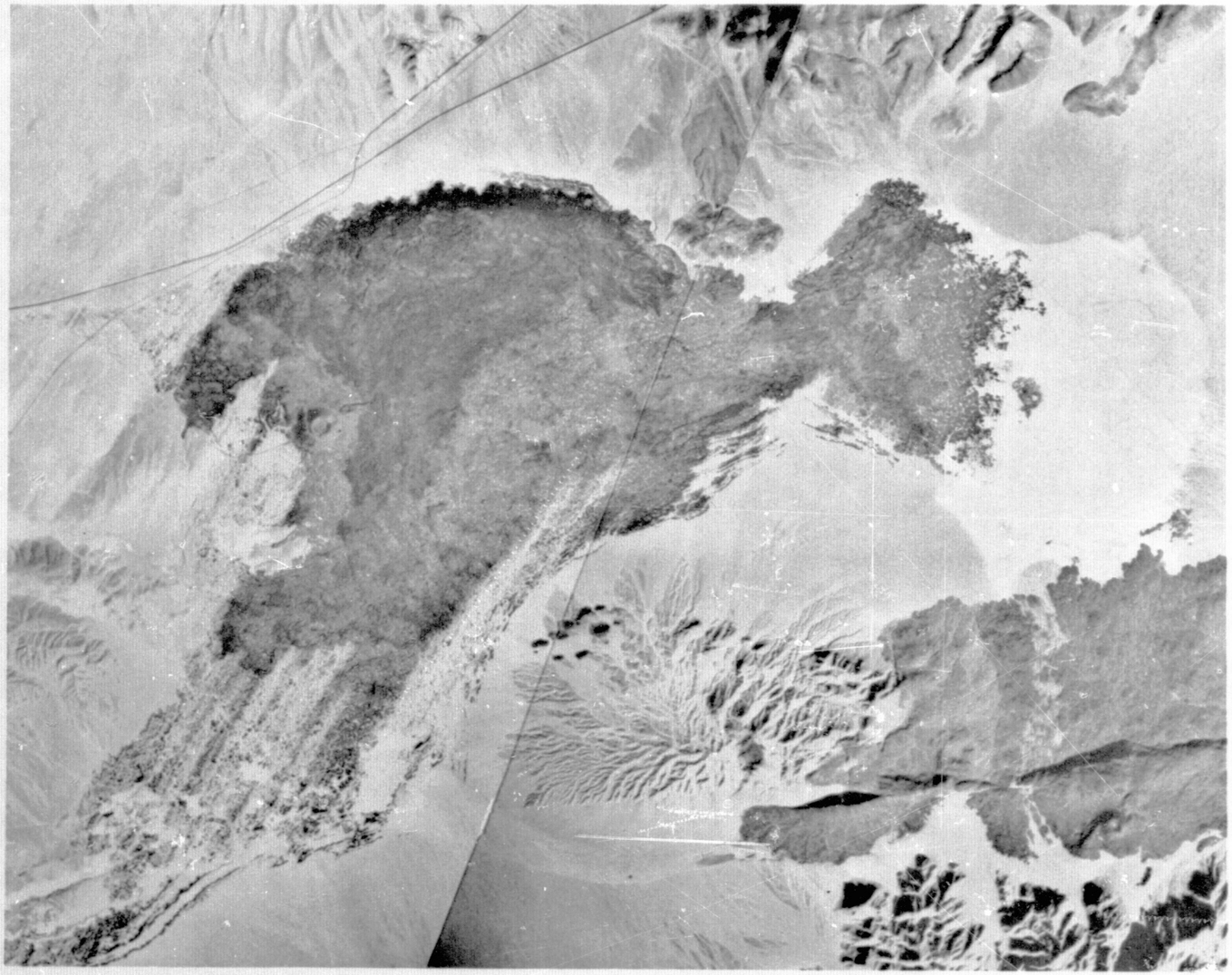

Figure 14-9.- Pisgah Crater, California.

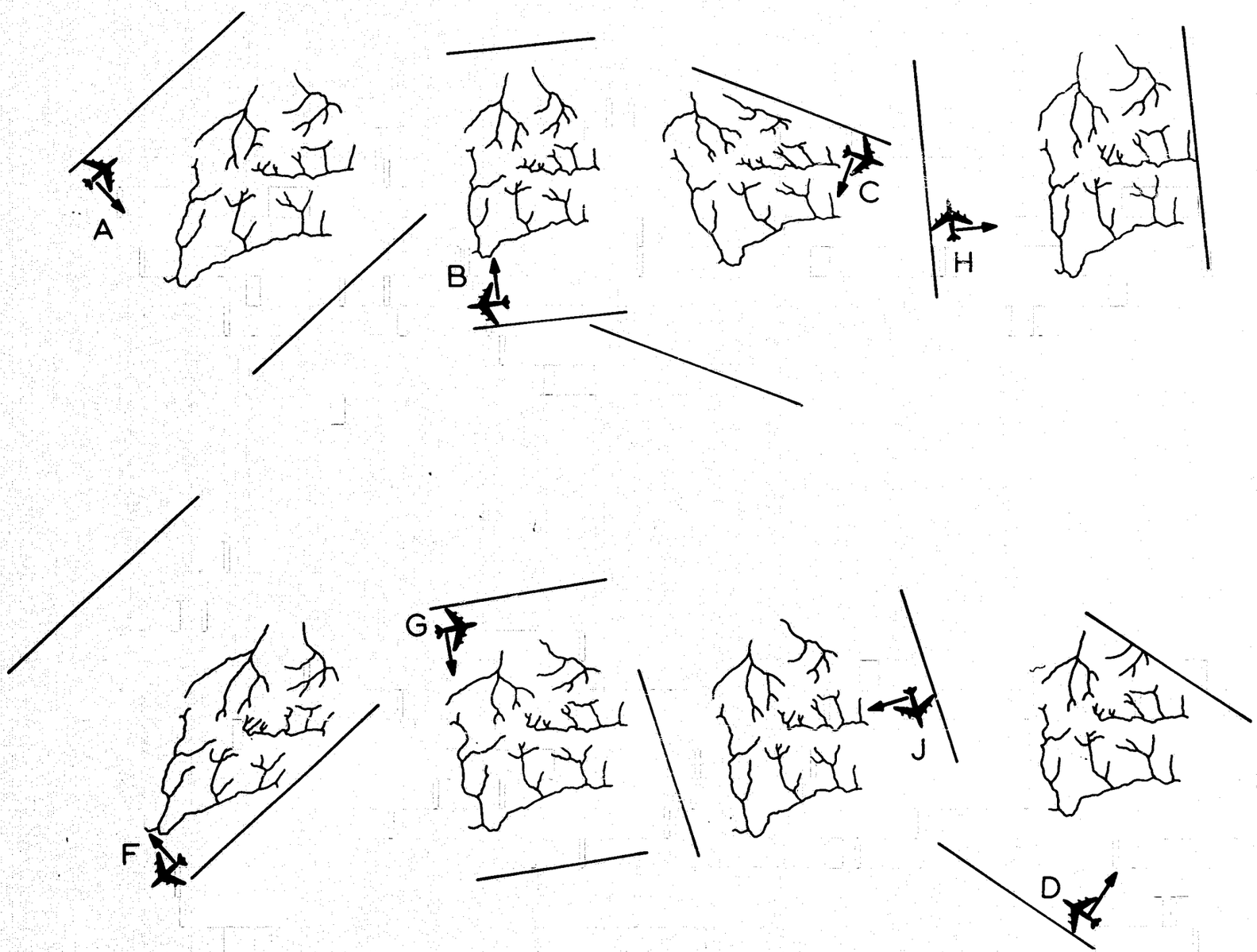

Figure 14-10.- Major drainage pattern in a portion of the test site showing apparent differences in stream orientation relative to position and orientation in the imagery.

APPENDIX 14A

TEST SITE 2, PISGAH CRATER, CALIFORNIA[a]

[Investigator, L. F. Dellwig; Discipline, Geology]

Flight/ run	Date flown	Data	Date received	Quality	Results
5/1 5/2 5/3 5/4 5/5 5/6 5/7 5/8 5/9 5/10 5/11	10/2/65	NRL P- and C-band side-looking airborne radar (SLAR)	Late '65	Poor	Comparisons of imagery from different systems reveals sufficient data to justify additional multiband imaging over this and other geologic test sites. Some penetration has been demonstrated, and variation of return intensity with variation in wavelength has been documented.

[a]Imagery from this set of flights is classified. Flights were indirectly supported by NASA funds.

PRECEDING PAGE BLANK-NOT FILMED.

TEST SITE 2, PISGAH CRATER, CALIFORNIA

[Investigator, L. F. Dellwig; Discipline, Geology]

Mission/ flight	Date flown	Data	Date received	Quality	Results
-/101 -/102	11/2/65 to 11/4/65	AN/APQ-97 K-band SLAR	12/15/65	Excellent	Geological content of simultaneously recorded like- and cross-polarized imagery far exceeds the content of a single polarization return. Separation of flows is look-direction dependent.

SUMMARY OF OBJECTIVES AT SITE 2

The Pisgah Crater-Lavic Lake area, California, is in a region of volcanic flows and associated bolson-type sediment which is essentially free of vegetation. The landscape has been considered to be potentially analogous to portions of the lunar surface. In a small area, it offered the opportunity to make preliminary evaluation of like- and cross-polarized imagery of lavas of a range of ages, of fine-grained lake sediments, of isolated patches of vegetation on the lake, and of a variety of gravels and coarser size fragmental materials of the relatively recent alluvium.

The extensive radar coverage with K-band imagery (AN/APQ-97 SLAR, 7/28/66) and the vast amount of ground data available provided a basis for comparison of imagery of wavelengths other than K-band when it subsequently became available. Although comparisons of nonsimultaneously recorded imagery are not without drawbacks, simultaneously recorded long- and short-wavelength imagery is not known to be available.

SUMMARY OF SCIENTIFIC ANALYSIS PERFORMED TO DATE

Of special interest in the NRL SLAR imagery is the contrast in the like- and cross-polarized return and the relationship between intensity and look direction. In addition to field data collected by other agencies, field investigations were conducted in areas in which there was strong contrast in like- and cross-polarized return and in imagery of diverse wavelengths. In simultaneously produced like- and cross-polarized imagery, information was obtained which was previously unobtainable from only like-polarized radar imagery. Comparison of long- and short-wavelength imagery demonstrated that the return signal from certain cultural and natural phenomena is strongly wavelength dependent. Although surface roughness appears to be the most strongly influencing parameter, the penetrative capability of long-wavelength imagery has been a significant factor in determining the magnitude of the return signal.

SUMMARY OF SCIENTIFIC ANALYSIS TO BE PERFORMED

No future work on existing imagery is anticipated.

PUBLICATIONS

Moore, R. K.; and Dellwig, L. F.: Terrain Discrimination by Radar Image Polarization Comparison. Proceedings of the Institute of Electrical and Electronics Engineers, vol. 54, no. 9, 1966, pp. 1213-1214.

Dellwig, L. F.; Bickford, M. E.; Kirk, J. N.; and Walters, R. L.: Remote Sensor Studies of the Pisgah Crater Area, California: A Preliminary Report. Kansas University CRES Technical Memorandum 61-18, 1965.

Dellwig, L. F.; and Moore, R. K.: The Geological Value of Simultaneously Produced Like- and Cross-Polarized Radar Imagery. Journal of Geophysical Research, vol. 71, no. 14, 1966, pp. 3597-3601.

Dellwig, L. F.: An Evaluation of Multiband Radar Imagery of the Pisgah Crater, California, Area. Kansas University CRES Technical Report 118-6. (In preparation.)

Published Paper in Which Reviews of the Cane Springs Research are Presented

Dellwig, L. F.; MacDonald, H. C.; and Kirk, J. N.: The Potential of Radar in Geological Exploration. Proceedings Fifth Symposium on Remote Sensing of Environment, University of Michigan. (In press.)

TEST SITE 3, MONO CRATERS, CALIFORNIA

TEST SITE 15, TWIN BUTTES, ARIZONA

TEST SITE 2, PISGAH CRATER, CALIFORNIA

TEST SITE 10, SAN FRANCISCO VOLCANIC FIELDS, ARIZONA

[Investigator, E. Gillerman; Discipline, Geology]

Mission/ flight	Date flown	Data	Date received	Quality	Results
-/100	11/1/65	AN/APQ-97 K-band SLAR	12/5/65	Excellent	Although glass content of bedrock appears to be of significance in depolarization of the transmitted signal, the effect of vegetation, roughness, and several other parameters could not be defined.
-/101	11/2/65	AN/APQ-97 K-band SLAR	12/5/65	Excellent	
-/102	11/4/65	AN/APQ-97 K-band SLAR	12/6/65	Excellent	
-/103	11/5/65	AN/APQ-97 K-band SLAR	12/6/65	Excellent	
-/104	11/8/65	AN/APQ-97 K-band SLAR	12/10/65	Excellent	

TEST SITE 3, MONO CRATERS, CALIFORNIA

TEST SITE 15, TWIN BUTTES, ARIZONA

TEST SITE 2, PISGAH CRATER, CALIFORNIA

TEST SITE 10, SAN FRANCISCO VOLCANIC FIELDS, ARIZONA - Concluded

[Investigator, E. Gillerman; Discipline, Geology]

Mission/ flight	Date flown	Data	Date received	Quality	Results
-/89	10/14/65	AN/APQ-97 K-band SLAR	11/20/65	Excellent	
-/94	10/17/65	AN/APQ-97 K-band SLAR	11/20/65	Excellent	

SUMMARY OF OBJECTIVE AT TEST SITES

The objective at the test sites was to test the hypothesis that the glass content of volcanic rocks affected the degree of radar return on cross-polarized radar imagery and to evaluate other parameters which might account for the differences in radar return on simultaneously produced like-polarized and cross-polarized AN/APQ-97 K-band radar imagery.

SUMMARY OF STUDIES PERFORMED TO DATE

To investigate the hypothesis, all available radar imagery was examined to detect differences in return on simultaneously produced like- and cross-polarized radar imagery. Noticeable differences were detected on imagery of the Mono Craters, Holloran Summit, and Pisgah Crater, California, areas and in the Twin Buttes and San Francisco Volcanic Fields, Arizona, volcanic areas. All are areas of volcanic rocks, some of which were known to be glassy. Imagery of the Obsidian Cliffs area, Yellowstone National Park, an area of glassy volcanic rocks, was also examined but no difference in return was detected.

The areas were then examined in the field, and field examination showed that while the glass content might be a contributory factor, it is not the determining factor that accounted for the lower radar return on cross-polarized imagery than on like-polarized imagery. Roughness, topography, vegetation differences, and rock composition (regardless of glass content) are important. The combination of factors governs the degree of return, the relative value of each depending upon its relationship to the total environment.

Microscopic examination of the rocks in an attempt to investigate more thoroughly the role of total rock composition and of glass content failed to give any more conclusive information.

SUMMARY OF STUDIES TO BE PERFORMED

To evaluate properly the reasons for the difference in return on simultaneously produced like- and cross-polarized radar imagery, much more detailed field investigations as well as laboratory and microscopic work need to be made, and test sites with better ground control are needed. In addition, radar imagery of more than one frequency (and polarization) should be examined, as well as imagery from other remote

sensors. At present, no further studies are being planned, nor are any contemplated in the near future. However, if the investigations are pursued, it would be in these directions.

PUBLISHED PAPER REPORTING ON CROSS-POLARIZED RADAR AND VOLCANIC ROCKS

Gillerman, Elliot: Investigation of Cross-Polarized Radar on Volcanic Rocks. CRES Technical Report 61-22, 1967.

TEST SITE 34, OUACHITA MOUNTAINS, ARKANSAS-OKLAHOMA

[Investigator, L. F. Dellwig; Discipline, Geology]

Mission/ flight	Date flown	Data	Date received	Quality	Results
-/83	9/15/65	AN/APQ-97 K-band SLAR	10/1/65	Excellent	1. Lineament displays which had been identified on previously obtained SLAR imagery were evaluated, and it was established that they were not radar-system dependent phenomena. 2. The Tuskahoma Syncline area in Oklahoma was geologically mapped on radar imagery in an effort to determine the feasibility of use of radar imagery as a primary mapping tool.
-/127	7/27/66	AN/APQ-97 K-band SLAR	8/22/66	Excellent	Effect of look direction in this terrain environment was evaluated; and it was determined that although geoscience information content was influenced by look direction, the effect was not sufficiently significant to justify multiple passes.

SUMMARY OF OBJECTIVES AT TEST SITE 34

The initial objective at test site 34 was to evaluate radar as a primary geologic mapping tool in a structurally complex and relatively heavily vegetated area. Although a great deal of ground data are available, the complexity of the area demands additional data for the complete understanding of its tectonic development. Geologic analysis of a relatively simple structural area would enable evaluation of radar as a mapping tool, whereas analysis of some of the more complex areas would determine the capability of radar to contribute unique geologic data in such a terrain environment.

The objectives were revised for the second flight (AN/APQ-97 flight 127) over the area. Identification of a north-south lineament trend in the Boston Mountains (Ouachitas) posed the question as to whether or not look direction was significant in their presentation. The flight was requested solely for the purpose of evaluating look direction and was recognized to be only a first step in any overall evaluation of that parameter.

SUMMARY OF SCIENTIFIC ANALYSIS PERFORMED TO DATE

The Tuskahoma Syncline area was mapped on radar imagery, and the results were evaluated in the light of published information and field data. The radar imagery proved to be an effective mapping tool, particularly in the depiction of gross patterns and in the revelation of lineaments, some of which had not been previously detected through mapping by more conventional methods. The lineaments revealed in the Boston Mountains were studied in the field in consultation with U.S. Geological Survey geologists who had recently mapped the area. The appearance of the pattern on radar was established as a unique data contribution of radar.

Imagery from the second flight was evaluated, and it was determined that in this particular terrain environment with the gross topographic expression of the lineaments involved, look direction affected the display of lineaments and drainage network, but not to a degree sufficiently significant to justify multiple passes.

Since it was recognized that radar displays lineament patterns well and permits the integration of seemingly isolated structures into regional patterns, an evaluation of tectonic relationships between the Ouachita and Arbuckle Mountains was undertaken in an effort to uncover significant data relative to the relationship of the two mountain belts

to each other. All necessary data have been plotted from the imagery, and the analysis is in progress.

SUMMARY OF SCIENTIFIC ANALYSIS TO BE PERFORMED

Except for the use of the imagery in analysis of several structurally complex areas, no additional work utilizing this imagery is anticipated.

PUBLISHED PAPERS REPORTING SPECIFICALLY ON RESEARCH AND RESULTS OF OUACHITA MOUNTAINS INVESTIGATION

Dellwig, L. F.; Kirk, J. N.; and Walters, R. L.: The Potential of Low Resolution Radar Imagery in Regional Geologic Studies. Journal of Geophysical Research, vol. 71, no. 20, 1966, pp. 4995-4998. NASA Contract NSR 17-004-003.

Kirk, J. N.; and Walters, R. L: Radar Imagery, A New Tool for the Geologist. The Compass of Sigma Gamma Epsilon, vol. 43, no. 2, 1966, pp. 85-93.

Kirk, J. N.; and Walters, R. L.: Preliminary Report on Radar Lineaments in the Boston Mountains of Arkansas. The Compass of Sigma Gamma Epsilon, vol. 45, no. 2, 1968, pp. 122-127.

Kirk, J. N.; Dellwig, L. F.; and Jefferis, L.: The Influence of Radar Look Direction on the Recording of Geologic Lineaments — A Study in the Boston Mountains, Arkansas. CRES Report 118-7, 1968.

TEST SITE 83, IRONTON (ST. FRANCOIS MOUNTAINS), MISSOURI

[Investigator, E. Gillerman; Discipline, Geology]

Mission/ flight	Date flown	Data	Date received	Quality	Results
-/128	7/28/66	AN/APQ-97 K-band SLAR	8/28/66	Excellent	Major lineaments and other fracture patterns were better displayed and extended for greater distances on radar than on aerial photographs.

SUMMARY OF OBJECTIVES

The study of AN/APQ-97 SLAR imagery in the St. Francois Mountain area of Southeastern Missouri had as its principal objective an attempt to ascertain what geologic features, obscure or difficult to recognize on aerial photographs or on the ground, were better recorded on radar imagery in an area of deciduous forest cover. As an auxiliary purpose, the possible importance of radar in mineral exploration was of interest. The study of the geology of the area, per se, was incidental to the primary goals.

SUMMARY OF STUDIES PERFORMED TO DATE

Radar imagery of the area was examined and comparisons were made of the information derived from it, principally the structural features, and of the information shown on aerial photographs and geologic maps. Investigations in the field tested some of the information hypothesized from a study of the radar imagery.

Results indicated that large-scale regional structural patterns that can be readily identified on radar imagery are obscure on aerial photographs. Linear features, representing faults and fractures, and circular patterns of possible significance appear on radar imagery in a manner superior to their portrayal on aerial photographs. Many of the features identified on the radar imagery are not distinguishable on the aerial photos or are obscure or poorly depicted. This superiority of radar over aerial photographs in the recognition of large-scale features is believed to be at least partly the result of the accentuation by radar of the gross features of the terrain and the consequent suppression of fine detail. This is coupled with the ability of radar to depict a large area on one photographic strip.

The value of radar in mineral exploration is linked to this ability to portray the broad regional pattern and to the accentuation of structural features which may be recognizable only with difficulty, if at all, by more conventional reconnaissance methods.

As a result of the studies, a previously unknown major lineament, traceable for more than 25 miles on available SLAR imagery, was recognized; it may extend for more than 125 miles in light of additional data from other sources. Its existence may be of significance in the distribution of the mineral deposits of the area. Other heretofore unmapped faults and fractures, identified on radar imagery, also appear to be associated with the localization of mineral deposits.

SUMMARY OF STUDIES TO BE PERFORMED

The geologic implications of a major lineament and of its relationships to the distribution of mineral deposits will be pursued by additional field investigations and hopefully by the study and comparison of radar imagery of other wavelengths. Further studies of the anomalous circular features will also be made.

PAPER ON RADAR STUDIES IN THE ST. FRANCOIS MOUNTAINS

Gillerman, Elliot: Circular Structural Features and Major Lineaments defined by SLAR, St. Francois Mountains, Missouri. CRES Report (being prepared).

TEST SITE 85, LAWRENCE, KANSAS

[Investigator, D. S. Simonett; Discipline, Geography and Geology]

Mi sion/ flight	Date flown	Data	Date received	Quality	Results
-/83	9/15/65	AN/APQ-97 K-band SLAR	10/1/65	Good	Analysis still in progress. Results obtained to date indicate considerable amounts of new geologic information may be obtainable from radar.

A SUMMARY OF OBJECTIVES OF STUDY IN SOUTHERN DOUGLAS COUNTY

The purpose of this study is to evaluate radar imagery as a geologic reconnaissance tool. It is specifically intended to determine the effectiveness of radar imagery in the determination of structural elements in flat-lying, gently deformed strata. The study involves the comparison of data obtained from radar imagery, aerial photographs, and field studies of the area.

It has been demonstrated in preliminary work in the study area that a close correlation exists between fracture patterns and aerial photography lineaments. Radar imagery from the same area also shows many of the lineaments obtained through aerial photography interpretation. However, a number of additional linear features were observed on the radar imagery. The problem is to determine the relationship between the radar lineaments and bedrock structures and to determine why the radar imagery apparently provides more lineament data than the aerial photographs.

SUMMARY OF ANALYSES PERFORMED TO DATE

In analysis and interpretation of AN/APQ-97 SLAR imagery, lineaments have been identified and mapped for the study area. Air photography data for the area have been studied to determine the type and amount of information available. These data have been plotted on base maps to allow comparison with the radar data.

A study of the major radar lineaments has been carried out in the field. Field studies have been performed to establish that the lineaments are more than an alinement of cultural features.

A study of the regional and local geology of the area has been undertaken to determine if geologic phenomenon other than fractures are coincident with the radar lineaments.

SUMMARY OF ANALYSIS TO BE PERFORMED

The following studies are planned for the Douglas County site.

1. Study of the regional fracture pattern. This study will be carried out by mapping the fractures exposed in available roadcuts and outcrops. These data will be compared with the radar data to determine if any correlations exist.

2. Geophysical survey. If deemed feasible, an electrical resistivity study is planned across a number of lineaments to determine if subsurface discontinuities exist where lineaments appear on the radar.

Interpretation and comparison of the results from the preceding outlined studies will determine the applicability of radar imagery in geologic studies. Radar and air photography lineament pattern observations will be plotted and analyzed on base maps and rose diagrams. These patterns will then be compared and correlated with fracture patterns identified during field studies. Results of geophysical studies may be a valuable source of additional information since they may indicate the existence or absence of subsurface fractures in areas where lineaments are found. The field study of lineaments should provide information about the causes of lineaments and determine whether lineaments are a reflection of geologic conditions in the bedrock or a fortuitous alinement of shadows. The study of the regional geology in the area may provide significant information about other possible causes of lineaments on radar imagery. Geologic structures and phenomena such as minor folds, contacts, unconformities, and strand lines will be studied to see if they correspond with radar lineaments.

TEST SITE 24, SAN ANDREAS FAULT ZONE, CALIFORNIA

[Investigator, L. F. Dellwig; Discipline, Geology]

Mission/ flight	Date flown	Data	Date received	Quality	Results
-/101	11/2/65	AN/APQ-97 K-band SLAR	12/3/65	Excellent	Used for in-progress fracture analysis, Cholame-Carrizo area, California

SUMMARY OF OBJECTIVES AT CHOLAME-CARRIZO, CALIFORNIA SITE

The San Andreas Fault (Cholame-Carrizo) investigation is designed to determine and document the extent to which SLAR imagery can be used to map fractures, particularly faults, and their imagery expressions and reliability. The Cholame-Carrizo area serves both for control and as a test site. Regarding the former, the area has previously been mapped in sufficient detail that surface geology, including most major faults, is known; hence, corresponding imagery manifestations can be readily identified and understood. This area includes the boundary zone between two segments of the San Andreas Fault with contrasting modes of tectonic adjustment, the segment to the south by sudden violent stress release and the segment to the north by perennial creep. Cholame-Carrizo is a test site in the special sense that SLAR imagery here could ideally permit mapping of significant faults previously unknown but understandably related to an active tectonic pattern about which much is already reliably known. The test site includes a predominance of Plio-Pleistocene outcrops, likely to reflect late fractures clearly, secondary to San Andreas movement, without the added complication of earlier folding and faulting.

The manner of SLAR fault expression, reliability, and relationship to look direction is under study. Inasmuch as this area was purposely imaged at right angles to the San Andreas Fault zone, it is possible to determine whether faults of particular bearings (relative to the San Andreas trace) show to advantage on SLAR and whether those of any other bearings are minimized.

Study of thermal infrared scanner imagery (NASA/MSC mission 8, June 3, 1965) permits an additional check on expression and validity of unknown fractures. SLAR imagery may show faults to better advantage than do large-scale aerial photographs, an additional premise for investigation.

SUMMARY OF SCIENTIFIC ANALYSES PERFORMED TO DATE

AN/APQ-97 SLAR imagery has been interpreted qualitatively for horizontal polarization and vertical polarization content. The potentiality for fracture mapping is dramatically illustrated by both known faults and a "family" of probable faults (a shatter zone) newly mapped using the SLAR imagery. Both categories of fracture lineaments have been related in terms of genesis and strain theory. This new mapping of a probable shatter zone by means of radar imagery, in an area as intensively mapped and studied heretofore as the subject area, dramatically illustrates the

potentiality of SLAR imagery for the mapping of faults in any area, even where surface expression of faulting is more subtle. Known and possible faults noted on SLAR imagery in the Cholame-Carrizo area are expressed clearly, regardless of orientation to the San Andreas lineation, although those parallel to or at right angles to the look direction show up most prominently. Although it was previously known that suspected fractures lineaments show well on certain SLAR imagery, this study confirms this for known faults and strengthens the hypothesis in terms of newly mapped probable faults of real significance not previously noted even through use of large-scale aerial photographs. A comparison of the SLAR fracture mapping to fracture mapping possible through use of large-scale areal photos shows qualitatively that SLAR has the greater utility owing to synoptic view, shaded relief effect, and suppression of smaller details which would otherwise obscure the continuity of surface traces of faults.

SUMMARY OF SCIENTIFIC ANALYSES TO BE PERFORMED

The San Andreas SLAR imagery clearly shows dipping strata in successive hogback ridges, most of which strike nearly parallel to the related San Andreas Fault; thus, look directions are at nearly right angles to obsequent/resequent slopes. Depending on flight direction, either obsequent or resequent slopes show up as potentially traceable high-return bands, an advantage over large-scale aerial photos. Further investigation is needed to determine the extent to which individual stratigraphic units may be mappable owing to this SLAR affect. Also, dip determinations by McCoy's method may be relatively accurate as slant-range lengths in the true dip direction are nearly parallel to look direction.

An angular thrust-fault discontinuity is strikingly apparent on SLAR imagery in the southern Diablo Range. The potentialities for mapping this type of geologic contact (including angular unconformities) using SLAR are also under investigation.

Certain rock types (e.g., serpentine) show distinctively on SLAR imagery largely because of distinctive topography, but perhaps for other reasons as well. This aspect bears further attention.

TEST SITE 51, CANE SPRINGS SEDIMENTARY SITE, ARIZONA

[Investigator, L. F. Dellwig; Discipline, Geology]

Mission/ flight	Date flown	Data	Date received	Quality	Results
-/103	11/5/65	AN/APQ-97	12/5/65	Excellent	Used in preparing geologic evaluation of the test site. Analysis of radar imagery with aerial photography has allowed extrapolation of some geologic information not available with a single sensor.

SUMMARY OF OBJECTIVES AT SITE 51

The Cane Springs area was selected by personnel at the University of Nevada as a fundamental sedimentary rock site where stratigraphic units of contrasting lithology are exposed with sparse vegetal cover in an area of limited areal extent. The objective of the scientists at the University of Nevada is to complete a multisensor analysis of this test site utilizing data other than radar gathered by the NASA aircraft. The analysis of the AN/APQ-97 radar imagery was conducted by personnel at the Center for Research in Engineering Science, University of Kansas, in an attempt to define the capabilities and limitations of radar in geologic studies where the terrain is relatively devoid of vegetation and to compare similarities and contrasts between panchromatic aerial photography and radar imagery from an area for which precise surface geologic data are available.

SUMMARY OF SCIENTIFIC ANALYSES PERFORMED TO DATE

Analysis of the Westinghouse AN/APQ-97 radar imagery has provided lithologic and structural information that was not as apparent on the aerial photography; however, the converse was also true. Interpretations also reveal the fundamental advantage of dual-sensor geologic reconnaissance in which several discrete parts of the electromagnetic spectrum are utilized. Comparison of images of the same area recorded by two different sensors will allow the extrapolation of some geologic information with increased confidence.

SUMMARY OF SCIENTIFIC ANALYSIS TO BE PERFORMED

Future studies at the sedimentary test site, utilizing additional multisensor data, will be conducted by personnel at the University of Nevada.

PUBLICATIONS

Published Paper Reporting Specifically on Research and Results of the Cane Springs Investigations

MacDonald, H. C.; Brennan, P. A.; and Dellwig, L. F.: Geologic Evaluation by Radar of NASA Sedimentary Test Site. IEEE Transactions on Geoscience Electronics, vol. GE-5, no. 3, 1967, pp. 72-78.

Published Paper in which Reviews of the Cane Springs Research are Presented

Dellwig, L. F.; MacDonald, H. C.; and Kirk, J. N.: The Potential of Radar in Geological Exploration. Proceedings Fifth Symposium on Remote Sensing of Environment, University of Michigan (in press) April 1968.

N71-16139

PROGRAM STATEMENT

FOR REGIONAL GEOLOGIC STUDIES IN REMOTE SENSING,

YELLOWSTONE NATIONAL PARK

By Harry W. Smedes
U.S. Geological Survey, Denver, Colorado

OBJECTIVES

The Yellowstone project (test site 11) was initiated in 1965 as a cooperative effort of the U.S. Geological Survey, the National Aeronautics and Space Administration, and the National Park Service. The U.S. Geological Survey has dual interests in the project and so plays a dual role. Along with the National Park Service, we are interested in deciphering the complex geologic history of the region. Along with NASA, we are interested in the project area for both development and testing of remote sensors.

Broadly stated, the objectives of the project as as follows:

1. For the geologic studies — to determine the geologic history and structural relations of the rocks and surficial deposits by means of reconnaissance and detailed geologic mapping and structural, stratigraphic, petrographic, geochemical, and geophysical studies.

2. For the remote-sensing studies — to evaluate the wide variety of remote-sensing data in terms of the geologic information. The ultimate aim is to determine what geologic data can be obtained in this kind of environment from remote sensors and to recommend types of remote sensing that will provide maximum geologic information. In addition, the scientists involved will become trained as specialists in the interpretation of remote-sensing data.

The first objective — the gathering of ground truth — is essential to the fulfillment of the second objective, which is interpretation. This is axiomatic.

The maps produced and information gathered during this present study would, we believe, make Yellowstone Park a suitable site for the testing and evaluation of sensors developed years hence.

ORGANIZATION AND FUNDING

The ground studies are of three fundamentally different types: a detailed study of the physical chemistry and geology of selected thermal areas; geophysical investigations including aeromagnetic and gravity surveys; and regional geologic mapping and related studies. This summary concerns only the last mentioned, the regional geologic aspects of the program.

At the outset, the Yellowstone project was supported entirely by NASA funding, but after the first year it has been supported increasingly with U.S. Geological Survey funds, so that to date, funding for the regional geologic studies has been approximately 75 percent by NASA and 25 percent by the U.S. Geological Survey.

The Yellowstone program of regional geologic studies consists primarily of five topically based projects, staffed by a total of nine full-time geologists, each an expert in one or more special fields. This topical approach has worked quite well, inasmuch as the major geologic units coincide with geographic units.

The projects are as follows:

1. Pretertiary geology of the northern part of Yellowstone Park. Mapping is completed, and reports are in preparation.

2. Pretertiary geology of the southern part of Yellowstone Park. Mapping is completed; a report has been prepared and is being reviewed.

3. Lower Tertiary volcanics. These principally make up the eastern third of Yellowstone Park and the northwest corner. Mapping is to be completed this season. Two quadrangle maps are complete; three other maps and one report are in preparation.

4. Upper Tertiary and Quaternary volcanics, in the central and western part of Yellowstone Park, and a large area to the west. Mapping is to be continued for two more seasons.

5. Surficial geology, glacial geology, and geomorphology of the entire Yellowstone Park and some of the surrounding region. Mapping is to be completed after one more season. Five quadrangle maps are ready to submit for publication.

We are on or ahead of schedule for all regional geologic project objectives. The original project proposal called for a geologic map of Yellowstone Park at a scale of 1:125 000, or about 2 miles to the inch. Without changes in timing and cost, or sacrifice of project objectives, we will be able to complete geologic mapping of the entire Yellowstone Park and some of the surrounding areas at a scale of 1:62 500, or

about 1 mile to the inch. We plan to publish these detailed maps in addition to the 1:125 000-scale map of the entire Yellowstone Park. Thus far, more detailed coverage and the ensuing increase in geologic data and understanding constitute a substantial bonus.

MISSIONS FLOWN

To date, four missions have been flown for us and have produced imagery which has been and is now being studied. The missions and sensors used are listed in table 15-I. As noted at the bottom of that table, there is an earlier University of Michigan infrared (IR) survey. That survey was flown for the Cold Regions Research and Engineering Laboratory (CRREL). Plans are being made for joint studies by the U.S. Geological Survey and CRREL to compare those data with the more recent data, looking for temporal changes in the thermal patterns.

GEOLOGIC RESULTS

Yellowstone Park, covering more than 3000 square miles, is almost completely mapped; mapping of nearly 1000 square miles of the surrounding area is completed. The only previous study of the entire area was that of the Hague survey conducted in the late 1890's. The total geologic picture that is emerging from these new studies is vastly more complicated and complete than previously known and differs in many fundamental respects.

Significant results of these geologic studies have been reported promptly through oral papers presented at meetings of the Geological Society of America and subsequently in the published abstracts of those papers. In this way, results of wide application and regional significance are made available.

REMOTE-SENSING RESULTS

Five reports on interpretation of imagery have been transmitted (refs. 15-1 to 15-5). To date, four of these reports (refs. 15-1 to 15-4) have been issued, and the fifth (ref. 15-5) is scheduled to be released soon, probably in October. Reference 15-6, dealing with the 1961 imagery, is included to complete the record of remote-sensing data for the Yellowstone region.

TABLE 15-I.- SUMMARY OF MISSIONS AND SENSORS[a]

Date	Mission flown by	Sensors
1965	Westinghouse	K-band side-looking radar, plane (HH) and cross-polarized (HV)
1966	H. R. B. Singer	3.5μ to 5.5μ IR (Reconofax IV) Color photographs of limited area
1966	NASA	8μ to 14μ IR Ultraviolet scanner Color film Multiband, film (nine lens camera) (Spectrac and scatterometer data recorded but never received by Yellowstone project)
1967	Willow Run Lab. (Univ. of Michigan)	Scanner spectrometer; 12 channels, 0.4μ to 1.0μ and five channels; 1.0μ to 14μ Ultraviolet scanner Color-IR film Color film Kodak IR film Kodak Plus-X film

[a]There is also 1961 University of Michigan 3.5μ to 5.5μ IR scanner imagery which has not yet been obtained for appraisal by the Yellowstone project personnel.

A comprehensive index to all existing imagery is about to be transmitted, and at least six reports are anticipated after completion of imagery study when personnel return from the field in a few weeks.

The radar mosaic of Yellowstone Park was completed this past summer. We will make a complete study of that mosaic this fall and winter.

Although it is not the purpose of this project statement to recount all the results detailed in the five reports transmitted, it is important to mention that several contain interpretation techniques, some of which can be and others of which previously have been utilized elsewhere. The following examples are presented.

The means of distinguishing between bedrock and unconsolidated cover by using radar images, as described in reference 15-2, could be of inestimable value to geologists working in the muskeg of Maine or in Alaska, where they spend most of their time looking for outcrops and may slog around for days without seeing any!

The IR detection of cold springs emerging on the floor of Yellowstone Lake made it possible to trace a fault beneath the lake (ref. 15-5). Previously, similar IR detection of cold springs emerging on the Pacific Ocean floor off the Hawaiian Coast provided important data that resulted in locating urgently needed sources of fresh water inland.

On the basis of the texture of the radar image, it was determined (ref. 15-1) that nearly all principal areas of rhyolite lava could be distinguished from rhyolite ash flows. Also, the degree of dissection by streams can be related to relative ages of individual flow units.

In forested regions of the Park, some areas of thick till have a general tone on thermal IR images that is slightly darker (cooler) than nearby forested areas where till does not mantle the bedrock. This is one of the many contributions to interpretation of IR imagery contained in reference 15-4.

Over Pretertiary terrane in the southern part of the Park (ref. 15-3), radar and IR imagery gave a good representation of the physiography, as elsewhere, but did not provide direct clues for the distinction of rock types and structure, which could be interpreted only to the extent that they are related to the physiography.

Most bedrock information has been inferred from the nature and distribution of soil, moisture, vegetative cover, and topographic expression because generally it is these secondary effects which are sensed. However, bedrock data have locally been inferred more directly from the sensor data. In places, differences in thermal properties of rocks directly affected the nighttime IR imagery; for example, limestone, dolomite, and rhyolite tuff showed as distinctly warmer than andesite and basalt (ref. 15-5).

CURRENT WORK

When we compare a thermal IR image or a radar image with an aerial photograph, we are in effect making two-band discriminations, the bands being rather broad. We have just started a study aimed at comparing the 3μ to 5μ and 8μ to 14μ IR imagery and aerial photographs of selected materials and environments. This involves making three-band discriminations.

We have also recently begun a study of the nine-lens multiband film using simultaneous projection and registry of images from four lantern slide projectors, similar to what has been done for some time by Professor Colwell for agricultural materials. This gives us many different combinations of four-band discrimination possibilities. Our preliminary work has already shown that selective use of filters on the projectors can result in substantial enhancement of some very subtle geologic contrasts in a bedded sedimentary sequence. This use of filters still further increases the number of combinations of four-band discrimination possibilities.

Our latest mission utilized a 12-channel spectrometer scanner. This provides a 12-band discrimination. This, of course, is far too much for handling by simple visual comparison, and a computer, using tapes from this scanner, can do a far more sophisticated job of discrimination and enhancement than the other techniques employed to date. The initial success with visual interpretation using the projectors and four channels strengthened our hopes for success using computer-processed data from 12 channels. This technique has tremendous potential for many geologic remote-sensing requirements, because it is a system that can scan, record, analyze, and automatically print selected geologic data. For this reason, I would like to describe our test of these scanner data, processed by Willow Run Laboratories of the University of Michigan.

The University of Michigan analog recognition processor, which can operate in real or slowed time, is a means of determining the correlations among all the data channels. If all 12 channels are used, this multidimensional correlation function is represented by a 12-by-12 covariance matrix. Once the image of the target outcrop has been analyzed and maximum-likelihood determinations made, the processor can be programed to detect and print as an image on film each resolution element scanned that has a correlation function which matches that of the target. Ideally, we would end up with an outcrop map of that rock type, or at least of outcrop with little vegetation cover. Repeating the process for another rock would, theoretically, give us an outcrop map of that rock type, and so on, until we have built up a fairly complete geologic outcrop map.

On our test, owing to some electronic problems, only nine of the 12 channels were used. We selected large well-exposed outcrops of basalt and of rhyolite as two of the targets — as ground control. The processor then came up with recognition data which were used to detect all areas of similar signature on the tape of the entire traverse.

The results indicate that we have a lot of work ahead, for when we used basalt as a target, the final print-out — ideally an outcrop map of basalt — showed more false than valid detections. Materials as

diverse as the following locally were "recognized" as being basalt: rhyolite, granite gneiss, glacial moraine, and outwash composed of various metamorphic stones, lake silt, bogs, clay soil, and sandy soil.

When rhyolite was used as a control, a similar diversity of false recognitions showed up. Not everywhere did the gneiss, outwash, bogs, et cetera, mentioned previously give the same results as in the basalt test, though in places the same spot was detected as being both rhyolite and basalt. In places, even segments of blacktop roads were detected as rhyolite.

In the first example, not all basalt was recognized as basalt, and in the second example, not all rhyolite was detected as rhyolite. This obviously will not be an easy test to interpret or an easy problem to solve. However, because of the potential of this technique in recognition and detection by remote sensing, we believe that it is important that we attempt to solve it.

The first anomaly studied in the field led us to conclude that moisture was the factor responsible for the false recognition. The next anomaly showed us that slope was the factor. Still another anomaly suggested that texture was the factor. Each time we thought we had reached the solution, and each time the next anomaly showed us to be wrong. Obviously, there are many factors and combinations of these factors effecting the false recognitions and the failure to make valid recognitions in many places where materials similar to the target material are present.

One of our first tasks is to determine the many parameters effecting these false recognitions. We have already determined that the reflectance spectra of the natural materials overlap. We hope that by using 12 rather than nine channels, we can greatly improve the discrimination ability of the processor. In this test the entire blue and blue-green spectrum (below 0.52μ) is lacking. However, that deficiency alone does not account for the problems. For example, the signature of rhyolites on a north-facing slope was found to be different from that of south-facing slopes, and both of these differ from rhyolite on level surfaces. Add to that the effect of scattered vegetation and soil, and the problems mount.

Our preliminary study disclosed one other important problem, and that is one of format. We must first transform the scanner imagery to a topographic base in order to be able to locate anomalies precisely and thereby know what specific material and environment contributes to the anomaly.

We are working with the University of Michigan engineers on interpretation of this recognition test and one involving thermal contouring.

Jal

We believe that continuation of contracts with them for further processing are essential and that an additional mission with their spectrometer scanner may be desirable in the near future.

Copies of the magnetic tapes of these traverses have been obtained from Michigan and will be converted to digital format so that some digital processing may be done utilizing sophisticated forms of decision theory. The results of this digital processing will provide a means of assessing the performance of the analog processor — a test of interest to both the U.S. Geological Survey and the University of Michigan.

Most of the interpretation to date has involved the study of imagery from one or two classes of sensors — the second one generally being aerial photographs — and comparison of these data with the geologic map. Our plans now call for integrating the data from several different sensors. This will involve us with the problem of incompatibility of different formats. We believe that this is the least of our problems and that it can be solved satisfactorily.

REFERENCES

15-1. Christiansen, R. L.; Pierce, K. L.; Prostka, H. J.; and Ruppel, E. T.: Preliminary Evaluation of Radar Imagery of Yellowstone Park, Wyoming. U.S. Geol. Survey Technical Letter NASA-30, July 1966.

15-2. Christiansen, R. L.: A Distinction Between Bedrock and Unconsolidated Deposits on 3μ to 5μ Infrared Imagery of the Yellowstone Rhyolite Plateau. U.S. Geol. Survey open-file report, May 22, 1968.

15-3. Keefer, W. R.: Evaluation of Radar and Infrared Imagery of Sedimentary Rock Terrane, South-Central Yellowstone National Park, Wyoming. U.S. Geol. Survey open-file report, June 21, 1968.

15-4. Pierce, K. L.: Evaluation of Infrared Imagery Applications to Studies of Surficial Geology — Yellowstone Park. U.S. Geol. Survey open-file report, June 21, 1968.

15-5. Smedes, H. W.: Geological Evaluation of Infrared Imagery, Eastern Part of Yellowstone National Park, Wyoming and Montana. U.S. Geol. Survey.

15-6. McLerran, J. H.: Thermal Mapping of Yellowstone National Park. Proc. Third Symposium on Remote Sensing of Environment, 2nd ed., Univ. of Michigan Willow Run Laboratories, 1965, pp. 517-530.

N71-16140

GEOTHERMAL INFRARED ANOMALIES OF LOW INTENSITY, YELLOWSTONE NATIONAL PARK

By Donald E. White and Lee D. Miller
U.S. Geological Survey, Menlo Park, California,
and Department of Recreation and Watershed Resources,
Colorado State University, Fort Collins, Colorado

INTRODUCTION

Infrared remote sensing of hot springs and other high-temperature geothermal phenomena has been feasible for many years; its usefulness in searching for inconspicuous anomalies of low intensity has not been demonstrated in the past. Future search for sources of geothermal energy must aim at deep reservoirs of hot water and steam at temperatures generally above 200° C. Hot springs are associated with some of these reservoirs, but most hot springs are unreliable evidence for commercial reservoirs. The most significant evidence for a concealed geothermal reservoir would be temperature gradients and heat flows three to 10 times higher than the worldwide averages. "Normal" gradients average about 1° C/50 meters in depth, and "normal" conductive heat flow averages 1.5 $\mu cal/cm^2 sec$. Solar energy is roughly 1000 times this value; therefore, the "noise" problem is severe.

OLD FAITHFUL TEST SITE

Infrared (IR) anomalies are actually differences in apparent surface temperature, which shows wide daily, seasonal, and microclimatic differences. Can IR anomalies also be calibrated in terms of heat flow, which is of more fundamental geothermal interest than temperature alone? A small area around Old Faithful was being used last year to test a new rapid method for mapping differences in heat flow, utilizing individual heavy snowfalls as calorimeters. These heat-flow data are also useful in attempting to calibrate IR data recently acquired and computer processed by the University of Michigan Infrared and Optical Sensor Laboratory for the U.S.G.S. Heat-flow contours of 1000 and 450 $\mu cal/cm^2 sec$ were mapped in this test area.

The oral presentation included the following:

1. A vertical color photograph of the test area, showing locations of Old Faithful and other thermal anomalies to be discussed and the different surface materials of the area

2. A heat-flow map of the test area

3. Analog thermal IR, 8μ to 14μ, conventional unprocessed scanner imagery, taken at 2:00 a.m. and showing the anomalies; of these, Old Faithful being the only visible conspicuous one

4. Analog computer processing of the original magnetic tape data, quantized between 0° and 20° C into eight levels, each with an interval of 2-1/2° C

5. Apparent surface temperatures, contoured by intervals of 5° C; not as effective in black and white as some other types of processing

6. Separate images, each of a different temperature interval, with 0° to 20° C divided into 16 different levels, each with 1-1/4° C temperature span

The first interval (16-1) includes all temperatures above 18-3/4° C. Several visually inconspicuous anomalies are more pronounced on IR than Old Faithful, but other anomalies are not yet evident. Representative levels or slices, with decreasing temperature, first show the appearance and then the enlargement of other anomalies. Separate images of temperature intervals below 10° C are especially useful. Interval 16-14 (2-1/2° to 3-3/4° C) shows anomalies that are similar in shape to the 1000-μcal contour, and interval 16-15 (1-1/4° to 2-1/2° C) is most nearly similar to the 450-μcal contour. The eastern anomalies have apparent surface temperatures 3° to 4° C lower than equivalent heat flows in the western part, because of differences either in real temperatures or in emissivities of ground materials.

BLACK SAND TEST SITE

Extensive physical studies have been made of a geothermal anomaly northwest of Old Faithful. Winter mapping of snow lines and snow depths adjacent to this warm ground provides qualitative differences in heat flow. Temperature-depth profiles permit calculation of heat flow by assuming reasonable thermal conductivities. A map of the radiation temperature of the warm area was made on the ground with a radiometer during one of the series of IR overflights. This radiation temperature map approximates a real surface temperature map for the surface material of

the area which is black sand with emissivity near 1 and little vegetative cover. Analog computer processing of the thermal IR imagery taken at this time produced multiple images, each representing the ground area with a different preselected 1-1/4° C radiation temperature range. Temperature separates were prepared for the temperature interval of -5° to 20° C. A system was developed for presenting these individual temperature separates in a single reconstituted color image by color coding the separates and rephotographing them. This color-coded image differs from a continuous-tone, black and white thermal IR image in that the boundaries between the colors represent isotherms of known value. The isothermal map obtained in this fashion correlated closely with the ground radiometer map. Heat flows between 5500 and 300 $\mu cal/cm^2 sec$ have been measured in this test area.

The oral presentation included the following:

1. A map presenting isolines of equal snow depth around the test site

2. Winter soil temperature profiles for various positions on the test site

3. A soil heat-flow map of the test area

4. An isoline map of radiation temperatures recorded on the site with a radiometer during the mission overflight

5. A color-coded thermal image of the site

Separate images representing each 1-1/4° C temperature span in the original 0° to 20° C, interval 8-14 image obtained at 2:00 a.m. were prepared. Each of these separate images was transformed into a colored image. A sandwich was made by registering these colored separates. A color photograph of the sandwich is a colored thermal image on which each color represents a different radiation temperature interval. The colors are selected so that the "hotter" colors such as red represent the warmer ground areas and so forth.

In summary, IR easily "sees" the obvious geothermal anomalies and also sees, by means of computer processing, inconspicuous anomalies not readily visible by ground inspection at intensity levels near and even below the average "noise" level. Low-intensity anomalies can be calibrated, at least roughly, in terms of heat flow at rates that range down to about 400 $\mu cal/cm^2 sec$ or somewhat less. Equal radiation ground temperatures at any instant, even in early morning, cannot be equated strictly with heat flow. We are still considerably above our hoped-for

objective of detecting heat flows only three to 10 times "normal," but major progress has been made in calibrating low-intensity anomalies and in computer processing of the data. The limits of both calibration and processing have not yet been fully tested; future investigations will explore these limits further.

N71-16141

RADAR AND INFRARED IMAGERY,

OREGON AND WASHINGTON COASTS

By Norman S. MacLeod and Parke D. Snavely, Jr.

INTRODUCTION

Radar and infrared imagery are being used to study the geology of coastal Oregon and Washington. The radar imagery includes a 10-mile-wide coastal strip extending from the Columbia River almost to the California border. The infrared imagery is of a 2-1/2- to 3-mile strip from near Cape Flattery on the northwestern Washington coast to near Seaside, Oregon. The radar and infrared imagery were obtained by NASA at the request of the U.S. Geological Survey.

Thick sequences of interbedded eugeosynclinal volcanic and sedimentary rocks of Tertiary age underlie the Washington coastal area and the northern three-fourths of the Oregon coastal belt; the terrain in the southern one-fourth of Oregon is composed of structurally complex sedimentary, igneous, and metamorphic rocks of Mesozoic age. Although reconnaissance geologic mapping has been largely completed, there remain many areas for which detailed mapping has yet to be undertaken. As part of the Office of Marine Geology and Hydrology's investigations of the continental shelf of the Pacific Northwest, the authors are currently completing detailed mapping of several quadrangles in the western part of the central Oregon coast range and, in conjunction with topical investigations, are mapping small areas throughout western Oregon and Washington. H. Edward Clifton, Richard J. Janda, and Robert G. Coleman of the U.S. Geological Survey are mapping and evaluating radar imagery in parts of southwestern Oregon.

Because of high rainfall (50 to over 100 inches a year), the coastal area of Oregon and Washington is characterized by a dense vegetative cover and thick soil profile which obscures the bedrock. Radar and infrared imagery of this area were requested in the anticipation that they would provide useful additional tools to aid in the field studies. Conversely, because the geology of much of this area has been investigated, the usefulness of radar and infrared imagery in areas covered by dense vegetation and thick soil zones can be evaluated.

RESULTS FROM THE USE OF RADAR DATA FROM NASA AIRCRAFT

The radar imagery was obtained with high-frequency side-looking radar that was operated in a polarizing mode. Images were acquired during two flights, one from south to north and the other north to south. For each flight, two simultaneous images were obtained: one image was horizontally polarized both in transmission and reception; the other image was horizontally polarized in transmission and vertically polarized on reception. The horizontally polarized image shows more tonal contrast. A storm at the time of the southward flight rendered much of the imagery useless. However, the vertically polarized image shows penetration through thin clouds in a few areas where ground definition was obscured on the horizontally polarized image on the southward flight. The distorted scale on the radar imagery does not seriously hamper imagery interpretation except in the narrow belt below the flight line. The radar imagery covers an area of approximately 3000 square miles, and a complete geologic analysis cannot be made in a short time period.

The radar imagery depicts on a single continuous strip the land form of a large area. Even small details of the topography can be discerned in areas of dense vegetation. The upper part of figure 17A-1 shows radar imagery of a 10-mile-wide area near Cape Perpetua on the central Oregon coast; the lower part shows a conventional aerial photograph of the same area (at a slightly larger scale than the radar image). The radar image shows more detail than the black and white aerial photograph; radar imagery is also superior to color aerial photographs and to actual sight observations from planes at various altitudes. This superiority greatly facilitates recognition of the topographic expression of lithologic and structural features. Areas underlain by contrasting rock types can in many places be delineated on the radar imagery because of differing topographic expression. Alined drainages and/or ridges are in places manifestations of faults or joints in the bedrock. These topographic lineations are more apparent on the radar imagery than on conventional aerial photographs. Tonal differences on the conventional photographs are largely produced by variations in the properties of the vegetative cover and tend to degrade topographic expression.

A radar image of a 10-mile-wide area near Lincoln City on the central Oregon coast is shown in figure 17A-2. The northeast-trending lineation is the topographic expression of a large fault. By field mapping, this fault has been demonstrated to extend at least 10 miles inland; ground magnetic studies completed in the summer of 1968 indicate that it continues at least as far west as the coastline through an area of poor exposures and alluvial cover. Subbottom acoustical profiling and aeromagnetic surveys along the offshore extension of this

fault were recently completed but have not yet been processed. Other similar lineations on the imagery have been shown to be fault controlled.

The large arcuate physiographic feature shown in figure 17A-3 is located 5 miles east of Seaside on the Oregon coast. The northern part of this structure is formed by a thick concordant-to-discordant gabbroic sill or sheet of middle-Miocene age. Preliminary fieldwork suggests that the gabbro was intruded along a preexisting structure, perhaps a collapse feature associated with middle-Miocene volcanism which produced extensive subaerial and submarine basalt flows in this region. An aeromagnetic survey of this area was completed in the summer of 1968, but results are not yet available.

The radar imagery of the Oregon coast extends only about 10 miles inland, and we consider acquisition of radar imagery of the entire coast range to be highly desirable. High-altitude (U-2) photography has been requested and may provide additional information. The high-altitude photography will serve as a basis for comparison of radar imagery and high-altitude aerial photography.

RESULTS FROM THE USE OF INFRARED DATA FROM NASA AIRCRAFT

Infrared imagery in the 8μ to 14μ range has been obtained for the coasts of Washington and Oregon. However, cloud cover obscures most of the Oregon imagery. Reconnaissance mapping of the area immediately adjacent to the Washington coast is near completion, and the infrared imagery is now being evaluated. Rocks are exposed along the coast on wave-cut platforms and sea cliffs, but dense vegetation and unconsolidated surficial deposits almost completely obscure bedrock in inland areas.

Although the most significant features shown on the infrared imagery of the Washington coast are current patterns in offshore waters, at least one fault previously mapped near Point Grenville can be discerned on the infrared image. The fault appears as a faint thermal lineation probably caused by water seepage along the fault trace. Kelp-covered reefs disturb current movement and are thus visible on the imagery. Many of these reefs are submerged strike ridges, and their positions and orientations as shown on the imagery provide additional data for geologic mapping.

Large-scale sand waves with amplitudes of several tens of feet are shown on the imagery of tidal flats in Willapa Bay. Smaller sand ripples are superimposed on the large sand waves but have a different orientation. The sand waves are probably produced by tidal current fluctuations on the flats.

Infrared images of current patterns along the coast are significant to geologic studies of the nearshore shelf areas because they provide information on direction of current movement, which in turn controls sediment transport and deposition. Interference patterns produced by reefs, small islands, and headlands allow determination of surface water-movement patterns. These current data are applicable to studies of recent sedimentation and heavy mineral distribution. A sequence of infrared images taken at different times of the year would provide useful data on the seasonal variations of these currents.

Perhaps the most spectacular infrared images are those of fresh-water plumes which extend seaward from the mouths of several of the larger rivers. They are particularly well developed off the mouths of the Hoh, Queets, and Quinault Rivers. Figure 17A-4 shows the fresh-water plume off the Quinault River at Taholah, Washington. The plumes consist of concentric thermal bands, the outward edges of which are warmer. In the plume off the mouth of the Quinault River, the concentric thermal bands are arranged in two similarly distinct sets; other plumes consist of only one set of concentric thermal bands or of one distinct set and a second faint set. The thermal bands in these plumes are thought to result from the interaction between river outflow and tidal fluctuation. Unfortunately, because of poor weather during the latter part of the summer (1968), a planned study of water temperature, salinity, and conductivity in the plumes had to be canceled. These data, as well as temporal variations in these parameters at points within the plumes, will be obtained later this fall (1968). This information is necessary for determination of the origin and rate of growth of the thermal bands. Successive infrared images taken over a period lasting from several hours to several days would also be very useful for the interpretation of plume origin.

In addition to the current patterns and plumes shown on the infrared imagery, fresh-water springs are discernible along the coast, particularly where sand covers the bedrock.

Enhanced false-color composite transparencies of an infrared image and a color aerial photograph have recently been prepared for an area near Ozette Island where the wave-cut platform is particularly wide. These composite transparencies have not yet been evaluated.

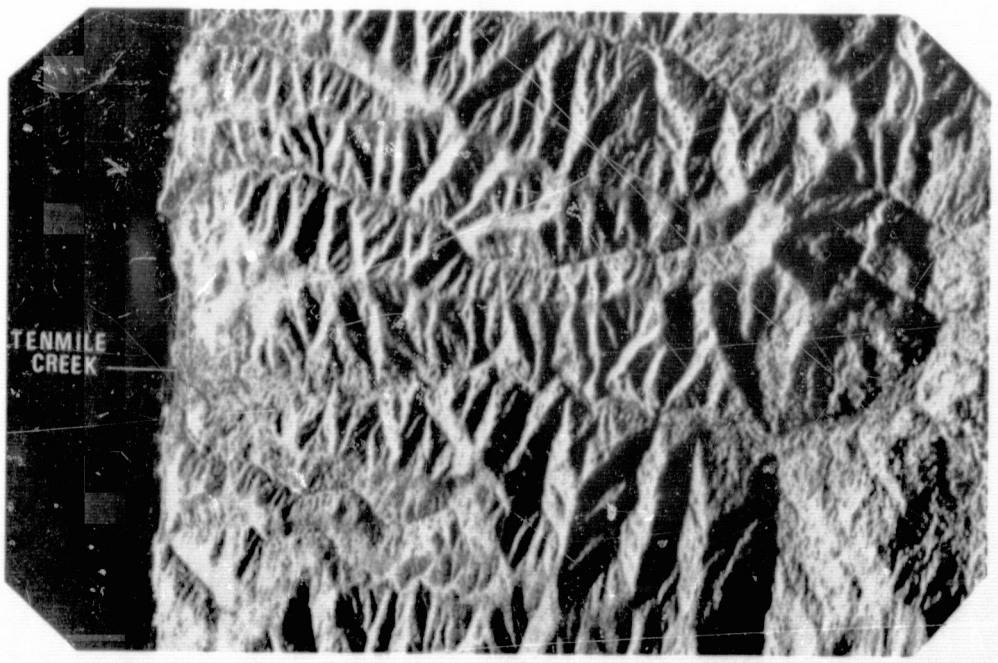

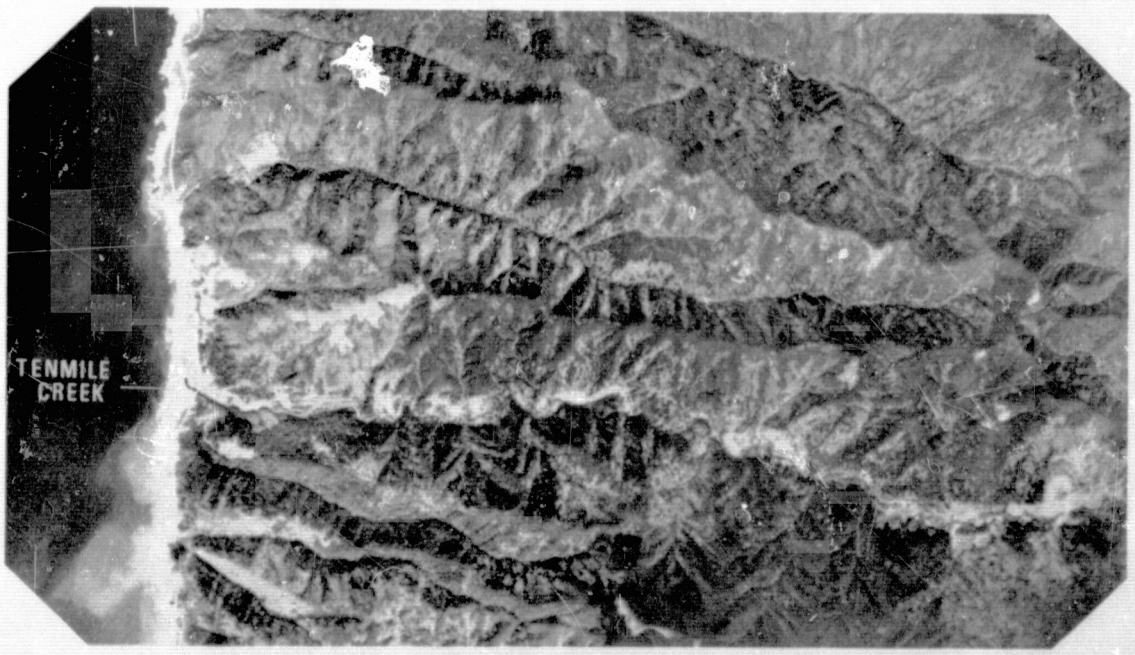

Figure 17A-1.- Comparison between photographically enlarged radar imagery (above) and conventional photography (below) in the Tenmile Creek area of coastal Oregon.

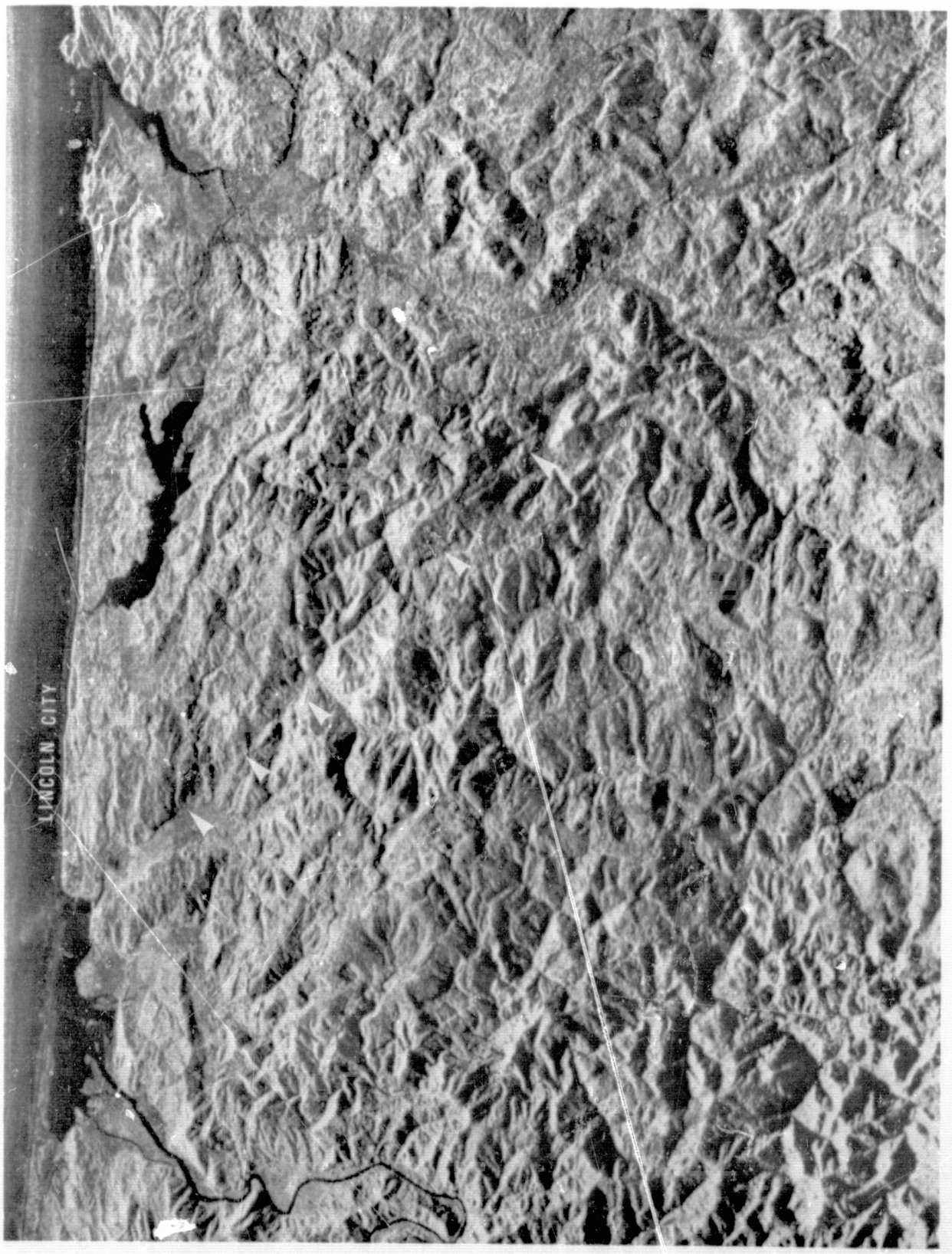

Figure 17A-2.- Radar image of area near Lincoln City, Oregon. Northeast trend of lineation is caused by large fault.

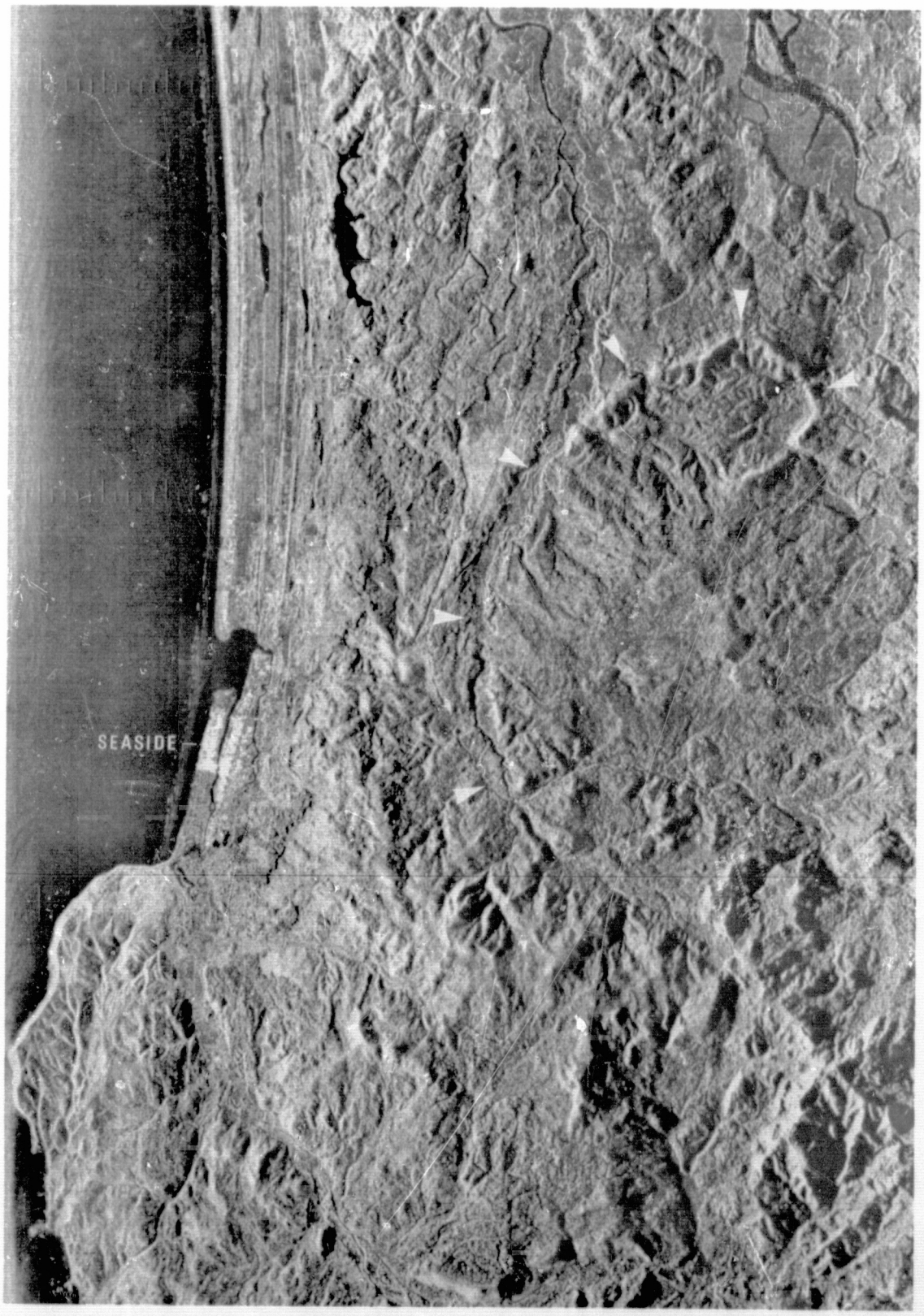

Figure 17A-3.- Radar image of area near Seaside, Oregon, showing arcuate feature (arrows in center of image). Miocene gabbroic intrusive underlies curved ridge on northern part of arc; physiographic expression in southern part of arc is a manifestation of a fault.

Figure 17A-4.- Infrared image of the Taholah, Washington, area showing thermal plume developed off the mouth of the Quinault River.

N71-16142

PROGRESS IN APPLICATION OF REMOTE-SENSING TECHNIQUES TO MARINE GEOLOGY AND HYDROLOGY

By Ernest H. Lathram

INTRODUCTION

This year is the first year in which NASA funds have been available to the U.S. Geological Survey for application of remote-sensing techniques specifically to marine geologic and hydrologic problems. Remote-sensing techniques, with the capability of repetitive viewing, will be of significant value in monitoring changes in state with time. This is particularly true of future orbital sensing, with its added synoptic capability. In the study of coastal areas, it is particularly important to identify changes with time of effects wrought by geologic and hydrologic processes, either natural or in response to modifications by man. Part of the effort this year has been devoted to a selection of problems most amenable to solution by remote-sensing techniques and to selection of initial sites for study. Three sites have been recommended for remote-sensing investigations — San Francisco Bay, Laguna Madre, and Puerto Rico. Aircraft data have been requested for all three sites; Laguna Madre has been scheduled, and aircraft data should be available by the end of calendar 1968. Ground studies are already underway on these three sites, hence remote-sensing data will provide immediate benefit to the marine program. As NASA aircraft data were not available for the three sites, the U.S. Geological Survey acquired color and infrared data, using its own funds, in order to begin acquisition and interpretation of necessary ground truth. In addition, other Interior Department funds have been made available for additional remote-sensing studies along the coast of the State of Washington. Some results of studies in two of these areas are reported below.

SAN FRANCISCO BAY

San Francisco Bay was selected as a site not only because of its importance to the civic and industrial development of a heavily populated and growing area, but also because a multidisciplinary study of hydrologic and geologic problems is currently being undertaken by the U.S. Geological Survey. Hence, close integration of remote-sensing and

ground-truth studies, and immediate application of results, are possible. Infrared imagery and radiometer surveys were flown over a portion of San Francisco Bay coincident with a systematic geochemical sampling of the water column and bottom sediments. The abundance of most major and minor ions in four cross sections of San Francisco Bay was determined. Enhanced composites of the infrared images are now being studied in an attempt to relate the photographs to variations in the physical and chemical properties of the suspended sediment and the water of the bay.

LAGUNA MADRE

Color photography covering the southern coastal area of Texas was acquired and interpreted in relation to ground studies of Padre Island and Laguna Madre. Comparison of these photographs with earlier photographs revealed that washover scars caused by Hurricane Beulah recurred in places that had previously been washed over, suggesting that areas of greatest probable damage can be predicted. Classification of land for housing or permanent development should be prevented in these washover areas. Furthermore, the photographs revealed that the dune field on Padre Island has been migrating westward. Comparison of the photographs with older charts shows this rate of migration to be 50 feet per year over the past 20 years. Padre Island is shown to be actively prograding into Laguna Madre, concomitant with an increase in island width of more than one-half mile since the 1880's. Deposition of sand over the mouths of the washover channels, and rehealing of the scars, proceeds at a rapid pace. Repetitive monitoring of the rehealing process and of the migration of the dune field will be of great value in the developmental planning for this seashore.

The data from the investigations will be compiled on an orthophotomap now being prepared by the U.S. Geological Survey. As remote-sensing data from orbital altitudes are essentially orthographic, direct comparison of these data to the orthophotomap will be possible. Hence, large areas may be monitored for changes in coastal configuration. An interesting field for development is the routine machine comparison of orbitally acquired data with orthophotomaps to automatically identify areas of change. This technique would permit the scientist to concentrate on those areas where change has occurred and to study the nature and cause of the change.

N71-16143

AIRBORNE MULTIFREQUENCY MICROWAVE RADIOMETRIC SENSING OF AN EXPOSED VOLCANIC PROVINCE*

By John C. Blinn III
Jet Propulsion Laboratory, California Institute of Technology

and

Peter Chapman and Jack Quade
NASA Project Office, University of Nevada

ABSTRACT

In support of the NASA Earth Resources Program, an empirical study was conducted, using airborne and ground-based sensors, to search for correlations between multispectral microwave brightness temperatures and geologic parameters. The test site, in the vicinity of Mount Lassen, California, was chosen because of its simple topography, large distinct areas of homogeneous composition, roughness characteristics, and lack of vegetation. Radiometers, operating at 9.3, 15.8, 22.2, and 34.0 gigahertz, were flown over preselected flight lines four times per flight to collect data.

Results of the ground-truth studies and analysis of the aircraft overflights show a distinction between cinder and lava, two chemically similar materials with different surface characteristics. Results from an area of cinder layered over lava show a distinctive response, which may be related to cinder thickness. An improved experiment (which uses more temperature probes, geologic cross sections, a ground-based microwave radiometer, and other refinements) is recommended.

---

*Published October 1968, as Jet Propulsion Laboratory Technical Memorandum 33-405.

INTRODUCTION

In support of the NASA Earth Resources Program, an empirical study was conducted in the vicinity of Mount Lassen, California, to determine correlations between multispectral microwave radiometric signatures and geologic parameters. The experimental portions of this study were completed on August 18 and 19, 1967, with the overflight tests using NASA remote-sensing Convair 240A aircraft 926. This report covers results of those tests, subsequent data analysis, and recommendations for an improved flight test for the test site. In addition, a summary of the principles of microwave radiometric sensing and a description of the airborne radiometric system are contained in appendixes 18A and 18B, respectively.

The investigation was accomplished as a joint effort by the University of Nevada and the California Institute of Technology Jet Propulsion Laboratory. The authors express gratitude for the support and services provided by the Earth Resources Program Office and the Flight Operations Office at the NASA Manned Spacecraft Center, Houston, Texas. In addition, the authors express their appreciation for the cooperation of the U.S. National Park Service at Mount Lassen.

Geology of Test Site

The test site is part of a volcanic province that contains a well-exposed series of eruptive rocks and a cinder cone about 10 miles east-northeast of Lassen Peak, Mount Lassen National Park (fig. 18-1). The cinder cone is a product of a series of pyroclastic eruptions, beginning several thousand years ago and concluding in 1851. After each eruption, there was an effusion of lava from the base of the cinder cone, followed by long periods of quiescence. Several other smaller primary cones exist in the southern and northern part of the flows, which complicates the dating and numbering of all the flows.

The lava flows dammed the drainage into Butte Lake, thus forming Snag Lake. Now 33 feet higher than Butte Lake, Snag Lake supplies water through the porous flows into Butte Lake. Prior to the last lava flows, deposition of diatomaceous earth accumulated in Butte Lake; vestiges of this deposit can still be found along the margins of the lake and lava flows.

A close inspection of the test site reveals that it may be divided into seven basic units. These can best be seen in a photograph of the test site (fig. 18-2) and in the supporting geologic map (fig. 18-3). The dark areas, designated as areas 5 and 6 on figure 18-2, consist

mainly of blocky lava, some aa, and even less pahoehoe, the latter being associated with the later flows. The last flow (area 6), which is distinctly black, can easily be traced from the breach in the southern end of the cone. The immediate vicinity of the cinder cone is covered with a pumiceous cinder, which overlies the dense lava associated with the flows. Where the cinder covered the lava directly (area 4), it was greatly altered by heat and fumerolic action. Where the cinder did not cover the molten lava (area 3), it shows little alteration and remains dark gray to black. The greatest percentage of lava material along both flight lines is homogeneous in texture and chemical composition.

Surface Characteristics

The surface characteristics of the basic test units (fig. 18-2) are described in terms of the roughness classification in appendix 18C.

1. Forest: classes II, III. Past experiments have shown that densely vegetated areas approximate blackbody radiators at microwave frequencies. Hence, the forested areas may serve as good calibration points for the radiometers.

2. Water: classes I, II. During both night and day, the surfaces of the lakes were nearly smooth. The lakes also provide good calibration points for the radiometers.

3. Unaltered cinder: class II. Except for the cinder cone, the areas of unaltered cinder are relatively flat and have a particle-size distribution between $\lambda/10$ and λ.

4. Altered cinder: classes II, IV. The altered cinder is a hilly area because of its superposition on the underlying flow. It has peak-to-valley variations on the order of 2 to 20 feet. Its variations are smoother (like dunes) than the characteristically angular variations in the basalts of the lava flows. The surface-particle distributions are the same as the unaltered cinder.

5. Lava flows: classes I, III, IV. The lava flows consist of sharp hills covered with lava blocks. The hill heights vary from approximately 5 to 30 feet. The blocks range in size from 30 to 60 centimeters and have smooth surfaces.

6. Lava flows of 1851. Most of the smooth-textured (pahoehoe) lava is associated with these recent dark black flows.

7. Cinder cone: classes II, IV. The cinder cone has a slope variation superimposed on the unaltered cinder.

Flight-Line Selection

The Mount Lassen Test Site is well suited for evaluating microwave radiometric techniques to sense geologic phenomena because it is relatively flat, with large homogeneous areas of similar chemical composition. Two flight lines were chosen to utilize the characteristics of the terrain to the fullest extent. Both flight lines originated over lakes, which offered geographic reference for flight lines and calibration points for the radiometer data. In each case, the lines traversed a course across lakes, basalt flows, cinder materials, and vegetated area. The chemistry, porosity, particle sizes, and surface geometry for individual units were remarkably similar along both flight lines. The steep topography of the cinder cone permits a study of slope effects. The remaining portions of the flight lines were relatively flat with little vegetation. The individual areas along both lines had uniform characteristics, permitting a more expeditious examination of the effects of surface roughness and material density on the microwave signatures. The dense vegetation bounding the flight lines offered the potential of a second calibration point for the radiometers.

MISSION STUDIES

Ground-Truth Studies

The investigations of the ground parameters at the Mount Lassen Test Site were initiated 2 months prior to the overflight. These studies included standard geologic mapping, particle-size measurements, petrographic and chemical studies, as well as density and moisture measurements. In the case of chemical and petrographic studies, a sampling grid was established along the general area of the flight lines (fig. 18-4). Samples were collected, numbered, and returned to the University of Nevada for laboratory analysis. Using a neutron gamma-gamma probe, direct field measurements for density and moisture were carried out on the altered cinder material. Samples were collected along both flight lines and returned to the laboratory for particle-size analysis. Results of the studies were used as the basis for establishing final positioning of the flight track and influenced the placement of ground monitoring stations manned during the overflight.

The only time-dependent variables monitored during the overflight were surface and subsurface temperatures, moisture content of the cinder, lake temperatures, and meteorological data taken from a weather station located at the center of the flight line. Important thermal and atmospheric parameters were measured during both the day (13:00 hours) and night (04:00 hours) overflights. However, data were affected by the presence of scattered cloud during the day flight. Because shadowing

effects from the cloud cover caused thermal variations on portions of the test site, efforts were concentrated on data gathered during the night flight.[1]

Chemical analysis.- Detailed studies of the rock chemistry have indicated little or no variation in the chemical makeup of the lava and cinder. The chemical consistency between cinder and lava virtually eliminates the possibility of the variation in microwave data being caused by changes in chemical compositions. Figure 18-5 indicates the results of the chemical analyses from a series of samples collected along flight line 2. The average chemical results are summarized in table 18-I.

Density and moisture measurements.- Density measurements of the cinder were performed at the test site with a neutron gamma-gamma probe. Resulting data indicate a very high porosity even for a vesicular material, with air occupying approximately 60 percent of the total volume. The vesicular cinder shows virtually no compaction, which helps account for the unusually high porosity. The highly permeable area of cinder is well drained, containing only about 3 percent moisture in the first 2 feet. Alteration, which occurs throughout the cinder deposits, seems to have produced little variation in the density measurements.

The soil moisture measurements were monitored over a period of several days prior to, as well as during, the overflights. The results are presented in table 18-II.

Particle-size analysis.- Particle sizes of the cinder were obtained by use of a square-root-of-two-series sieve set. These measurements indicated that a great majority of the cinder particles were comparable or smaller in size than the wavelengths received by the microwave radiometers. In contrast, the lava material consisted of large basalt blocks, 30 to 60 centimeters in size, many times larger than any of the wavelengths. The particular size variations of the cinder are presented in figure 18-6. The composite grain-size distribution for the 16 samples is shown in figure 18-7.

Measurements During Overflight

At the beginning and end of both flight lines, stations were manned to provide communications for aircraft guidance, and to obtain temperatures and meteorological measurements (fig. 18-8). A fifth station was

---

[1]Only a portion of the ground-truth data is presented in this paper. The complete preflight and inflight studies can be found in University of Nevada Technical Letters 8 and 10.

used as a meteorological station, while a sixth station was mobile along the junction of both flight lines, gathering infrared (IR) radiometric measurements. A seventh (unmanned) station consisted of temperature probes at various depths within the cinder fields.

The meteorological station operated radiosondes on a tethered balloon up to aircraft elevation, before, after, and during the overflights. By taking soundings along the entire interface between the ground and the aircraft, the total moisture in the atmospheric column, through which the sensors were looking, was established. Wet and dry bulb temperatures, using a sling psychrometer, were recorded at each of the manned stations to enhance the overall meteorological information.

Contact and IR radiometric temperatures were taken of the lava flows, cinder fields, and lakes over as wide a range of locations as each station could observe during the limited time frames. Upon completion of the night and day missions, soil moisture samples were collected from selected areas along the flight line. In addition to those tasks, the end stations along the flight line provided floodlights for aircraft guidance during the night mission. A summary of the temperatures taken at different stations during the overflights is given in table 18-III.

By the use of thermistor probes on the surface and at varied depths in the cinder, a temperature profile was established over the course of several days before and during the overflight. These measurements indicated a wide daily variation of temperature at the surface and a fairly constant temperature at the 12-inch depth. Below 12 inches, the temperatures most likely reflect seasonal variations. Figure 18-9 plots results of temperature measurements for a 24-hour cycle at various cinder depths. It would have been desirable to measure temperatures from the lava fields at varied depths, but, without hard-rock drilling equipment, such attempts proved unsatisfactory.

AIRCRAFT SYSTEMS PERFORMANCE

Description of Flights

The long-term test site studies conducted prior to the flights were instrumental in establishing both the flight lines and flight scheduling. Day and night flights were flown to determine diurnal influences on the microwave signature. Although maximum surface temperatures occurred between 1:00 and 3:00 p.m., the day mission was scheduled for 11:00 a.m. because of the afternoon cloud buildup, which has a drastic effect on IR temperatures. However, mechanical difficulties caused a 2-hour aircraft delay, and scattered clouds were over the test site at the time of the overflight.

Flight line 1 was flown south to north, and flight line 2 was flown from northeast to southwest in a "figure 8" pattern. Four runs were flown over each line in the same direction and at constant altitude, with radiometer beam settings of 10° E, 10° H, 45° E, and 45° H. The lowest possible altitude was desired to maximize spatial resolution of the radiometers. Considerations of low-level turbulence (day) and aircraft safety (night) determined the flying altitude, 4000 feet above the terrain. Ground-resolution elements for this altitude are listed in table 18A-I of appendix 18A.

Aircraft Performance

Aircraft ground tract.- Aircraft altitude and position over the flight lines are of prime consideration when comparing a number of passes over the same target. Using aerial photography, the exact track of the aircraft was plotted for the day mission. The plots indicate the pilot had difficulty in holding flight line 1 because of excessive crosswinds and limited ground visibility. The night mission runs were plotted from the Reconofax IV thermal IR imagery and indicated less difficulty in holding the flight path in the absence of crosswinds.

Variations in aircraft velocity were corrected by scaling the distance between lakes located at the ends of the flight lines and recording the number of integrations made by the radiometers. By superimposing the data on the known flight track, it was found that the velocity between different runs varied only slightly. The only critical target on the flight line was the cinder cone, over which plots of the aircraft position are represented in figure 18-10.

A single-channel radiometer response is included to show the comparison between the temperature measured by the radiometer and the track of the aircraft. Because the data were good and the cinder areas appeared as thermal anomalies to the microwave radiometers, some determination of aircraft position on the flight lines could be made directly from the microwave data itself. Figure 18-11 shows the composite plots of all runs made by the aircraft during the day. Only data representing flights over the same target on the ground were used for comparative studies.

Drift angle effects.- The radiometer beam intercept along the ground was offset from the aircraft ground track when the aircraft was forced to crab into the wind. This offset D is given by

$$D = H \tan \alpha \sin \theta$$

where H = altitude above ground

α = radiometer look angle

θ = drift angle

Table 18-IV summarizes the offsets for the day flight (number 5). There was no drift angle during the night flight (number 6).

Aircraft stability.- Superimposed on the offsets in beam position, caused by aircraft track and drift angles, is a randomly varying offset caused by roll, pitch, and yaw of the aircraft. The magnitude and peak deviations of the roll, pitch, and yaw rates, and altitude for each of the flight lines are listed in table 18-V. No attempt was made to correct for these effects, which were generally small.

Radiometer System Performance

Recorder evaluation.- An indication of recorder performance for the 9.3-gigahertz channel is shown in figures 18-12 to 18-14. Figure 18-12 shows the recorder deviation from the linear equation established by the 1.5- and 3.0-volt calibration points. Over the entire 5-volt range, the maximum deviation is 30 millivolts, which corresponds to 0.6 percent of full scale. The deviation over the range of most of the data, 0.5 to 3.5 volts, is 12 millivolts (0.25 percent).

Figures 18-13 and 18-14 show the 1.5- and 3.0-volt calibrations for flights 5 and 6, respectively. For each run, several 1-second samples are plotted for the calibrations recorded before and after the run. Samples within the run show that recorder noise levels were satisfactorily low, except for the following cases: preflight calibration and run 4, flight line 2 of flight 5; and preflight calibration, run 3, flight line 2, and run 4, flight line 1 of flight 6. In these cases, recorder wow caused peak excursions up to 70 millivolts (1.4 percent). Wow greatly reduced the usefulness of the data in which it was present. The single deviation in the flight 5, run 3, flight line 2, 1.5-volt calibration was the result of recorder dropout, a phenomenon which occurs occasionally in the data.

Except for the noisy runs, figures 18-13 and 18-14 show that the recorder drift is less than ±8 millivolts, which is acceptable performance for the recorder.

Radiometer evaluation.- A summary of the radiometer calibrations is shown in table 18-VI. The base-line voltage is the voltage output for an absorber temperature of 290° K. The value listed is the average

of the preflight and postflight calibrations. The deviation is one-half of the difference in degrees Kelvin between the preflight and postflight values. The scale factor is the gain of the instrument in degrees Kelvin per volt. Its deviation in percentage is one-half the difference between preflight and postflight values, divided by the average.

The deviations for the 15.8-gigahertz channel are within the limits imposed by the radiometer noise alone. The gain deviations for the 22.2- and 34.0-gigahertz channels are also within the radiometer noise limitations. However, the base-line variations are two to four times greater than those expected from instrument noise alone. This would indicate that the 22.2- and 34.0-gigahertz channels were less stable than the 15.8-gigahertz channel. Both deviations for the 9.3-gigahertz channel are considerably out of the expected range and render run-to-run comparisons of the 9.3-gigahertz data somewhat questionable.

An examination of the postflight calibration data for flight 6 indicates that the peak noise fluctuation over a 50-second interval was 3.0° K, or less, for the 15.8-, 22.2-, and 34.0-gigahertz channels. This compares favorably with the laboratory results discussed in appendix 18A. However, the 9.3-gigahertz peak-noise fluctuations were on the order of 30° K, which is considerably higher than the laboratory results. This may be attributed in part to a lower gain in the 9.3-gigahertz channel, which increases noise contributions resulting from the recorder. Radar interference is also frequently experienced on the 9.3-gigahertz channel. The fluctuations ΔT_{p-p} are shown by brackets on the flight data to indicate how much of the fluctuations along a flight line may be attributed to inherent system noise.

Since these calibrations are measures of the instrument status before and after the flight, it is assumed that they are representative of instrument status during the flight. In some instances (e.g., flight 5), the ambient temperature during preflight and postflight calibrations varied significantly from that encountered at flight altitude. Because the instrument was not in a temperature-controlled environment, this could have caused change in base line and gain between calibration and the overflight. However, with the possible exception of the 9.3-gigahertz channel, the radiometers are known to be stable in a constant-temperature environment. Hence, base-line and gain drifts during the overflight are expected to be small.

An indication of instrument performance during flight can be obtained by observing the flight data. Neither theoretical nor experimental values are available for microwave brightness temperatures; therefore, evaluation of the instruments data output can be done on a qualitative basis only. With this in mind, refer to table 18-VII, which lists antenna temperatures at selected points over water and forest at either end of

the flight line. Comparing the E- and H-plane polarization data, over water for 10° and 45° look angles, and using the definitions of polarization in table 18B-I of appendix 18B, it can be seen that qualitatively the radiometers behave as expected. That is, (1) vertical polarizations yield higher antenna temperatures than horizontal temperature polarizations, and (2) antenna temperatures at 45° are lower than those at 10° for horizontal polarizations and are higher than those at 10° for vertical polarizations. Comparison of day and night antenna temperatures over the forested area at a 10° look angle was made to determine the validity of day-night comparisons of antenna temperatures for a given channel. The forest was chosen because it has a high emissivity and most closely approximates a blackbody. In all cases, antenna temperatures were less at night than during the day (in most cases, from 10° to 13° K). This is in good comparison with the 11° to 13° K difference in vegetation temperature measured with the IR radiometer. Day-night comparisons of results are valid within the uncertainty limits imposed by the preflight and postflight calibrations.

If adequate field and/or theoretical values for brightness temperatures over the water and forests were available, it would be possible to calibrate the radiometers in terms of a temperature that would be a first-order approximation of brightness temperature (loss effects removed; side-lobe contributions not removed).

MULTISPECTRAL MICROWAVE RESULTS

The reduced aircraft radiometer data were analyzed with respect to the ground studies and within the limits of system performance discussed in previous sections. The analysis includes further verification of system performance by observation of the data, examination of the effects of surface roughness and layering on the data, and discussion of limitations on the experiment because of both its design and inherent system characteristics. These considerations serve as bases for experiments proposed in the conclusions and recommendations. Details of the reduction of the raw data to antenna temperature are presented in the section on data reduction in appendix 18B.

Figure 18-15, the 34.0-gigahertz radiometer response for the four night runs over flight line 1, demonstrates that the various elements along the flight line are differentiable with a microwave radiometer. Every run shows a distinctive return for water, lava, cinder cone, and forest. This consistency in results indicates that the response is caused by systematic changes in terrain, rather than by random instrumental errors.

Multiple-frequency microwave radiometers offer the potential of differentiating between various parameters of the terrain that are observed. Since the microwave data contained herein are in terms of antenna (not brightness) temperatures, only relative comparisons among the different frequency channels are valid. Because antenna beam widths and side-lobe structures are different for each of the channels, it is assumed that the area observed at each instant is uniform for all of the beam intercepts and that variations resulting from different side-lobe structures are negligible.

Thermal Effects

The thermal properties of the cinder and lava materials are controlled primarily by albedo (reflectivity at solar wavelengths) and thermal diffusivity. The photograph of the test site (fig. 18-2) shows the basaltic lava flows to be darker in color than the cinder field. Hence, the lava flows will have a lower albedo than the cinder and will absorb more solar thermal energy during the day. The thermal IR imagery taken during the day flight (fig. 18-16) shows that the basalt is cooler than the cinder. Since it is absorbing more energy than the cinder, its coolness must be the result of higher thermal diffusivity (i.e., ability to conduct the solar energy received at the surface to subsurface zones). (Because of an automatic gain control on the IR imager, the gray scale is not uniquely related to temperature. Temperatures of the water (lakes), cinder, and lava flows are given in table 18-III.)

The IR imagery from the night flight is shown in figure 18-16. The relative surface temperatures have reversed themselves from those of the day flight because of the higher thermal diffusivity of the basalt, which is being heated at the surface by the energy stored at depth. Although the cinder has a relatively warm zone at a depth of 12 inches (25° C), it is such a good insulator (low thermal diffusivity) that its surface equilibrates roughly with the air temperature (10° C).

Average measured values of antenna temperatures over water, lava, and unaltered cinder of flight 6 (night) are shown diagrammatically in figure 18-17. As indicated by the IR and 34.0-gigahertz microwave radiometers, the surface temperature of the lava is significantly warmer than that of the cinder. However, at the depth sensed by the 9.3-gigahertz radiometer, the subsurface temperature of the lava is cooler than that of the cinder. The 22.2- and 15.8-gigahertz channels show intermediate responses, with the 15.8-gigahertz response indicating no temperature change between the two substances. The low temperature over water is the result of the low emissivity of water in the microwave portion of the spectrum.

There are several factors that may contribute to the signal differences between the lava and unaltered cinder: chemical composition, moisture content, surface characteristics, microwave penetration depth, and thermal properties. Since the chemical composition of the cinder and the lava were essentially the same by choice, it was not a contributing factor. Moisture has the effect of lowering the brightness temperature and decreasing the depth of penetration. The moisture content was low for both materials, and the microwave return did not show consistently cooler temperatures at all frequencies over either of the materials. Surface roughness (surface area exposure) affects cooling rates and hence microwave brightness temperatures. It is expected that these effects would cause consistent trends in the data; that is, all channels would show the lava to be cooler than the cinder or vice versa. Since this supposition is not supported by the responses in figure 18-17, moisture and surface roughness do not appear to be controlling factors in these microwave responses.

Radiometric penetration depth will certainly influence the observed brightness temperature. If the penetration depth of the cinder was greater than that of the basalt and if all other factors were equal, the 9.3-gigahertz channel would show the cinder to be warmer than the lava at night, as indicated by the data. However, the surface temperature would be the same for both materials. This is not supported by the IR and 34.0-gigahertz data.

The controlling factor in the response appears to be the thermal properties of the material. The better thermal conductor of two materials will show a warmer surface temperature and a cooler temperature at depth during the night. Of course, there will be an isothermal depth at which the temperatures of the two materials are equal. Although the first four factors, especially the penetration depth, certainly contribute to the signal, the explanation that the cinder (because of its porosity) is not as good a thermal conductor as the basalt, best fits the observed data. This conclusion is further confirmed by consideration of a similar response diagram for the day flights. Figure 18-18 shows a temperature reversal in the 9.3- and 15.8-gigahertz channels. Scattered clouds rendered surface thermal considerations inconclusive during the day flight.

In differentiating between the lava and the altered cinder for the night flight, the 9.3- and 34.0-gigahertz channels are more graphic than the 15.8- and 22.2-gigahertz channels. The actual responses for these two channels for two runs are shown in figure 18-19. For these runs, the 34.0-gigahertz channel consistently shows the lava to be warmer than the cinder, and the 9.3-gigahertz channel consistently shows the lava to be cooler than the cinder. This consistency indicates that these are

systematic changes caused by the terrain, rather than random instrumental changes. Figure 18-19 also indicates that the position of the maximum temperature at 9.3 gigahertz does not correspond to minimum 34.0-gigahertz temperatures.

The altered cinder covers the lava in varying thicknesses and will have varying thermal gradients. The radiometer response will depend on these thermal properties and on the radiometric penetration depth for the two materials. A more complete knowledge of the geologic cross section and diurnal heating characteristics is required for detailed interpretation of the responses of figure 18-19. An improved experiment over the same test area would include more extensive determination of the geologic cross section and diurnal measurements of contact and radiometric (with a ground-based instrument) temperatures in the cinder, lava, and layered areas.

Cinder Cone

The principal reason for flying the cinder-cone flight line was to measure the effect of slope on the antenna temperature. These cinder-cone data were then to be compared with data generated along the flat-lying cinder on flight line 2. Again, only night data were reduced for comparison. The microwave data indicated that the subsurface temperatures (9.3 gigahertz) of the cone varied greatly from the north to the south side. This anomaly is primarily a product of the sun angles on the cone. During the day, the sun heats the south side of the cinder cone to temperatures well in excess of those on the north side. Night IR imagery indicated that there was no north-south variation in surface thermal temperature, evidence that the surface cinder material is more sensitive to the surrounding air temperature than to subsurface temperatures.

Figure 18-20 is a sample of the data received over the cinder cone, which is located directly in the center of the data. The length of the cone represents eight integrations or 8 seconds of flight. The 34.0-gigahertz channel and the IR imagery give similar readings for surface temperatures on the north and south sides of the cinder cone, whereas the 9.3-gigahertz channel shows clearly that the subsurface temperatures on the south side of the cone were above those of the north side. Because of the wide variation in subsurface temperatures on the cinder cone, no attempt was made to compare these data with those collected over the flat cinder areas.

Surface Roughness Effects

As indicated in appendix 18B, the microwave radiometer has a response that is different as a function of incidence angle for horizontal and vertical polarizations. For a smooth surface, the vertically polarized temperature component will be greater than the horizontally polarized component, and that difference will be greater at 45° than at 10°. This phenomenon can be observed in the graph of temperature differences over Snag Lake (fig. 18-21, water), and demonstrates the differences between vertical and horizontal polarization temperatures over a body of water. For increasingly rougher surfaces, this difference would be expected to decrease. Differences in temperature graphs for the lava and the altered cinder, which have markedly different surface characteristics, are also shown in figure 18-21. Two features of the graph are noteworthy: (1) in certain cases, the vertically polarized apparent temperature T_A is smaller than the horizontally polarized T_A, a phenomenon unexpected and unexplained, except possibly by a difference in radome loss between the two polarizations; (2) on all channels, the differences in the 10° plots are approximately the same for the two materials, whereas the 45° plots show a noticeable positive departure for cinder when compared to lava. Hence, the cinder behaves more like a specular reflector than the lava.

While these measurements are inconclusive in defining a set of roughness-identifying parameters, they have indicated that the radiometers are capable of differentiating between similar materials with different roughness characteristics.

CONCLUSIONS AND RECOMMENDATIONS

The mission over the Mount Lassen Test Site and subsequent data analysis demonstrated requirements for exploring the potential of multispectral microwave radiometers for sensing geologic parameters.

1. A relatively simple test site is preferable in studying the effect of individual geologic parameters on the microwave signal.

2. Knowledge of the parameters affecting the radiometric signature, (i.e., thermal diffusity, albedo, surface roughness, density, temperatures, and weather conditions) are required for analysis of the data.

A thorough understanding of the aircraft and sensing-instrument limitations and capabilities is also required. Several operational limitations were observed which may be of value in future mission planning.

1. The aircraft can fly more accurate tracks at night because of lighting along the flight line and because lighter winds and calmer air are usually encountered at night.

2. Cloud buildup can greatly compromise the usefulness of collected data.

3. An intermittent recorder wow reduced the usefulness of approximately 25 percent of the radiometer data. A method of checking the recorder in real time for wow should be valuable.

Since the microwave data are in terms of antenna temperatures, comparisons between channels can be made on a relative basis only. Examination of the data indicates that the instrument performance was not significantly degraded from that observed in the laboratory. Results showed the following:

1. There was definite correlation between basic geologic units and radiometric temperatures.

2. The longer wavelength radiometers are capable of sensing subsurface temperatures.

3. There appears to be a correlation between layer thickness and multispectral return for a layered area.

4. The roughness of two chemically similar areas is differentiable using a dual-polarization radiometer.

These qualitative conclusions indicate that further efforts to define quantitative models and obtain quantitative results are warranted.

The experiment revealed several interesting features which warrant further investigation. A future mission and further field studies are recommended for the Mount Lassen Test Site. Improvements in the experiment and the tools necessary to implement them are outlined in the form of specific recommendations.

In order to examine the responses resulting from layering, discussed in the section on Multispectral Microwave Results, it is desirable to obtain geologic profiles for the layered areas and to define a flight line to fly over the most promising profile. A small seismic thumper could be utilized for obtaining these profiles. Hard-rock drilling equipment is needed to obtain temperatures at depth in the basalt lava. More probes of temperature as a function of depth are also required. Automatic self-contained recording units would greatly facilitate thermal temperature measurements. In addition, thermal parameters of the unaltered cinder, the altered cinder, and the lava should be measured in the laboratory.

Ground-based radiometers would permit measurement of brightness temperatures of the lakes and other areas which could be used as calibration points for the aircraft radiometers. They could also be used for more detailed studies of interesting phenomena, such as a surface roughness or diurnal temperature variations.

Finally, it is recommended that flights be made at lower altitudes and that radiometer integration times be decreased to improve instrument resolution.

TABLE 18-I.- SUMMARY OF CHEMICAL ANALYSES IN PERCENTAGE

Chemical	Lava flow	Unaltered cinder	Altered cinder
SiO_2	55.55	55.25	53.68
Al_2O_3	15.67	14.55	13.62
K_2O	1.49	1.48	1.29
CaO	9.64	9.21	9.83
TiO_2	.79	.80	.78
[a]Fe_2O_3	8.21	8.00	8.27
MgO	8.22	8.33	9.06
Na_2O	3.12	3.02	2.44
Total	102.69	100.64	98.97

[a]Total iron as Fe_2O_3.

TABLE 18-II.- NEUTRON GAMMA-GAMMA PROBE DATA FROM ALTERED CINDER

Site	Wet density	Dry density	Water, percent	Porosity, percent (a)
Ridge top	1.35	1.34	1.2	47.8
Valley adjacent to exposed lava	1.05	1.03	3.5	60.0
Level cinders	1.14	1.11	2.3	56.6
15° slope	1.16	1.14	2.3	55.6
In depression	1.18	1.16	1.2	54.7
Dry streambed	1.14	1.09	4.2	57.5
Base of knoll	.88	.84	3.6	66.9
35° slope	1.10	1.06	3.4	58.4
Average	1.13	1.10	2.6	58.2

[a]Calculation based on a solid density of 2.7.

TABLE 18-III.- AVERAGE TEMPERATURE MEASUREMENTS FOR DAY AND NIGHT FLIGHTS

Station (method)	Day, °C	Night, °C
Lava flows (IR)	44	16.5
Cinder (IR)	47	10.5
Butte Lake (contact)	21.5	20.5
Snag Lake (contact)	21	20.5
Twin Lake (contact)	21	20

TABLE 18-IV.- BEAM POSITION OFFSETS CAUSED BY DRIFT, FLIGHT 5

Line	Run	Polarization	Look angle, deg	Offset, D (a)
1	1	E	10	74L
2	1	H	10	15R
1	2	E	45	490L
2	2	H	45	140R
1	3	H	10	30R
2	3	E	10	44R
2	4	E	45	200L
1	5	H	45	140L

[a]Left is indicated by "L"; right is indicated by "R."

TABLE 18-V.- MAGNITUDE AND PEAK DEVIATIONS OF AIRCRAFT ROLL, PITCH, AND YAW RATES AND ALTITUDE

Flight	Line	Run	No. of samples	Roll, deg/sec (a)	Pitch, deg/sec (b)	Yaw, deg/sec (a)	Altitude, ft above mean sea level
5	1	1	6	-	+0.2 (-0.2, +0.5)	-0.2 (-0.6, +1.2)	9 800 (-80, +100)
	2	1	7	-	0.0 (±0.2)	-0.1 (-1.6, +2.1)	9 890 (±60)
	1	2	6	-	0.0 (±0.3)	-0.2 (-0.7, +0.5)	10 010 (-20, +10)
	2	2	8	-	+0.1 (±0.3)	+0.5 (-0.8, +2.9)	9 990 (-70, +90)
	1	3	5	-	+0.2 (±0.5)	+0.3 (-0.8, +0.4)	9 830 (±0)
	2	3	7	-	-0.2 (-2.0, +0.7)	+0.5 (-1.0, +1.5)	9 890 (-10, +20)
	2	4	7	-	+0.1 (±0.3)	-0.1 (-1.3, +0.6)	9 960 (-40, +30)
	1	5	6	-	+0.2 (-0.5, +1.2)	-0.7 (-1.8, +1.0)	9 900 (-20, +10)
6	1	1	1	-	0.0	0.7	9 880
	2	1	6	-	0.0 (-0.2, +0.1)	-0.4 (-0.3, +0.4)	9 810 (-30, +40)
	1	2	7	-	-0.1 (-0.4, +0.1)	-0.2 (-0.5, +0.3)	10 000 (-70, +20)
	2	2	10	-	0.0	0.0 (-0.4, +0.3)	9 960 (-70, +40)
	1	3	7	-	-0.1 (-0.7, +0.4)	-0.3 (-1.5, +0.5)	9 940 (-40, +80)
	2	3	11	-	0.0 (-0.3, +0.1)	0.0 (±0.7)	10 000 (-20, +10)
	1	4	6	-	0.0 (-0.1, +0.0)	-0.1 (±0.1)	9 950 (±50)
	2	4	9	-	0.0 (-0.0, +0.1)	0.0 (-0.7, +0.5)	9 900 (-50, +90)

[a] Right is indicated by +; left is indicated by -.

[b] Up is indicated by +; down is indicated by -.

TABLE 18-VI.- RADIOMETER CALIBRATIONS

Flight	Calibrations	Channel, GHz			
		9.3	15.8	22.2	34.0
5	Base-line voltage, V	1.033	1.439	1.266	1.305
	Base-line deviation, °K	8.0	.2	3.3	--
	Scale factor, °K/V	260.0	92.7	88.0	--
	Deviation, percent	5.8	.9	.5	--
6	Base-line voltage, V	1.068	1.409	1.179	1.277
	Base-line deviation, °K	--	.3	3.9	1.7
	Scale factor, °K/V	272.4	86.4	85.9	126.7
	Deviation, percent	--	2.2	.7	.6

TABLE 18-VII.- ANTENNA TEMPERATURES OF SELECTED POINTS IN DEGREES KELVIN

Surface	Flight, look angle	Channel, GHz							
		34.0		9.3		22.2		15.8	
		Polarization							
		E (a)	H (b)	E (a)	H (b)	E (a)	H (b)	E (a)	H (b)
Over water	5, 10°	--	183.9	58.0	54.0	193.6	199.5	165.2	163.9
	5, 45°	211.0	166.5	85.0	37.2	191.0	224.7	192.0	155.3
Over forest	5, 10°	--	279.0	202.0	200.0	286.0	289.2	262.5	265.0
	6, 10°	261.5	266.3	192.0	193.0	275.5	276.8	252.0	252.5
	ΔT (day-night)	--	12.7	10.0	7.0	10.5	12.4	10.5	12.5

[a] E-plane vertical.

[b] E-plane horizontal.

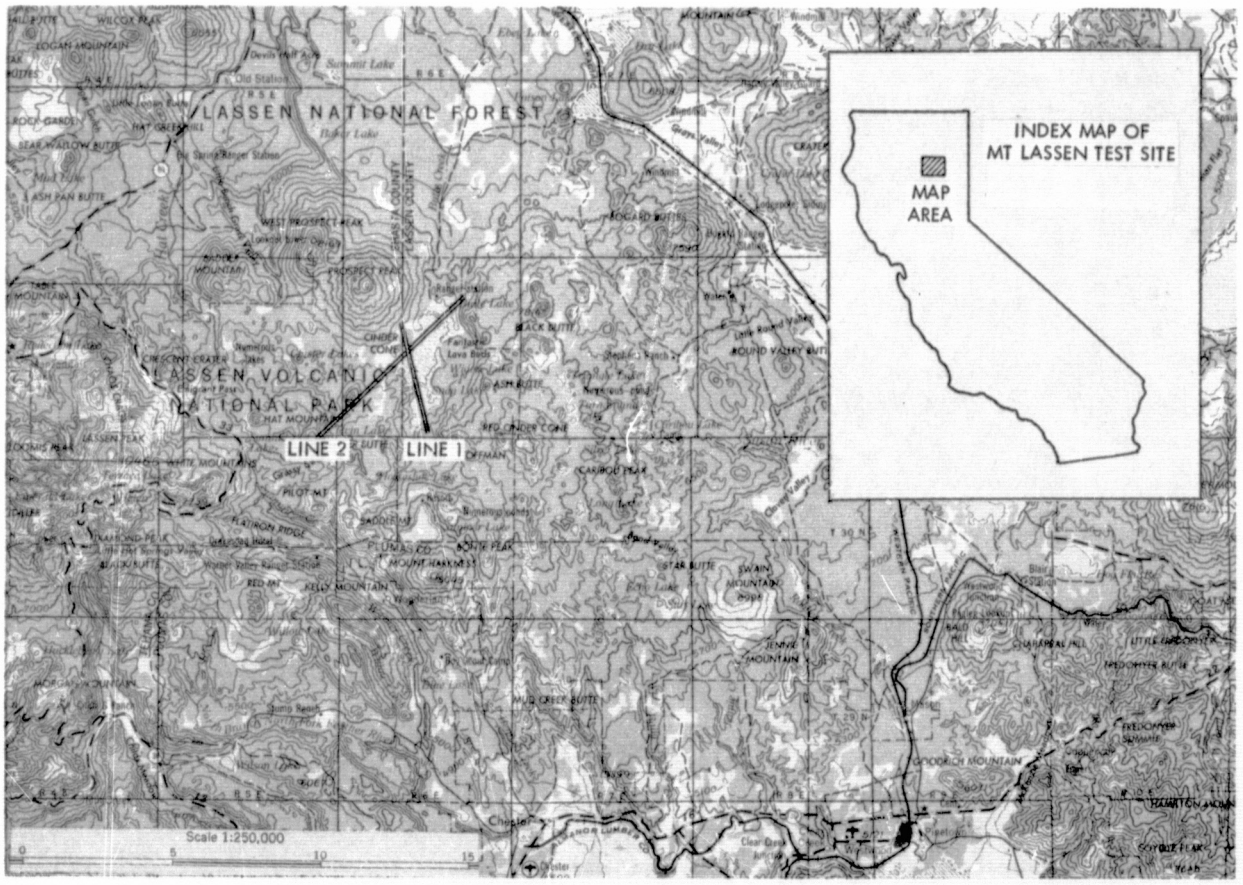

Figure 18-1.- Index map of Mount Lassen Test Site.

Figure 18-2.- Aerial view of test site area.

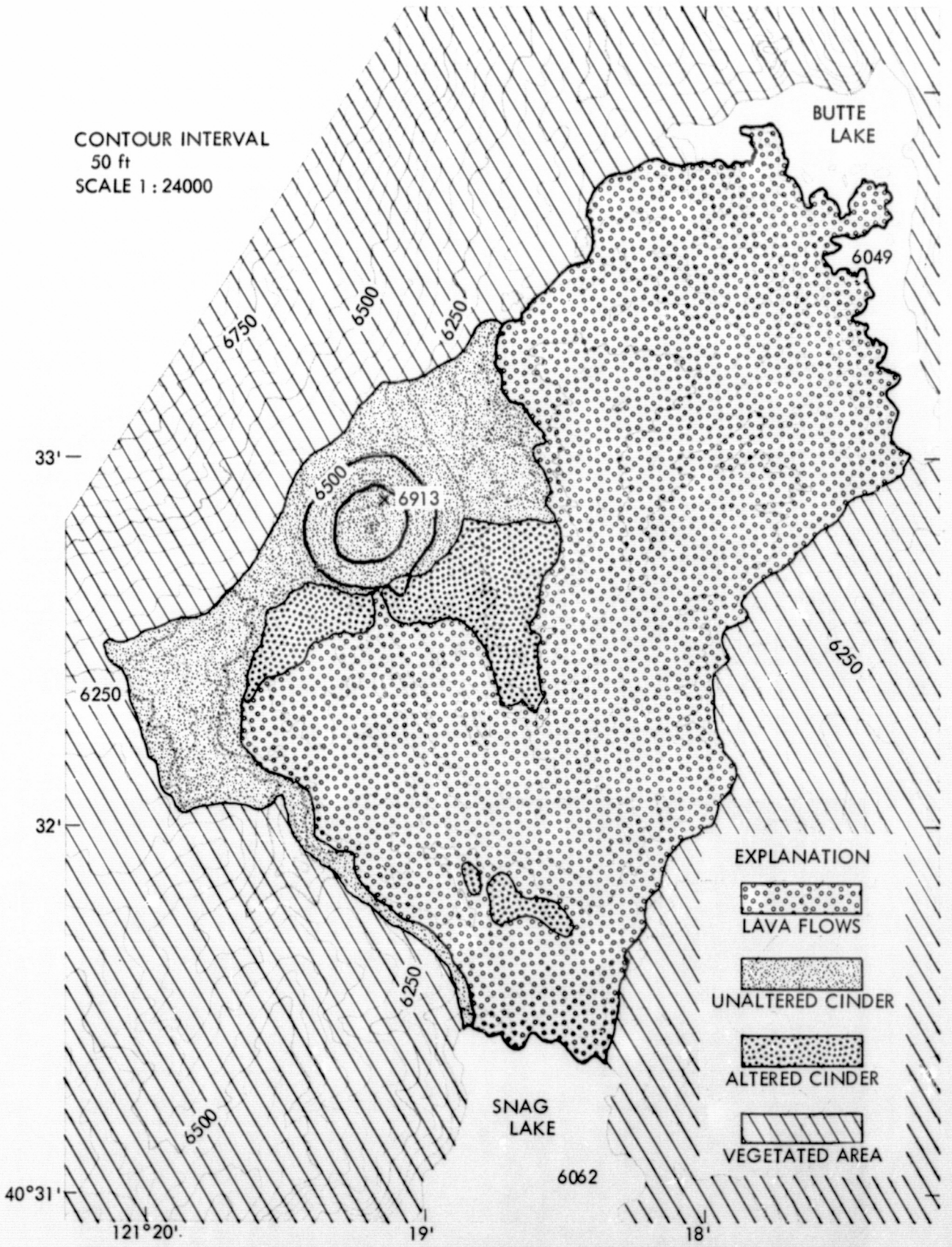

Figure 18-3.- Geologic map of test site area.

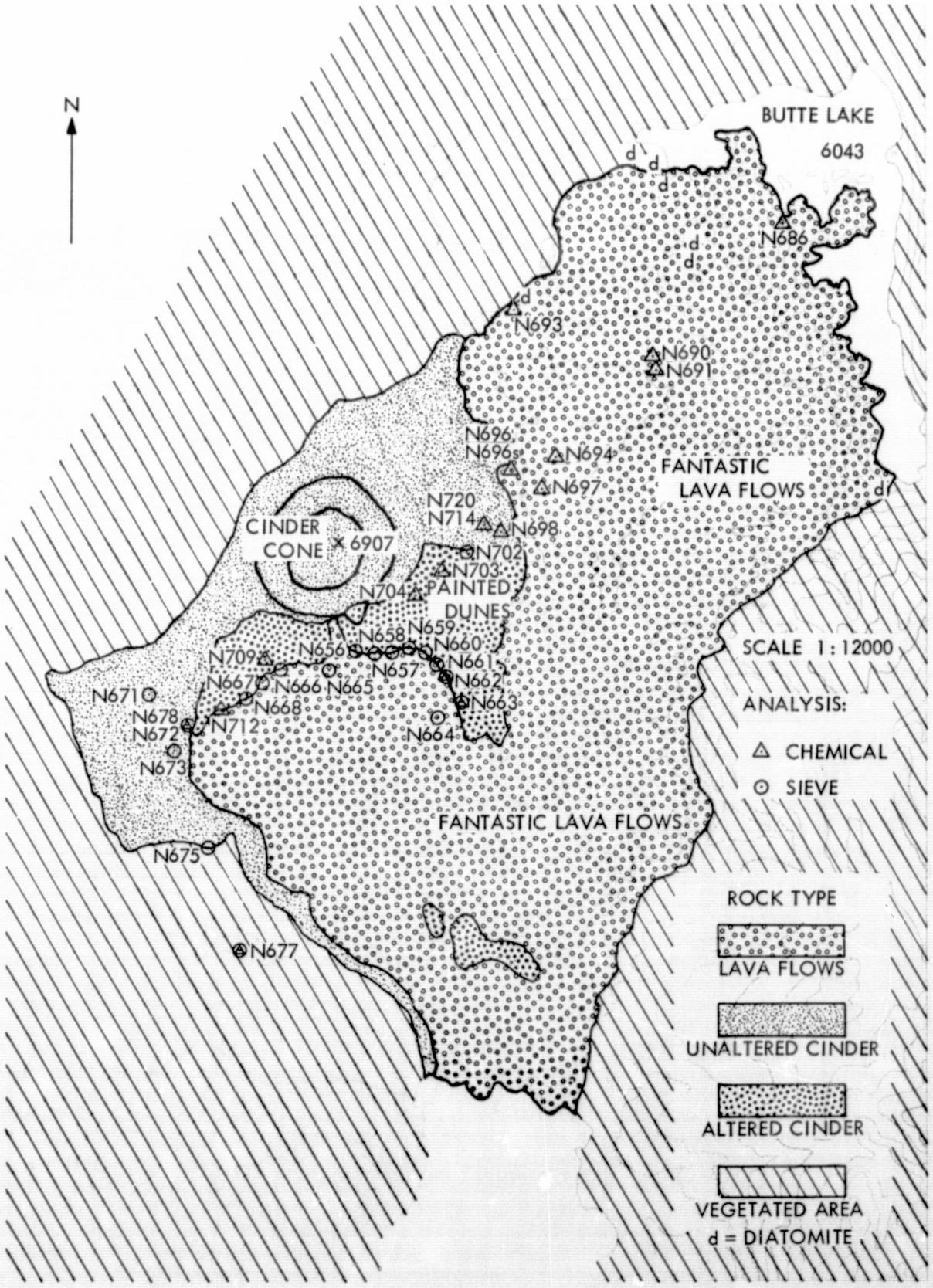

Figure 18-4.- Sample location map showing sampling points for preflight studies.

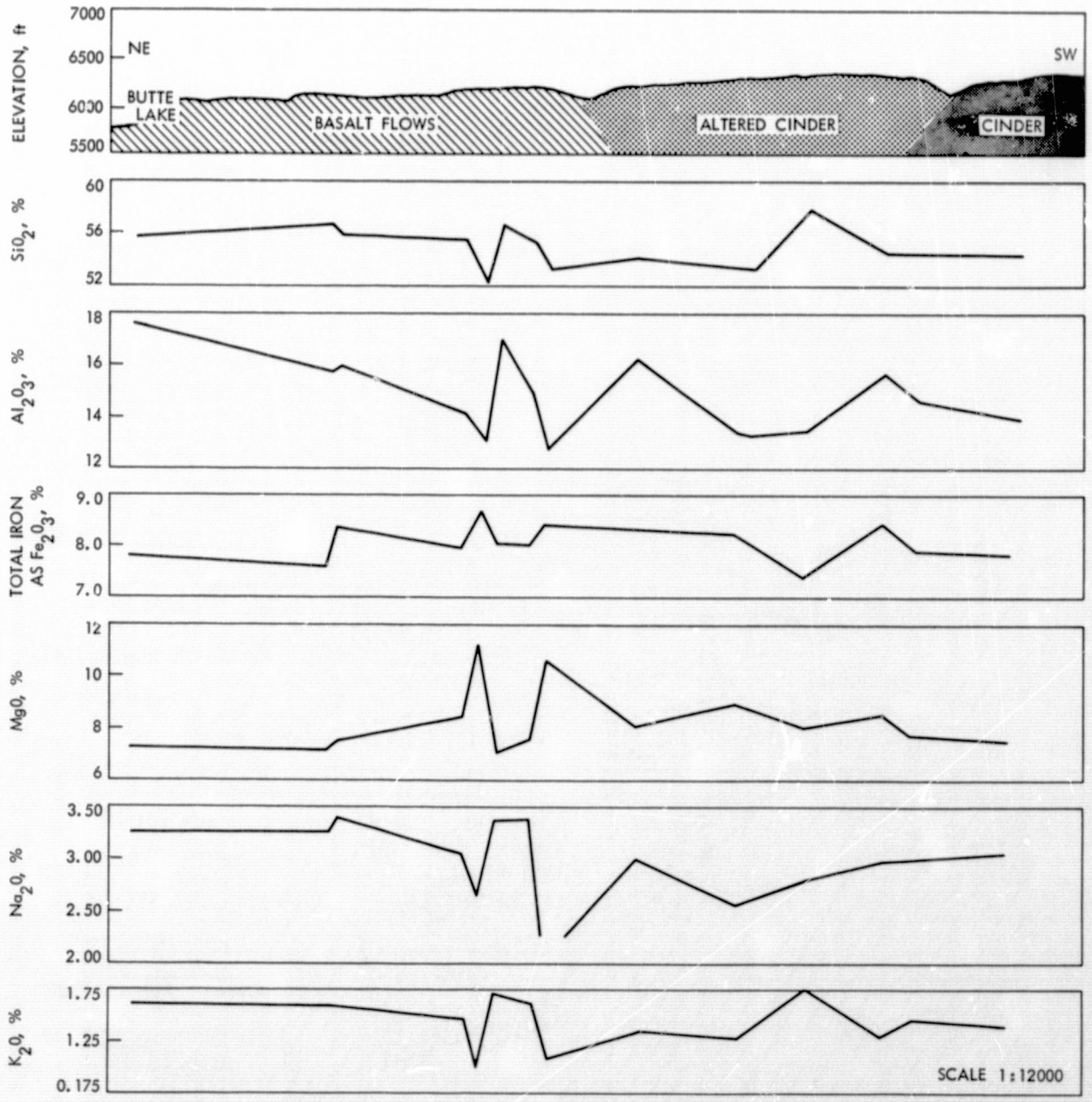

Figure 18-5.- Major chemical variations along flight line 2.

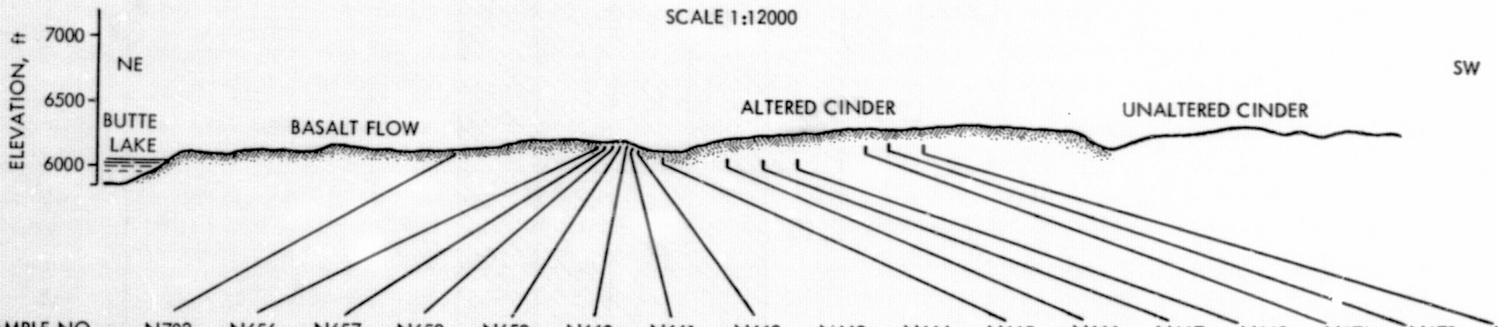

SAMPLE NO.	N702	N656	N657	N658	N659	N660	N661	N662	N663	N664	N665	N666	N667	N668	N671	N673	N675
Ø MEAN	-3.25	-2.44	-1.79	-3.01	-1.84	-2.16	-1.39	-2.54	-2.39	-3.61	-2.75	-2.04	-1.56	-0.37	-0.67	-1.19	-2.01
Ø DEVIATION	1.52	0.73	1.09	0.46	0.81	1.14	0.97	1.03	1.04	0.79	0.60	1.15	0.88	1.25	1.16	1.14	0.99
SKEWNESS	0.53	0.48	0.59	3.29	0.18	0.45	0.10	0.81	0.75	2.23	1.86	0.75	0.04	0.03	0.06	0.23	0.36
KURTOSIS	-1.61	5.63	2.23	81.51	1.63	1.35	0.19	4.12	3.35	28.71	31.04	1.54	1.56	0.43	0.33	0.50	0.76

Figure 18-6.- Particle-size variations along flight line 2.

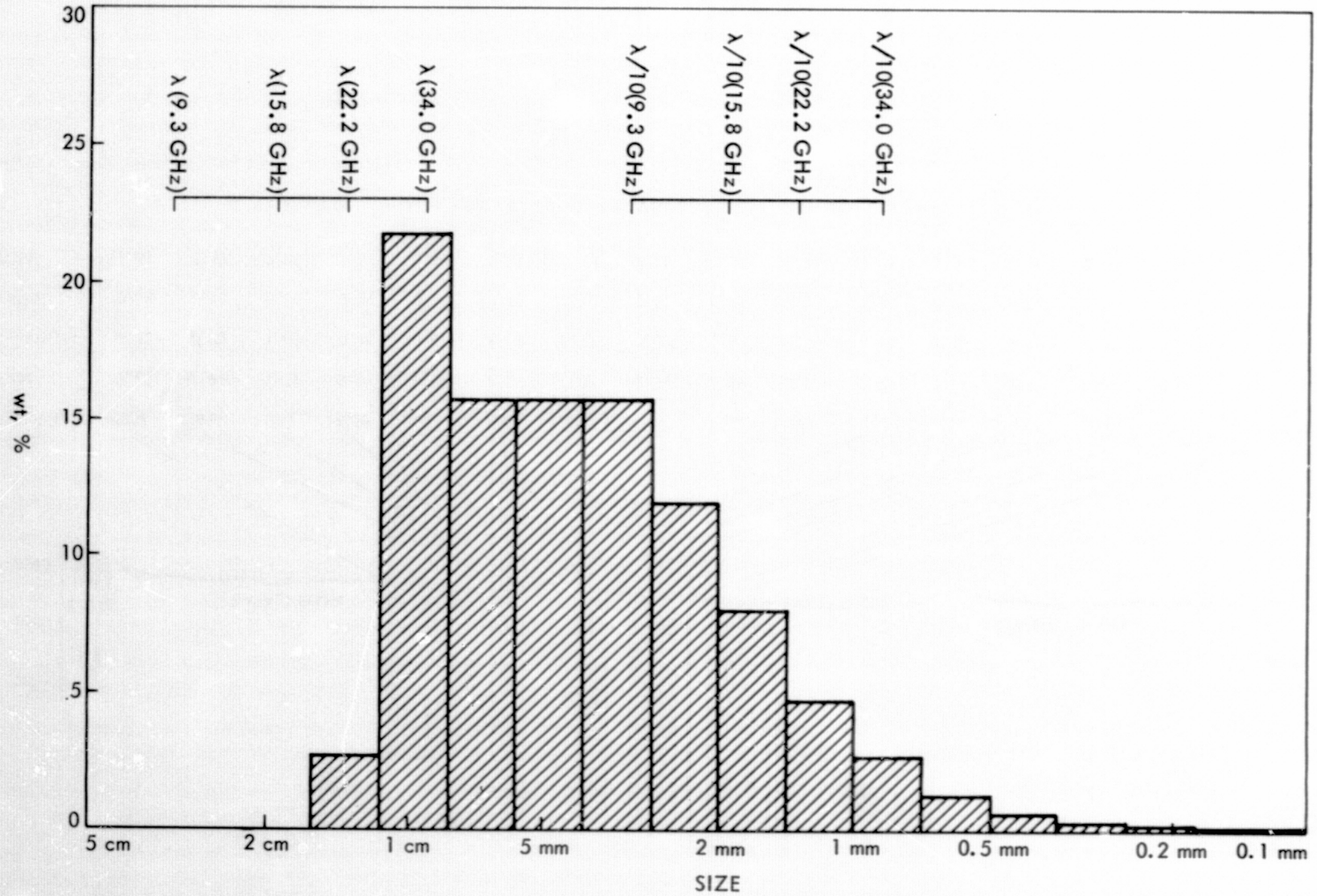

Figure 18-7.- Cinder grain-size distribution and comparisons with radiometer wavelengths.

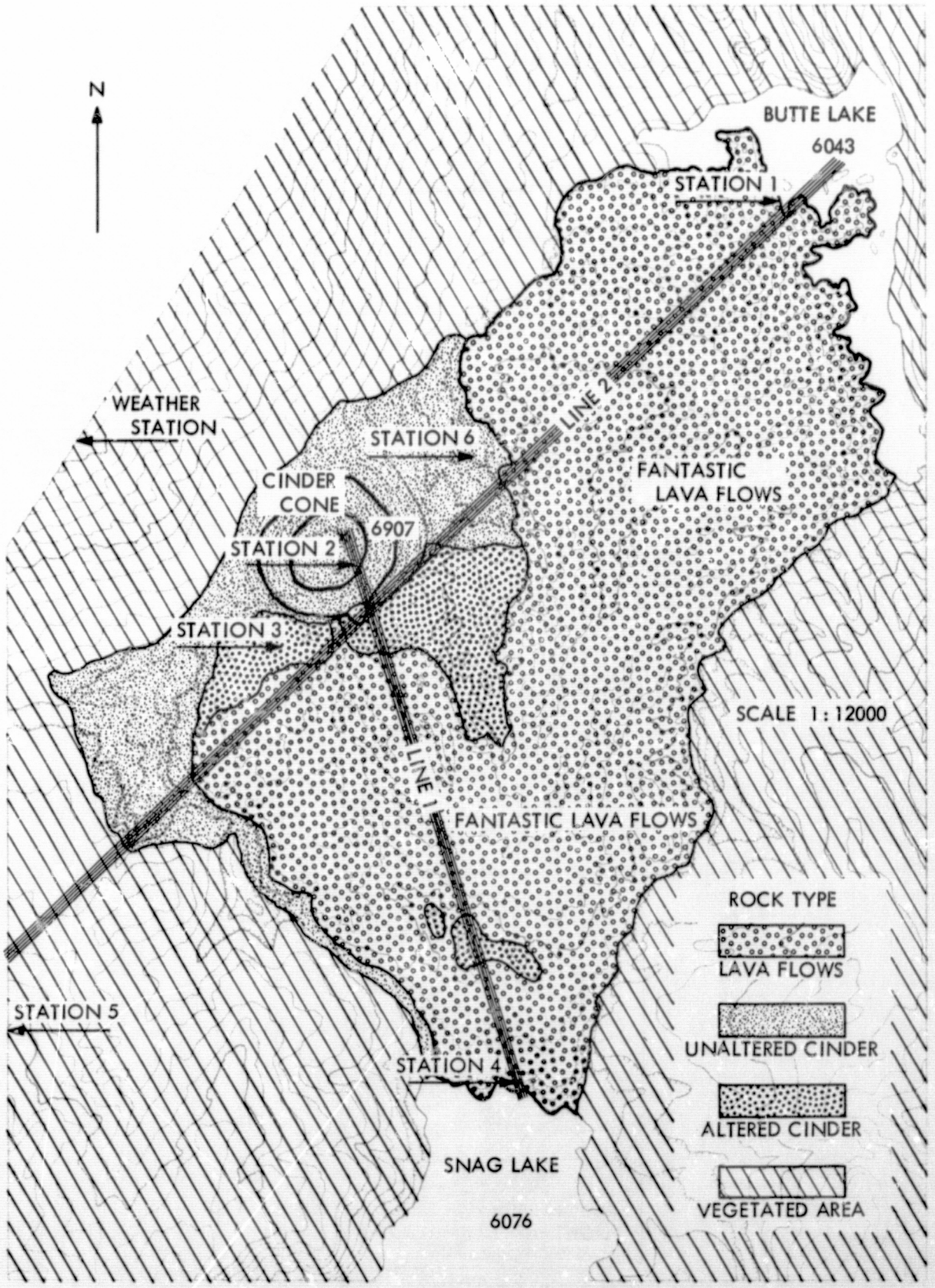

Figure 18-8.- Locations of overflight stations.

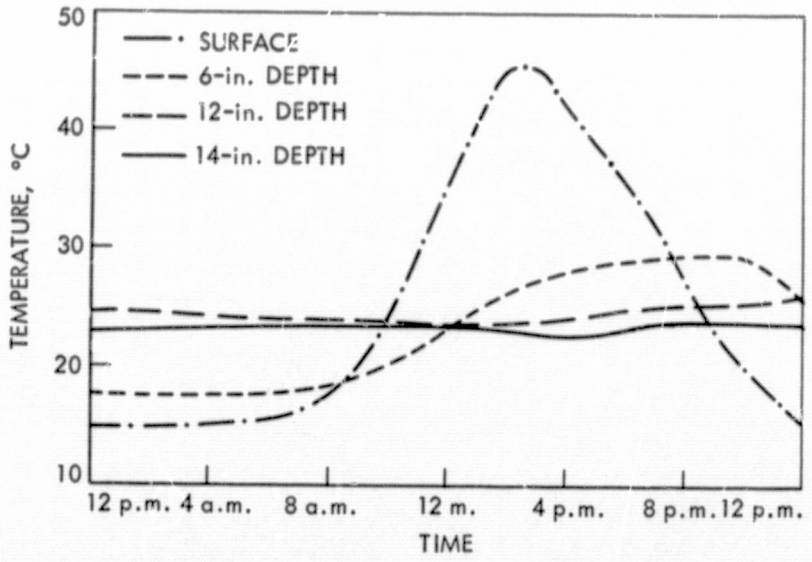

Figure 18-9.- Diurnal heating--cooling curves for basalt cinder.

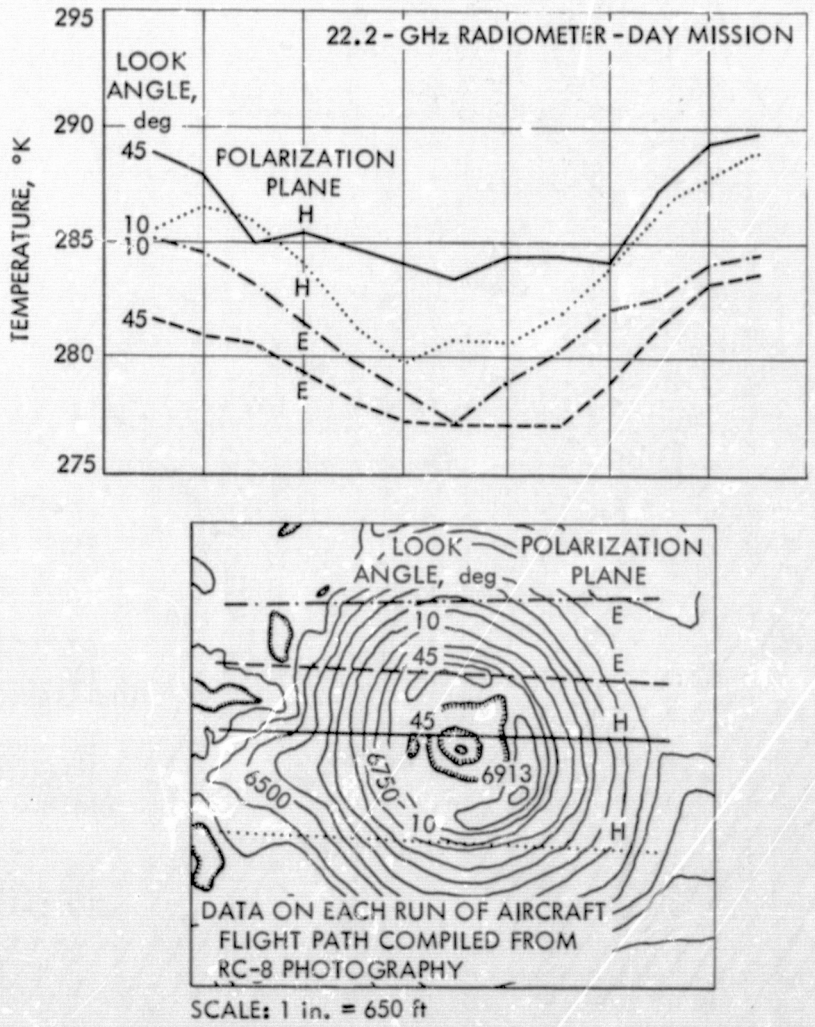

Figure 18-10.- Aircraft flight path and radiometer response over cinder cone, flight 5.

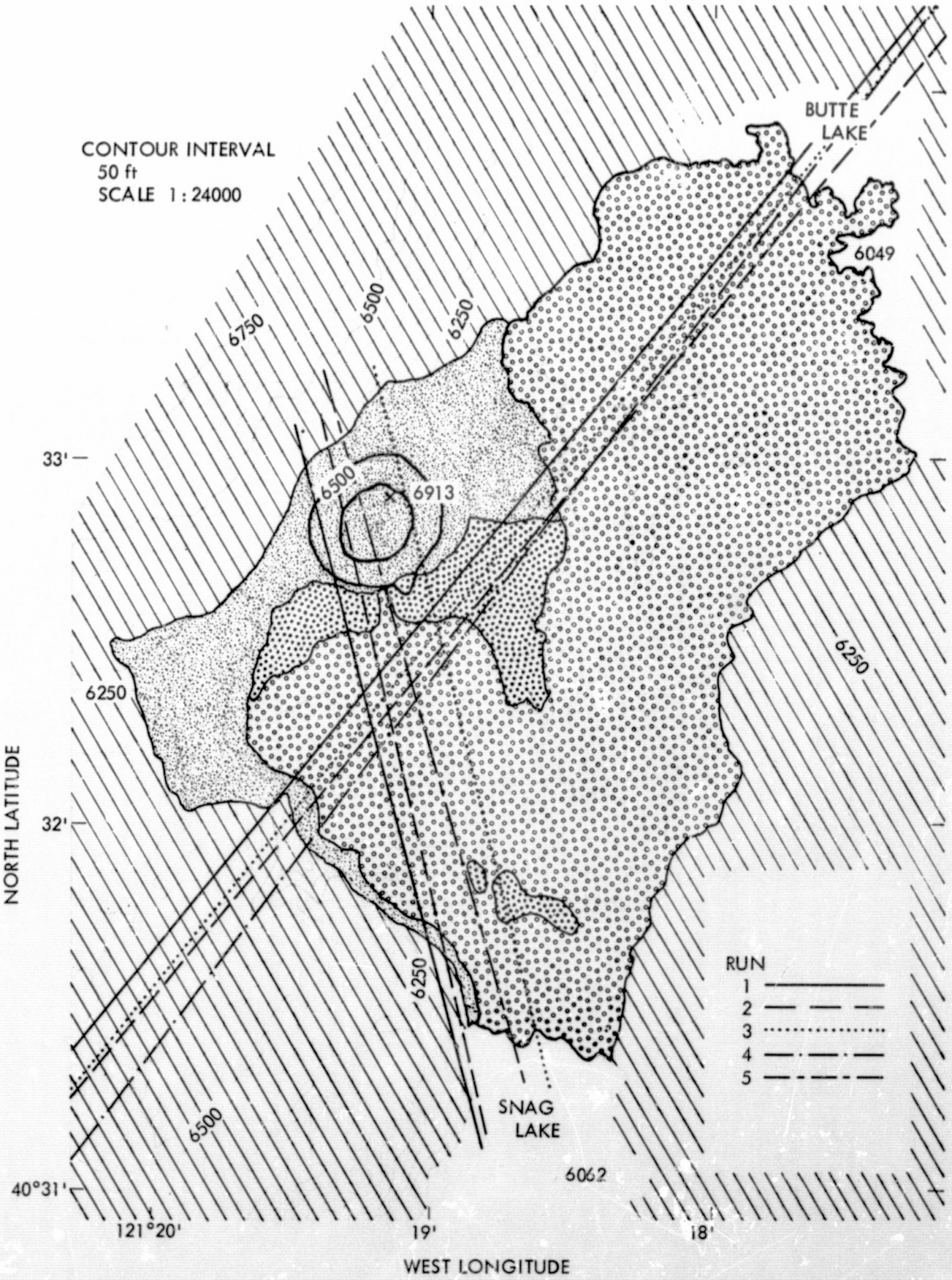

Figure 18-11.- Aircraft flight path, day flight.

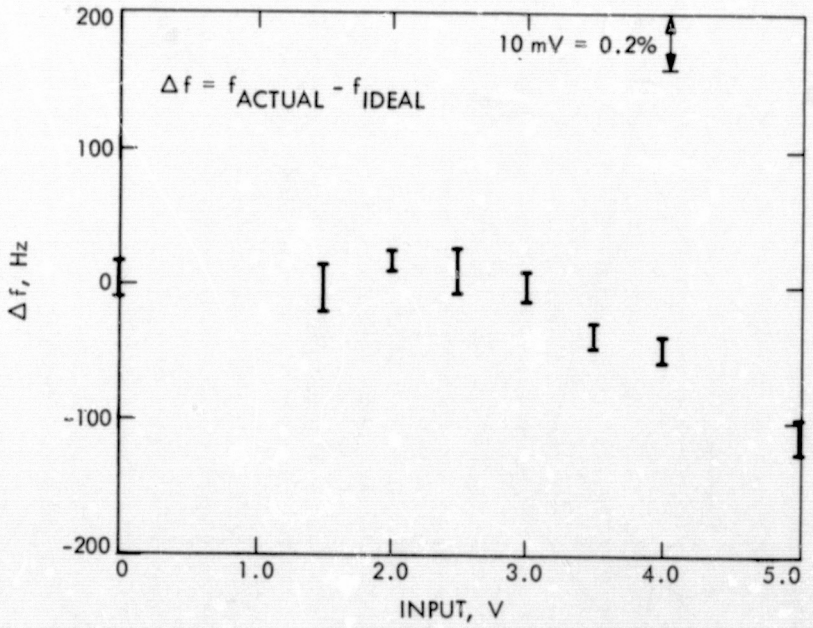

Figure 18-12.- Recorder deviation from linearity, 9.3-gigahertz channel.

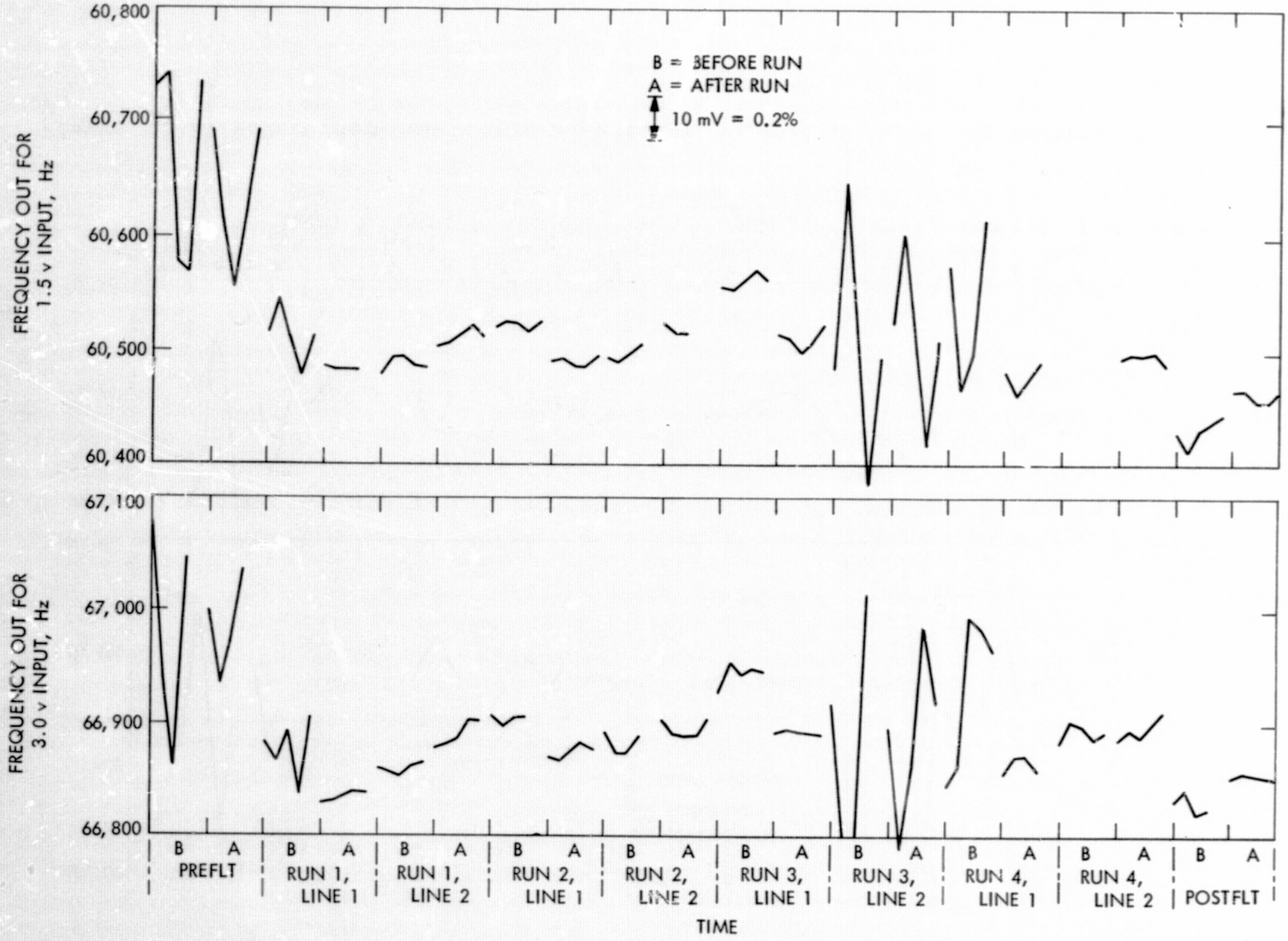

Figure 18-13.- Recorder calibrations, mission 55, flight 5, 9.3-gigahertz channel.

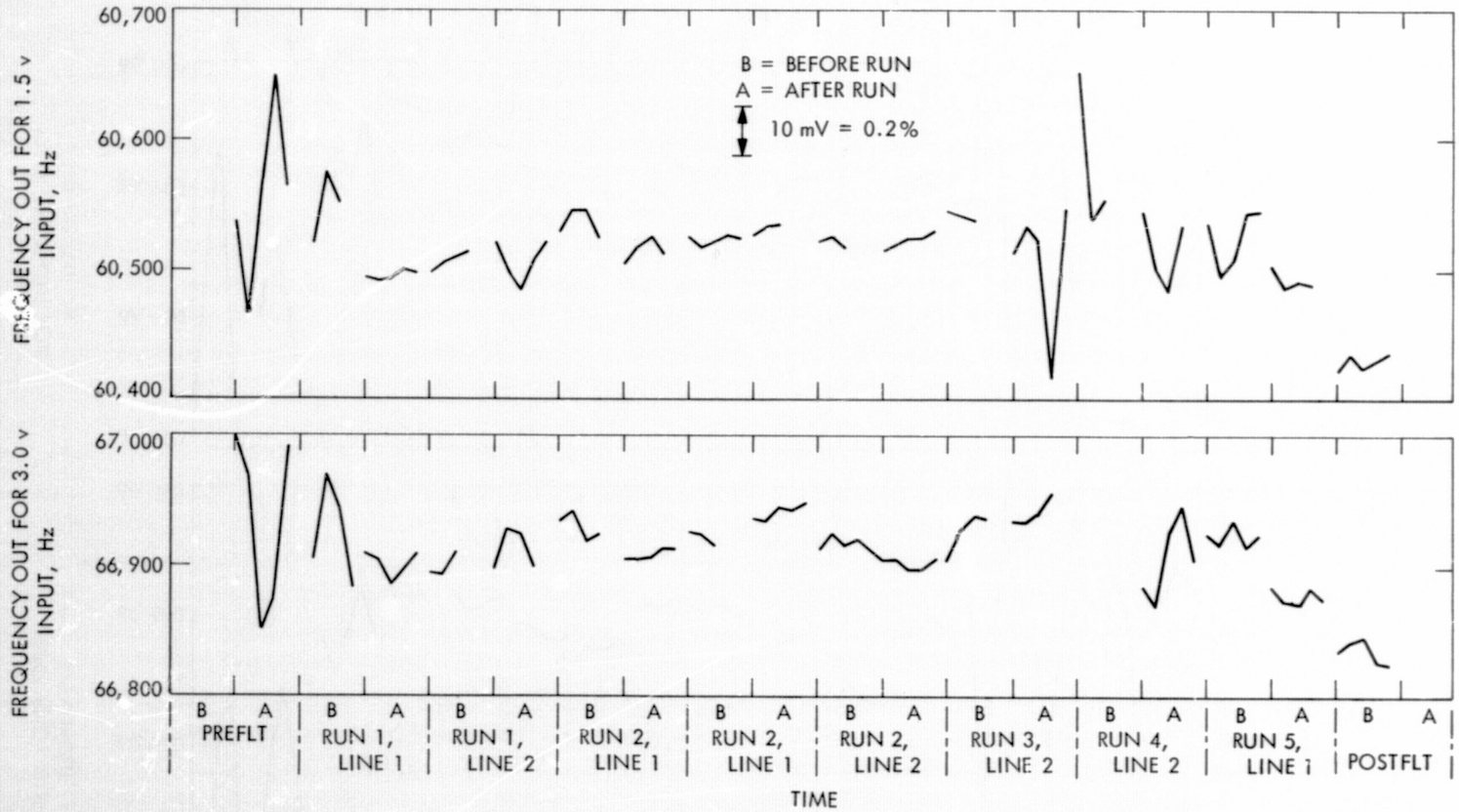

Figure 18-14.- Recorder calibrations, mission 55, flight 6, 9.3-gigahertz channel.

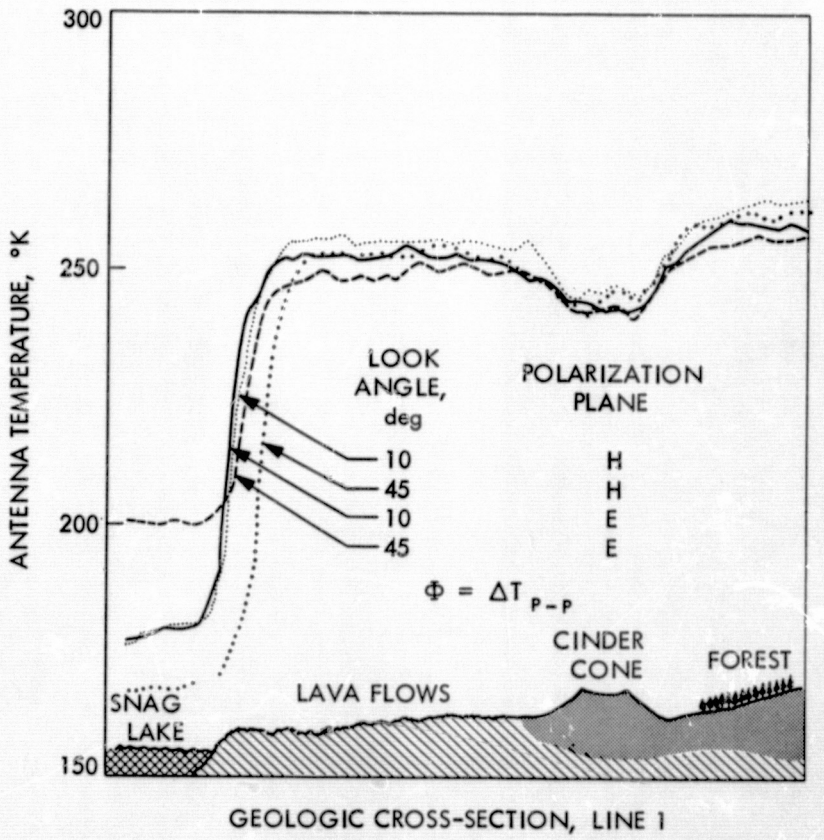

Figure 18-15.- Response of 34.0-gigahertz channel over flight line 1.

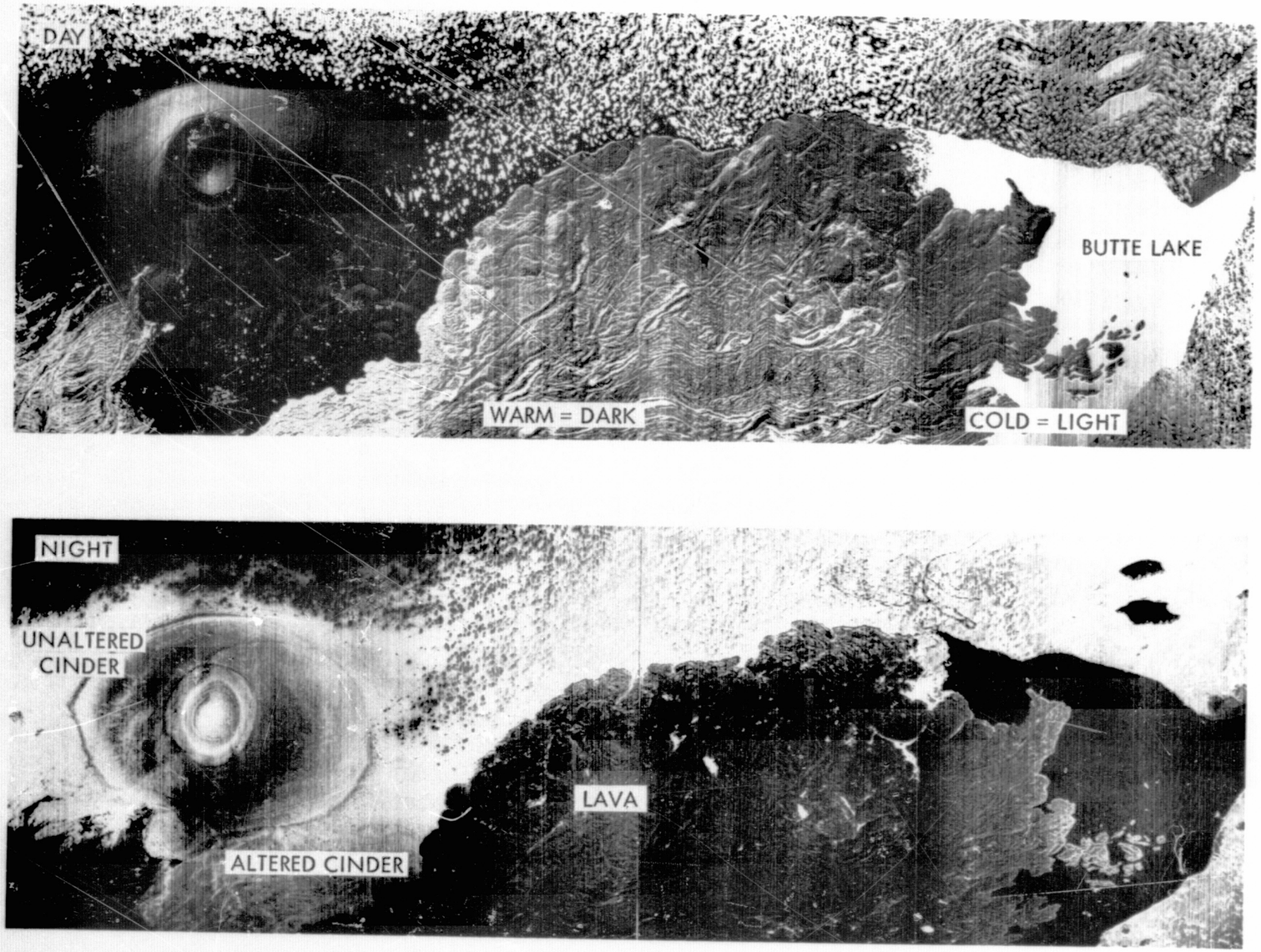

Figure 18-16.- Thermal IR imagery (8μ to 14μ).

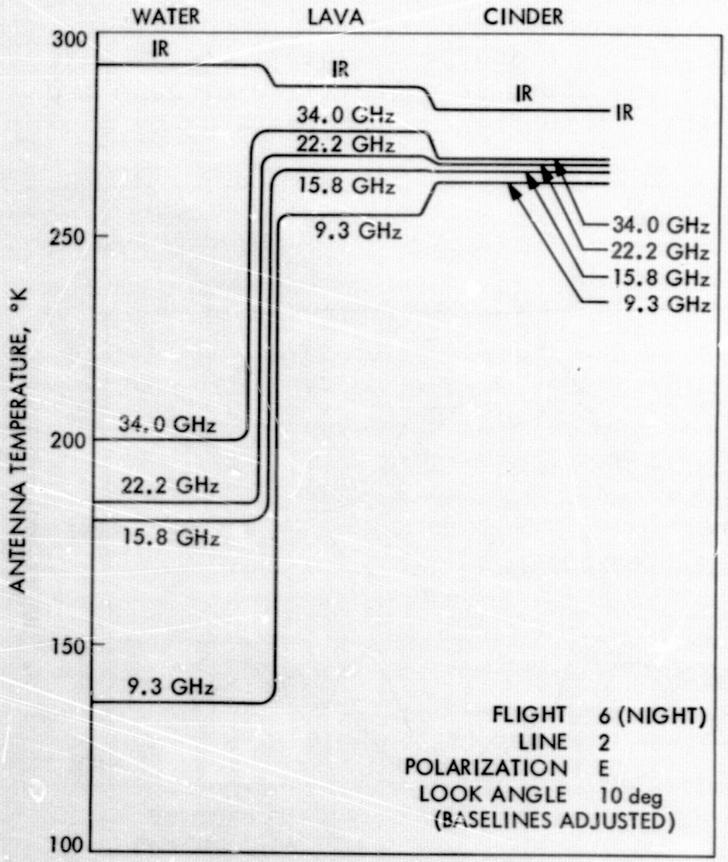

Figure 18-17.- Radiometer responses over water, lava, and cinder, flight 6, diagrammatic representation.

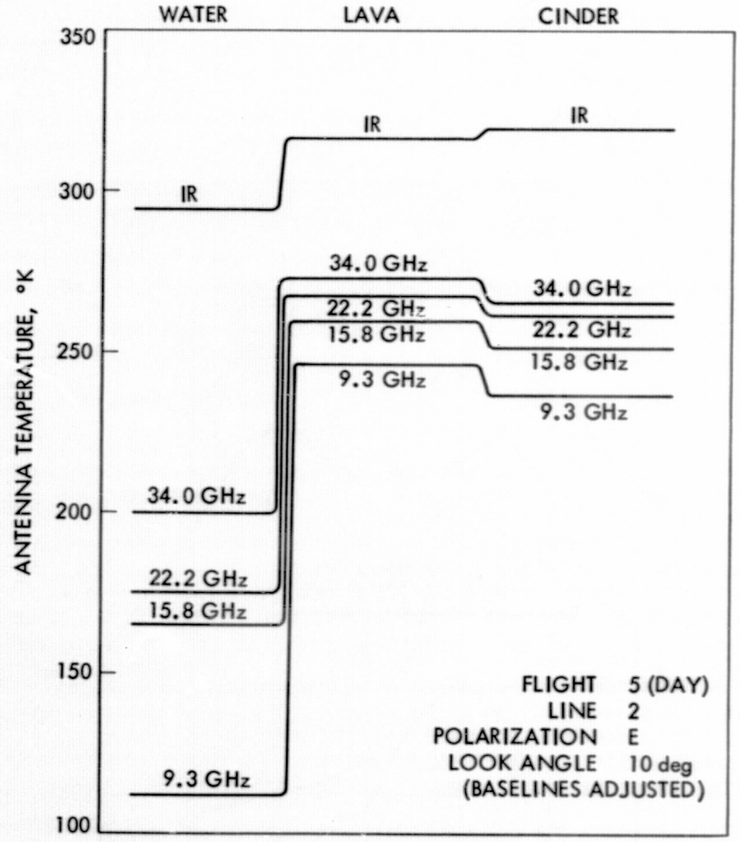

Figure 18-18.- Radiometer responses over water, lava, and cinder, flight 5, diagrammatic representation.

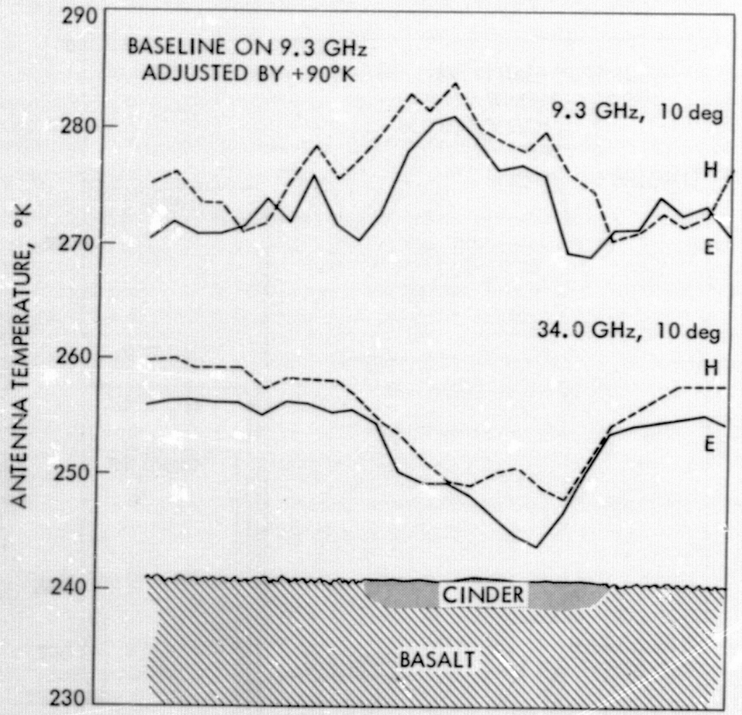

Figure 18-19.- Radiometer responses, cinder over lava, flight 6 at night (base line on 9.3 gigahertz adjusted by +90° K).

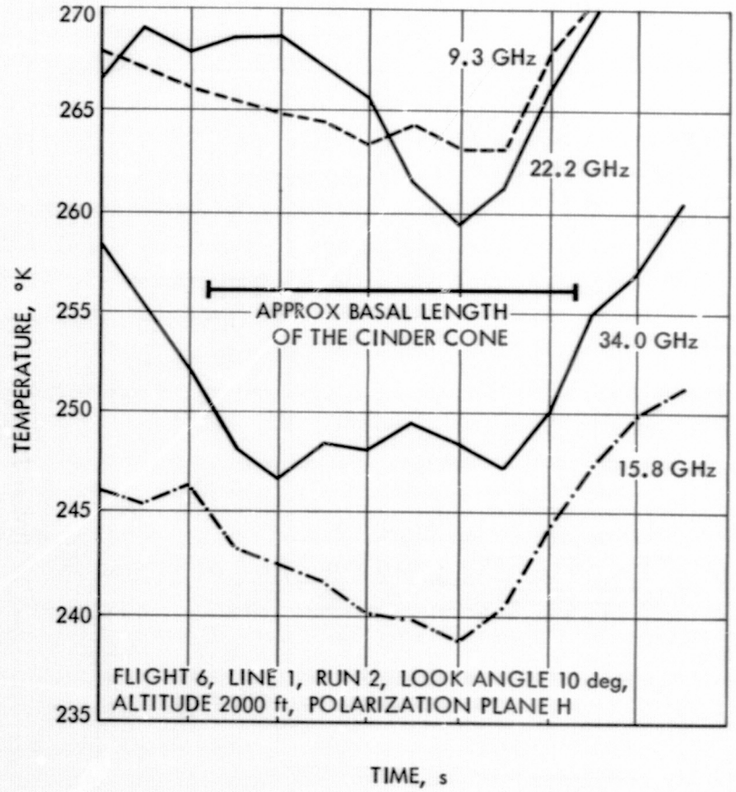

Figure 18-20.- Radiometer responses over cinder cone, base lines adjusted.

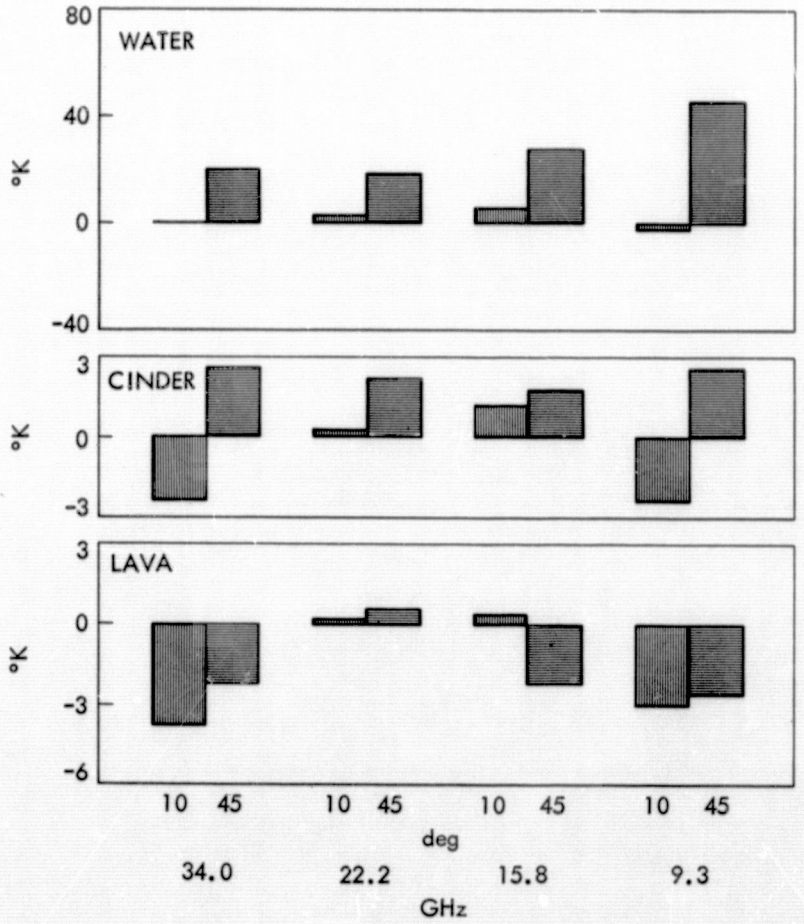

Figure 18-21.- Temperature differences between vertically and horizontally polarized data.

APPENDIX 18A

MICROWAVE RADIOMETRIC SENSING OF TERRAIN

Brightness Temperature

In simplest terms, the microwave radiometer is an antenna and receiver combination that senses the thermal radiation from the terrain it views. The radiation received, referred to as the brightness temperature, is calibrated with respect to the radiation emitted by a blackbody at temperature T_B. For a specular (smooth) reflector, T_B is related to physical parameters by the relation

$$T_B = eT_p + (1 - e)T_s$$

where T_p = physical temperature of the terrain

T_s = microwave temperature of the sky

e = emmissivity

$1 - e$ = reflectivity of the surface

Furthermore, the reflectivity is given (ref. 18-1) by

$$r_h = \frac{\sin \zeta - \left(\gamma^2 - \cos^2 \zeta\right)^{1/2}}{\sin \zeta + \left(\gamma^2 - \cos^2 \zeta\right)^{1/2}}$$

$$r_v = \frac{\gamma^2 \sin \zeta - \left(\gamma^2 - \cos^2 \zeta\right)^{1/2}}{\gamma^2 \sin \zeta + \left(\gamma^2 - \cos^2 \zeta\right)^{1/2}}$$

where h = horizontal polarization

v = vertical polarization

ζ = grazing angle

$\gamma^2 = \varepsilon_{rc}/\mu_{rc}$

$\varepsilon_{rc} = K' - jK''$ = relative complex dielectric constant

μ_{rc} = relative complex permeability constant

Curves of T_B versus ζ for several different substances, frequencies, and physical temperatures have been calculated by Marindino (ref. 18-2). Typical curves for sea water and limestone (and desert sand), are shown in figures 18A-1 and 18A-2, respectively. The curves start at a common point at the nadir, diverge with increasing look angle [$\alpha = (90° - \zeta)$], and then begin to converge as α approaches 90°, where they both sense sky temperature. These curves are for a specular reflector. For increasingly rougher surfaces, the curves tend to converge. Adequate models of the surface-roughness phenomenon do not exist at this time.

Penetration Depth

Because the surface is not a perfect conductor, the radiation associated with T_B has subsurface, as well as surface, components. The effective depth of the radiation is related to the skin depth δ of the material. This is the depth of material required to attenuate incoming radiation to 1/e of its original value. For the case $\mu = 1$, δ is given (ref. 18-3) by

$$\delta = \frac{c}{4\pi f(\varepsilon)^{1/2}} \left[-\frac{1}{2} + \frac{1}{2}\left(1 + \frac{2\sigma}{\varepsilon f}\right)^{1/2} \right]^{-1/2}$$

where c = speed of light

f = frequency

ε = dielectric constant

σ = electrical conductivity, $\sigma(f)$

Because of the dependence of δ on f, the effective depth of radiation (penetration depth) will increase with decreasing frequency (increasing wavelengths).

Influence of Instrument Parameters on Measurement

In addition to the complex relation of terrain parameters to brightness temperature, microwave measurements are further complicated by the influence of instrument parameters. The receiver of the radiometer detects the apparent temperature T_A at the output port of the antenna. The antenna has a beam pattern $D(\theta,\phi)$ which receives radiation components from all directions, not only from the direction of interest. In addition, losses associated with both the antenna and the radome attenuate the signal and add a reradiation component to it. Assuming no atmospheric losses, T_A is related to T_B by terrain component + antenna reradiation component + radome reradiation component

$$T_A = \frac{\eta_a}{4\pi}\int_{4\pi} \eta_R(\theta,\phi)T_B(\theta,\phi)D(\theta,\phi)\, d\Omega + \left(1 - \eta_a\right)T_{ant} + \frac{\eta_a}{4\pi}\int_{4\pi} [1 - \eta_R(\theta,\phi)]T_R(\theta,\phi)D(\theta,\phi)\, d\Omega$$

where η_a = antenna efficiency = 1 - ℓ (dissipative loss)

η_R = power transmission coefficient of radome

T_R = physical temperature of radome

T_{ant} = physical temperature of antenna

If the radome is at a uniform temperature, then the third term reduces to

$$\eta_a\left(1 - \overline{\eta_R}\right)T_R$$

where $\overline{\eta_R}$ = average value of $\eta_R(\theta,\phi)$. If it is further assumed that the antenna has a pencil beam pointing in direction (θ_0,ϕ_0) and has no side lobes, T_A reduces to

$$T_A = \eta_a \eta_R(\theta_0,\phi_0) T_B(\theta_0,\phi_0) + (1 - \eta_a) T_{ant} + \eta_a [1 - \overline{\eta_R}] T_R$$

Inversion of this equation to determine T_B is straightforward, yielding

$$T_B(\theta_0,\phi_0) = \frac{T_A - (1 - \eta_a) T_{ant} + \eta_a [1 - \overline{\eta_R}] T_R}{\eta_a \eta_R}$$

where η_a and η_R are laboratory-determined constants; T_{ant} and T_R are physical varying temperatures, recorded during experiment; and T_A is the calibrated output of the instrument.

Spatial Resolution

The spatial resolution of the radiometers is determined by the angular extent of the antenna beam (beam width θ_B), look angle α, and integration time τ of the radiometer and by ground speed V_g and altitude H of the aircraft. For a stationary radiometer looking at angle α, the beam projection will be an oval with down track length of

$$d_{dt} = H\theta_B \sec^2 \alpha$$

and across track width of

$$d_{at} = H\theta_B \sec \alpha$$

In addition to beam smearing, the radiometer has a response (integration) time τ, which causes an additional ground coverage of $d_{vt} = V_g \tau$ along track. Hence, the total resolution element has a "race track" shape with length

$$w_{dt} = V_g \tau + H\theta_B \sec^2 \alpha$$

and width

$$w_{at} = H\theta_B \sec \alpha$$

Dimensions w_{dt} and w_{at} for mission 55 are shown in table 18A-I.

Temperature Resolution

The radiometer is limited in its ability to detect changes in antenna flux by inherent instrument noise ΔT. The ΔT's for the Convair 240A MR-62 and MR-64 radiometers have been measured with $\tau = 1$ second in the laboratory and are shown in table 18A-II.

REFERENCES

18-1. Beckman, P.; and Spizzichino, A.: The Scattering of Electromagnetic Waves from Rough Surfaces. Pergamon Press, New York, 1963.

18-2. Marindino, G. E.: Microwave Signatures from Various Terrain. B.S. Thesis, Massachusetts Institute of Technology, Cambridge, Mass., May 1967.

18-3. Troitsky, V. S.: "Radio Emission of the Moon, its Physical State, and the Nature of its Surface," in The Moon. Academic Press, New York, 1962.

TABLE 18A-I.- RADIOMETER RESOLUTION ELEMENTS FOR MISSION 55

[H = 4000 ft

V_g = 180 knots = 300 ft/sec]

Elements	Channel, GHz			
	9.3	15.8	22.2	34.0
w_{dt} (10°)	560	516	444	386
w_{at} (10°)	256	212	142	84
w_{dt} (45°)	800	720	580	468
w_{at} (45°)	354	300	200	120

TABLE 18A-II.- THE ΔT's FOR MR-62 AND MR-64 RADIOMETERS

Channel, GHz	ΔT_{rms}, °K	ΔT_{peak}, °K (100 samples)
9.3	1.9	10.4
15.8	.31	1.3
22.2	.70	3.7
34.0	.72	3.4

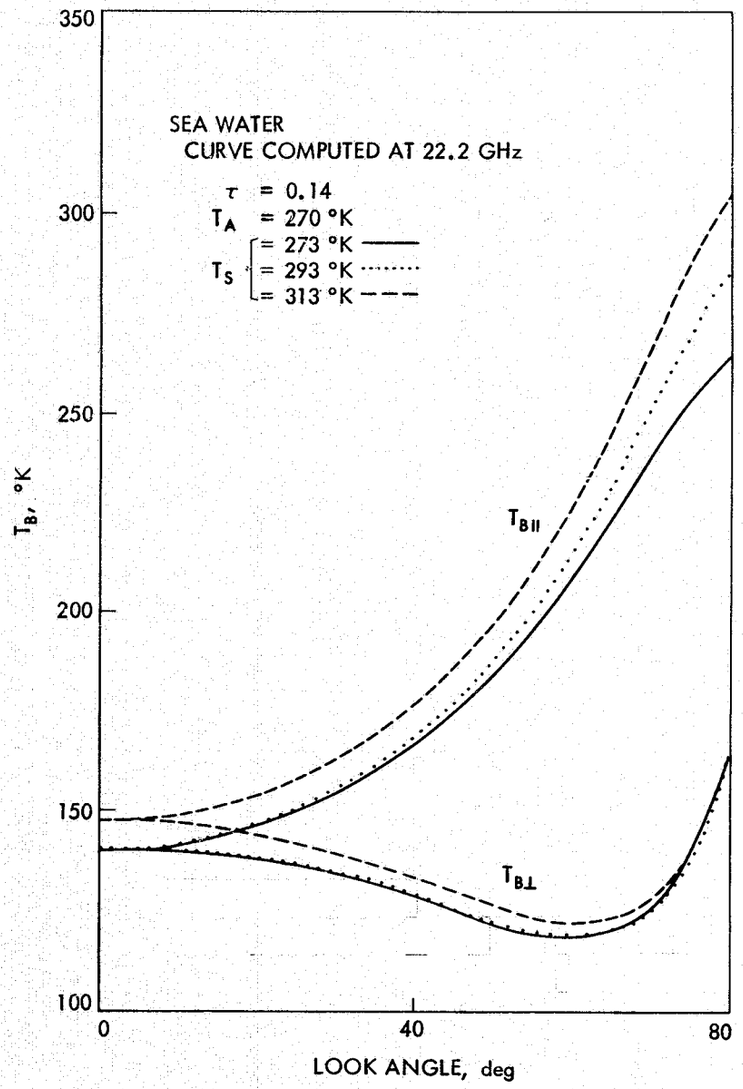

Figure 18A-1.- Radiometric temperature of sea water (ref. 18-2).

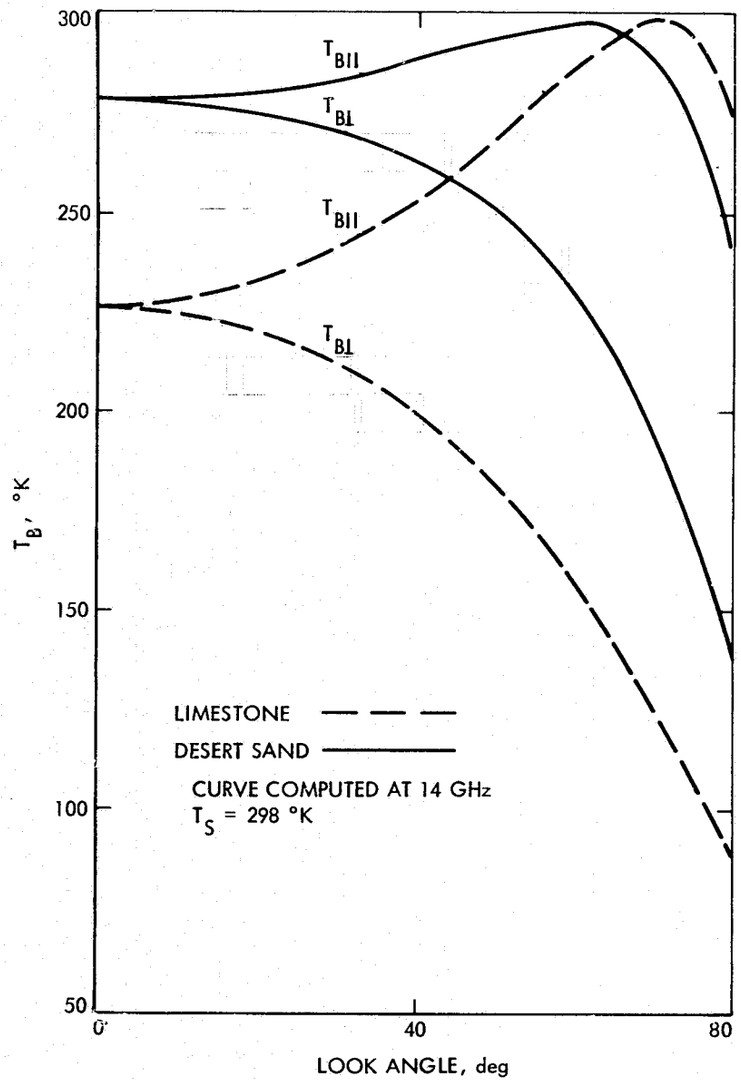

Figure 18A-2.- Radiometric temperatures of limestone and sand (ref. 18-2).

APPENDIX 18B

CONVAIR 240A AIRBORNE RADIOMETRIC SYSTEM

System Description

A schematic diagram of the microwave radiometric system aboard the Convair 240A aircraft is shown in figure 18B-1. The two dual-channel radiometers, designated MR-62 and MR-64, operate at 15.8 and 22.2 gigahertz; and at 9.3 and 34.0 gigahertz, respectively. They are mounted in the nose of the aircraft on a servocontrolled platform, which permits a remote selection of looking angles from the nadir (0°) to 45° forward of the nadir, with a read-out that is accurate to ±0.5°. There is no transverse scan capability.

Two polarizations, the E- and H-planes, are also remotely selected. The radiometer polarizations corresponding to these designations are shown in table 18B-I. It should be noted that the two channels in the MR-62 radiometer are crosspolarized.

The radiometers are protected from the airstream by an 11-layer radome, specially designed to minimize loss at the four operating frequencies. The temperature of the radome is monitored at two positions by thermistors. In addition to the radiometer and temperature outputs, voice commentary, a precision-frequency, binary scanner, and a system-annotation channel are simultaneously recorded on a 14-track analog magnetic tape recorder. (A complete description of the radiometer system is available on request from the author.)

Operational Procedures

The radiometers are turned on approximately 1 hour prior to flight time. While they are warming up, the radome is unbolted, absorbing material is placed over the antenna feeds, and the temperature of the absorber is recorded. A minimum of 30 minutes after turnon, preflight calibration data are recorded on the magnetic tape and strip-chart recorders. These data consist of dc-levels from the recorder calibration unit, followed by several minutes of radiometer data with the noise sources periodically on and off. The absorber is then removed, the radome is secured, and the flight is begun. The radiometers remain on until the flight and a similar postflight calibration are completed.

During the flight, the recorders are turned on 30 to 45 seconds prior to line start. Calibrations are accomplished during this time. Run, start, and stops are marked on the data by appropriate use of the zero calibration level.

Over the Mount Lassen Test Site, four runs were flown over each line in the same direction at constant altitude. The angle and polarization settings for the four runs were 10° E, 10° H, 45° E, and 45° H. The strip-chart recording for a typical run over the site is shown in figure 18B-2. Worthy of note are the voltage calibrations before and after the run, use of "zero" levels to mark line start and stop, and the strong signals from the lakes at the start of the flight line. These signals can be used to relate the data, in units of time, to position on the ground. In the absence of a boresite camera, such use of known features for spatial orientation is essential for analyzing the data.

Data Reduction

The recorded voltage data from the radiometer are converted to antenna temperature, as shown in figure 18B-3. Laboratory calibrations for the noise tube outputs, recorder calibrations, and the preflight and postflight calibration data are used to establish the relationship between antenna temperature and voltage output. Both the recorder and radiometer are assumed to be linear. These radiometer calibrations and recorder calibrations for the run are then used to convert recorder run data into antenna temperatures. Note that the data are in terms of antenna temperature with no corrections for antenna patterns or system losses; hence, temperatures among channels cannot be compared on an absolute basis. However, the data can be compared on a relative basis. Examples of the plotted and printed data from flight 6 are shown in figures 18B-4 and 18B-5, respectively.

TABLE 18B-I.- RADIOMETER POLARIZATIONS CORRESPONDING TO E- AND H-PLANES

Radiometer	Frequency, GHz	E-plane (a)	H-plane (a)
MR-64	9.3	Vertical	Horizontal
	34.0	Vertical	Horizontal
MR-62	15.8	Vertical	Horizontal
	22.2	Horizontal	Vertical

[a]Vertical indicates $\overline{E}$ parallel to the plane of motion; horizontal indicates $\overline{E}$ perpendicular to the plane of motion. The plane of motion is the plane defined by the aircraft velocity vector and the antenna boresight axis.

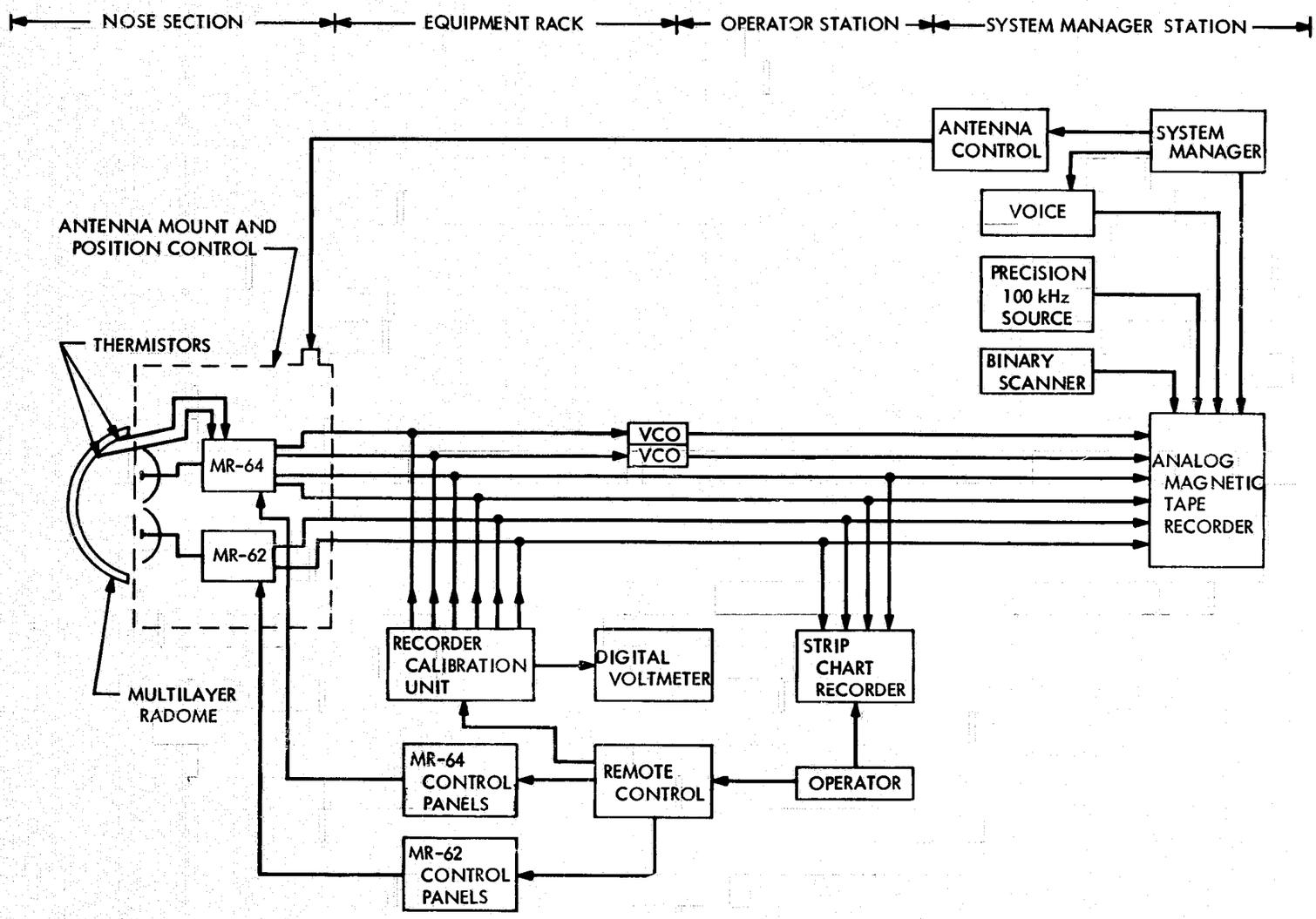

Figure 18B-1.- System diagram of the Convair 240A aircraft microwave radiometer.

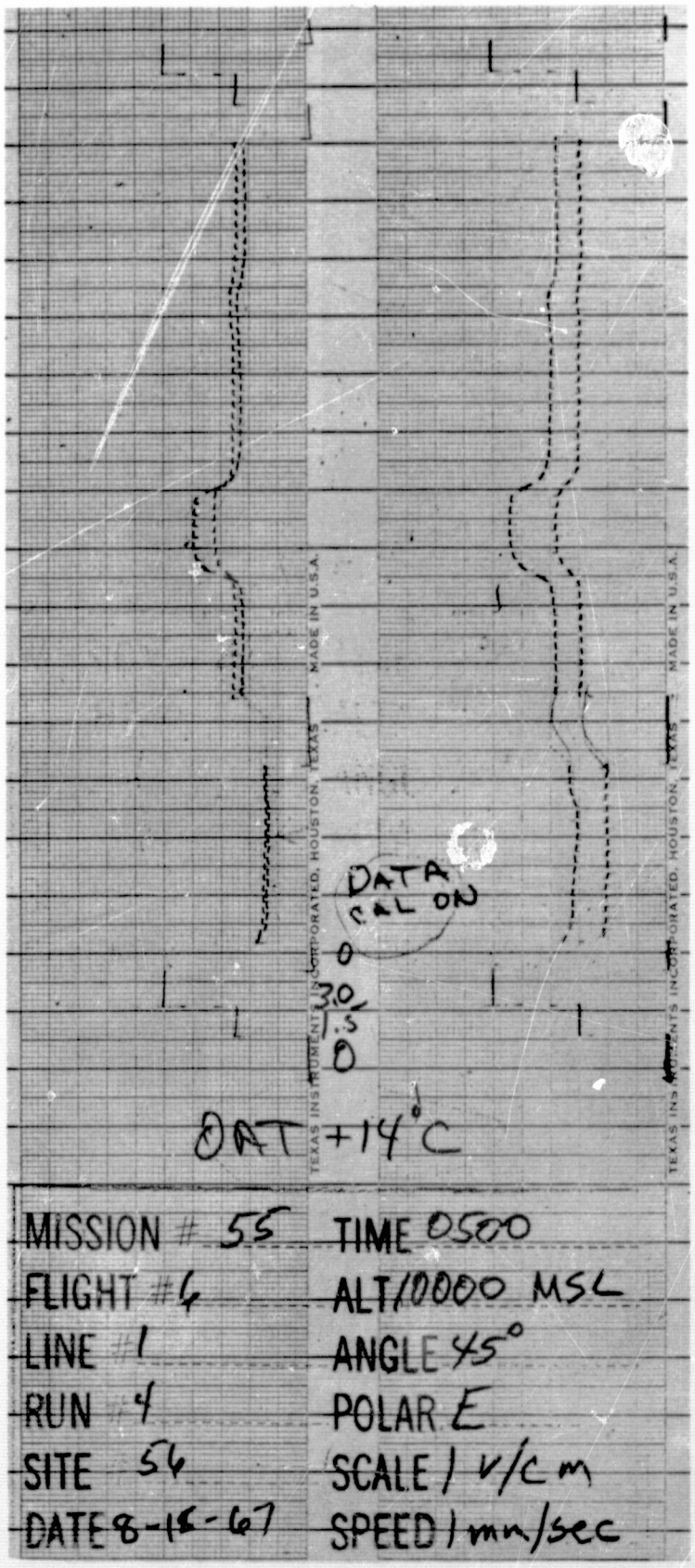

Figure 18B-2.- Aircraft strip-chart recording.

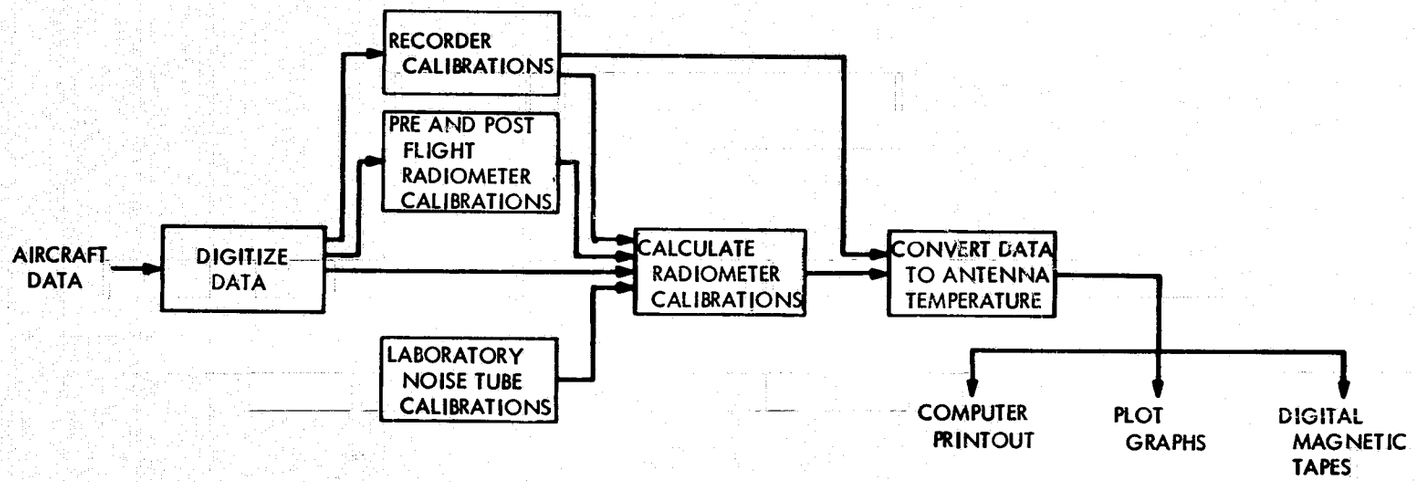

Figure 18B-3.- Steps in conversion of raw flight data to calibrated data.

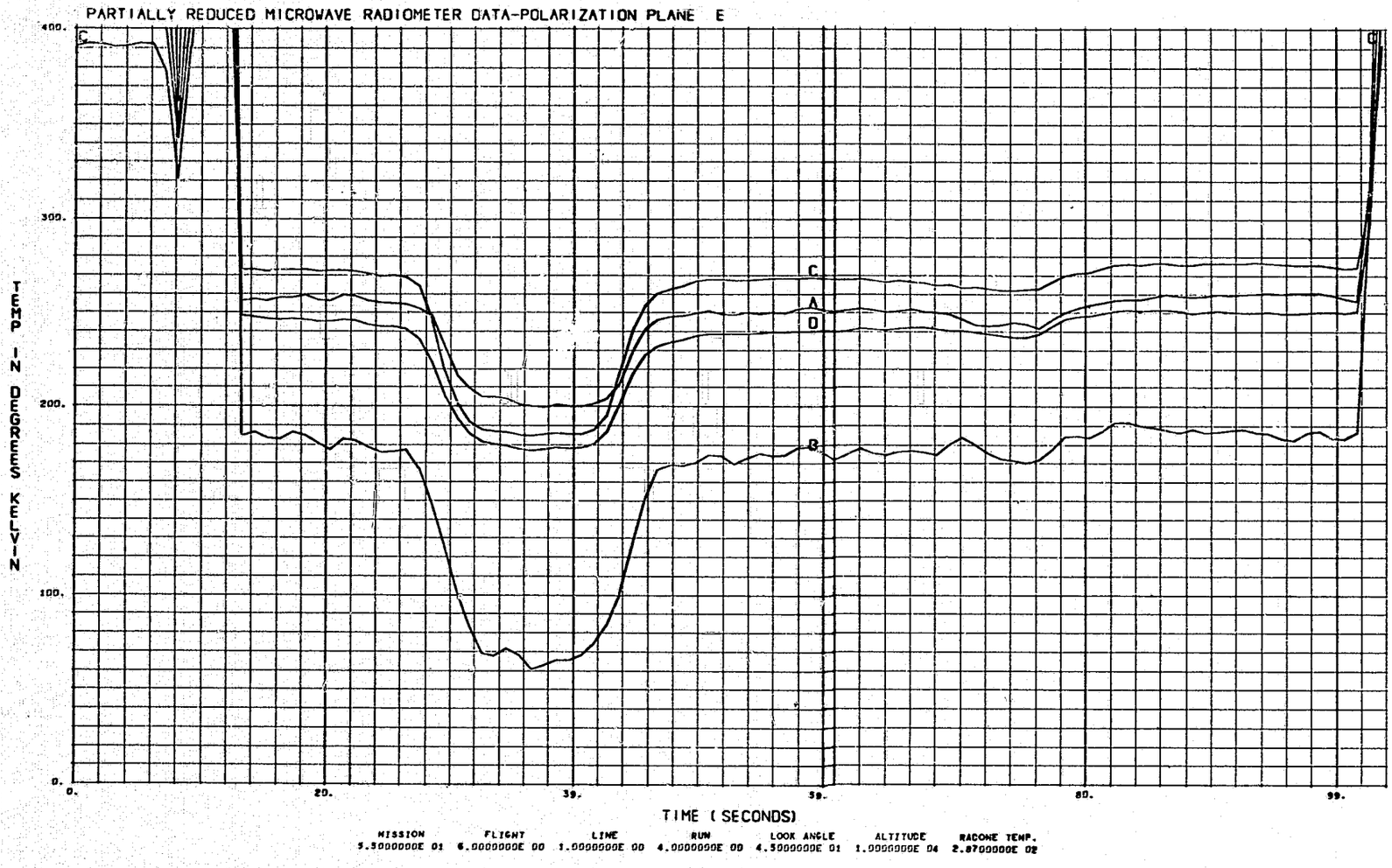

Figure 18B-4.- Computer plot of radiometer data.

PARTIALLY REDUCED MICROWAVE RADIOMETER DATA FROM NASA 926 CONVAIR 240A AIRCRAFT

TEST SITE MOUNT LASSEN

MISSION 55 FLIGHT 6

AUGUST 18, 1967

LINE 1 LOOK ANGLE 45 DEGREES ALTITUDE 10000 FEET
RUN 4 POLARIZATION E-PLANE RADOME TEMP 287.0 DEGREES

TIME SECONDS	MR-64 RADIOMETER CHANNELS 34.0 GHZ DEGREES KELVIN	9.2 GHZ DEGREES KELVIN	MR-62 RADIOMETER CHANNELS 22.2 GHZ DEGREES KELVIN	15.8 GHZ DEGREES KELVIN
0	452.8	583.7	391.2	413.2
1	454.8	588.4	392.5	414.6
2	454.2	587.3	392.1	414.1
3	452.2	583.1	390.8	412.8
4	452.7	584.0	391.1	413.1
5	454.6	588.1	392.4	414.5
6	454.1	587.1	392.0	414.1
7	432.4	540.5	377.4	399.1
8	349.1	361.6	321.0	341.9
9	451.9	582.2	390.5	412.5
10	558.6	811.4	462.7	485.9
11	557.0	807.9	461.7	484.8
12	533.1	758.4	446.7	466.4
13	256.4	184.5	272.8	248.4
14	257.0	186.3	273.1	247.6
15	256.3	183.2	272.3	246.5
16	258.0	182.7	272.9	246.3
17	258.1	186.3	273.1	246.6
18	259.2	184.7	273.0	246.4
19	256.8	180.6	272.3	245.5
20	256.3	177.0	272.4	245.3
21	259.3	183.0	272.5	246.3
22	258.9	181.9	272.0	245.8
23	256.2	178.5	270.8	243.6
24	255.6	175.9	269.4	242.8
25	254.9	176.3	269.9	242.7
26	254.7	177.1	269.1	241.3
27	252.3	167.6	264.5	236.6
28	248.2	148.0	246.3	223.1
29	232.7	126.0	215.3	206.2
30	216.6	101.4	201.7	194.2
31	209.7	83.3	192.1	186.1
32	204.7	69.1	187.6	181.4
33	204.7	67.7	186.7	180.2
34	203.8	71.6	186.2	179.3
35	200.8	68.1	185.1	177.5
36	200.2	60.7	184.5	176.8
37	199.8	62.8	185.6	177.7
38	200.7	65.6	186.1	178.3
39	199.9	65.3	185.4	178.0
40	199.9	68.0	185.4	178.4
41	201.5	74.3	187.5	180.3
42	203.8	84.2	195.3	186.7
43	211.5	99.8	217.8	200.9
44	229.0	126.6	240.0	216.9
45	240.9	150.7	253.3	227.1
46	246.1	166.6	260.0	232.2
47	247.7	169.1	262.5	234.2
48	248.5	168.7	264.2	235.7
49	249.7	170.7	266.6	237.7
50	251.2	174.3	267.8	238.5
51	249.4	173.9	267.8	238.8
52	248.8	169.5	267.3	238.7
53	250.0	172.6	267.4	238.5
54	249.2	175.2	267.8	239.3
55	249.9	174.0	268.0	239.6
56	249.5	174.3	267.9	239.6
57	251.9	178.5	268.2	239.8
58	252.8	178.8	268.7	240.1
59	251.6	175.8	268.2	240.3
60	250.7	171.9	267.9	239.8
61	251.4	175.0	267.8	240.5
62	252.2	178.1	268.3	241.8
63	251.6	175.4	267.3	241.2
64	250.4	174.5	266.5	240.9
65	250.8	176.1	267.3	241.9
66	251.8	176.8	268.4	242.3
67	250.6	175.8	265.9	242.2
68	250.0	174.6	264.8	241.3
69	249.3	180.3	265.1	240.6
70	246.7	183.7	263.5	240.6
71	243.6	180.0	263.6	239.7
72	243.3	175.4	262.8	238.5
73	243.7	172.3	261.9	237.9
74	244.8	171.3	262.0	237.1
75	244.1	170.2	262.3	237.0
76	241.9	171.8	262.9	238.8
77	246.3	177.0	266.2	242.8
78	250.1	184.3	270.1	246.4
79	252.5	184.5	271.4	247.8
80	254.0	183.8	271.8	248.2
81	255.6	187.2	273.8	249.6
82	256.7	191.8	275.6	251.0
83	257.0	191.5	276.0	251.3
84	257.2	189.9	275.4	250.9
85	258.5	189.0	276.6	251.4
86	259.6	187.7	276.7	251.3
87	258.7	186.6	275.6	250.9
88	258.6	188.1	275.4	249.8
89	258.8	186.6	276.4	250.6
90	259.8	186.7	276.6	251.2
91	259.1	187.6	276.6	250.8
92	260.0	187.9	276.4	249.9
93	260.1	186.4	277.1	250.0
94	260.8	186.0	276.7	250.3
95	260.3	183.2	276.0	249.8
96	260.6	182.4	275.5	249.6
97	260.7	186.5	275.7	249.9
98	260.8	187.2	275.7	250.3
99	259.3	183.1	274.9	250.5
100	257.6	183.2	273.7	250.1
101	256.3	186.9	274.3	251.0
102	315.0	303.4	309.5	298.6
103	453.5	586.2	391.7	413.6

CALIBRATION DATA

		34.0 GHZ	9.3 GHZ	22.2 GHZ	15.8 GHZ
1.5 VOLTS	BEFORE RUN (COUNTS)	60650	60550	60350	60550
	AFTER RUN (COUNTS)	60620	60480	60360	60540
	AVERAGE (COUNTS)	60635	60515	60355	60545
	DEVIATION (MV)	0	0	0	0
3.0 VOLTS	BEFORE RUN (COUNTS)	67050	66900	66750	66900
	AFTER RUN (COUNTS)	67030	66865	66743	66825
	AVERAGE (COUNTS)	67040	66882	66746	66862
	DEVIATION (MV)	0	0	0	0
SCALE FACTOR	BEFORE RUN (MVOLT/C)	0.2344	0.2362	0.2344	0.2362
	AFTER RUN (MVOLT/C)	0.2340	0.2349	0.2350	0.2387
	AVERAGE (MVOLT/C)	0.2342	0.2356	0.2347	0.2374
	DEVIATION (PER CENT)	0.1	0.3	-0.1	-0.5

Figure 18B-5.- Computer print-out of radiometer data.

APPENDIX 18C

SURFACE ROUGHNESS CLASSIFICATION

In the absence of a quantitative measure of surface variations, five general categories of roughness are defined to classify qualitatively the surface characteristics of the site.

Class I: Surface variations are smooth compared to a wavelength λ. Surface variations are less than $\lambda/8$, and the laws of a specular surface apply.

Class II: Surface variations are comparable to a wavelength. Resonance phenomena may influence signature.

Class III: Surface variations are small compared to a resolution element but large compared to λ. This may be modeled as an ensemble of specular reflectors with a statistical distribution of look angles.

Class IV: Surface variations are comparable to the ground-resolution element. These are distinguishable units that contribute to the short-term variation in radiometer signal. These units may be missed from flight to flight because of flight-line position uncertainties and drift-angle effects.

Class V: Surface variations are large with respect to the resolution elements. These "hills and valleys" have the effect of slowly modulating the mean look angle of the other classes of roughness superimposed on the site. The effects are easily separable.

It should be noted that class I and II surfaces are independent of altitude. The effect of flying a given site at higher altitudes is to convert class IV and V surfaces into class III surfaces. A given surface may be the superposition of all of these surfaces.

N71-16144

APPLICATION OF ULTRAVIOLET REFLECTANCE AND STIMULATED LUMINESCENCE TO THE REMOTE DETECTION OF NATURAL MATERIALS*

By William R. Hemphill
U.S. Geological Survey

ABSTRACT

Carbonate rocks and evaporite deposits commonly exhibit relatively high reflectance in the ultraviolet region (<3600 angstroms), and some outcrops of these materials are selectively shown on ultraviolet imagery. Other materials which are commonly strongly imaged on ultraviolet imagery and photography include water, snow, concrete, and metallic objects, particularly aluminum.

Outdoor tests of an active ultraviolet imaging system have demonstrated the feasibility of imaging ultraviolet-stimulated luminescence of such minerals as talc, dolomite, and deweylite along quarry faces from distances of several hundred feet. The system features a cathode-ray-tube transmitter, an image-dissector receiver, and a video monitor on which the distribution of luminescent material is imaged as the outcrop is scanned.

A pulsed ultraviolet laser emitting at 3371 angstroms has been used successfully in the laboratory to stimulate phosphorescence of selected rock and mineral specimens and to discriminate between them on the basis of decay time, which ranges from less than 3 to more than 10 microseconds. Initial results suggest that sodic feldspars have longer decay periods than calcic feldspars. Some granites also appear to have decay periods significantly different from other types of granite in the same locality.

Outdoor tests with a high-resolution grating spectrometer were successful in detecting luminescent materials by means of the so-called

---

* Presented at the 1968 American Society of Photogrammetry Convention, March 11-15, Hilton Hotel, Washington, D.C., Session B, Application of Remote Sensing.

"Fraunhofer line-depth method." This method is advantageous because it uses the sun as an ultraviolet source and therefore is independent of low-powered artificial sources such as cathode-ray tubes, lasers, and mercury-vapor lamps. A Fraunhofer line-discriminator suitable for aircraft operation has been constructed, and initial on-the-ground tests are being performed on Rhodamine WT, a luminescent dye used by hydrologists and oceanographers in studies of current dynamics in streams and estuaries.

INTRODUCTION

The U.S. Geological Survey and NASA are jointly sponsoring a program aimed at determining the application of the ultraviolet spectrum in discriminating natural materials. The U.S. Geological Survey is interested in the terrestrial applications of detecting and mapping selected rocks and other materials, in both surface and airborne studies and from orbital altitudes. NASA is interested in similar applications for study of the earth and moon, as well as other planetary bodies.

This paper discusses the program in terms of the two properties to be detected and measured. These properties are ultraviolet reflectance and ultraviolet-stimulated luminescence.

ULTRAVIOLET REFLECTANCE

Laboratory Studies

Most materials show a gradual reduction in spectral reflectance with reduction in wavelength from the visible into the ultraviolet region. Exceptions to this generalization include snow, concrete, aluminum, and certain other materials which strongly reflect ultraviolet energy.

Spectral reflectance of more than a hundred rock specimens and common rock-forming minerals have been measured in the laboratory (refs. 19-1 to 19-3), and figure 19-1 typifies the spectral-distribution patterns of most of them. Carbonates, evaporites, and some phosphate rocks commonly show comparatively high reflectance values in both the ultraviolet and the visible regions; this response is exemplified by the curve for the limestone specimen. Acidic rocks also tend to have high reflectance values in the visible region and low values in the ultraviolet region, as, for example, the granite specimen shown in figure 19-1. Basic rocks such as the basalt specimen seen in figure 19-1 commonly show low reflectances which are nearly the same in both the visible and ultraviolet

regions. A few materials such as the monzonite in figure 19-1 and asphalt show more reflectance in the ultraviolet region than in the visible region, but these are exceptions. Also, although a higher ultraviolet response is fairly common for asphalt, it is not necessarily typical for monzonite and intermediate rocks.

The limestone and granite specimens, with reflectances on the order of 35 to 40 percent in the visible region, would appear on a photograph at nearly the same density or grayness, and only slightly brighter than the rhyolite with a reflectance of 25 to 30 percent. At best, image brightness in the visible region for these three specimens would tend to be similar.

At 2500 angstroms in the ultraviolet region, less energy is reflected by the limestone, granite, and rhyolite specimens. However, limestone shows more than 2-1/2 times the reflectance of the granite and more than 10 times the reflectance of the rhyolite. Despite the fact that there is less total energy, image contrast would be greater in this part of the ultraviolet region than at longer wavelengths. This possibility of achieving greater contrast for some materials is the single most important advantage of imaging in the ultraviolet region.

In lunar orbit, the contrast property can be exploited to the utmost by imaging in the 2500-angstrom band where contrast is at maximum. However, earth applications are more limited because nearly all ultraviolet energy shorter than 3000 angstroms is absorbed by ozone and oxygen in the atmosphere and does not reach the surface of the earth. At longer wavelengths, ultraviolet energy is extremely scattered. Nevertheless, the 3000- to 3500-angstrom band is particularly interesting because this is where abrupt changes in spectral reflectance begin to occur.

Ultraviolet Photography and Imagery

To date, two systems have been used to acquire ultraviolet imagery. One is a 35-millimeter photographic system, and the other is a line-scanner similar to that used for infrared (IR) imaging, except that an ultraviolet-sensitive photomultiplier has been substituted for the cooled IR detector.

Several instrumentation problems plague operations in the near-ultraviolet region. Most severe is the fact that all filters transmitting near-ultraviolet light also leak light in the red and near-IR regions where photomultipliers retain marginal sensitivity.

Red leakage of filters is shown in the extreme right-hand part of figure 19-2. The response curve of the S-13 photocathode commonly used in the ultraviolet photomultiplier also extends into this area. Many

early attempts to image in the ultraviolet, using line scanners, resulted inadvertently in red or IR imagery. This red leakage can be reduced to tolerable levels, but at the sacrifice of the spatial resolution.

A neat way of avoiding this filter leakage problem is to use a camera with a special ultraviolet film that has a longwave limit of about 5500 angstroms. However, conventional camera lenses have little or no transmittance in the 3000- to 3500-angstrom band of interest. There are ultraviolet-transmitting lens elements composed of quartz and lithium fluoride available, but they are expensive. Also, a lens-film system generally has a slower response time than a photomultiplier.

Another disadvantage of the camera approach is that rays striking an interference filter at angles of more than 5° to 10° off the axis are tuned to wavelengths longer than the center frequency of the filter. This precludes the use of wide-angle lenses in an ultraviolet camera system. Still another disadvantage is the fact that surface texture of some components in the ultraviolet filter stack approaches the center wavelength of the filter pass band; consequently, a significant amount of energy in the filter pass band is scattered by the filter, reducing photographic contrast and resolution. Thus, although an ultraviolet camera and a selected film neatly avoids the problem of red leakage of ultraviolet filters, there are other disadvantages that must be weighed against a photomultiplier line-scan system. To date, the most successful results have been achieved with the line-scan system from altitudes of less than 6000 feet above terrain.

Figure 19-3 shows imagery taken by the University of Michigan over the Paoha Island, Mono Lake, California. The scanner is an elaborate device of 18 channels, 12 of which are time coincident. Of the 18 channels, three are shown in the figure; ultraviolet is on the left, limited to wavelengths shorter than 3750 angstroms. Blue is in the middle, and red is on the right. The spectral range for all 18 channels is from 3000 angstroms to 14 micrometers.

All channels are tape recorded and have the same format. This permits playback and print-out of the tape in the laboratory. Those bands which are time coincident can be integrated electronically in various combinations. Image-density data can be stored and collated by means of a computer.

The imagery in figure 19-3 was taken at an altitude of about 5000 feet above terrain. Evaporite deposits (at area a in the figure) appear with marked contrast on the ultraviolet band, but are less apparent in the blue and red bands. However, other materials, for example, basalt lava flows (at area c in the figure) on the north end of the island appear more clearly in the blue or red bands. Each band contributes its own unique spectral contrast. The most significant application

of the ultraviolet reflectance appears to be in a truly multispectral approach in which several bands in the ultraviolet, visible, and IR regions are used simultaneously to discriminate natural materials.

An instrument that produces 18 channels of imagery simultaneously puts a user in the dangerous position of being overwhelmed with data. At best, attempting to collate 12 or 18 channels of imagery by simple inspection and channel-to-channel comparison is inefficient and generally ineffective.

Figure 19-4 also shows Paoha Island. For comparison, one of the film print-outs is shown on the right in the figure. On the left is a composite made from three channels in the blue, red, and near-IR regions. The ultraviolet region could not be included because it is not a part of the 12-channel spectrometer and therefore is not time coincident. This composite of three channels was made with the aid of Purdue University's IBM 360-44 computer, using a program designed to use data from Michigan's 12-channel imaging spectrometer. This program involves determining the probability description of two or more classes (for example, rock types) in two or more channels. Each data point in the imagery is then analyzed and classified on the basis of its similarity or nonsimilarity to previously determined probability descriptions. Automatic data processing as applied to the classification of agricultural crops is reported by Landgrebe (ref. 19-4) and Purdue University (ref. 19-5).

The computer output shown in figure 19-4 is actually a two-dimensional plot on which different materials are symbolized by different letters. Water is denoted by an "I," basalt by a "B," rhyolite by an "R," and lake and surficial deposits by blank space. The false-alarm rate for rhyolite is probably quite large in the northern part of the island. The basalt at the north end of the Paoha Island and the adjacent island is surprisingly accurate, however, as are the surficial deposits and water. The area shown in the figure covers about 1 square mile; ground distance of the entire computer print-out is more than 12 miles, and it was produced in less than 2 minutes.

Neither the ultraviolet region nor the IR region is time coincident, but it is believed that the example shown in figure 19-4 illustrates a technique of data handling which is promising. These are very crude attempts; more sophisticated computer programs hopefully will be even more effective in discriminating between materials, particularly with the addition of ultraviolet (<3500 angstroms) and IR (8 to 14 micrometers) channels.

ULTRAVIOLET-STIMULATED LUMINESCENCE

The other property that we propose to detect and to measure is luminescence; that is, the property of some materials to emit energy at longer wavelengths when illuminated by ultraviolet light.

Ultraviolet-stimulated luminescence is a property that has been used for a number of years in detecting and discriminating between some natural materials. Small hand-carried ultraviolet lamps have been used in the exploration for luminescing minerals. However, these portable ultraviolet sources are low powered and are rarely effective more than a few feet from the outcrop.

Ultraviolet Imaging System

The ultraviolet imaging system shown in figure 19-5 was designed originally for a military application, but was later modified by Westinghouse Aerospace Division for use by the U.S. Geological Survey (ref. 19-6). Basic components of this system include an ultraviolet transmitter and an image-dissector receiver.

The transmitter consists of a cathode-ray tube with an ultraviolet phosphor and a raster scan. Electron bombardment of the phosphor stimulates an ultraviolet emission peaking at 3700 angstroms. This radiation is projected by means of the optics and instantaneously illuminates a spot in the subject field. The raster scan enables the ultraviolet transmitter to sequentially illuminate all elements in the target field.

The receiver consists of an image dissector sensitive to visible light. This device provides a scannable aperture slightly larger than the transmitter flying spot and synchronized with the transmitter beam. The small instantaneous spot size or field of view of both the transmitter and receiver reduces the amount of ultraviolet back scatter normally encountered in floodlight ultraviolet systems, thereby extending useful range and improving contrast of imaged features (ref. 19-7).

Figure 19-6 shows the components of the system — the transmitter A and the receiver B, both of which are directed toward the subject in the background. The receiver output is connected to an oscilloscope C and television monitor D for simultaneous measurement and observation of the intensity of luminescence in the visible region of the spectrum.

The U.S. Geological Survey originally became interested in this imaging system to evaluate its application in the exploration for materials such as scheelite, phosphate, and other materials which are known to luminesce in some localities. It was also hoped that by using the

device in a pulsed mode, the decay time of phosphorescent materials could be measured, but preliminary tests in the laboratory showed that design limitations of the prototype instrument precluded measurement of decay time.

The instrument was used successfully, however, to image luminescing materials in outcrops and along quarry faces from distances as great as 200 feet in the Baltimore, Maryland, area. The transmitter-receiver was transported in a small delivery truck and positioned in such a way that it could be directed toward the rock exposure to be imaged. The tests were conducted at night in order to avoid solar illumination.

Figure 19-7 is a photograph of the television monitor. The three bright areas in the upper half of the figure are the result of the luminescence of deweylite, a mineral of the serpentine group which crops out along a fracture set in a quarry near Baltimore. Other bright spots in the image are merely electronic noise in the system. The distance between the imaging system and the quarry face is 64 feet; the distance represented across figure 19-7 is about 20 feet. For comparison, figure 19-8 shows the same area photographed during daylight with a camera. Although the photograph is rather nondescript, the television image indicates luminescing areas that could be of interest to the geologist. Discrimination of deweylite and several other minerals with an ultraviolet-imaging system is little more than a scientific curiosity; however, the study does serve to demonstrate the technique.

A possible application of an ultraviolet-imaging system concerns the discrimination of limestone along inaccessible faces in quarries in central Indiana (ref. 19-2). Spectral measurements in the laboratory show that peak excitation for most of the limestones is in the 2600- to 2800-angstrom region, a part of the ultraviolet region which does not receive solar illumination. The spectral measurements also show that these limestones differ in their luminescence intensities and that some of these differences could be used to distinguish varying grades of quarriable limestone, if a suitable field device were available. This work was done as a cooperative effort by the U.S. Geological Survey and the Geological Survey of Indiana.

Ultraviolet Laser

In 1966, Avco-Everett laboratories in Boston perfected a nitrogen-gas laser emitting at 3371 angstroms in the ultraviolet region. The laser, shown in figure 19-9, can only be operated in the pulsed mode, but this feature is considered to be ideal for the type of source that is required to measure luminescence-decay time. Pulse rate can be as fast as 100 pulses per second and output power is extremely high, as much as 200 kilowatts.

Recently, 75 samples of selected rocks and rock-forming minerals were illuminated with 3371-angstrom light, using the Avco laser and an S-11 photomultiplier arranged in the simple configuration shown in figure 19-10. Filters effectively block all ultraviolet light reflected from the sample so that the photomultiplier sees only the time-dependent emission in the visible region. Some early results of the work are encouraging.

Figure 19-11 shows the oscilloscope traces for a suite of five feldspars. In each trace, the laser pulse is followed by a relatively high fluorescence peak on the left and then a gradual decay or decrease in intensity toward the right. Peaks displayed on the decay curves are caused by ringing in the output signal, which is caused by the photomultiplier responding to the high-voltage discharge of the laser power supply. Horizontal sweep is one-half microsecond per square. Thus, decay time ranges from less than 2 microseconds for bytownite to more than 5 microseconds for oligoclase. Of feldspar specimens measured to date, decay time tends to be the longest for sodic feldspars — on the order of 5 to 10 microseconds. Similar work suggests that measurement of decay time of laser-stimulated luminescence may be useful in distinguishing between some granites of different mineralogic composition and between oils which are secreted by schools of some commercial fish and which may form a thin layer on the surface of the water.

Fraunhofer Line-Depth Method

Both the ultraviolet-imaging system and the pulsed-laser sources are significant improvements over the portable mercury-vapor lamps of 10 to 20 years ago. However, compared to the sun, both these systems are low powered and rarely would be effective more than a few hundred feet from the outcrop. Also, it is imperative that the work be done at night in order to avoid obscuring the luminescence by daytime solar background.

During the 1950's, the Russian astronomer Kozyrev (ref. 19-8) detected luminescence on the lunar surface by means of an earth-based spectrometer and a method that has since become known as the "Fraunhofer line-depth method" or "method of line depths." This method involves observing a selected Fraunhofer line reflected from the lunar surface, measuring the ratio of the central intensity to the continuum, and comparing this ratio with its conjugate observed in the solar spectrum directly. Diagram 1 in figure 19-12 is an idealized Fraunhofer line in the solar spectrum, wherein the central intensity or minimum B constitutes a narrow region less than 1 angstrom wide where solar emission is absorbed or occluded by gases in the solar atmosphere. Typically, the central intensity B is 10 to 20 percent of the continuum A. Thus, Kozyrev looked at the sun, scanned across the Fraunhofer line in question,

and obtained a profile and a $\underline{B}/\underline{A}$ ratio, that is, an $\underline{R}_s$ such as is shown in diagram 1 in figure 19-12. Then, Kozyrev looked at a small area on the moon, scanned the same spectrum, and obtained $\underline{R}_m$ shown in diagram 2 in figure 19-12. If there is no luminescence, both ratios will be equal. If there is luminescence, as shown in diagram 3 of figure 19-12, then both the central intensity and the continuum will be increased an equal amount as shown in diagram 4 of figure 19-12. However, the ratio $\underline{R}_m$ will then exceed $\underline{R}_s$ by an amount proportional to the amount of luminescence.

This line-depth method is amazing in its simplicity and in the past 10 years has been used successfully by a number of astronomers to detect luminescence in specific areas on the lunar surface (refs. 19-8 to 19-14).

About 2 years ago, in cooperation with the IIT Research Institute, Chicago, Illinois, outdoor tests of the Fraunhofer line-depth method were performed on hand specimens of colemanite, phosphate, and calcite, using an Ebert grating spectrometer and using the sun as a source. The tests were successful and demonstrated the feasibility of detecting ultraviolet-stimulated luminescence of natural materials during the day against a high solar background. These tests also pointed out that the crude instrumentation that was used was inadequate outside the lab. For example, rapid fluctuations of the solar ultraviolet flux, probably caused by pollutants in the atmosphere, commonly exceeded the scan rate of the grating spectrometer. It was obvious that instrumentation with a faster response would be required. Additional basic design requirements of a more elaborate instrument are described by Hemphill (ref. 19-15).

Early in 1968, the Perkin-Elmer Corporation completed design and construction of a prototype Fraunhofer line discriminator that will be adequate for trial field use, perhaps from an aircraft. Figure 19-13 is a schematic showing the optical unit of this line discriminator. The instrument has two entrance apertures. One is directed upward toward the skylight and sunlight and the other, with a 1° field of view, is directed downward toward the ground.

The key components of the Perkin-Elmer design are two glass-spacer Fabry-Perot filters with half-widths of less than 1 angstrom and a peak transmission of more than 50 percent. This extremely narrow bandwidth and high peak transmission represents a state-of-the-art advance in filter fabrication. The center wavelength of the filters may be tuned by a precision thermostatic control.

In the configuration shown in figure 19-13, one filter is tuned to the central intensity of the Fraunhofer line, and the other filter is

tuned to a convenient point on the continuum adjacent to the line. Low-noise photomultipliers are located behind each filter. A system of lenses, beamsplitters, and choppers permits the instrument to "look" alternately downward at the ground and upward toward the sky, and to monitor the ratio of the central intensity to the continuum in each look. An analog computer compares the ratio in the solar look and ground look and converts any difference that may be present into a signal that is proportional to the amount of luminescence in the ground target. This signal is plotted as a function of time on a strip-chart recorder.

Figure 19-14 shows the completed prototype line discriminator. This prototype instrument is designed to detect Rhodamine dye in concentrations of 20 parts per billion or less.

Luminescent dyes such as Rhodamine WT are used by hydrologists and oceanographers to monitor current dynamics in rivers and estuaries. The reason for selecting Rhodamine dye as a design target for this first prototype instrument is one of convenience (ref. 19-15). First, Rhodamine dye is readily available and lends itself ideally to quantitative testing of the instrument. Second, conventional dye monitoring methods are extremely laborious and awkward; it is believed that if this airborne semiautomated method were successful, the method would be of immediate practical benefit in dye studies (ref. 19-16).

Figure 19-15 shows the excitation and emission spectra of Rhodamine dye. Peak excitation occurs near 5400 angstroms, and peak emission is near 5800 angstroms. Accordingly, the prototype instrument is filtered to look at the nearby sodium Fraunhofer line at 5890 angstroms.

Following completion of initial tests on Rhodamine WT, it is tentatively planned to modify the instrument to operate at shorter wavelengths, specifically the calcium Fraunhofer line at 3868 angstroms in the ultraviolet region where a variety of materials are known to luminesce, notably oil slicks, detergents, and other water pollutants, as well as some phosphate rocks and other minerals. The potential role of the instrument appears to be especially promising in water-pollution studies, although it is realized that the emission spectra of materials may vary widely with locality and occurrence. Because of this and other factors, specific applications of the technique are difficult to predict at this time.

SUMMARY

Work to date shows that some materials exhibit more contrast when imaged in the ultraviolet region than at longer wavelengths. The University of Michigan's 18-channel imaging spectrometer is a promising research tool because its spectral range extends from the ultraviolet

region to the far-IR region. Output is tape recorded and can be computer processed.

Active ultraviolet systems permit both imaging of luminescing materials and measurement of luminescing decay time.

The Fraunhofer line-depth method is the only technique that permits detection of luminescence during daylight against a high solar background, and shows great promise particularly in water-resource and water-pollution studies.

REFERENCES

19-1. Watts, H. V.: Reflectance of Rocks and Minerals to Visible and Ultraviolet Radiation. U.S. Geol. Survey Tech. Letter NASA-32, 1966.

19-2. Watts, H. V.; and Goldman, H. J.: Visible and Ultraviolet Reflectance and Luminescence from Various Saudi Arabian and Indiana Limestone Rocks. U.S. Geol. Survey open-file rep., 1967.

19-3. Thorpe, A. N.; Alexander, C. M.; and Senftle, F. E.: Preliminary Ultraviolet Reflectance of Some Rocks and Minerals from 2000A to 3000A. U.S. Geol. Survey Tech. Letter NASA-37, 1966.

19-4. Landgrebe, David A., and staff: Automatic Identification and Classification of Wheat by Remote Sensing. Purdue Univ. Lab. for Agricultural Remote Sensing, Information Note 212567, Research Progress Rep. 279, 1967.

19-5. Purdue Univ.: Remote Multispectral Sensing in Agriculture. Lab. for Agricultural Remote Sensing (LARS), vol. 2, no. 832, 1967.

19-6. Hemphill, W. R.; and Carnahan, S. U.: Ultraviolet Absorption and Luminescence Investigations, Progress Report. U.S. Geol. Survey Tech. Letter NASA-6, 1965.

19-7. Horn, E. F.; and Hubbard, R. N.: Considerations For The Application of an Ultraviolet Illuminator to Night Aerial Photographic Reconnaissance. Unpub. U.S. Air Force Tech. Report AFAL-TR-67-205, 1967, pp. 5 and 36.

19-8. Kozyrev, N. A.: The Luminescence of the Lunar Surface and the Intensity of the Solar Corpuscular Radiation. Izv. Krymskoi Astroizitcheskoy Observatorye, vol. 16, 1956, pp. 148-161.

19-9. Grainger, J. F.; and Ring, J.: The Luminescence of the Lunar Surface. Physics and Astronomy of the Moon, ed., Z. Kopal, Academic Press (New York), 1962, pp. 385-405.

19-10. Grainger, J. F.; and Ring, J.: Anomalous Fraunhofer Line Profiles. Nature, vol. 193, 1962, p. 762.

19-11. Spinrad, H.: Lunar Luminescence in the Near Ultraviolet. Icarus, vol. 3, 1964, pp. 500-501.

19-12. Kopal, Zdenek: The Luminescence of the Moon. Sci. Am., vol. 212, no. 5, 1965, pp. 28-37.

19-13. Noxon, J.; and Goody, R. M.: Noncoherent Scattering of Skylight. Bull., Atmospheric and Oceanic Physics Series, vol. 1, no. 3, 1965, pp. 275-281.

19-14. McCord, Thomas B.: Observational Study of Lunar Visible Emission. Journ. Geophys. Res., vol. 72, no. 8, 1967, pp. 2087-2097.

19-15. Hemphill, W. R.: Ultraviolet Absorption and Luminescence Studies. Progress report for the period from Apr. to Dec. 1967. U.S. Geol. Survey open-file report, Tech. Letter NASA-100, 1968.

19-16. Betz, H. T.: The Remote Measurement of Rhodamine B Concentration When Used as Fluorescent Tracer in Hydrologic Studies. U.S. Geol. Survey open-file report, Tech. Letter NASA-101, 1968.

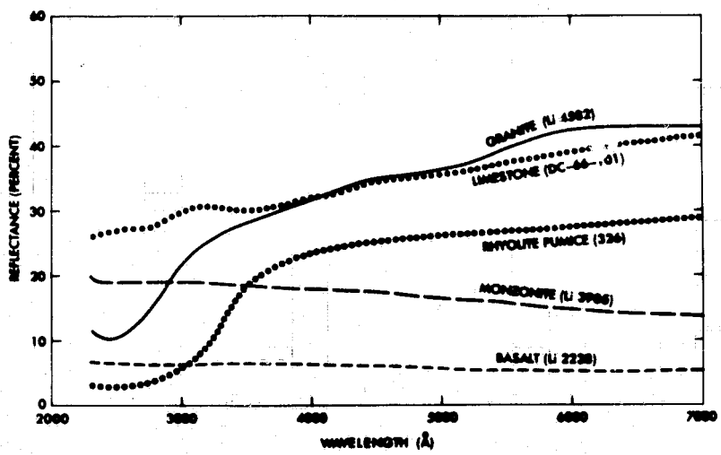

Figure 19-1.- Curves showing ultraviolet and visible spectral reflectance of some common rocks.

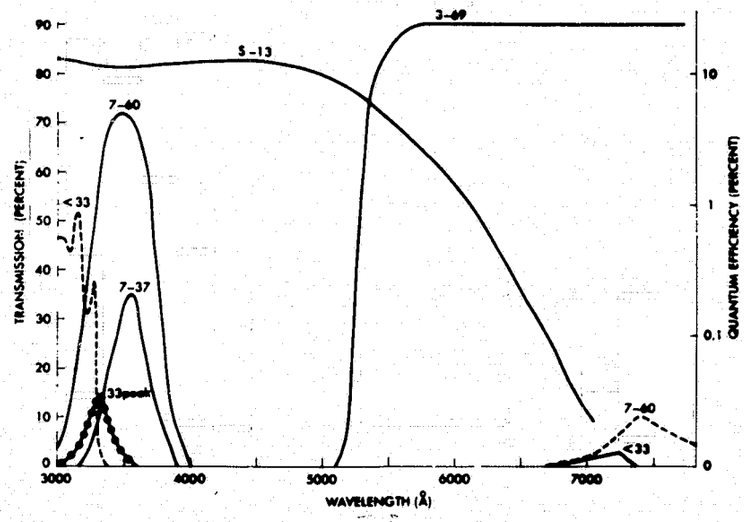

Figure 19-2.- Curves showing transmission of specific ultraviolet and visible filters and the quantum efficiency of the S-13 photocathode.

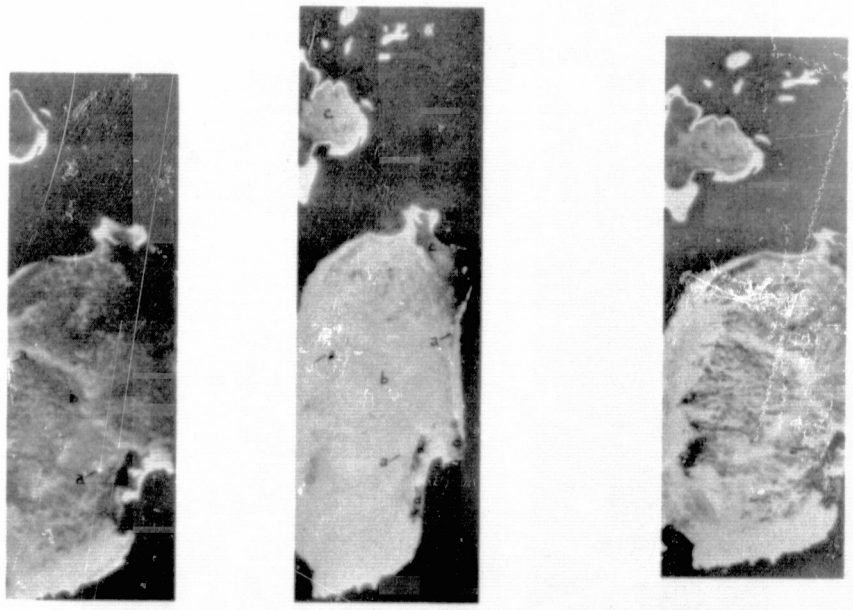

Figure 19-3.- Multiband imagery acquired with the University of Michigan's 18-channel scanner over Paoha Island, Mono Lake, California.

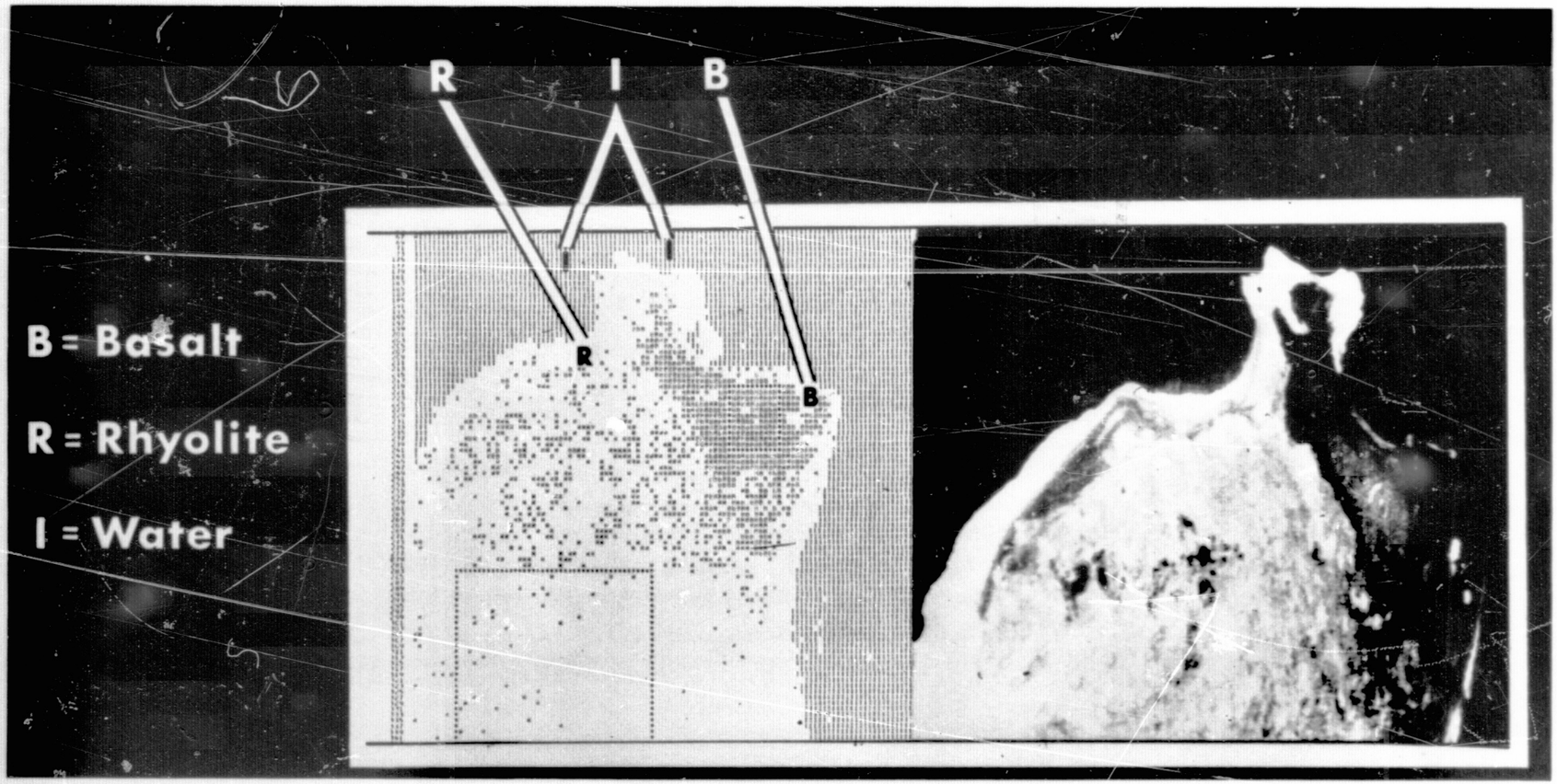

Figure 19-4.- Computer print-out of part of Paoha Island, Mono Lake, California, showing bedrock and surficial materials symbolized by letter. (Prepared in cooperation with the Department of Agriculture and Purdue University.)

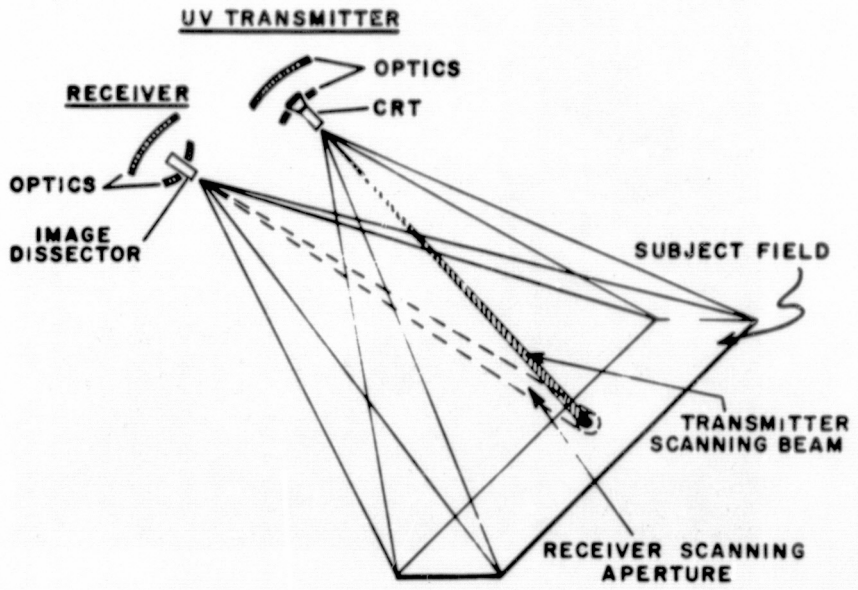

Figure 19-5.- Diagram showing operational components of an active ultraviolet imaging system.

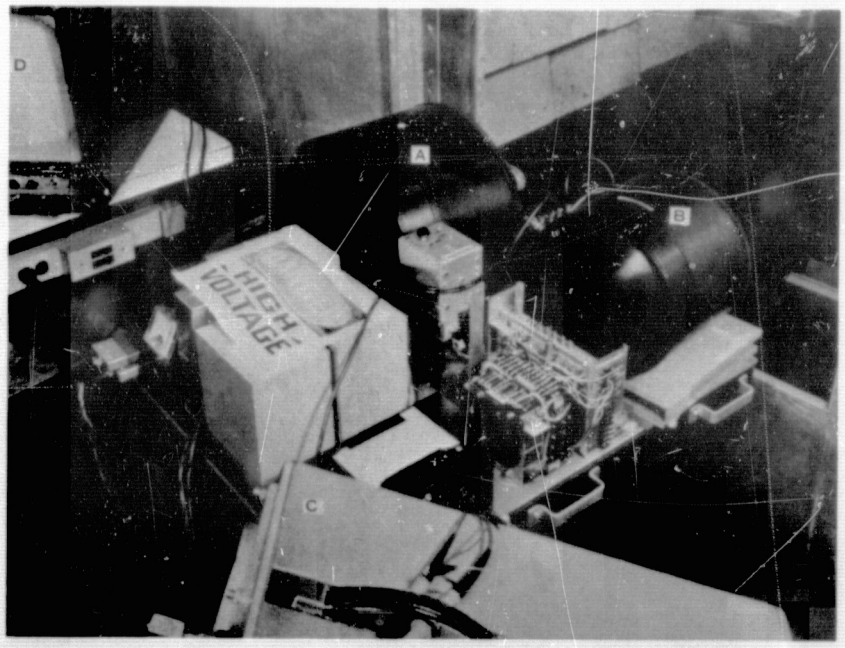

Figure 19-6.- Photograph showing ultraviolet imaging system set up in laboratory. Transmitter, A; receiver, B; oscilloscope, C; and video monitor, D.

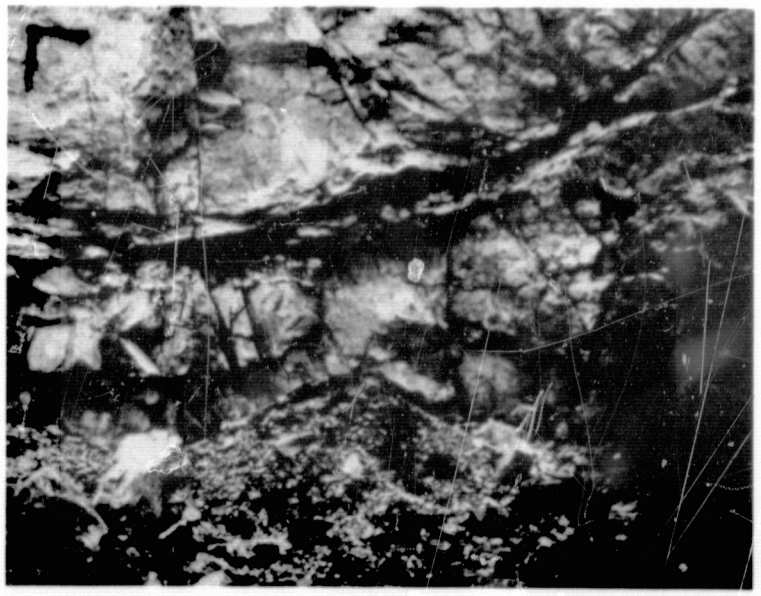

Figure 19-7.- Video monitor image indicating luminescence of deweylite in a quarry near Baltimore. Distance from the transmitter to the quarry face is 64 feet.

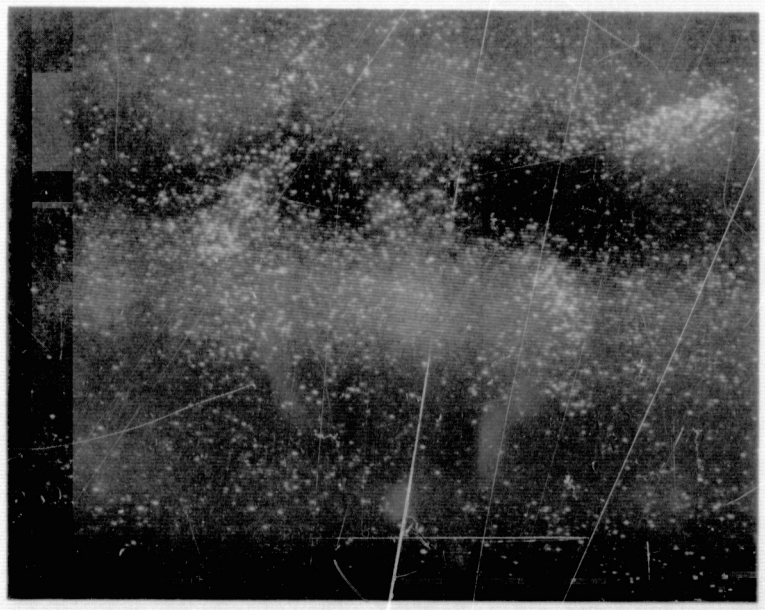

Figure 19-8.- Conventional photograph of same area shown in figure 19-7.

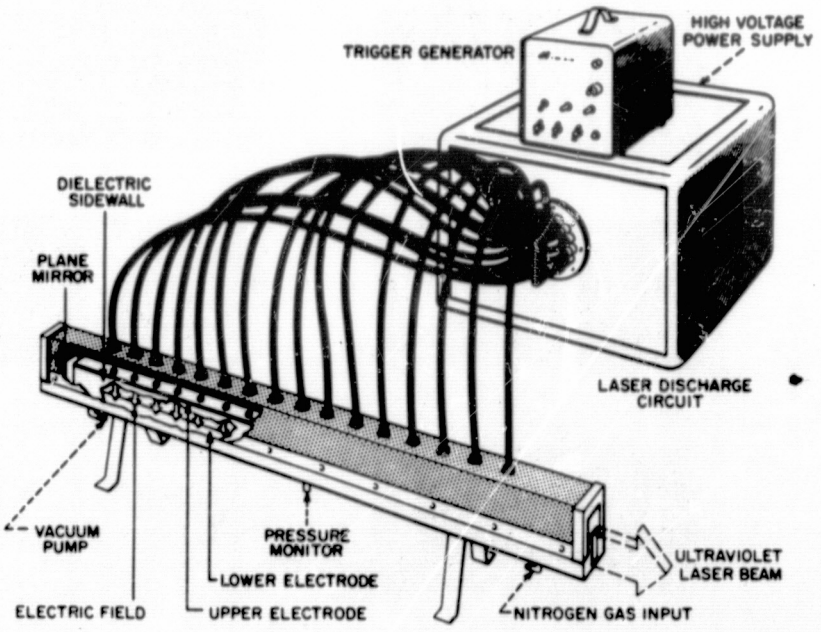

Figure 19-9.- Ultraviolet laser. (Courtesy of the Avco-Everett Research Laboratory.)

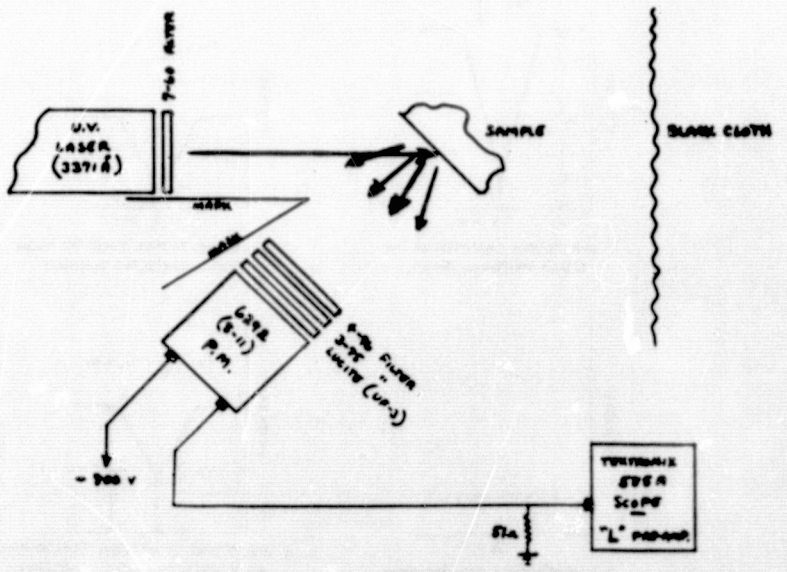

Figure 19-10.- Diagram showing position of laser, sample, and photomultiplier detector for measurement of luminescent decay time.

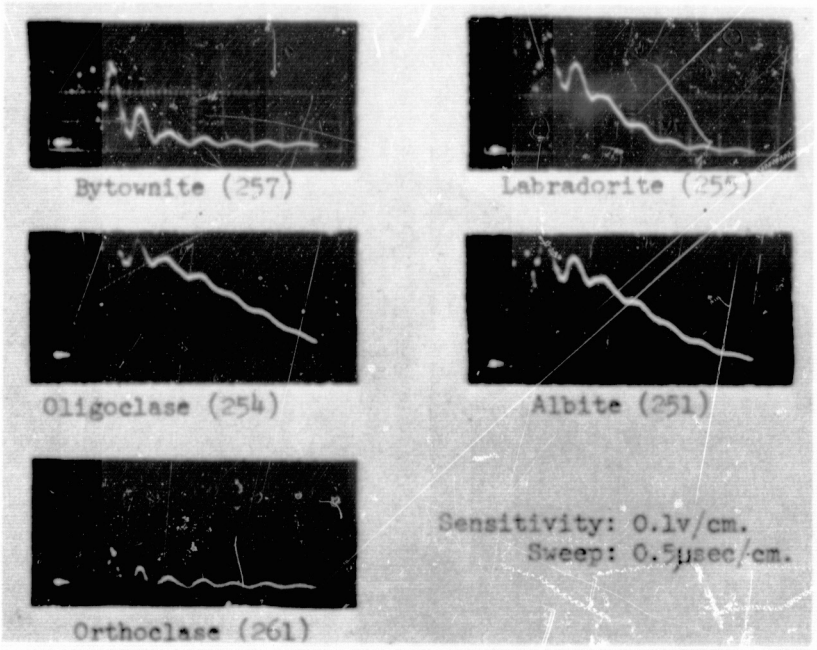

Figure 19-11.- Oscilloscope traces for a suite of five feldspars.

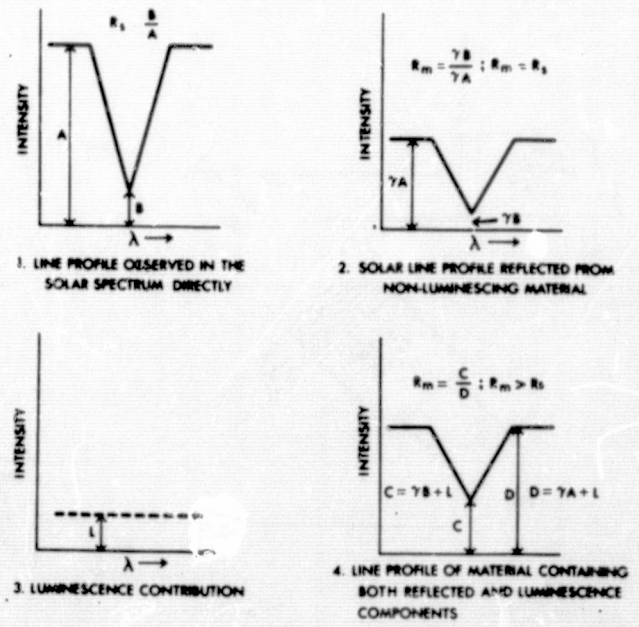

Figure 19-12.- Diagrams illustrating the Fraunhofer line-depth method.

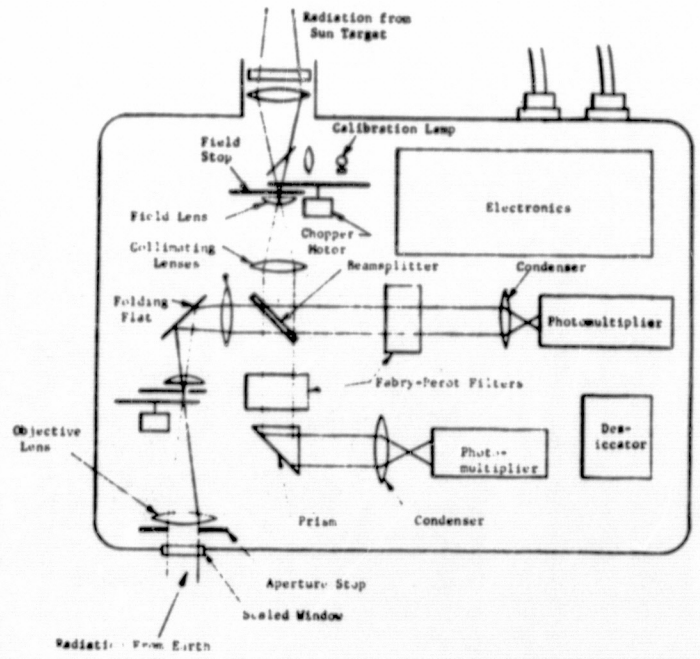

Figure 19-13.- Schematic showing design of the optical unit of the line-discriminator prototype. (Courtesy of the Perkin-Elmer Corp.)

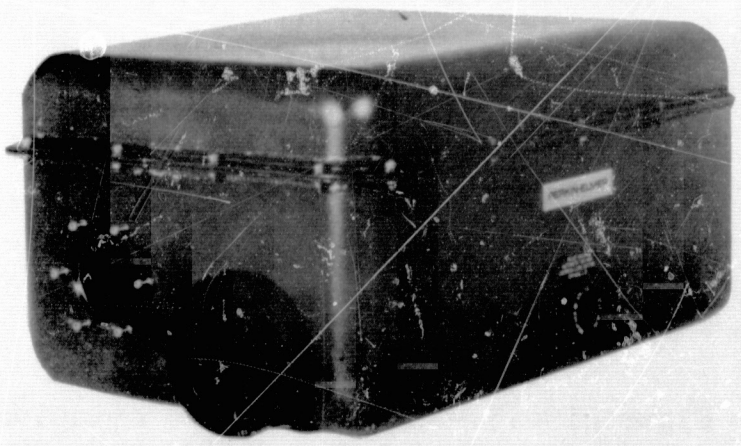

a. Optical unit.

Figure 19-14.- Prototype line discriminator showing the optical unit and the control console. (Courtesy of the Perkin-Elmer Corp.)

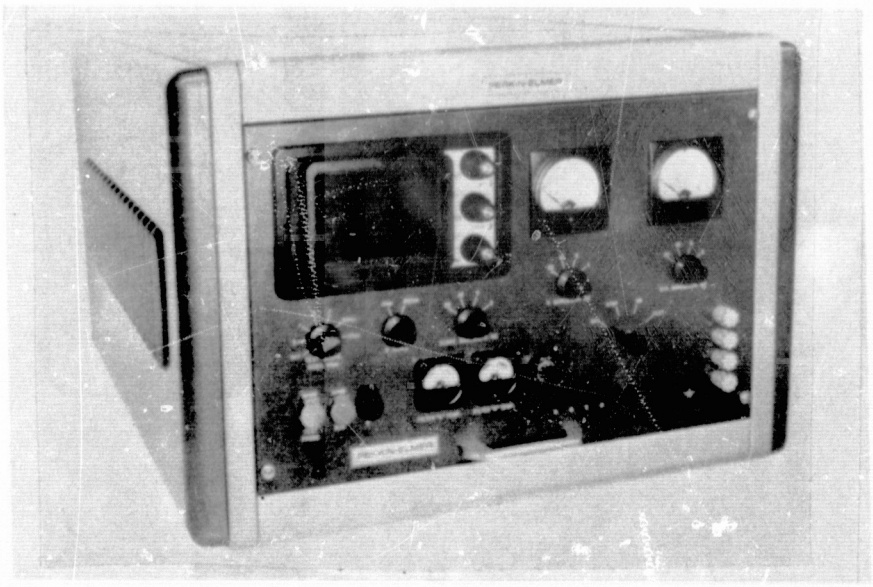

b. Control console.

Figure 19-14.- Concluded.

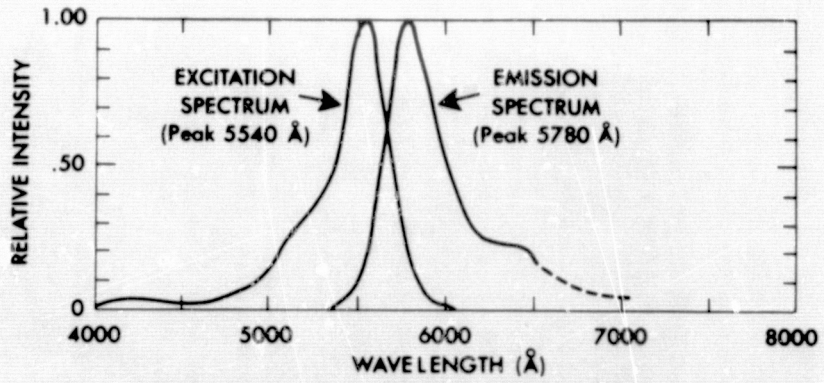

Figure 19-15.- Excitation and emission spectra of Rhodamine dye. (After spectrofluorometric analyses furnished by G. K. Turner Associates, Palo Alto, California.)

N71-16145

RADAR PROGRESS IN THE NASA EARTH RESOURCES AIRCRAFT PROGRAM

By R. K. Moore
Center for Research in Engineering Science
University of Kansas

INTRODUCTION

Much progress has been made in the application of radar to the earth sciences in the 4 years since what is now the NASA Earth Resources Aircraft Program began. In 1964, the word scatterometer had not been invented. Although the scatterometer had been proposed for sea-state measurement, the available data were much poorer than those obtained to date in the NASA Program. Use of a scatterometer to measure parameters of the land had never been attempted. Today, enough measurements have been made to show that scatterometry can be a useful tool for land geoscience, at least from aircraft. In 1964, very few studies had been conducted (nearly all by the U.S. Army) on the use of imaging radar for earth-resources-type applications. In 1968, some geologic uses of radar have been proved and many others are indicated. Preliminary evidence is at hand that radar will be useful in discriminating both cultivated and natural vegetation. Land-use studies have been conducted by using radar on at least a preliminary experimental basis. At least one hydrologic application of radar, determining drainage basin parameters, has been shown to be promising. In 1964, multipolarization radar imagery had never been tested for earth resources application and seldom for any other purpose. In 1968, the value of multiple-polarization images has been clearly indicated by numerous experiments. In 1964, polychromatic radar had been postulated, but no polychromatic image studies had been made. In 1968, a beginning test at Pisgah Crater has been completed, and the potentially great value of multiple frequencies has been indicated, at least for that environment.

The NASA Earth Resources Aircraft Program and its predecessors have contributed, we believe, more to the peaceful uses of radar mapping (imaging) systems than all previous efforts. In 1964, the application of radar to earth resources was speculation. In 1968, although most applications need to be really proved, enough experiments have been conducted to show that radar has a prominent place in earth resources

studies. We believe, in fact, that it may play the primary role when short-time repetitive coverage is required in areas with frequent cloud cover.

This report primarily covers the activities of the past year, but it necessarily depends upon work done in the previous years. No radar system yet flying on a NASA Manned Spacecraft Center aircraft was designed or even procured for this program. Results to date have been based on use of the 13.3-gigahertz scatterometer originally procured to obtain engineering data for the Apollo landing radars. The Westinghouse AN/APQ-97, owned by the U.S. Army but flown under NASA-funded contract; the U.S. Air Force Avionics Laboratory AN/APQ-56, flown under NASA contract; and the Naval Research Laboratory (NRL) four-frequency radar (equipped for imaging by NASA funding through the University of Kansas to the University of Michigan) have provided the images studied so far. We look forward to the new radars that will be installed on the NASA Manned Spacecraft Center aircraft and to improvements in the NRL system, so that the years ahead may be even more productive than those just past.

This report is concerned first with the scatterometer and then with the imaging radar. The scatterometer is a specialized instrument with an output that is difficult for most users to interpret. The radar imager, however, at least superficially, should be much easier for a wide variety of user disciplines to apply.

Details of specific mission results are given in the reports by Dellwig, McCoy, Pierson, Rouse, and Simonett.

RADAR SCATTEROMETER

The radar scatterometer is an instrument permitting measurement of the radar differential scattering coefficient (radar reflectivity). The scatterometers used in the NASA Earth Resources Aircraft Program determine scattering coefficient as a function of angle of incidence. Other scatterometers can be built to vary such parameters as polarization and frequency, as well as angle of incidence.

Aircraft Program Measurements

Sea-state measurement is probably the most promising spacecraft application of radar scatterometry. Details of the sea-state measurements under the program have been reported here by Pierson and will not be repeated. The sea-state measurements may be unique in that they are the first in which the complete curve of scattering coefficient versus angle is provided for each patch of sea. Thus, the measurements in this program should be and, in fact, are more consistent than those

in many other programs. "Sea truth" in this program has been more complete than in nearly every other program of radar sea-return measurements. Sea returns have been measured in this program from seas with stronger winds and higher waves than in other programs.

The scatterometer has shown itself, in a first test, to be able to discriminate different kinds of polar sea ice, at least from aircraft altitudes. Rouse has reported on this elsewhere (ref. 50-1), and the details are not given here. We believe that this is the first time a scatterometer has been flown over sea ice, although radar imagers have been used over the sea ice and have shown great promise in distinguishing kinds of ice (refs. 50-2, 50-3, and 50-4).

The radar scatterometer has been flown over several land test sites. Its resolution on these test sites is of the order of 30 to 150 meters; therefore, extrapolation of the results to space where the resolution will be kilometers is dangerous. Nevertheless, the results have indicated possible values of the scatterometer as an aircraft instrument, and data-processing techniques are being investigated that should apply when scatterometers are flown in spacecraft over the land.

The only land scatterometer data thoroughly investigated to date are from Pisgah Crater, where the ability of the scatterometer to distinguish the different geologic units has been shown (refs. 50-5, 50-6, and 50-7). Data-processing techniques have also been studied in connection with these flights. Figure 50-1 shows an aerial photograph of the Pisgah Crater area with the curves of differential scattering coefficient σ° as a function of angle indicated for each of the separate geologic units. Clearly, such an ensemble of curves is difficult to interpret. An attempt to improve the situation was made by plotting the difference between each individual curve and an average curve for the entire flight line, as shown in figure 50-2. Differences between alluvial material and lava are more clearly indicated on this illustration than on figure 50-1. Even so, the results are difficult to interpret.

A principal components analysis of the scatterometer data indicates that three components contain more than 90 percent of the variance of the data. Thus, it seems reasonable to express the results in terms of only three components. The three principal components actually contain information from more than three angles of incidence. However, a simpler experiment was conducted in which the scattering coefficient measurement at each of three angles of incidence was used to set the intensity of a light with one of the primary colors. Superposition of these three colored lights gives a resultant color that is the result of the combination of the three scattering coefficients (fig. 50-3). Although figure 50-3 is not as quantitative a presentation as figure 50-1 or 50-2, figure 50-3 is much easier to interpret when compared with a

photograph. Several other desplay techniques were tried, but this one was found most acceptable to the geologists involved in analysis of Pisgah Crater radar data. More details are given by Masenthin (ref. 50-6).

The next area subjected to this type of analysis is the Garden City agricultural test site. Because of difficulties in alining the scatterometer data with the photographs, insufficient time has been available to produce the color output such as that in figure 50-3. Figures 50-4 and 50-5, however, show the sort of variation in scattering coefficient curve and deviation of the scattering coefficient from the mean curve indicated for the Pisgah Crater data in figures 50-1 and 50-2. Further analysis of the Garden City data will be forthcoming. These Garden City observations have also been subjected to pattern recognition computations like those reported in another section of this report.

Techniques for alining scatterometer outputs with aerial photographs have been under development for some time. When the auxiliary data annotation set (ADAS) system is operating, the alinement presumably will be easy, but it is far from easy without the ADAS. The technique used now depends on a continuous recording of the scatterometer output at a particular angle of incidence. Correlation of data-panel photographs, aerial photographs of the area, tape-recorder annotations, and the scatterometer trace should make it possible to aline the scatterometer trace with the photographs. To accomplish this, a clearly defined boundary is required. Such clearly defined boundaries were located rather easily with the polar sea ice and somewhat less easily at Pisgah Crater. At Garden City, the boundaries seem to be much harder to find. Part of this appears to be caused by the switch from analog filtering to digital filtering in producing the output traces. Some characteristics of the digital-filtering process used makes the outputs less susceptible to interpretation than the analog process used. An extensive investigation is underway to determine the difference since the two filtering processes should give the same results. A final determination cannot be made until the computer program flow chart and the computer program itself are supplied to the University of Kansas.

Experience over the past year in working with the Garden City scatterometer data emphasizes the need both for better data correlation (which ADAS is expected to do) and for selection of a flight line in which outstanding isolated boundaries are included near the end of the line that should appear in both the photograph and the scatterometer trace.

In 1965, the U.S. NRL four-frequency radar aircraft conducted a series of measurements of radar sea return off Puerto Rico in conjunction with the Applied Physics Laboratory of John Hopkins University. A ship near the area of radar measurements made stereophotographs of the ocean surface. Unfortunately, most of the data were obtained while winds were

less than 16 knots, and only one point above that (at 18 knots) appears in the data (ref. 50-8).

A most significant result of these measurements is the relative independence of frequency for radar sea return. Of course, the applicability of this result to wind speeds of more interest in foul-weather conditions is unknown. The average data are shown for horizontal and vertical polarizations in figures 50-6 and 50-7. No cross-polarized data on frequency dependence were reported. If this result applies at higher wind speeds, the choice of frequency for a spaceborne radar scatterometer for sea-state measurements should be determined almost completely by equipment considerations, since it appears that any frequency will give about the same variation of sea return with winds/waves.

Aircraft Program Equipment

The 400-megahertz scatterometer system was in Houston at the time of the meeting. The antenna was reworked and was scheduled for pattern measurements in October. Should it pass these tests, the system will be ready for installation. A 1.6-gigahertz system has been recommended for purchase, and it is our understanding that negotiations are underway.

A system somewhere between 1.6 and 13.3 gigahertz would be desirable if no plans were made to provide images in that frequency region. If an imaging radar can be obtained in that region, no further scatterometers are required for the low-altitude aircraft.

Flight of a scatterometer in the B57 should give evidence of two differences of spacecraft measurements from the low-altitude aircraft measurements, although the B57 does not actually fly high enough to test either fairly. Over the sea, the high altitude should permit averaging over a sufficiently large area so that local variations in the wind will have less effect on the data than they do at low altitudes. At satellite altitudes, the illuminated area will be so large that a truly excellent average should be obtained. The B57 at least approaches this. Over land, the scatterometer and other poor-resolution instruments should be tested at high altitudes to see what they can do. Many of the low-altitude experiments over land for poor-resolution instruments are relatively meaningless in terms of application to spacecraft because the resolution is so important to the results of the experiment. We believe that the radar scatterometer will have considerable value over land when flown in a spacecraft, but because of the poor angular resolution, it will be difficult to predict such uses without testing them in a platform such as the B57.

Accordingly, we believe that the B57 should be equipped with a scatterometer. Since a new one will have to be designed to work at that altitude, an intermediate frequency such as 3 gigahertz (or perhaps even 6 gigahertz) may well be appropriate.

Related Theory and Experiment

Radar return theory has been the subject of many papers over the years. At the University of Kansas, this work has been supported by the National Science Foundation[1] and, to a limited extent, by the Earth Resources Aircraft Program through the Naval Oceanographic Office.[2] All theories assume some sort of rough surface that may be statistically described. In order to make the theories analytically tractable, the statistical description is customarily greatly simplified and, in fact, is usually given in terms of an autocorrelation function selected for its integrability rather than for its relation to reality. Comparison between radar returns as modeled with an ultrasonic simulator for a known surface and the theoretical calculations for this known surface have been underway at the University of Kansas for some time, with varying degrees of success (refs. 50-9 and 50-10).

The boundary between the ocean and the air would appear to be a much simpler boundary to describe analytically than most land boundaries. This is true not only because it is simpler than one involving vegetation, but also because the sea is (for radar purposes) a homogeneous half space, with the air being another homogeneous half space. Over land, however, the land itself is far from homogeneous and, in fact, is usually made up in layers which frequently contain inhomogeneities themselves. Thus, the prospect of determining the radar return from the sea using the actual sea statistical description appeared, at first sight, to be easy.

The results for computation of the radar backscatter from the sea, using the spectrum for a fully developed sea to determine the autocorrelation function of the surface, are not very encouraging. Computed scattering shows almost no variation with wind speed (ref. 50-11); whereas, in fact, measurements at all frequencies indicate that the scattering coefficient varies strongly with wind speed (ref. 50-12). Apparently, the spectrum normally valid for most oceanographic uses neglects some factors that are most important for scatter of the short radar wavelengths. Pierson believes that these factors may include

---

[1]Grants GP-2259, GK-875, and GK-1153.

[2]Contract N62306-67-C-0044.

nonlinear effects, the short-crested nature of actual waves (assuming in the theory that the waves are all going in the direction of the wind), and the effects of foam, spray, and breaking waves. None of these is covered in the gross theory, since the linear theory is intended more to describe the components of the waves that are significant for ship navigation rather than the components that contribute most strongly to the radar signal.

Progress has recently been made both at the University of Kansas and at the NRL in application of a small-perturbation model to describe the small structure on the surface of the ocean. Wright at the NRL has used this small perturbation alone (ref. 50-13), whereas Fung at the University of Kansas has combined it with the description for the full-scale ocean (ref. 50-14). Thus, Fung's approach might be characterized as a two-component description of the sea: large-scale effects and small-scale effects. Unfortunately, it is difficult to know where to draw the line between large- and small-scale effects; therefore, this is only a preliminary attempt at explanation of sea return. Nevertheless, the results obtained for variation of scattering coefficient with angle appear hopeful and seem to describe the experimental results somewhat better than methods using the full-scale wave description alone. It appears that the description of the ocean surface is not as simple as one might hope in developing a radar theory!

With Naval Oceanographic Office sponsorship, ultrasonic simulation of scatter from the ocean is underway at the University of Kansas. The recently observed data are presently being checked; therefore, no curves are presented. The conclusions are clear, however. A combination of relatively long surface waves generated by a plunger and very short surface waves generated by a fan indicates that even when the short waves are much lower than the long waves, they are the major contributors to the off-vertical radar return. This seems to be in accord both with theoretical discussions and with the general feeling of all who are working in radar sea-return research that the small structure (which is wind dependent) is the primary determinant for radar return from the ocean. Of course, this technique does not permit the modeling of breaking waves, foam, or spray.

Use of multifrequency or swept-frequency radar scatterometers and imagers should give the same kind of "signatures" (but different ones) found in the visible and infrared (IR) regions. An acoustic simulation of the frequency variation of radar return over approximately a three-to-one frequency range was recently completed by Rouse (ref. 50-15). His results clearly show, for the targets investigated, that frequency signature is indeed feasible in the radar region.

Rouse's ultrasonic simulation involved two targets. The first was a rough surface of known characteristics used also for comparison

between theory and experiment. Figure 50-8 shows the frequency variation of scattering coefficient observed for this target. The target was relatively smooth. It had no undulations with lengths comparable with the wavelength of the illuminating radiation at any of the wavelengths used. All undulations were much larger. This target was then covered thinly with fine sand particles with diameters near a wavelength at the high-frequency end of the range. The result is shown in figure 50-9. A radar scatterometer operating across this frequency range would obviously be able to distinguish between the target with and without the sand, as indicated by the two figures.

A 4- to 8-gigahertz frequency-swept ground-based radar system is being completed at the University of Kansas under sponsorship of the Advanced Research Projects Agency and the Engineering Topographic Laboratories of the U.S. Army Corps of Engineers (ref. 50-16). Except for a system going into use at the U.S. Army Waterways Experiment Station, this is, we believe, the only octave-bandwidth earth-oriented radar in existence. It will be used to verify the potential of broad-spectrum radar measurements both for determining signatures and checking swept-frequency scatterometry and for improving image gray scale, as discussed later.

Use of the instrument as a ground-truth device in connection with NASA aircraft overflights, particularly when an imaging radar system operating within the band of this system is provided on one of the NASA aircraft, will provide interesting comparisons comparable to those now provided in the IR region. We hope that such comparisons can be made soon.

New Techniques

Radar scatterometers operated in spacecraft, or even in aircraft, may be power limited. Techniques by which the power required can be reduced are, therefore, always of interest. At the University of Kansas recently, a radar receiver concept has been analyzed that uses a receiver for the scatterometer, similar to that for a Dicke radiometer. In the Dicke radiometer, the receiver input is switched alternately to a known temperature source and to the antenna which is observing an unknown temperature. Thus, a continuous calibration is obtained. By integrating the signal from the known source long enough, the effective temperature of the receiver may be determined very accurately. A comparable integration of the unknown source determines the combination of a signal and receiver noise accurately, so that the difference between signal plus noise and noise alone may be ascertained with great precision. In applying this technique to the scatterometer, one need not use a known temperature source. The total noise at the input to the scatterometer is a combination of the receiver noise and the noise

picked up by the antenna (radiation from the target). By integrating long enough, this noise may be accurately determined. Similar integration of the signal plus noise, when the radar transmitter is activated, gives an accurate value for signal plus noise. The difference may thus be determined accurately. With a signal-to-noise ratio of unity, an accuracy of about ±0.7 decibel can be achieved with the integration time involved in one example system for space (ref. 50-17).

Several authors have indicated the value of using radars and radiometers together (ref. 50-18). The radiometer measures the product of emissivity and temperature, and emissivity is closely related to the radar cross section (ref. 50-19). Thus, making both measurements together may well permit using the radiometer as a temperature-measuring device, even with varying emissivities. Calculations made recently show that the amount of radar power required is very small with a radiometer which must use a very high gain antenna to achieve its spatial resolution. For example, a power of about 50 milliwatts is all that is required for one system operating at nimbus altitudes with about 2.5° beamwidth. Introduction of such a small transmitter on a time-shared basis into the radiometer system should be easy. The only modification in the receiver is a separate narrowband receiver channel for the radar, and this may be added after the low-noise part of the receiver. Because of the narrow pass band, either a stable transmitter and receiver local oscillator is required, or an automatic frequency control must be used for the receiver.

IMAGING RADAR

Most earth scientists make extensive use of spatial relations and texture in analyzing remote-sensor observations. Thus, they prefer either photographs or images that have some of the characteristics of photographs, as obtained by line scanners or side-looking airborne radars. Because of the importance of spatial context in analysis, we believe the imaging radar to be a much more important tool for the land geoscientist than the scatterometer, and research emphasis should be placed accordingly. Multispectral radars (polychromatic systems) are urgently needed in the program, for preliminary indications are that such radars will indeed prove valuable in the earth resources activities, whether they are flown in aircraft or spacecraft. Multispectral systems call for elaborate data processing if the results are to be applied efficiently.

Aircraft Measurements

No new radar images have been produced within the past year under NASA Earth Resources Program sponsorship. This is most unfortunate, but the big backlog of images provided by the AN/APQ-97 in previous years is still being analyzed. The need for additional measurements with careful experiment design is clear, however.

New analyses completed or published within the past year have been reported here by Simonett, Dellwig, McCoy, and several U.S. Geological Survey personnel. Dellwig's report on the first analysis of four-frequency radars at Pisgah Crater is most encouraging and important.

The NRL four-frequency imaging radar[3] has been flown experimentally several times within the past year under sponsorship of the NRL and other Department of Defense (DOD) agencies as well as the Coast Guard. A mission was flown north of Point Barrow over the Arctic ice in April 1968 for the Naval Oceanographic Office. Preliminary investigation of the images indicates that resolution appears adequate, but gray scale leaves much to be desired. The NRL has recently installed new amplifiers in the receiver, which should improve the dynamic range. We have not heard the results of this change; although signal films have been obtained, they had not been processed to produce images by the time of writing.

Should the gray scale of the NRL images be significantly improved by addition of this amplifier, we believe that every effort should be made to reincorporate this aircraft in the Earth Resources Aircraft Program, so that polychromatic images can be obtained as soon as possible.

The AN/DPD-2 is, we understand, presently in Houston awaiting installation on the P3A. When it is installed, we hope that a significant set of experiments can be scheduled to test its capabilities.

We believe it to be most urgent that a new multifrequency synthetic-aperture system be procured for the NASA aircraft program. Such a system should have between three and five frequencies in the range between 1 and 10 gigahertz. Although it would be desirable to fly all frequencies at once, a system permitting single frequencies to be flown on each path and changing frequency from one flight path to the next would be acceptable for the early experiments.

---

[3]This system was built for DOD missions but equipped for imaging by the University of Michigan through a subcontract from the University of Kansas/NASA contract in 1965 and 1966. Improvements have since been made at DOD expense.

Related Experiments

Most synthetic-aperture radars and many real-aperture radars obtain only one independent look at each target. Since tens to hundreds of looks are required to obtain reasonable average values of the radar scattering cross section, the individual look at each target means that the observed strength of the target echo may vary widely. The result is a speckled image. The same phenomenon can be seen in photographs produced with laser (monochromatic) illumination.

One possible way to overcome this monochromatic illumination problem for radars is use of a panchromatic system, just as in optics. A system might be used, for instance, in which a range of frequencies is used so that frequency averaging removes much of the uncertainty and produces a reasonable average value for each target echo.

A demonstration of the value of the panchromatic radar was recently conducted by Rouse using the ultrasonic simulator (ref. 50-15). Figure 50-10 shows two images, one produced with a monochromatic source and the other with a panchromatic source. The structure shown in the monochromatic image is not relevant to the description of the target, which should appear relatively smooth in an image. Clearly, the panchromatic image accomplishes this purpose.

Figure 50-11 demonstrates this even more strikingly. Here, a set of monochromatic images produced at different single frequencies is compared with two panchromatic images, one with ±3-percent frequency variation and the other with ±6-percent variation.

The 4- to 8-gigahertz electromagnetic system being assembled now will be used to produce panchromatic images, as well as scatterometer data.

We believe that airborne or spaceborne radar systems in the future will use the polypanchromatic concept shown in figure 50-12. Here, the radar uses a somewhat broad spectrum about each of three isolated center frequencies. Because each center frequency has a "panchromatic" character, good average values for the echoes are obtained. The lowest frequency may be assigned red, the middle frequency green, and the higher frequency blue in an image-combining system, and the result should be a consistent color every time the target is imaged. Without the panchromatic nature, consistency would exist over an area, but at individual points there would be considerable variation in color.

Data Processing

The production of multispectral image data, whether in the microwave range or in some other frequency range, makes some sort of automatic or semiautomatic data processing almost essential. Difficulty of going from one image to another to pick out the differences is indeed great. Work has proceeded at the University of Kansas since 1964 along two parallel lines: (1) semiautomated development involving extensive use of a human operator, but with color presentation of the results so that the human interpreter's eye-brain communication channel can best be used, and (2) the computer recognition of multispectral (and, for the scatterometer, multiangle) information.

We believe that the general-purpose computer, which is relatively slow and expensive, should be used to determine the program settings for a real-time processor, either on an absolute signature basis or by comparison with a learning set of observations over a ground-truth site to determine the signature at the time of imaging.

The image discrimination enhancement and combination system (IDECS), developed at the University of Kansas with NASA funds and recently improved and expanded with DOD funds, permits real-time combination and enhancement of images. Furthermore, through use of its "spectrance selector" (formerly called "signature selector"), signatures are recognized and presented on a color TV display in the form of colored maps of recognized areas. Unfortunately, few adequate signatures are available at present to program the spectrance selector.

Modifications currently underway will permit coupling the IDECS to magnetic tape units so that images may be scanned in the IDECS, digitized and processed on a digital computer, and the results displayed in color, with and without further IDECS processing. Figure 50-13 is a block diagram showing the IDECS and associated equipment. The only equipment missing is the small computer for which funds have never become available. The following is a list of the characteristics of the IDECS:

1. High-speed image processing

2. Acceptance of single- or multiple-input images

3. Variety of outputs, including enhanced images, false-color images, thematic map format, area totals

4. Capability of using a variety of "pattern-recognition techniques" to identify selected features

Numerous improvements have been made in the IDECS within the past year. These are indicated in the following list of IDECS investigations during the year ending August 1968.

1. Application to a variety of image formats and test areas

2. Development of computer programs to determine optimum settings for IDECS controls

3. Breadboard of circuits to give capabilities for area measurement and texture discrimination

4. Design of interface equipment between IDECS and digital tape

5. Completion and initial application of the spectrance selector

Although the IDECS has been used with multiple-polarization radar imagery, the lack of multispectral radar imagery has led to testing with multispectral photographs. The tests described here were performed with multispectral photographs of the Bucks Lake forestry test site obtained by the NASA aircraft (figs. 50-14 to 50-18). This work has been conducted cooperatively with Colwell's group at the University of California. Following is an extract from a report by Estes, Draeger, and Haiman, graduate students of Colwell, who came to Lawrence and applied the IDECS to the multispectral images for their test site (ref. 50-20).

"The false-color image in Figure 14 was used to differentiate the serpentine-derived soils, which on this image appear green in color. The Dubakella and Cohasset are the two soil types involved, and no attempt was made to further discriminate between them....

"In Figure 15 well-stocked mature timber stands appear black, while areas of medium-stand density appear mottled green. Areas with little or no timber cover appear blue, white, or red.

"In Figure 16 areas of dense timber appear in red. In Figure 17 areas of intermediate timber densities appear in green. By a simultaneous interpretation of these two images, a regional stratification can be made, based on density criteria (sparse, intermediate, and dense)....

"The false-color-enhanced image in Figure 18 effectively discriminates meadow and riparian vegetation from a forest matrix. The result indicates drainage patterns as well as vegetational differentiation. The red areas are higher in soil moisture.

"Preliminary interpretation indicates that many important ground conditions in this area can be analyzed through the use of electronically enhanced imagery. Soil and vegetation types (riparian and meadow versus

other associations in the area) can be differentiated, leading to still further inferences, such as estimates of soil moisture content."

These preliminary tests show this technique to be valid but requiring a great deal of attention from the human operator. Whether adequate signatures permitting use of the spectrance selector can be derived either in the visible or radar region remains to be determined by further experiment. Perhaps, because illumination with radar is better controlled, radar signatures will be more suitable for such quantitative application than visible and IR signatures.

The University of Kansas has also investigated a group of digital data compaction and pattern-recognition techniques for multiple images and multiparameter scatterometer data, using both real and artificial data. The techniques are as follows:

1. Bayes' statistical decision theory
2. Principal components analysis
3. Nonlinear adaptive learning
4. Spatial clustering
5. Measurement space clustering

Bayes' statistical decision theory is a classification technique applicable when a priori knowledge exists of the statistics of the desired categories, as might be obtained by analysis of data from a ground-truth region. Principal components analysis may be used for data compaction. The other three techniques assume no prior knowledge of data statistics for known categories. They may be used to find natural classes in the observations, which may then be identified with desired classifications by a user. Application of such techniques avoids unproductive efforts at use of categories not really distinguishable by the sensor.

Bayes' theory (ref. 50-21) leads to a statistically optimum decision rule on the basis of our prior knowledge of the probability distributions of the categories we consider and on the basis of our economic gains and losses for correct and incorrect identifications. A Bayes' classification was constructed for two sets of Garden City agricultural radar imagery

(ref. 50-22). The first set consisted of three images in time sequence with the following polarization combinations:

1. HH polarization taken in August 1965
2. HH polarization taken in September 1965
3. HV polarization taken in September 1965

The second set consisted of four images taken simultaneously:

1. HH polarization taken in July 1966
2. HV polarization taken in July 1966
3. VH polarization taken in July 1966
4. VV polarization taken in July 1966

Each data set was randomly divided in half. The first half was used to estimate the conditional probability statistics, and the second half was identified on the basis of a Bayes' classification. A unit one was gained for a correct identification, and a zero was gained for an incorrect identification. The identification of the second half of each data set produced the results shown in figures 50-19 and 50-20. Ninety percent of the types of surface cover, grouped as shown, were correctly identified for the "time sequential" set (August plus two-polarization data in September); 78 percent of the types of surface cover, grouped as shown, were correctly identified in the "simultaneous" set (July). September simultaneous two-polarization data would give better results than July four-polarization data (as discussed in the report by Simonett), but September data have been used only with the time-sequential analysis/ application of Bayes' theory.

A Bayes' classification was also constructed for Pisgah Crater scatterometry data. The four geologic formation categories were alluvial material, porphyritic olivine basalt flows of the second and final eruptive phases, microporphyritic olivine basalt flows of the first eruptive phase, and playa-lake sediment. The gain function was the same one used with the Garden City data. The data set was randomly divided in half. The first half was used to estimate the conditional probabilities, and the second half was identified on the basis of the Bayes' classification; 82 percent was identified correctly. Figure 50-21 summarizes these results.

Principal components analysis provides a way for reducing the dimensionality of the data while the essential data structure is preserved

(ref. 50-23). The method works particularly well if most of the elements in measurement space which have high probability lie in a linear subspace or flat. Both the Garden City image data sets, as well as the Pisgah Crater scatterometry data set, showed that most of the data do indeed lie in a flat (ref. 50-22). This is an important fact because it means that data of high dimensionality may be collected by radar imagers and scatterometers, and they can be compacted and stored or transmitted with low dimensionality. The compacted form may be expanded by linear transformation, and the original data set may be reproduced with little loss of information.

The technique may also be applied to reduce the dimensionality of the input patterns employed with other pattern-recognition algorithms. This enables the data-processing time and cost to be lessened. The results of principal components analysis for various data sets are as follows. Ninety-eight percent of the variance of the three-dimensional time-sequential Garden City image data is accounted for in a two-dimensional flat. Ninety-five percent of the variance of the four-dimensional simultaneous Garden City image data is accounted for in a two-dimensional flat. Ninety-two percent of the variance of the eight-dimensional Pisgah Crater scatterometer data is accounted for in a three-dimensional flat. Eighty-eight percent of the variance of one set of the nine-dimensional ice scatterometry data was accounted for in a three-dimensional flat. Ninety-two percent of the variance of another set of nine-dimensional ice scatterometry data was accounted for in a three-dimensional flat. Figures 50-22 and 50-23 illustrate the data projected onto the principal two-dimensional flat for the simultaneous Garden City image data.

The adaptive learning algorithm has a structure similar to Rosenblatt's five-layer perception device (ref. 50-24). However, the weights are interpreted as measures of association between the corresponding output patterns δ of the sensor units and the output categories η of the association units. The weight matrix for the fourth layer is the transpose of the weight matrix in the second layer. The predictive reinforcement procedure is based on the following consideration. If the output category is a good one and if g_{ij} is indeed a measure of association between the jth pattern component and the ith category component, then from the output category η, a good prediction should be made of the input pattern δ. If the problem has a solution and if some of the predicted components are wrong, then the corresponding weights are reinforced in such a way that they take on values more nearly consistent with the measure of association the problem is supposed to represent. Within a few hundred reinforcements, the algorithm constructed category groups from the Garden City image data, which it was able to identify almost as well as the Bayes' decision algorithm did (fig. 50-19, ref. 50-25). In a very noisy set of made-up data, the algorithm converged to a perfect answer within a few thousand iterations.

The spatial clustering technique is specifically designed for multi-image data. Data structure is examined from the perspective of spatial closeness, measurement space closeness, and the empirical probability distribution on measurement space. A chaining procedure is defined which constructs the classification by finding center sets and then links the most similar points to each of the respective center sets. By this means, it is not necessary to compute the astronomic number of distances between each pair of points on the multiple image as would be required with the multiple-linkage clustering method employed in numerical taxonomy (ref. 50-26).

With a set of three made-up images, each with dimensions of 80 by 80 (figs. 50-24, 50-25, and 50-26) with normally distributed noise 0.27 variance added, the spatial clustering algorithm identified the 12 categories 99.5 percent correctly (fig. 50-27).

The measurement space clustering method is similar to the spatial clustering method except that spatial closeness is not taken into account, and a more exacting definition is required for measurement space similarity. With the same set of three made-up images, the measurement space clustering identified the 12 categories 98.5 percent correctly (fig. 50-28, ref. 50-26).

EXPERIMENT PHILOSOPHY

Scatterometer

The scatterometer is a poor-resolution instrument by nature. The microwave radiometer is also naturally a poor-resolution instrument. Some IR devices are poor-resolution instruments as well. This poor resolution must always be kept in mind when considering space applications of the scatterometer, for the type of thing that can be done from an aircraft may not be feasible with a spacecraft which is at a much higher altitude and, consequently, has a much larger resolution cell.

We believe, as indicated by Pierson, that the validity of the scatterometer for measuring sea roughness parameters closely related to the surface winds has been demonstrated, although it has certainly not been calibrated. Sea roughness and winds do not require fine resolutions. In fact, coarse resolutions are probably better for the synoptic scale computations required for oceanwide wave/wind mapping.

The scatterometer probably can be used to determine the major ice boundaries in the Arctic and perhaps major features of the Antarctic continent. Certainly, ice types are differentiated at small scale;

whether they will be equally well differentiated at large scale remains to be determined. Gross boundaries, such as those between grasslands and forests, between frozen and unfrozen ground, and between dry land and land that has recently been wet down by rain can possibly be determined by the scatterometer from space. The poor resolution should not stand in the way of the scatterometer for this function, but these applications have not been fully tested with aircraft to determine whether, in fact, the scatterometer return is different on the opposite sides of the boundaries.

A gross-resolution sensor may well have other applications from space. For example, the gross-resolution sensors in Tiros have been used in providing maps of the Sahara (ref. 50-27). The sort of application we will find with a resolution cell that is kilometers or tens of kilometers across will be difficult to establish before the scatterometer is flown in space; however, its generalizing capability may well be of great significance. It is difficult to see how this sort of application can be checked using an aircraft; perhaps use of the B57 at maximum altitude will permit at least a preliminary check in some areas.

The aircraft scatterometer can be used to check the applications of spaceborne scatterometers for which the size of the resolution cell does not matter. Over the ocean, as long as the aircraft is high enough so that major wave structures are illuminated completely, this certainly should be true. The same may be true over the ice, and the aircraft can be used for checking the ability to determine frozen-unfrozen boundaries, wet-dry boundaries, and forest-grassland boundaries. Low-altitude aircraft measurements with 50-foot to a few-hundred-foot resolution probably will not be too helpful in determining other spacecraft uses of scatterometers.

Aircraft scatterometers, however, can be used in the absence of appropriate aircraft imaging radar to learn many useful pieces of information about potential applications of imaging radars in space. Thus, an aircraft mission at low altitudes using the 400-megahertz scatterometer should be able to determine the difference between a signal at this frequency and one at 13.3 gigahertz, or at the 16.5 gigahertz of the DPD-2. In the absence of an imager near 400 megahertz, this will give very useful information about the potential of the polychromatic imager. When a calibrated imager with its ability to provide good spatial context is available, however, the aircraft scatterometer will fade into the background for this application.

Radar scatterometers were originally installed in aircraft to obtain system design information for radars (imagers, altimeters, autonavigators, etc.). Because most of the programs to obtain such information had limited objectives and little or no ground truth, information is still spotty on the values of scattering coefficient to be used in radar system design.

As a consequence, designs are probably more conservative than they need be; hence, a more extensive use of aircraft scatterometers should provide system design data which would permit lower power space radar systems and should provide knowledge of possible penalties to be paid for using the lower power. Furthermore, the aircraft scatterometer can be used to determine the variation of scattering coefficient with incident angle so that an optimum angle of incidence can be picked for a spacecraft or aircraft radar imager. This, we believe, is an important application of the radar scatterometer in aircraft; but data analysis is primarily important for the radar designer. The user scientist is important here only to guarantee that the designer is meeting the user's real needs rather than those imagined by the radar engineer.

Radar Imager

Obtaining multifrequency multipolarization radar imagers for use in the NASA Program is most important. Multifrequency imagers will certainly be important in space.

It is easy for the radar imager to cover large areas. The large-area coverage obtained with the AN/APQ-97 has been used to advantage in both geographic and geologic studies. The use of very small test sites in which extensive ground truth is gathered may be appropriate for some radar applications, but the experiments for the imager should also include large-area "test sites" in which the generalizing capability of the imager can be used to advantage. Furthermore, the simplicity of operation for obtaining wide-area coverage may make it desirable to obtain images for users not in the NASA Earth Resources Aircraft Program while going from one place to another as a part of the program. Thus, a larger group of the scientific community would be drawn into the program, at least superficially, and more users will be ready when images are available from space.

Numerous experiments should be conducted using the radar imager to determine such things as the effect of look angle, angle of incidence, repeatability of the imaging, the effect of the "pebbliness" of synthetic aperture image on interpretation, and similar information. Much work remains to be done along these lines.

CONCLUSION

The NASA Earth Resources Aircraft Program has led to a great expansion in our knowledge of geoscience-resource applications of radar, even though the MSC aircraft are just being equipped with a radar imager and multifrequency/polarization scatterometers. Multifrequency imaging

radar, preferably "polypanchromatic," should give even more important results. The progress in multiimage data processing shows great potential of both semi-real-time and general-purpose computer techniques, but progress here, too, will be even greater when multifrequency radar data are available.

REFERENCES

50-1. Rouse, J. W., Jr.: Arctic Ice Type Identification by Radar. Tech. Report 121-1, CRES, Univ. of Kansas, Aug. 1968.

50-2. Simonett, D. S.; and Brown, D. A.: Spacecraft Radar as a Means for Studying the Antarctic. Proceedings of the VII Congress International Quaternary Assoc., Boulder, Colo., Sept. 1965. Also published as CRES Tech. Report 61-4.

50-3. Anderson, V. H.: Radar Imagery of Arctic Pack Ice, Kane Basin to North Pole. U.S. Army CRREL Special Report 94, 1962.

50-4. Anderson, V. H.: High-Altitude, Side-Looking Radar Images of Sea Ice in the Arctic. Proceedings of the Fourth Symposium on Remote Sensing of Environment, Univ. of Michigan, April 1966, pp. 845-857.

50-5. Dalke, G. W.: Identification of Remote Objects by Means of Scatterometry Data and Applications to Pisgah Crater. Tech. Report 61-17, CRES, Univ. of Kansas, Feb. 1967.

50-6. Masenthin, H. W.: Scatterometer Data Analysis Techniques. Tech. Report 118-3, CRES, Univ. of Kansas, July 1967.

50-7. Lundien, J. R.: Analysis of Scatterometry Data from Pisgah Crater. Tech. Report 118-2, CRES, Univ. of Kansas, Aug. 1967.

50-8. Daley, J. C.: Sea Clutter Measurements on Four Frequencies. Presented at Fall Meeting, U.S. National Committee, URSI, Northeastern Univ., Sept. 1968.

50-9. Parkins, B. E.: The Omnidirectional Scattering of Acoustic Waves from Rough Surfaces with Application to Electromagnetic Scattering. Tech. Report 48-4, CRES, Univ. of Kansas, June 1965.

50-10. Fung, A. K.; and Leovaris, A.: Frequency Dependence of Ultrasonic Scatter from Statistically Known Rough Surfaces. 1968 WESCON Technical Papers, Session 22. WESCON, Los Angeles, Aug. 1968.

50-11. Chia, R. C.: The Theory of Radar Scatter from the Ocean. Tech. Report 112-1, CRES, Univ. of Kansas, Oct. 1968.

50-12. Pierson, W. J.: Radar Sea Return as a Function of Wave Height and Wind Speed for Fully Developed Seas. Earth Resources Aircraft Program Status Review, 1968.

50-13. Wright, J. W.: A New Model for Sea Clutter. IEEE Trans., vol. AP-16, Mar. 1968.

50-14. Fung, A. K.: Backscattering of Waves by Composite Rough Surfaces. Presented at Spring Meeting, U.S. National Committee, URSI, National Academy of Science, Washington, D.C., Apr. 1968.

50-15. Rouse, J. W., Jr.: Frequency Dependence of Backscatter from Rough Surfaces. Interim Tech. Report 133-4, CRES, Univ. of Kansas, Aug. 1968.

50-16. Ellermeier, R. D.: Project THEMIS: A Center for Remote Sensing Semi-Annual Technical Report. CRES, Univ. of Kansas, Apr. 1968.

50-17. Pierson, W. J.; and Moore, R. K.: Global Radar for Ocean Waves and Winds (GROW), An Experiment Submitted to NASA for Flight on a NIMBUS E or NIMBUS F Spaceflight. CRES, Univ. of Kansas and NYU School of Engrg. & Science, Feb. 1968.

50-18. Janza, F. J.: A Comparison of the Microwave Scatterometer and Radiometer for Sea State Measurements. Presented at the 49th Annual Meeting, AGU, Washington, Apr. 1968.

50-19. Peake, W. H ; Riegler, R. L.; and Shultz, C. H.: The Mutual Interpretation of Active and Passive Microwave Sensor Outputs. Proceedings of the Fourth Symposium on Remote Sensing of Environment, Univ. of Michigan, Apr. 1966, pp. 771-777.

50-20. Dalke, G. W.: Multi-Image Correlation Systems Study for MGI Phase II Technical Report. CRES, Univ. of Kansas, June 1968.

50-21. Raiffa, H.; and Schlaife, R.: Applied Statistical Decision Theory. Harvard Univ. Press, 1961.

50-22. Haralick, R. M., et al.: A Statistical and Conditional Probability Study of Crop Discrimination Using Radar Images. Presented at the International IEEE Meeting, New York, Mar. 1968. Also appears as CRES Tech. Memo. 133-5, 1968.

50-23. Kendall, M.; and Stuart, A.: The Advanced Theory of Statistics. Hafner, (London), 1966.

50-24. Rosenblatt, F.: Principles of Neurodynamics. Spartan Books, 1962.

50-25. Haralick, R. M.: Adaptive Pattern Recognition of Agriculture in Western Kansas by Using a Predictive Model in Construction of Similarity Sets. Proceedings of the Fifth Symposium on Remote Sensing of Environment, Univ. of Mich., Apr. 1968.

50-26. Haralick, R. M.: Pattern Recognition Using Likelihood Functions. Tech. Report 118-4, CRES, Univ. of Kansas, Aug. 1967.

50-27. Pouquet, J.: Remote Detection of Terrain Features from NIMBUS I High Resolution Infrared Radiometer Nighttime Measurements. NASA TN D-4603, 1968.

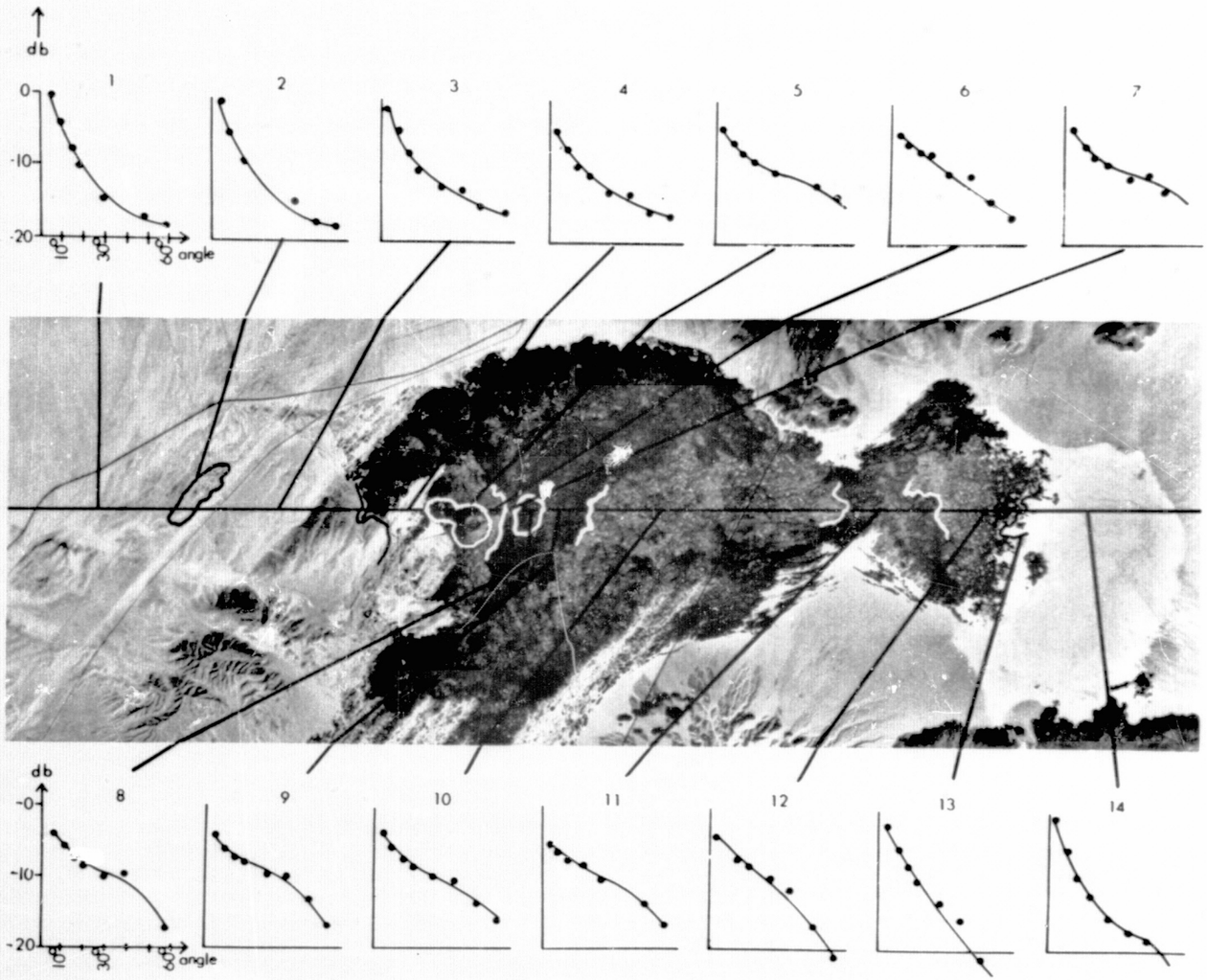

Figure 50-1.- Curves of radar differential scattering coefficient versus angle of incidence compared with photograph showing regions from which the data were obtained using the 13.3-gigahertz scatterometer.

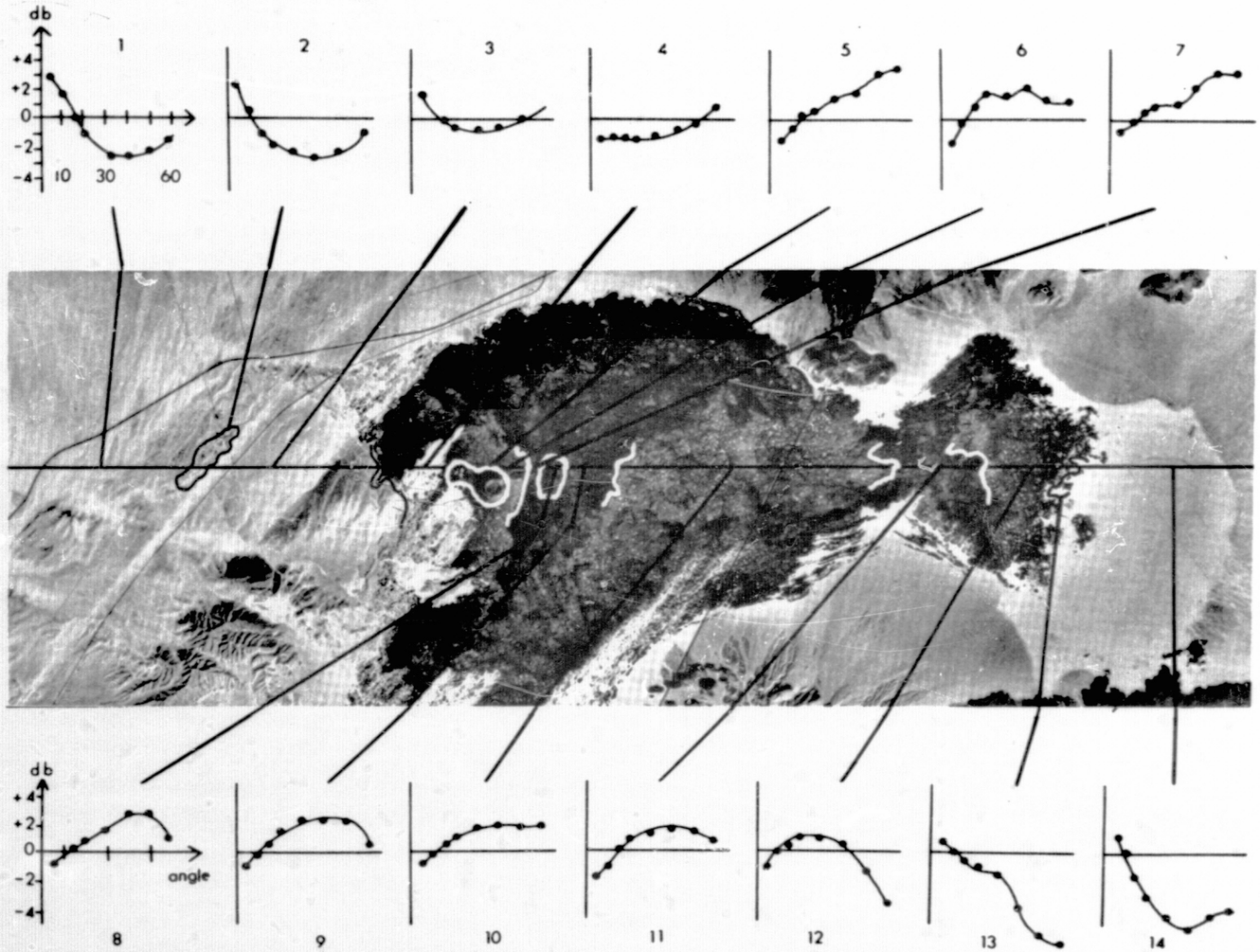

Figure 50-2.- Curves of difference between radar differential scattering coefficient and values for a mean curve compared with photograph of Pisgah Crater area from which the data were obtained by the 13.3-gigahertz scatterometer.

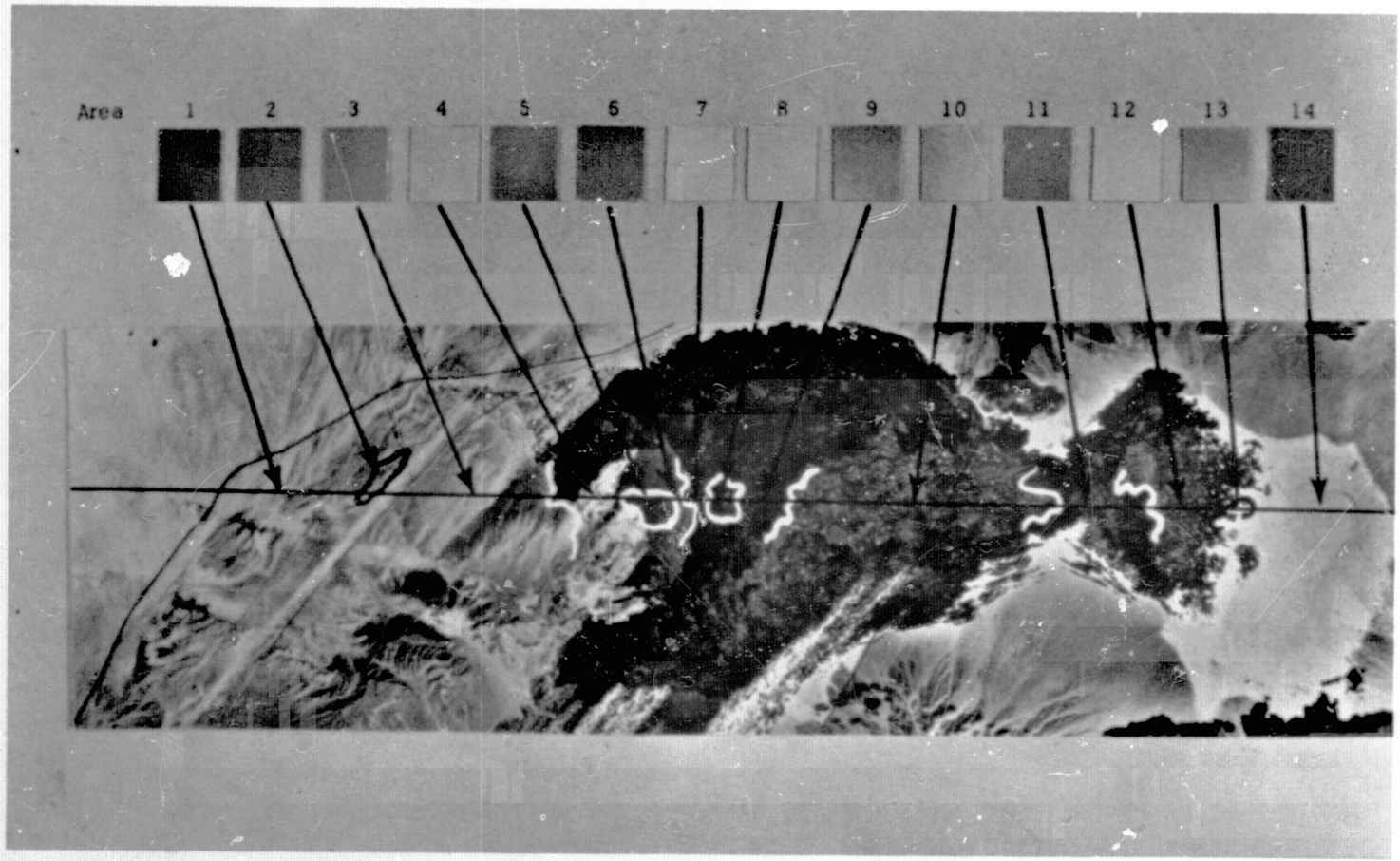

Figure 50-3.- Color codes for the information obtained by scatterometer from the Pisgah Crater area, compared with a photograph of the area.

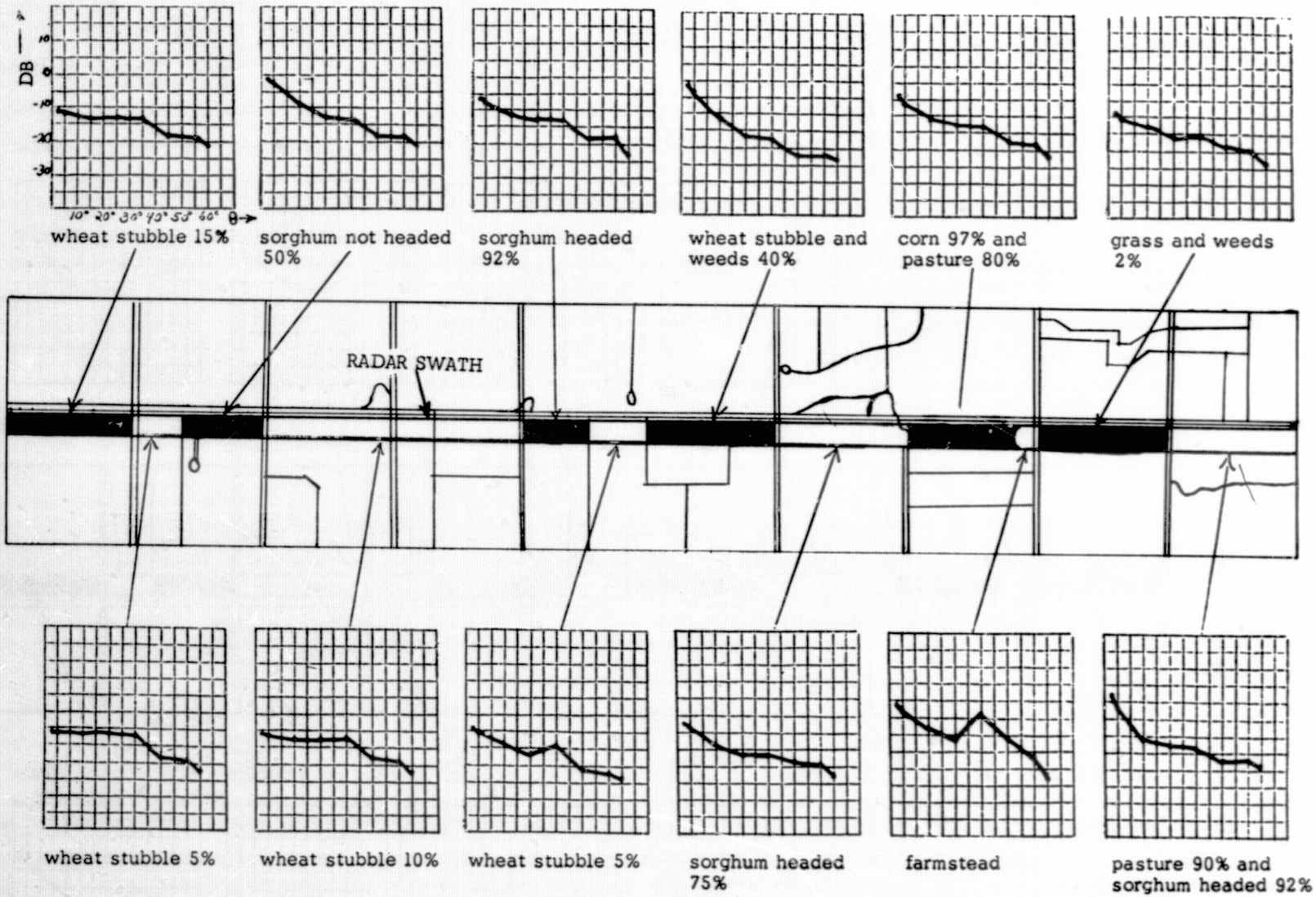

Figure 50-4.- Curves of radar differential scattering coefficient versus angle of incidence compared with a line map of the Garden City Test Site area from which the data were obtained with the 13.3-gigahertz scatterometer.

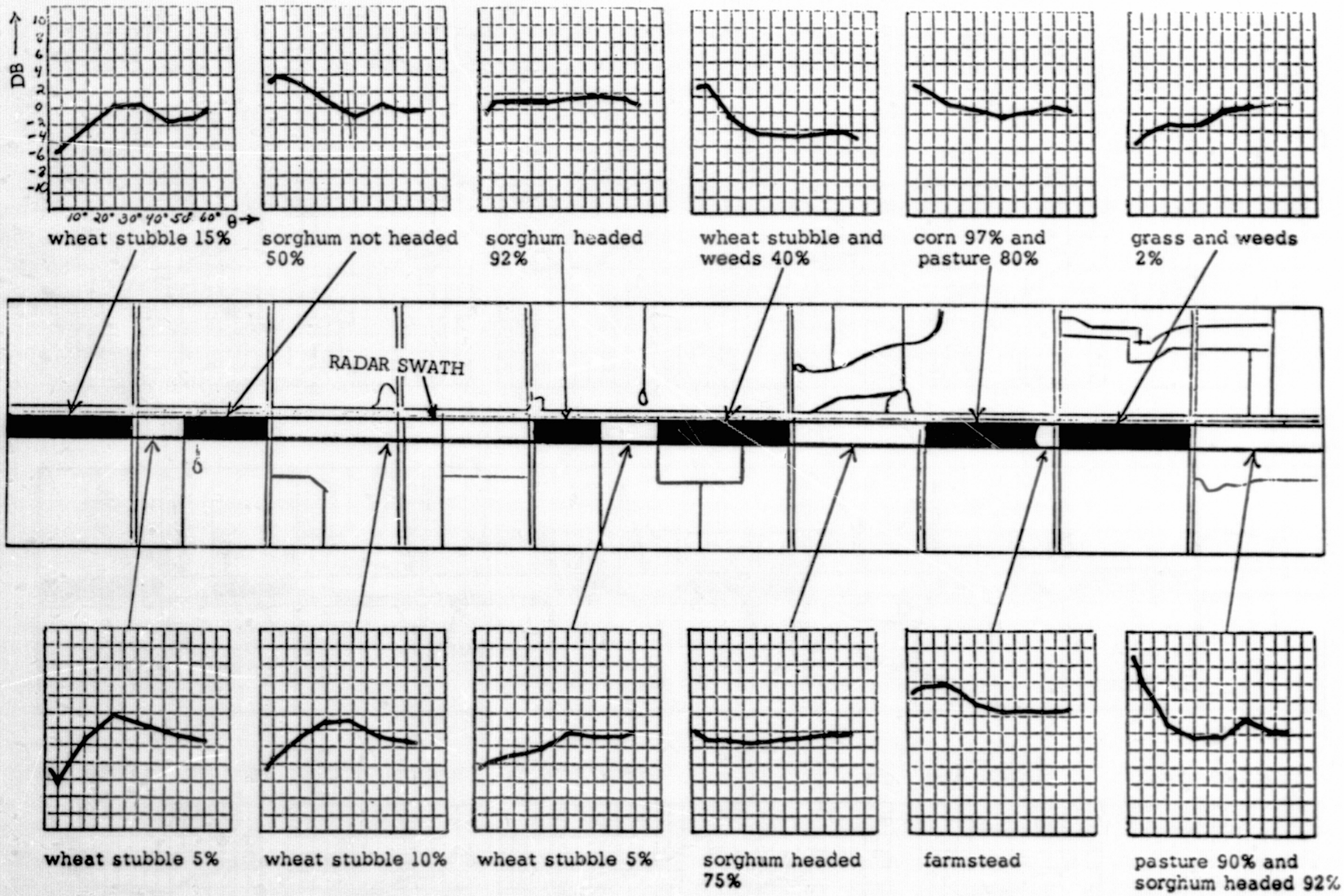

Figure 50-5.- Curves of difference between radar differential scattering coefficient and values for a mean curve compared with a line map of the Garden City Test Site area from which the data were obtained with the 13.3-gigahertz scatterometer.

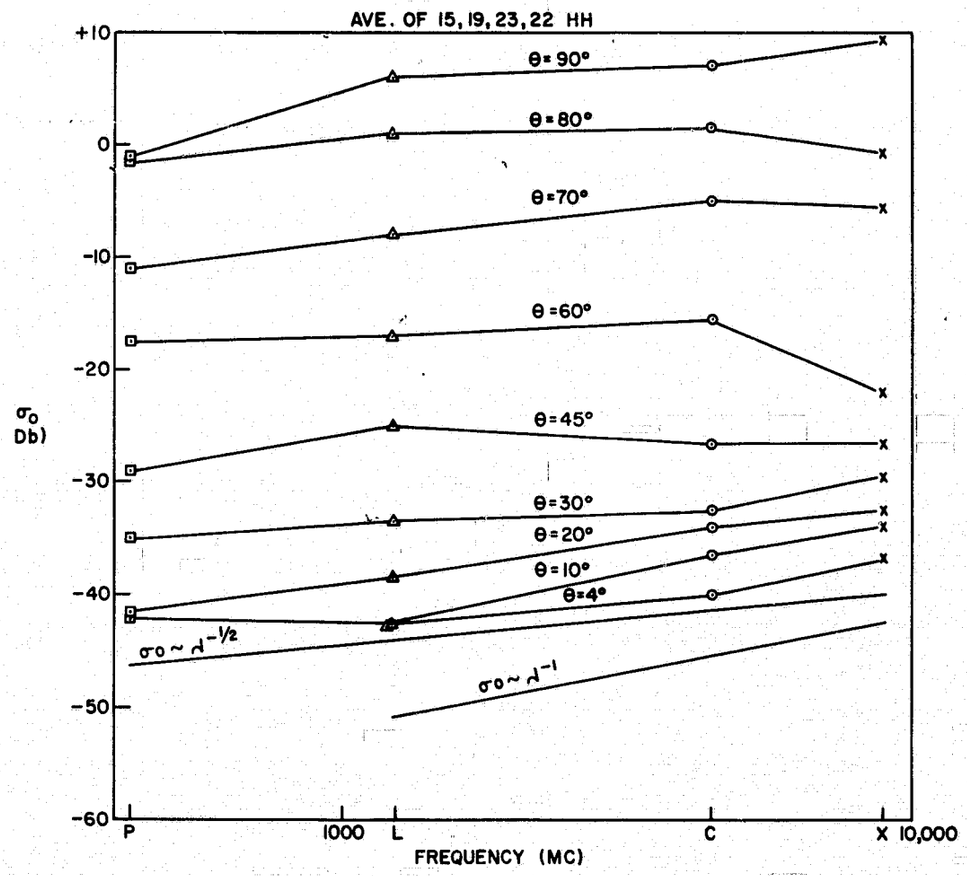

Figure 50-6.- Variation of radar differential scattering cross section with frequency as reported by Daley of NRL (horizontal polarization). The parametric angle is the elevation angle, the complement of the angle of incidence.

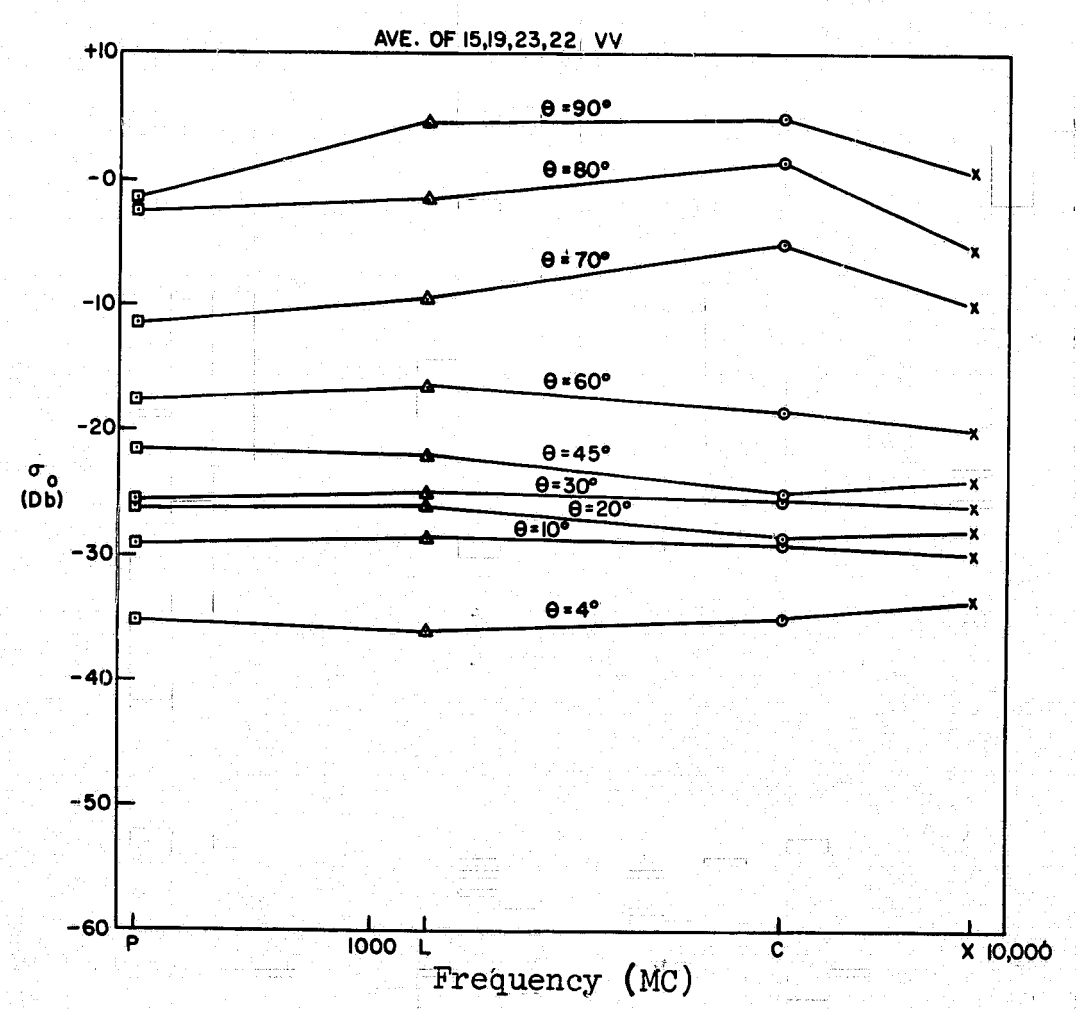

Figure 50-7.- Variation of radar differential scattering cross section with frequency as reported by Daley of NRL (vertical polarization). The parametric angle is the elevation angle, the complement of the angle of incidence.

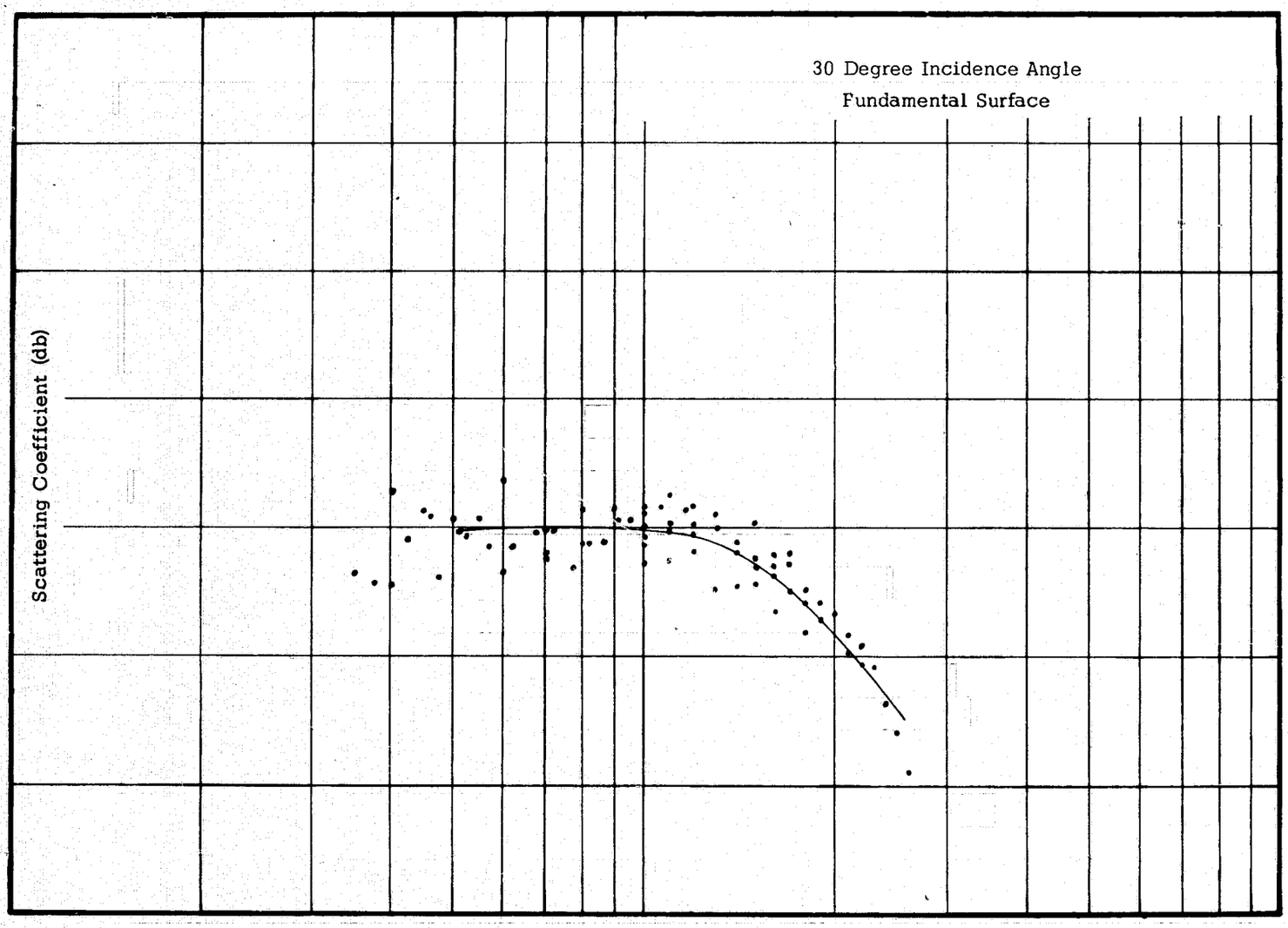

Figure 50-8.- Frequency dependence of scattering coefficient obtained by ultrasonic simulation (undulating surface).

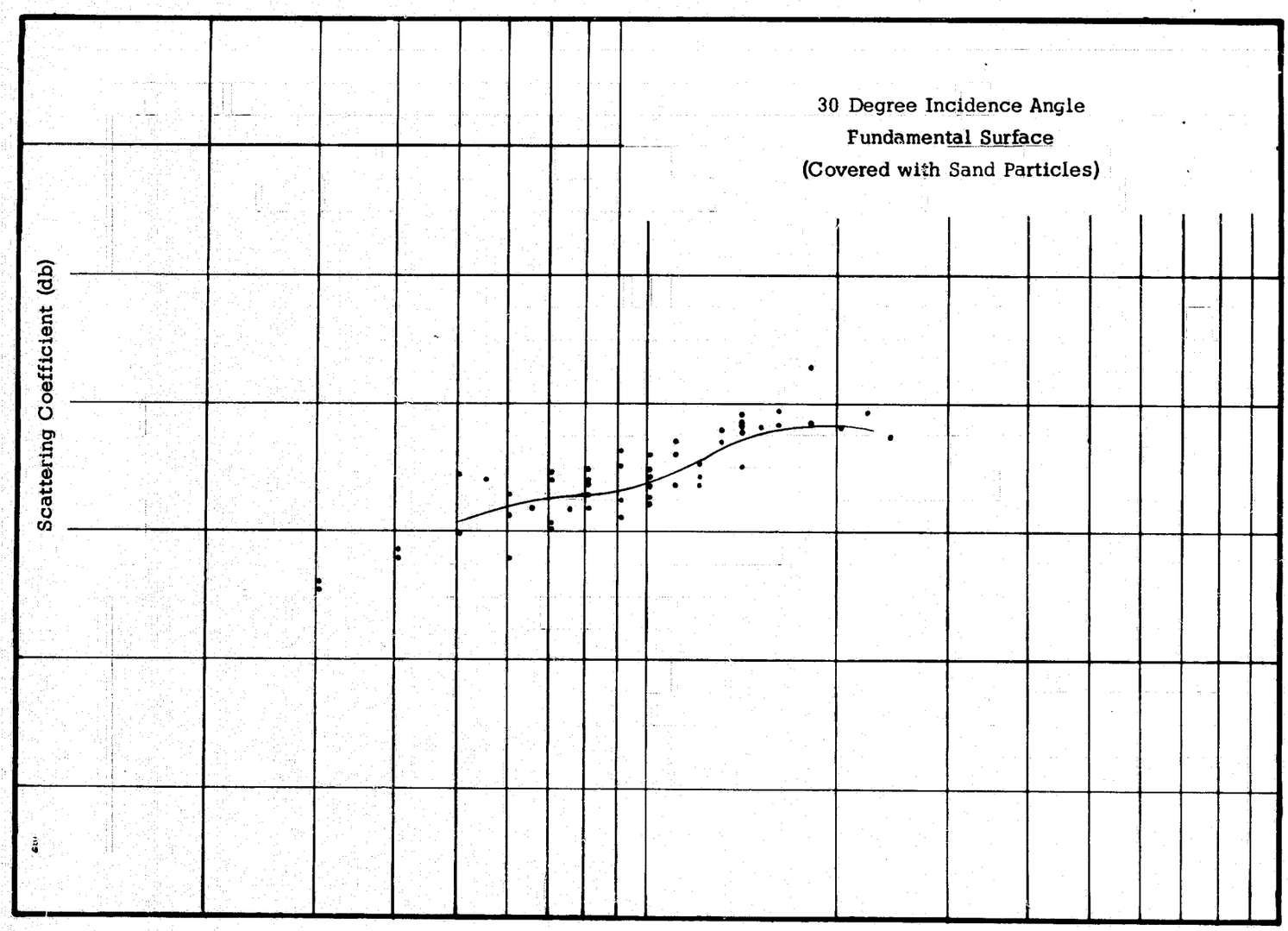

Figure 50-9.- Frequency dependence of scattering coefficient obtained by ultrasonic simulation (undulating surface roughened with sand particles).

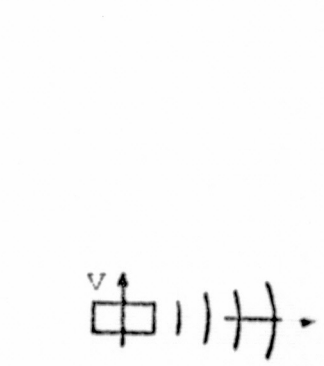

(a) Monochromatic image of two spheres
(f= 1.5 MHz)

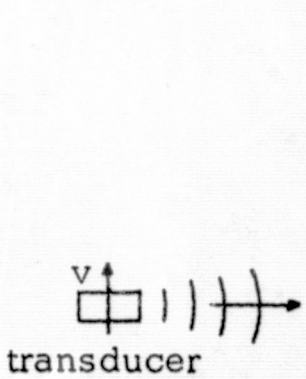

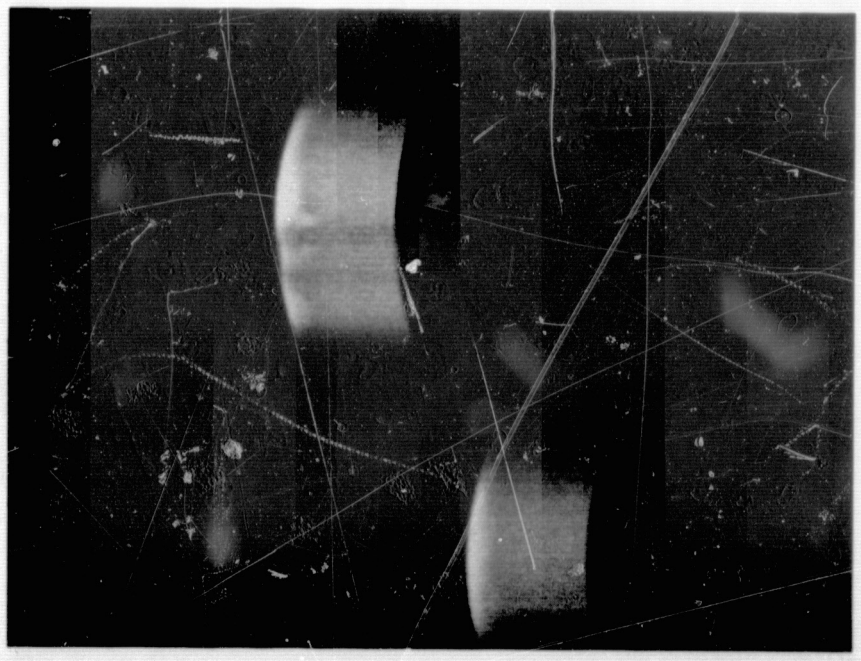

(b) Swept frequency image of two spheres
(f= 1.5 MHz ± 10%)

Figure 50-10.- Effect of frequency average on image of sphere targets.

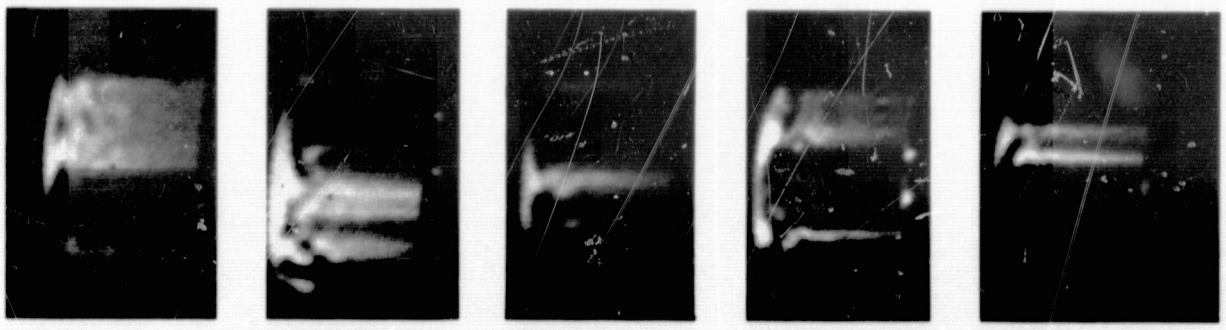

f = 1.43 MHz f = 1.52 MHz f = 1.64 MHz f = 1.74 MHz f = 1.82 MHz

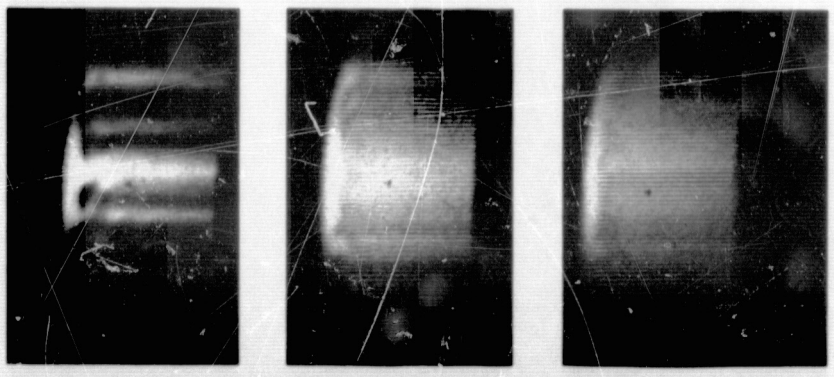

F = 1.64 MHz f = 1.64 ± 0.05 MHz f = 1.64 ± 0.1 MHz

Figure 50-11.- Monochromatic images of the same target made at nearby frequencies compared with panchromatic images with ±3-percent and ±6-percent frequency variation. These images were produced in the ultrasonic simulator.

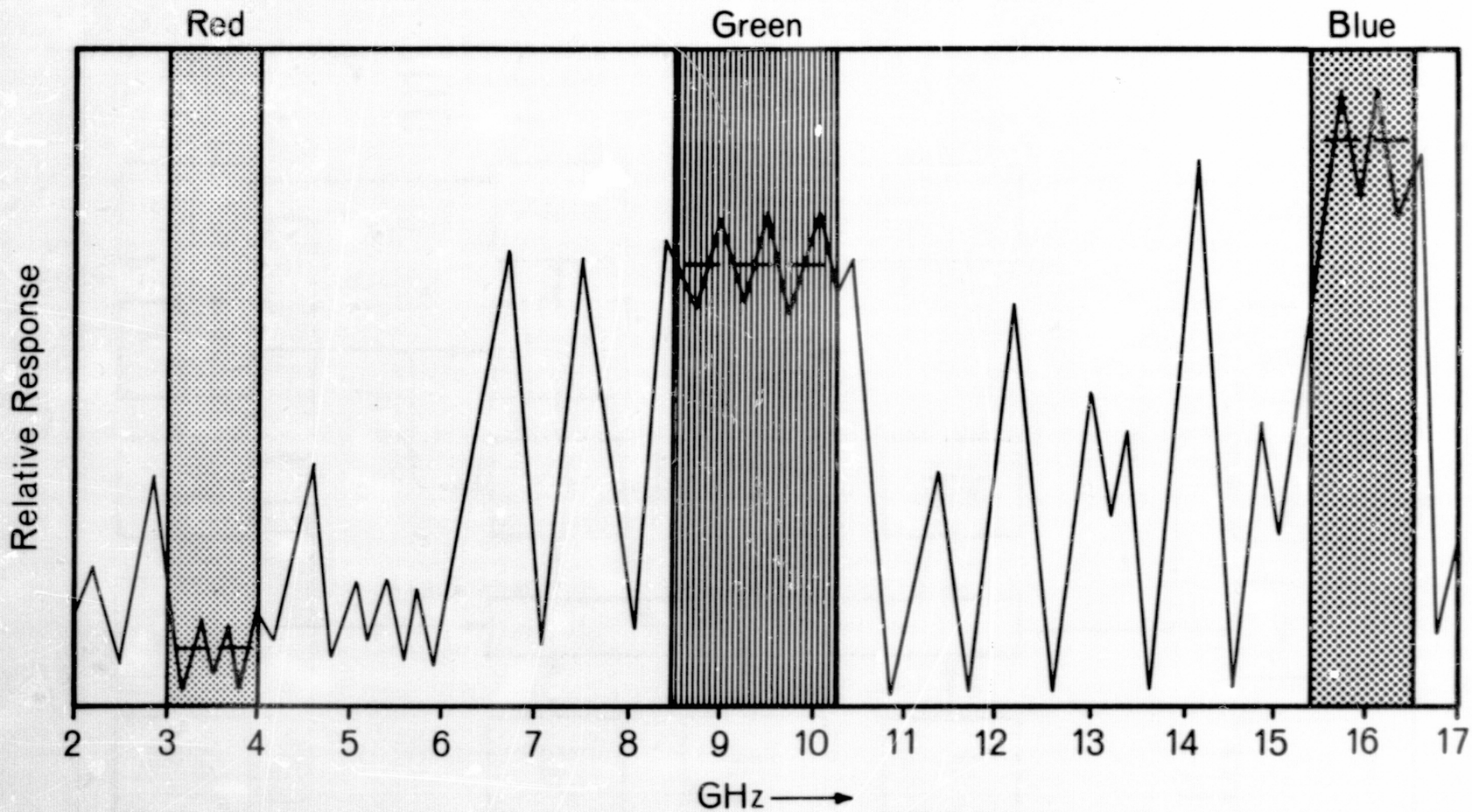

Figure 50-12.- Example of possible spectral-response-separated trichromatic radar.

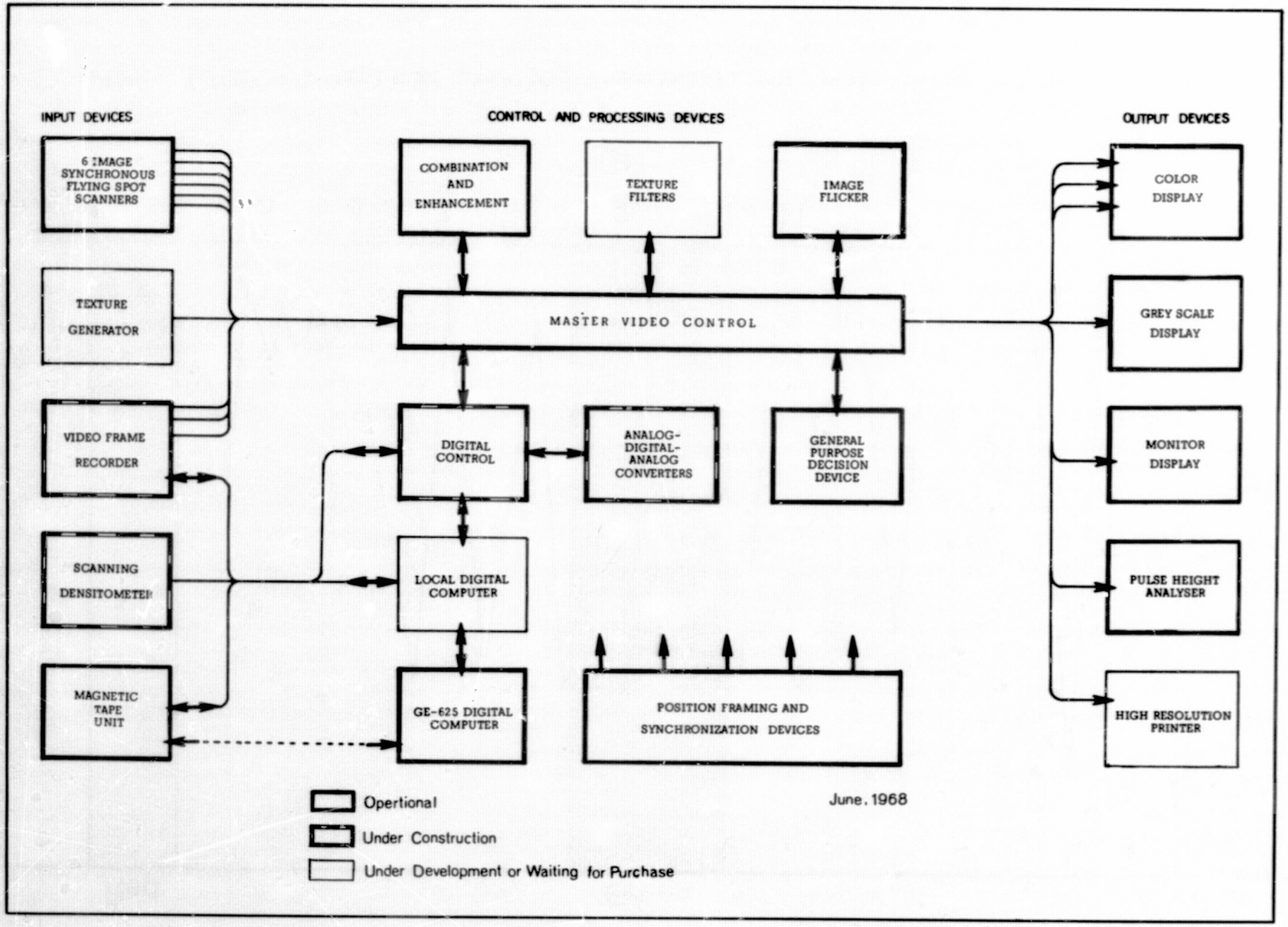

Figure 50-13.- Block diagram of the IDECS and associated equipment.

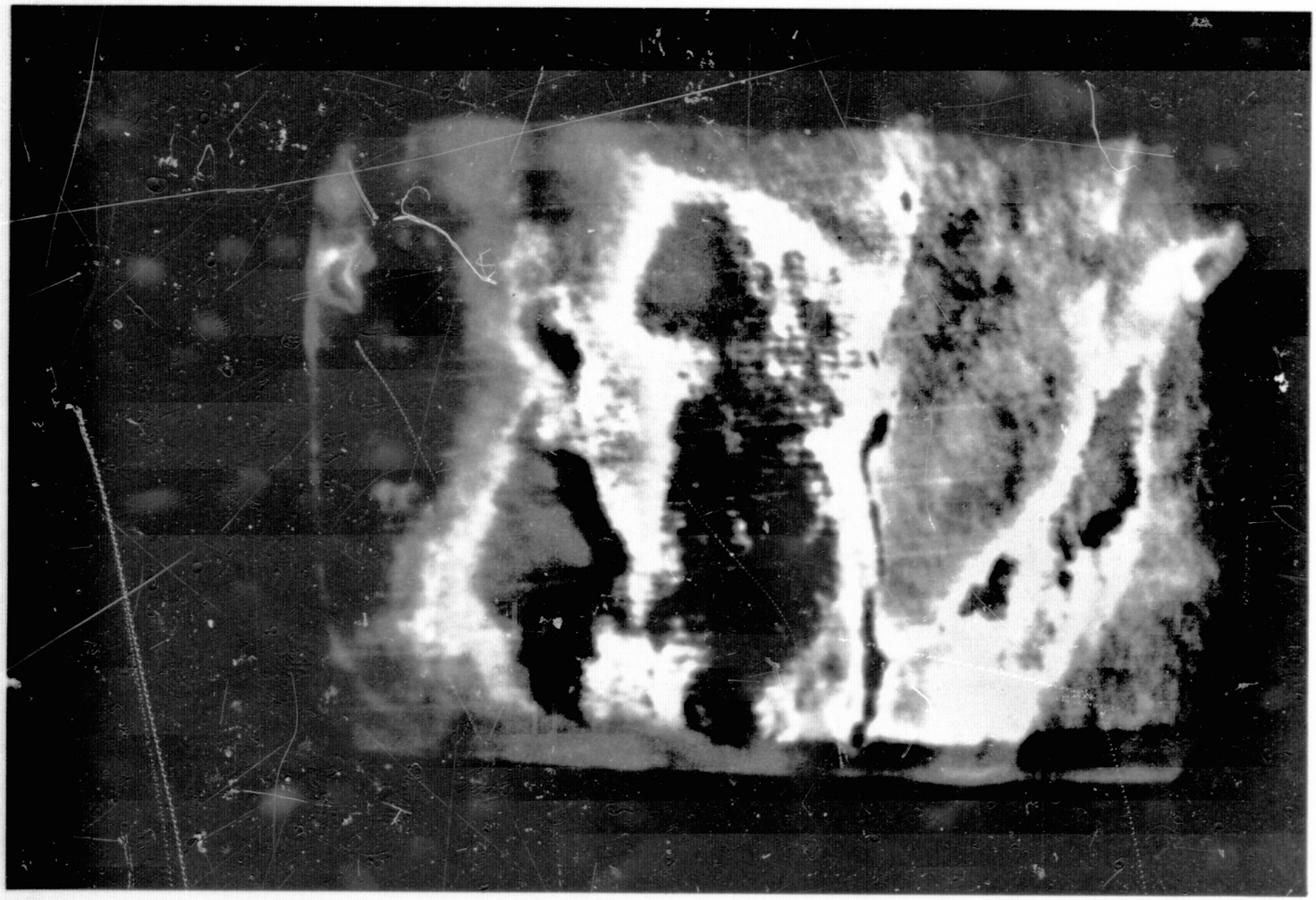

Figure 50-14.- False-color IDECS-enhanced image of Bucks Lake Test Site. Original data multi-spectral photographs from NASA aircraft 926 overflight.

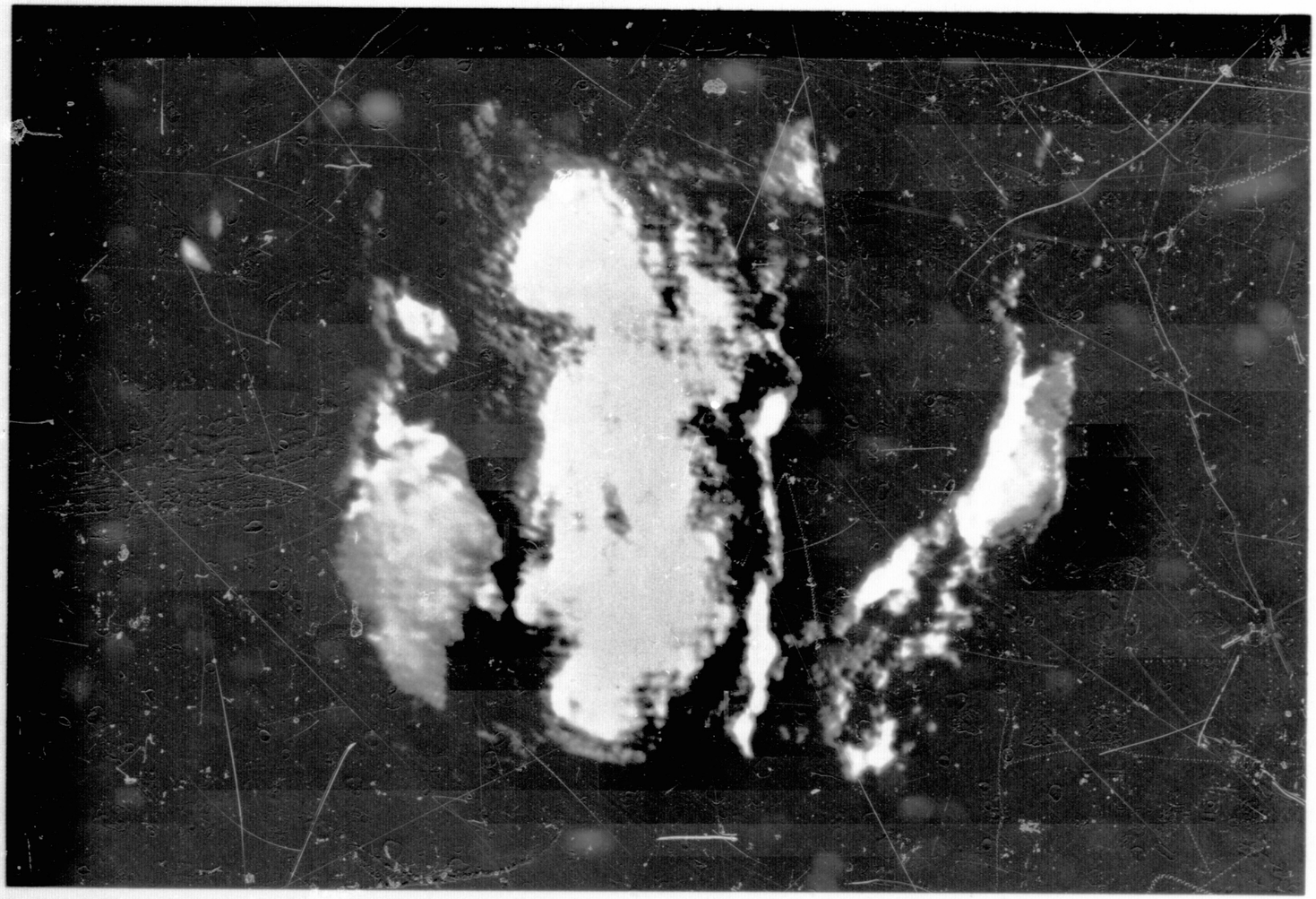

Figure 50-15.- False-color IDECS-enhanced image of Bucks Lake Test Site. Original data multi-spectral photographs from NASA aircraft 926 overflight.

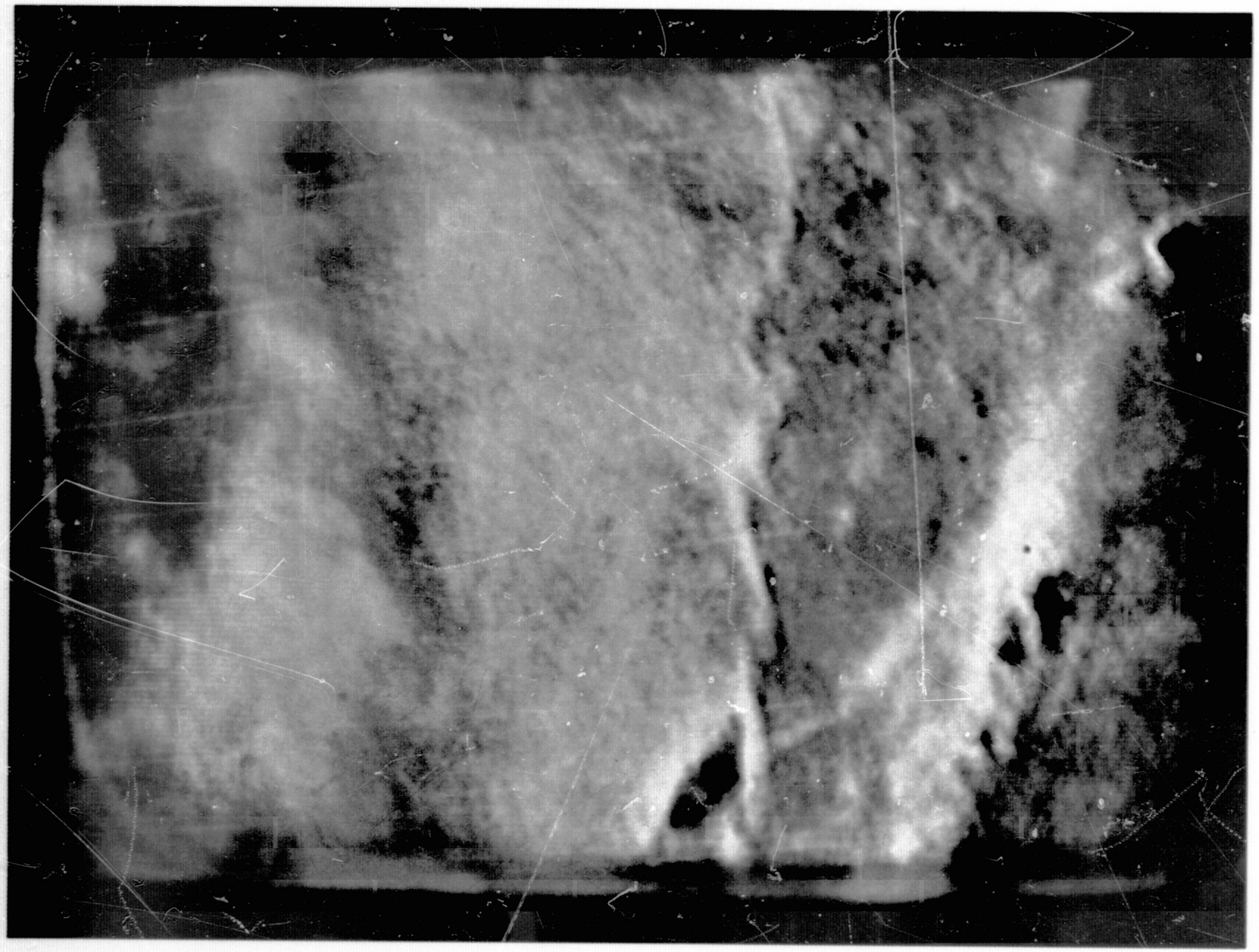

Figure 50-16.- False-color IDECS-enhanced image of Bucks Lake Test Site. Original data multi-spectral photographs from NASA aircraft 926 overflight.

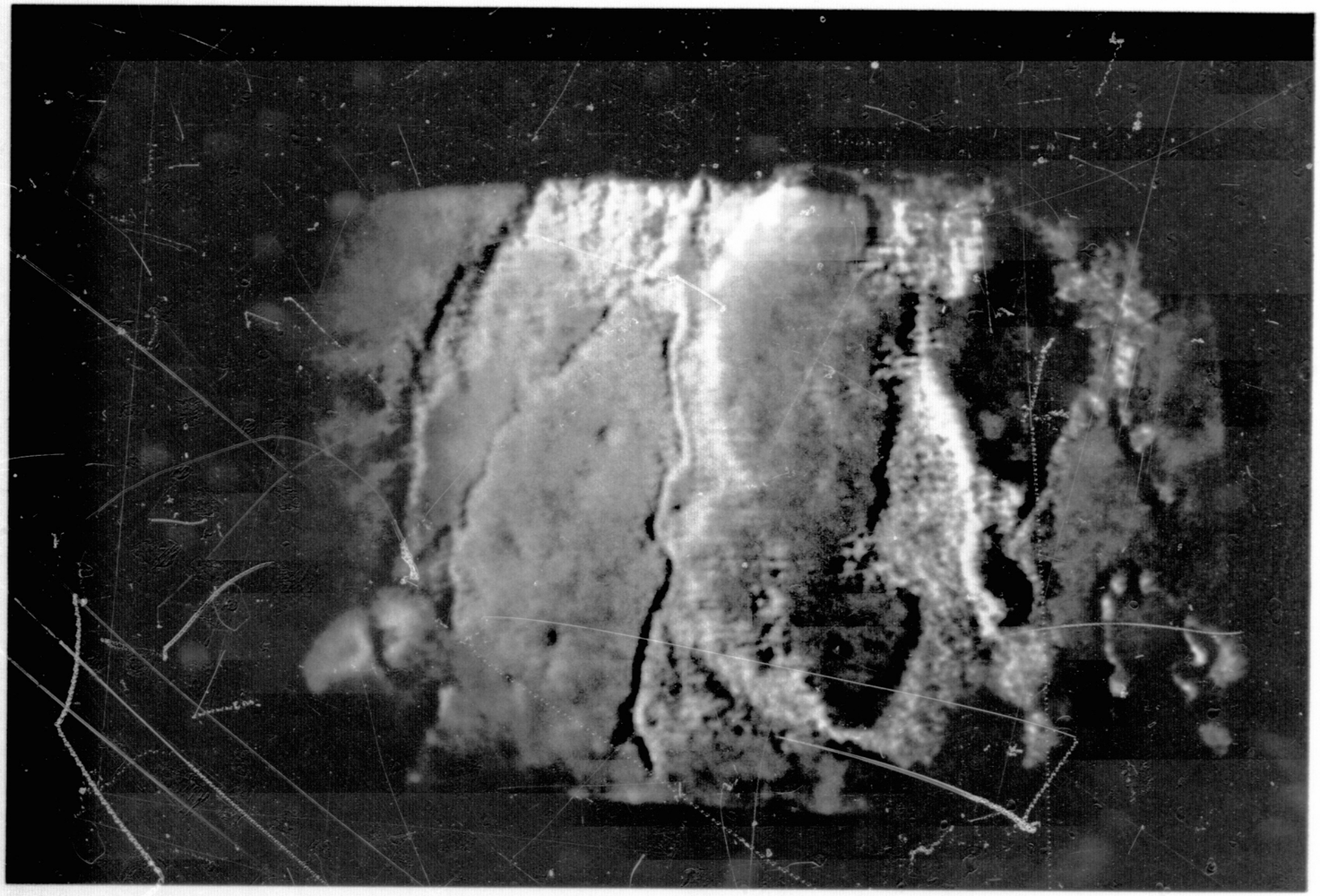

Figure 50-17.- False-color IDECS-enhanced image of Bucks Lake Test Site. Original data multi-spectral photographs from NASA aircraft 926 overflight.

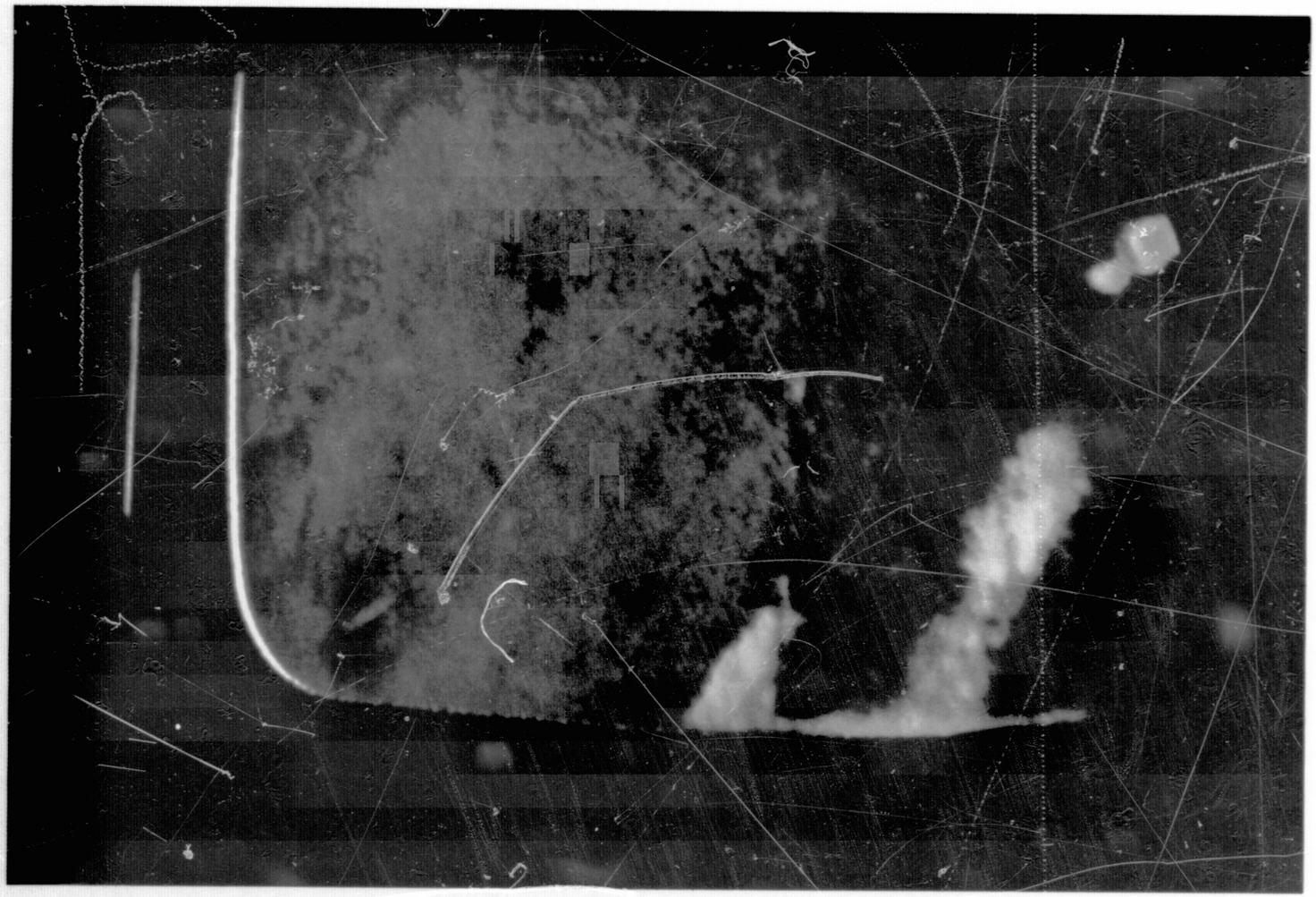

Figure 50-18.- False-color IDECS-enhanced image of Bucks Lake Test Site. Original data multi-spectral photographs from NASA aircraft 926 overflight.

Surface Cover Actually Measured:	Number of Measurements Identified as: (a) bare ground pasture	(b) grain sorghum, bare ground-wht., alfalfa wheat stubble-weeds	(c) corn	(d) sugar beets
(a) bare ground pasture	22 (91% cor. id.)	2	0	0
(b) grain sorghum, wheat stubble-weeds, alfalfa, bare ground-wheat	5	73 (91% cor. id.)	2	0
(c) corn	0	0	2 (67% cor. id.)	1
(d) sugar beets	0	0	1	5 (83% cor. id.)

Figure 50-19.- Identification accuracy for August-September 1965 radar imagery. A random sample of 113 measurements of field averages from a total set of 226 were used to train a Bayes' decision classifier, and the other 113 measurements of field averages were classified on the basis of the Bayes' decision rule. Ninety percent of the types of surface cover, grouped as shown, were correctly identified. Each field had the indicated type of surface cover for both the months of August and September, the exception being bare ground/wheat, which was bare ground in August and wheat in September. (The 91-percent-correct identification in groups a and b means that 91 of the measurements in each of these groups were actually identified as being in that group. In general, the individual types of surface cover within each group were completely confused with one another.)

Surface Cover Actually Measured:	Number of Measurements Identified as: (a) bare ground	(b) corn, alfalfa, grain sorghum, weeds, pasture, wheat stub.	(c) sugar beets
(a) bare ground	14 (52% cor. id.)	13	0
(b) corn, alfalfa, grain sorghum, weeds, pasture, wheat stubble	11	75 (85% cor. id.)	2
(c) sugar beets	0	1	6 (86% cor.id.)

Figure 50-20.- Identification accuracy for July 1966 radar imagery. A random sample of 129 measurements of field averages from a total set of 251 were used to train a Bayes decision classifier, and the other 122 measurements of field averages were classified on the basis of the Bayes decision rule. Of the types of surface cover shown, 78 percent were correctly identified in the groupings. (The 85-percent-correct identification means that 85 percent of the measurements in group b were actually identified as being in group b. In general, the individual types of surface cover in group b were completely confused with one another.)

NUMBER OF MEASUREMENTS IDENTIFIED AS:

Surface Cover Actually Measured	Alluvial Material	Porphyritic Olivine Basalt Flows of the Second and Final Eruptive Phases	Microporphysitic Olivine Basalt Flows of the First Eruptive Phase	Playa Lake Sediment
Alluvial Material	20	0	0	1
Porphyritic Olivine Basalt Flows of the Second and Final Eruptive Phases	15	67	3	3
Microporphysitic Olivine Basalt Flows of the First Eruptive Phase	0	0	7	0
Playa Lake Sediment	2	0	0	16

Figure 50-21.- Identification accuracy for Pisgah Crater scatterometer data. A random sample of 134 measurements from a total set of 268 was used to train a Bayes' decision classifier, and the other 134 measurements were classified on the basis of the Bayes' decision rule. Eighty-two percent of the measurements were identified correctly.

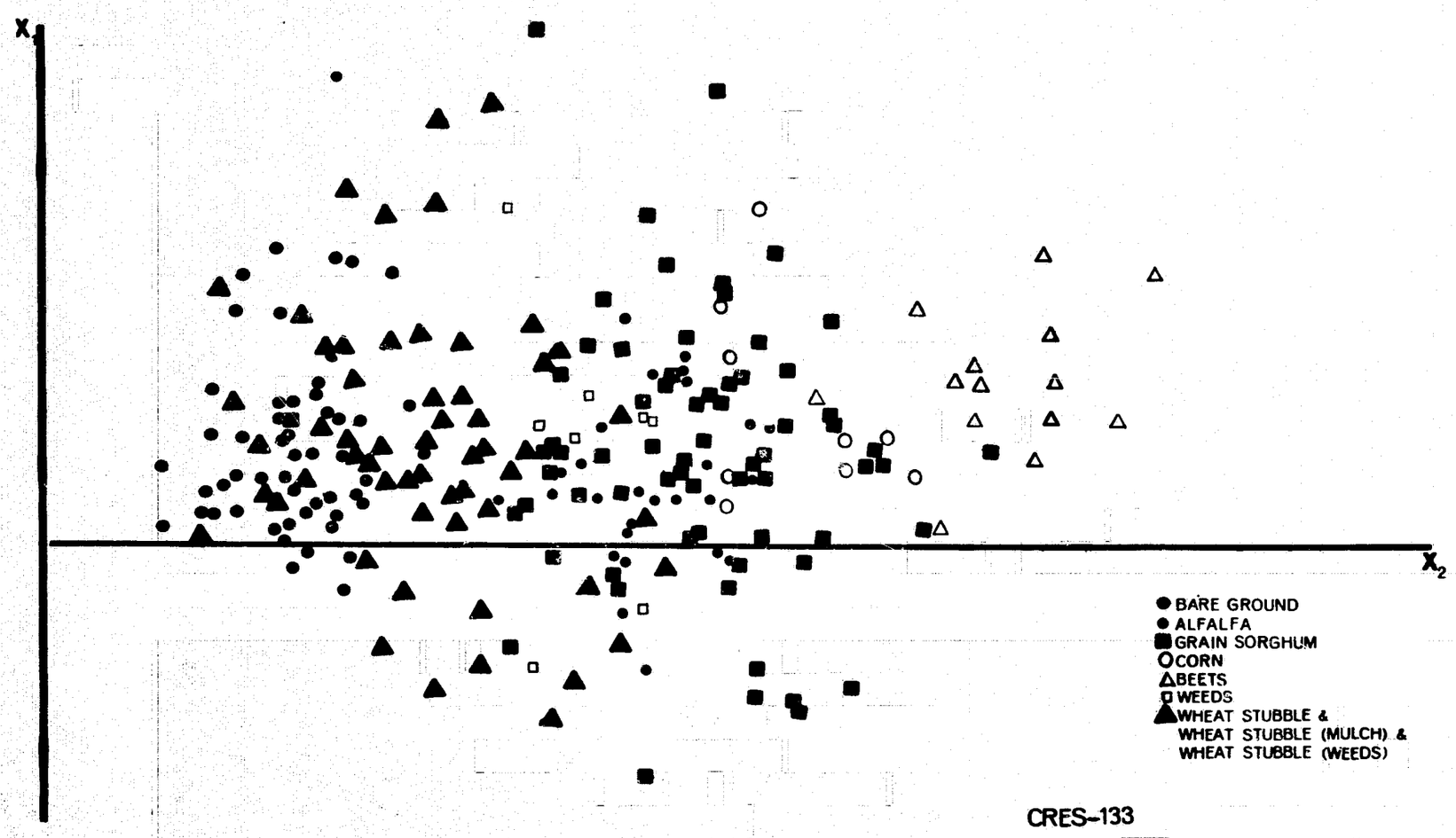

Figure 50-22.- Scattergram of July 1966 Garden City radar image data projected on its first two principal axes.

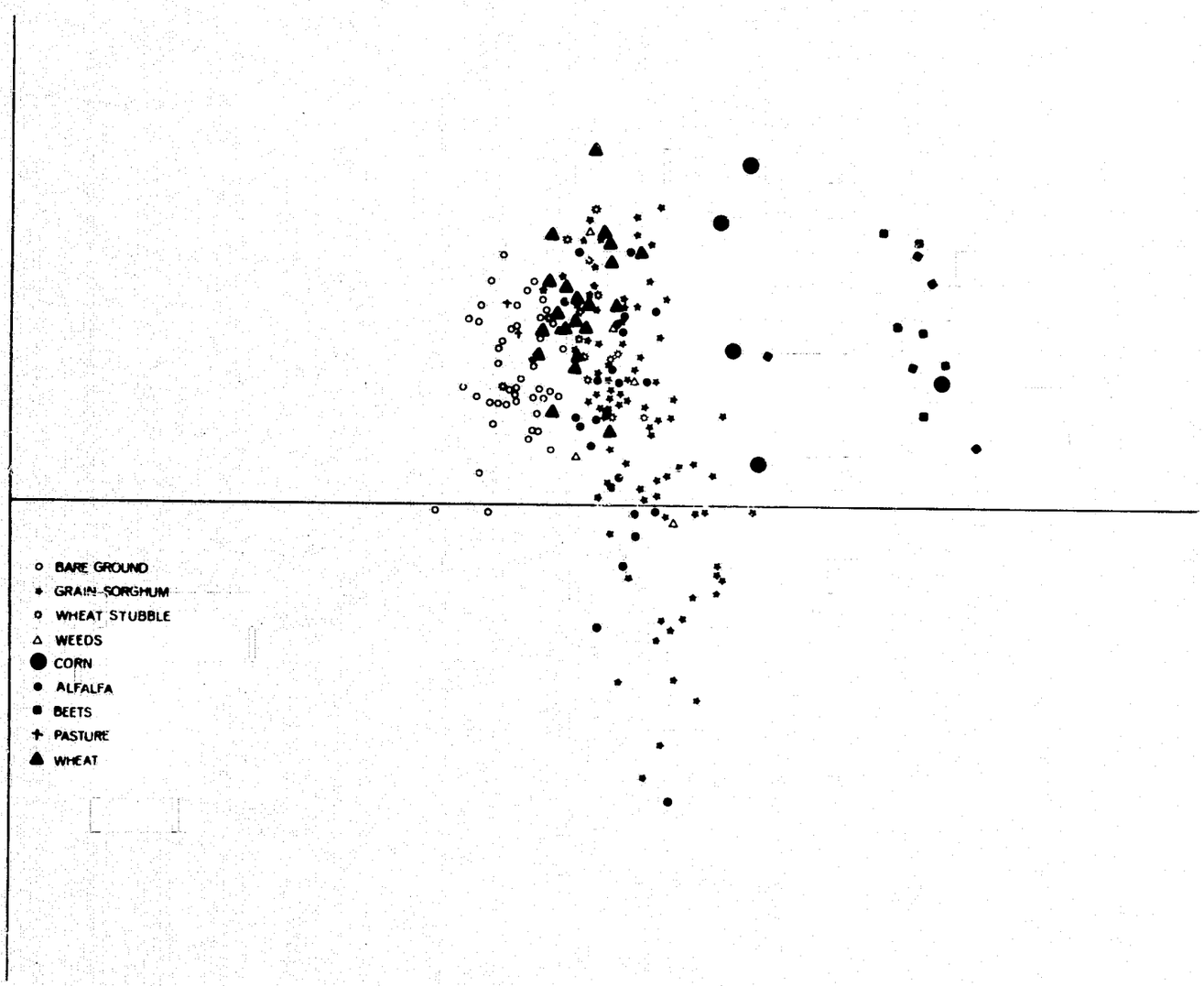

Figure 50-23.- Scattergram of August 1965 to September 1965 Garden City radar image data projected on its first two principal axes.

PHOTO 1 N(0,, 3)

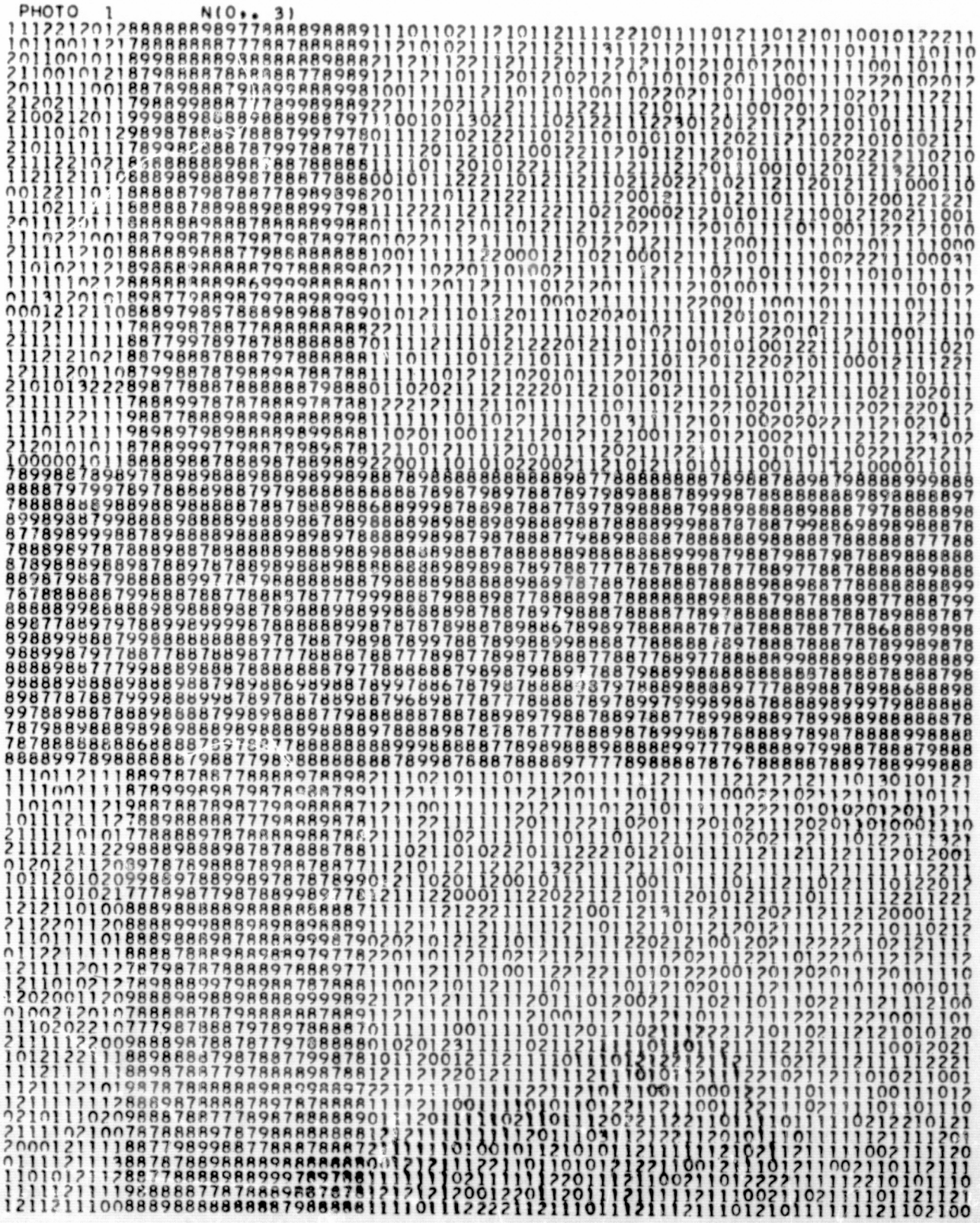

Figure 50-24.- Image 1 of made-up data.

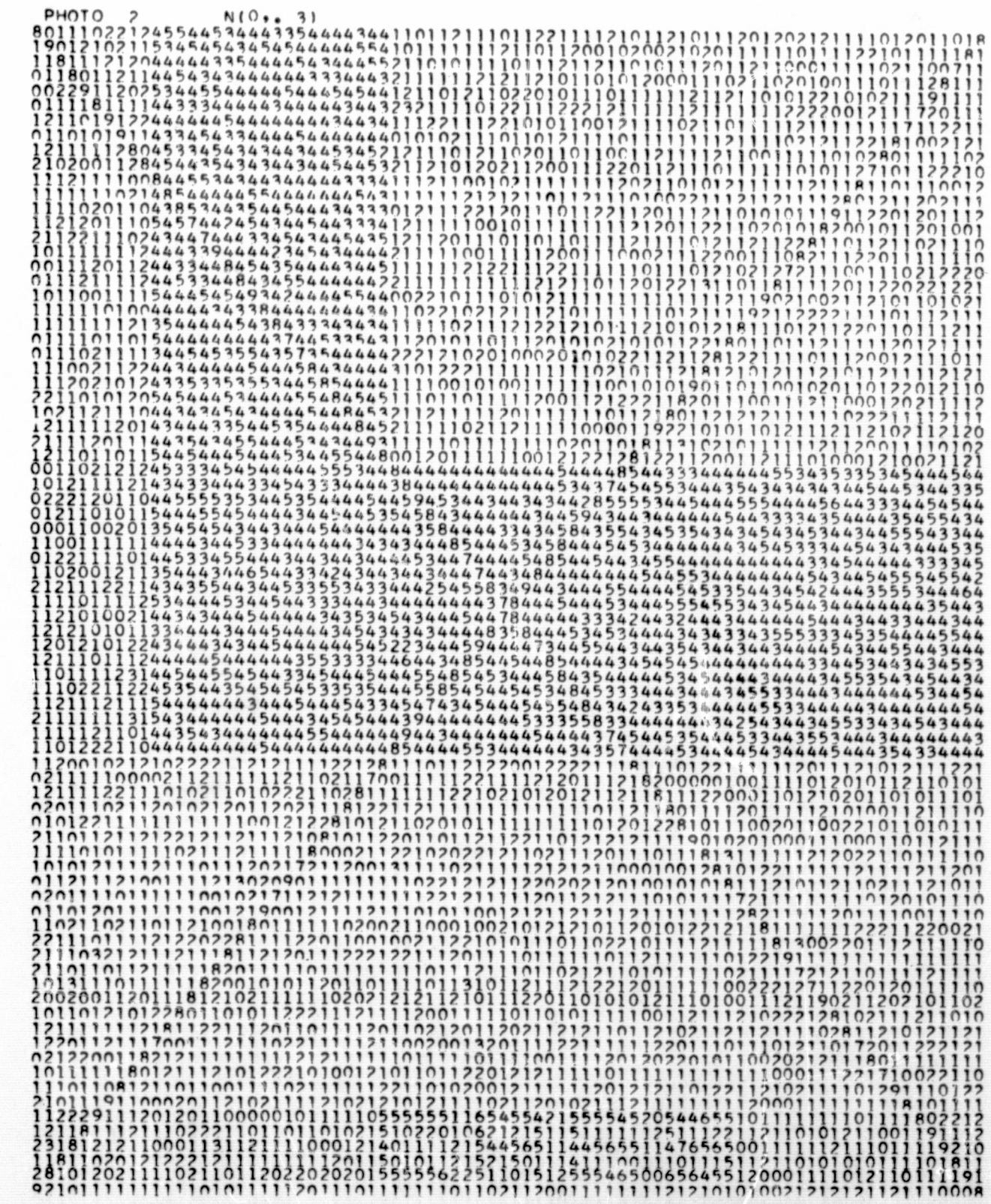

Figure 50-25.- Image 2 of made-up data.

PHOTO 3 N(0,, 3)

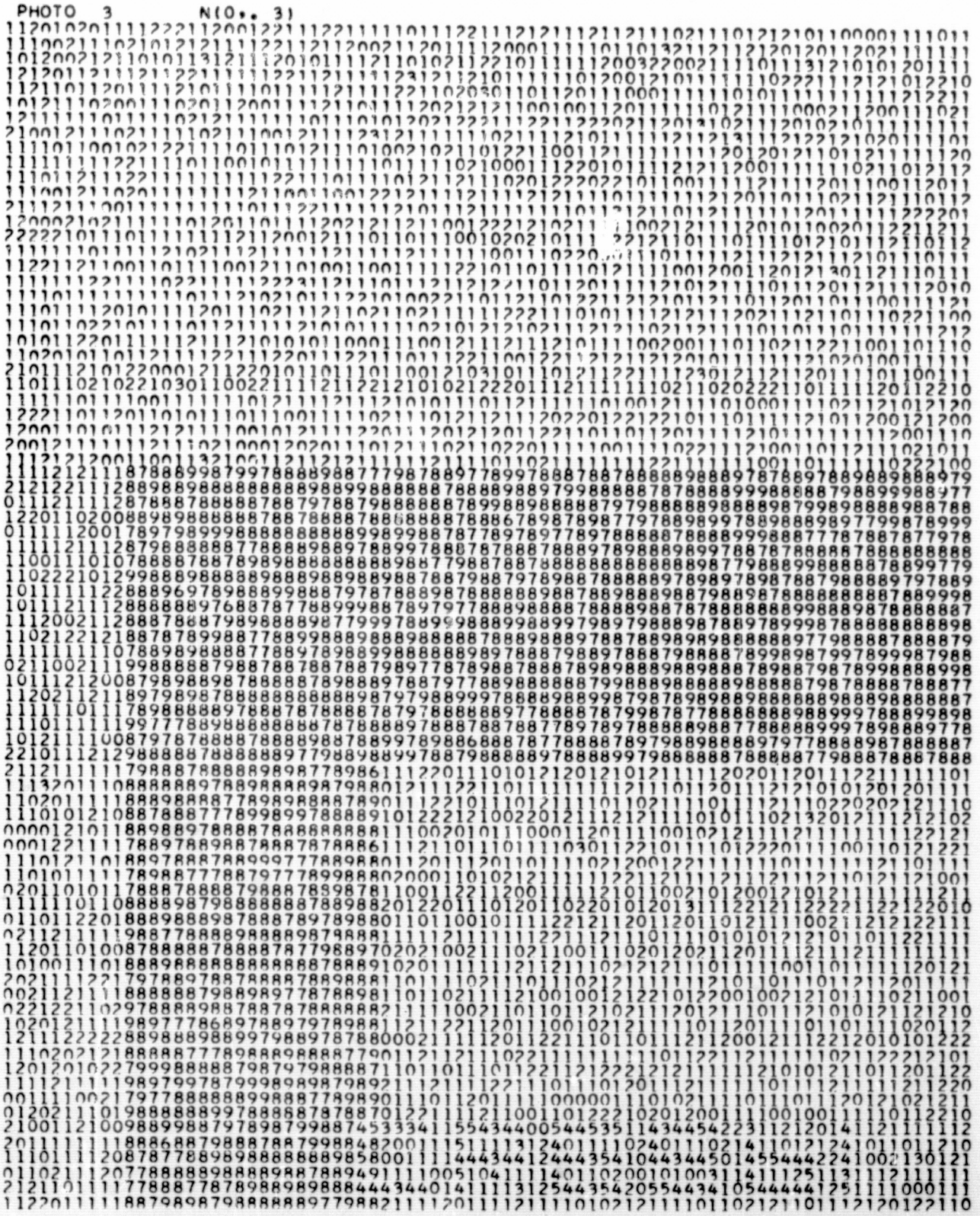

Figure 50-26.- Image 3 of made-up data.

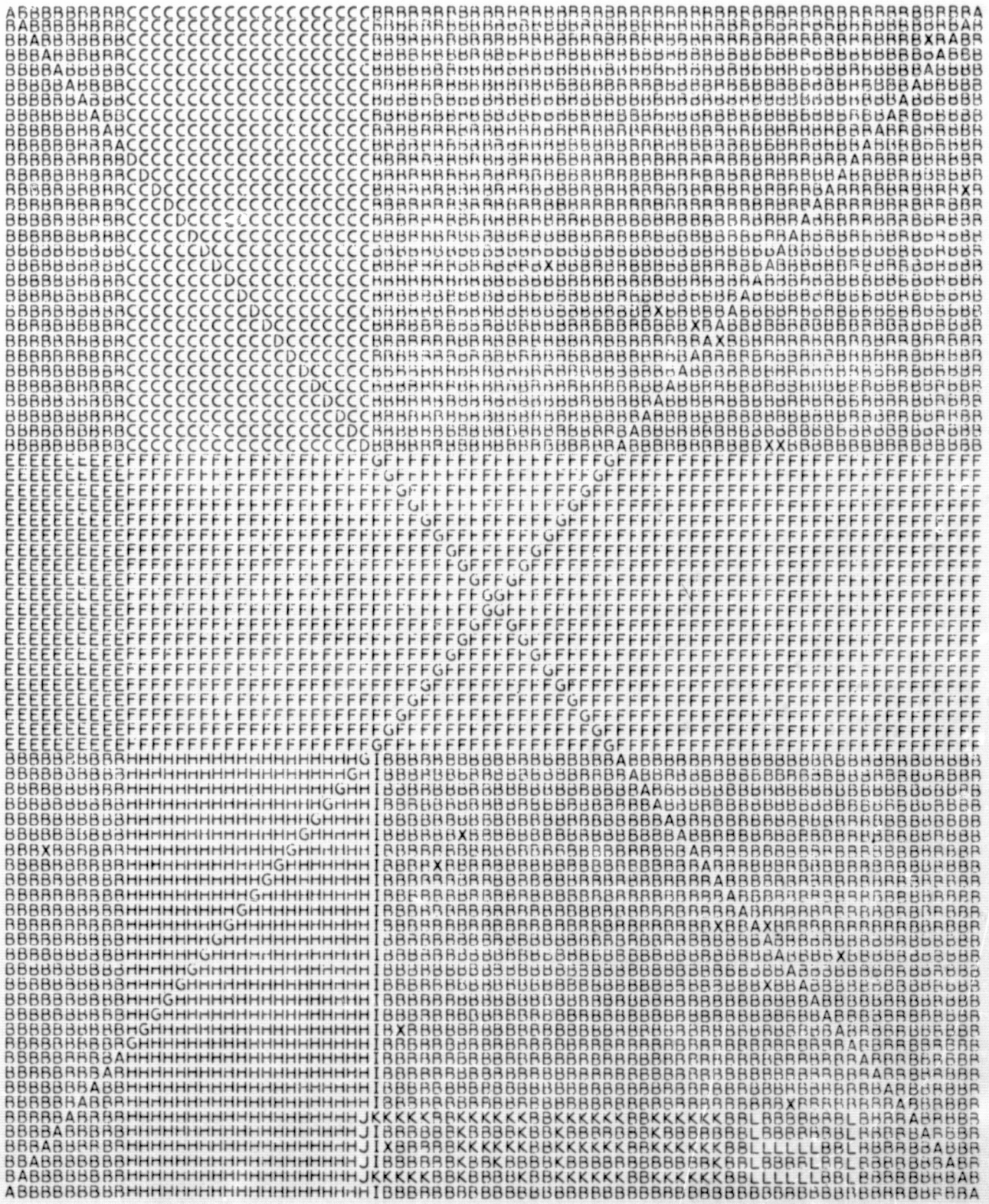

Figure 50-27.- Classified image of made-up data using spatial clustering.

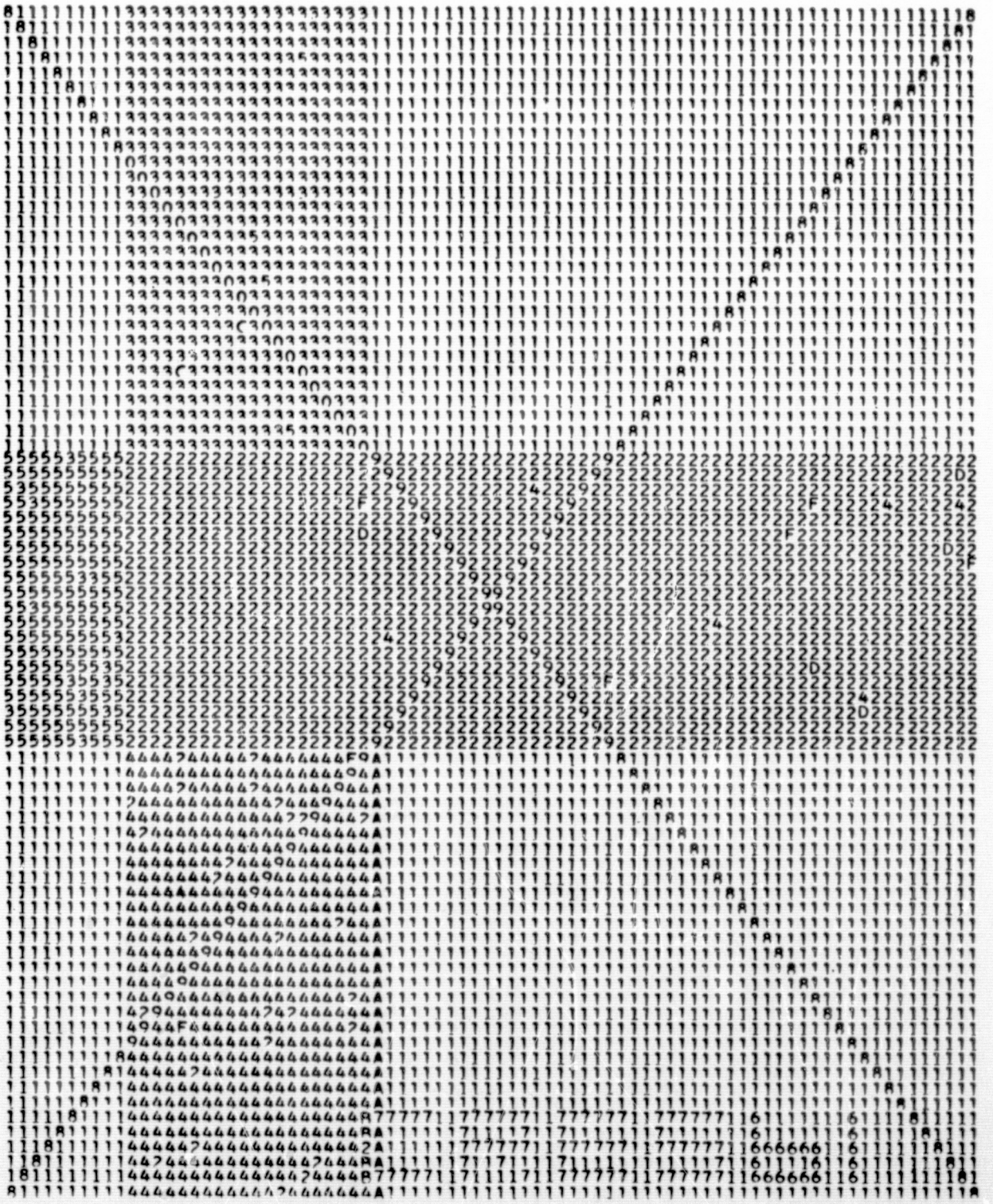

Figure 50-28.- Classified image of made-up data using measurement space clustering.

N71-16146

INFRARED STUDIES

By D. S. Lowe
University of Michigan

The NASA Remote Sensing Aircraft Program uses infrared (IR) scanners for thermal mapping and multispectral sensing. This paper discusses a few aspects of what can or cannot be done with the current scanner instrumentation.

Optical-mechanical scanning is a well-established technique despite the many engineering problems that seem to plague scanners. Some examples of optical-imaging scanners are early television systems, aerial reconnaissance scanners, the Nimbus scanning radiometers, and more recently, the Soumi spin-scan camera in the ATS satellite. Compared with cameras of comparable resolution, the scanner, though simple, is relatively complex. Why then, use scanners? The following are some of the advantages:

1. The scanners can operate in any region of the optical spectrum.

2. The electrical signal can be readily transmitted, recorded, analyzed, or processed as needed or desired.

3. The detectors generally have a very large dynamic range, and the detection process is reversible. (That is, unlike photographic film the detectors are reusable.)

4. The sensor is amenable to calibration and can yield quantitative data.

5. Collection of data simultaneously in many wavelength channels is possible.

To be detected, an object must be contrasted with its background. To identify, one needs additional information which is gleaned from such parameters as shape, tone, texture, environment, and knowledge of the subject matter. We have seen a number of examples of investigators searching for the optimum wavelength of best contrast. About 6 years ago, researchers at Michigan recognized that conventional black and white images are limiting in their ability to contrast an object in a large variety of backgrounds. In large-area search, it is apparent that

some means of object-to-background contrast enhancement would be desirable for quick detection. Since spectral information is lost in systems that record broadband reflectance or emittance, the question was asked whether or not a sensor could be developed which would use the spectral information in a scene so that the resulting image contrast takes advantage of this spectral information. For example, perhaps the tone in the resulting image may represent how well the spectrum of a scene point correlates with one known to exist for the object being sought. If contrast is enhanced to the point that all backgrounds are suppressed, one then has spectral recognition of the object. The multispectral sensor described in the following discussion was designed to investigate the feasibility of developing such a sensor.

In an IR scanner the detector is used as the field stop, and a filter is placed in the radiation path to limit the wavelength of operation. Instead of throwing away this unwanted radiation, the entrance slit of a multichannel spectrometer can be used as the field stop (fig. 51-1). In such a system, each detector of the spectrometer observes the same resolution element of the scene, but in a different wavelength region.

The airborne multispectral instrumentation at Michigan obtains data in 18 bands simultaneously in the wavelength interval of 0.32μ to 13.5μ. Four scanners are used to obtain this coverage. Twelve channels are collected with a multichannel spectrometer so that the signals are registered and can be mixed or processed electrically. Two of the scanners are fitted with filtered three-element arrays of InSb and InAs detectors. The detectors are alined to scan a scene point sequentially, and the video signal can be brought into registration through time-delay lines. Other spectral bands are obtained with a filtered ultraviolet (UV) photomultiplier and/or filtered single-element InSb and Ge:Hg detectors.

The output signal from each detector element is a video signal corresponding to the scene brightness in the particular wavelength region of operation. The tape-recorded multichannel video signals can be displayed and analyzed in a number of ways to obtain information about the spectral characteristics of signatures necessary for designing an optimum signal processor for an operational spectrum-matching sensor.

Figure 51-2 shows typical A-scope traces from two channels of data. In this format, the detector signal deflects the oscilloscope beam in the y-direction, while the scan position within a line is the x-direction. This format is not too unlike a microdensitometer trace over a photograph. In the two traces of figure 51-2, at the left the detector is looking inside the dark scanner. As the detector moves to the right, it scans the scene below the aircraft and then back inside the scanner and two calibration sources.

Another useful way to examine the data is shown in figure 51-3. This figure shows two examples where the video signals from two channels are used to deflect the beam of an oscilloscope in the x- and y-directions. Since the deflection in the x-direction is determined by the signal from one wavelength channel (color) and the signal in the y-direction from another channel, this x-y plot can be considered to represent a two-dimensional color space. As the tape-recorded data are played back, the position of the oscilloscope beam is determined by the brightness of the resolution element in the two bands used to deflect the beam. Inspection of data played back in this manner allows one to make judgments of the color variations in the scene.

The video signals from the multiple detectors can be sampled to determine the spectral distribution of the radiation from scene elements. Figure 51-4 shows a sampled raw spectrum of a calibration panel as observed by the 12-channel scanner, and figure 51-5 shows the reduced spectrum of the panel. The solid curve is the spectrum as measured in the laboratory. This measurement is what is called hemispherical reflectance. In the field, hemispherical reflectance is not observed, since direct solar illuminance, plus down-welling radiation from the clouds and sky, are available. The circles represent the spectrum value measured by a spectrometer on the ground under natural illumination during the overflight of the aircraft. The x's are the reflectance values observed with the airborne scanner as it flew over, taking approximately 20 000 spectra/sec. These spectra do not have to be reduced manually. Rather, the data can be digitized and analyzed by a digital computer.

To determine the effect of observation and illumination angles on the spectral signature of crops, the aircraft is flown low over large fields so that they subtend a large angle beneath the aircraft. Figure 51-6 shows a computer print-out of the manner in which the radiance of a wheat field varies with scan angle in four wavelength channels. Each scan line represents the mean value of as many as 100 scan lines. It can be noted that there is correlation among channels (i.e., all the signals increasing with angle). The cause of this effect is illustrated in figure 51-7, in which the aircraft heading with respect to the sun is changed. When the scan plane is parallel to the sun, the scanner observes the field under highlighted and backlighted conditions. Under this condition, the signal varies strongly with angle. When the scanner scans perpendicular to the plane of illumination, the signal is relatively constant with scan angle.

While the variation in reflectance with angle at first appears too formidable to correct, it is interesting to see how the spectral information varies with angle. Figure 51-8 plots the signal from a wheat field in color space using the signals from channels 5 and 10 of the multispectral scanner. It is noted that there is a strong correlation

in variation of the signals from these two channels as the angle of observation changes. With the knowledge of the spectral characteristics of objects and their background it is possible to develop optimum decision rules for making the spectral discriminations as shown by Hoffer, Landgrebe, and Holter.

The current multispectral scanner has the serious shortcoming that it operates in a narrow interval of the optical spectrum. In 1966, the University of Michigan performed a design study for NASA and came up with the specifications of an instrument given in table 51-I. This scanner would cover the spectral interval of 0.32μ to 13.5μ in as many as 29 bands with perfect time and space registration.

TABLE 51-I.- SCANNER-SPECTROGRAPH SPECIFICATIONS

Velocity/height (VH), radians/sec^{-1}	0.1
Angular resolution β, radians	0.003
Collector aperture, cm	15 (6 in.)
Scan mirror rate, rpm	2000
Amplifier bandwidths, kcps	35
Spectral resolving power, $\lambda/\delta\lambda$, at 0.6μ and 10μ	20
Performance, (1) NE Δρ, percent for direct solar illumination and $\lambda < 2\mu$	<1

Turning now to IR imagery, I would like to make two comments regarding tonal distortions. Many of the earth resource applications require a scanner to determine surface temperature on a quantitative or semi-quantitative basis. For ease of signal handling and recording, the electronics of scanners developed by the military are ac coupled. As a result, the average signal level at the output of the electronics is zero, and the instantaneous signal is known only as to its value with respect to this average. In such a system, the tone of an object in an image is dependent upon other objects that lie within the scan lines which determine the average signal level. Consider a scanner flying parallel to a land/water interface. Assume that the land is warmer than the water and that two passes are flown, one directly over the shoreline and the other off shore. The resulting video signals from ac-coupled

electronics are hypothesized in figure 51-9, along with the average signal level. As shown in figure 51-9, the signal difference B between land and water is independent of the flight line, while the magnitude of the voltage representing land A is smaller when the scanner is flown over the shoreline than when it is flown over the water. Thus, when the scanner is flown off shore, both the land and the water appear warmer in the imagery than when the scanner is flown directly over the shoreline. The difference in signal between land and water, however, is the same. By similar synthesis of video signals over terrain, it can be shown that the tone of any object in the imagery is affected by the signal from other objects within its environment. Figure 51-10 shows imagery generated with an ac-coupled scanner without dc restoration. It should be noted that thermal patterns are clearly evident, but that some of the tonal variations (vertical striations) are an artifact of the instrument arising from ac coupling.

This problem of nonquantitative tones in ac-coupled imaging systems can be readily corrected by a technique known as dc restoration. This technique requires that the video signal contain a repetitive signal of constant level from a source whose position in the video is known. One such signal may be the inside of the scanner housing, provided it can be made constant throughout the data-collection mission. Since the relative magnitudes of the signals are preserved in an ac-coupled system, if the tone of the source known to be constant is maintained constant, the tones of all other objects are quantitative, provided the amplification gain is constant and the sensor is calibrated. The circuitry for dc restoration is well known and is used in television systems. The circuitry requires electronically sampling the output level of the known and constant signal and adding or subtracting a dc voltage to make the signal constant.

While dc restoration, or clamping, makes the tone of an object independent of its environment, the tone is quantitative if, and only if, the system response (volts out/watts in) is constant and known. If the response is constant, which implies fixed detector response and amplifier gains, then the response can be computed from the observation of two or more sources of known radiance (watts/cm^2ster). If the response is linear, two sources will suffice. Because the detector response is temperature dependent, frequent calibration is desirable, which leads to a scanner that carries its own reference and calibration sources. Even with these calibrations, one can only be quantitative with respect to the apparent radiance, the true surface radiance as modified by atmospheric absorption and emission. By observing sources on the ground of known radiance, the atmospheric effects can be determined. Surface temperature is then related to the radiance through emissivity and the Planck radiation law for blackbodies. The NASA MSC is concerned about the lack of dc restoration in its scanners, and plans are underway to

correct this deficiency in scanners aboard their aircraft. The dual-channel scanner under procurement will have calibration sources, as well as dc restoration.

Another source of tonal distortions in IR imagery is from the limited dynamic range of the display and/or recording medium. The output signal from the detector is generally linear with respect to the radiation input over the levels encountered in the thermal mapping of natural features. When one is interested in observing thermal details of a particular feature, the gain setting for photographic recording is usually adjusted to give optimum contrast of the feature being investigated. As an example, figure 51-11 is a stripmap which NASA generated over test site 162. The mission was to map the thermal patterns in Lake Michigan. With the gain setting properly adjusted to observe this feature the thermal features on the land were "washed out." Thus, it is highly important that the investigator inform the operator as to the purpose of his data so that the proper gain setting be made. Had the operator adjusted the gain in figure 51-10 to avoid saturation of the land feature, the fine thermal detail in the water would be lost. Solutions exist for overcoming the limited dynamic range of the recording medium such as parallel recording of the data at different gain levels and automatic gain control. The University of Michigan is currently studying this problem with particular emphasis on space applications for which telemetry and recording bandwidths are a premium. Preferred methods for recording the full dynamic range of the scanner signal will be recommended.

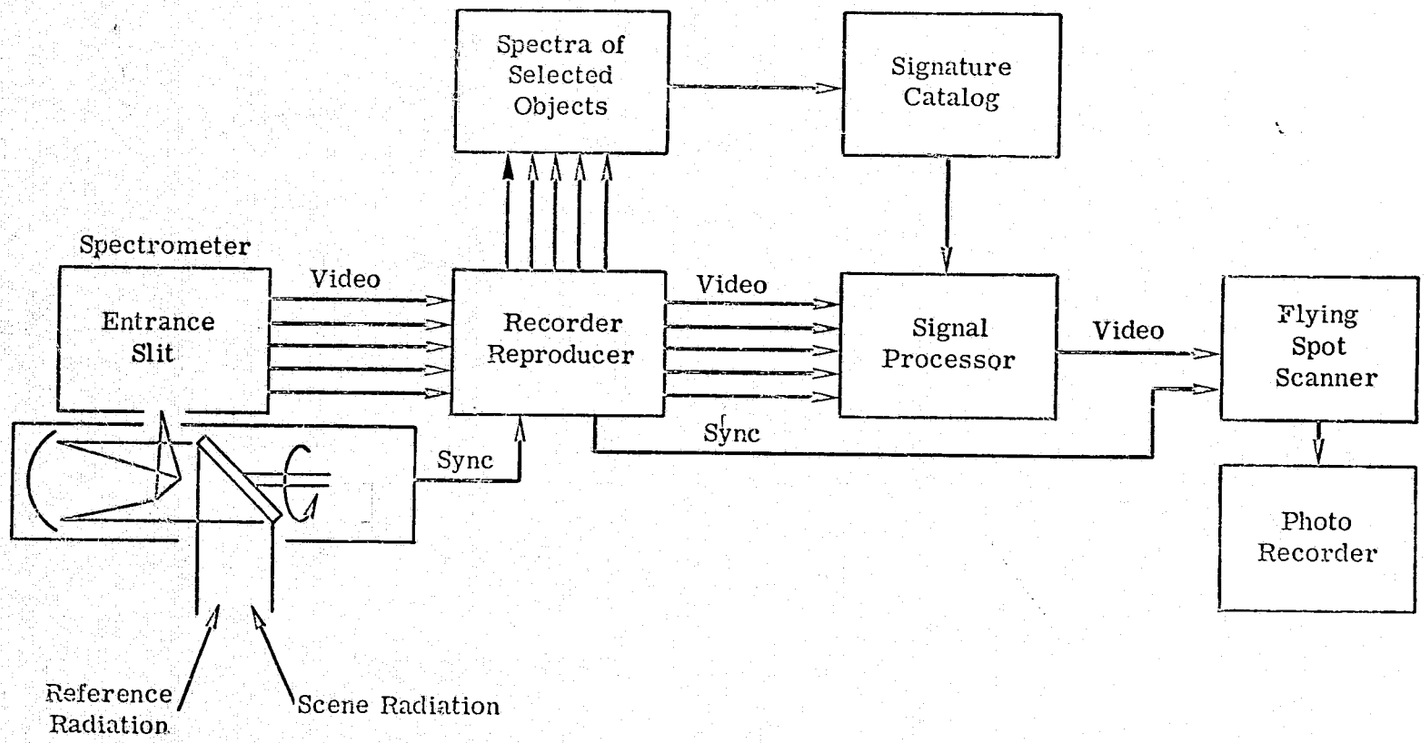

Figure 51-1.- Schematic of multispectral scanner and data processor.

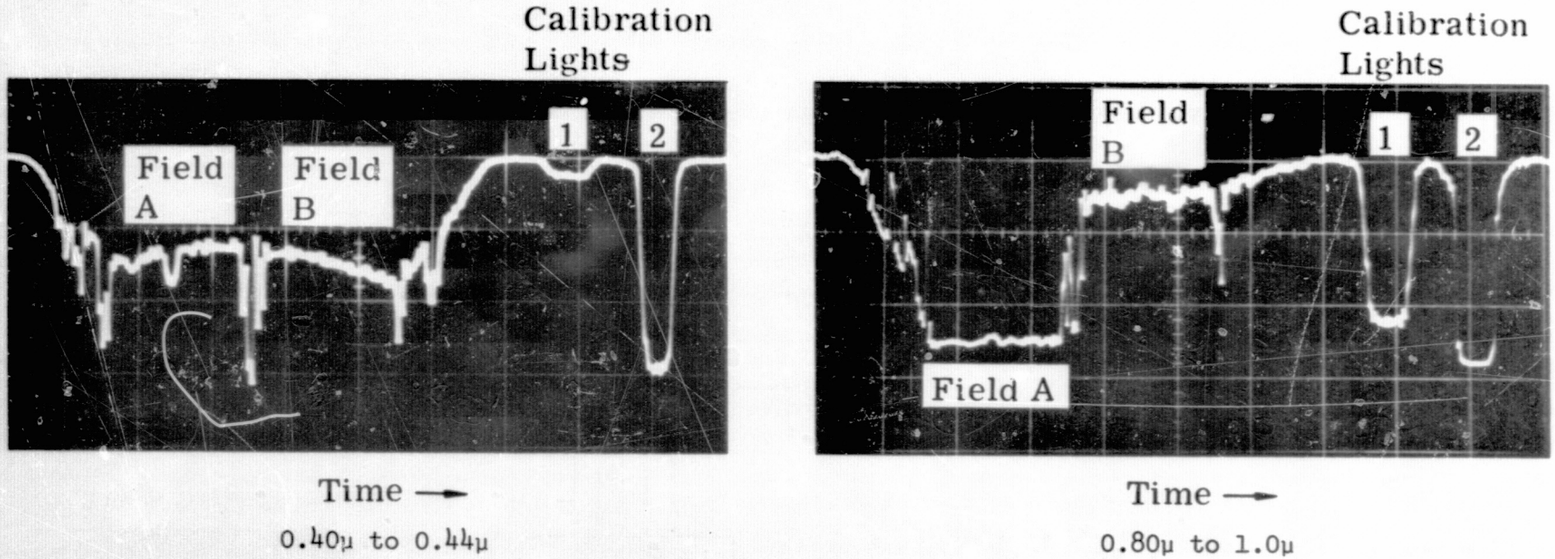

Figure 51-2.- Typical spectrometer video data (U). California Rice Fields 5/26/66 at 1400 hours.

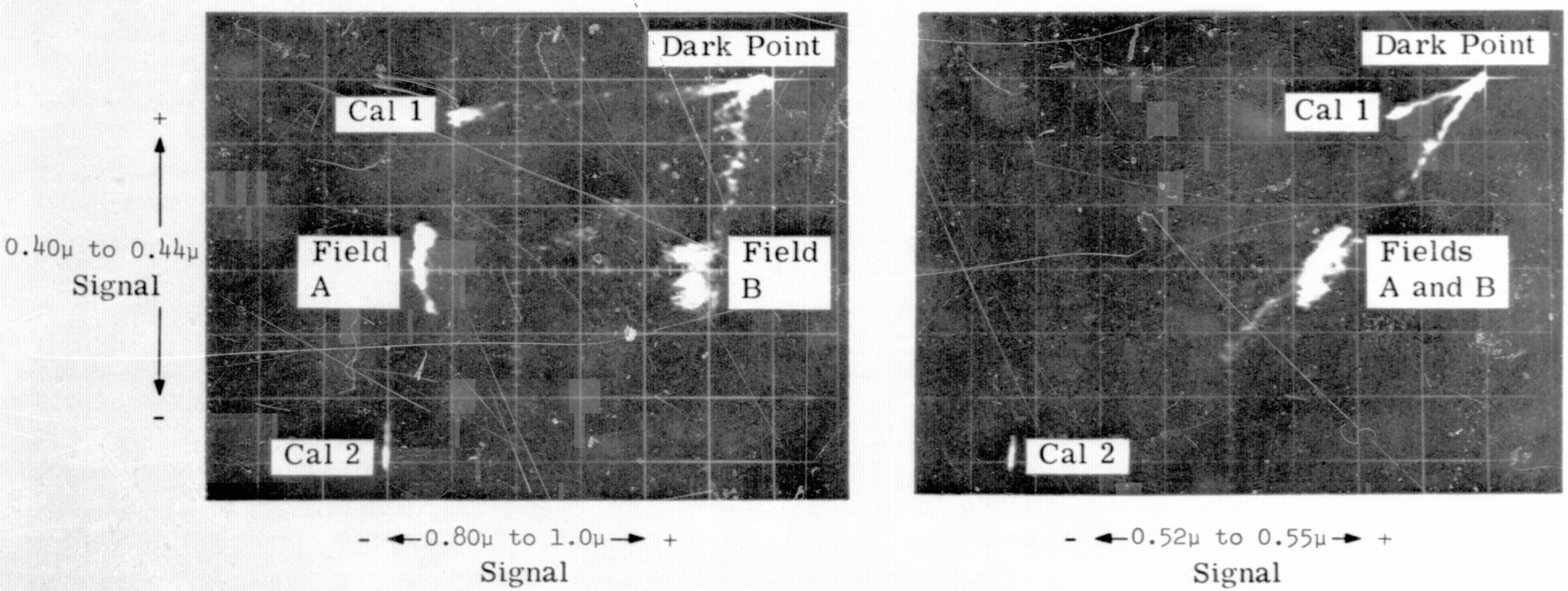

Figure 51-3.- Typical x-y scope pictures (U). California Rice Fields 5/26/66 at 1400 hours.

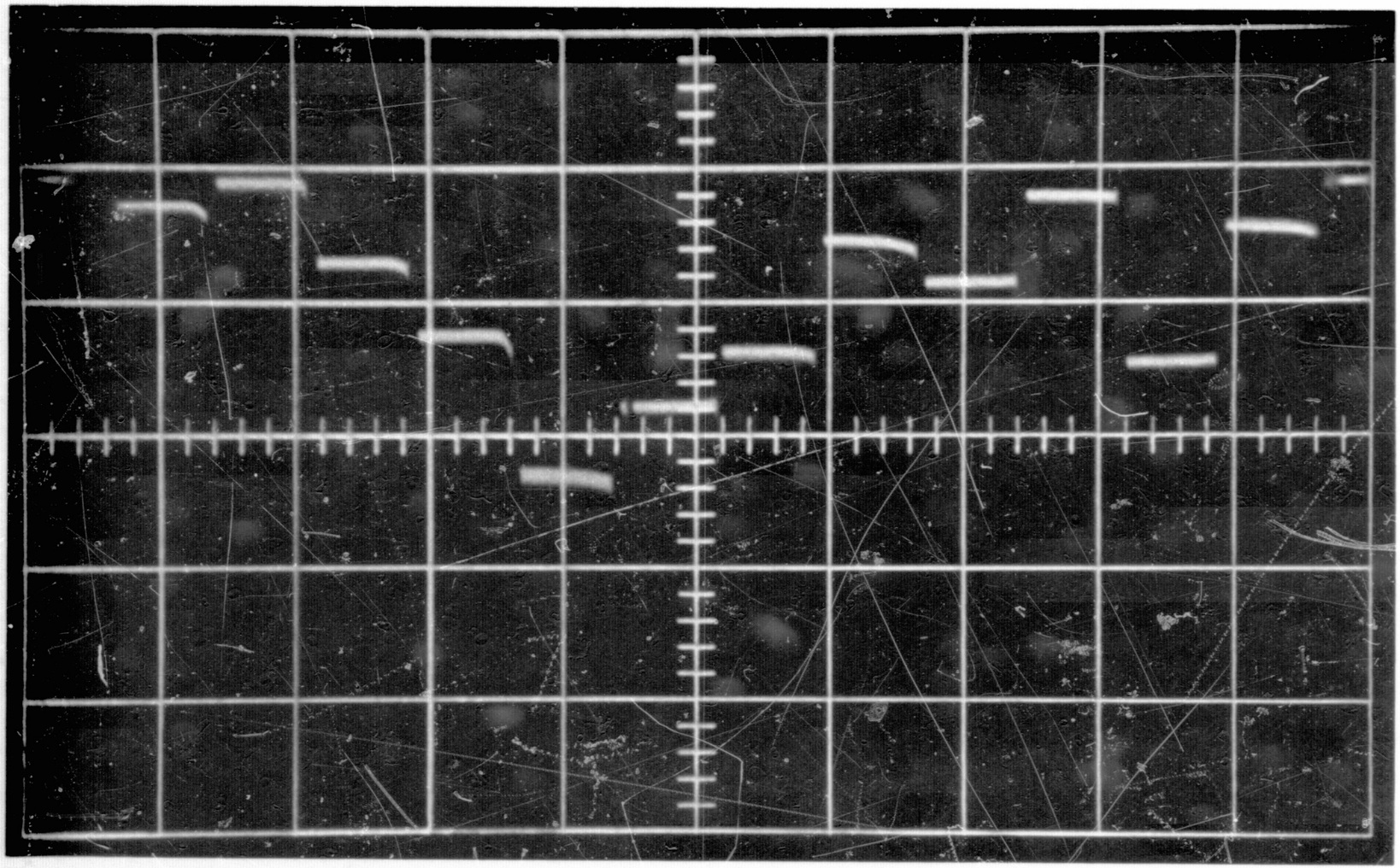

Figure 51-4.- Raw spectrum of green paint.

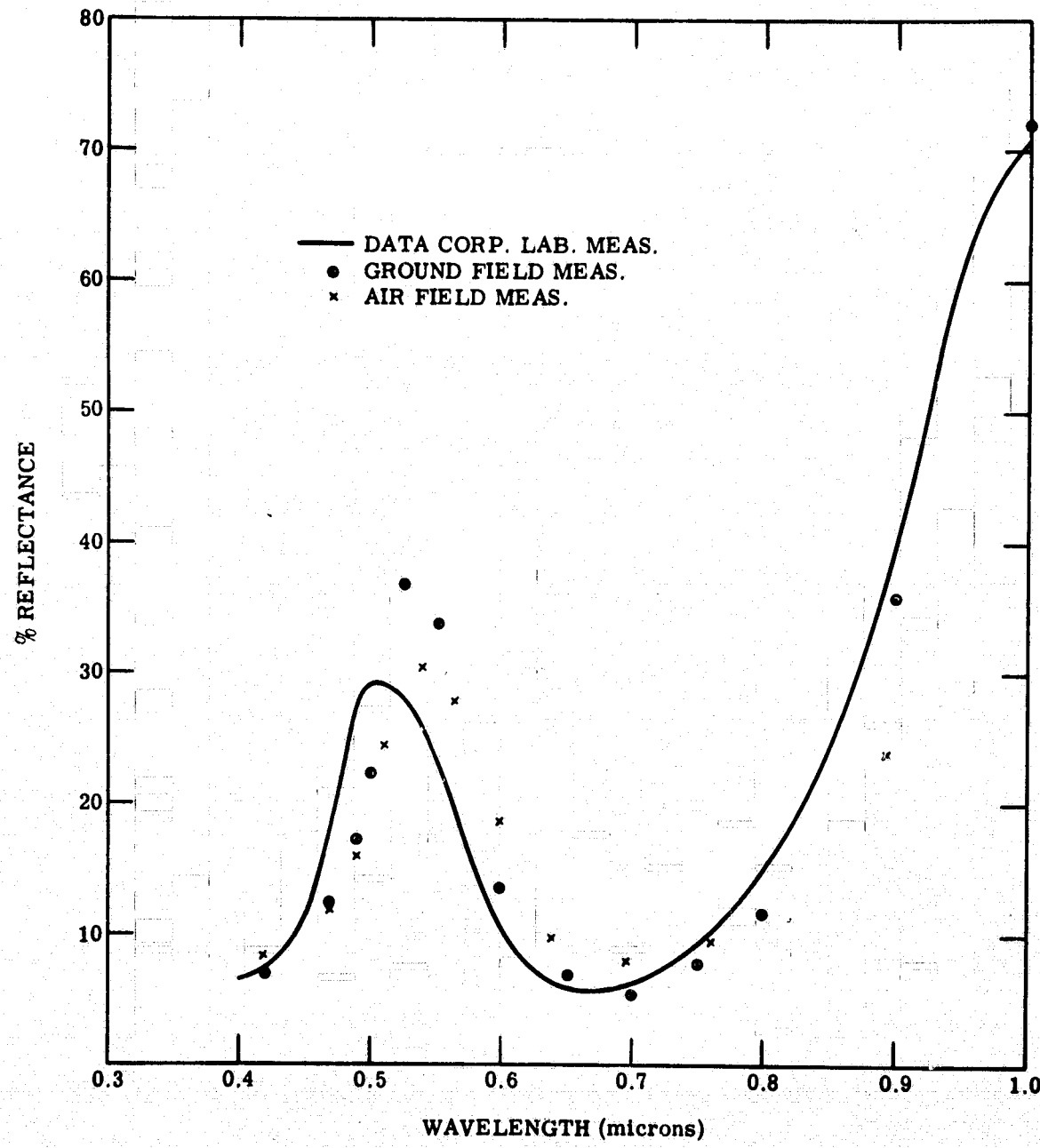

Figure 51-5.- Light-green standard reflectance panel.

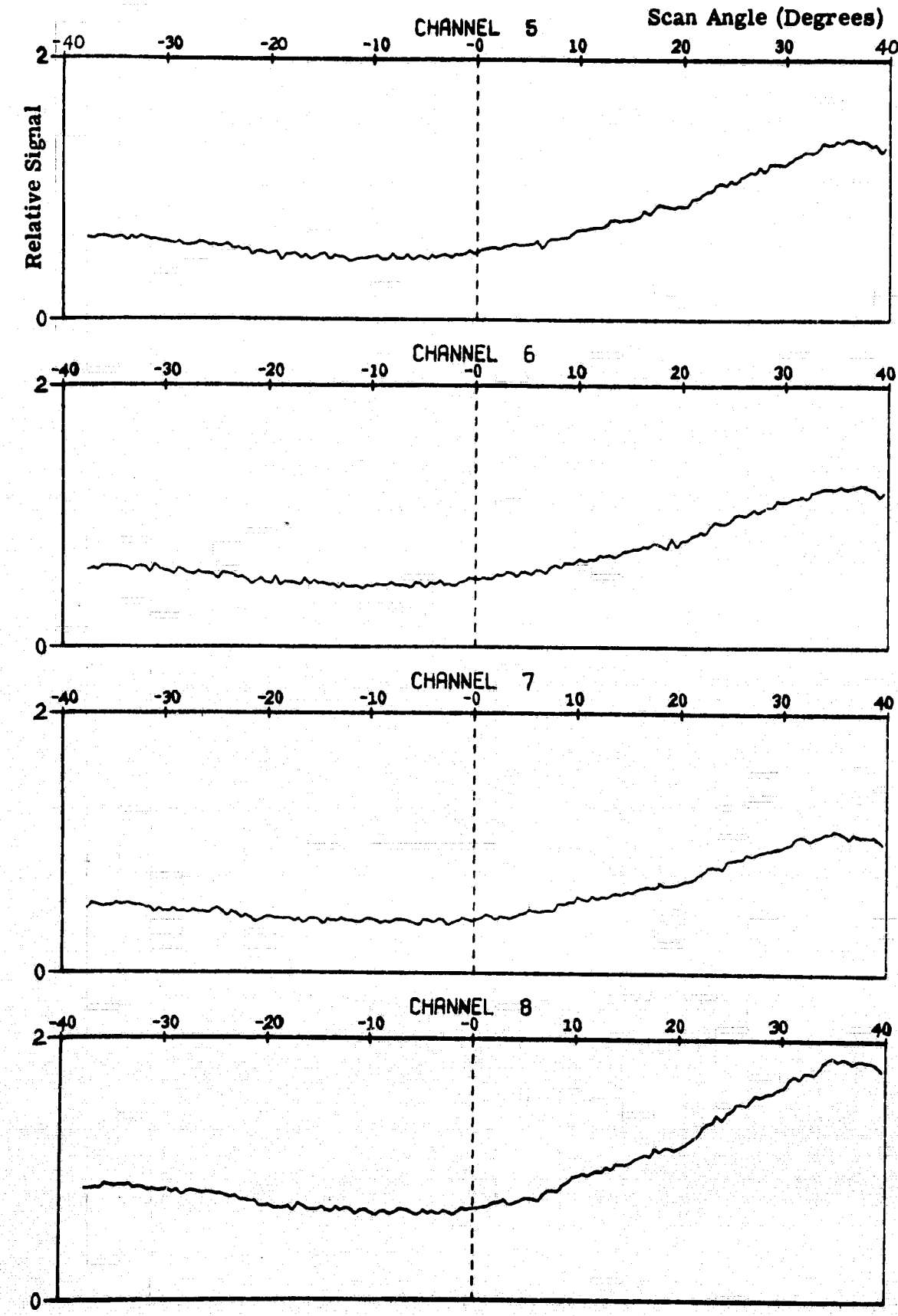

Figure 51-6.- Illustrative plots of relative signal versus scan angle for wheat field; data acquired June 30, 1966, 09:06 hours.

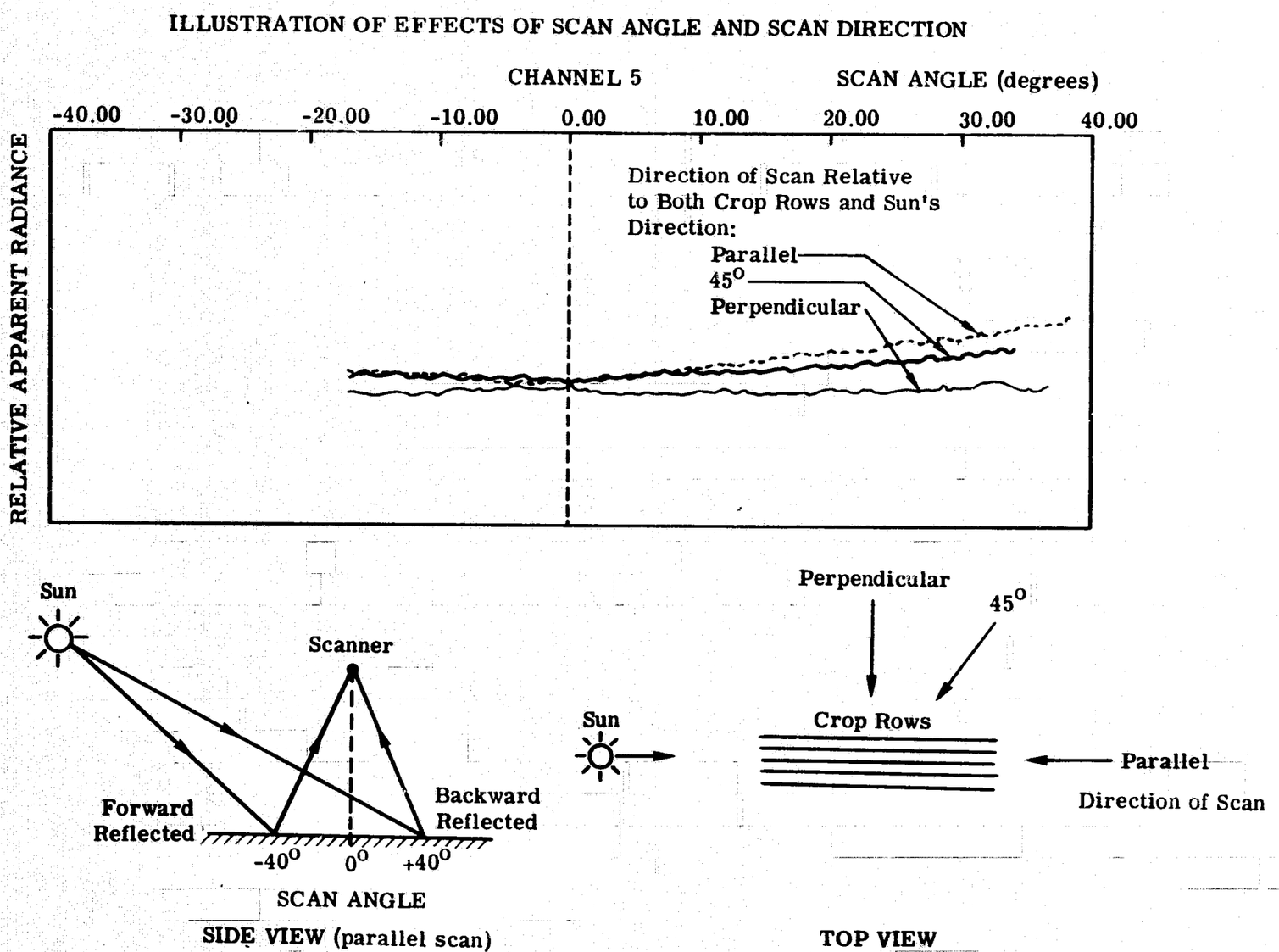

Figure 51-7.- Signal variation as a function of scan angle and direction.

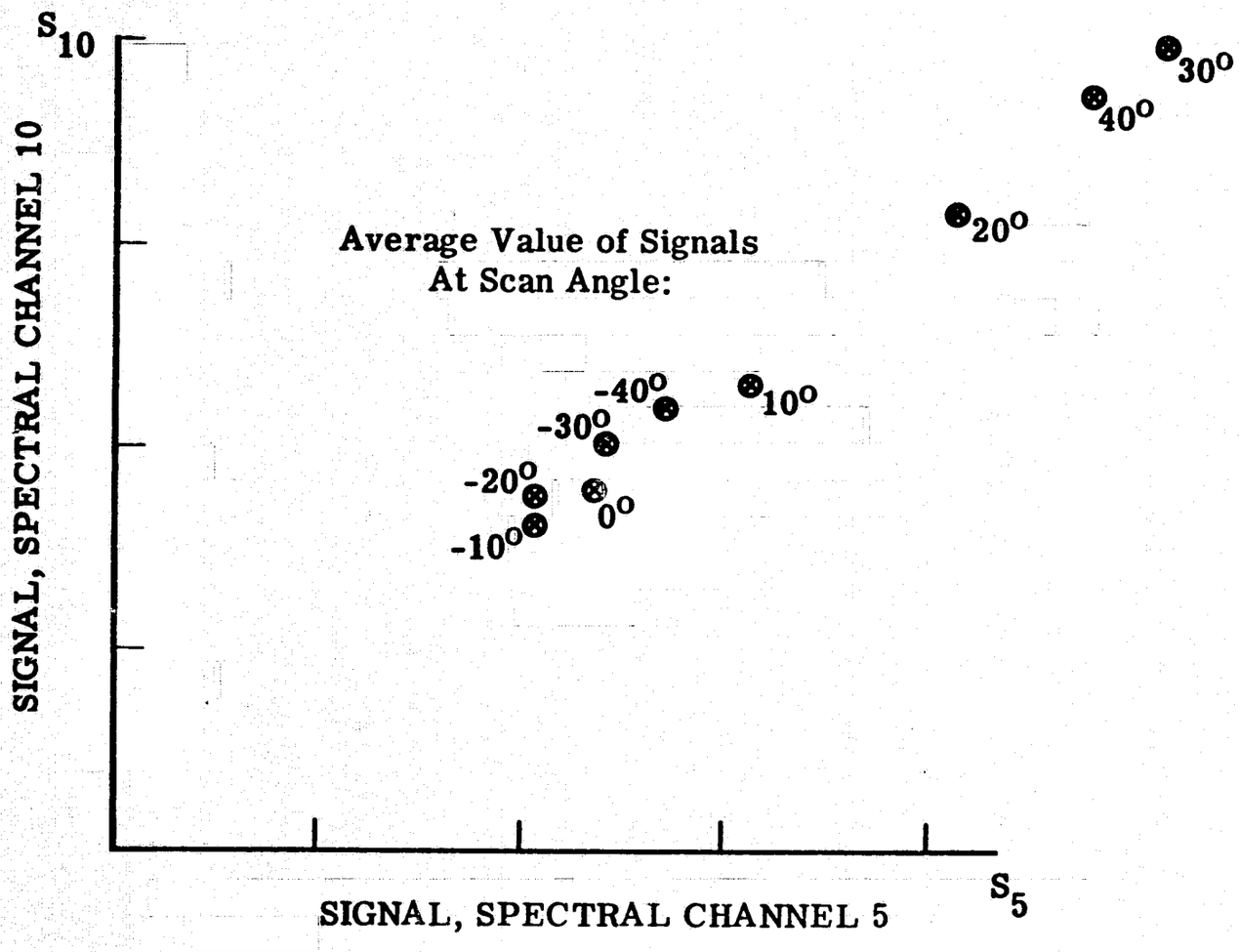

Figure 51-8.- Distribution of wheat-field signals data taken June 30, 1966, 09:06 hours.

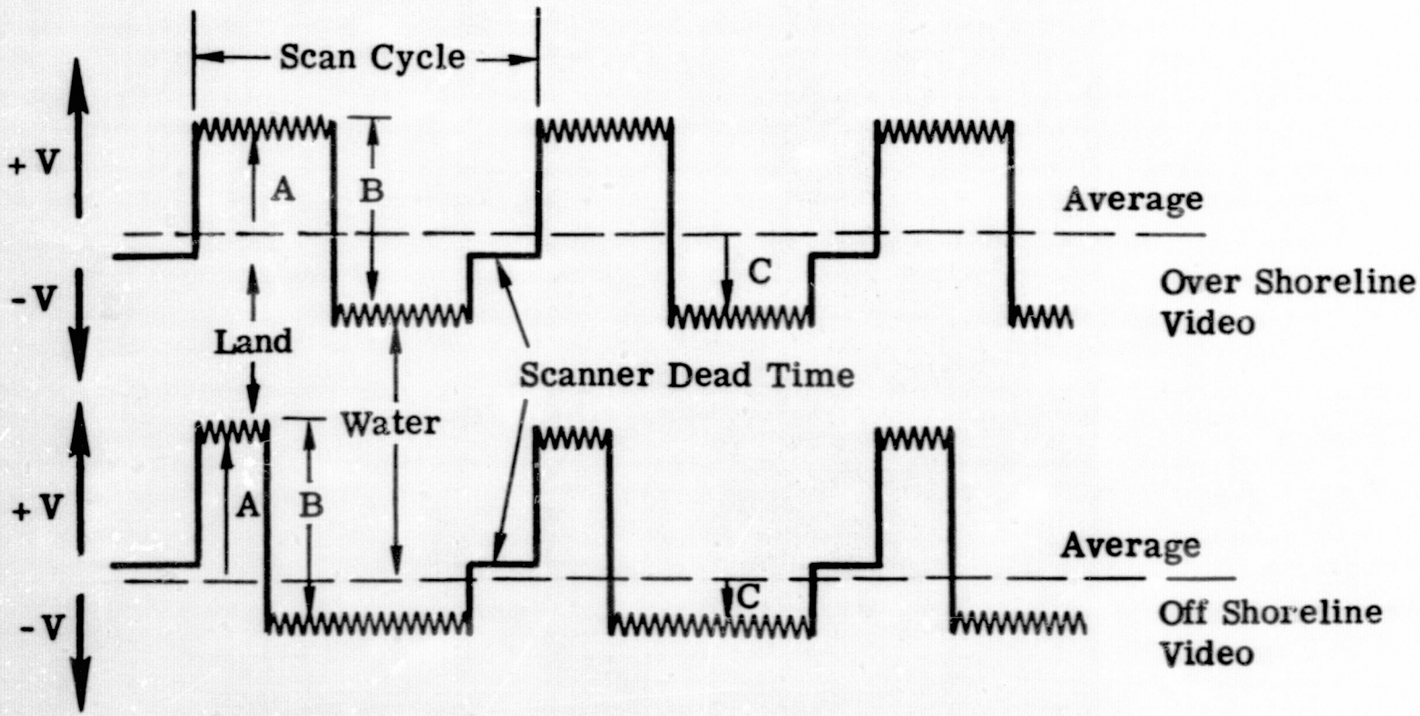

Figure 51-9.- Typical signal relationships of dwell time on land to water changes.

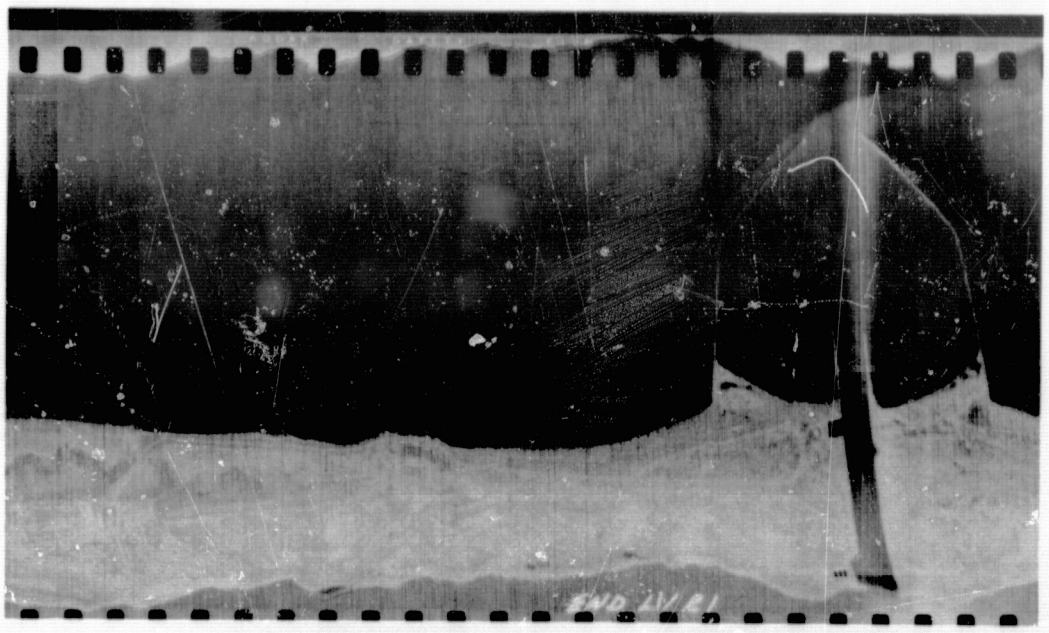

Figure 51-10.- Tonal variations arising from ac coupling.

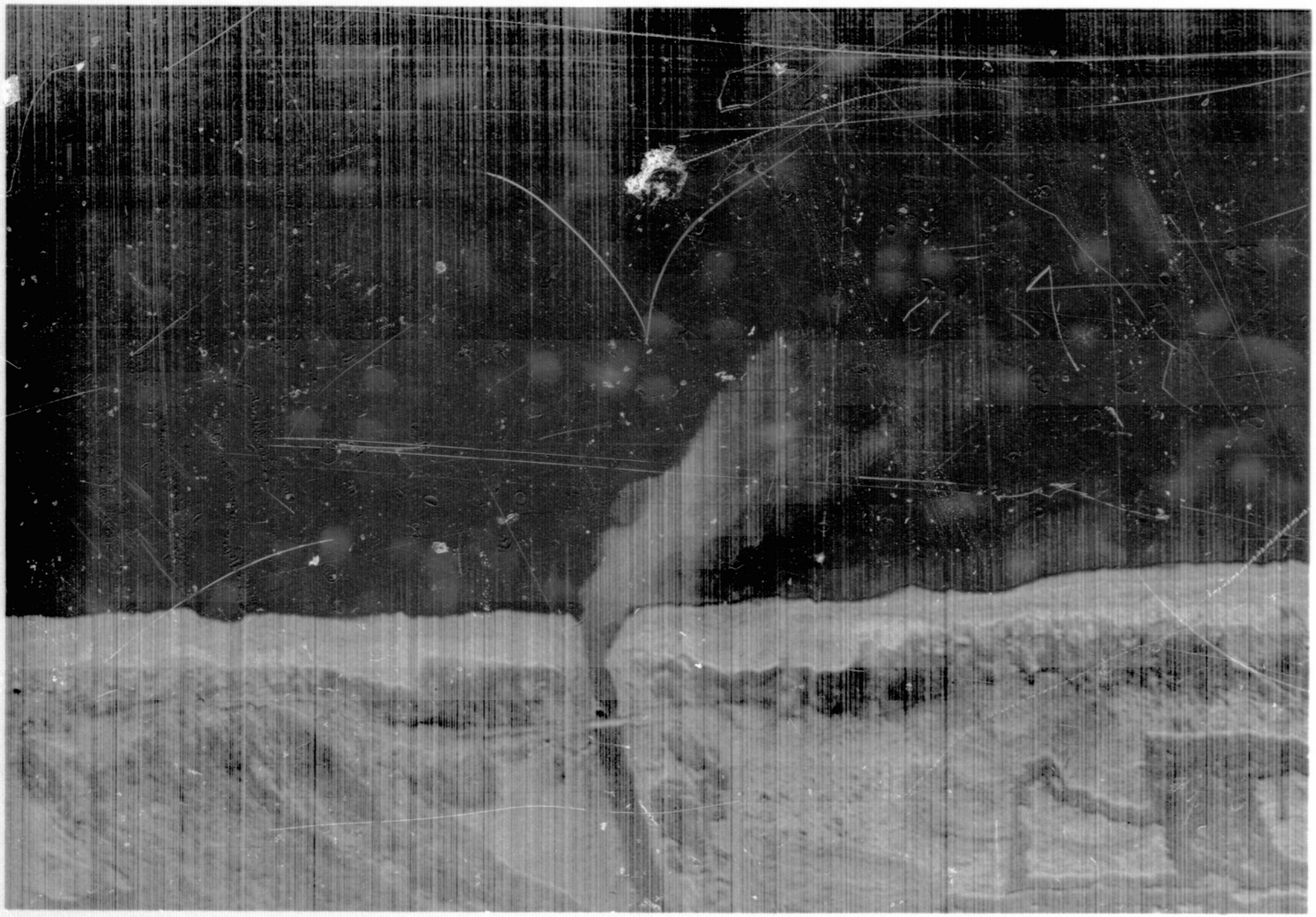

Figure 51-11.- Thermal stripmap with gain set to observe thermal patterns in water.

ERRATA

EARTH RESOURCES AIRCRAFT PROGRAM

STATUS REVIEW

VOLUME I

GEOLOGY, GEOGRAPHY, AND SENSOR STUDIES

The errata in this issue represent the results of each author's review of his edited manuscript. Only those editorial changes that affected the technical accuracy of the report are included. Changes submitted to update the original manuscript could not be accepted.

Errata received after September 1, 1969, will be distributed in a separate issue.